Complexity

Modern Applications of Bioconvection with Fractional Derivatives

Lead Guest Editor: Muhammad Imran Asjad
Guest Editors: Dumitru Vieru, Ali Akgül, Nehad Ali Shah, and Esra Karatas Akgül

Modern Applications of Bioconvection with Fractional Derivatives

Complexity

Modern Applications of Bioconvection with Fractional Derivatives

Lead Guest Editor: Muhammad Imran Asjad
Guest Editors: Dumitru Vieru, Ali Akgül, Nehad Ali Shah, and Esra Karatas Akgül

Contents

Contents

Hindawi
Complexity
Volume 2021, Article ID 5058751, 16 pages
https://doi.org/10.1155/2021/5058751

Research Article

Computational Study on Three-Dimensional Convective Casson Nanofluid Flow past a Stretching Sheet with Arrhenius Activation Energy and Exponential Heat Source Effects

P. Ragupathi,[1] **S. Saranya**,[2] **H.V.R. Mittal**,[3] **and Qasem M. Al-Mdallal**[2]

[1]*Department of Mathematics, Sri Ramakrishna Mission Vidyalaya College of Arts and Science, Coimbatore-641 020, India*
[2]*Department of Mathematical Sciences, UAE University, P.O. Box 15551, Al-Ain, UAE*
[3]*Computer, Electrical and Mathematical Sciences and Engineering Division, King Abdullah University of Science and Technology, (KAUST), Thuwal 23955-6900, Saudi Arabia*

Correspondence should be addressed to Qasem M. Al-Mdallal; q.almdallal@uaeu.ac.ae

Received 13 June 2021; Accepted 21 August 2021; Published 30 November 2021

Academic Editor: Ali Akgül

The effective applications of Casson fluid in drilling processes, biological treatments, food processing, and bio-engineering activities have caught the interest of a wide range of researchers. The suitable knowledge of heat transfer via non-Newtonian fluid is essential for the achievement of best quality products in industry. Thus, the three-dimensional Casson nanofluid flow over a stretching sheet with Arrhenius activation energy and exponential heat source effects is investigated in this paper using a computational process based on iterative power series (IPS) method. To provide useful insights into the physical and dynamic examinations of this topic, convective heat and convective mass boundary conditions are used. The developed model of nonlinear partial differential equations (PDEs) has been transformed into ordinary differential equations (ODEs) using similarity transformations. The numerical solution of the transformed ODEs is obtained by employing the IPS technique combined with shooting iteration approach. The results of this study are validated with the previous studies, and excellent agreements have been obtained. The behavior of various capable physical parameters is analyzed. It is observed that the thermal and concentration fields show an enhancement with respect to the exponential heat source parameter and thermal and concentration Biot numbers. Further, the Arrhenius activation energy parameter has shown a significant effect on the concentration field.

1. Introduction

A better understanding of engineering and industrial technology difficulties requires taking into account the boundary layer phenomenon of non-Newtonian liquids with heat transport. Non-Newtonian physiological liquids are used in various engineering processes such as manufacturing of fiberglass, paper, crystals and plastic sheets, food production, petroleum drilling, and transportation of slurries. Non-Newtonian fluids have a tendency to modify their viscosity or flow behavior under stress. Under the influence of an unexpected stress, certain non-Newtonian fluids such as Casson fluids, micropolar fluids, Carreau fluids, power law fluids, Prandtl fluids and Eyring–Powell fluids may behave similar to a solid due to an increase in their viscosity. However, some situations might result in a reverse action where the fluid viscosity can decrease and fluids become thinner under the application of an unexpected stress. On the removal of these unexpected stresses, these liquids revert to their original flow behavior. Casson liquids have interesting properties and perform a significant part in non-Newtonian fluid experimentation, and in past few years they have gained the attention among researchers. The Casson fluid model was developed by Casson and Mill [1] for the prevision of pigment–oil suspension stream conduction. Shafiq et al. [2] analyzed the Darcy–Forchheimer Casson water/glycerin rotating nanofluid flow with uniform magnetic field. Saeed et al. [3] considered three-dimensional (3D) nano-Casson slender film stream created on a slanting rotating plate. Reddy et al. [4] analyzed the Buongiorno

model with respect to the rotating flow of Casson liquids on an extended surface with thermophoresis and Brownian motion. The Casson nanofluid 3D stream over the permeable layers of a slender sheet in a graphene nanoparticulate suspension was investigated by Durgaprasad et al. [5]. Later, Durgaprasad et al. [6] studied the 3D slip stream of a chemically reactive Casson liquid flowing over a thin penetration layer with nonuniform heat source or sink. Raza [7] contemplated the impacts of radiation and slip on the magnetohydrodynamic stagnation point stream of Casson liquids past a convective stretching sheet. Thumma et al. [8] considered the impacts of the viscous dissipation and heat generation of nanofluid streams past an impermeable extending sheet. Murthy et al. [9] investigated the thermophoresis and Brownian movement effects in case of an exponentially extended surface in a 3D magnetohydrodynamic slip stream of the Casson nanofluid.

Investigations of non-Newtonian fluid flows created by a stretching sheet for MHD flow and heat transfer find many applications in engineering and industry such as melt spinning, extrusion, glass fiber processing, heat rolling, plastic wire drawing, rubber sheet manufacturing, and cooling of a solid steel plate in a pool. Sometimes sheets are continually stretched during manufacture to produce the necessary thickness. It demonstrates that the final outcome is determined by the sheet's stretching and cooling rate. For example, when molten polymers are extruded through a slit die to make plastic sheets, the sheet is stretched. In such operations, the pace of cooling determines the final product's qualities. When such a sheet is drawn in an electrically conducting Casson fluid under the influence of a magnetic field, the pace of cooling may be regulated, resulting in the desired final product. Crane [10] examined a Newtonian fluid boundary layer flow caused by the stretching elastic flat plate. He focused on the case of linear stretching elastic flat plate for discussing the heat conduction properties. Wang [11] analyzed a 3D flow past a stretching sheet. Freidoonimehr and Rahimi [12] studied the Brownian motion effect on the heat transfer of a 3D nanofluid flow past a stretched sheet with velocity slip. Hamid et al. [13] investigated the effects of linear thermal radiation and presented a dual solution for both steady and unsteady flows of the Casson fluid over the stretching sheet. Aziz and Afify [14] analyzed the Casson fluid flow and showed that the production of entropy increased with increasing magnetization. In addition, a reverse behavior was observed with the Hall effect. Shankar et al. [15] demonstrated the 3D flow in a Casson fluid considering the Cattaneo–Christov heat flux and the Joule effect at the boundary of the stretching sheet. Mahanta et al. [16] discussed the Brownian and thermophoresis flow effects on the Casson nanofluid over a stretching sheet in the presence of magnetic field.

Activation energy is defined as the minimum needed energy that reactants must receive to envision a chemical reaction. The activation energy has various focal points with respect to the design of chemical production, manufacturing of food items, geothermal repository, oil emulsion formation, etc. Activation energy investigations of a nano Casson fluid flow were carried out by Gireesha et al. [17] with an exponential spatial source of thermal energy and a binary chemical reaction. Hayat et al. [18] detailed the Arrhenius activation energy on the nanofluid 3D Darcy–Forchheimer stream based on the impacts of the binary chemical reaction in a rotating frame. Umar et al. [19] presented a numerical treatment of the 3D Eyring–Powell liquid stream over an expanding sheet with velocity slip and activation energy. Hayat et al. [20] introduced the properties of activation energy in the Carreau liquid stream with cross-dissemination and exponential heat source effects. Rashid et al. [21] introduced a 3D rotating Darcy–Forchheimer stream with activation energy. In the MHD third-grade nanofluid system, Hayat et al. [22] developed a computational model for studying the impact of the Arrhenius activation energy through a nonlinear extending surface under convective temperature and mass conditions. Rashid et al. [23] proposed a similar work with activation energy on an Oldroyd-B nanofluid. Rashid et al. [24] also used Arrhenius energy for rotating the Maxwell nanomaterial. The activation energy in case of a squeezed liquid with a binary chemical reaction was examined by Ahmad et al. [25].

Researchers recently expressed their enthusiasm in the progress of methodologies, including heat generation/absorption due to its immense usage in the fields of information science and mechanical engineering (Nadeem et al. [26], Shehzad et al. [27], Mishra et al. [28], Rehman et al. [29], and Ragupathi et al. [30]). Except for the traditional component of the heat source, an irregular part of the heat source (thermal and exponential space-based source) is optimal for systems that require high-temperature distribution mechanisms. Mahanthesh et al. [31] examined the changes associated with radiative dusty nanofluid flow when subjected to the heat sources (exponential space-based) and Marangoni convection. Kumar et al. [32] considered exponential heat source effects on a fluid passing over a melting surface. Similarly, Sandeep et al. [33], Krishna et al. [34], Zia et al. [35], etc. contributed to establish the functioning of the heat source which is exponential space-based.

The nonlinear boundary value problems (BVPs) govern various phenomena in science and engineering. Accordingly, BVPs have therefore drawn great interest from researchers and technologists in obtaining and evaluating their solutions. BVPs are not trivial, and it is very difficult to find empirical solutions to nonlinear BVPs. The BVPs of real-life problems (fluid flow problems) are typically nonlinear and involve numerical and analytical algorithms with great accuracy in their solutions. Several numerical methods have been developed for solving such problems. The power series approach is perhaps the simplest and most effective approach compared with other nonlinear differential equation approaches (Liao and Tan [36]). This approach is frequently used on many problems including chaotic processes as almost a suitable mathematical approach. This approach has led to the development of a number of numerical methods and algorithms. An iterative method called the Iterative Power Series (IPS), based on recursive power series expansions, provides such a highly accurate numerical scheme (Burden and Faires [37]). The IPS procedure aims to ensure high precision by showing that the radius convergence of the

solution can be altered to any major value by accuracy. In theory, this value reaches infinity, which produces exact solutions. The IPS solutions to $\operatorname{sech}(x)$ and nonlinear differential equations were presented by Al-Khawaja and Al-Mdallal [38]. The numerical IPS method was applied to study the fluid stream past a shrinking infinite permeable long cylinder by Al-Sakkaf et al. [39]. Their observations reported that the iterative numerical scheme obtained via this process is more useful than conventional numerical systems.

Based on the detailed literature survey, no study has investigated the 3D convective Casson nanofluid flow with Arrhenius activation energy and exponential heat source effects past a stretching sheet. This analysis therefore incorporates some new aspects, which are described hereinafter.

(i) Convective heat and mass boundary conditions are added to explore and enhance the dynamical investigations.

(ii) A notable shooting procedure and IPS method are employed to examine the influence of numerous parameters (magnetic, exponential heat source, and Arrhenius activation energy) on velocity, energy, and concentration profiles.

(iii) Present numerical results are compared with those obtained by Umar et al. [19], Freidoonimehr and Rahimi [12], and Wang [11]. They observed the movement of 3D fluid flow over a stretching layer, which was observed herein to exhibit perfect coordination.

(iv) The appearance of capable physical quantities with respect to standard profiles is visualized and analyzed.

The current study contributes to the literature by looking into the factors that influence the flow, heat, and mass transfer rate. Hence, the following research questions are central to the empirical part:

(i) Does the magnetic field and the sheets stretching rate increase the coefficient of skin friction?

(ii) Does the exponential heat source parameter influence the heat and mass transfer rate?

(iii) Does the thermal and concentration Biot numbers support the thermal and concentration profiles?

(iv) Does the Arrhenius activation energy supports thermal heat and mass transfer rate?

The remaining of the manuscript is organized in the following pattern. Section 2 gives the generalized formulation Casson model. Section 3 holds the description on Arrhenius activation equation and exponential heat source. Section 4 deals with the problem formulation, corresponding governing equations and boundary conditions. In Section 5, the algorithm for IPS procedure and properties are explained. Section 6 explains the numerical algorithm of the IPS procedure followed by the validation of our numerical scheme in Section 7. Results and discussions are presented in Section 8, and finally the major conclusions are drawn in Section 9.

2. Generalized Casson Fluid Model

The rheological state for the Casson model is represented as [33]

$$\tau^* = \tau_0 + \mu\gamma^*, \tag{1}$$

or

$$\tau_{ij} = \begin{cases} 2\left(\dfrac{\sqrt{2\prod}\,\mu_B + p_y}{\sqrt{2\prod}}\right)e_{ij}, & \prod_c < \prod, \\ 2\left(\dfrac{\sqrt{2\prod}_c\mu_B + p_y}{\sqrt{2\prod_c}}\right)e_{ij}, & \prod_c > \prod, \end{cases} \tag{2}$$

where $\Pi = e_{ij}e_{ij}$ is the product of the component of the deformation rate, e_{ij} is the $(i, j)^{\text{th}}$ component of deformation rate, Π_c is the critical value of this product, μ_B is the plastic dynamic viscosity of the fluid, and $p_y = \mu_B\sqrt{2\Pi}/\beta$ is the yield stress of the fluid. To retain a steady strain rate, there are certain fluids that involve a progressive rise in shear stress and are known as rheopectic fluid. In case of Casson fluid where $\Pi > \Pi_c$:

$$\mu = \mu_B + \frac{p_y}{\sqrt{2\Pi}}, \tag{3}$$

By substituting p_y in equation (3), we can observe the dependency of kinematic viscosity ν of the Casson fluid on plastic dynamic viscosity μ_B, density ρ, and Casson parameter β as follows:

$$\nu = \frac{\mu_B}{\rho}\left(1 + \frac{1}{\beta}\right). \tag{4}$$

3. Activation Energy and Exponential Heat Source

3.1. The Arrhenius Equation. In 1889, Swedish scientist Svante Arrhenius discovered the presence of activation energy. To describe the relationship between temperature and reaction rate, Arrhenius devised his eponymous equation. The Arrhenius equation is essential for determining chemical reaction rates and, more critically, the amount of energy required to initiate them.

$$K = Ae^{-E_a/\mathrm{RT}}, \tag{5}$$

where K is the reaction rate coefficient (the rate of reaction), A is the frequency factor (how often molecules collide), R is the universal gas constant, T represents the absolute temperature, and E_a is the activation energy.

3.2. Exponential Heat Source. Chemical or nuclear processes produce heat energy within a body as an interior energy source/sink. Its importance can be seen in combustion research, nuclear reactors, heat exchangers, plastic, paper, and steel production, thermal insulation, and fusion reactors, etc. The effects of an internal heat source/sink can be studied using two models. The first is a uniform temperature-dependent internal heat source/sink process $(Q_0(T - T_\infty))$, and the second is a nonuniform space and a thermal based heat source in which two dimensionless parameters appear in the energy equation, one for thermal based heat source analysis and the other for space-based heat source analysis. These two models may not be able to achieve more heat transmission in the fluid boundary layer, according to science. An exponential heat source effect $(Q_0(T - T_\infty) e^{-m\sqrt{a/\nu}z})$ has been developed as a new model for intensive heating processes in light of these findings.

4. Modeling and Description

We consider the steady, laminar, and incompressible 3D flow of the Casson fluid past over a stretching sheet. The sheet is positioned at $z = 0$, and the flow is assumed to occur in the domain $z > 0$. Let the sheet's stretching velocity in x-direction be $u = U_w(x) = ax$ and the y-direction stretching velocity be $v = V_w(y) = by$. Convective heat (T_f) and mass (C_f) conditions are imposed at the bottom of the sheet surface with coefficients h_f and h_s. The schematic diagram of the physical domain of the problem is presented in Figure 1. The magnetic field is uniformly distributed with an impact force B_0 in a direction normal to the fluid flow. The induced magnetic field is neglected because of the small magnetic Reynolds number. The impacts of viscous dissipation are also neglected because the magnetic field is not considerably high. Attention is devoted to the novel Arrhenius activation energy and exponential heat source effects, which are comprehensively examined.

Based on all the above-stated assumptions, the following sequence of equations governing the flow is obtained.

$$\frac{\partial u}{\partial x} + \frac{\partial v}{\partial y} + \frac{\partial w}{\partial z} = 0, \tag{6}$$

$$u\frac{\partial u}{\partial x} + v\frac{\partial u}{\partial y} + w\frac{\partial u}{\partial z} = \nu\left(\beta^{-1} + 1\right)\frac{\partial^2 u}{\partial z^2} - \frac{\sigma B_0^2 u}{\rho}, \tag{7}$$

$$u\frac{\partial v}{\partial x} + v\frac{\partial v}{\partial y} + w\frac{\partial v}{\partial z} = \nu\left(\beta^{-1} + 1\right)\frac{\partial^2 v}{\partial z^2} - \frac{\sigma B_0^2 v}{\rho}, \tag{8}$$

$$u\frac{\partial T}{\partial x} + v\frac{\partial T}{\partial y} + w\frac{\partial T}{\partial z} = \alpha^*\frac{\partial^2 T}{\partial z^2} + \tau\left[D_B\frac{\partial C}{\partial T}\frac{\partial T}{\partial z} + \frac{D_T}{T_\infty}\left(\frac{\partial T}{\partial z}\right)^2\right] + \frac{Q_0(T - T_\infty)}{\rho C_p}e^{-m\sqrt{a/\nu}z}, \tag{9}$$

$$u\frac{\partial C}{\partial x} + v\frac{\partial C}{\partial y} + w\frac{\partial C}{\partial z} = D_B\left(\frac{\partial^2 C}{\partial z^2}\right) + \frac{D_T}{T_\infty}\left(\frac{\partial^2 T}{\partial z^2}\right) - K_s^2(C - C_\infty)\left(\frac{T}{T_\infty}\right)^r e^{(-E_a/k_1 T)}, \tag{10}$$

where u, v, and w are the x, y, and z components of velocity, ν is the kinematic viscosity of the nanofluid, β is the Casson parameter, ρ is the density of the nanofluid, T is the temperature of the fluid, Q_0 is the heat generation/absorption variable, and D_B and D_T represent the coefficient of Brownian and thermophoresis diffusions, K_s is the reaction rate, E_a is the activation energy, and k_1 is the Boltzmann constant, respectively.

The corresponding boundary conditions are as follows:

$$\left.\begin{aligned} &u = U_w(x), v = V_w(y), w = 0, \\ &\frac{\partial T}{\partial z} = -\frac{h_f}{k_f}\left(T_f - T\right), \frac{\partial C}{\partial z} = -\frac{h_s}{D_B}\left(C_f - C\right) \end{aligned}\right\} \text{at } z = 0, \tag{11}$$

$$\text{such that } u \longrightarrow 0, v \longrightarrow 0, w \longrightarrow 0, T \longrightarrow T_\infty, C \longrightarrow C_\infty \text{ as } z \longrightarrow \infty.$$

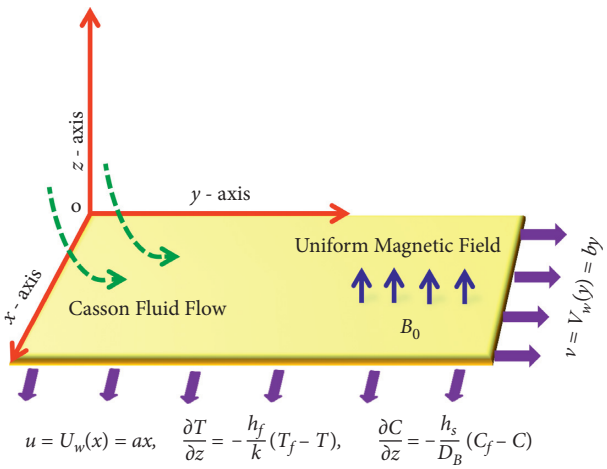

Figure 1: Schematic model of the physical coordinate system of the problem.

The variables for the similarity solution are given as follows:

$$\eta = z\sqrt{\frac{a}{\nu}}, u = axf'(\eta), v = ayg'(\eta), w = -\sqrt{a\nu}(f(\eta) + g(\eta)), \tag{12}$$
$$\theta(\eta) = \frac{T - T_\infty}{T_f - T_\infty}, \phi(\eta) = \frac{C - C_\infty}{C_f - C_\infty}.$$

By substituting the similarity variables from equation (12) into Equations (6)–(10), the transformed dimensionless equations can be written as

$$\left(\beta^{-1} + 1\right)f''' + (f + g)f'' - f'^2 - Mf' = 0, \tag{13}$$

$$\left(\beta^{-1} + 1\right)g''' + (f + g)g'' - g'^2 - Mg' = 0, \tag{14}$$

$$\theta'' + \Pr(f + g)\theta' + \Pr Nb\theta'\phi' + \Pr Nt\theta'^2 + \Pr Q\theta e^{-m\eta} = 0, \tag{15}$$

$$\phi'' + Le(f + g)\phi' + \frac{Nt}{Nb}\theta'' - Le\Lambda(1 + \Gamma\theta)^r e^{(-E/1+\Gamma\theta)} = 0. \tag{16}$$

After modifications, the boundary condition can be represented as follows:

$$\left.\begin{aligned} &f = 0, g = 0, f' = 1, g' = \alpha, \\ &\theta' = -Bi_1(1 - \theta(0)), \phi' = -Bi_2(1 - \phi(0)) \end{aligned}\right\} \text{at } \eta = 0,$$
$$f' \longrightarrow 0, g' \longrightarrow 0, \theta \longrightarrow 0, \phi \longrightarrow 0, \text{ as } \eta \longrightarrow \infty. \tag{17}$$

The nondimensional parameters used in equations (13)–(17) and their corresponding expressions are represented in Table 1.

Table 1: Nondimensional parameters and their expression.

Expression	Names
$\alpha = b/a$	Stretching ratio parameter
$M = \sigma B_0^2/\rho a$	Magnetic parameter
$Pr = \nu/\alpha$	Prandtl number
$Nb = \tau D_B/\nu(C_f - C_\infty)$	Brownian motion parameter
$Nt = \tau D_T/\nu T_\infty(T_f - T_\infty)$	Thermophoresis parameter
$Q = Q_0/a\rho C_p$	Exponential heat source parameter
$Le = \nu/D_B$	Lewis number
$\Lambda = K_s^2/c$	Reaction rate constant
$\Gamma = (T_f - T_\infty)/T_\infty$	Nondimensional fluid parameter
$E = Ea/k_1T_\infty$	Arrhenius activation energy parameter
$Bi_1 = h_f/k_f\sqrt{\nu/a}$	Thermal biot number
$Bi_2 = h_s/D_B\sqrt{\nu/a}$	Concentration biot number

The local skin friction coefficients, C_{fx} and C_{fy}, the local Nusselt number, Nus_x, and the local Sherwood number, Sh_x, are given as

$$C_{fx} = \frac{\tau_{wx}}{\rho U_w^2},$$
$$C_{fy} = \frac{\tau_{wy}}{\rho V_w^2},$$
$$\mathrm{Nus}_x = \frac{xq_w}{k\left(T_f - T_\infty\right)}, \tag{18}$$
$$\mathrm{Sh}_x = \frac{xq_m}{D_B\left(C_f - C_\infty\right)},$$

where $\tau_{wx} = \mu(\partial u/\partial z)_{z=0}$ and $\tau_{wy} = \mu(\partial v/\partial z)_{z=0}$ are the shear stress values along the surface of the sheet, $q_w = -k(\partial T/\partial z)_{z=0}$ is the heat flux, and $q_m = -D_B(\partial C/\partial z)_{z=0}$ is the mass flux.

The dimensionless form of equation (18) can be written as:

$$\mathrm{Re}_x^{1/2}C_{fx} = \left(\beta^{-1} + 1\right)f''(0),$$
$$\alpha^{3/2}\mathrm{Re}_y^{1/2}C_{fy} = \left(\beta^{-1} + 1\right)g''(0), \tag{19}$$
$$\mathrm{Re}_x^{-1/2}\mathrm{Nus}_x = -\theta'(0),$$
$$\mathrm{Re}_x^{-1/2}\mathrm{Sh}_x = -\phi'(0).$$

In the above expressions, both $\mathrm{Re}_x = U_w x/\nu$ and $\mathrm{Re}_y = V_w y/\nu$ are the local Reynolds numbers.

5. Generalized Algorithm for IPS Method

This section explains the algorithm to generate a convergent power series for a function in general and its properties.

Properties

(1) Around $\eta = 0$, the function $f(\eta)$ is expanded in a Taylor series. The infinite Taylor series is an exact representation of $f(\eta)$ for $\eta < R$, where R is the radius of convergence. This Taylor series diverges when $\eta \geq R$.

Step 1: As is customary, we expand the function $f(\eta)$ in a power series, say about $\eta = 0$.
Step 2: The coefficients, $f^{(n)}(\eta)$, are then re-expressed in terms of $f(\eta)$. These creates a recursion relationship in between higher-order coefficients, $f^{(n)}(0)$, and the lower-order coefficients, $f^{(0)}(0)$, and $f^{(1)}(0)$, allowing the power series to be represented in terms of simply these two coefficients.
Step 3: The series and its derivative are then computed at $\eta = h$, where $h(= \eta_\infty - \eta_0/N)$ is substantially less than the radius of convergence of the power series.
Step 4: At $\eta = h$, a new power series expansion is performed.
Step 5: Accordingly, the higher order coefficients, $f^{(0)}(h)$ and $f^{(1)}(h)$, are re-expressed in terms of the lower-order coefficients. $f^{(0)}(h)$ and $f^{(1)}(h)$ are given the value of the previous series and its derivative determined at $\eta = h$, respectively.
Step 6: Then, around $2h$, a new expansion is executed, using the lowest order coefficients from the preceding series, and so on. This iterative process is performed an infinite number of times. At $\eta = Nh$, the final series corresponds to a convergent series.

Algorithm 1: Steps of solutions using IPS method.

(2) Truncating the Taylor series at $k_{\max}$ introduces an error of order $h^{k_{\max}+1}$. This error will be magnified N times due the recursive substitutions. The total error is then estimated by

$$\text{Error} = \left(\frac{\eta}{N}\right)^{k_{\max}+1} N. \tag{20}$$

For more details, the reader is referred to the reference Al-Khawaja and Al-Mdallal [38]).

6. Numerical Method for the Solution

This section discusses briefly the numerical algorithm used to resolve the equation (13)–(16) with the boundary conditions given by equation (17). The IPS method given by Al-Khawaja and Al-Mdallal [38] and Al-Sakkaf et al. [39] will be followed. However, the shooting iteration approach for the equations (13)–(16) needs to be characterized. Hence, equations (13)–(16) are converted to IVPs of the following form:

$$f''' = \mathbf{F_f}(\eta, f, f', f'', g, g', g''), 0 \le \eta \le \infty, f(0) = 0, f'(0) = 1, f''(0) = \chi, \tag{21}$$

$$g''' = \mathbf{F_g}(\eta, f, f', f'', g, g', g''), 0 \le \eta \le \infty, g(0) = 0, g'(0) = \alpha, g''(0) = \zeta, \tag{22}$$

$$\theta'' = \mathbf{F}_\theta(\eta, f, g, \theta, \theta', \phi, \phi'), 0 \le \eta \le \infty, \theta'(0) = -Bi_1(1 - \theta(0)), \theta(0) = \lambda, \tag{23}$$

$$\phi'' = \mathbf{F}_\phi(\eta, f, g, \theta, \theta', \phi, \phi'), 0 \le \eta \le \infty, \phi'(0) = -Bi_2(1 - \phi(0)), \phi(0) = \xi. \tag{24}$$

The final values of χ, ζ, λ, and ξ are calculated by employing an iterative procedure, so that the solutions satisfy the remaining boundary conditions, $f'(\infty) = 0$, $g'(\infty) = 0, \theta(\infty) = 0$ and $\phi(\infty)) = 0$, such that

$$\lim_{i \longrightarrow \infty} f'(\eta_\infty, \chi_i) = 0, \tag{25}$$

$$\lim_{i \longrightarrow \infty} g'(\eta_\infty, \zeta_i) = 0, \tag{26}$$

$$\lim_{i \longrightarrow \infty} \theta(\eta_\infty, \lambda_i) = 0, \tag{27}$$

$$\lim_{i \longrightarrow \infty} \phi(\eta_\infty, \xi_i) = 0. \tag{28}$$

We start with appropriate initial guesses χ_0, ζ_0, λ_0, and ξ_0 to solve the IVPs (21)–(24) iteratively. The approximate solutions to f, g, θ, ϕ are generated after updating the values of χ, ζ, λ, ξ at each iteration step "i." Readers are referred to [37–39] for more details.

Denote $\mathfrak{B} = (\beta^{-1} + 1)$ for simplicity. The functions $\mathbf{F_f}$, $\mathbf{F_g}$, $\mathbf{F}_\theta$, and $\mathbf{F}_\phi$ are presented as

$$\begin{aligned}
\mathbf{F_f} &= -\frac{1}{\mathfrak{B}}\left\{(f+g)f'' - f'^2 - Mf'\right\},\\
\mathbf{F_g} &= -\frac{1}{\mathfrak{B}}\left\{(f+g)g'' - g'^2 - Mg'\right\},\\
\mathbf{F}_\theta &= -\left\{Pr(f+g)\theta' + PrNb\theta\prime\phi\prime + PrNt\theta'^2 + PrQ\theta e^{-m\eta}\right\},\\
\mathbf{F}_\phi &= -\left\{Le(f+g)\phi' + \frac{Nt}{Nb}\theta'' - Le\Lambda(1+\Gamma\theta)^r e^{(-E/1+\Gamma\theta)}\right\}.
\end{aligned} \tag{29}$$

We divide the interval $[0, \eta_\infty]$ into N uniform subintervals $\Omega_n = [\eta_n, \eta_{n+1}]$ for $n = 0, 1, 2, 3, \ldots, N-1$ in order to solve the IVPs (21)–(24) iteratively using the IPS procedure. Let $\mathbb{Z}_N = \{\eta_n = nh\colon n = 0, 1, 2, 3, \ldots, N-1\}$ where $h = \eta_\infty - \eta_0/N$. The exact solution of equations (21)–(24) can be shown here as a piecewise polynomial on each Ω_n at given $\chi = \chi_i$, $\zeta = \zeta_i$, $\lambda = \lambda_i$, and $\xi = \xi_i$ for $i \ge 1$, i.e.,

$$f(\eta,\chi_i) \approx f_n(\eta) = \sum_{k=0}^{j} a_{n,k}(\eta-\eta_n)^k, \tag{30}$$

$$g(\eta,\zeta_i) \approx g_n(\eta) = \sum_{k=0}^{j} b_{n,k}(\eta-\eta_n)^k, \tag{31}$$

$$\theta(\eta,\lambda_i) \approx \theta_n(\eta) = \sum_{k=0}^{j-1} c_{n,k}(\eta-\eta_n)^k, \tag{32}$$

$$\phi(\eta,\xi_i) \approx \phi_n(\eta) = \sum_{k=0}^{j-1} d_{n,k}(\eta-\eta_n)^k. \tag{33}$$

Note that here j denotes the degree of the polynomials. The functions f, g, θ, and ϕ are assumed to be continuously differentiable on $[0,\eta_\infty]$ to obtain the recursion relations between the coefficients. By applying the IPS technique with $j=4$, we obtain the following recursion relations between coefficients for $n=0,1,2,3,\ldots,N-1$ (Al Sakkaf et al. [39]):

$$a_{n,0} = a_{n-1,0} + ha_{n-1,1} + h^2a_{n-1,2} + h^3a_{n-1,3} + h^4a_{n-1,4}, \tag{34}$$

$$a_{n,1} = a_{n-1,1} + 2ha_{n-1,2} + 3h^2a_{n-1,3} + 4h^3a_{n-1,4}, \tag{35}$$

$$a_{n,2} = a_{n-1,2} + 3ha_{n-1,3} + 6h^2a_{n-1,4}, \tag{36}$$

$$a_{n,3} = \frac{1}{6\mathfrak{B}}\left\{-2a_{n,2}\left(a_{n,0}+b_{n,0}\right) + Ma_{n,1} + a_{n,1}^2\right\}, \tag{37}$$

$$a_{n,4} = -\frac{1}{24\mathfrak{B}^2}\left\{-2a_{n,2}\left(\mathfrak{B}a_{n,1} - \mathfrak{B}b_{n,1} + b_{n,0}^2 + \mathfrak{B}M\right) + a_{n,0}\left(-4a_{n,2}b_{n,0} + Ma_{n,1} + a_{n,1}^2\right) + a_{n,1}b_{n,0}\left(a_{n,1}+M\right) - 2a_{n,2}a_{n,0}^2\right\}. \tag{38}$$

$$b_{n,0} = b_{n-1,0} + hb_{n-1,1} + h^2b_{n-1,2} + h^3b_{n-1,3} + h^4b_{n-1,4}, \tag{39}$$

$$b_{n,1} = b_{n-1,1} + 2hb_{n-1,2} + 3h^2b_{n-1,3} + 4h^3b_{n-1,4}, \tag{40}$$

$$b_{n,2} = b_{n-1,2} + 3hb_{n-1,3} + 6h^2a_{n-1,4}, \tag{41}$$

$$b_{n,3} = \frac{1}{6\mathfrak{B}}\left\{-2b_{n,2}\left(a_{n,0}+b_{n,0}\right) + Mb_{n,1} + b_{n,1}^2\right\}, \tag{42}$$

$$b_{n,4} = \frac{1}{24\mathfrak{B}^2}\left\{2\mathfrak{B}b_{n,2}\left(-a_{n,1}+b_{n,1}+M\right) + 2b_{n,0}^2b_{n,2} - a_{n,0}\left(Mb_{n,1} + b_{n,1}^2 - 4b_{n,0}b_{n,2}\right) + 2a_{n,0}^2b_{n,2} - b_{n,0}b_{n,1}\left(b_{n,1}+M\right)\right\} \tag{43}$$

$$c_{n,0} = c_{n-1,0} + hc_{n-1,1} + h^2c_{n-1,2} + h^3c_{n-1,3} + h^4c_{n-1,4}, \tag{44}$$

$$c_{n,1} = c_{n-1,1} + 2hc_{n-1,2} + 3h^2c_{n-1,3} + 4h^3c_{n-1,4}, \tag{45}$$

$$c_{n,2} = -\frac{1}{2(Nt\,\mathrm{Pr}+1)}\left\{\mathrm{Pr}e^{-hmn}\left(c_{n,1}e^{hmn}\left(Nb\,a_{n,1} + b_{n,0} + d_{n,0}\right) + Qc_{n,0}\right)\right\}, \tag{46}$$

$$\begin{aligned} c_{n,3} = \frac{1}{6(Nt\,\mathrm{Pr}+1)^2}\Big\{&\mathrm{Pr}e^{-hmn}\Big(Qc_{n,0}\left(Nb\,\mathrm{Pr}a_{n,1} + \mathrm{Pr}b_{n,0} + \mathrm{Pr}d_{n,0} + mNt\,\mathrm{Pr} + m\right) \\ &- c_{n,1}\left(-2Nb\,\mathrm{Pr}a_{n,1}e^{hmn}\left(b_{n,0}+d_{n,0}\right) + Nb^2\mathrm{Pr}a_{n,1}^2\left(-e^{hmn}\right)\right. \\ &+ 2Nb\,(Nt\,\mathrm{Pr}+1)a_{n,2}e^{hmn} - 2\mathrm{Pr}b_{n,0}d_{n,0}e^{hmn} + Nt\,\mathrm{Pr}b_{n,1}e^{hmn} - \mathrm{Pr}b_{n,0}^2e^{hmn} + b_{n,1}e^{hmn} \\ &+ Nt\,\mathrm{Pr}d_{n,1}e^{hmn} - \mathrm{Pr}d_{n,0}^2e^{hmn} + d_{n,1}e^{hmn} + Nt\,\mathrm{Pr}Q + Q\Big)\Big)\Big\}, \end{aligned} \tag{47}$$

$$d_{n,0} = d_{n-1,0} + hd_{n-1,1} + h^2d_{n-1,2} + h^3d_{n-1,3} + h^4d_{n-1,4}, \tag{48}$$

$$d_{n,1} = d_{n-1,1} + 2hd_{n-1,2} + 3h^2d_{n-1,3} + 4h^3d_{n-1,4}, \tag{49}$$

$$d_{n,2} = \frac{1}{2Nt}\left\{Nb\left(Le\left(\Gamma e^{-E/\Gamma d_{n,0}+1}\left(\Gamma d_{n,0}+1\right)^{r} - a_{n,1}\left(b_{n,0}+c_{n,0}\right)\right) - 2a_{n,2}\right)\right\}, \tag{50}$$

$$\begin{aligned} d_{n,3} = \frac{1}{6Nt}\Bigg\{ Nb\Bigg(& -\frac{Ma_{n,1}+a_{n,1}^{2}-2a_{n,2}\left(a_{n,0}+b_{n,0}\right)}{\mathfrak{B}} - 2Le\, a_{n,2}b_{n,0} - Le\, a_{n,1}b_{n,1} - Le\left(2a_{n,2}c_{n,0}+a_{n,1}c_{n,1}\right) \\ & + \Gamma^{2}Le\, d_{n,1}e^{-E/\Gamma d_{n,0}+1}\left(\Gamma d_{n,0}+1\right)^{r-2}\left(\Gamma r d_{n,0}+E+r\right)\Bigg)\Bigg\}. \end{aligned} \tag{51}$$

The process continues until the boundary conditions, equations (25)–(28), are satisfied, i.e., $|f'(\eta_\infty,\chi_i)| < \varepsilon$, $|g'(\eta_\infty,\zeta_i)| < \varepsilon$, $|\theta(\eta_\infty,\lambda_i)| < \varepsilon$, and $|\phi(\eta_\infty,\xi_i)| < \varepsilon$. Here ε is the tolerance fixed to 10^{-10}, and the optimal choice for η_∞ is discussed in Section 7.

7. Validation

In the present section, we intend to assess the performance and efficiency of the present numerical scheme for solving (21)–(24). We will concentrate on equation (21), which can be written as

$$\left(\beta^{-1}+1\right)f''' + (f+g)f'' - f'^{2} - Mf' = 0, \tag{52}$$

with the conditions

$$f(0) = 0,\ f'(0) = 1,\ f''(0) = \chi, \tag{53}$$

where the value χ is modified using the shooting technique in order to satisfy $f'(\infty) = 0$.

We discuss the relevance of choosing the numerical parameter, η_∞, in order achieve accurate numerical data. Table 2 presents the values of χ as a function of η for distinct values of η_∞ in order to obtain an optimal value of η_∞. As mentioned earlier, the values of the parameter χ are updated at every iteration until it becomes sufficiently close to $f'(\infty) = 0$. Table 2 shows that the values of χ become nearly constant after few iterations as $\eta_\infty > 7$. Therefore, $\eta_\infty = 15$ is the optimal value. However, the range of values up to $\eta_\infty = 7$ is considered for plotting the figures.

The associated residuals to (21)–(24) are, respectively, given by

$$\mathrm{Res}_f(\eta) = \left(\beta^{-1}+1\right)f''' + (f+g)f'' - f'^{2} - Mf', \tag{54}$$

$$\mathrm{Res}_g(\eta) = \left(\beta^{-1}+1\right)g''' + (f+g)g'' - g'^{2} - Mg', \tag{55}$$

$$\mathrm{Res}_\theta(\eta) = \theta'' + \Pr(f+g)\theta' + \Pr Nb\theta'\phi' + \Pr Nt\theta'^{2} + \Pr Q\theta e^{-m\eta}, \tag{56}$$

$$\mathrm{Res}_\phi(\eta) = \phi'' + Le(f+g)\phi' + \frac{Nt}{Nb}\theta'' - Le\Lambda(1+\Gamma\theta)^{r}e^{(-E/1+\Gamma\theta)}. \tag{57}$$

In Table 3, we present the residual error values for $\mathrm{Res}_f(\eta)$ in equation (54) corresponding to each η_∞ using the IPS method. The findings demonstrate an accuracy of order 10^{-10}.

To guarantee the convergence of the solution, we present Tables 4 and 5 , which compare the numerical results obtained for $f'(\eta)$ and $g'(\eta)$ using the IPS method with the approximate solution derived using Runge–Kutta method of fourth order for various values of η.

To validate our numerical solution, the estimated numerical results for $f''(0)$ and $g''(0)$ are compared with the available literature. Table 6 compares $f''(0)$ and $g''(0)$ values obtained in the present research with those of Umar et al. [19], Freidoonimehr and Rahimi [12], and Wang [11]. It is clear that the results are in very good agreement with an accuracy of 10^{-5}.

8. Results and Discussion

The results obtained for equations (13)–(16) by transforming into IVPs given by equations (21)–(24) and using the IPS method combined with the shooting approach are discussed in this section. Now onwards, $f'(\eta)$, $g'(\eta)$, $\theta(\eta)$, and $\phi(\eta)$ have been used to mention the x component of velocity, y component of the velocity, temperature, and concentration profiles, respectively. Similarly, we mention momentum boundary layer as MBL, thermal boundary layer as TBL, and concentration boundary layer as CBL, respectively. The parameter are values are varied between the following ranges: $0.5 \le M \le 2.0$, $0.6 \le \alpha \le 0.9$, $2.0 \le Q \le 5.0$, $0.1 \le E \le 0.25$, $0.1 \le M \le 0.25$, $1.0 \le Bi_1 \le 2.5$, $0.5 \le Bi_2 \le 0.8$, $2.0 \le Nb \le 5.0$, $0.2 \le Nt \le 0.8$, $0.5 \le \Gamma \le 2.0$, $0.6 \le Le \le 0.75$, $3.0 \le \Pr \le 4.5$, and $0.1 \le \Lambda \le 0.25$. The value of β is fixed to 0.5 and m and n to 1 throughout this study.

Table 7 presents the calculated values of the local skin friction coefficients in the x-and y-directions. Following the effects of the Casson parameter (β), $\mathrm{Re}_x^{1/2}C_{fx}$ and $\alpha^{3/2}, \mathrm{Re}_y^{1/2}C_{fy}$ are enhanced, while it is decreased following the effect of magnetic parameter (M) in both directions. Interestingly, for the case of α, the friction coefficient,

Table 2: Values of parameter χ corresponding to η_∞, calculated by using shooting method with $M = 1.0$, $\beta = 0.5$, $\alpha = 0.3$, and absolute error in the subsequent values of η_∞.

η_∞	χ	Absolute Error
7	−0.92126708636310317	—
8	−0.92113408041491218	1.33×10^{-4}
9	−0.92109189943454539	4.22×10^{-5}
10	−0.92107847137819310	1.34×10^{-5}
11	−0.92107419566890625	4.28×10^{-6}
12	−0.92107282577059646	1.37×10^{-6}
13	−0.92107238794947266	4.38×10^{-7}
14	−0.92107224800468002	1.40×10^{-7}
15	−0.92107220327054939	4.47×10^{-8}

Table 3: Residual error ($\mathrm{Res}_f(\eta)$) corresponding to η_∞, calculated by using IPS method with $M = 1.0$, $\beta = 0.5$, and $\alpha = 0.3$.

η_∞	Error
7	0.0000130877
8	2.50503×10^{-7}
9	-2.01555×10^{-7}
10	2.81436×10^{-6}
11	-1.68648×10^{-7}
12	-6.91890×10^{-7}
13	-3.96241×10^{-8}
14	-1.14731×10^{-7}
15	-8.83440×10^{-10}

Table 4: Estimations of error for $f'(\eta)$ by setting $M = 0.5$, $\alpha = 0.5$, and $\beta = 0.5$.

η	$f'_{\mathrm{IPS}}(\eta)$	$f'_{\mathrm{RK4}}(\eta)$	Error $(f'_{\mathrm{IPS}}(\eta) - f'_{\mathrm{RK4}}(\eta))$
1	1.000000000000	1.000000000000	0.00
2	0.460525220817	0.460525181476	3.9341×10^{-8}
3	0.204915558646	0.204915533345	2.53006×10^{-8}
4	0.089670147015	0.089670097323	4.96921×10^{-8}
5	0.038942267210	0.038942231873	3.53371×10^{-8}
6	0.016855052694	0.016855116531	-6.38367×10^{-8}
7	0.007284282287	0.007284365925	-8.36375×10^{-7}
8	0.003145699764	0.003145804840	-1.05076×10^{-7}
9	0.001357621734	0.001357770701	-1.48967×10^{-7}
10	0.000585300711	0.000585480549	-1.79839×10^{-7}

Table 5: Estimations of error for $g'(\eta)$ by setting $M = 0.5$, $\alpha = 0.5$, and $\beta = 0.5$.

η	$g'_{\mathrm{IPS}}(\eta)$	$g'_{\mathrm{RK4}}(\eta)$	Error $(g'_{\mathrm{IPS}}(\eta) - g'_{\mathrm{RK4}}(\eta))$
1	0.500000000000	0.500000000000	0.00
2	0.243218922052	0.243218869936	5.21155×10^{-8}
3	0.110964835767	0.110964849780	-1.40132×10^{-8}
4	0.049098390961	0.049098373377	1.75844×10^{-8}
5	0.021425892132	0.021425880937	1.11958×10^{-8}
6	0.009293015758	0.009293079577	-6.38193×10^{-8}
7	0.004019793239	0.004019881570	-8.8331×10^{-8}
8	0.001736581704	0.001736693904	-1.122×10^{-7}
9	0.000749555748	0.000749706482	-1.50734×10^{-7}
10	0.000323117550	0.000323302343	-1.84793×10^{-7}

$\mathrm{Re}_x^{1/2} C_{fx}$, increases, and $\alpha^{3/2}\mathrm{Re}_y^{1/2} C_{fy}$ decreases according to the directions. Table 8 lists the numerical values for the local Nusselt number and local Sherwood number for different values of the relevant physical parameters. From this table, it is clear that the heat transfer rate increases with the thermal Biot number (Bi_1), exponential heat source parameter (Q), and Lewis number (Le). Likewise, the local Sherwood number shows an enhancement with the concentration Biot number (Bi_2), Lewis number, (Le), and reaction rate constant (Λ). It is noteworthy to mention that the local Nusselt and Sherwood numbers reduce following the effects of Arrhenius activation energy.

Figures 2–5 present the behavior of the velocity profiles in x and y directions ($f'(\eta)$ and $g'(\eta)$, respectively), temperature ($\theta(\eta)$), and concentration ($\phi(\eta)$) profiles with respect to η for the variations in the magnetic parameter (M) and stretching ratio parameter (α). It is observed that $f'(\eta)$ and $g'(\eta)$ show a gradual decrease in the flow domain with an increase in the values of M from 0.5 to 2. A charged molecule moving across a magnetic field is acted upon by a force that is perpendicular to the direction applied field and to the direction in which the particle is moving. The interactions between the applied magnetic field and the magnetic field generated by the moving particle lead to development of a force, termed as the Lorentz force. This force acts as a drag-like force, opposite to the direction of fluid motion. Therefore, an increase in the strength of the magnetic field applied in the direction perpendicular to the fluid flow tends to reduce the fluid velocities along both x-and y-directions, as depicted in Figures 2 and 3. Similar observations are reported by Nadeem et al. [26]. Lorentz forces tend to increase the heat transmission in the fluid domain by considerably reducing the flow velocities. Hence, $\theta(\eta)$ enhances significantly with M as shown in Figure 4. Even though the temperature distribution under the influence of M is considerably high, the concentration profile of the fluid reduces considerably with an increase in M as depicted in Figure 5.

Figures 2–5 also demonstrate the effect of α on the parameters $f'(\eta)$, $g'(\eta)$, $\theta(\eta)$, and $\phi(\eta)$. A gradual increase in α from 0.6 to 0.9 leads to an enhancement in the transverse velocity $g'(\eta)$, whereas $f'(\eta)$ diminishes. $\alpha(= b/a)$ is a quantitative relation between the stretching velocities in x and y directions, represented as $U_w = ax$ and $V_w = by$. On increasing α, the sheet stretching force significantly increases in the transverse direction. This is attributed to the relation of direct proportionality between α and the transverse velocity ($g'(\eta)$). On the other hand, the axial velocity field ($f'(\eta)$), which is inversely proportional to α, decreases with an increase in α (see Figures 2 and 3). The enhanced values of α seem not to influence the TBL, and $\theta(\eta)$ continues to decline. This is due to the fact that the cooler fluid from the ambient region progresses towards the sheet relatively faster due to the stretching of the sheet. As a result the temperature gradient near the sheet is increased and thus the TBL grows thinner. This leads to decreased temperature profile (see Figure 4). In addition, stretching of the sheet leads to a decrease in the values of $\phi(\eta)$. The CBL thickness decreases with an increase in the values of α in Figure 5.

Table 6: Comparison of the present numerical results for α, $f''(0)$, and $g''(0)$ with Umar et al. [19], Freidoonimehr and Rahimi [12], and Wang [11].

	α	Umar et al. [19]	Freidoonimehr and Rahimi [12]	Wang [11]	Present Result	Maximum Error
$f''(0)$	0	−1.0000	−1.0000	−1.0000	−1.0000000	—
	0.25	−1.0490	−1.04881	−1.0488	−1.0488110	-1.1×10^{-5}
	0.5	−1.0932	−1.09309	−1.0930	−1.0930950	-9.5×10^{-5}
	0.75	−1.1345	−1.13450	−1.1344	−1.1344857	-8.57×10^{-5}
	1.0	−1.1737	−1.17372	−1.1737	−1.1737207	-2.07×10^{-5}
$g''(0)$	0	0.00000	0.00000	0.0000	0.0000000	—
	0.25	−0.19457	−0.19457	−0.1945	−0.1945638	-1.38×10^{-3}
	0.5	−0.46532	−0.46520	−0.4652	−0.4652048	-4.8×10^{-6}
	0.75	−0.79470	−0.79462	−0.7946	−0.7946182	-1.8×10^{-5}
	1.0	−1.17372	−1.17372	−1.1737	−1.1737207	-2.07×10^{-5}

Table 7: Values of $\mathrm{Re}_x^{1/2} C_{fx}$ and $\alpha^{3/2}\, \mathrm{Re}_y^{1/2} C_{fy}$ corresponding to M, α, and β.

M	α	β	$\mathrm{Re}_x^{1/2} C_{fx}$	$\alpha^{3/2} \mathrm{Re}_y^{1/2} C_{fy}$
0.0			−0.91263354	−0.10486921
0.3			−1.14686424	−0.19773170
0.6			−1.36502137	−0.28057038
	0.0		−1.67539238	−0.00000000
	0.25		−1.64024018	−0.30972771
	0.5		−1.60811195	−0.67453871
		0.5	−1.63359047	−0.37845134
		1.0	−1.28109625	−0.29421997
		3.0	−0.99679321	−0.22663912

Table 8: Values of $\mathrm{Re}_x^{-1/2} \mathrm{Nus}_x$ and $\mathrm{Re}_x^{-1/2} \mathrm{Sh}_x$ corresponding to $M, Bi_1, Bi_2, Nb, Nt, Le, E, \Lambda, Q$, and β.

M	Bi_1	Bi_2	Nb	Nt	Le	E	Λ	Q	β	$\mathrm{Re}_x^{-1/2} \mathrm{Nus}_x$	$\mathrm{Re}_x^{-1/2} \mathrm{Sh}_x$
0.0										0.73049067	0.16449552
0.3										0.72902988	0.17600451
0.6										0.72753576	0.18873343
	0.1									0.09741008	0.23319547
	0.2									0.18945977	0.22896889
	0.3									0.27593479	0.22506826
		0.1								0.72556403	0.20629971
		0.2								0.71283726	0.39898561
		0.3								0.70031755	0.57950017
			0.1							0.72941262	0.07371255
			0.2							0.72846414	0.15657457
			0.3							0.72750619	0.18419747
				0.1						0.78918148	0.23318320
				0.2						0.77992473	0.22807811
				0.3						0.77015236	0.22320023
					0.5					0.72556403	0.20629971
					1.0					0.73741327	0.22744454
					1.5					0.74486116	0.23559864
						0.1				0.72563138	0.23770808
						0.2				0.72560205	0.22122394
						0.3				0.72556403	0.20629971
							0.1			0.72437632	0.09197616
							0.2			0.72469919	0.12056004
							0.3			0.72500447	0.14914185
								0.1		0.74194053	0.20491889
								0.2		0.73812455	0.20524079
								0.3		0.73413256	0.20557744
									0.5	0.72556403	0.20629971
									1.0	0.72425929	0.21507536
									3.0	0.72287366	0.22407199

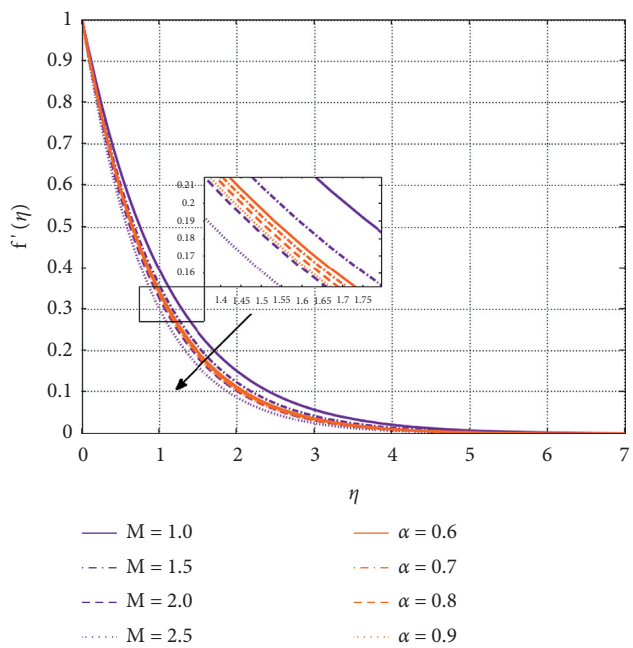

Figure 2: Behavior of $f'(\eta)$ with respect to η for $1 \le M \le 2.5$ and $0.6 \le \alpha \le 0.9$.

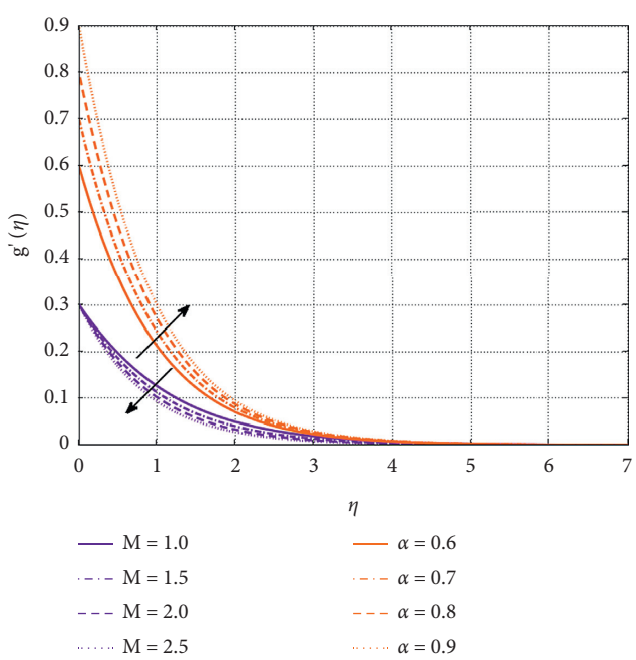

Figure 3: Behavior of $g'(\eta)$ with respect to η for $1 \le M \le 2.5$ and $0.6 \le \alpha \le 0.9$.

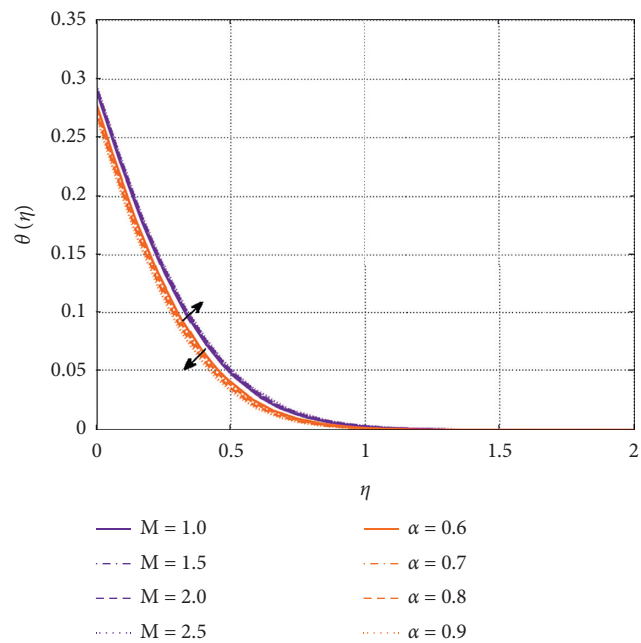

Figure 4: Behavior of $\theta(\eta)$ with respect to η for $1 \le M \le 2.5$ and $0.6 \le \alpha \le 0.9$.

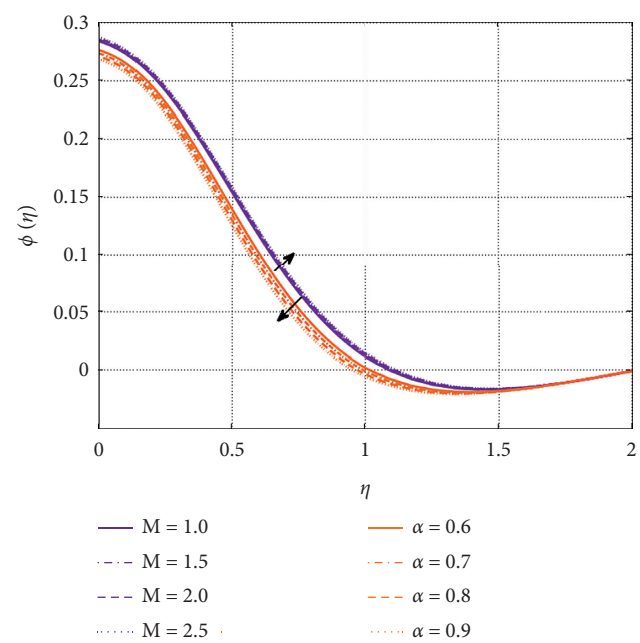

Figure 5: Behavior of $\phi(\eta)$ with respect to η for $1 \le M \le 2.5$ and $0.6 \le \alpha \le 0.9$.

Figures 6 and 7 present the impact of the exponential heat source parameter (Q) and the Brownian motion parameter (Nb) on the parameters $\theta(\eta)$ and $\phi(\eta)$, respectively. The exponential heat source provides heat to the fluid, leading to a strong thermal environment, which justifies the behavior of Q with $\theta(\eta)$. Similarly, Nb displays an opposite behavior with $\theta(\eta)$. The unpredictable migration of fluid molecules increases with increasing Nb. This migration can be attributed to a reduction in the TBL thickness, which eventually leads to a decrease in the temperature in the whole domain.

In Figure 7, the curves of the concentration profile can be analyzed with values of Q ranging from 2.0 to 5.0. Initially,

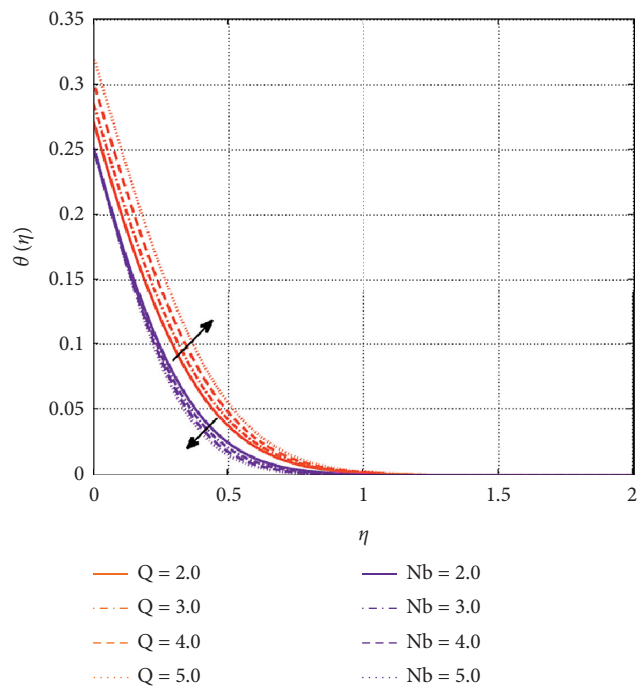

Figure 6: Behavior of $\theta(\eta)$ with respect to η for $2 \leq Q \leq 5.0$ and $2.0 \leq Nb \leq 5.0$.

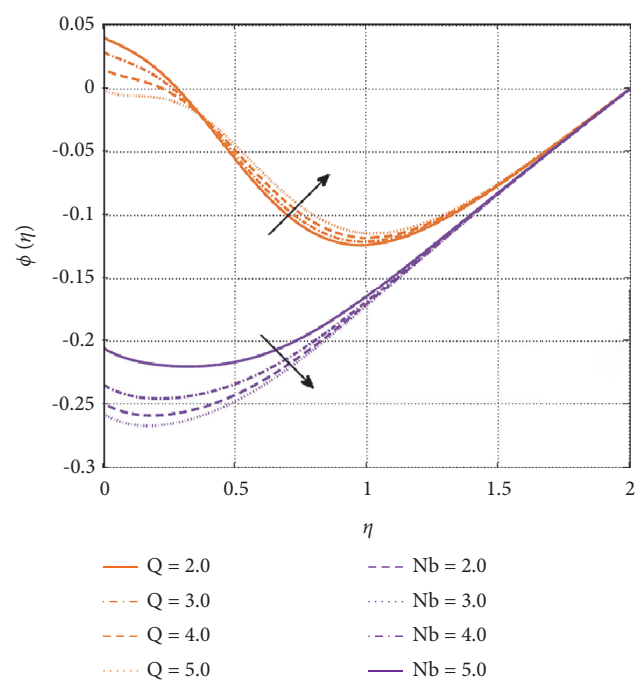

Figure 7: Behavior of $\phi(\eta)$ with respect to η for $2 \leq Q \leq 5.0$ and $2.0 \leq Nb \leq 5.0$.

the concentration decreases in the region close to the sheet surface ($0 \leq \eta \leq 0.4$), and as η approaches the free stream region, the concentration increases. This is due to the fact that the particles in the liquids remain very close to each other near the surface that tend to increase the concentration gradient. This increment tends to a decrease in the TBL thickness and it further affects the temperature profile in the vicinity of the sheet surface. But, as the fluid particles move at a considerable distance from the sheet surface, concentration gradient effects are less perceived and therefore the TBL thickness is larger here. Hence, the concentration profiles far away from the sheet show an increase. We also observe that an increase in the Brownian motion parameter (Nb) tends to reduce the concentration profile. Mechanically, Nb tends to induce a continual acceleration between the fluid molecules. Such an acceleration boosted particles move faster as they acquire kinetic energy, which leads to higher collision rates and an increased diffusion rate. Thus, the greater the migration of particles to regions of lower concentration, the lower the values of $\phi(\eta)$.

Figures 8 and 9 present the behavior of $\theta(\eta)$ and $\phi(\eta)$ against the Prandtl number (Pr) and the thermophoresis parameter (Nt), Pr, which is represented as the ratio of energy diffusiveness to warm diffusiveness, and helps to reduce $\theta(\eta)$ and $\phi(\eta)$. The general thickening of MBL, TBL, and CBL in heat transfer problems is well known to be controlled by Pr (Shehzad et al. [27]). If Pr is small (smaller than 1), the MBL is considerably less than those of the TBL and CBL. Thus, increasing the values of Pr from 3.0 to 4.5 may decrease the thicknesses of TBL and CBL. This leads to a reduction with $\theta(\eta)$ and $\phi(\eta)$. Similar observations have been documented by Shehzad et al. [27].

Figures 8 and 9 depict the variations in the thermal and concentration profiles with respect to Nt. If a temperature gradient exists in a liquid, suspended particles tend to move from a region of high temperature to a region of low temperature. The force responsible for this behaviour is termed as thermophoretic force. Particles colliding with the particles lying in region of high temperature have higher velocities than those colliding with the particles lying in the region of lower temperature. This leads to a net force towards the low temperature regions. Thus, more fluid gets heated that leads to a rise in the temperature, as observed in Figure 8. However, in Figure 9, an increase in $\phi(\eta)$ has been observed. This is attributed to the fact that the thermophoresis present in the domain tends to agitate the particles. The random oscillations do not possess a particular direction. Hence, the particles tend to spread equally throughout the domain over a period of time, from regions of high concentration to regions of lower concentration. This phenomenon is also called diffusion. Therefore, diffusion tends to improve the concentration boundary layer and it leads to an increase in $\phi(\eta)$, as depicted in Figure 9.

Figure 10 shows the dynamics of the Arrhenius activation energy parameter (E) and the reaction rate constant (Λ) with $\phi(\eta)$. The expression, $E = E_a/k_1 T_\infty$, describes the connection of temperature with the speed of a chemical reaction. Here, E_a denotes the activation energy for the reaction and k_1 denotes the reaction rate constant. As the activation energy increases, the generative chemical reaction is initiated, which leads to an enhanced concentration profile. Meanwhile, an increase in Λ results in the decrease of $\phi(\eta)$ to ensure an enormous concentration gradient on the wall, which lowers the thickness of CBL.

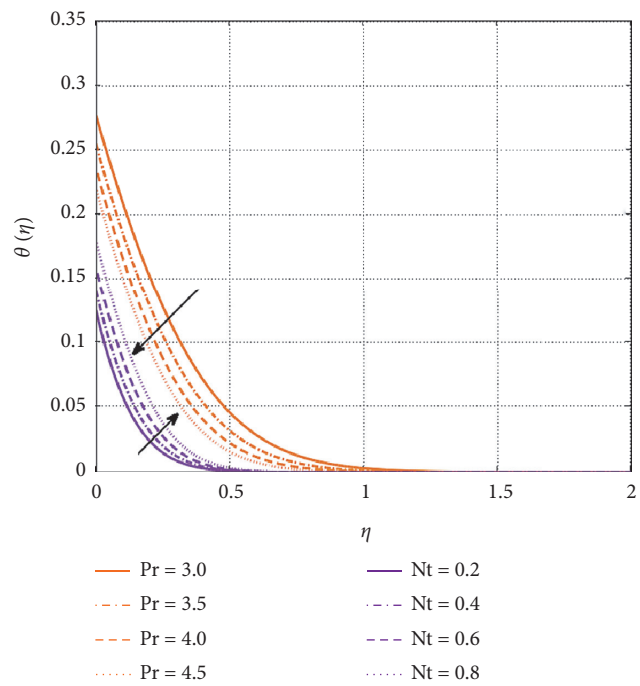

Figure 8: Behavior of $\theta(\eta)$ with respect to η for $3.0 \leq Pr \leq 4.5$ and $0.2 \leq Nt \leq 0.8$.

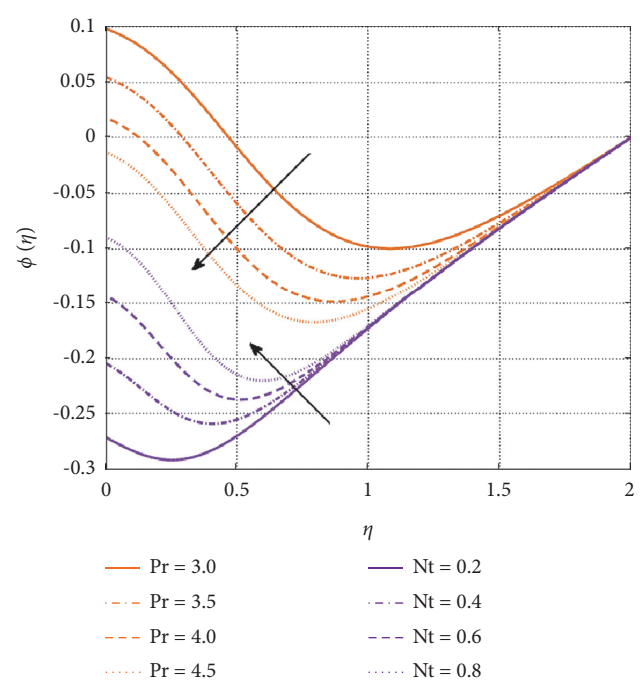

Figure 9: Behavior of $\phi(\eta)$ with respect to η for $3.0 \leq Pr \leq 4.5$ and $0.2 \leq Nt \leq 0.8$.

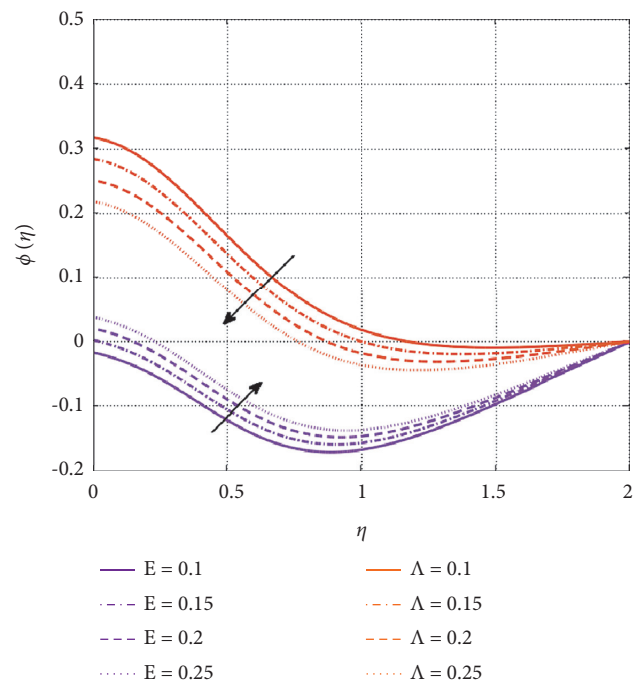

Figure 10: Behavior of $\phi(\eta)$ with respect to η for $0.1 \leq E \leq 4.5$ and $0.1 \leq \Lambda \leq 0.25$.

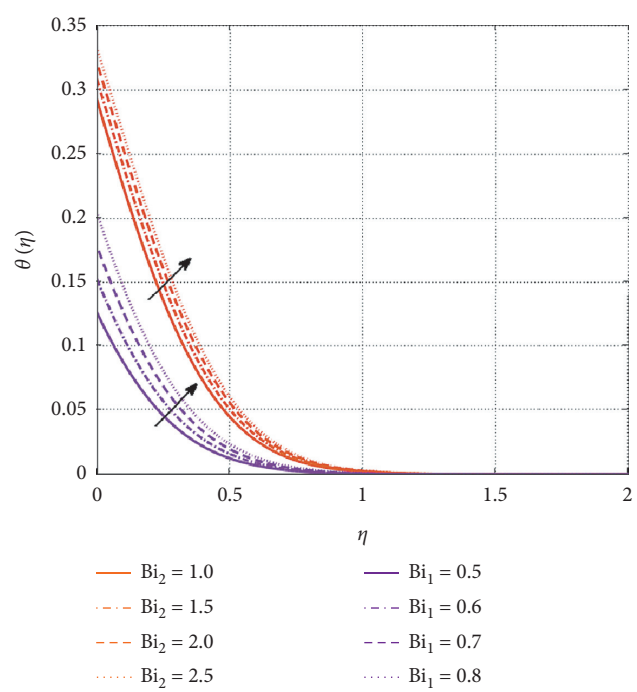

Figure 11: Behavior of $\theta(\eta)$ with respect to η for $1.0 \leq Bi_1 \leq 2.5$ and $0.5 \leq Bi_2 \leq 0.8$.

Figures 11 and 12 present the impacts of Bi_1 and Bi_2 on $\theta(\eta)$ and $\phi(\eta)$, respectively. Here, Bi_1 and Bi_2 denote the thermal and concentration Biot numbers, respectively. Similarly, the fixed temperature of the wall $\theta(0) = 1$ and the concentration $\phi(0) = 1$ are achieved using the values of Bi_1 and Bi_2. An increment in the values of Bi_1 and Bi_2 leads to an increase in the values of heat and mass transfer coefficients. This increase in the values of these coefficients enhances the temperature and the concentration profiles. The variations in $\phi(\eta)$ against the nondimensional fluid parameters (Γ) and Lewis number (Le) are depicted in Figure 13. This figure

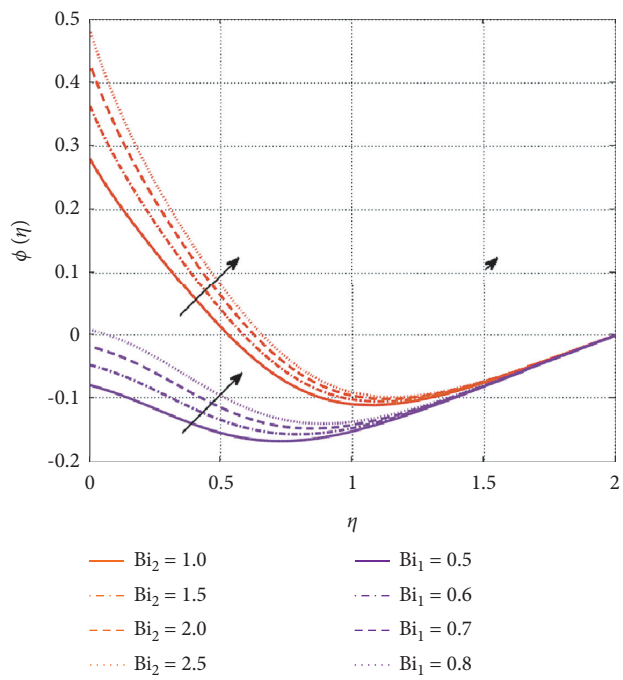

Figure 12: Behavior of $\phi(\eta)$ with respect to η for $1.0 \le Bi_1 \le 2.5$ and $0.5 \le Bi_2 \le 0.8$.

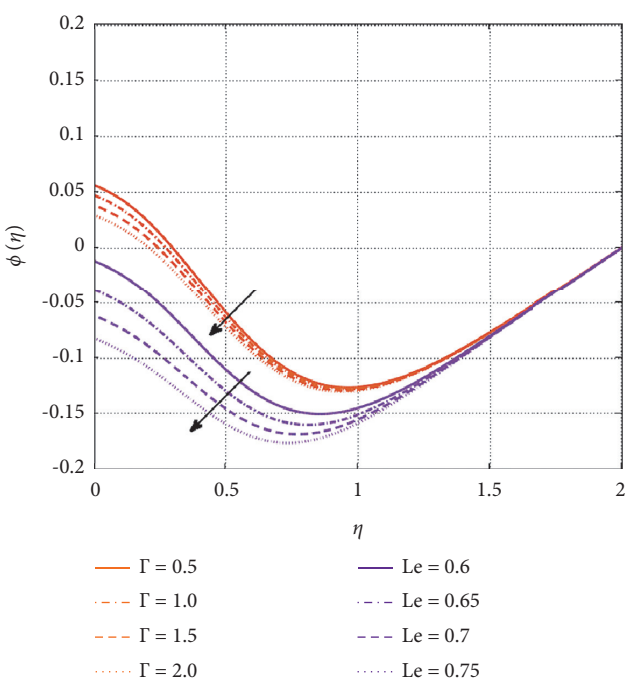

Figure 13: Behavior of $\theta(\eta)$ with respect to η for $0.5 \le \Gamma \le 2.0$ and $0.6 \le Le \le 0.75$.

shows that $\phi(\eta)$ is a diminishing relation of Γ and Le. The Lewis number, Le, is a dimensional number that is defined as the ratio of thermal diffusivity and mass diffusivity. It has been used to model fluid flows where the heat transfer and mass transfer phenomena are observed to occur simultaneously. In the boundary layer flow, if Le increases, heat diffuses more easily than the solute. Therefore, the thickness of TBL is greater than the thickness of CBL. Note that a reduction in the CBL reflects a reduction in the concentration profile.

9. Conclusion

The considered problem is quite significant in the field of engineering and technology. It has great importance in the production of cosmetics, pharmaceuticals, chemicals, oil, gas, food, and several others. In this study, we investigated the three-dimensional Casson nanofluid flow over a stretching sheet with Arrhenius activation energy and exponential heat source effects with convective heat and mass boundary condition. The numerical solution of the ODEs is obtained using a computational process based on iterative power series (IPS) method combined with shooting iteration approach. The following are some key characteristics of various physical constraints on various flow variables in the problem:

(i) When the magnetic parameter, M, increases, the x– and y–direction velocities, $f'(\eta)$ and $g'(\eta)$, decreases. But the rising values of magnetic parameter improve the temperature and concentration distribution.

(ii) The x–direction velocity, $f'(\eta)$, temperature, $\theta(\eta)$, and concentration, $\phi(\eta)$, are reduced for larger values of stretching ratio parameter, α, whereas for the same values of α, the y–direction velocity, $g'(\eta)$, is enhanced.

(iii) The exponential heat source parameter, Q, improves the temperature profile. For the concentration profile, we note a decrement initially in the region close to the surface $(0 \le \eta \le 0.4)$ and an increment after that.

(iv) Skin friction coefficient is increased by enhancing the Casson parameter, β, and is decreased for magnetic parameter, M, and stretching ratio parameter, α.

(v) The strength of the Arrhenius activation energy, E, intensifies the concentration field. Also, enhancement in the thermal and concentration Biot numbers augments the temperature and concentration profiles.

(vi) The heat and mass transfer rates are observed to decline with an increment in the Arrhenius activation energy parameter, E.

(vii) The mass transfer rate is enhanced and the heat transfer rate decreased with an increase in the exponential heat source parameter, Q.

The results obtained indicate very clearly that thermal and concentration profiles of Casson fluid are enhanced by an exponential heat source and by Arrhenius activation energy. Also, from these concluded points, we have achieved clear-cut answers for the research questions raised in Section 1.

Data Availability

All the data are available within this article.

Conflicts of Interest

The authors declare no conflicts of interest.

Acknowledgments

The authors would like to acknowledge and express their gratitude to the United Arab Emirates University, Al Ain, UAE, for providing financial support with Grant No. 12S086.

References

[1] N. Casson and C. C. Mill, *Rheology of Disperse Systems*, pp. 84–104, Pergamon Press, Elmsford, NY, USA, 1959.

[2] A. Shafiq, G. Rasool, H. Alotaibi et al., "Thermally enhanced Darcy-Forchheimer Casson-water/glycerine rotating nanofluid flow with uniform magnetic field," *Micromachines*, vol. 12, no. 6, p. 605, 2021.

[3] A. Saeed, Z. Shah, S. Islam et al., "Three-dimensional Casson nanofluid thin film flow over an inclined rotating disk with the impact of heat generation/consumption and thermal radiation," *Coatings*, vol. 9, no. 4, p. 248, 2019.

[4] M. G. Reddy, P. A. Dinesh, and J. Basavaraj, "3D rotating flow of Casson fluid over an elongated surface with thermophoresis and Brownian moment: Buongiorno model," *Journal of Nanofluids*, vol. 8, no. 7, pp. 1479–1484, 2019.

[5] P. Durgaprasad, S. V. K. Varma, M. M. Hoque, and C. S. K. Raju, "Combined effects of Brownian motion and thermophoresis parameters on three-dimensional (3D) Casson nanofluid flow across the porous layers slendering sheet in a suspension of graphene nanoparticles," *Neural Computing & Applications*, vol. 31, no. 10, pp. 6275–6286, 2019.

[6] P. Durgaprasad, S. Saleem, S. V. K. Varma, and C. S. K. Raju, "Three dimensional slip flow of a chemically reacting Casson fluid flowing over a porous slender sheet with a non-uniform heat source or sink," *Journal of the Korean Physical Society*, vol. 74, no. 9, pp. 855–864, 2019.

[7] J. Raza, "Thermal radiation and slip effects on magnetohydrodynamic (MHD) stagnation point flow of Casson fluid over a convective stretching sheet," *Propulsion and Power Research*, vol. 8, no. 2, pp. 138–146, 2019.

[8] T. Thumma, S. R. Mishra, and M. Shamshuddin, "Effect of heat generation and viscous dissipation on MHD 3D Casson nanofluid flow past an impermeable stretching sheet," in *Numerical Heat Transfer and Fluid Flow. Lecture Notes in Mechanical Engineering*, D. Srinivasacharya and K. Reddy, Eds., Springer, Berlin, Singapore, pp. 575–585, 2019.

[9] M. K. Murthy, S. Sreenadh, P. Lakshminarayana, G. Sucharitha, B. Rushikumar, and J. Nanofluids, "Thermophoresis and Brownian motion effects on three dimensional magnetohydrodynamics slip flow of a Casson nanofluid over an exponentially stretching surface," *Journal of Nanofluids*, vol. 8, no. 6, pp. 1267–1272, 2019.

[10] L. J. Crane, "Flow past a stretching plate," *Zeitschrift für angewandte Mathematik und Physik ZAMP*, vol. 21, no. 4, pp. 645–647, 1970.

[11] C. Y. Wang, "The three-dimensional flow due to a stretching flat surface," *Physics of Fluids*, vol. 27, no. 8, pp. 1915–1917, 1984.

[12] N. Freidoonimehr and A. B. Rahimi, "Brownian motion effect on heat transfer of a three-dimensional nanofluid flow over a stretched sheet with velocity slip," *Journal of Thermal Analysis and Calorimetry*, vol. 135, no. 1, pp. 207–222, 2019.

[13] M. Hamid, M. Usman, Z. H. Khan, R. Ahmad, and W. Wang, "Dual solutions and stability analysis of flow and heat transfer of Casson fluid over a stretching sheet," *Physics Letters A*, vol. 383, no. 20, pp. 2400–2408, 2019.

[14] M. Abd El-Aziz and A. A. Afify, "MHD Casson fluid flow over a stretching sheet with entropy generation analysis and Hall influence," *Entropy*, vol. 21, no. 6, p. 592, 2019.

[15] D. G. Shankar, C. S. K. Raju, M. S. J. Kumar, and O. D. Makinde, "Cattaneo-Christov heat flux on an MHD 3D free convection Casson fluid flow over a stretching sheet," *Engineering Transactions*, vol. 68, no. 3, pp. 223–238, 2020.

[16] G. Mahanta, M. Das, S. Shaw, and M. L. Mahanta, "Heat and mass transfer of Casson nanofluid flow over a stretching sheet in the presence of magnetic field with Brownian and thermophoretic effects," *Journal of Engineering Science & Technology*, vol. 14, no. 5, pp. 3046–3061, 2019.

[17] B. J. Gireesha, M. Archana, B. Mahanthesh, and B. C. Prasannakumara, "Exploration of activation energy and binary chemical reaction effects on nano Casson fluid flow with thermal and exponential space-based heat source," *Multidiscipline Modeling in Materials and Structures*, vol. 15, no. 1, pp. 227–245, 2019.

[18] T. Hayat, A. Aziz, T. Muhammad, and A. Alsaedi, "Effects of binary chemical reaction and Arrhenius activation energy in Darcy-Forchheimer three-dimensional flow of nanofluid subject to rotating frame," *Journal of Thermal Analysis and Calorimetry*, vol. 136, no. 4, pp. 1769–1779, 2019.

[19] M. Umar, R. Akhtar, Z. Sabir et al., "Numerical treatment for the three-dimensional Eyring-Powell fluid flow over a stretching sheet with velocity slip and activation energy," *Advances in Mathematical Physics*, vol. 2019, Article ID 9860471, 2019.

[20] T. Hayat, I. Ullah, M. Waqas, and A. Alsaedi, "Attributes of activation energy and exponential based heat source in flow of Carreau fluid with cross-diffusion effects," *Journal of Nonequilibrium Thermodynamics*, vol. 44, no. 2, pp. 203–213, 2019.

[21] S. Rashid, T. Hayat, S. Qayyum, M. Ayub, and A. Alsaedi, "Three-dimensional rotating Darcy-Forchheimer flow with activation energy," *International Journal of Numerical Methods for Heat & Fluid Flow*, vol. 29, no. 3, pp. 935–948, 2019.

[22] T. Hayat, R. Riaz, A. Aziz, and A. Alsaedi, "Influence of Arrhenius activation energy in MHD flow of third grade nanofluid over a nonlinear stretching surface with convective heat and mass conditions," *Physica A: Statistical Mechanics and Its Applications*, vol. 549, Article ID 124006, 2020.

[23] S. Rashid, T. Hayat, S. Qayyum, M. Ayub, and A. Alsaedi, "Local similar solutions for flow of an Oldroyd-B nanofluid with activation energy," *International Journal of Numerical Methods for Heat & Fluid Flow*, vol. 29, no. 8, pp. 2911–2931, 2019.

[24] S. Rashid, M. I. Khan, T. Hayat, M. Ayub, and A. Alsaedi, "Numerical treatment for rotating Maxwell nanomaterial flow with Arrhenius energy," *Applied Nanoscience*, vol. 10, no. 8, pp. 2665–2672, 2020.

[25] S. Ahmad, M. Farooq, N. A. Mir, A. Anjum, and M. Javed, "Magneto-hydrodynamic flow of squeezed fluid with binary chemical reaction and activation energy," *Journal of Central South University*, vol. 26, no. 5, pp. 1362–1373, 2019.

[26] S. Nadeem, R. U. Haq, N. S. Akbar, and Z. H. Khan, "MHD three-dimensional Casson fluid flow past a porous linearly stretching sheet," *Alexandria Engineering Journal*, vol. 52, no. 4, pp. 577–582, 2013.

[27] S. Shehzad, T. Hayat, and A. Alsaedi, "Three-dimensional MHD flow of Casson fluid in porous medium with heat generation," *Journal of Applied Fluid Mechanics*, vol. 9, no. 1, pp. 215–223, 2016.

[28] S. R. Mishra, I. Khan, Q. M. Al-Mdallal, and T. Asifa, "Free convective micropolar fluid flow and heat transfer over a shrinking sheet with heat source," *Case Studies in Thermal Engineering*, vol. 11, pp. 113–119, 2018.

[29] K. U. Rehman, Q. M. Al-Mdallal, and M. Y. Malik, "Symmetry analysis on thermally magnetized fluid flow regime with heat source/sink," *Case Studies in Thermal Engineering*, vol. 14, Article ID 100452, 2019.

[30] P. Ragupathi, A. K. A. Hakeem, Q. M. Al-Mdallal, B. Ganga, and S. Saranya, "Non-uniform heat source/sink effects on the three-dimensional flow of Fe_3O_4/Al_2O_3 nanoparticles with different base fluids past a Riga plate," *Case Studies in Thermal Engineering*, vol. 15, Article ID 100521, 2019.

[31] B. Mahanthesh, B. J. Gireesha, B. C. PrasannaKumara, and N. S. Shashikumar, "Marangoni convection radiative flow of dusty nanoliquid with exponential space dependent heat source," *Nuclear Engineering and Technology*, vol. 49, no. 8, pp. 1660–1668, 2017.

[32] A. Kumar, J. V. R. Reddy, V. Sugunamma, and N. Sandeep, "MHD flow of Carreau fluid over a variable thickness melting surface subject to Cattaneo-Christov heat flux," *Multidiscipline Modeling in Materials and Structures*, vol. 15, no. 1, pp. 999–1016, 2018.

[33] N. Sandeep and I. L. Animasaun, "Theoretical exploration of exponential heat source and thermal stratification effects on the motion of 3-dimensional flow of Casson fluid over a low heat energy surface at initial unsteady stage," *Journal of Theoretical and Applied Mechanics*, vol. 47, no. 2, pp. 61–82, 2017.

[34] P. M. Krishna, N. Sandeep, and R. P. Sharma, "Computational analysis of plane and parabolic flow of MHD Carreau fluid with buoyancy and exponential heat source effects," *The European Physical Journal-Plus (EPJ Plus)*, vol. 132, no. 5, pp. 1–15, 2017.

[35] Z. Zia Q, I. Ullah, M. Waqas, A. Alsaedi, and T. Hayat, "Cross diffusion and exponential space dependent heat source impacts in radiated three-dimensional (3D) flow of casson fluid by heated surface," *Results Physics*, vol. 8, pp. 1275–1282, 2018.

[36] S. Liao and Y. Tan, "A general approach to obtain series solutions of nonlinear differential equations," *Studies in Applied Mathematics*, vol. 119, no. 4, pp. 297–354, 2007.

[37] R. L. Burden and J. D. Faires, "Numerical Analysis," in *Cengage Learning*, 1 Brooks/Cole, Pacific Grove, CA, USA, 9th edition, 2021.

[38] U. Al Khawaja and Q. M. Al-Mdallal, "Convergent power series of sech (x) and solutions to nonlinear differential equations," *International Journal of Differential Equations*, vol. 2018, Article ID 6043936, 2018.

[39] L. Y. Al Sakkaf, Q. M. Al-Mdallal, and U. Al Khawaja, "A numerical algorithm for solving higher-order nonlinear BVPs with an application on fluid flow over a shrinking permeable infinite long cylinder," *Complexity*, vol. 2018, Article ID 8269541, 2018.

Hindawi
Complexity
Volume 2021, Article ID 4570605, 13 pages
https://doi.org/10.1155/2021/4570605

Research Article

The Numerical Investigation of Fractional-Order Zakharov–Kuznetsov Equations

Pongsakorn Sunthrayuth,[1] **Farman Ali**,[2] **A. A. Alderremy**,[3] **Rasool Shah**,[4] **Shaban Aly**,[5] **Y. S. Hamed**,[6] **and Jeevan Katle**[7]

[1]*Department of Mathematics and Computer Science, Faculty of Science and Technology, Rajamangala, University of Technology Thanyaburi (RMUTT), Pathumthani 12110, Thailand*
[2]*Department of Software, Sejong Unversity, Seoul 05006, Republic of Korea*
[3]*Department of Mathematics, Faculty of Science, King Khalid University, Abha 61413, Saudi Arabia*
[4]*Department of Mathematics, Abdul Wali Khan University, Mardan 23200, Pakistan*
[5]*Department of Mathematics, Faculty of Science, AL-Azhar University, Assiut, Egypt*
[6]*Department of Mathematics and Statistics, College of Science, Taif University, P O. Box 11099, Taif 21944, Saudi Arabia*
[7]*Central Department of Mathematics, Tribhuvan University, Kritipur, Nepal*

Correspondence should be addressed to Jeevan Katle; jeevan.kafle@cdmath.tu.edu.np

Received 1 May 2021; Revised 19 May 2021; Accepted 2 November 2021; Published 27 November 2021

Academic Editor: Dan Selişteanu

In this article, a modified method called the Elzaki decomposition method has been applied to analyze time-fractional Zakharov–Kuznetsov equations. In this method, the Adomian decomposition technique and Elzaki transformation are combined. Two problems are investigated to show and validate the efficiency of the suggested method. It is also shown that the solutions achieved from the current producer are in good contact with the exact solutions to show with the help of graphs and table. It is observed that the suggested technique is to be reliable, efficient, and straightforward to implement for many related models of engineering and science.

1. Introduction

Nonlinear fractional partial differential equations play important role in demonstrating different physical appearances identified with solid-state physics, fluid mechanics, chemical kinetics, population dynamics, plasma physics, nonlinear optics, protein chemistry, soliton theory, etc. These nonlinear problems, just as their scientific arrangements, are of tremendous enthusiasm for suitable subjects. In many above-discussed science and engineering areas, the nonlinear problems perform a key factor in many phenomena. Differential equations demonstrate several frameworks and the majority of them are nonlinear [1–4].

The Zakharov–Kuznetsov (ZK) equation is an extremely appealing model equation for investigating vortices in geophysical streams. The ZK problems show up in numerous regions of material science, implemented arithmetic, and designing. Specifically, it appears in the territory of quantum physics [5–9]. The ZK problems administer the conduct of feebly nonlinear particle acoustic plasma waves, including cold particles and hot isothermal electrons within sight of a smooth magnetic field [10, 11]. Solitary wave arrangements were produced by determining the nondirect higher order of broadened KdV conditions for the free surface removal [12]. By utilizing fractional strategy, the precise expository structures of some nonlinear advancement equations in numerical material science, to be specific, space time-fractional Zakharov–Kuznetsov and modified Zakharov–Kuznetsov equations, were obtained [13]. It has been investigated in the past decades by many with the

techniques such as new iterative Sumudu transform method [14], homotopy perturbation transform method [15], extended direct algebraic method [16], natural decomposition method, and q-homotopy analysis transform method [17].

In the last three decades, fractional differential conditions have picked up importance and ubiquity, mostly since its exhibited uses in various fields of material science and design. Numerous significant phenomena in electromagnetics, acoustics, viscoelasticity, electrochemistry and material science, likelihood and measurements, electrochemistry of erosion, concoction physical science, and sign preparation are depicted in fractional differential equations [18–23]. Consequently, special consideration has been given to discover solutions of fractional differential equations.

The investigation of these equations and their solutions has extraordinary enthusiasm for numerous specialists because of its different applications. To refer to a couple, Wazwaz [24] used the Adomian disintegration strategy as a dependable method for treating Schrodinger conditions. In Wazwaz [25], the variational emphasis technique was utilized to obtain specific solutions for both linear and nonlinear Schrodinger equations. Additionally, Shah et al. [26] utilized He's recurrence definition as a technique to look for Schrodinger equations arrangements. The arrangements decided to end up being in good concurrence with the outcomes decided in [24, 25]. Notwithstanding, we mean to couple the Elzaki transform built up as late by Elzaki [27] with the commended technique for the 80th Adomian decay strategy [28, 29]. Recently, many researchers obtained the results of FPDEs; interested readers can see [30–36].

In this present work, the Elzaki decomposition technique is applied to investigate the result of the fractional-order ZK equation. The fractional derivatives are defined by the Caputo operator. The result of the given problems shows the validity of the suggested method. The solutions of the suggested technique are analyzed and shown with the help of the table and figures. Applying the current method, the results of time-fractional equations and integral-order equations are investigated. The given method is very helpful in solving other fractional-order of PDEs.

2. Basic Definitions

2.1. Definition. The fractional-order Riemann–Liouville $\rho > 0$, of a function $f \in C_1$, $\rho \geq -1$, is given as [27]

$$J^{\rho} h(\xi) = \frac{1}{\Gamma(\rho)} \int_0^{\xi} (\xi - 1)^{\rho-1} h(\eta) \partial\eta \ , \quad \rho, \xi > 0,$$
$$J^{\rho} h(\xi) = h(\xi). \tag{1}$$

The operator of some properties:

For $h \in C_1$, $\rho \geq -1$, $\rho, \beta \geq 0$, and $\rho > -1$,

$$J^{\rho} J^{\beta} h(\xi) = J^{\rho+\beta} h(\xi),$$
$$J^{\rho} J^{\beta} h(\xi) = J^{\rho} J^{\beta} h(\xi),$$
$$J^{\beta} \xi^{\rho} = \frac{\Gamma(\rho + 1)}{(\beta + \rho + 1)} \xi^{\beta+\rho}. \tag{2}$$

2.2. Lemma. If $\imath - 1 < \rho \leq \imath$, $\imath \in \mathrm{N}$ and $h \in C_1$, $\rho \geq -1$, then $D^{\rho} J^{\rho} h(\xi) = h(\xi)$ [18–20],

$$D^{\rho} J^{\rho} h(\xi) = h(\xi) - \sum_{\imath=0}^{m-1} h^{(\imath)}(0) \frac{\xi^{\imath}}{\imath!}, \quad \xi > 0. \tag{3}$$

The basic theory of the Elzaki transformation:

A new transform called the Elzaki transform defines the function exponential order that we found in the set A, define by [27]

$$A = \left\{ h(\mathfrak{I}) \colon \sum \left| M, k_1, k_2 > 0, \left| h(\mathfrak{I}) \right| < M e^{|\mathfrak{I}|/k_{\imath}}, \quad \text{if } (\mathfrak{I}) \in (-\imath)^{\imath} \times [0, \infty). \right. \right. \tag{4}$$

The finite number M must be constant, k_1 and k_2 of infinite or finite, for a specified function in the set. The Elzaki transformation is defined throughout the following integral problem:

$$\mathrm{E}[h(\mathfrak{I})] = T(s) = s\int_0^{\infty} h(\mathfrak{I})e^{-\mathfrak{I}/s}\mathrm{d}\mathfrak{I}, \quad \mathfrak{I} \geq 0, k_1 \leq s \leq k_2. \tag{5}$$

We can obtain the next solution from the explanation and the basic investigation

$$\begin{aligned} E[\mathfrak{I}^n] &= m!s^{m+2}, \\ E[h'(\mathfrak{I})] &= \frac{T(s)}{s} - sh(0), \\ E[h''(\mathfrak{I})] &= \frac{T(s)}{s^2} - h(0) - sh'(0), \\ E\left[h^{(m)}(\mathfrak{I})\right] &= \frac{T(s)}{s^m} - \sum_{k=0}^{n-1} s^{2-m+k}h^{(k)}(0). \end{aligned} \tag{6}$$

2.3. Theorem. The Elzaki Riemann–Liouville transform of the derivative can be defined as given if $T(s)$ is the Elzaki transformation of $(\mathfrak{I})$ [27]:

$$E[D^{\rho}h(\mathfrak{I})] = s^{-\rho}\left[T(s) - \sum_{k=1}^{m}\left\{D^{\rho-k}h(0)\right\}\right], \quad -1 < m-1 \leq \rho < m. \tag{7}$$

proof. Taking the Laplace transformation of $h\prime(\mathfrak{I}) = d/\mathrm{d}\mathfrak{I}h(\mathfrak{I})$, we have

$$\begin{aligned} L[D^{\rho}h(\mathfrak{I})] &= s^{\rho}T(s) - \sum_{k=0}^{m-1} s^k\left[D^{\rho-k-1}h(0)\right] \\ &= s^{\rho}T(s) - \sum_{k=0}^{m-1} s^{k-1}\left[D^{\rho-k}h(0)\right] = s^{\rho}T(s) - \sum_{k=0}^{m-1} s^{k-2}\left[D^{\rho-k}h(0)\right] \\ &= s^{\rho}T(s) - \sum_{k=0}^{m-1} \frac{1}{s^{-k+2}}\left[D^{\rho-k}h(0)\right] = s^{\rho}T(s) - \sum_{k=0}^{m-1} \frac{1}{s^{\rho-k+2-\rho}}\left[D^{\rho-k}h(0)\right] \\ &= s^{\rho}T(s) - \sum_{k=0}^{m-1} s^{\rho}\frac{1}{s^{\rho-k+2}}\left[D^{\rho-k}h(0)\right] \\ L[D^{\rho}h(\mathfrak{I})] &= s^{\rho}\left[T(s) - \sum_{k=0}^{m-1}\left(\frac{1}{s}\right)^{\rho-k+2}\left[D^{\rho-k}h(0)\right]\right]. \end{aligned} \tag{8}$$

Therefore, the fractional-order Elzaki transform of $h(\mathfrak{I})$ is

$$E[D^{\rho}h(\mathfrak{I})] = s^{-\rho}\left[T(s) - \sum_{k=0}^{m}(s)^{\rho-k+2}\left[D^{\rho-k}h(0)\right]\right]. \tag{9}$$

□

2.4. Definition. Using Theorem 1, the fractional Caputo ET is provided as [18–20]

$$\mathrm{E}\left[D_{\mathfrak{I}}^{\rho}g(\mathfrak{I})\right] = s^{\rho}\mathrm{E}[g(\mathfrak{I})] - \sum_{k=0}^{\imath-1} s^{2-\rho+k}g^{(k)}(0), \quad \text{where } \imath - 1 < \rho < \imath. \tag{10}$$

3. The General Implementation of Elzaki Decomposition Technique

In this section, we present the Elzaki decomposition technique producer for fractional partial differential equation.

$$D^{\rho}\Psi(\xi,\mathfrak{I})+L\Psi(\xi,\mathfrak{I})+N\Psi(\xi,\mathfrak{I})=q(\xi,\mathfrak{I}),\quad \xi,\mathfrak{I}\geq 0, \imath-1<\rho<\imath, \tag{11}$$

and the initial condition is

$$\Psi(\xi,0)=k(\xi). \tag{12}$$

Applying the Elzaki transform to equation (11), we get

$$E\left[D^{\rho}\Psi(\xi,\mathfrak{I})\right]+E[L\Psi(\xi,\mathfrak{I})+N\Psi(\xi,\mathfrak{I})]=E[q(\xi,\mathfrak{I})]. \tag{13}$$

Using the Elzaki transform differentiation property,

$$\begin{gathered}\frac{1}{s^{\rho}}E[\Psi(\xi,\mathfrak{I})]-s^{2-\rho}\Psi(\xi,0)=E[q(\xi,\mathfrak{I})]-E[L\Psi(\xi,\mathfrak{I})+N\Psi(\xi,\mathfrak{I})]\\ E[\Psi(\xi,\mathfrak{I})]=s^{2}\Psi(\xi,0)+s^{\rho}E[q(\xi,\mathfrak{I})]-s^{\rho}E[L\Psi(\xi,\mathfrak{I})+N\Psi(\xi,\mathfrak{I})].\end{gathered} \tag{14}$$

Now, $\Psi(\xi,0)=k(\xi)$ and hence

$$E[\Psi(\xi,\mathfrak{I})]=s^{2}k(\xi)+s^{\rho}E[q(\xi,\mathfrak{I})]-s^{\rho}E[L\Psi(\xi,\mathfrak{I})+N\Psi(\xi,\mathfrak{I})], \tag{15}$$

where $\Psi(\xi,\mathfrak{I})$ is defined as

$$\Psi(\xi,\mathfrak{I})=\sum_{\imath=0}^{\infty}\Psi_{\imath}(\xi,\mathfrak{I}). \tag{16}$$

The nonlinearity of Adomian polynomials terms N is defined as

$$N\Psi(\xi,\mathfrak{I})=\sum_{\imath=0}^{\infty}A_{\imath}, \tag{17}$$

$$A_{\imath}=\frac{1}{\imath!}\left[\frac{d^{\imath}}{d\lambda^{\imath}}\left[N\sum_{\imath=0}^{\infty}\left(\lambda^{\imath}\Psi_{\imath}\right)\right]\right]_{\lambda=0},\quad \imath=0,1,2,\ldots. \tag{18}$$

Putting equation (16) and (17) into (15), we have

$$E\left[\sum_{\imath=0}^{\infty}\Psi_{\imath}(\xi,\mathfrak{I})\right]=s^{2}k(\xi)+s^{\rho}E[q(\xi,\mathfrak{I})]-s^{\rho}E\left[L\sum_{\imath=0}^{\infty}\Psi_{\imath}(\xi,\mathfrak{I})+\sum_{\imath=0}^{\infty}A_{\imath}\right]. \tag{19}$$

Now using EDM, we have

$$E\left[\Psi_{0}(\xi,\mathfrak{I})\right]=s^{2}k(\xi)+s^{\rho}E[q(\xi,\mathfrak{I})]. \tag{20}$$

Generally, we can write

$$E\left[\Psi_{\imath+1}(\xi,\mathfrak{I})\right]=-s^{\rho}E\left[L\Psi_{\imath}(\xi,\mathfrak{I})+A_{\imath}\right],\quad \imath\geq 1. \tag{21}$$

Taking the inverse Elzaki transform of equation (21), we have

$$\begin{gathered}\Psi_{0}(\xi,\mathfrak{I})=k(\xi)+E^{-1}\left[s^{\rho}E[q(\xi,\mathfrak{I})]\right],\\ \Psi_{\imath+1}(\xi,\mathfrak{I})=-E^{-1}\left[s^{\rho}E\left[L\Psi_{\imath}(\xi,\mathfrak{I})+A_{\imath}\right]\right].\end{gathered} \tag{22}$$

4. Main Results

Example 1. Consider the two-dimensional Zakharov–Kuznetsov equation as

$$D_{\mathfrak{I}}^{\rho}\Psi+\left(\Psi^{2}\right)_{\xi}+\frac{1}{8}\left(\Psi^{2}\right)_{\xi\xi\xi}+\frac{1}{8}\left(\Psi^{2}\right)_{\xi\zeta\zeta}=0,\quad 0<\rho\leq 1, \tag{23}$$

and the initial condition is

$$\Psi(\xi,\zeta,0)=\frac{4}{3}\eta\sinh^{2}(\xi+\zeta), \tag{24}$$

where η is an arbitrary constant.

Taking Elzaki transform of equation (23), we have

$$\begin{gathered}E\left[\frac{\partial^{\rho}\Psi}{\partial\mathfrak{I}^{\rho}}\right]=E\left[-\left(\Psi^{2}\right)_{\xi}-\frac{1}{8}\left(\Psi^{2}\right)_{\xi\xi\xi}-\frac{1}{8}\left(\Psi^{2}\right)_{\xi\zeta\zeta}\right],\\ \frac{1}{s^{\rho}}E[\Psi(\xi,\zeta,\mathfrak{I})]-s^{2-\rho}[\Psi(\xi,\zeta,0)]=E\left[-\left(\Psi^{2}\right)_{\xi}-\frac{1}{8}\left(\Psi^{2}\right)_{\xi\xi\xi}-\frac{1}{8}\left(\Psi^{2}\right)_{\xi\zeta\zeta}\right].\end{gathered} \tag{25}$$

Applying the inverse Elzaki transform, we have

$$\begin{aligned}\Psi(\xi,\zeta,\mathfrak{J}) &= E^{-1}\left(s^2\Psi(\xi,\zeta,0)\right) + E^{-1}\left[s^{\rho}E\left[-\left(\Psi^2\right)_{\xi} - \frac{1}{8}\left(\Psi^2\right)_{\xi\xi\xi} - \frac{1}{8}\left(\Psi^2\right)_{\xi\zeta\zeta}\right]\right],\\ \Psi(\xi,\zeta,\mathfrak{J}) &= \frac{4}{3}\eta\sinh^2(\xi+\zeta) + E^{-1}\left[s^{\rho}E\left[-\left(\Psi^2\right)_{\xi} - \frac{1}{8}\left(\Psi^2\right)_{\xi\xi\xi} - \frac{1}{8}\left(\Psi^2\right)_{\xi\zeta\zeta}\right]\right].\end{aligned} \tag{26}$$

Using ADM procedure, we get

$$\sum_{\imath=0}^{\infty}\Psi_{\imath}(\xi,\zeta,\mathfrak{J}) = \frac{4}{3}\eta\,\sinh^2(\xi+\zeta) + E^{-1}\left[s^{\rho}E\left[-N(\Psi)_{\xi} - \frac{1}{8}N(\Psi)_{\xi\xi\xi} - \frac{1}{8}N(\Psi)_{\zeta\zeta\xi}\right]\right], \tag{27}$$

where the nonlinear terms can be defined by Adomian polynomials in the above equations.

$$N(\Psi) = \Psi^2 = \sum_{\imath=0}^{\infty}\mathscr{A}_{\imath}(\Psi), \tag{28}$$

Adomian polynomials are given as

$$\begin{aligned}\mathscr{A}_0 &= \Psi_0^2,\\ \mathscr{A}_1 &= 2\Psi_0\Psi_1,\\ \mathscr{A}_2 &= 2\Psi_0\Psi_2 + \Psi_1^2,\\ \Psi_0(\xi,\zeta,\mathfrak{J}) &= \frac{4}{3}\eta\sinh^2(\xi+\zeta),\\ \Psi_{\imath+1}(\xi,\zeta,\mathfrak{J}) &= E^{-1}\left[s^{\rho}E\left[-\left(\sum_{\imath=0}^{\infty}\mathscr{A}_{\imath}(\Psi)\right)_{\xi} - \frac{1}{8}\left(\sum_{\imath=0}^{\infty}\mathscr{A}_{\imath}(\Psi)\right)_{\xi\xi\xi} - \frac{1}{8}\left(\sum_{\imath=0}^{\infty}\mathscr{A}_{\imath}(\Psi)\right)_{\zeta\zeta\xi}\right]\right],\end{aligned} \tag{29}$$

for $\imath = 0, 1, 2, \ldots,$

$$\begin{aligned}\Psi_1(\xi,\zeta,\mathfrak{J}) &= E^{-1}\left[s^{\rho}E\left[-\left(\Psi_0^2\right)_{\xi} - \frac{1}{8}\left(\Psi_0^2\right)_{\xi\xi\xi} - \frac{1}{8}\left(\Psi_0^2\right)_{\xi\zeta\zeta}\right]\right],\\ \Psi_1(\xi,\zeta,\mathfrak{J}) &= \left(-\frac{224}{9}\eta^2\sinh^3(\xi+\zeta)\cosh(\xi+\zeta) - \frac{32}{3}\eta^2\sinh(\xi+\zeta)\cosh^3(\xi+\zeta)\right)E^{-1}\left(s^{\rho+2}\right)\\ \Psi_1(\xi,\zeta,\mathfrak{J}) &= \left(-\frac{224}{9}\eta^2\sinh^3(\xi+\zeta)\cosh(\xi+\zeta) - \frac{32}{3}\eta^2\sinh(\xi+\zeta)\cosh^3(\xi+\zeta)\right)\frac{\mathfrak{J}^{\rho}}{\Gamma(\rho+1)}.\end{aligned} \tag{30}$$

The few terms of the given methods are

$$\begin{aligned}
\Psi_2(\xi,\zeta,\mathfrak{J}) &= E^{-1}\left[s^{\rho}E\left[-(2\Psi_0\Psi_1)_{\xi}-\frac{1}{8}(2\Psi_0\Psi_1)_{\xi\xi\xi}-\frac{1}{8}(2\Psi_0\Psi_1)_{\xi\zeta\zeta}\right]\right],\\
\Psi_2(\xi,\zeta,\mathfrak{J}) &= \frac{128}{27}\eta^3\left(1200\cosh^6(\xi+\zeta)-2080\cosh^4(\xi+\zeta)+968\cosh^2(\xi+\zeta)-79\right)\frac{\mathfrak{J}^{2\rho}}{\Gamma(2\rho+1)},\\
\Psi_3(\xi,\zeta,\mathfrak{J}) &= E^{-1}\left[s^{\rho}E\left[-\left(2\Psi_0\Psi_2+\Psi_1^2\right)_{\xi}-\frac{1}{8}\left(2\Psi_0\Psi_2+\Psi_1^2\right)_{\xi\xi\xi}-\frac{1}{8}\left(2\Psi_0\Psi_2+\Psi_1^2\right)_{\xi\zeta\zeta}\right]\right],\\
\Psi_3(\xi,\zeta,\mathfrak{J}) &= -\frac{2048}{81}\eta^4\sinh(\xi+\zeta)\cosh(\xi+\zeta)\left[88400\cosh^6(\xi+\zeta)-160200\right.\\
&\quad\left.\cosh^4(\xi+\zeta)+85170\cosh^2(\xi+\zeta)-11903\right]\frac{\mathfrak{J}^{3\rho}}{\Gamma(3\rho+1)}.
\end{aligned}\tag{31}$$

The EDM result is

$$\begin{aligned}
\Psi(\xi,\zeta,\mathfrak{J}) &= \Psi_0(\xi,\zeta,\mathfrak{J})+\Psi_1(\xi,\zeta,\mathfrak{J})+\Psi_2(\xi,\zeta,\mathfrak{J})+\Psi_3(\xi,\zeta,\mathfrak{J})+\cdots,\\
\Psi(\xi,\zeta,\mathfrak{J}) &= \frac{4}{3}\eta\sinh(\xi+\zeta)-\left(\frac{224}{9}\eta^2\sinh^3(\xi+\zeta)\cosh(\xi+\zeta)+\frac{32}{3}\eta^2\sinh(\xi+\zeta)\cosh^3(\xi+\zeta)\right)\frac{\mathfrak{J}^{\rho}}{\Gamma(\rho+1)}\\
&\quad+\frac{128}{27}\eta^3\left(1200\cosh^6(\xi+\zeta)-2080\cosh^4(\xi+\zeta)+968\cosh^2(\xi+\zeta)-79\right)\frac{\mathfrak{J}^{2\rho}}{\Gamma(2\rho+1)}-\frac{2048}{81}\eta^4\sinh(\xi+\zeta)\\
&\quad\cosh(\xi+\zeta)\left[88400\cosh^6(\xi+\zeta)-160200\cosh^4(\xi+\zeta)+85170\cosh^2(\xi+\zeta)-11903\right]\frac{\mathfrak{J}^{3\rho}}{\Gamma(3\rho+1)}+\cdots.
\end{aligned}\tag{32}$$

For $\rho = 1$, we have

$$\Psi(\xi,\mathfrak{J}) = \frac{4}{3}\eta\sinh^2(\xi+\zeta-\eta\mathfrak{J}).\tag{33}$$

In Figure 1, the exact and the EDM solutions of problem 1 at $\rho = 1$ are shown by Figures 1(a) and 1(b), respectively. From the given figures, it can be seen that both the EDM and exact results are in close contact with each other. Also, in Figures 1(c) and 1(d), the EDM solutions of problem 1 are investigated at different fractional-order $\rho = 0.8$ and 0.6. It is analyzed that time-fractional problem results are convergent to an integer order effect as time-fractional analysis to integer order. In Figure 2, the first graph shows the two dimensions of exact and analytical solutions with respect to ξ and $\mathfrak{J}$ and second one shows the different fractional-order graph with respect to ξ and $\mathfrak{J}$. Table 1 shows the different fractional-order absolute error.

Example 2. Consider the three-dimensional Zakharov–Kuznetsov equation as

$$D_{\mathfrak{J}}^{\rho}\Psi+\left(\Psi^3\right)_{\xi}+2\left(\Psi^3\right)_{\xi\xi\xi}+2\left(\Psi^3\right)_{\xi\zeta\zeta}=0,\quad 0<\rho\le 1,\tag{34}$$

and the initial condition is

$$\Psi(\xi,\zeta,0) = \frac{3}{2}\eta\sinh\left[\frac{1}{6}(\xi+\zeta)\right],\tag{35}$$

where η is an arbitrary constant.

Taking Elzaki transform of equation (34), we have

$$\begin{aligned}
E\left[\frac{\partial^{\rho}\Psi}{\partial\mathfrak{J}^{\rho}}\right] &= E\left[-\left(\Psi^3\right)_{\xi}-2\left(\Psi^3\right)_{\xi\xi\xi}-2\left(\Psi^3\right)_{\xi\zeta\zeta}\right],\\
s^{\rho}E[\Psi(\xi,\zeta,\mathfrak{J})]-s^{2-\rho}[\Psi(\xi,\zeta,0)] &= E\left[-\left(\Psi^3\right)_{\xi}-2\left(\Psi^3\right)_{\xi\xi\xi}-2\left(\Psi^3\right)_{\xi\zeta\zeta}\right].
\end{aligned}\tag{36}$$

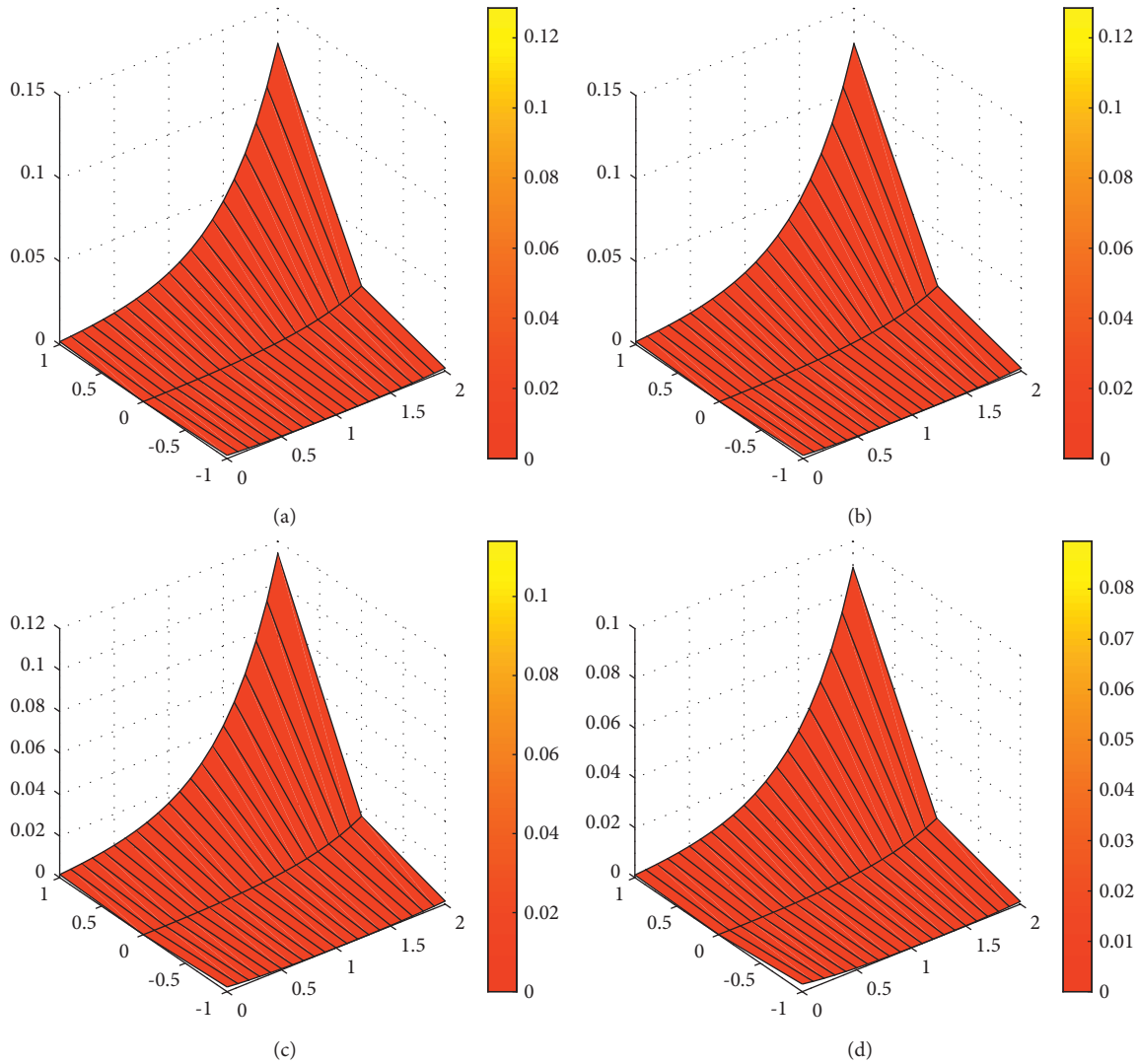

Figure 1: (a) The exact solution figure of $\Psi(\xi, \mathfrak{I})$ of Example 1. (b) The EDM solution figure of $\Psi(\xi, \mathfrak{I})$ of Example 1. (c) The graph EDM result of $\Psi(\xi, \mathfrak{I})$ at $\rho = 0.8$ problem 1. (d) The graph EDM result of $\Psi(\xi, \mathfrak{I})$ at $\rho = 0.6$ problem 1.

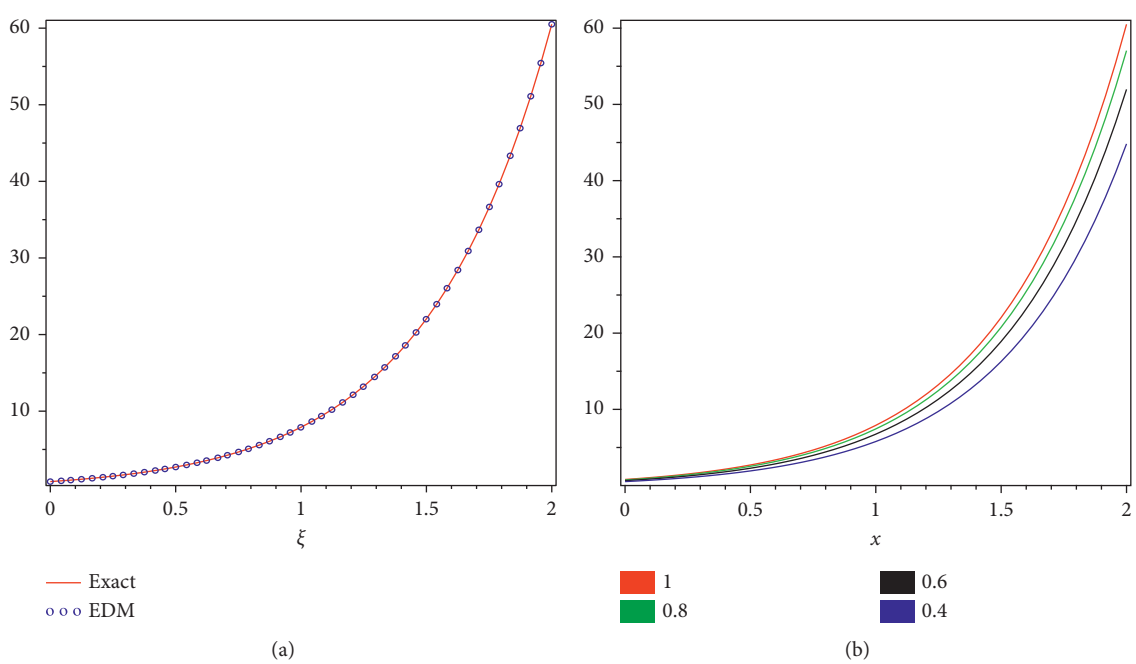

Figure 2: Continued.

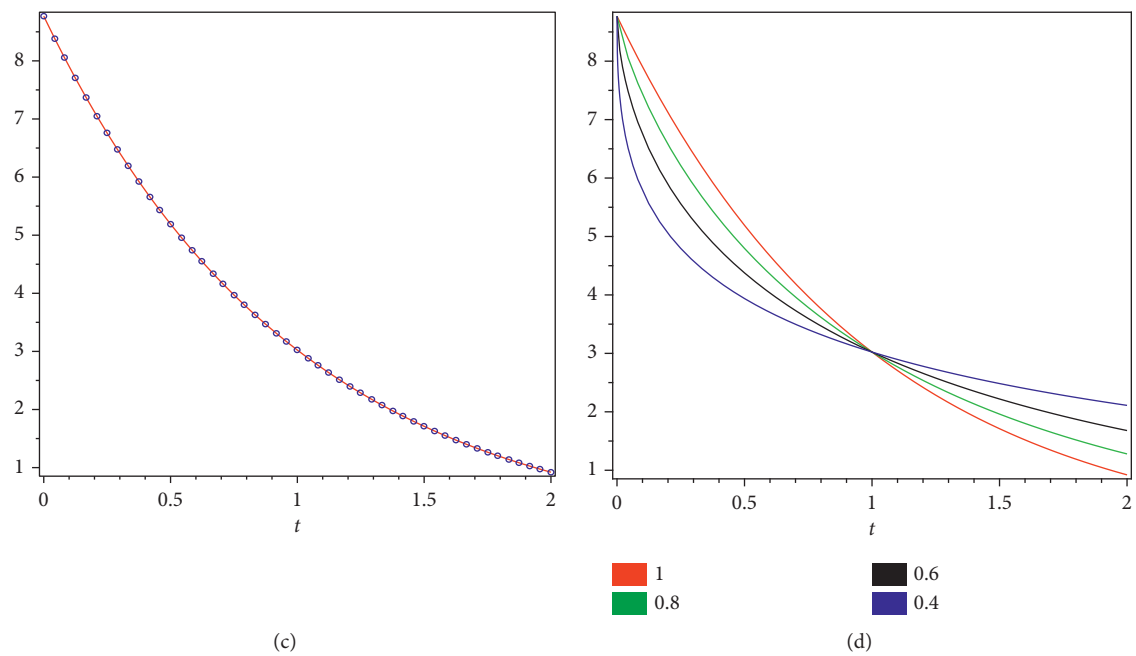

Figure 2: (a) The exact and EDM solution figure of $\Psi(\xi, \mathfrak{I})$ of Example 1. (b) The EDM solution figure of different fractional-order of ρ at $\Psi(\xi, \mathfrak{I})$ of Example 1. (c) The exact and EDM solution figure of $\Psi(\xi, \mathfrak{I})$ with respect to $\mathfrak{I}$ Example 1. (d) The EDM solution figure of different fractional-order of ρ with respect to $\mathfrak{I}$ of Example 1.

Table 1: EDM result for a different value of ρ when $\eta = 0.001$ and absolute error of Example 1.

			EDM				
ξ	ζ	$\mathfrak{I}$	$\rho = 0.6$	$\rho = 0.8$	EDM ($\rho = 1$)	Exact (E)	AE (E) ($\rho = 1$)
		0.1	$6.347977E-5$	$6.378034E-5$	$4.461135E-5$	4.488458-5	2.7323-7
0.2	0.2	0.3	$6.374898E-5$	$6.397867E-5$	$4.441928E-5$	4.499518-5	5.76800-7
		0.5	$6.329478E-5$	$6.358477E-5$	$4.393236E-5$	4.488588-5	8.92644-7
		0.1	$3.961810E-3$	$3.992936E-3$	$4.124545E-3$	4.148347-3	2.3802-5
0.5	0.5	0.3	$3.918638E-3$	$3.937942E-3$	$2.767287E-3$	2.868188-3	1.00902-4
		0.5	$2.851320E-3$	$3.986888E-3$	$3.014248E-3$	3.144685-3	1.31437-4
		0.1	$2.651681E-2$	$2.755798E-2$	$2.78556E-02$	2.864629-2	7.9069-4
1.0	1.0	0.3	$2.147458E-2$	$2.554775E-2$	$2.69884E-02$	2.863881-2	1.65041-3
		0.5	$3.686988E-3$	$3.286775E-2$	$2.55842E-02$	2.861074-2	3.02654-3

Using inverse Elzaki transformation,

$$\begin{aligned}\Psi(\xi,\zeta,\mathfrak{I}) &= E^{-1}\left[s^2\Psi(\xi,\zeta,0) + s^{\rho}E\left[-\left(\Psi^3\right)_{\xi} - 2\left(\Psi^3\right)_{\xi\xi\xi} - 2\left(\Psi^3\right)_{\xi\zeta\zeta}\right]\right],\\ \Psi(\xi,\zeta,\mathfrak{I}) &= \frac{3}{2}\eta\,\sinh\left[\frac{1}{6}(\xi+\zeta)\right] + E^{-1}\left[s^{\rho}E\left[-\left(\Psi^3\right)_{\xi} - 2\left(\Psi^3\right)_{\xi\xi\xi} - 2\left(\Psi^3\right)_{\xi\zeta\zeta}\right]\right].\end{aligned} \tag{37}$$

Applying the procedure of ADM, we get

$$\sum_{i=0}^{\infty}\Psi_i(\xi,\zeta,\mathfrak{I}) = \frac{3}{2}\eta\,\sinh\left[\frac{1}{6}(\xi+\zeta)t\right] + E^{-1}\left[s^{\rho}E\left[-N(\Psi)_{\xi} - 2N(\Psi)_{\xi\xi\xi} - 2N(\Psi)_{\xi\zeta\zeta}\right]\right], \tag{38}$$

where the nonlinear terms can be defined by Adomian polynomials in the above equations.

$$N(\Psi) = \Psi^3 = \sum_{\imath=0}^{\infty} \mathscr{B}_\imath(\Psi). \tag{39}$$

Adomian polynomials are given as

$$\begin{aligned}
\mathscr{B}_0 &= \Psi_0^3,\\
\mathscr{B}_1 &= 3\Psi_0^2\Psi_1,\\
\mathscr{B}_2 &= 3\Psi_0^2\Psi_2 + 3\Psi_0^2\Psi_1^2,\\
\Psi_0(\xi,\zeta,\mathfrak{J}) &= \frac{3}{2}\eta\,\sinh\left[\frac{1}{6}(\xi+\zeta)\right],\\
\Psi_{\imath+1}(\xi,\zeta,\mathfrak{J}) &= E^{-1}\left[s^\rho E\left[-\sum_{\imath=0}^{\infty}\mathscr{B}_\imath(\Psi)_\xi - 2\sum_{\imath=0}^{\infty}\mathscr{B}_\imath(\Psi)_{\xi\xi\xi} - 2\sum_{\imath=0}^{\infty}\mathscr{B}_\imath(\Psi)_{\xi\zeta\zeta}\right]\right],
\end{aligned} \tag{40}$$

for $\imath = 0, 1, 2, \ldots,$

$$\begin{aligned}
\Psi_1(\xi,\zeta,\mathfrak{J}) &= E^{-1}\left[s^\rho E\left[-\left(\Psi_0^3\right)_\xi - 2\left(\Psi_0^3\right)_{\xi\xi\xi} - 2\left(\Psi_0^3\right)_{\xi\zeta\zeta}\right]\right],\\
\Psi_1(\xi,\zeta,\mathfrak{J}) &= -\left[3\eta^3\sinh^2\left[\frac{1}{6}(\xi+\zeta)\right]\cosh\left[\frac{1}{6}(\xi+\zeta)\right] + \frac{3}{8}\eta^3\cosh^3\left[\frac{1}{6}(\xi+\zeta)\right]\right]E^{-1}\left(\frac{1}{s^{\rho+2}}\right),\\
\Psi_1(\xi,\zeta,\mathfrak{J}) &= -\left[3\eta^3\sinh^2\left[\frac{1}{6}(\xi+\zeta)\right]\cosh\left[\frac{1}{6}(\xi+\zeta)\right] + \frac{3}{8}\eta^3\cosh^3\left[\frac{1}{6}(\xi+\zeta)\right]\right]\frac{\mathfrak{J}^\rho}{\Gamma(\rho+1)}.
\end{aligned} \tag{41}$$

The subsequent terms are

$$\begin{aligned}
\Psi_2(\xi,\zeta,\mathfrak{J}) &= E^{-1}\left[s^\rho E\left[-\left(3\Psi_0^2\Psi_1\right)_\xi - 2\left(3\Psi_0^2\Psi_1\right)_{\xi\xi\xi} - 2\left(3\Psi_0^2\Psi_1\right)_{\xi\zeta\zeta}\right]\right],\\
&= \frac{3}{32}\eta^5\sinh\left[\frac{1}{6}(\xi+\zeta)\right]\left[765\,\cosh^4\left[\frac{1}{6}(\xi+\zeta)\right] - 729\,\cosh^2\left[\frac{1}{6}(\xi+\zeta)\right] + 91\right]\frac{\mathfrak{J}^{2\rho}}{\Gamma(2\rho+1)},\\
\Psi_3(\xi,\zeta,\mathfrak{J}) &= E^{-1}\left[s^\rho E\left[-\left(3\Psi_0^2\Psi_2 + 3\Psi_0^2\Psi_1^2\right)_\xi - 2\left(3\Psi_0^2\Psi_2 + 3\Psi_0^2\Psi_1^2\right)_{\xi\xi\xi} - 2\left(3\Psi_0^2\Psi_2 + 3\Psi_0^2\Psi_1^2\right)_{\xi\zeta\zeta}\right]\right],\\
&= -\frac{3}{128}\cosh\left[\frac{1}{6}(\xi+\zeta)\right]\left[171738\,\cosh^6\left[\frac{1}{6}(\xi+\zeta)\right] - 349884\,\cosh^4\left[\frac{1}{6}(\xi+\zeta)\right] + 215496\,\cosh^2\left[\frac{1}{6}(\xi+\zeta)\right]\right.\\
&\quad \left. - 36907\right]\frac{\mathfrak{J}^{2\rho}}{\Gamma(2\rho+1)}.
\end{aligned} \tag{42}$$

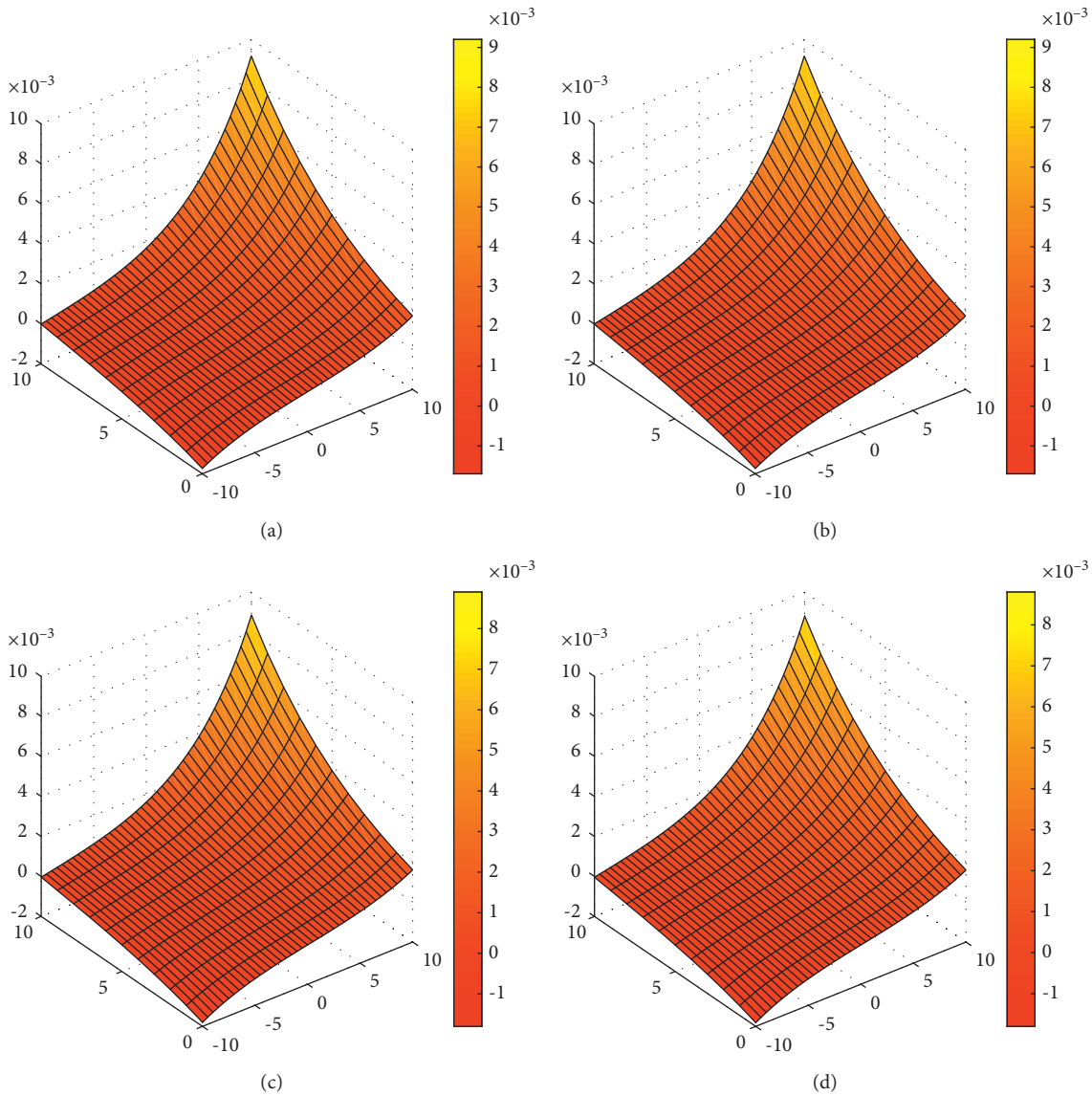

Figure 3: (a) The exact solution figure of $\Psi(\xi, \mathfrak{I})$ of Example 2. (b) The EDM solution figure of $\Psi(\xi, \mathfrak{I})$ of Example 2. (c) The EDM solution figure of $\Psi(\xi, \mathfrak{I})$ at $\rho = 0.8$ Example 2. (d) The EDM solution figure of $\Psi(\xi, \mathfrak{I})$ at $\rho = 0.6$ Example 2.

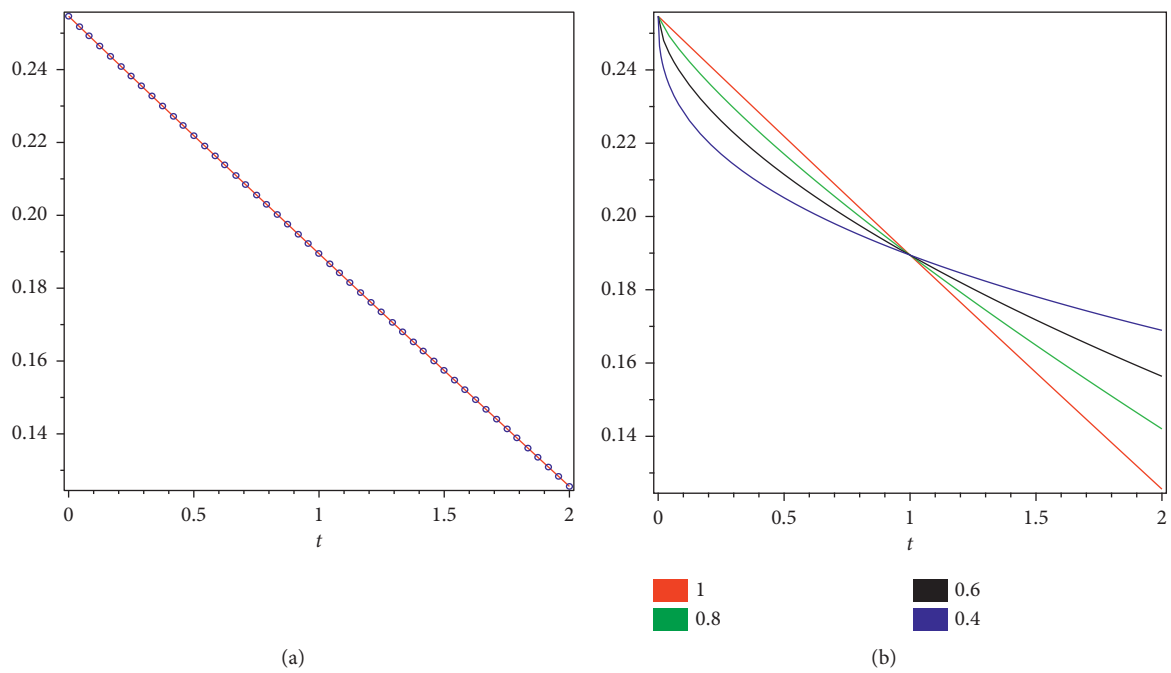

Figure 4: (a) The exact and EDM solution of $\Psi(\xi, \mathfrak{I})$ with respect to $\mathfrak{I}$ Example 1. (b) The EDM solution figure of different fractional-order of ρ with respect to $\mathfrak{I}$ of Example 1.

The EDM result is

$$\begin{aligned}
\Psi(\xi,\zeta,\mathfrak{I}) &= \Psi_0(\xi,\zeta,\mathfrak{I}) + \Psi_1(\xi,\zeta,\mathfrak{I}) + \Psi_2(\xi,\zeta,\mathfrak{I}) + \Psi_3(\xi,\zeta,\mathfrak{I}) + \cdots,\\
\Psi(\xi,\zeta,\mathfrak{I}) &= \frac{3}{2}\eta\,\sinh\left[\frac{1}{6}(\xi+\zeta)\right] - \left[3\eta^3\sinh^2\left[\frac{1}{6}(\xi+\zeta)\right]\cosh\left[\frac{1}{6}(\xi+\zeta)\right]\right.\\
&\quad \left.+\frac{3}{8}\eta^3\cosh^3\left[\frac{1}{6}(\xi+\zeta)\right]\right]\frac{\mathfrak{I}^{\rho}}{\Gamma(\rho+1)} + \frac{3}{32}\eta^5\sinh\left[\frac{1}{6}(\xi+\zeta)\right]\\
&\quad \left[765\,\cosh^4\left[\frac{1}{6}(\xi+\zeta)\right] - 729\,\cosh^2\left[\frac{1}{6}(\xi+\zeta)\right] + 91\right]\frac{\mathfrak{I}^{2\rho}}{\Gamma(2\rho+1)}\\
&\quad -\frac{3}{128}\cosh\left[\frac{1}{6}(\xi+\zeta)\right]\left[171738\,\cosh^6\left[\frac{1}{6}(\xi+\zeta)\right] - 349884\right.\\
&\quad \left.\cosh^4\left[\frac{1}{6}(\xi+\zeta)\right] + 215496\,\cosh^2\left[\frac{1}{6}(\xi+\zeta)\right] - 36907\right]\frac{\mathfrak{I}^{2\rho}}{\Gamma(2\rho+1)} + \cdots.
\end{aligned} \tag{43}$$

For $\rho = 1$,

$$\Psi(\xi,\mathfrak{I}) = \frac{3}{2}\eta\,\sinh\left[\frac{1}{6}(\xi+\zeta-\eta\mathfrak{I})\right]. \tag{44}$$

In Figure 3, the exact and the EDM solutions of Example 2 at $\rho = 1$ are shown by Figures 3(a) and 3(b), respectively. From the given figures, it can be seen that both the EDM and exact solutions are in close contact with each other. Also, in Figures 3(c) and 3(d), the EDM results of problem 2 are investigated at different fractional-order $\rho = 0.8$ and 0.6. It is analyzed that time-fractional problem results are convergent to an integer order effect as time-fractional analysis to integer order. In Figure 4, the first graph shows the two dimensions of exact and analytical solutions with respect to $\mathfrak{I}$ and the second one shows the different fractional-order graph with respect to $\mathfrak{I}$.

5. Conclusion

In this article, we investigated the time-fractional Zakharov–Kuznetsov equations using an Elzaki decomposition method. The given test examples illustrate the leverage and

effectiveness of the suggested method. The obtained solutions are demonstrated by tables and graphs. The Elzaki decomposition method solution is in close contact with the actual result of the given problems. The figures show that the time-fractional solutions obtained have verified the convergence towards the integer order solutions. Moreover, the current technique is simple and straightforward as compared to other analytical techniques; the proposed method can solve other linear and nonlinear fractional-order partial differential equations.

Data Availability

The numerical data used to support the findings of this study are included within the article.

Disclosure

Pongsakorn Sunthrayuth and Farman Ali are the co-first authors.

Conflicts of Interest

The authors declare that there are no conflicts of interest regarding the publication of this article.

Authors' Contributions

Pongsakorn Sunthrayuth and Farman Ali contributed equally to this work.

Acknowledgments

The authors extend their appreciation to the Deanship of Scientific Research at King Khalid University, Saudi Arabia, for funding this work through Research Groups Program under grant number (R.G.P2./99/41).

References

[1] A. Ekinci and M. Ozdemir, "Some new integral inequalities via riemann-liouville integral operators," *Applied and Computational Mathematics*, vol. 18, 2019.

[2] Q. Li, Z. Zheng, S. Wang, and J. Liu, *Lattice Boltzmann Model for Nonlinear Heat Equations*, Springer, Berlin, Germany, 2012.

[3] H. Khan, R. Shah, M. Arif, and S. Bushnaq, "The Chebyshev wavelet method (CWM) for the numerical solution of fractional HIV infection of CD T cells model," *International Journal of Algorithms, Computing and Mathematics*, vol. 6, no. 2, pp. 1–17, 2020.

[4] J. Nathan Kutz, J. L. Proctor, and S. L. Brunton, "Applied Koopman theory for partial differential equations and data-driven modeling of spatio-temporal systems," *Complexity*, vol. 2018, Article ID 6010634, 16 pages, 2018.

[5] V. E. Zakharov and E. A. Kuznetsov, "Three-dimensional solitons," *Soviet Physics Uspekhi*, vol. 39, pp. 285-286, 1974.

[6] A.-M. Wazwaz, "The extended tanh method for the Zakharov-Kuznetsov (ZK) equation, the modified ZK equation, and its generalized forms," *Communications in Nonlinear Science and Numerical Simulation*, vol. 13, no. 6, pp. 1039–1047, 2008.

[7] A. Biswas and E. Zerrad, "Solitary wave solution of the Zakharov-Kuznetsov equation in plasmas with power law nonlinearity," *Nonlinear Analysis: Real World Applications*, vol. 11, no. 4, pp. 3272–3274, 2010.

[8] H.-L. Zhen, B. Tian, H. Zhong, and Y. Jiang, "Dynamic behaviors and soliton solutions of the modified Zakharov-Kuznetsov equation in the electrical transmission line," *Computers & Mathematics with Applications*, vol. 68, no. 5, pp. 579–588, 2014.

[9] A. R. Seadawy, "Stability analysis for two-dimensional ion-acoustic waves in quantum plasmas," *Physics of Plasmas*, vol. 21, no. 5, Article ID 52107, 2014.

[10] A. H. Khater, D. K. Callebaut, W. Malfliet, and A. R. Seadawy, "Nonlinear dispersive Rayleigh-taylor instabilities in magnetohydrodynamic flows," *Physica Scripta*, vol. 64, no. 6, pp. 533–547, 2001.

[11] A. H. Khater, D. K. Callebaut, and A. R. Seadawy, "Nonlinear dispersive instabilities in kelvin-helmholtz magnetohydrodynamic flows," *Physica Scripta*, vol. 67, no. 4, pp. 340–349, 2003.

[12] A. R. Seadawy, "Fractional solitary wave solutions of the nonlinear higher-order extended KdV equation in a stratified shear flow: Part I," *Computers & Mathematics with Applications*, vol. 70, no. 4, pp. 345–352, 2015.

[13] S. S. Ray and S. Sahoo, "New exact solutions of fractional zakharov-kuznetsov and modified zakharov-kuznetsov equations using fractional sub-equation method," *Communications in Theoretical Physics*, vol. 63, no. 1, pp. 25–30, 2015.

[14] A. Prakash, M. Kumar, and D. Baleanu, "A new iterative technique for a fractional model of nonlinear Zakharov-Kuznetsov equations via Sumudu transform," *Applied Mathematics and Computation*, vol. 334, pp. 30–40, 2018.

[15] D. Kumar, J. Singh, and S. Kumar, "Numerical computation of nonlinear fractional Zakharov-Kuznetsov equation arising in ion-acoustic waves," *Journal of the Egyptian Mathematical Society*, vol. 22, no. 3, pp. 373–378, 2014.

[16] A. R. Seadawy, "Three-dimensional nonlinear modified Zakharov-Kuznetsov equation of ion-acoustic waves in a magnetized plasma," *Computers & Mathematics with Applications*, vol. 71, no. 1, pp. 201–212, 2016.

[17] P. Veeresha and D. G. Prakasha, "Solution for fractional Zakharov-Kuznetsov equations by using two reliable techniques," *Chinese Journal of Physics*, vol. 60, pp. 313–330, 2019.

[18] M. G. Saker, F. Erdogan, and A. Yildirim, "Variational iteration method for the time fractional Fornberg–Whitham equation," *Computers & Mathematics with Applications*, vol. 63, no. 9, pp. 1382–1388, 2012.

[19] K. S. Miller and B. Ross, *An Introduction to the Fractional Calculus and Fractional Differential Equations*, Wiley, New York, NY, USA, 1993.

[20] A. A. Kilbas, H. M. Srivastava, and J. J. Trujillo, *Theory and Applications of Fractional Differential Equations*, Elsevier, Amsterdam, Netherland, 2006.

[21] H. Khan, R. Shah, P. Kumam, B. Dumitru, and M. Arif, "Laplace decomposition for solving nonlinear system of fractional order partial differential equations," *Advances in Difference Equations*, vol. 1, pp. 1–18, 2020.

[22] M. A. E. Herzallah, M. A. El-Sayed, and D. Baleanu, "On the fractional-order diffusion-wave process," *Romanian Journal of Physics*, vol. 55, no. 3-4, pp. 274–284, 2010.

[23] D. Baleanu, O. Defterli, and O. P. Agrawal, "A central difference numerical scheme for fractional optimal control problems," *Journal of Vibration and Control*, vol. 15, no. 4, pp. 583–597, 2009.

[24] A. M. Wazwaz, "A reliable technique for solving linear and nonlinear Schrodinger equations by Adomian decomposition method," *Bulletin of institute of mathematics*, vol. 29, no. 2, pp. 125–134, 2001.
[25] A.-M. Wazwaz, "A study on linear and nonlinear Schrodinger equations by the variational iteration method," *Chaos, Solitons & Fractals*, vol. 37, no. 4, pp. 1136–1142, 2008.
[26] R. Shah, H. Khan, D. Baleanu, P. Kumam, and M. Arif, "The analytical investigation of time-fractional multi-dimensional Navier-Stokes equation," *Alexandria Engineering Journal*, vol. 59, no. 5, pp. 2941–2956, 2020.
[27] T. M. Elzaki, "The new integral transform "Elzaki Transfrom"," *Global Journal of Pure and Applied Mathematics*, vol. 7, no. 1, pp. 57–64, 2011.
[28] G. Adomian, "Solution of physical problems by decomposition," *Computers & Mathematics with Applications*, vol. 27, no. 9-10, pp. 145–154, 1994.
[29] G. Adomian, "A review of the decomposition method in applied mathematics," *Journal of Mathematical Analysis and Applications*, vol. 135, no. 2, pp. 501–544, 1988.
[30] E. Aksoy, A. C. Çevikel, and A. Bekir, "Soliton solutions of (2+1)-dimensional time-fractional zoomeron equation," *Optik*, vol. 127, no. 17, pp. 6933–6942, 2016.
[31] R. I. Nuruddeen, "Elzaki decomposition method and its applications in solving linear and nonlinear Schrodinger equations," *Sohag Journal of Mathematics*, vol. 4, no. 2, pp. 1–5, 2017.
[32] A. Akbulut and M. Kaplan, "Auxiliary equation method for time-fractional differential equations with conformable derivative," *Computers & Mathematics with Applications*, vol. 75, no. 3, pp. 876–882, 2018.
[33] K. Hosseini, A. Korkmaz, A. Bekir, F. Samadani, A. Zabihi, and M. Topsakal, "New wave form solutions of nonlinear conformable time-fractional zoomeron equation in (2+1)-dimensions," *Wave Random Complex*, vol. 31, 2019.
[34] D. Kumar and M. Kaplan, "New analytical solutions of (2 + 1)-dimensional conformable time fractional Zoomeron equation via two distinct techniques," *Chinese Journal of Physics*, vol. 56, pp. 2173–2185, 2018.
[35] H. K. Mishra and R. K. Pandey, "Time-fractional nonlinear dispersive type of the Zakharov- Kuznetsov equation via HAFSTM," *Proceedings of the National Academy of Sciences, India Section A: Physical Sciences*, vol. 91, pp. 1–14, 2020.
[36] M. Odabasi, "Traveling wave solutions of conformable time-fractional Zakharov-Kuznetsov and Zoomeron equations," *Chinese Journal of Physics*, vol. 64, pp. 194–202, 2020.

Hindawi
Complexity
Volume 2021, Article ID 9576873, 16 pages
https://doi.org/10.1155/2021/9576873

Research Article

Analytical Solution of Fractional Oldroyd-B Fluid via Fluctuating Duct

Ying Qing Song,[1] Aamir Farooq,[2] Muhammad Kamran,[3] Sadique Rehman,[4] Muhammad Tamoor,[5,6] Rewayat Khan,[2] Asfand Fahad,[7] and Muhammad Imran Qureshi[7]

[1]*School of Science, Hunan City University, Yiyang 413000, China*
[2]*Department of Mathematics, Abbottabad University of Science and Technology, Havelian 22500, Pakistan*
[3]*Department of Mathematics, COMSATS University Islamabad, Wah Campus, Islamabad 47040, Pakistan*
[4]*Department of Pure and Applied Mathematics, University of Haripur, Haripur, KPK, Haripur, Pakistan*
[5]*Key Laboratory of Green Process and Engineering, Institute of Process Engineering, Chinese Academy of Sciences, Beijing 100190, China*
[6]*University of Chinese Academy of Sciences, Beijing 100049, China*
[7]*Department of Mathematics, COMSATS University Islamabad, Vehari Campus, Vehari 61100, Pakistan*

Correspondence should be addressed to Muhammad Imran Qureshi; imranqureshi18@gmail.com

Received 25 April 2021; Revised 1 June 2021; Accepted 24 October 2021; Published 22 November 2021

Academic Editor: Muhammad Imran Asjad

This investigation focuses on the mixed initial boundary value problem with Caputo fractional derivatives. The studied pour an incompressible fractionalized Oldroyd-B fluid prompted by fluctuating rectangular tube. The explicit expression of the velocity field and shear stresses for the fractional model are obtained by utilizing the integral transforms, i.e., double finite Fourier sine transform and Laplace transform. Furthermore, the confirmation of the analytical solutions is also analyzed by utilizing the Tzou's and Stehfest's algorithms in the tabular form. In limited cases, ordinary Oldroyd-B fluid similar solutions and classical Maxwell and fractional Maxwell fluid are derived. The flow field's graphs with the influences of relevant parameters are also mentioned.

1. Introduction

The liquids which change their viscosity under force to either more liquid or solid are famous. These liquids are known as non-Newtonian fluids. The understanding can be improved by studying such types of fluids. A French physicist and engineer along with a mathematician named (Anglo-Irish, Claude-Louis Navier, and George Gabriel Stokes) described fluid flow through its environment. After it, these equations are known by their names like the Navier–Stokes equations. Navier–Stokes equations could describe the form and presentation of non-Newtonian fluids' flow quite well. These were proved useful in various areas of science and engineering. Petroleum engineers reveal how oil flows from well or pipe using mathematical modeling exactly in the same way as biomedical investigators for blood flow Non-Newtonian fluids have gained prominence because of their many uses in commerce and architecture, as well as medicine.

The non-Newtonian behavior understanding is generally more complicated than the Newtonian one. According to Hartnett and Kostic [1], in non-Newtonian fluids, the theoretical predictions yield low estimates of the heat transfer under laminar flow conditions. The motion of non-Newtonian fluid in containers is a very functional issue in dynamics. First, Stokes [2] presented the precise result of oscillatory motion in a classical linearly viscous fluid. Rajagopal [3] answered the models of non-Newtonian fluids in regards to their motion. Rajagopal and Bhatnagar [4] studied the Oldroyd-B fluid solutions in Bessel function for torsional and the longitudinal oscillations of an enormously

lengthy dowel. Mahmood et al. [5] used Laplace and finite Hankel transform and acquired the exact velocity's solutions and sinusoidal shear stress corresponding to second-grade fluid's flow. Hayat et al. [6] found out the five particular results used for the problems of an Oldroyd-B fluid, i.e., (i) Stokes problem, (ii) modified Stokes problem, (iii) the time-periodic Poiseuille flow due to an oscillating pressure gradient, (iv) the nonperiodic flows between two boundaries, and (v) symmetric flow with an arbitrary initial velocity.

In the last decades, fractional calculus (FC) underwent intensive research and development [7]. The working and comprehension of artificial and characteristic frameworks require the conventional derivative and integral which are significant for innovation experts. The derivative operators and calculus integral can be characterized by fractional calculus which is the field of math wherein the fractional powers are utilized instead of integer powers. Therefore, noninteger derivatives are portrayed by some memory impacts that are imparted to various materials such as polymers and viscoelastic materials and furthermore its uses in anomalous diffusions. By [8], we obtained exact solutions using an expansion theorem of Steklov for flows satisfying no-slip boundary conditions. Waters and King [9] evaluated the exact solution with the Laplace transform. They investigated that the velocity sketches intensely subject to the flexible parameters and fluctuates approximately on their central position. Wood [10] studied start-up helical flows for Oldroyd-B in straight tubes of the annular and rounded cross-section. They added that the fluid is originally at rest for completing the process of the solution.

Electromagnetic, viscoelasticity, fluid mechanics, electrochemistry, biological population models, optics, and signal processing are just a few of the engineering and science fields where fractional calculus is used. Ray et al. [11] discussed fractional calculus as a modeling tool for engineering and physical advancements that are defined vigorously by fractional differential equations. Systems that require precise damping modeling used fractional derivative models to accurately model it. Various analytical and numerical techniques, as well as their presentations to new complications, have been projected in these fields [12, 13].

Researches in fluid flow problems are present in terms of fractional derivatives. They had observed the influence of fractional parameters on the flow profiles [14, 15]. They referred to the obtained governing equations as fractional partial differential equations. Moreover, through discrete Laplace transform and Fourier transform along with some well-known special functions, they got precise results [16]. Few scholars considered Oldroyd-B fluid for various models in terms of fractional derivatives. Fetecau et al. [17, 18] solved Stokes's first problem of the velocity profile and the related tangential tension parallel to an Oldroyd-B fluid flow above abruptly stimulated smooth bowl analytically. Fetecau et al. [19] investigated the tangential pressures and velocity field between two perpendicular walls in the trembling flow of Oldroyd-B fluid by continuously accelerating a plate. They obtained the exact solution with the utilization of the Fourier transform method. Different geometries exist in different types of solutions. In industry, ducts are normally used for managing different flows. Therefore, as a prime process part in industrial units, it gained high importance. The rotational flow of fractional Oldroyd-B fluid in cylindrical domains was studied in [20, 21]. Fetecau and Fetecau [22] used a rectangular cross-sectional channel and introduced precise results for two different kinds of trembling flows of an Oldroyd-B fluid. Nazar et al. [23] determined sine oscillations of the rectangular tube through studying the mandatory time-period to reach the steady-state. Riaz et al. [21] used fractional derivatives and investigated the rotating flow of an Oldroyd-B fluid caused by an infinite circular tube with a continuous couple. Ghada and Ahmed [24] find out the trembling flow of broad Oldroyd-B fluid by studying the analytic solution and the flow of fluid was in the oscillating rectangular tube.

Furthermore, Wang et al. [25] used an extended rectangular cross-sectional tube and investigated the vibratory flow of Maxwell fluid. The exact solution's singularities and appropriate expressions of velocity and phase variation were studied clearly. Sun et al. [26] used an isosceles right triangular cross-sectional lengthy tube and modeled the vibratory flow of the Maxwell fluid. They obtained analytical terms for the flow compelled by the periodic pressure gradient. Farooq et al. [27] studied the generalized Maxwell fluid flow with magnetic and porous factors via quadrilateral duct. Sultan et al. [28] found out the trembling magnetohydrodynamic (MHD) flow of Oldroyd-B fluid through analytic solution in a permeable rectangular cross-section. Some studies related to time-fractional derivatives have obtained interesting results of such flow problems [29–35]. This paper aims to express the oscillatory motion of an Oldroyd-B fluid through a rectangular duct. The unsteady boundary layer equations of Oldroyd-B fluid are formulated. Then, the exact solutions are derived for the comprehensive Oldroyd-B fluid through integral transform. More precisely, the researchers want to know the relation of the vibratory motion of the fractionalized Oldroyd-B fluid by discovering the shear stress and velocity motion, and the first "time" derivative of the velocity is taken "zero" as its extra condition to simplify the model at time $t = 0$. Furthermore, the effects and features are graphically represented that are relevant to velocity field's parameters.

The remainder of this article is designed in such a way that, after the introduction, the statement of the problem is discussed in Section 2. In Section 3, we presented the exact solution of related velocity field and tangential stresses specific to Oldroyd-B fluid inside a vibratory rectangular tube with fractional derivatives. Section 4 discusses limited cases of the fractional Oldroyd-B fluid. The graphical results and the derived exact solutions compared with numerical results are investigated in Section 5. The conclusion of the paper is presented in Section 6. Also, see Table 1 for the dimension of the physical parameters.

2. Statement of the Problem

This paper considers the incompressible fractional Oldroyd-B fluid (FOBF) in the quadrilateral tube in Figure 1. The dimensions of the sides are $\mathscr{X} = 0$, $\mathscr{X} = d$, $\mathscr{Y} = 0$, and

Table 1: Nomenclature.

Symbols	Quantity
Ω	$\mathscr{Z}$-direction velocity (ms^{-1})
λ_1	Relaxation time (s)
λ_2	Retardation time (s)
μ	Dynamic viscosity ($kgm^{-1}s^{-1}$)
U_0	Amplitude (m)
ω	Angular frequency ($rads^{-1}$)
d	Length of duct (m)
h	Height of duct (m)
ρ	Density of fluid (kgm^{-3})
α, β	Fractional parameters
LT	Laplace transform
$\mathbf{V}$	Velocity of fluid (ms^{-1})
$\mathbf{S}$	Tangential stress (Nm^{-2} or Pa)
p	Pressure ($kgm^{-1}s^{-2}$)

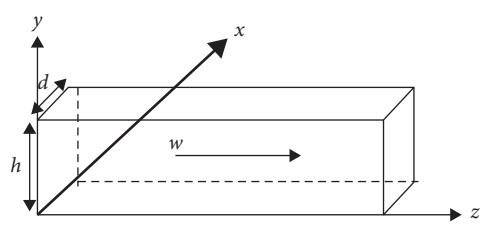

Figure 1: Flow through rectangular duct.

$\mathscr{Y} = h$. At time $t = 0^+$, the tube starts to vibrate along $\mathscr{Z}$-axis. Due to these oscillations, an oscillatory motion in fluid gets started inside along the duct's boundary. The considered velocity field and tangential stress are as follows:

$$\mathbf{V}(\mathscr{X}, \mathscr{Y}, \mathscr{Z}) = \mathbf{\Omega}(\mathscr{X}, \mathscr{Y}, t)\mathbf{k} = (0, 0, \Omega)\mathbf{S} = \mathbf{S}(\mathscr{X}, \mathscr{Y}, t), \tag{1}$$

where $\mathbf{k}$ is the unit vector aiming in $\mathscr{Z}$-direction. Remember the first $\mathbf{B}$ kinematic tensor can be given from Rivlin-Ericksen as

$$\mathbf{B} := \nabla\mathbf{V} + (\nabla\mathbf{V})^{\dagger}, \tag{2}$$

where † represents the operation transpose. The stress tensor $\mathbf{T}$ is

$$\mathbf{T} := -p\mathbf{I} + \mathbf{S}. \tag{3}$$

This equation indicates p, $\mathbf{I}$, and $\mathbf{S}$ which are the hydrostatic pressure, identity tensor, and extra stress tensor, respectively. The extra stress tensor [36] can be written as by the following relation:

$$(1 + \lambda_1\mathscr{D}_t)[\mathbf{S}] = \mu(1 + \lambda_2\mathscr{D}_t)[\mathbf{B}]. \tag{4}$$

In (4) $\mu > 0$, λ_1 and λ_2 are the dynamic viscosity, relaxation time, and retardation time, respectively. The operator denotes the Oldroyd derivative [36] $\mathscr{D}_t$ and is given below

$$\mathscr{D}_t[\mathbf{S}] := \partial_t\mathbf{S} + (\mathbf{V}.\nabla)\mathbf{S} + (\nabla\mathbf{V})\mathbf{S} + \mathbf{S}(\nabla\mathbf{V})^{\dagger}. \tag{5}$$

Furthermore, the initial conditions for the considered fluid flow are

$$\mathbf{S}(\mathscr{X}, \mathscr{Y}, 0) = 0 = \partial_t\mathbf{S}(\mathscr{X}, \mathscr{Y}, 0). \tag{6}$$

The assumed governing equations for an incompressible fluid system are

$$\begin{aligned} \nabla.\mathbf{V} &= 0, \\ \rho[\partial_t\mathbf{V} + (\mathbf{V}.\nabla)\mathbf{V}] &= \nabla.\mathbf{S}, \end{aligned} \tag{7}$$

while $\rho > o$; for ease, body strength and pressure gradient are overlooked.

2.1. Flow Problem. Firstly, the researchers carefully weighed the flow of Oldroyd-B fluid and the possible constitutive equations for it. Then, after the exact modification, the researchers found out the desired results for the fluids' flow. (1) satisfies the equation of continuity, i.e., (6). While (1), (2) and (4), (3), together with the initial conditions, i.e., (5), we can get for all $t > 0$,

$$S_{xx} = S_{yy} = 0, \tag{8}$$

$$(1 + \lambda_1\partial_t)S_{xz} = \mu(1 + \lambda_2\partial_t)\partial_{\mathscr{X}}\Omega, \tag{9}$$

$$(1 + \lambda_1\partial_t)S_{yz} = \mu(1 + \lambda_2\partial_t)\partial_{\mathscr{Y}}\Omega. \tag{10}$$

Using the same procedure [28] and with the help of (1) and (8)–(10), we can reduce (7) to

$$\rho(1 + \lambda_1\partial_t)\partial_t\Omega = \mu(1 + \lambda_2\partial_t)\left(\partial^2_{\mathscr{X}}\Omega + \partial^2_{\mathscr{Y}}\Omega\right). \tag{11}$$

The appropriate conditions are

$$\begin{aligned} &\Omega(\mathscr{X}, \mathscr{Y}, 0) = \partial_t\Omega(\mathscr{X}, \mathscr{Y}, 0) = 0, \\ &\Omega(0, \mathscr{Y}, t) = \Omega(d, \mathscr{Y}, t) = \Omega(\mathscr{X}, 0, t) = \Omega(\mathscr{X}, h, t) \\ &\qquad = U_0H(t)\cos(\omega t), \quad t > 0, \\ &\Omega(\mathscr{X}, \mathscr{Y}, 0) = \partial_t\Omega(\mathscr{X}, \mathscr{Y}, 0) = 0, \\ &\Omega(0, \mathscr{Y}, t) = \Omega(d, \mathscr{Y}, t) = \Omega(\mathscr{X}, 0, t) = \Omega(\mathscr{X}, h, t) \\ &\qquad = U_0\sin(\omega t), \quad t > 0, \end{aligned} \tag{12}$$

where U_0 is the amplitude, $H(t)$ is a unit step function, and ω is the velocity frequency of edge. While forgetting the fractional Oldroyd-B fluid flow equations, the researchers need to change the inner time derivatives (11) with left-sided Caputo fractional time derivatives ∂_t^{α} and ∂_t^{β} for $0 < \alpha \le \beta < 1$, and it can be diverted into the model with the same original boundary conditions accurately,

$$\rho(1 + \lambda_1^{\alpha}\partial_t^{\alpha})\partial_t\Omega = \mu\left(1 + \lambda_2^{\beta}\partial_t^{\beta}\right)\left(\partial^2_{\mathscr{X}}\Omega + \partial^2_{\mathscr{Y}}\Omega\right), \tag{13}$$

where the Caputo's fractional derivative [13] is

$$D_t^{\wp}f(t) = \frac{1}{\Gamma(1 - \wp)}\int_0^t \frac{f'(\tau)}{(t - \tau)^{\wp}}\mathrm{d}\tau, \quad 0 \le \wp < 1, \tag{14}$$

and $\Gamma(.)$ is the gamma function.

To balance the dimension of (13), we bring into the power α and β on λ_1 and λ_2, respectively. Moreover, we will use the following dimensionless quantities to normalize the (13).

$$\begin{aligned}
\widehat{\mathcal{X}} &= \frac{\mathcal{X}}{d},\\
\widehat{\mathcal{Y}} &= \frac{\mathcal{Y}}{h},\\
\widehat{\Omega} &= \frac{\Omega}{u_0},\\
\widehat{t} &= \frac{\mu t}{\rho\ dh},\\
\widehat{\lambda_1} &= \frac{\mu\lambda_1}{\rho\ dh},\\
\widehat{\lambda_2} &= \frac{\mu\lambda_2}{\rho\ dh},\\
\widehat{\omega} &= \frac{\rho\ dh\ \omega}{\mu},\\
\gamma &= \frac{d}{h}.
\end{aligned} \tag{15}$$

With the help of the above dimensionless quantities and dropping the hats sign, the (13) will become

$$\left(1+\lambda_1^{\alpha}\partial_t^{\alpha}\right)\partial_t\Omega = \frac{1}{\gamma}\left(1+\lambda_2^{\beta}\partial_t^{\beta}\right)\left(\partial_{\mathcal{X}}^2\Omega+\gamma^2\partial_{\mathcal{Y}}^2\Omega\right), \tag{16}$$

$$\begin{aligned}
&\Omega(\mathcal{X},\mathcal{Y},0) = \partial_t\Omega(\mathcal{X},\mathcal{Y},0) = 0,\\
&\Omega(0,\mathcal{Y},t) = \Omega(1,\mathcal{Y},t) = \Omega(\mathcal{X},0,t),\\
&\Omega(\mathcal{X},1,t) = H(t)\cos(\omega t), \quad t>0,
\end{aligned} \tag{17}$$

or

$$\begin{aligned}
&\Omega(\mathcal{X},\mathcal{Y},0) = \partial_t\Omega(\mathcal{X},\mathcal{Y},0) = 0,\\
&\Omega(0,\mathcal{Y},t) = \Omega(1,\mathcal{Y},t) = \Omega(\mathcal{X},0,t),\\
&\Omega(\mathcal{X},1,t) = \sin(\omega t), \quad t>0.
\end{aligned} \tag{18}$$

3. Solution of Velocity Profile

3.1. $\Omega(0,\mathcal{Y},t) = \Omega(1,\mathcal{Y},t) = \Omega(\mathcal{X},0,t) = \Omega(\mathcal{X},1,t) = \sin(\omega t)$. Operating $\sin(\alpha_l\mathcal{X})\sin(\beta_n\mathcal{Y})$ on (16), then integrating concerned $\mathcal{X}$ and $\mathcal{Y}$ over $[0,1]\times[0,1]$, and utilizing the transmuted original and boundary conditions (18), we will get

$$\begin{aligned}
&\left(1+\lambda_1^{\alpha}D_t^{\alpha}\right)\partial_t\Omega_{lp}(t) + \frac{\lambda_{lp}^2}{\gamma}\left(1+\lambda_2^{\beta}D_t^{\beta}\right)\Omega_{lp}(t)\\
&= \frac{a_{lp}\lambda_{lp}^2}{\gamma}\left(1+\lambda_2^{\beta}D_t^{\beta}\right)\sin(\omega t),
\end{aligned} \tag{19}$$

where $\alpha_l = l\pi$, $\beta_p = p\pi$, $a_{lp} = [1-(-1)]^l[1-(-1)^p]/\alpha_l\beta_p$, and $\lambda_{lp}^2 = \alpha_l^2+\gamma^2\beta_p^2$, and

$$\Omega_{lp}(t) = \int_0^1\int_0^1 \Omega(\mathcal{X},\mathcal{Y},t)\sin(\alpha_l\mathcal{X})\sin\left(\beta_p\mathcal{Y}\right)\mathrm{d}\mathcal{X}\mathrm{d}\mathcal{Y}, \quad l,p = 1,2,3\ldots, \tag{20}$$

is the binary Fourier alteration of $\Omega(\mathcal{X},\mathcal{Y},t)$.

By applying Laplace transformation and appropriate transform conditions on equation (15) we will get $\overline{\Omega}_{lp}(q)$ as

$$\overline{\Omega}_{lp}(q) = \frac{a_{lp}\lambda_{lp}^2}{\gamma}\frac{\omega}{q^2+\omega^2}\frac{1+\lambda_2^{\beta}q^{\beta}}{q+\lambda_1^{\alpha}q^{\alpha+1}+\left(\lambda_{lp}^2/\gamma\right)\left(1+\lambda_2^{\beta}q^{\beta}\right)}, \tag{21}$$

or

$$\overline{\Omega}_{lp}(q) = \frac{a_{lp}\lambda_{lp}^2}{\gamma}\frac{\omega}{q^2+\omega^2}\overline{F_{lp}(q)}, \tag{22}$$

where

$$\overline{F_{lp}(q)} = \frac{1+\lambda_2^{\beta}q^{\beta}}{q+\lambda_1^{\alpha}q^{\alpha+1}+\left(\lambda_{lp}^2/\gamma\right)\left(1+\lambda_2^{\beta}q^{\beta}\right)}, \tag{23}$$

which can be written as

$$\overline{F_{lp}(q)} = \frac{\gamma}{\lambda_{lp}^2} - \frac{1+\lambda_1^{\alpha}q^{\alpha}}{1+\lambda_1^{\alpha}q^{\alpha}+\left(\lambda_{lp}^2/\gamma\right)\left(1+\lambda_2^{\beta}q^{\beta}\right)q^{-1}}\frac{\gamma}{\lambda_{lp}^2}, \tag{24}$$

and the Laplace transform of $\Omega_{lp}(t)$ is $\overline{\Omega}_{lp}(q) = \int_0^{\infty}\Omega_{lp}(t)e^{-qt}\mathrm{d}t$ (22) which becomes

$$\begin{aligned}
\overline{\Omega}_{lp}(q) &= a_{lp}\frac{\omega}{q^2+\omega^2} - a_{lp}\omega\frac{q}{q^2+\omega^2}\\
&\quad\times\frac{q^{-1}+\lambda_1^{\alpha}q^{\alpha-1}}{1+\lambda_1^{\alpha}q^{\alpha}+\left(\lambda_{lp}^2/\gamma\right)\left(1+\lambda_2^{\beta}q^{\beta}\right)q^{-1}}.
\end{aligned} \tag{25}$$

So it is denoted by

$$\overline{F}(q) = \frac{q\left(q^{-1}+\lambda_1^{\alpha}q^{\alpha-1}\right)}{q^2+\omega^2}, \tag{26}$$

and the inverse LT of the $\overline{F}(q)$ is

$$\begin{aligned}
f(t) = L^{-1}\{\overline{F}(q)\} &= \frac{\lambda_1^{\alpha}}{\Gamma(1-\alpha)}\int_0^t\frac{\cos(\omega t)}{(t-\psi)^{\alpha}}\mathrm{d}\psi\\
&\quad+\frac{\sin(\omega t)}{\omega}, \quad 0<\alpha<1.
\end{aligned} \tag{27}$$

Now, we consider the function

$$\overline{A}_{lp}(q) = \frac{1}{1+\lambda_1^{\alpha}q^{\alpha}+\left(\lambda_{lp}^2/\gamma\right)\left(1+\lambda_2^{\beta}q^{\beta}\right)q^{-1}}. \tag{28}$$

With the help of $1/(x+a) = \sum_{k=0}^{\infty}(-1)^k(x^k/a^{k+1})$, $(a+b)^k = \sum_{m=0}^{k}(k!/(k-m)!m!)a^m b^{(k-m)}$, the expression for $\overline{A}_{lp}(q)$ can be written as

$$\overline{A}_{lp}(q)=\sum_{k=0}^{\infty}\sum_{n=0}^{k}\left(\frac{-\lambda_{lp}^{2}}{\gamma}\right)^{k}\frac{k!\lambda_{2}^{\beta n}}{n!(k-n)!\lambda_{1}^{\alpha(k+1)}}\times\frac{q^{\beta n-k}}{\left(q^{\alpha}+\lambda_{1}^{-\alpha}\right)^{k+1}}. \tag{29}$$

The inverse LT of the expression (29) is

$$a_{lp}(t)=\sum_{k=0}^{\infty}\sum_{n=0}^{k}\left(\frac{-\lambda_{lp}^{2}}{\gamma}\right)^{k}\frac{k!\lambda_{2}^{\beta n}}{n!(k-n)!\lambda_{1}^{\alpha(k+1)}}\times G_{\alpha,\beta n-k,k+1}\left(-\lambda_{1}^{-\alpha},t\right), \tag{30}$$

where $G_{e,f,g}(h,t)$ is the generalized G-function as defined in [37].

$$G_{e,f,g}(h,t)=\sum_{i=0}^{\infty}\frac{d^{i}\Gamma(r+i)}{\Gamma(r)\Gamma(1+i)}\frac{t^{(r+i)a-b-1}}{\Gamma[(r+i)a-b]}. \tag{31}$$

The transformed velocity can be rewritten as

$$\overline{\Omega}_{lp}(q)=a_{lp}\frac{\omega}{q^{2}+\omega^{2}}-a_{lp}\omega\overline{F}(q)\overline{A}_{lp}(q). \tag{32}$$

The inverse LT of the (32) is

$$\Omega_{lp}(t)=a_{lp}\sin(\omega t)-a_{lp}\omega\left(f(t)*a_{lp}(t)\right), \tag{33}$$

where $f(t)*a_{lp}(t)=\int_{o}^{t}f(t-q)a_{lp}(t)\mathrm{d}q$ denotes the convolution product. Taking the inverse Fourier transform to (33) and using the formula [38], the velocity field for sin oscillation is

$$\Omega_{s}(\mathcal{X},\mathcal{Y},t)=\sin(\omega t)-4\sum_{l,p=1}^{\infty}a_{lp}\omega\sin(\alpha_{l}\mathcal{X})\sin\left(\beta_{p}\mathcal{Y}\right)\times\left(f(t)*a_{lp}(t)\right). \tag{34}$$

It can be rewritten as

$$\Omega_{s}(\mathcal{X},\mathcal{Y},t)=\sin(\omega t)-16\omega\sum_{l,p=0}^{\infty}\frac{\sin((2l+1)\pi\mathcal{X})}{(2l+1)\pi}\times\frac{\sin((2p+1)\pi\mathcal{X})}{(2p+1)\pi}\left(f(t)*a_{(2l+1)(2p+1)}(t)\right). \tag{35}$$

The dimensionless tangential stresses T_1 and T_2 associated with the fractional Oldroyd-B fluid in such motions are given by

$$\left(1+\lambda_{1}^{\alpha}D_{t}^{\alpha}\right)T_{1s}(\mathcal{X},\mathcal{Y},t)=\left(1+\lambda_{2}^{\beta}D_{t}^{\beta}\right)\partial_{\mathcal{X}}\Omega(\mathcal{X},\mathcal{Y},t), \tag{36}$$

$$\left(1+\lambda_{1}^{\alpha}D_{t}^{\alpha}\right)T_{2s}(\mathcal{X},\mathcal{Y},t)=\left(1+\lambda_{2}^{\beta}D_{t}^{\beta}\right)\partial_{\mathcal{Y}}\Omega(\mathcal{X},\mathcal{Y},t), \tag{37}$$

where $T_{1s}=\mathrm{d}S_{xz}/\mu u_{0}$ and $T_{2s}=hS_{yz}/\mu u_{0}$.

Taking the Laplace transform of (36), we can get

$$\overline{T}_{1s}(\mathcal{X},\mathcal{Y},q)=\frac{1+\lambda_{2}^{\beta}q^{\beta}}{1+\lambda_{1}^{\alpha}q^{\alpha}}\partial_{\mathcal{X}}\overline{\Omega_{s}}(\mathcal{X},\mathcal{Y},q). \tag{38}$$

Rewrite (38) as

$$\overline{T}_{1s}(\mathcal{X},\mathcal{Y},q)=\left[1+\frac{\lambda_{2}^{\beta}}{\lambda_{1}^{\alpha}}\frac{q^{\beta}}{q^{\alpha}+\lambda_{1}^{-\alpha}}-\frac{q^{\alpha}}{q^{\alpha}+\lambda_{1}^{-\alpha}}\right]\times\partial_{\mathcal{X}}\overline{\Omega}(\mathcal{X},\mathcal{Y},q), \tag{39}$$

where

$$\overline{\Omega}(\mathcal{X},\mathcal{Y},q)=\frac{\omega}{q^{2}+\omega^{2}}-16\omega\sum_{l,p=0}^{\infty}\frac{\sin((2l+1)\pi\mathcal{X})}{(2l+l)\pi}\times\frac{\sin((2p+1)\pi\mathcal{Y})}{(2p+1)\pi}\left(\overline{F}(q)\overline{A}_{(2l+1)(2p+1)}(q)\right). \tag{40}$$

Invoking $\partial_{\mathcal{X}}\overline{\Omega}(\mathcal{X},\mathcal{Y},t)$ in (40), we will get

$$\overline{T}_{1s}(\mathcal{X},\mathcal{Y},q)=\left[1+\frac{\lambda_{2}^{\beta}}{\lambda_{1}^{\alpha}}\frac{q^{\beta}}{q^{\alpha}+\lambda_{1}^{-\alpha}}-\frac{q^{\alpha}}{q^{\alpha}+\lambda_{1}^{-\alpha}}\right]\times-16\omega\sum_{l,p=0}^{\infty}\cos((2l+1)\pi\mathcal{X})\frac{\sin((2p+1)\pi\mathcal{Y})}{(2p+1)\pi}\times\left(\overline{F}(q)\overline{A}_{(2l+1)(2p+1)}(q)\right). \tag{41}$$

The inverse LT of the above relation is

$$\begin{aligned}T_{1s}(\mathcal{X},\mathcal{Y},t)=&-16\sum_{l,p=0}^{\infty}\omega\cos((2l+1)\pi\mathcal{X})\frac{\sin((2p+1)\pi\mathcal{Y})}{(2p+1)\pi}\times f(t)*a_{(2l+1)(2p+1)}(t)-\frac{16\lambda_{r}^{\beta}}{\lambda^{\alpha}}\sum_{l,p=0}^{\infty}\omega\cos\\&\cdot((2l+1)\pi\mathcal{X})\times\frac{\sin((2p+1)\pi\mathcal{Y})}{(2p+1)\pi}\cdot f(t)*g(t)*a_{(2l+1)(2p+1)}(t)\\&+16\sum_{l,p=0}^{\infty}\omega\cos((2l+1)\pi\mathcal{X})\frac{\sin((2p+1)\pi\mathcal{Y})}{(2p+1)\pi}\times f(t)*g(t)*a_{(2l+1)(2p+1)}(t).\end{aligned} \tag{42}$$

where $g(t)=L^{-1}(q^{\beta}/q^{\alpha}+\lambda_{1}^{-\alpha})=R_{\alpha,\beta}(-\lambda_{1}^{-\alpha},t)$, $h(t)=L^{-1}(q^{\alpha}/q^{\alpha}+\lambda_{1}^{-\alpha})=H(t)-(1/\lambda_{1}^{\alpha})R_{\alpha,0}(-\lambda_{1}^{-\alpha},t)$, and $R_{a,b}(e,f,t)=\sum_{p=0}^{\infty}e^{p}(t-f)^{(p+1)a-b-1}/\Gamma[(p+1)a-b]$.

Similarly, we can calculate T_{2s} from (37).

3.2. $\Omega(0,\mathcal{Y},t)=\Omega(1,\mathcal{Y},t)=\Omega(\mathcal{X},0,t)=\Omega(\mathcal{X},1,t)=H(t)\cos(\omega t)$. Operating $\sin(\alpha_{l}\mathcal{X})\sin(\beta_{p}\mathcal{Y})$ on (16), then integrating with respect to $\mathcal{X}$ and $\mathcal{Y}$ over $[0,1]\times[0,1]$, and

together with the transformed boundary conditions (17), we obtain

$$\begin{aligned}&\left(1+\lambda_1^{\alpha}D_t^{\alpha}\right)\partial_t\Omega_{lp}(t)+\frac{\lambda_{lp}^2}{\gamma}\left(1+\lambda_2^{\beta}D_t^{\beta}\right)\Omega_{lp}(t)\\&=\frac{a_{lp}\lambda_{lp}^2}{\gamma}\left(1+\lambda_2^{\beta}D_t^{\beta}\right)H(t)\cos(wt).\end{aligned}\tag{43}$$

Now, taking the LT of (43) with an appropriate transform condition, we will obtain the expression for $\overline{\Omega}_{lp}(q)$ as

$$\overline{\Omega}_{lp}(q)=\frac{a_{lp}\lambda_{lp}^2}{\gamma}\frac{q}{q^2+\omega^2}\frac{1+\lambda_2^{\beta}q^{\beta}}{q+\lambda_1^{\alpha}q^{\alpha+1}+\left(\lambda_{lp}^2/\gamma\right)\left(1+\lambda_2^{\beta}q^{\beta}\right)},\tag{44}$$

or

$$\overline{\Omega}_{lp}(q)=\frac{a_{lp}\lambda_{lp}^2}{\gamma}\frac{q}{q^2+\omega^2}\overline{F_{lp}(q)}.\tag{45}$$

Putting $F_{lp}(q)$ in (45),

$$\begin{aligned}\overline{\Omega}_{lp}(q)&=a_{lp}\frac{q}{q^2+\omega^2}-a_{lp}\frac{q}{q^2+\omega^2}\\&\quad\times\frac{1+\lambda_1^{\alpha}q^{\alpha}}{1+\lambda_1^{\alpha}q^{\alpha+1}+\left(\lambda_{lp}^2/\gamma\right)\left(1+\lambda_2^{\beta}q^{\beta}\right)q^{-1}},\end{aligned}\tag{46}$$

where $\overline{K}(q)=q(1+\lambda_1^{\alpha}q^{\alpha})/q^2+\omega^2$, the inverse LT of the $\overline{K}(q)$ is

$$\begin{aligned}k(t)=L^{-1}\{\overline{K}(q)\}&=\frac{\lambda_1^{\alpha}}{\Gamma(-\alpha)}\int_0^t\frac{\cos(\omega t)}{(t-\tau)^{\alpha+1}}\mathrm{d}\tau\\&\quad+\cos(\omega t),\quad 0<\alpha<1.\end{aligned}\tag{47}$$

Rewrite $\overline{\Omega}_{lp}(q)$,

$$\overline{\Omega}_{lp}(q)=a_{lp}\frac{q}{q^2+\omega^2}-a_{lp}\overline{K}(q)\overline{A}_{lp}(q).\tag{48}$$

The inverse LT (48) is

$$\Omega_{lp}(t)=a_{lp}\cos(\omega t)-a_{lp}\left(k(t)*a_{lp}(t)\right),\tag{49}$$

where $k(t)*a_{lp}(t)=\int_o^t f(t-s)a_{lp}(t)\mathrm{d}s$ denotes the convolution product of $k(t)$ and $a_{lp}(t)$. Taking the inverse Fourier alteration of (49) and utilizing the formula [38], the velocity profile is

$$\begin{aligned}\Omega_c(\mathcal{X},\mathcal{Y},t)&=\cos(\omega t)-4\sum_{l,p=1}^{\infty}a_{lp}\sin(\alpha_l\mathcal{X})\sin\left(\beta_p\mathcal{Y}\right)\\&\quad\times\left(k(t)*a_{lp}(t)\right).\end{aligned}\tag{50}$$

Rewrite (50),

$$\begin{aligned}\Omega_c(\mathcal{X},\mathcal{Y},t)&=\cos(\omega t)-16\sum_{l,p=0}^{\infty}\frac{\sin((2l+1)\pi\mathcal{X})}{(2l+1)\pi}\\&\quad\times\frac{\sin((2p+1)\pi\mathcal{Y})}{(2p+1)\pi}\left(k(t)*a_{(2l+1)(2p+1)}(t)\right).\end{aligned}\tag{51}$$

Using the same technique as of the above section, we can find the tangential stresses under the forms:

$$\begin{aligned}T_{1c}(\mathcal{X},\mathcal{Y},t)&=-16\sum_{l,p=0}^{\infty}\cos((2l+1)\pi\mathcal{X})\frac{\sin((2p+1)\pi\mathcal{Y})}{(2p+1)\pi}\\&\quad\times f(t)*a_{(2l+1)(2p+1)}(t)\\&\quad-\frac{16\lambda_2^{\beta}}{\lambda_1^{\alpha}}\sum_{l,p=0}^{\infty}\cos((2l+1)\pi\mathcal{X})\\&\quad\times\frac{\sin((2p+1)\pi\mathcal{Y})}{(2p+1)\pi}f(t)*g(t)*a_{(2l+1)(2p+1)}(t)\\&\quad+16\sum_{l,p=0}^{\infty}\cos((2l+1)\pi\mathcal{X})\frac{\sin((2p+1)\pi\mathcal{Y})}{(2p+1)\pi}\\&\quad\times f(t)*h(t)*a_{(2l+1)(2p+1)}(t).\end{aligned}\tag{52}$$

Similarly, we can calculate T_{2c}.

4. Limiting Cases

4.1. Classical Oldroyd-B Fluid. Creating $\alpha\longrightarrow 1$ and $\beta\longrightarrow 1$ into (35), (42), (51), and (52), we can acquire a similar solution of the velocity distribution of both cases for trembling flows of an ordinary Oldroyd-B fluid. Thus, the velocity field and shear stresses decrease to

$$\begin{aligned}\Omega s(\mathcal{X},\mathcal{Y},t)&=\sin(\omega t)-16\omega\sum_{l,p=0}^{\infty}\frac{\sin((2l+1)\pi\mathcal{X})}{(2l+1)\pi}\\&\quad\times\frac{\sin((2p+1)\pi\mathcal{Y})}{(2p+1)\pi}\left(f(t)*a_{(2l+1)(2p+1)}(t)\right),\end{aligned}$$

$$\Omega_c(\mathcal{X},\mathcal{Y},t)=\cos(\omega t)-16\sum_{l,p=0}^{\infty}\frac{\sin((2l+1)\pi\mathcal{X})}{(2l+1)\pi}$$

$$\times \frac{\sin((2p+1)\pi_Y)}{(2p+1)\pi}\left(k(t) * a_{(2l+1)(2p+1)}(t)\right),$$

$$T_{1s}(\mathcal{X},\mathcal{Y},t) = -16\sum_{l,p=0}^{\infty} \omega \cos((2l+1)\pi\mathcal{X}) \times \frac{\sin((2p+1)\pi\overline{Y})}{(2p+1)\pi} f(t) * a_{(2l+1)(2p+1)}(t)$$
$$-\frac{16\lambda_r}{\lambda}\sum_{l,p=0}^{\infty} \omega \cos((2l+1)\pi\mathcal{X}) \times \frac{\sin((2p+1)\pi\mathcal{Y})}{(2p+1)\pi} f(t) * h(t) * a_{(2l+1)(2p+1)}(t)$$
$$+16\sum_{l,p=0}^{\infty} \omega \cos((2l+1)\pi\mathcal{X}) \frac{\sin((2p+1)\pi\mathcal{Y})}{(2p+1)\pi} \times f(t) * h(t) * a_{(2l+1)(2p+1)}(t),$$

$$T_{1c}(\mathcal{X},\mathcal{Y},t) = -16\sum_{l,p=0}^{\infty} \cos((2l+1)\pi\mathcal{X}) \times \frac{\sin((2p+1)\pi\mathcal{Y})}{(2p+1)\pi} f(t) * a_{(2l+1)(2p+1)}(t)$$
$$-\frac{16\lambda_r}{\lambda}\sum_{l,p=0}^{\infty} \cos((2l+1)\pi\mathcal{X}) \times \frac{\sin((2p+1)\pi\mathcal{Y})}{(2p+1)\pi} f(t) * h(t) * a_{(2l+1)(2p+1)}(t)$$
$$+16\sum_{l,p=0}^{\infty} \cos((2l+1)\pi\mathcal{X}) \frac{\sin((2p+1)\pi\mathcal{Y})}{(2p+1)\pi} \times f(t) * h(t) * a_{(2l+1)(2p+1)}(t), \tag{53}$$

where $a_{lp}(t) = \sum_{k=0}^{\infty}\sum_{n=0}^{k}(-\lambda_{lp}^2/\gamma)^k (k!(\lambda_2^n)/n!(k-n)!\lambda_1^{(k+1)})G_{1,l-1,k+1}(-\lambda_1^{-1},t)$, $f(t) = \lambda_1\cos(\omega t) + (\sin(\omega t)/\omega)$, $k(t) = \lambda_1\cos(\omega t) + \lambda_1(H(t) - \omega\sin(\omega t))$, $\alpha = 1$, and $h(t) = L^{-1}(q/q + \lambda_1^{-1}) = H(t) - (1/\lambda_1)R_{1,0}(-\lambda_1^{-1},t)$.

4.2. Fractional Maxwell Fluid. Making $\lambda_2 \longrightarrow 0$ into (35), (42), (51), and (52), then we can acquire both cases of identical solution of velocity dispersion and shear stress for generalized Maxwell fluid's flows [38]. Thus, the velocity field and shear stresses decrease to

$$\Omega_s(\mathcal{X},\mathcal{Y},t) = \sin(\omega t) - 16\omega\sum_{l,p=0}^{\infty} \frac{\sin((2l+1)\pi\mathcal{X})}{(2l+1)\pi} \times \frac{\sin((2p+1)\pi\mathcal{Y})}{(2p+1)\pi}\left(f(t) * a_{(2l+1)(2p+1)}(t)\right),$$

$$\Omega_c(\mathcal{X},\mathcal{Y},t) = \cos(\omega t) - 16\sum_{l,p=0}^{\infty} \frac{\sin((2l+1)\pi\mathcal{X})}{(2l+1)\pi} \times \frac{\sin((2p+1)\pi\mathcal{Y})}{(2p+1)\pi}\left(k(t) * a_{(2l+1)(2p+1)}(t)\right),$$

$$T_{1s}(\mathcal{X},\mathcal{X},t) = -16\sum_{l,p=0}^{\infty} \omega \cos((2m+1)\pi\mathcal{X}) \times \frac{\sin((2p+1)\pi\mathcal{Y})}{(2p+1)\pi} f(t) * a_{(2l+1)(2p+1)}(t)$$
$$+16\sum_{l,p=0}^{\infty} \omega \cos((2l+1)\pi\mathcal{X}) \frac{\sin((2p+1)\pi\mathcal{Y})}{(2p+1)\pi} f(t) * h(t) * a_{(2l+1)(2p+1)}(t), \tag{54}$$

$$T_{1c}(\mathcal{X},\mathcal{Y},t) = -16\sum_{l,p=0}^{\infty} \cos((2l+1)\pi\mathcal{X}) \times \frac{\sin((2p+1)\pi\mathcal{Y})}{(2p+1)\pi} f(t) * a_{(2l+1)(2p+1)}(t)$$
$$+16\sum_{l,p=0}^{\infty} \cos((2l+1)\pi\mathcal{X}) \frac{\sin((2p+1)\pi\mathcal{Y})}{(2p+1)\pi} f(t) * h(t) * a_{(2l+1)(2p+1)}(t),$$

where

$$a_{lp}(t) = \sum_{k=0}^{\infty}\left(\frac{-\lambda_{lp}^2}{\gamma}\right)^k \frac{1}{\lambda_1^{\alpha(k+1)}} G_{\alpha,-1,k+1}(-\lambda_1^{-\alpha},t). \tag{55}$$

4.3. Classical Maxwell Fluid. Making $\lambda_2 \longrightarrow 0$ and $\alpha \longrightarrow 1$ into (35), (42), (51), and (52), we can acquire a similar solution of velocity distribution and shear stresses of both the cases for trembling flows of classical Maxwell fluid [23]. Thus, the velocity field and shear stresses decrease to

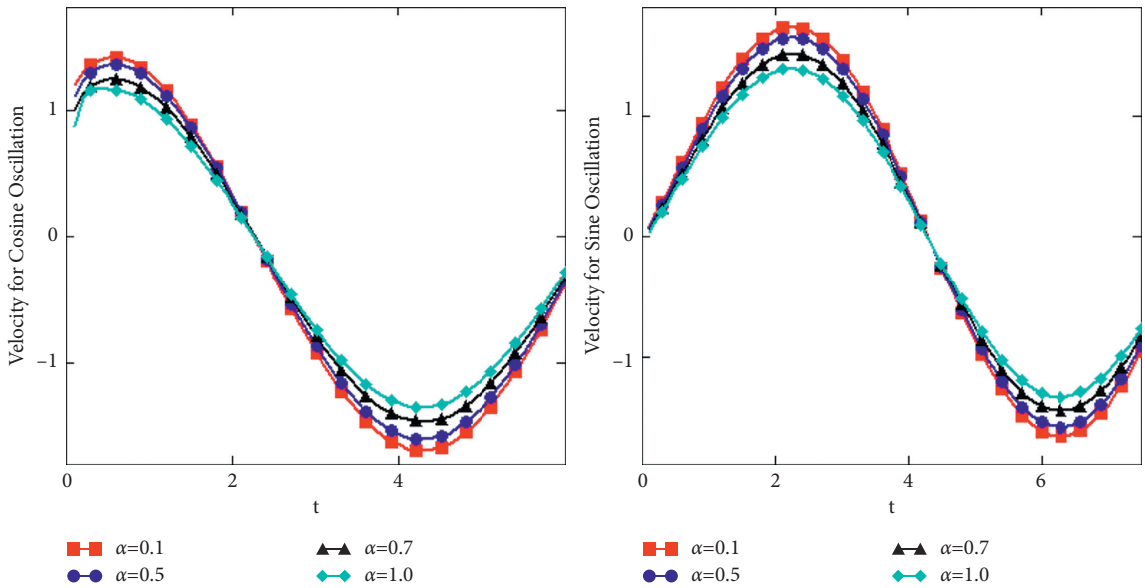

FIGURE 2: The variation of α for both the oscillations with $\omega = \pi/4$, $\lambda = 0.8$, $\lambda_r = 0.5$, $\beta = 0.8$, $\gamma = 2$, $\mathcal{X} = 0.45$, and $\mathcal{Y} = 0.1$.

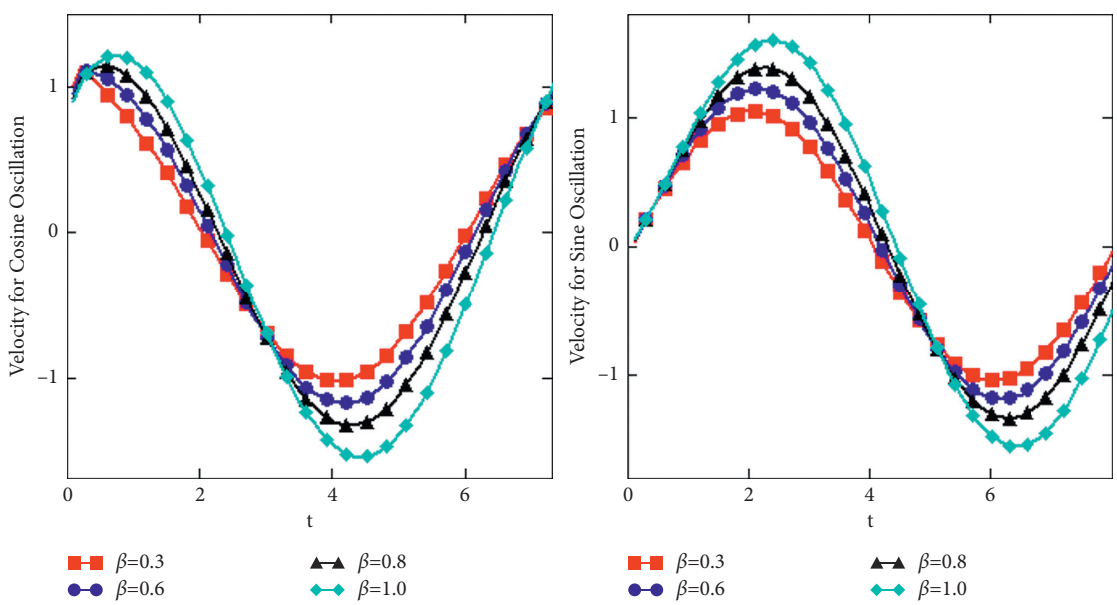

FIGURE 3: The variation of β for both the oscillations with $\omega = \pi/4$, $\lambda_1 = 0.8$, $\lambda_2 = 0.5$, $\alpha = 0.8$, $\gamma = 2$, $\mathcal{X} = 0.45$, and $\mathcal{Y} = 0.1$.

$$\Omega s(\mathcal{X}, \mathcal{Y}, t) = \sin(\omega t) - 16\omega \sum_{l,p=0}^{\infty} \frac{\sin((2l+1)\pi\mathcal{X})}{(2l+1)\pi} \times \frac{\sin((2p+1)\pi\mathcal{Y})}{(2p+1)\pi} \left(f(t) * a_{(2l+1)(2p+1)}(t)\right),$$

$$\Omega_c(\mathcal{X}, \mathcal{Y}, t) = \cos(\omega t) - 16 \sum_{l,p=0}^{\infty} \frac{\sin((2l+1)\pi\mathcal{X})}{(2l+1)\pi} \times \frac{\sin((2p+1)\pi\mathcal{Y})}{(2p+1)\pi} \left(k(t) * a_{(2l+1)(2p+1)}(t)\right),$$

$$T_{1s}(\mathcal{X}, \mathcal{Y}, t) = -16 \sum_{l,p=0}^{\infty} \omega \cos((2l+1)\pi\mathcal{X}) \times \frac{\sin((2p+1)\pi\mathcal{Y})}{(2p+1)\pi} f(t) * a_{(2l+1)(2p+1)}(t)$$

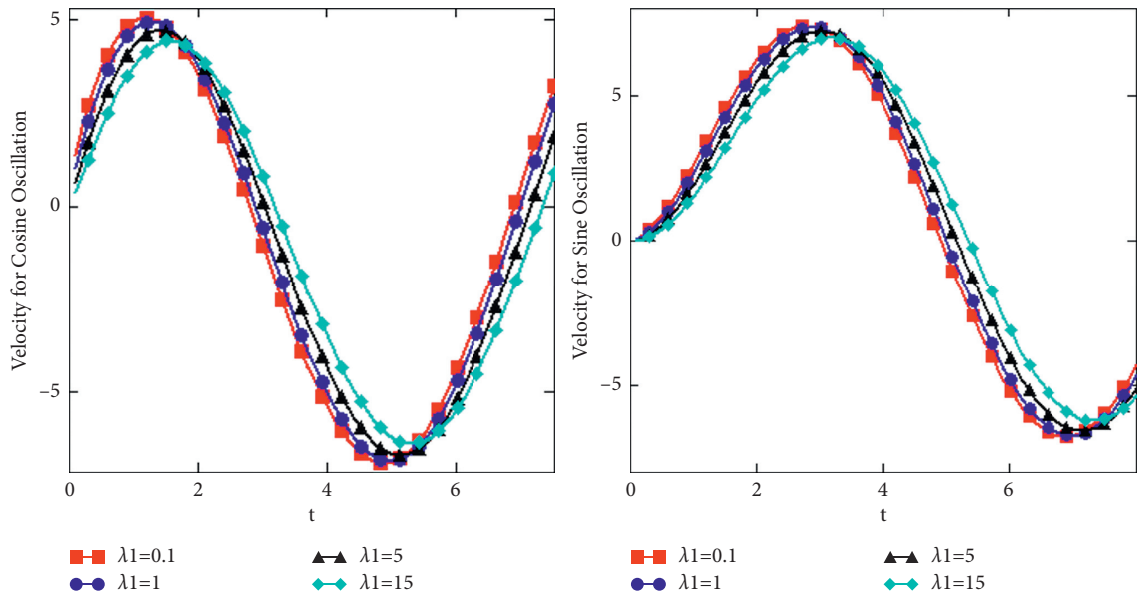

FIGURE 4: The variation of λ_1 for both the oscillations with $\omega = \pi/4$, $\alpha = 0.5$, $\lambda_2 = 0.07$, $\beta = 0.9$, $\gamma = 2$, $\mathscr{X} = 0.25$, and $\mathscr{Y} = 0.1$.

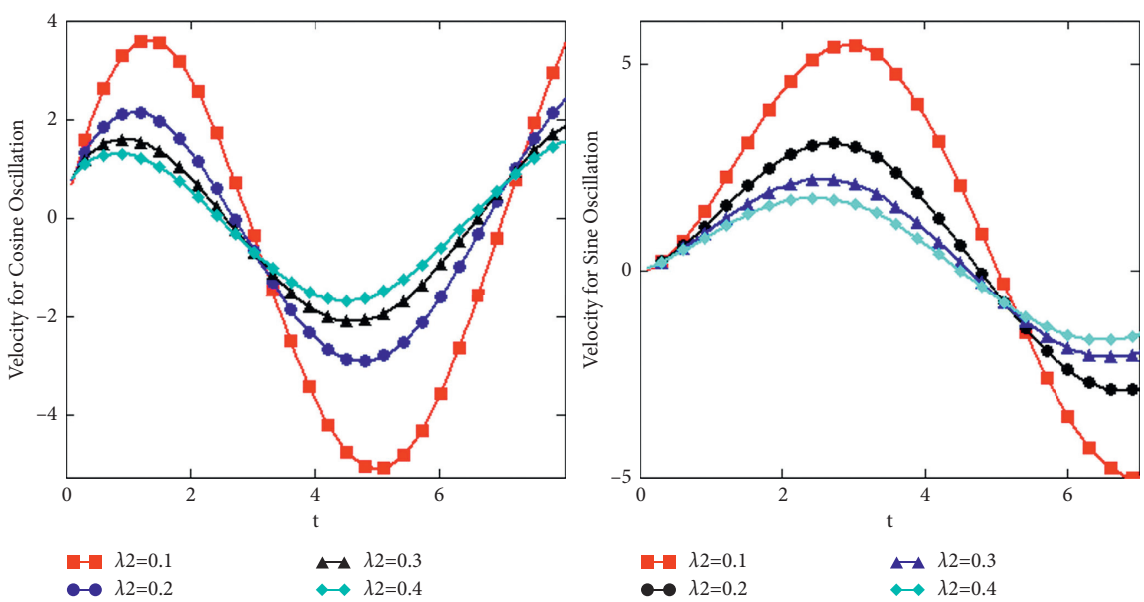

FIGURE 5: The variation of λ_2 for both the oscillations with $\omega = \pi/4$, $\lambda_1 = 5$, $\alpha = 0.5$, $\beta = 0.9$, $\gamma = 2$, $\mathscr{X} = 0.25$, and $\mathscr{Y} = 0.1$.

$$
\begin{aligned}
&+ 16 \sum_{l,p=0}^{\infty} \omega \cos((2l+1)\pi\mathscr{X}) \frac{\sin((2p+1)\pi\mathscr{Y})}{(2p+1)\pi} \times f(t) * h(t) * a_{(2l+1)(2p+1)}(t), \\
T_{1c}(\mathscr{X}, \mathscr{Y}, t) = &-16 \sum_{l,p=0}^{\infty} \cos((2l+1)\pi\mathscr{X}) \times \frac{\sin((2p+1)\pi\mathscr{Y})}{(2p+1)\pi} f(t) * a_{(2l+1)(2p+1)}(t) \\
&+ 16 \sum_{l,p=0}^{\infty} \cos((2l+1)\pi\mathscr{X}) \frac{\sin((2p+1)\pi\mathscr{Y})}{(2p+1)\pi} \times f(t) * h(t) * a_{(2l+1)(2p+1)}(t),
\end{aligned} \tag{56}
$$

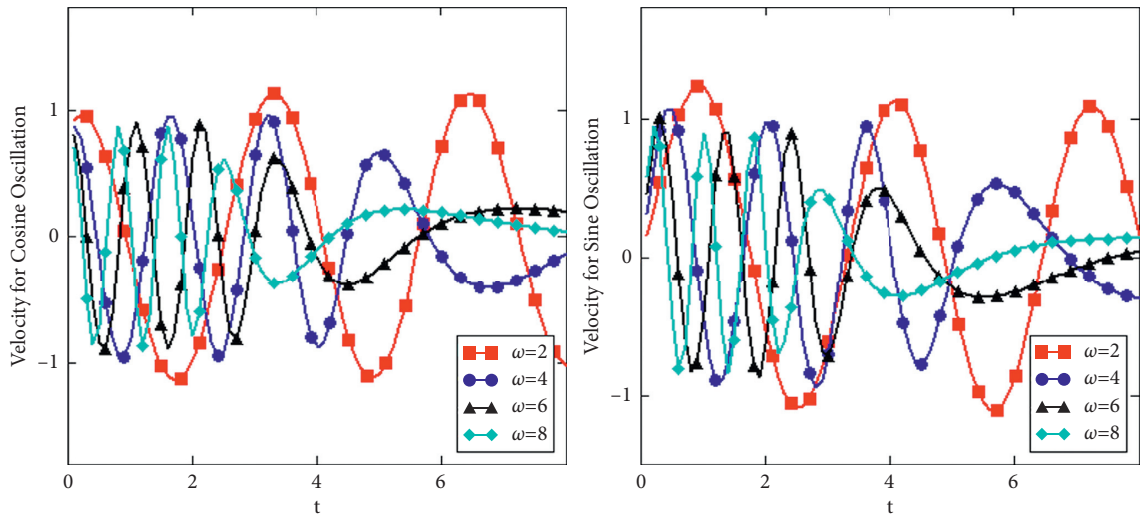

FIGURE 6: The variation of ω for both the oscillations with $\gamma = 2$, $\alpha = 0.5$, $\lambda_1 = 0.8$, $\beta = 0.9$, $\lambda_2 = 0.5$, $\mathscr{X} = 0.25$, and $\mathscr{Y} = 0.1$.

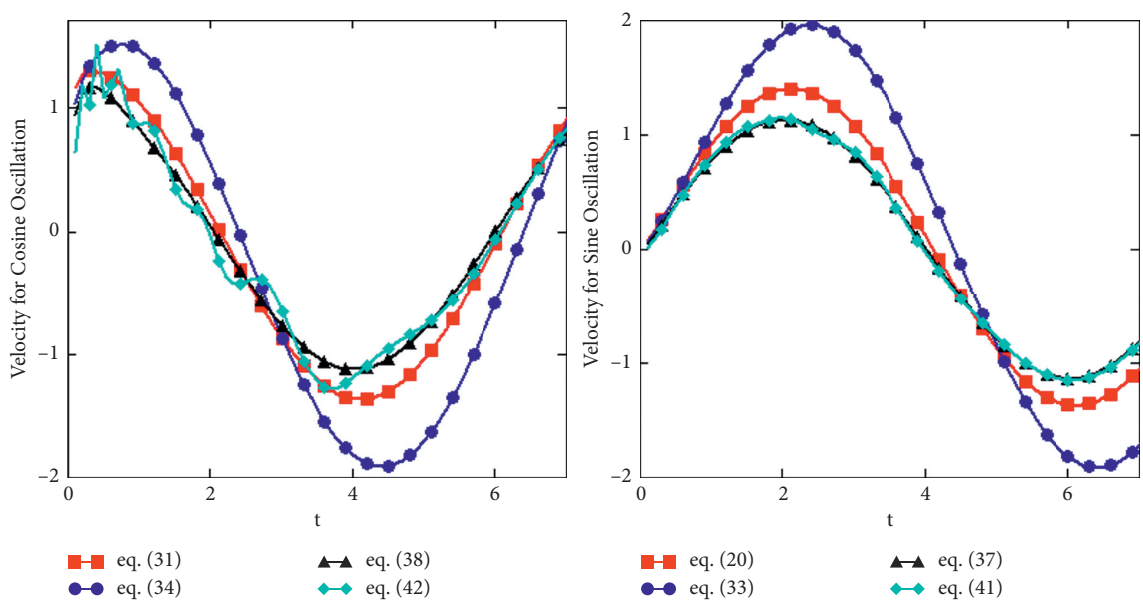

FIGURE 7: Velocity profiles of fractional Oldroyd-B fluid, classical Oldroyd-B fluid, fractional Maxwell fluid, and classical Maxwell fluid for both cos and sin.

where

$$a_{lp}(t) = \sum_{k=0}^{\infty} \left(\frac{-\lambda_{lp}^2}{\gamma} \right)^k \frac{1}{\lambda_1^{(k+1)}} G_{1,-1,k+1}\left(-\lambda_1^{-1}, t\right). \tag{57}$$

5. Numerical Results

In this section, we will give graphically results for the velocity and shear stresses profiles for the various parameters. Also, we will show a comparison between the analytical and numerical results in a tabular form. The numerical results were obtained by Stehfest's and Tzou's numerical inverse Laplace algorithms. The access of the various physical parameters for time is graphically presented in Figures 2 to 13.

In Figure 2, the researchers strategized the absolute values of the velocity field versus time. The given diagrams are strategized for four values of the fractional coefficient α. The velocity of the fluid decreases (absolute values) is observed as $\alpha \longrightarrow 1$ for the back and forth moment of both sine and cosine vibrations. In Figure 3, the researchers drew the consequences of the second fractional parameter β on the velocity field versus time. It was expected an opposite behavior concerning the first fractional parameter α and seen it comes true in the plot of Figure 3. In Figures 4 and 5, the effect of the relaxation parameter and the delay time on fluid motion is seen. From this figure, it is observed that its behavior is identical to that of a fractional parameter α, and when the fractional derivative parameter extends to 1 for the back and forth moment of both sine and cosine, the velocity

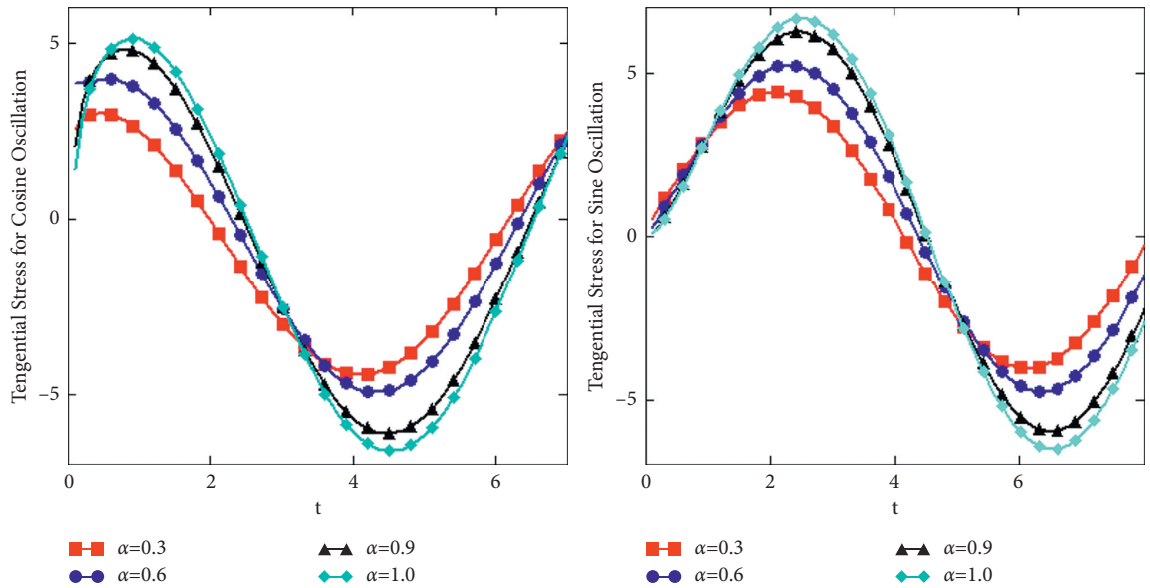

Figure 8: The variation of α for both the oscillations with $\omega = \pi/4$, $\lambda_1 = 0.8$, $\lambda_2 = 0.5$, $\beta = 0.8$, $\gamma = 2$, $\mathscr{X} = 0.55$, and $\mathscr{Y} = 0.15$.

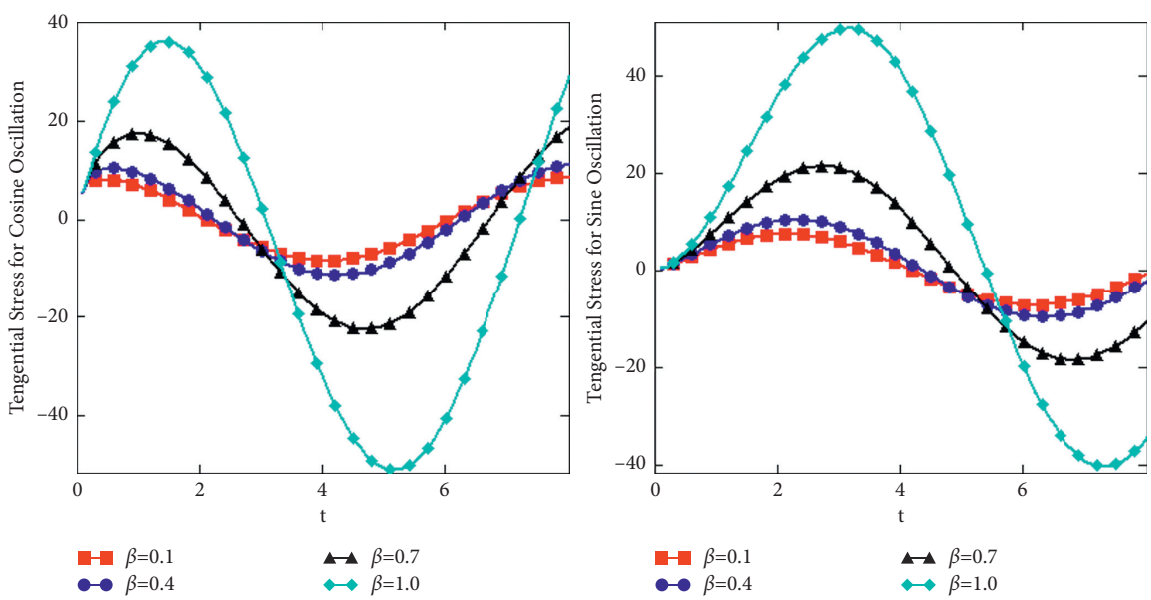

Figure 9: The variation of β for both the oscillations with $\omega = \pi/4$, $\lambda_1 = 0.08$, $\lambda_2 = 0.05$, $\alpha = 0.8$, $\gamma = 2$, $\mathscr{X} = 0.55$, and $\mathscr{Y} = 0.15$.

of the fluid reduces (nonabsolute values). Figure 6 exhibits the fluid factor w on the fluids flow. It shows the same behavior like Figures 2, 4, and 5, i.e., it describes that the fluid flow decreases with the enlargement of such parameter. The comparison of dimensionless velocities for fractional Oldroyd-B, ordinary Oldroyd-B, fractional Maxwell fluid, and ordinary Maxwell fluid is presented in Figure 7. It is clear that fractional Oldroyd-B fluid is the hastiest and fractional Maxwell fluid is the slowest in absolute values.

In Figure 8, the dimensionless shear stress versus t drew for various values of fractional coefficient α. The given diagrams are strategized for three values of the α. The stress on the fluid decreases for half interval of time, and the next half, it increases for sine oscillation because the standards of fractional parameter α increase. Figure 9 is sketched to show the dimensionless shear stress versus t directed for various values of fractional coefficient β. It can be observed that the effect of parameter β on the fluid motion has an opposite behavior compared to parameter α. Figures 10 and 11 are showing the effects of relaxation and retardation time on fluid motion. They have the opposite effect on stress as expected due to the relation between the return of a perturbed system into equilibrium and delayed response to an applied force or stress. Figure 12 gives the impact of frequency factor w on the shear stress. From Figure 12, it is clearly sighted that shear stress of the fluid goes to decay due to the increase of w. The comparison of dimensionless shear stresses for fractional Oldroyd-B, ordinary Oldroyd-B,

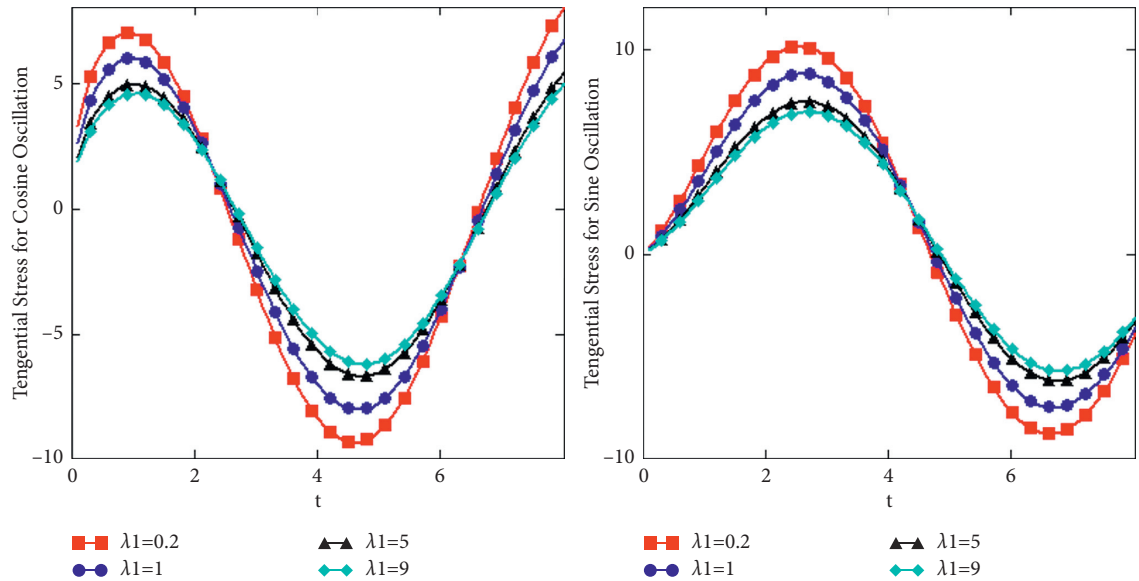

FIGURE 10: The variation of λ_1 for both the oscillations with $\omega = \pi/4$, $\beta = 0.7$, $\lambda_2 = 0.1$, $\alpha = 0.2$, $\gamma = 2$, $\mathscr{X} = 0.55$, and $\mathscr{Y} = 0.15$.

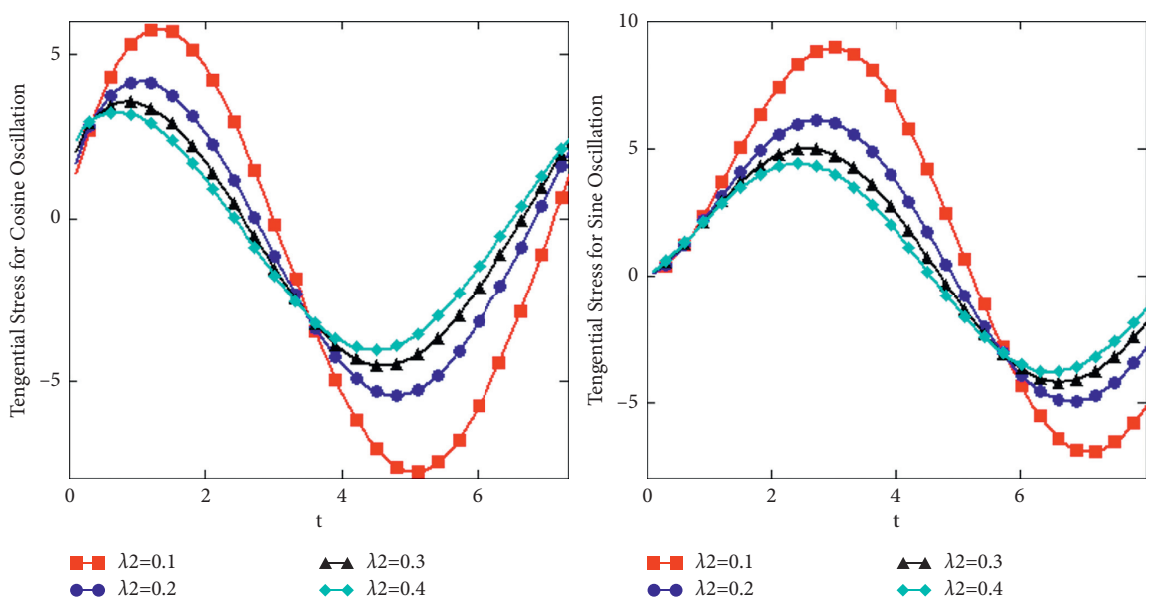

FIGURE 11: The variation of λ_2 for both the oscillations with $\omega = \pi/4$, $\beta = 0.7$, $\lambda_1 = 2$, $\alpha = 0.5$, $\gamma = 2$, $\mathscr{X} = 0.55$, and $\mathscr{Y} = 0.15$.

fractional Maxwell fluid, and ordinary Maxwell fluid is presented in Figure 13. From Figure 13, we noticed that the fractional parameter shows the increasing behavior for both the Oldroyd-B and Maxwell fluid as compared to the classical Oldroyd-B and Maxwell fluid.

It is clear from Tables 2 to 5 that the analytical solutions are nearly equal to the numerical results. The Stehfest's algorithm shows quite good agreement with our analytical solutions as compared to the numerical results obtained by Tzou's algorithm.

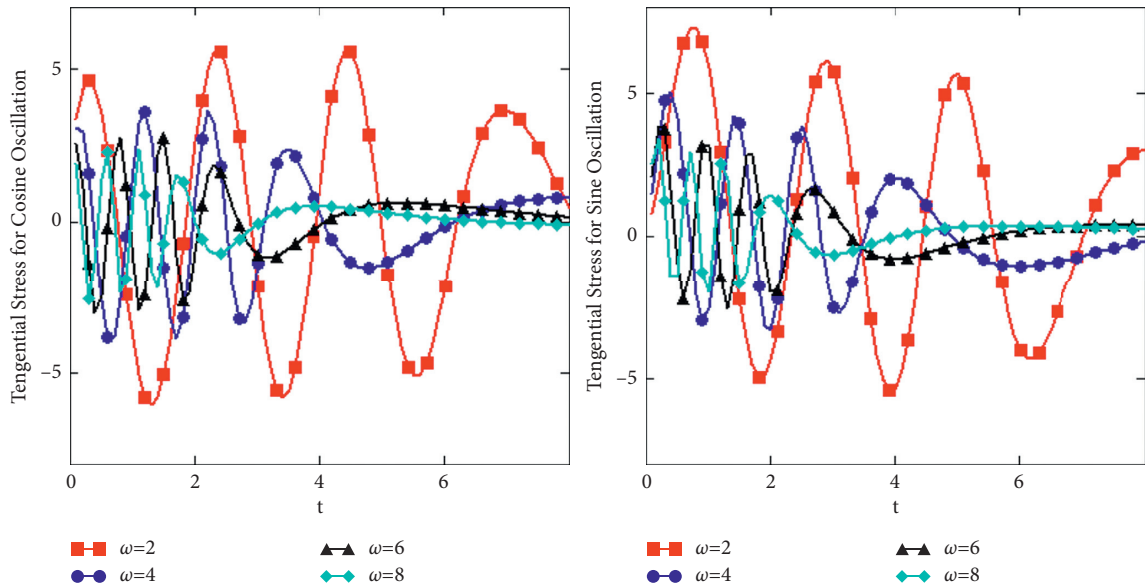

Figure 12: The variation of ω for both the oscillations with $\lambda_2 = 0.1$, $\beta = 0.7$, $\lambda_1 = 0.3$, $\alpha = 0.5$, $\gamma = 2$, $\mathscr{X} = 0.55$, and $\mathscr{Y} = 0.15$.

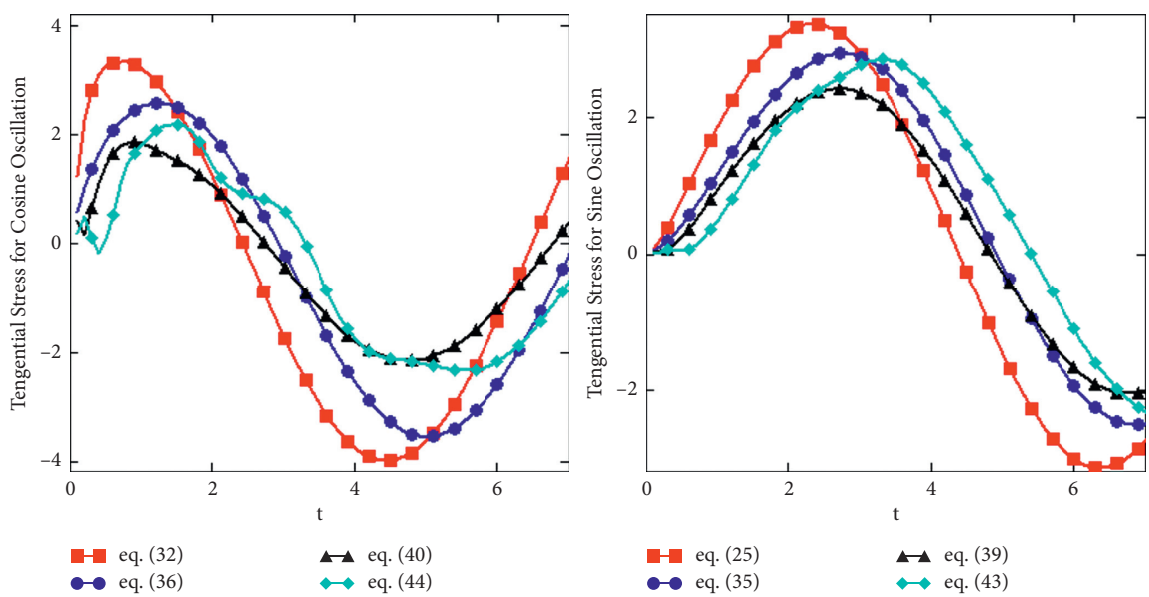

Figure 13: Tangential stresses of fractional Oldroyd-B fluid, classical Oldroyd-B fluid, fractional Maxwell fluid, and classical Maxwell fluid for both cos and sin.

Table 2: Comparison of analytical and numerical solution for velocity profile of sin oscillation.

t	λ_1	λ_2	α	β	Velocity (analytical)	Velocity (Stehfest's)	Velocity (Tzou's)
0.3					0.19679	0.19679	0.19698
0.6					0.49046	0.49044	0.49108
0.9					0.79985	0.79982	0.8005
	0.1				0.92838	0.92846	0.92026
	1				0.90133	0.90131	0.90187
	5				0.72345	0.72345	0.72371
		0.1			2.15514	2.15642	2.15508
		0.3			1.19366	1.19364	1.19391
		0.5			0.91705	0.91709	0.91542
			0.1		0.82248	0.82249	0.81367

Table 2: Continued.

t	λ_1	λ_2	α	β	Velocity (analytical)	Velocity (Stehfest's)	Velocity (Tzou's)
			0.5		0.83191	0.83194	0.82416
			0.9		0.84186	0.84194	0.83695
				0.2	0.7179	0.71795	0.71603
				0.5	0.72393	0.72382	0.72608
				0.7	0.72725	0.72696	0.73064

Table 3: Comparison of analytical and numerical solution for velocity profile of cos oscillation.

t	λ_1	λ_2	α	β	Velocity (analytical)	Velocity (Stehfest's)	Velocity (Tzou's)
0.3					1.10340	1.09977	1.05517
0.6					1.16489	1.16141	1.11978
0.9					1.11031	1.10694	1.06528
	0.1				1.11259	1.10913	1.07161
	1				1.1023	1.09865	1.05327
	5				1.09359	1.08982	1.03876
		0.1			1.77775	1.77494	1.68597
		0.3			1.26878	1.26496	1.19361
		0.5			1.09359	1.08982	1.03876
			0.1		1.1023	1.09865	1.05327
			0.5		1.1172	1.11542	0.92388
			0.9		1.2042	1.20333	1.23378
				0.2	1.03804	1.04065	0.98972
				0.5	1.08693	1.0851	0.88743
				0.7	1.10415	1.09827	0.95289

Table 4: Comparison of analytical and numerical solution for shear stresses of sin oscillation.

t	λ_1	λ_2	α	β	Shear stress (analytical)	Shear stress (Stehfest's)	Shear stress (Tzou's)
0.3					0.23055	0.23055	0.22853
0.6					0.49964	0.49965	0.49531
0.9					0.76883	0.76883	0.76204
	0.1				0.3223	0.3223	0.31942
	1				0.31801	0.31802	0.31525
	5				0.31444	0.31445	0.31178
		0.1			0.45165	0.45166	0.45033
		0.3			0.35301	0.35301	0.35062
		0.5			0.3194	0.3194	0.3166
			0.1		0.29581	0.29582	0.2927
			0.5		0.29495	0.294971	0.29309
			0.9		0.29711	0.29709	0.29765
				0.2	0.28779	0.28777	0.28832
				0.5	0.29213	0.29214	0.29181
				0.7	0.29412	0.29414	0.2924

Table 5: Comparison of analytical and numerical solution for shear stresses of cos oscillation.

t	λ_1	λ_2	α	β	Shear stress (analytical)	Shear stress (Stehfest's)	Shear stress (Tzou's)
0.3					0.99845	0.9926	0.76837
0.6					0.96564	0.95701	0.73931
0.9					0.85766	0.84791	0.6461
	0.1				0.99529	0.98762	0.77642
	1				0.97397	0.97164	0.7738
	5				0.9397	0.94018	0.81115
		0.1			1.45506	1.45601	1.40114
		0.3			1.17962	1.17937	1.03098

Table 5: Continued.

t	λ_1	λ_2	α	β	Shear stress (analytical)	Shear stress (Stehfest's)	Shear stress (Tzou's)
		0.5			1.0676	1.06564	0.87715
			0.1		1.47842	1.47583	1.36826
			0.5		1.41951	1.4202	1.41206
			0.9		1.32882	1.32841	1.31978
				0.2	1.25973	1.25822	1.28592
				0.5	1.409	1.40928	1.41688
				0.7	1.43243	1.43337	1.38511

6. Conclusion

This communication aims to provide exact solutions for the fractionalized Oldroyd-B fluid in a fluctuating quadrilateral duct by applying the discrete Laplace and double finite Fourier transforms. Also, a comparison is shown in tables for the analytical and numerical results. The corresponding results were not studied before and have important remarks concerning the prevailing equations for the nontrivial shear stress. These results fulfill all the executed initial and boundary conditions and were easily converted into parallel solutions. The parallel solutions for fractional Maxwell fluid, classical Oldroyd-B, and Maxwell fluid were regained as regulating case of the conventional solution. The following conclusions were drawn:

(i) Both sine and cosine oscillations of the velocity field decrease with the increase of fractional parameter α and vice versa for β

(ii) An increase in the values of λ_1 and λ_2 decreases the velocity profile of both sine and cosine oscillations

(iii) Dimensionless velocities comparison figured out fractional Oldroyd-B fluid is swiftest than fractional Maxwell fluid

(iv) Dimensionless shear stress changes behavior after half interval, and the opposite effect was seen between α and β fractional parameters

(v) Also, the analytical solutions show good agreement with the numerical results

In future, we will study, what will be the effects on fractional Oldroyd-B fluid via a fluctuating duct by adding the magnetic and porous factors.

Data Availability

No data were used to support the findings of this study.

Conflicts of Interest

The authors declare that they have no conflicts of interest.

References

[1] J. P. Hartnett and M. Kostic, "Heat transfer to Newtonian and non-Newtonian fluids in rectangular ducts," in *Advances in Heat Transfer*vol. 19, , pp. 247–356, Elsevier, 1989.

[2] G. G. Stokes, "On the effect of the rotation of cylinders and spheres about their axis in increasing the logarithmic decrement of the arc of vibration," 1886.

[3] K. R. Rajagopal, "Longitudinal and torsional oscillations of a rod in a non-Newtonian fluid," *Acta Mechanica*, vol. 49, no. 3, pp. 281–285, 1983.

[4] K. R. Rajagopal and R. K. Bhatnagar, "Exact solutions for some simple flows of an oldroyd-b fluid," *Acta Mechanica*, vol. 113, no. 1, pp. 233–239, 1995.

[5] A. Mahmood, N. A. Khan, I. Siddique, and S. Nazir, "A note on sinusoidal motion of a viscoelastic non-Newtonian fluid," *Archive of Applied Mechanics*, vol. 82, no. 5, pp. 659–667, 2012.

[6] T. Hayat, A. M. Siddiqui, and S. Asghar, "Some simple flows of an oldroyd-b fluid," *International Journal of Engineering Science*, vol. 39, no. 2, pp. 135–147, 2001.

[7] D. Valério, J. Machado, and V. Kiryakova, "Some pioneers of the applications of fractional calculus," *Fractional Calculus and Applied Analysis*, vol. 17, no. 2, pp. 552–578, 2014.

[8] C. Fetecau, "Analytical solutions for non-Newtonian fluid flows in pipe-like domains," *International Journal of Non-Linear Mechanics*, vol. 39, no. 2, pp. 225–231, 2004.

[9] N. D. Waters and M. J. King, "The unsteady flow of an elastico-viscous liquid in a straight pipe of circular cross section," *Journal of Physics D: Applied Physics*, vol. 4, no. 2, p. 204, 1971.

[10] W. P. Wood, "Transient viscoelastic helical flows in pipes of circular and annular cross-section," *Journal of Non-Newtonian Fluid Mechanics*, vol. 100, no. 1-3, pp. 115–126, 2001.

[11] S. S. Ray, A. Atangana, S. C. Noutchie, M. Kurulay, N. Bildik, and A. Kilicman, "Fractional calculus and its applications in applied mathematics and other sciences," *Mathematical Problems in Engineering*, vol. 2014, Article ID 849395, 2 pages, 2014.

[12] L. Debnath, "Recent applications of fractional calculus to science and engineering," *International Journal of Mathematics and Mathematical Sciences*, vol. 2003, no. 54, pp. 3413–3442, 2003.

[13] I. Podlubny, *Fractional Differential Equations: An Introduction to Fractional Derivatives, Fractional Differential Equations, to Methods of Their Solution and Some of Their Applications*, Elsevier, Amsterdam, Netherland, 1998.

[14] N Ali Shah and I. Khan, "Heat transfer analysis in a second grade fluid over and oscillating vertical plate using fractional caputo–fabrizio derivatives," *The European Physical Journal C*, vol. 76, no. 7, pp. 1–11, 2016.

[15] I. Khan, N. A. Shah, Y. Mahsud, and D. Vieru, "Heat transfer analysis in a maxwell fluid over an oscillating vertical plate using fractional caputo-fabrizio derivatives," *The European Physical Journal Plus*, vol. 132, no. 4, pp. 1–12, 2017.

[16] L. Debnath, *Transforms and Their Applications*, 2007.

[17] C. Fetecau and C. Fetecau, "The first problem of Stokes for an oldroyd-b fluid," *International Journal of Non-linear Mechanics*, vol. 38, no. 10, pp. 1539–1544, 2003.

[18] M. Jamil, N. A. Khan, and M. A. Imran, "New exact solutions for an oldroyd-b fluid with fractional derivatives: Stokes' first problem," *International Journal of Nonlinear Sciences and Numerical Stimulation*, vol. 14, no. 7-8, pp. 443–451, 2013.

[19] C. Fetecau, M. Nazar, and C. Fetecau, "Unsteady flow of an oldroyd-b fluid generated by a constantly accelerating plate between two side walls perpendicular to the plate," *International Journal of Non-Linear Mechanics*, vol. 44, no. 10, pp. 1039–1047, 2009.

[20] M. Kamran, M. Imran, M. Athar, and M. A. Imran, "On the unsteady rotational flow of fractional oldroyd-b fluid in cylindrical domains," *Meccanica*, vol. 47, no. 3, pp. 573–584, 2012.

[21] M. B. Riaz, M. A. Imran, and K. Shabbir, "Analytic solutions of oldroyd-b fluid with fractional derivatives in a circular duct that applies a constant couple," *Alexandria Engineering Journal*, vol. 55, no. 4, pp. 3267–3275, 2016.

[22] C. Fetecau and C. Fetecau, "Unsteady flows of oldroyd-b fluids in a channel of rectangular cross-section," *International Journal of Non-linear Mechanics*, vol. 40, no. 9, pp. 1214–1219, 2005.

[23] M. Nazar, F. Shahid, M. Saeed Akram, Q. Sultan, and Q. Sultan, "Flow on oscillating rectangular duct for maxwell fluid," *Applied Mathematics and Mechanics*, vol. 33, no. 6, pp. 717–730, 2012.

[24] H. I. Ghada and A. M. Abdulhadi, "Flow through an oscillating rectangular duct for generalized oldroyd-b fluid with fractional derivatives," *IOSR Journal of Mathematics*, vol. 10, no. 5, 2014.

[25] S. Wang, P. Li, and M. Zhao, "Analytical study of oscillatory flow of maxwell fluid through a rectangular tube," *Physics of Fluids*, vol. 31, no. 6, Article ID 063102, 2019.

[26] X. Sun, S. Wang, and M. Zhao, "Oscillatory flow of maxwell fluid in a tube of isosceles right triangular cross section," *Physics of Fluids*, vol. 31, no. 12, Article ID 123101, 2019.

[27] A. Farooq, M. Kamran, Y. Bashir, H. Ahmad, A. Shahzad, and Y.-M. Chu, "On the flow of MHD generalized maxwell fluid via porous rectangular duct," *Open Physics*, vol. 18, no. 1, pp. 989–1002, 2020.

[28] Q. Sultan, M. Nazar, U. Ali, and M. Imran, "Unsteady flow of oldroyd-b fluid through porous rectangular duct," *International Journal of Nonlinear Science*, vol. 15, no. 3, pp. 195–211, 2013.

[29] S. Wang and M. Zhao, "Analytical solution of the transient electro-osmotic flow of a generalized fractional maxwell fluid in a straight pipe with a circular cross-section," *European Journal of Mechanics-B: Fluids*, vol. 54, pp. 82–86, 2015.

[30] X. Guo and H. Qi, "Analytical solution of electro-osmotic peristalsis of fractional jeffreys fluid in a micro-channel," *Micromachines*, vol. 8, no. 12, p. 341, 2017.

[31] X. Wang, H. Qi, B. Yu, Z. Xiong, and H. Xu, "Analytical and numerical study of electroosmotic slip flows of fractional second grade fluids," *Communications in Nonlinear Science and Numerical Simulation*, vol. 50, pp. 77–87, 2017.

[32] A. U. Awan, M. D. Hisham, and N. Raza, "The effect of slip on electro-osmotic flow of a second-grade fluid between two plates with caputo–fabrizio time fractional derivatives," *Canadian Journal of Physics*, vol. 97, no. 5, pp. 509–516, 2019.

[33] N. A. Shah, X. Wang, H. Qi, S. Wang, and H. Ahmad, "Transient electro-osmotic slip flow of an oldroyd-b fluid with time-fractional caputo-fabrizio derivative," *Journal of Applied and Computational Mechanics*, vol. 5, no. 4, pp. 779–790, 2019.

[34] B. Wang, M. Tahir, M. Imran, M. Javaid, and C. Y. Jung, "Semi analytical solutions for fractional oldroyd-b fluid through rotating annulus," *IEEE Access*, vol. 7, pp. 72482–72491, 2019.

[35] M. Kamran, Y. Bashir, A. Farooq et al., "Study on the helicoidal flow through cylindrical annuli with prescribed shear stresses," *Results in Physics*, vol. 23, Article ID 103993, 2021.

[36] J. G. Oldroyd, "On the formulation of rheological equations of state," *Proceedings of the Royal Society of London-Series A: Mathematical and Physical Sciences*, vol. 200, pp. 523–541, 1950.

[37] S. C. Pandey, "The Lorenzo-Hartley's function for fractional calculus and its applications pertaining to fractional order modelling of anomalous relaxation in dielectrics," *Computational and Applied Mathematics*, vol. 37, no. 3, pp. 2648–2666, 2018.

[38] M. Nazar, M. Zulqarnain, M. Saeed Akram, and M. Asif, "Flow through an oscillating rectangular duct for generalized maxwell fluid with fractional derivatives," *Communications in Nonlinear Science and Numerical Simulation*, vol. 17, no. 8, pp. 3219–3234, 2012.

Hindawi
Complexity
Volume 2021, Article ID 9992022, 9 pages
https://doi.org/10.1155/2021/9992022

Research Article

Study on Preparation Technology and Physical Fingerprint of Chuilian Jianpi Granules Based on QbD

Guangjiao Zhou,[1,2] **Xiao-Wei Li**,[3] **Jin-Cai Li**,[1] **and Xue-Hua Feng**[4]

[1]*Bozhou Chinese Medicine Institute, Anhui Academy of Chinese Medicine, Bozhou 236800, China*
[2]*Bozhou Vocational and Technical College, Bozhou 236800, China*
[3]*Meng Cheng Hospital of Chinese Medicine, Bozhou 236800, China*
[4]*Anhui Xinhua University, Hefei 230088, China*

Correspondence should be addressed to Guangjiao Zhou; 403621620@qq.com

Received 30 March 2021; Accepted 21 August 2021; Published 30 September 2021

Academic Editor: Ali Akgül

Objective. To optimize the preparation formula and technology of Chuilian Jianpi granules. *Methods*. The formulation and preparation process were optimized by single factor experiment and response surface analysis, with the molding rate, hygroscopicity, and fluidity of particles as the comprehensive evaluation indexes, and the comprehensive score as the response value according to different weights. To further evaluate the stability and feasibility of the preparation formulation and technology, the physical fingerprint of the granules was constructed by seven indicators including particle tap density, bulk density, hygroscopicity, water content, angle of repose, Hausner ratio, and relative homogeneity index. *Results*. The optimum formula conditions of Chuilian Jianpi granules were as follows: the dosage ratio of drug to adjuvant was 1 : 0.8, lactose:mannitol = 1.5 : 1, and the amount of wetting agent (90% ethanol) was 25% of the granules, with high-speed stirring granulation. The similarity of the physical fingerprints of the 10 batches of Chuilian Jianpi granules was high, which is above 98.5%. *Conclusion*. The optimized preparation technology was stable and feasible, which can provide reference for the development of Chuilian Jianpi granules and other Chinese medicine granules.

1. Introduction

The Chuliani Jianpi granule is a prescription developed by the Mengcheng County Hospital of Traditional Chinese Medicine of Anhui Province based on modern pharmacological studies. The Mengcheng County Hospital has exclusive ownership of the prescription. This prescription is composed of 17 traditional Chinese medicines, including Spreading Hedyotis Herba, Sedi Herba, Scutellariae Barbatae Herba, Polygoni Cuspidati Rhizoma Et Radix, Pheretima, Poria, Galli Gigerii Endothelium Corneum, Crataegi Fructus, Citri Sarcodactylis Fructus, Aurantii Fructus, Moutan Cortex, Rhei Radix Et Rhizoma, Artemisiae Scopariae Herba, Schisandrae Chinensis Fructus, Glycyrrhizae Radix Et Rhizoma, Astragali Radix, and Coptidis Rhizoma. Years of clinical verification by the Mengcheng County Hospital of Traditional Chinese Medicine proved its functions of clearing away heat and toxic materials, soothing liver, and regulating qi, as well as fortifying the spleen and disinhibiting dampness. It is mainly used for chest pain caused by dampness and heat in the liver and gallbladder, mouth pain, nausea and vomiting, dysuria or yellowish urine, yellowing of body and eyes, chronic hepatitis, and ascites due to cirrhosis. However, in clinical practice, this prescription shows poor stability and portability. Our research group developed it into "Chuilian Jianpi granules", which featured portability and stability, thus better serving the patients. Focusing on the quality by design (QbD), this paper adopted the molding rate, moisture absorption rate, and fluidity of granules as evaluation indexes [1–6]. The team optimized the preparation formula and production procedures of Chuilian Jianpi granules by single-factor-based Box–Behnken experiment. The physical fingerprint of the particles was established based on physical properties such as stacking,

fluidity, stability, and uniformity [7–10]. The particles were fully evaluated to ensure the stable and controllable quality of the particles, thus providing experimental data for the preparation, production, and quality control of the prescription.

2. Testing Instruments and Materials

2.1. Main Experimental Instruments. GHL-150 high-speed stirring granulator (Changzhou Subang Drying Equipment Co. Ltd.) and RXH-5-C hot air circulation drying box (Shanghai Tianxiang Pharmaceutical Machinery) were used in this study.

2.2. Materials. Seventeen kinds of decoction pieces, such as Spreading Hedyotis Herba, Sedi Herba, Scutellariae Barbatae Herba, Polygoni Cuspidati Rhizoma Et Radix, Pheretima, Poria, Galli Gigerii Endothelium Corneum, Crataegi Fructus, Citri Sarcodactylis Fructus, Aurantii Fructus, Moutan Cortex, Rhei Radix Et Rhizoma, Artemisiae Scopariae Herba, Schisandrae Chinensis Fructus, Glycyrrhizae Radix Et Rhizoma, Astragali Radix, and Coptidis Rhizoma, were purchased from Yonggang Decoction Pieces Factory in Bozhou of Anhui Province. Chen Na, Associate Professor of Bozhou Vocational and Technical College Pharmacy School, confirmed that the Spreading Hedyotis Herba conforms to the requirements specified in the 2008 edition of Shanghai Chinese Herbal Pieces Processing Standard. The rest also meet the requirements specified in the first edition of Chinese Pharmacopoeia, 2020. Mannitol and lactose (Anhui Shanhe Pharmaceutical Accessories Co., Ltd.) and ethanol (Xinxiang Xianfeng Pharmaceutical New Materials Co., Ltd.) were analytically pure, and purified water was made by the laboratory.

3. Method and Result

3.1. Preparation of Chuilian Jianpi Granules. According to previous experimental studies, 17 kinds of Chinese herbal pieces, including Spreading Hedyotis Herba, Sedi Herba, Sophorae Tonkinensis Radix Et Rhizoma, Scutellariae Barbatae Herba, Polygoni Cuspidati Rhizoma Et Radix, Pheretima, Poria, Galli Gigerii Endothelium Corneum, Crataegi Fructus, Citri Sarcodactylis Fructus, Aurantii Fructus, Moutan Cortex, Rhei Radix Et Rhizoma, Artemisiae Scopariae Herba, and Schisandrae Chinensis Fructus, were decocted with 10 times of water and boiled twice, with the first time lasting 1.5 hours and the second time one hour. Then, it was filtered and mixed and concentrated to a relative density of 1.15 ~ 1.25 before being dried under reduced pressure at 80°C to obtain dry paste. After being crushed, it was mixed with 2 times of auxiliary materials (lactose: mannitol = 1.5 : 1). Then, the 90% ethanol was used as wetting agent in an amount of 25% of the total material. Then, the mixture was stirred at high speed to make wet granules and dried [10–12].

3.2. Granule Evaluation. In the pre-experiment, the lactose and mannitol were found to be ideal diluents to dissolve granules. Therefore, factors like the molding rate, moisture absorption, and fluidity instead of the solubility were taken as indicators for evaluation. The granules were evaluated according to the weight coefficients of 40, 30, and 30, with a full score of 100 points. The final score = molding rate × 40/maximum molding rate + minimum moisture absorption rate × 30/moisture absorption rate + minimum angle of repose × 30/angle of repose [13–16]. Based on the physical properties of particles, the physical fingerprint of particles is constructed with four primary properties of stacking, stability, fluidity, and uniformity and seven secondary parameters of tap density, bulk density, hygroscopicity, water content, angle of repose, Hausner ratio, and relative homogeneity [9, 10]. The stacking property of particles is characterized by tap density and bulk density, the stability featured by hygroscopicity and water content, the fluidity of particles by repose angle and Hausner ratio, and the uniformity of particles by relative homogeneity. The measurement of each indicator is as follows.

3.2.1. Molding Rate. The dried granules were weighed and marked as W_1, which then passed through No. 1 sieve and No. 5 sieve, respectively. Granules that passed through No. 1 sieve but got stuck in No. 5 sieve were collected, weighed, and marked as W_2. The forming rate = $W_2{}^*100\%/W_1$.

3.2.2. Bulk Density. Five grams of Chuilian Jianpi granules were taken and marked as W and then slowly added into a dry and clean measuring cylinder of 25 mL. The volume (V_a) of granules was read, and the bulk density was calculated according to the following formula: bulk density = W/V_a.

3.2.3. Tap Density. The measuring cylinder filled with particles was vibrated up and down for 200 times at a frequency of 2 s/time. The volume (V_C) of particles was read, and the tap density of particles was calculated according to the following formula: tap density = W/V_C.

3.2.4. Moisture Absorption [16]. Three grams of particles dried to constant weight were accurately weighed and marked as m_1. Then, they were placed in a closed environment with a relative humidity of 75% and stored in a constant temperature incubator at 25°C. 24 hours later, they were weighed and marked as m_2. The moisture absorption rate was calculated according to the following formula: moisture absorption rate = $(m_1 - m_2)/m_1 \times 100\%$.

3.2.5. Water Content. Two grams of particles were placed in a sample tray and heated to constant weight at 105°C. Then, a quick moisture analyzer was used to read their water content.

3.2.6. Angle of Repose. The funnel was used for determining the angle of repose, which was horizontally fixed at a height h from the graph paper. The particles were slowly poured into it until the top of the particles touched the top of the funnel, and the particles formed a cone with the height h and radius r. The angle of repose was calculated according to $\alpha = h/r$.

3.2.7. Hausner Ratio. It was calculated based on the following formula: Hausner ratio = tap density/loose density.

3.2.8. Relative Homogeneity. Based on approaches proposed by previous literatures [4, 9], the Chuilian Jianpi granules were screened by 24, 50, 65, 120, 180, and 325 meshes in turn and oscillated for 5 min, after which the mass of the granules intercepted on each screen was recorded, respectively. The relative homogeneity was calculated by taking particles trapped by screens with average pore diameters of 603, 303, 188, 108, and 83 μm.

3.3. Optimized Single-Factor Experiment. In the pre-experiment, it was found that the dry paste of Chuilian Jianpi recipe has a strong viscosity in the presence of water. When dextrin, starch, or their mixture is used as diluent, it is not easy to form a fixed shape in addition to its poor solubility. However, the mixture of lactose and mannitol features much greater solubility and formability [17, 18]. Based on evaluation indicators under "Section 2.2," the effect of adjuvant ratio, lactose and mannitol ratio, wetting agent, and various dosages on the final score of Chuilian Jianpi granules was investigated.

This paper also studied the effect of adjuvant ratio (in the ratio of 0.5 : 1, 1 : 1, 1.5 : 1, 2 : 1, and 2.5 : 1), lactose and mannitol (in the ratio of 0.5 : 1, 1 : 1, 1.5 : 1, 2 : 1, and 2.5 : 1), ethanol concentration of wetting agent (60%, 70%, 80%, 90%, and 95%), and the dosage of wetting agent (10%, 15%, 20%, 25%, and 30%) on the performance of Chuilian Jianpi granules, as shown in Table 1.

The preparation was carried out based on the above parameters, with the value of single-factor parameter as abscissa and the overall evaluation (marked as "Y") as ordinate. The data were used to create a graph, as shown in Figure 1. In Figure 1, there is a rise in the efficiency with the ratio of adjuvant drugs increasing between 0.5 : 1 and 1.5 : 1, while there was no significant change in the efficiency when it varies between 1.5 : 1 and 2.5 : 1. With the increasing ratio of adjuvant drugs, the daily dosage of granules will go up as well. This paper took the ratio of 1 : 1, 1 : 1, and 2 : 1 as ideal option considering the final score and daily dosage. The efficacy increases before going down with the increase of lactose: mannitol ratio, which peaks at the ratio of 2 : 1. Therefore, the ratio of 1.5 : 1, 2 : 1, and 2.5 : 1 is taken as possible option. When the concentration of ethanol is 90%, the efficiency is significantly higher than other concentrations. Therefore, the 90% ethanol is selected as the wetting agent for granule preparation. The efficiency of the granules also shows the trend of rise and fall with the increase of ethanol dosage, which peaked at the dosage of 25%. Therefore, the dosages of 20%, 25%, and 30% were taken as options for optimization.

3.4. Optimization of Granulation by Response Surface Methodology

3.4.1. Design of the Response Surface Experiment. On the basis of single-factor pre-experiment, factors including adjuvant ratio (marked as "A"), lactose: mannitol (marked as "B"), and ethanol consumption (marked as "C") were taken as the investigation factors. According to the principles of response surface methodology, three levels were set for the three investigation factors, which were expressed by code values −1, 0, and 1, as shown in Table 2.

3.4.2. Results and Variance Analysis of the Response Surface Experiment. Based on the design of the Box–Behnken experiment, the prescription was optimized with the 90% ethanol as the wetting agent. The method under "Section 3.2" was used to calculate the final score, which was taken as the response value. The analysis was done using Analysis using software and Box–Behnken response surface method. The results are shown in Tables 3 and 4. The variance analysis and multiple regression fitting were performed, with the $P < 0.01$ and $R^2 = 0.9593$, indicating statistical significance of the model. The values were consistent with the predictions. The lack of fit had $P > 0.05$, indicating the feasibility of the equation in preparing the Chuilian Jianpi granules. The quadratic multiple regression equation is given by

$$Y = 94.03 + 2.55A + 1.01B + 1.49C + 2.37AB + 2.81AC + 0.61BC - 3.09A^2 - 4.71B^2 - 3.91C^2. \quad (1)$$

In the simple linear regression model, A had high significance while B and C had no significance. For interaction terms, both A and C were significant. In the quadratic term, A^2 had certain significance, while B^2 and C^2 were highly significant. Other items were not significant. In conclusion, the effect of the three factors on the preparation of Chuilian Jianpi granules is ranked as follows: adjuvant ratio (A) > ethanol dosage (C) > lactose: mannitol ratio (B).

3.4.3. Analysis of Optimization by Response Surface Methodology. The 3D graph of the response surface was made based on the model and experimental results, as shown in Figure 2. The Design-Expert 11.0.4.0 software, combined with the results of the quadratic regression model, was used to determine the optimized conditions: adjuvant ratio = 1.88 : 1, lactose: mannitol = 1.66 : 1, and the proportion of ethanol at 27.45% of the total granule weight. Under this condition, the predicted value of the final score is 95.54. To facilitate the preparation procedures, the optimal parameters were set as follows: adjuvant ratio = 2 : 1, lactose: mannitol = 1.5 : 1, and the proportion of ethanol at 25%.

3.4.4. Verification of the Optimal Prescription. Three batches of Chuilian Jianpi dry paste were taken and processed into

Table 1: The change conditions of single factor.

Factor	Single-factor change condition	Other fixed conditions
Adjuvant ratio (marked as "*A*")	0.5 : 1, 1 : 1, 1.5 : 1, 2 : 1, 2.5 : 1	Lactose and mannitol ratio = 1.5 : 1, ethanol concentration = 90%, ethanol dosage = 25%
Lactose and mannitol ratio (marked as "*B*")	0.5 : 1, 1 : 1, 1.5 : 1, 2 : 1, 2.5 : 1	Adjuvant ratio = 2 : 1, ethanol concentration = 90%, ethanol dosage = 25%
Ethanol concentration of wetting agent (marked as "*C*")	60, 70, 80, 90, 95	Lactose and mannitol ratio = 1.5 : 1, adjuvant ratio = 2 : 1, ethanol dosage = 25%
Dosage of wetting agent (marked as "*D*," %)	10, 15, 20, 25, 30	Lactose and mannitol ratio = 1.5 : 1, adjuvant ratio = 2 : 1, ethanol concentration = 90%

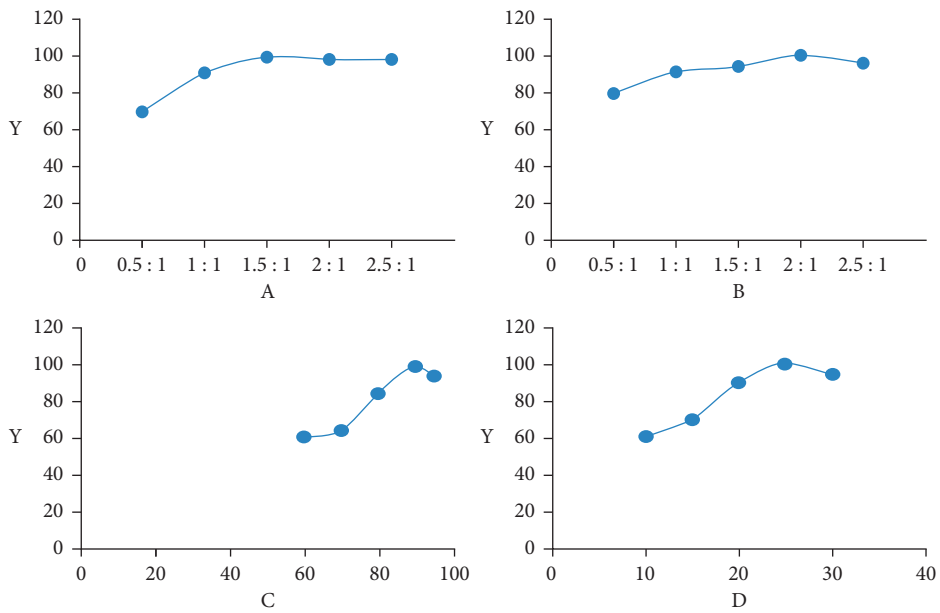

Figure 1: The influence of each single factor on the comprehensive score.

Table 2: Analysis of factors and level coding of response surface methodology.

Adjuvant ratio (*A*)	Lactose : mannitol (*B*)	Dosage of ethanol (*C*) (%)	Level
1 : 1	1.5 : 1	20	−1
1.5 : 1	2 : 1	25	0
2 : 1	2.5 : 1	30	1

granules by high-speed stirring, granulating, drying, and grading based on the optimal prescription for verification. The molding rate, moisture absorption rate, and angle of repose were measured, and the results are shown in Table 5. It was found that there was no significant difference in the three batches of granules in terms of the above three factors. Also, the average value was basically consistent with predictions of the response surface, indicating the reliability and accuracy of the evaluation system and the quadratic multiple regression fitting model.

3.5. Physical Fingerprint of Chuilian Jianpi Granules

3.5.1. Determination and Standardization of Physical Properties of Chuilian Jianpi Granules. To verify the stability and feasibility of the optimized preparation process, 10 batches of Chuilian Jianpi granules were prepared based on the optimal prescription, with the batch numbers of 20201101, 20201102, 20201103, 20201104, 20201105, 20201106, 20201107, 20201108, 2020110, 20201110, and 20201102, respectively. According to Section 3.2, the stability and feasibility of the prescription were investigated in terms of seven physical parameters, including tap density, bulk density, moisture absorption, water content, angle of repose, Hausner ratio, and relative homogeneity, which served as the secondary indicators of the physical fingerprint. The value of each parameter was determined by the method described in Section 3.2 for the 10 batches of granules, and the results are shown in Table 6. To ensure consistency, the measured values were standardized and converted to the numerical range of 0–10 specified by the Chinese Pharmacopoeia 2020 edition and related literatures [4, 9, 19], as shown in Table 7.

Table 3: Experimental design and results of response surface for granulation process.

Number	A	B	C (%)	Formability (%)	Hygroscopicity (%)	Angle of repose	Comprehensive scores (marked as "Y")
1	1	0	1	94.35	4.05	25.1	95.15
2	0	1	−1	91.52	5.08	29.21	84.37
3	0	0	0	95.01	4.07	25.18	95.19
4	0	0	0	94.92	4.26	24.86	94.38
5	1	−1	0	86	4.71	28.77	84.18
6	0	0	0	95.13	4.28	24.63	94.64
7	0	−1	−1	94.11	5.15	29.73	84.67
8	0	0	0	88.04	3.54	29.31	91.96
9	0	1	1	98.71	4.62	31.59	87.37
10	0	0	0	96.54	4.26	25.72	94.00
11	−1	−1	0	86.89	5.33	25.68	85.14
12	1	1	0	96.73	4.57	26.01	92.06
13	−1	0	−1	94.21	5.01	30.62	84.53
14	−1	0	1	88.64	5.07	29.38	83.09
15	0	−1	1	89.41	4.61	29.65	85.25
16	−1	1	0	89.32	5.02	29.41	83.55
17	1	0	−1	89.93	4.61	29.79	85.34

Table 4: Analysis of variance.

Source	Sum of squares	Df	Mean square	F value	P value
Model	354.14	9	39.35	18.33	**0.0005
A	52.12	1	52.12	24.28	0.0017
B	8.22	1	8.22	3.83	0.0912
C	17.85	1	17.85	8.31	0.0235
AB	22.42	1	22.42	10.44	0.0144
AC	31.64	1	31.64	14.74	*0.0064
BC	1.46	1	1.46	0.68	0.4362
A^2	40.32	1	40.32	18.78	*0.0034
B^2	93.29	1	93.29	43.45	**0.0003
C^2	64.44	1	64.44	30.01	**0.0009
Residual	15.03	7	2.15		
Lack of fit	8.90	3	2.97	1.94	0.2653
Pure error	6.13	4	1.53		
Cor total	369.17	16	$R^2 = 0.9593$		

*Signifying salience; **signifying high salience.

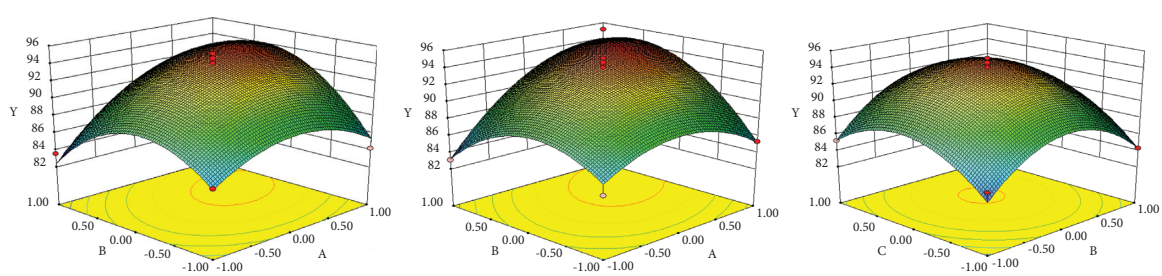

Figure 2: Response surface 3D map of each dependent variable relative to its respective variable.

Table 5: Results of verification ($n = 3$).

Batch	Formability (%)	Hygroscopicity (%)	Angle of repose
First batch	94.51	3.69	26.25
Second batch	93.68	3.71	26.41
Third batch	94.01	3.75	26.65
Average value	94.07	3.72	26.44

Table 6: The physical evaluation index results of ten batches of granules ($n = 10$).

Batch number	Index						
	Tap density	Bulk density	Hygroscopicity (%)	Water content (%)	Hausner ratio	Angle of repose (°C)	Relative homogeneity index
20201101	0.46	*0.33*	3.67	3.89	1.39	26.75	0.0096
20201102	0.47	*0.33*	3.54	3.75	1.42	27.15	0.0098
20201103	0.45	*0.32*	3.49	3.64	1.41	27.56	0.0102
20201104	0.49	*0.35*	3.65	3.86	1.40	26.96	0.0101
20201105	0.48	*0.35*	3.81	4.02	1.37	27.13	0.0096
20201106	0.47	*0.35*	3.76	3.98	1.34	27.45	0.0102
20201107	0.48	*0.34*	3.69	3.82	1.41	26.56	0.0095
20201108	0.47	*0.33*	3.82	3.63	1.42	27.02	0.0096
20201109	0.47	*0.34*	3.58	4.11	1.38	26.35	0.0101
20201110	0.45	0.32	3.6	3.73	1.41	26.89	0.0097
Average value	0.47	0.34	3.66	3.84	1.40	26.98	0.0098

Table 7: Standardized conversion method of secondary physical indexes.

Level indicators	The secondary indicators	Numerical range (x)	Conversion formula
Bulk property	Tap density (g/mL^{-1})	0 ~ 1	$10x$
	Bulk density (g/mL^{-1})	0 ~ 1	$10x$
Stability	Hygroscopicity (%)	20% ~ 0	$10-(x/2)$
	Water content (%)	10% ~ 0	$10-x$
Mobility	Hausner ratio	0 ~ 3	$(30-10x)/2$
	Angle of repose (°)	50 ~ 0	$10-(x/5)$
Uniformity	Relative homogeneity index	0 ~ 0.02	$500x$

3.5.2. Establishing Physical Fingerprint of Chuilian Jianpi Granules. The values of the seven physical parameters for the 10 batches of drugs were transformed, based on which the radar charts of each batch were drawn to establish the physical fingerprint of Chuilian Jianpi granules. The average values of the converted parameters were used to draw the radar charts as the control physical fingerprint, as shown in Figure 3.

3.5.3. Similarity Analysis of Physical Fingerprint. The similarities between the physical fingerprints of the above 10 batches of Chuilian Jianpi granules and the control physical fingerprints were analyzed by the cosine method of SPSS 17.0. The closer the similarity to 1, the more stable and uniform the product. The results showed that the physical fingerprint similarity of the 10 batches of Chuilian Jianpi granules was 99.2% and 98.9%, respectively, all of which are above 98.5%. The result suggests little difference in the physical properties of each batch of granules, indicating stability of the prescription.

4. Discussion

4.1. Preparation Method and Selection of Adjuvant Materials. Chuilian Jianpi offers a variety of options and features large total dose and a high rate of paste extraction in the presence of water. Increase in the amount of wet adjuvant materials would increase the daily dosage, which would be too strong for patients. Therefore, it is recommended to process the material into dry paste before being applied in drug production. The dry paste has strong water absorption and high viscosity when it meets water. In the preparation, high-concentration ethanol was selected as the wetting agent, and lactose and mannitol were used as diluents.

4.2. Establishment of the Granule Evaluation System. In the pre-experiment, the granules prepared under any ratio of lactose and mannitol showed good solubility. Therefore, the solubility was not taken into the single-factor evaluation and response surface optimization experiment.

4.3. The Concept of QbD and Physical Fingerprint. The principle of QbD emphasizes the role of procedures in ensuring product quality [18, 19]. The traditional evaluation method based on particle forming rate and substance content can no longer fully evaluate the prescription and preparation procedures. In particular, the substance content would not cause significant changes because of the simple forming procedures. In the pre-experiment, the preparation procedure was found to have little effect on the parameters,

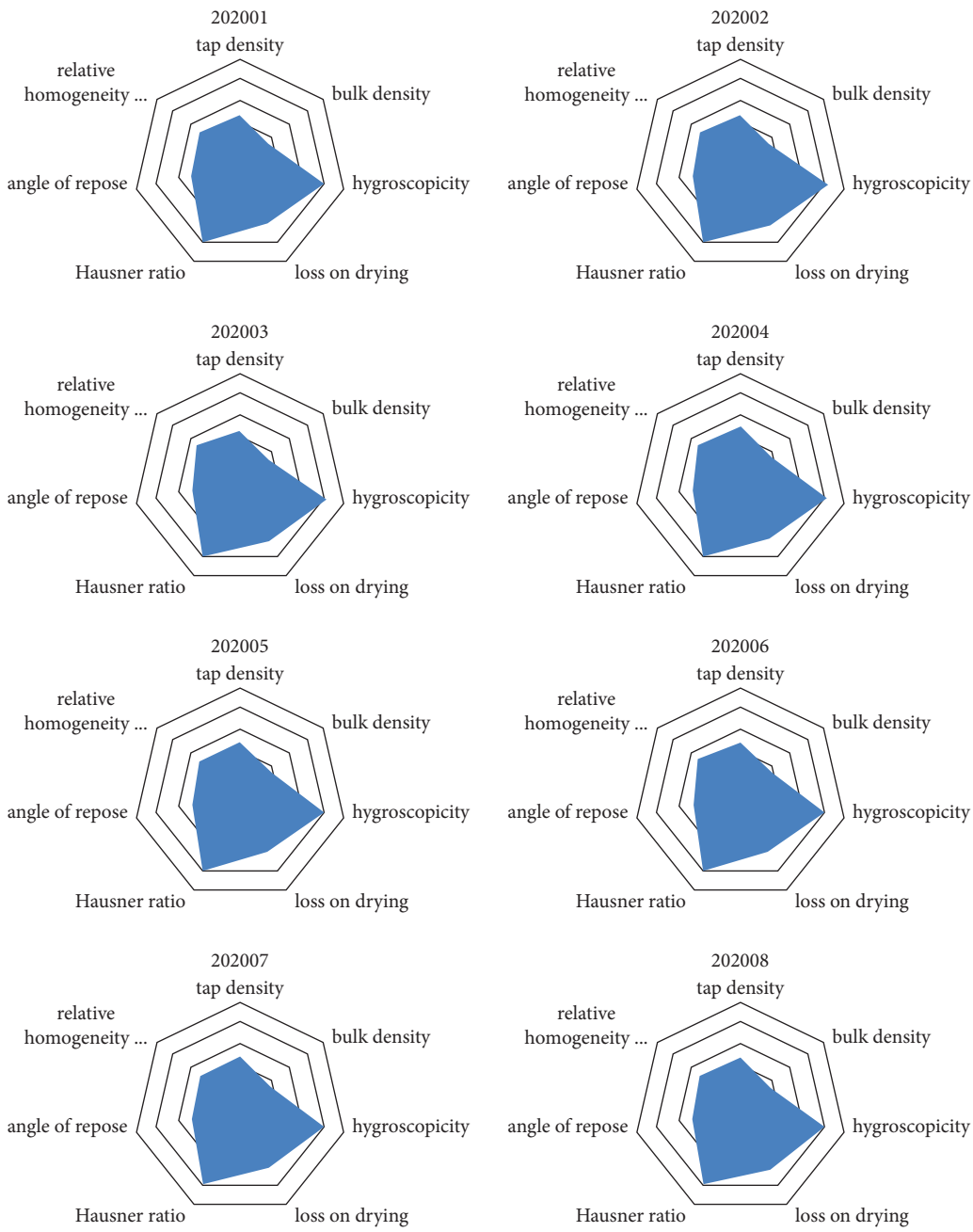

(a)

Figure 3: Continued.

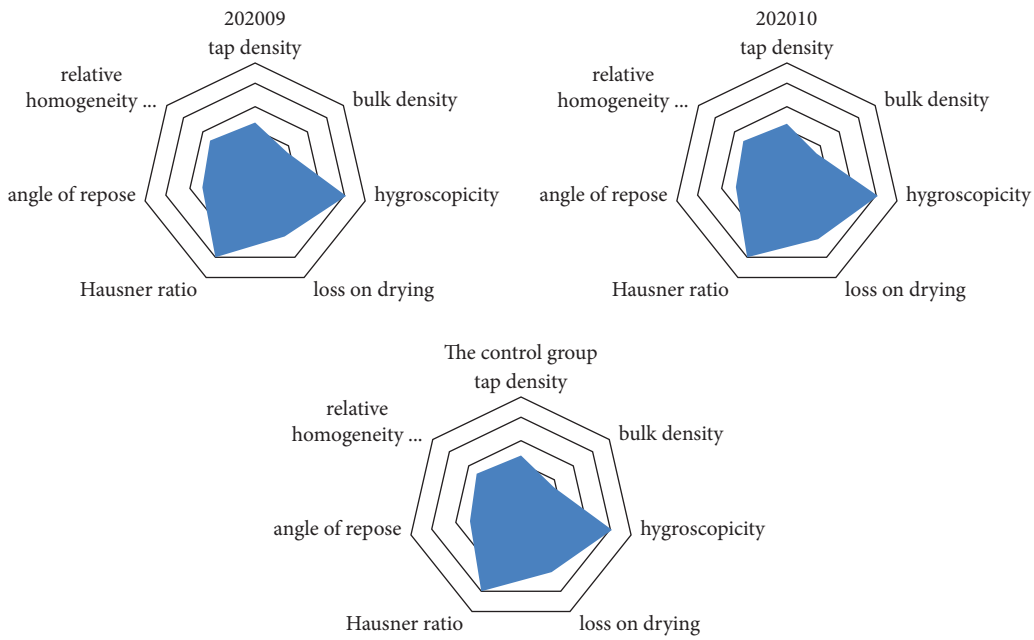

(b)

Figure 3: Physical fingerprint spectrum of Chuilian Jianpi granules.

with no significant difference in the parameters of the granule. Therefore, it was used in the evaluation of granules. In this paper, seven parameters, including tap density, bulk density, and moisture absorption, were used to establish physical fingerprint to evaluate the stability and feasibility of the preparation formula and procedures. The idea is consistent with QbD, and therefore it is worthy of promotion.

Data Availability

The data used to support the findings of this study are available from the corresponding author upon request.

Conflicts of Interest

The authors declare that there are no conflicts of interest regarding the publication of this paper.

Acknowledgments

This study was supported by the Technical Innovation and Social Service Team of Bozhou Vocational and Technical College (no. yptd001), Key Research Project of Bozhou Institute of Traditional Chinese Medicine of Anhui Academy of Traditional Chinese Medicine (nos. ykzzd008 and ykzyb011), Key Project of Anhui Vocational Adult Education Association (no. AGZ18011), and Natural Science Research Foundation of the Department of Education of Anhui Province (no. KJ2020A0789).

References

[1] L. Wang, *Study on the Effect of Design on the Quality of Traditional Chinese Medicine*, Zhejiang University, Hangzhou, China, 2015.

[2] S. Mehtap and T. Sevgi, "Development and in-vitro evaluation of pH-independent release matrix tablet of weakly acidic drug valsartan using quality by design (QbD) tools," *Drug Development and Industrial Pharmacy*, vol. 12, no. 44, pp. 1905–1917, 2018.

[3] Y. Xu, M. Xie, Y. Liang, W. Zhang, X. Cao, and T. Liu, "Optimized preparation of Chuanminshen violaceum buccal tablets based on QbD," *Chinese Journal of Experimental Traditional Medical Formulae*, vol. 24, no. 17, pp. 14–19, 2018.

[4] L. Deng, C. Chang, Y. Wang et al., "Establishment of safflower extract concentrating process and physical parameter model based on QbD," *Chinese Traditional Medicine Journal*, vol. 45, no. 19, pp. 4633–4642, 2020.

[5] W. Jamshed and K. S. Nisarl, "Computational single-phase comparative study of a Williamson nanofluid in a parabolic trough solar collector via the Keller box method," *Internatinal Journal of Energy Research*, vol. 45, no. 7, pp. 10636–10718, 2021.

[6] W. Jamshed, S. U. Devi, and K. S. Nisar, "Single phase based study of Ag-Cu/EO Williamson hybrid nanofluid flow over a stretching surface with shape factor," *Physica Scripta*, vol. 96, no. 6, p. 65202, 2021.

[7] W. Jamshed, E. Karatas Akgül, K. Sooppy Nisar, Esra, and Kottakkaran, "Keller box study for inclined magnetically driven Casson nanofluid over a stretching sheet: single phase model," *Physica Scripta*, vol. 96, no. 6, p. 65201, 2021.

[8] W. Jamshed, K. S. Nisar, R. J. P. Gowda, R. N. Kumar, and B. C. Prasannakumara, "Radiative heat transfer of second grade nanofluid flow past a porous flat surface: a single-phase mathematical model," *Physica Scripta*, vol. 96, no. 6, p. 64006, 2021.

[9] P. Li, T. Liu, W. Zhang, Y. Liang, J. Zhang, and B. Li, "Study on preparation and physical fingerprint of Huanghuai tablets based on QbD," *Chinese Herbal Medicine*, vol. 49, no. 7, pp. 1576–1582, 2018.

[10] Y. Wang, C. Chang, L. Deng et al., "Study on the preparation technology and physical fingerprint of safflower granules based on the idea that quality is determined by the design," *Chinese Herbal Medicine*, vol. 50, no. 17, pp. 4123–4130, 2019.
[11] G. Zhou, X. Huang, and F. Xuehua, "Optimization of the preparation of compound Wuhua granules," *Chinese Patent Medicine*, vol. 41, no. 6, pp. 1389–1391, 2019.
[12] S. Gui, W. Li, Y. Huang, and J. Wang, "Investigation on the prescription and preparation technology of Peiyuan granules," *Chinese Experimental Prescription Science*, vol. 21, no. 22, pp. 31–3339, 2015.
[13] Y. Diao, J. Ban, Q. Xie et al., "Effects of two preparation processes on the formability of compound Qishu granules," *Chinese Patent Medicine*, vol. 39, no. 2, pp. 414–417, 2017.
[14] A. Sun, B. Yuan, N. Li et al., "Study on dry granulation technology of kidney-warming and bone-strengthening granules," *Chinese Herbal Medicine*, vol. 49, no. 3, pp. 1324–1330, 2018.
[15] Q. Wang, X. Meng, T. Xue, and S. Sun, "Optimization of extraction and preparation of rust-brown Crotalaria granules," *Chinese Patent Medicine*, 2020, https://kns.cnki.net/kcms/detail/31.1368.R.20201111.0922.002.html.
[16] S. Guo, Q. He, H. Guo et al., "Study on the preparation technology of lily granules," *Jiangxi Traditional Chinese Medicine*, vol. 51, no. 6, pp. 67–69, 2020.
[17] L. Lu, X. Wang, Y. Wang et al., "Selection of adjuvant material for wind-coursing and panting stabilizer granules," *Chinese Patent Medicine*, vol. 39, no. 4, pp. 731–736, 2017.
[18] H. Yan, C. Zou, and H. Lu, "Study on moisture-proof adjuvant material of Trichosanthes granules," *Chinese Patent Medicine*, vol. 37, no. 4, pp. 902–905, 2015.
[19] European Pharmacopeia, "Dosage forms monographs," 2013.

Hindawi
Complexity
Volume 2021, Article ID 7792422, 17 pages
https://doi.org/10.1155/2021/7792422

Research Article

Analytical Investigation of Magnetohydrodynamic Non-Newtonian Type Casson Nanofluid Flow past a Porous Channel with Periodic Body Acceleration

N. Thamaraikannan,[1] **S. Karthikeyan**,[1] **Dinesh Kumar Chaudhary**,[2] **and Safak Kayikci**[3]

[1]*Department of Mathematics, Erode Arts and Science College, Erode 638 009, Tamilnadu, India*
[2]*Department of Physics, Amrit Campus, Tribhuvan University, Kathmandu, Nepal*
[3]*Department of Computer Engineering, Bolu Abant Izzet Baysal University, Bolu, Turkey*

Correspondence should be addressed to N. Thamaraikannan; kthamkar@gmail.com and Dinesh Kumar Chaudhary; din.2033@gmail.com

Received 18 June 2021; Revised 27 August 2021; Accepted 28 August 2021; Published 17 September 2021

Academic Editor: Muhammad Imran Asjad

The consequence of periodic body acceleration and thermal radiation in the pulsating flow of MHD Casson nanofluid through a porous channel is addressed. A flow of the nanofluid injected through the lower plate is considered while sucked out through the upper plate with a similar velocity. The thermal radiation term is incorporated in the heat transfer equation. The governing equations corresponding to velocity and temperature are converted from partial differential equations to a system of ordinary differential equations by employing similarity variables. The perturbation technique is applied to solve the governing flow equations. The impact of diverse parameters on flow features is graphically analyzed. The result reveals that adding the nanoparticle has enhanced the velocity profile of the base fluid. Moreover, an increase in the periodic body acceleration results in enlarging velocity and temperature.

1. Introduction

The foremost principle of MHD is that forces are formed by the magnetic field, which stimulates a current through a moving conducting fluid. The importance of MHD in various areas such as astrophysics, biomedical research, and geophysics motivates us to investigate MHD flow. Concerning the shear strain-stress relationship, Casson fluid is a non-Newtonian fluid, which becomes firm when the yield stress is more significant than shear stress. However, it begins to deform when the yielded stress becomes less significant than shear stress. The MHD flow of Casson fluid in a porous channel is a field of dynamic research due to its applicability in industry and medical technology such as paper production, condensation, and blood flow in the human body. Due to its applications in heat storage beds and fossil fuels, heat and mass transfer through a porous medium have been developed into an exciting topic for the most recent decades. Tamoor et al. [1] focused on "MHD Casson fluid flow above a stretching cylinder." Reddy [2] examined the "MHD Casson fluid flow over an exponentially inclined permeable stretching surface with the influence of thermal radiation and chemical reaction on the flow of the MHD Casson fluid flow over an exponentially inclined permeable stretching surface."

Fluids with suspended nanoparticles have an extensive range of applications in the heat transfer process because an increment in thermal conductivity in fluids was noticed while mixing nanoparticles. This attempt was taken first by Choi [3] subsequently succeeded by Sandeep et al. [4] and Nisar et al. [5]. They suggested that "the nanoparticle-containing gold can be used to treat and trounce cancer." Next, Abolbashari et al. [6]

analyzed "the mass and heat transfer characteristics of Casson nanofluid over a stretching surface." Finally, Tassaddiq et al. [7] analyzed "the Newtonian heating effects for the generalized Casson fluid MHD flow with porous effects." They found that velocity augments with escalating porosity and the Casson parameter control the fluid flow. Menni et al. [8, 9], Khan et al. [10], and Maouedj et al. [11] simulated the applicability of nanofluid in the solar channels.

Thermal radiation has a crucial role in many manufacturing processes. Irfan et al. [12] and Vellanki [13] investigated the radiation effect on Casson nanofluid and bio-nanofluid flow through a porous medium. MHD flow across porous channel between two parallel plates has vast application such as petrochemical engineering, polymer technology, food production technology, and biomedical research. Falede and Adensanya [14] explored "the oscillatory flow of MHD fluid through a porous channel." "MHD flow through a vertical channel with porous medium" was investigated by Dwivedi et al. [15]. "MHD nanofluid flow and heat transfer in rotating horizontal annulus were numerically simulated with thermal radiation" by Peng et al. [16]. The important visualization about the influence of magnetic field and radiation with assorted flow geometries is established in the literature [17–28].

The importance of the pulsating flow in a porous channel is well known, and it has many biological and industrial applications. Srinivas et al. [29] considered the MHD pulsating Casson fluid flow with chemical reaction and magnetic field through a porous channel. Kumar et al. [30] considered the "Joule heating and thermal radiation effects on the pulsatile MHD flow of Casson nanofluid through a vertical porous space." The study related to periodic body acceleration has enormous applications, particularly analyzing blood flow in the cardiovascular system. In many situations, such as driving in a vehicle, running, and jogging, the human body accelerates periodically (vibration). The sudden velocity change in the human body disturbs the blood flow, which causes most health problems. Vishali and Sarojamma [31] investigated the "flow of a fluid through a catheterized artery with the effect of a periodic body acceleration" in which they concluded that "the body acceleration enhanced velocity." Sulochana [32] discussed "the influence of body acceleration on an unsteady pulsatile flow of MHD couple stress fluid."

Over the years, nonlinear differential equations have been solved by approximate analytical methods such as the homotopy analysis method, weighted residual method, differential transformation methods, perturbation method, and so on. However, the non-perturbation approximate analytical methods have operational limitations that fussily tapered their performance domain, and they may sometimes lead to erroneous results while routinely implemented. Moreover, the conversion of the nonlinear equation and the evolution of corresponding recurrence equations using differential transformation methods are complex in some nonlinear systems. Consequently, the demand for reasonably simple, flexible, standard, and high precise total approximate analytical solutions is well acknowledged. One of such techniques applied for the quest is the perturbation method, which can solve nonlinear problems with high precision, while the perturbation method gives enhanced results for small perturbation parameters, further having a useful mathematical formulation with better accurateness, even for comparatively huge values of the perturbation parameter. Due to its unfussiness and high accuracy, the perturbation method was applied for solving various heat transfer and fluid mechanics problems [29–34].

To this extent, our literature review authenticates that there are no existing papers for MHD pulsating Casson nanofluid flow past a porous channel with periodic body acceleration effect. An examination was made for "pulsating Casson nanofluid flow through a porous channel with radiation" [35]. However, similar research for Casson nanofluid with periodic body acceleration effects was not investigated yet. Hence, we prolonged our effort to pulsative Casson nanofluid that passes through a porous channel between two parallel plates with periodic body acceleration and magnetic field impacts. The considered problem has massive application in manufacturing and biological processes. The perturbation technique was employed to solve the resulting similarity equations. The velocity and temperature fields are illustrated for several pertinent flow parameters.

2. Mathematical Formulation

Consider the influence of uniform traverse applied magnetic field on the pulsatile incompressible flow of a Casson nanofluid in a porous channel between two parallel plates, in which one plate is at rest and another plate moves in a parallel direction. The flow is driven by a pulsating pressure gradient [29].

$$\frac{1}{\rho_{nf}}\frac{\partial p^*}{\partial x^*} = -A\left\{1 + \varepsilon e^{i\omega t^*}\right\}, \tag{1}$$

where ρ_{nf} is the "density of the nanofluid," p^* is the "pressure," $\varepsilon \ll 1$ is suitably chosen positive quantity, A is a constant, and ω is the "frequency." The physical flow system is noted in Figure 1.

We consider that X^*-axis is taken along the lower plate, and the perpendicular axis is noted as Y^*-axis. The lower plate is at rest, maintaining the temperature T_0. The upper plate is moving with the velocity $U_w^* = (A/\omega)\{1 + \varepsilon e^{i\omega t^*}\}$ parallel to the X^*-axis and maintains the temperature $T_1\,(T_0 < T_1)$. The nanofluid is injected from the lower plate into the porous channel with the velocity v_0, and it is sucked out from the porous medium via the upper plate with the similar velocity. "Uniform magnetic field" (B_0) is imposed along the usual direction to the flow. The periodic body acceleration is assumed as $G^* = g_0 \cos\psi$, where ψ is the phase difference and g_0 is the amplitude of the body acceleration.

The Casson nanofluid rheological equation is stated as

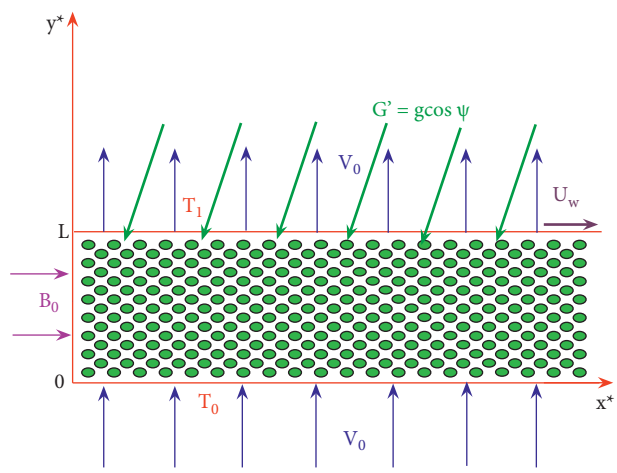

Figure 1: Physical model and coordinate system.

$$T_{ij} = \begin{cases} \left(2\mu_{B_{nf}} + \dfrac{p_y}{\sqrt{(\pi_c/2)}}\right)e_{mn}, & \pi_c > \pi, \\ \left(2\mu_{B_{nf}} + \dfrac{p_y}{\sqrt{(\pi/2)}}\right)e_{mn}, & \pi_c < \pi, \end{cases} \tag{2}$$

where "π_c" is the critical value of "π" based on the non-Newtonian model, T_{mn} is the (m,n)-th stress tensor component, $\pi = e_{mn}$ with e_{mn} being the (m,n)-th deformation rate, $\mu_{B_{nf}}$ is the plastic "dynamic viscosity" of the "non-Newtonian" nanofluid, and p_y is the "yield stress" of the fluid.

The governing equations of the flow problem are stated as follows:

$$\frac{\partial u^*}{\partial x^*} = 0, \tag{3}$$

$$\frac{\partial u^*}{\partial t^*} + v_0\frac{\partial u^*}{\partial y^*} = -\frac{1}{\rho_{nf}}\frac{\partial p^*}{\partial x^*} + \frac{\mu_{nf}}{\rho_{nf}}\left(1 + \frac{1}{\beta}\right)\frac{\partial^2 u^*}{\partial y^{*2}} - \frac{\sigma B_0^2}{\rho_{nf}}u^* - \frac{\mu_{nf}\Phi}{\rho_{nf}k}u^* + g_0\cos\psi, \tag{4}$$

$$0 = -\frac{1}{\rho_{nf}}\frac{\partial p^*}{\partial y^*}, \tag{5}$$

$$\frac{\partial T^*}{\partial t^*} + v_0\frac{\partial T^*}{\partial y^*} = \frac{\kappa_{nf}}{(\rho C_p)_{nf}}\frac{\partial^2 T^*}{\partial y^{*2}} + \frac{\mu_{nf}}{(\rho C_p)_{nf}} \cdot \left(1 + \frac{1}{\beta}\right)\left(\frac{\partial u^*}{\partial y^*}\right)^2 + \frac{\sigma B0^2}{(\rho C_p)_{nf}}u^{*2} + \frac{4\sigma^*}{3K^*(\rho C_p)_{nf}}\frac{\partial^2 T^{*4}}{\partial y^{*2}} + \frac{Q_0}{(\rho C_p)_{nf}}(T^* - T_0). \tag{6}$$

The boundary conditions for the present analysis are

$$\begin{aligned} u^* &= 0, \\ T^* &= T_0, \quad \text{at } y^* = 0, \\ u^* &= U_w^* = \frac{A}{\omega}\left\{1 + \varepsilon e^{i\omega t^*}\right\}, \\ T^* &= T_w, \quad \text{at } y^* = L, \end{aligned} \tag{7}$$

where Q_0 is "heat source/sink parameter," β is the "Casson parameter," u^* is the "dimensional velocity in X-direction," k and Φ are the "permeability and porosity of the porous medium," σ is the "electrical conductivity" of the fluid, $C_{p_{nf}}$ is the "specific heat at constant pressure of nanofluid," μ_{nf} is the "dynamic viscosity" of the nanofluid, ρ_{nf} is the "density" of the nanofluid, $(\rho C_p)_{nf}$ is the "heat capacity of the nanofluid," ν_{nf} is the "kinematic viscosity of the Casson nanofluid," κ_{nf} is the "thermal conductivity" of the nanofluid, K^* is "Rosseland mean absorption coefficient," and σ^* is the "Stefan–Boltzmann constant" [16].

$$\begin{aligned} \rho_{nf} &= (1-\varphi)\rho_f + \varphi\rho_n, \\ \mu_{nf} &= \frac{\mu_f}{(1-\varphi)^{2.5}}, \\ (\rho C_p)_{nf} &= (1-\varphi)(\rho C_p)_f + \varphi(\rho C_p)_n, \\ \nu_{nf} &= \frac{\mu_{nf}}{\rho_{nf}}, \\ \frac{\kappa_{nf}}{\kappa_f} &= \frac{(2\kappa_f + \kappa_n) - 2\varphi(\kappa_f - \kappa_n)}{(2\kappa_f + \kappa_n) + \varphi(\kappa_f - \kappa_n)}, \end{aligned} \tag{8}$$

where φ is the nanoparticle volume fraction and the subscripts nf, f, and n represent the nanofluid, base fluid, and nanoparticles correspondingly. The use of the above expression for (κ_{nf}/κ_f) is restricted to spherical nanoparticles only.

We assume that the temperature variation within the fluid flow can be expanded in a Taylor's series about T_0. By neglecting the higher-order terms, we obtain

$$T^{*4} \cong 4T_0^3 T^* - 3T_0^4. \tag{9}$$

We establish the dimensionless variables as follows:

$$\begin{aligned} x &= \frac{x^*}{L}, \\ y &= \frac{y^*}{L}, \\ t &= t^* \omega, \\ u &= \frac{u^* \omega}{A}, \\ p &= \frac{p^*}{\rho_{nf} A L}, \\ U_w &= \frac{\omega U_w^*}{A}, \\ \theta &= \frac{T^* - T_0}{T_w - T_0}. \end{aligned} \tag{10}$$

By applying equations (3), (5), (8), (9), and (10), in equations (4), (6), and (7),

$$\begin{aligned} &\frac{(1+(1/\beta))}{(1-\varphi)^{2.5}\left(1-\varphi+\left(\varphi\rho_n/\rho_f\right)\right)}\frac{\partial^2 u}{\partial y^2} - \mathrm{Re}\frac{\partial u}{\partial y} \\ &-\left(\frac{Ha^2}{\left(1-\varphi+\left(\varphi\rho_n/\rho_f\right)\right)} + \frac{1}{\left(1-\varphi+\left(\varphi\rho_n/\rho_f\right)\right)(1-\varphi)^{2.5}\mathrm{Da}}\right) \\ &\cdot u = H^2\left(\frac{\partial u}{\partial t} + \frac{\partial p}{\partial x}\right) - G\cos\psi, \end{aligned} \tag{11}$$

$$\begin{aligned} &\frac{\left((4/3)\mathrm{Rd} + \left(k_{nf}/k_f\right)\right)}{\mathrm{Pr}}\frac{\partial^2\theta}{\partial y^2} - \left(1-\varphi+\frac{\varphi\left(\rho C_p\right)_n}{\left(\rho C_p\right)_f}\right)\mathrm{Re}\frac{\partial\theta}{\partial y} \\ &+ Q\theta = H^2\left(1-\varphi+\frac{\varphi\left(\rho C_p\right)_n}{\left(\rho C_p\right)_f}\right)\frac{\partial\theta}{\partial t} \\ &- \mathrm{Ec}\left(\frac{(1+(1/\beta))}{(1-\varphi)^{2.5}}\left(\frac{\partial u}{\partial y}\right)^2 + \mathrm{Ha}^2 u^2\right). \end{aligned} \tag{12}$$

The new boundary conditions are

$$\begin{aligned} &u = 0, \\ &\theta = 0, \quad \text{at } y = 0, \\ &u = U_w = \left\{1 + \varepsilon e^{it}\right\}, \\ &\theta = 1, \quad \text{at } y = 1, \end{aligned} \tag{13}$$

where $\mathrm{Da} = k/\Phi L^2$ is the "Darcy number of the porous media," $H = L\sqrt{\omega}/\sqrt{\nu_f}$ is the frequency parameter, $\mathrm{Ha} = B_0 L\sqrt{\sigma}/\sqrt{\mu_f}$ is the Hartmann number, $\mathrm{Re} = V_0 L/\nu_f$ is the cross-flow Reynolds number, $\mathrm{Ec} = ((A/\omega)^2/(C_p)_f(T_w - T_0))$ is the Eckert number, $Q = (Q_0 L^2/(\rho C_p)_f \nu_f)$ is the "heat source/sink parameter," $\mathrm{Rd} = (4T_0^3\sigma^*/k_f K^*)$ is the radiation parameter, $\mathrm{Pr} = (\mu C_p)_f/k_f$ is the Prandtl number, and $G = L^2\omega g_0/A\nu_f$ is the body acceleration parameter.

3. Method of Solution

The velocity u and temperature θ can be supposed to have the form:

$$u = u_1(y) + \varepsilon u_2(y)e^{it} + \varepsilon^2 u_3(y)e^{2it}, \tag{14}$$

$$\theta = \theta_1(y) + \varepsilon\theta_2(y)e^{it} + \varepsilon^2\theta_3(y)^{2it}. \tag{15}$$

Now, substituting equations (1), (14), and (15) into equations (11)–(13) and then equating the coefficients of various powers of ε, we get

$$\alpha_1 u_1^{ll} - \mathrm{Re}\, u_1^l - \alpha_2 u_1 = -H^2 - G\cos\psi, \tag{16}$$

$$\alpha_1 u_2^{ll} - \mathrm{Re}\, u_2^l - \alpha_3 u_2 = -H^2, \tag{17}$$

$$\alpha_1 u_3^{ll} - \mathrm{Re}\, u_3^l - \alpha_4 u_3 = -H^2, \tag{18}$$

$$\beta_1\theta_1^{ll} - \beta_2\theta_1^l - Q\theta_1 = -\beta_3 u_1^{l2} - \beta_4 u_1^2, \tag{19}$$

$$\beta_1\theta_2^{ll} - \beta_2\theta_2^l - \beta_5\theta_2 = -2\beta_3 u_1^l u_2^l - 2\beta_4 u_1 u_2, \tag{20}$$

$$\beta_1\theta_3^{ll} - \beta_2\theta_3^l - \beta_6\theta_3 = -\beta_3 u_2^{l2} - \beta_4 u_2^2. \tag{21}$$

The new boundary conditions are

$$\begin{aligned} u_1 &= 0, \\ u_2 &= 0, \\ u_3 &= 0, \\ \theta_1 &= 0, \\ \theta_2 &= 0, \\ \theta_3 &= 0, \quad \text{at } y = 0, \\ u_1 &= 1, \\ u_2 &= 1, \\ u_3 &= 1, \\ \theta_1 &= 1, \\ \theta_2 &= 0, \\ \theta_3 &= 0, \quad \text{at } y = 1. \end{aligned} \tag{22}$$

Solving the six ODEs (16)–(21) with the boundary conditions (22), we obtain

$$
\begin{aligned}
u_1 &= A_1 e^{m_1 y} + A_2 e^{m_2 y} + A_3,\\
u_2 &= A_4 e^{m_3 y} + A_5 e^{m_4 y} + A_6,\\
u_3 &= A_7 e^{m_5 y} + A_8 e^{m_6 y} + A_9,\\
\theta_1 &= B_8 e^{m_7 y} + B_7 e^{m_8 y} + B_1 e^{2m_1 y} + B_2 e^{2m_2 y} + B_3 e^{m_1 y} + B_4 e^{m_2 y} + B_5 e^{(m_1+m_2)y} + B_6,\\
\theta_2 &= B_{18} e^{m_9 y} + B_{19} e^{m_{10} y} + B_9 e^{(m_1+m_3)y} + B_{10} e^{(m_1+m_4)y} + B_{11} e^{(m_2+m_3)y} + B_{12} e^{(m_2+m_4)y}\\
&\quad + B_{13} e^{m_1 y} + B_{14} e^{m_2 y} + B_{15} e^{m_3 y} + B_{16} e^{m_4 y} + B_{17},\\
\theta_3 &= B_{37} e^{m_{11} y} + B_{36} e^{m_{12} y} + B_{20} e^{2m_3 y} + B_{21} e^{2m_4 y} + B_{22} e^{(m_3+m_4)y} + B_{23} e^{(m_3+m_1)y} + B_{24} e^{(m_1+m_4)y}\\
&\quad + B_{25} e^{(m_3+m_2)y} + B_{26} e^{(m_2+m_4)y} + B_{27} e^{(m_5+m_1)y} + B_{28} e^{(m_6+m_1)y} + B_{29} e^{(m_5+m_2)y}\\
&\quad + B_{30} e^{(m_6+m_2)y} + B_{31} e^{m_3 y} + B_{32} e^{m_4 y} + B_{33} e^{m_5 y} + B_{34} e^{m_6 y} + B_{35},
\end{aligned}
\tag{23}
$$

where m's, A's, and B's are constants given in Appendix.

The dimensionless Nusselt number at the plates is given by

$$
\mathrm{Nu} = -\left(\frac{\partial \theta}{\partial y}\right)_{y=0,1} = -\left(\theta_1'(y) + \varepsilon\,\theta_2'(y) e^{it} + \varepsilon^2 \theta_3'(y) e^{2it}\right)_{y=0,1}. \tag{24}
$$

4. Results and Discussion

The effect of diverse material parameters on the non-dimensional heat transfer and velocity is discussed in this section. The values of the Nusselt number are compared with previously available results obtained by Srinivas et al. [29] for the various assumptions of the Hartmann number, Reynolds number, radiation parameter, and heat source parameter to assess the validity of the current results, and the outcome is shown in Table 1. Throughout the computation, the parameters are taken as $t = \pi/4, \varepsilon = 0.01, \mathrm{Re} = 2, \phi = 0.1, \mathrm{Ha} = 1, \beta = 5, \mathrm{Da} = 0.2, \mathrm{Ec} = 0.2, Q = 0.5, \mathrm{Rd} = 3, \mathrm{Pr} = 14, \psi = 60^{\circ}$, and $G = 1$ unless otherwise stated. Figures 2(a) and 2(b) represent the effect of nanoparticle volume fraction (φ) and Hartmann number (Ha) on the velocity distribution $u(y)$. It is noticed that $u(y)$ improves with an escalation in φ. Furthermore, the velocity is diminishing function of Ha since the applied magnetic field generates the Lorentz forces, which acts opposite to the flow direction. Figures 3(a) and 3(b) exhibit the effect of H and G on velocity distribution $u(y)$. It is noticed that $u(y)$ improves with an escalation in frequency parameter (H) and body acceleration parameter (G). Figure 4(a) elucidates the effect of Da on velocity distribution $u(y)$. It is evident that $u(y)$ improves with an escalation in Darcy number (Da) because Da is inversely proportional to the Darcy drag force. Figure 4(b) shows that an augment in Casson fluid parameter (β) escalates velocity distribution $u(y)$.

Figures 5(a) and 5(b) show the influence of (Ec) and (G) on the temperature distribution $\theta(y)$. The observations conclude that the temperature distribution $\theta(y)$ upsurges with a rise in Ec. In addition, it is obvious that the escalating periodic body acceleration slightly improves the temperature.

Figures 6(a) and 6(b) displays persuade of (Re) and (Pr)on the temperature distribution $\theta(y)$. From Figure 6(a), the observations show that the temperature distribution $\theta(y)$ reduces with an upsurge in cross-flow Reynolds number. Figure 6(b) depicts that the temperature diminished for increasing values of Pr. The Prandtl number diminishes the thermal boundary layer thickness. In addition, it controls the thickness of the thermal boundary layer. Fluids with lower Prandtl number have higher thermal conductivity so that the heat can diffuse from the plate faster than higher Prandtl number fluids [29]. Figures 7(a) and 7(b) reveal the influence of Q and Rd on $\theta(y)$. Figure 7(a) depicts that the temperature distribution boosts up with a rise in the heat source/sink parameter (Q). From Figure 7(b), one can observe a rise in $\theta(y)$ with intensification in Rd. This is in agreement with the physical reality that the thermal boundary layer thickness enhances with growing Rd.

The effect of Eckert number (Ec), Darcy number (Da), body acceleration parameter (G), radiation parameter (Rd), the nanoparticle volume fraction (φ), Hartmann number (Ha), heat source/sink parameter (Q), and Prandtl number (Pr) on unsteady temperature $\theta_t(y)$ is shown in Figures 8–11. From Figure 8(a), it is observed that the enhancement in Eckert number (Ec) produces an increasing tendency in unsteady temperature $\theta_t(y)$. Figure 8(b) depicts that the unsteady temperature $\theta_t(y)$ is oscillating with increasing Darcy number (Da). From Figure 9(a), it is observed that the increase in body acceleration parameter (G) produces an increase in unsteady temperature $\theta_t(y)$. Figure 9(b) shows that the unsteady temperature $\theta_t(y)$ is oscillating with increasing Hartmann number (Ha).

Figure 10(a) shows that the amplification in the nanoparticle volume fraction (φ) produces an insurgence in unsteady temperature $\theta_t(y)$ at the lower half of the channel; however, it begins osculating near the upper wall. From Figure 10(b), it is evident that the increase in Pr escalates the unsteady temperature.

From Figure 11(a), the influence of Q is minimal in the lower part of the channel. However, the unsteady temperature slightly decreases on the upper part of the channel for the increasing values of Q. From Figure 11(b), it is noticed

Table 1: Comparison of Nusselt number for Newtonian and non-Newtonian fluids with Srinivas et al. [29] for the limiting case of $\varphi = 0, G = 0, \varepsilon = 0.01, H = 3, \beta = 2, \mathrm{Ec} = 1, \mathrm{Da} = 0.1, \mathrm{Pr} = 21$, and $t = \pi/4$.

Parameter	Values	$\mathrm{Nu} = -(\partial\theta/\partial y)_{y=0}$				$\mathrm{Nu} = -(\partial\theta/\partial y)_{y=1}$			
		Newtonian		Non-Newtonian		Newtonian		Non-Newtonian	
		[29]	Present	[29]	Present	[29]	Present	[29]	Present
Ha	0	−2.7033	−2.7033	−2.6361	−2.6361	3.1771	3.1771	2.7457	2.7457
	2	−2.2726	−2.2726	−2.2307	−2.2307	3.5754	3.5754	2.7261	2.7261
	4	−1.5615	−1.5615	−1.5380	−1.5380	2.6740	2.6740	1.8116	1.8116
Re	0	−7.6829	−7.6829	−7.1678	−7.1678	6.1846	6.1846	5.6695	5.6695
	1	−2.2726	−2.2726	−2.2307	−2.2307	3.5754	3.5754	2.7261	2.7261
	2	−1.1585	−1.1585	−1.2067	−1.2067	−1.9577	−1.9577	−2.8056	−2.8056
Q	0	−2.5506	−2.5506	−2.4868	−2.4868	1.6763	1.6763	1.2142	1.2142
	0.5	−2.6712	−2.6712	−2.6064	−2.6064	3.2306	3.2306	2.7556	2.7556
	1	−2.8333	−2.8333	−2.7671	−2.7671	5.4356	5.4356	4.9425	4.9425
Rd	0	−4.2702	−4.2702	−4.1034	−4.1034	19.2777	19.2777	17.4188	17.4188
	1	−3.3850	−3.3850	−3.2904	−3.2904	6.2590	6.2590	5.4984	5.4984
	2	−2.8333	−2.8333	−2.7671	−2.7671	3.2303	3.2303	2.7556	2.7556

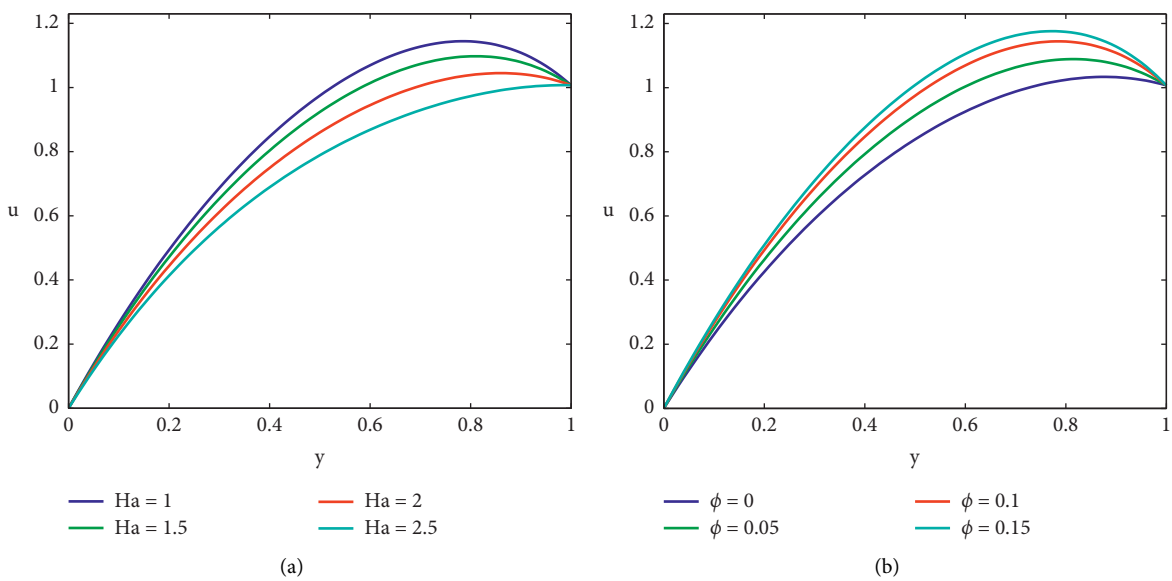

Figure 2: (a) Effect of Ha on the "velocity distribution" when $\varphi = 0.1$. (b) Effect of φ on the "velocity distribution" when Ha = 1.

that the increase in radiation parameter (Rd) produces a diminishing tendency in unsteady temperature.

Figure 12(a) shows the influence of the nanoparticle volume fraction (φ) on the Nusselt number (Nu) distribution. It is observed that a given rise in φ results in the decrease of Nusselt number (Nu) at the lower plate, although it increases at the upper plate. Figure 12(b) shows the influence of the body acceleration parameter (G) on the Nusselt number (Nu) distribution. It is observed that a given increase in body acceleration at the lower plate results in the decrease of Nusselt number (Nu), while it increases at the upper plate.

Figure 13 shows the influence of Rd on the Nusselt number (Nu) distribution. It is observed that a given increase in the Rd results in the decline of the Nusselt number (Nu) at the upper plate, while it increases

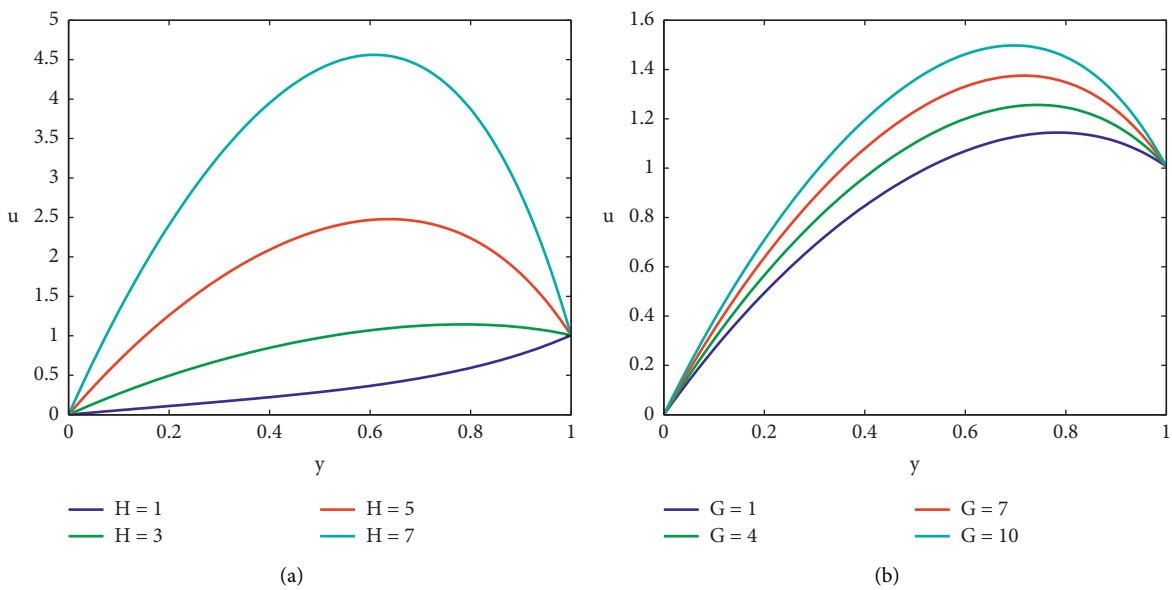

Figure 3: (a) Effect of H on the "velocity distribution" when $G = 1$. (b) Effect of G on the velocity distribution when $H = 5$.

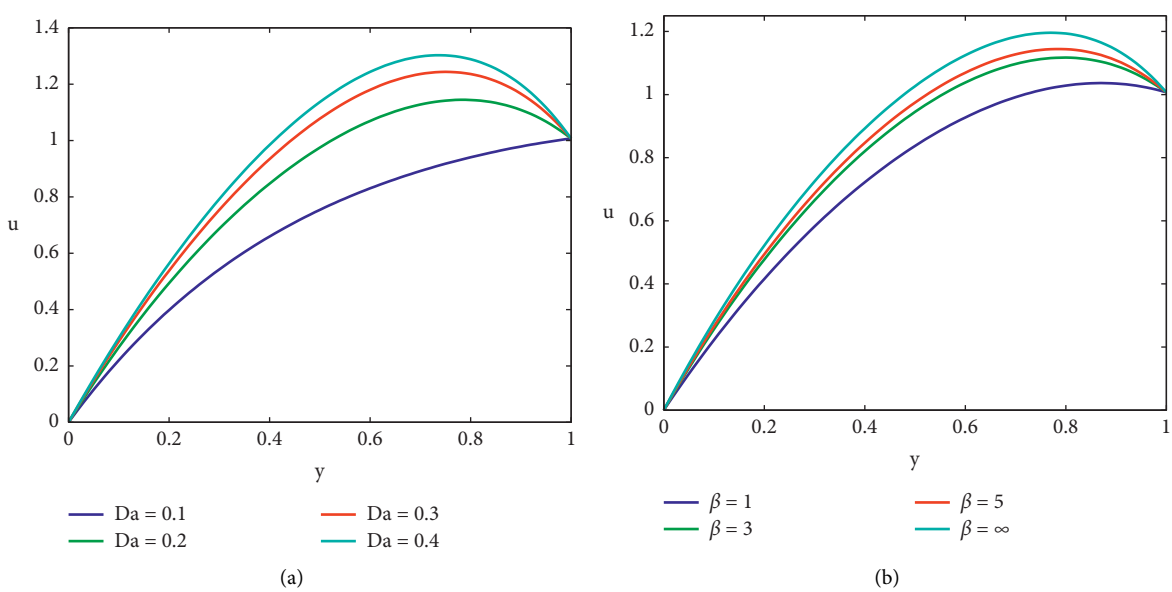

Figure 4: (a) Effect of Da on the "velocity distribution" when $\beta = 5$. (b) Effect of β on the "velocity distribution" when Da = 0.2.

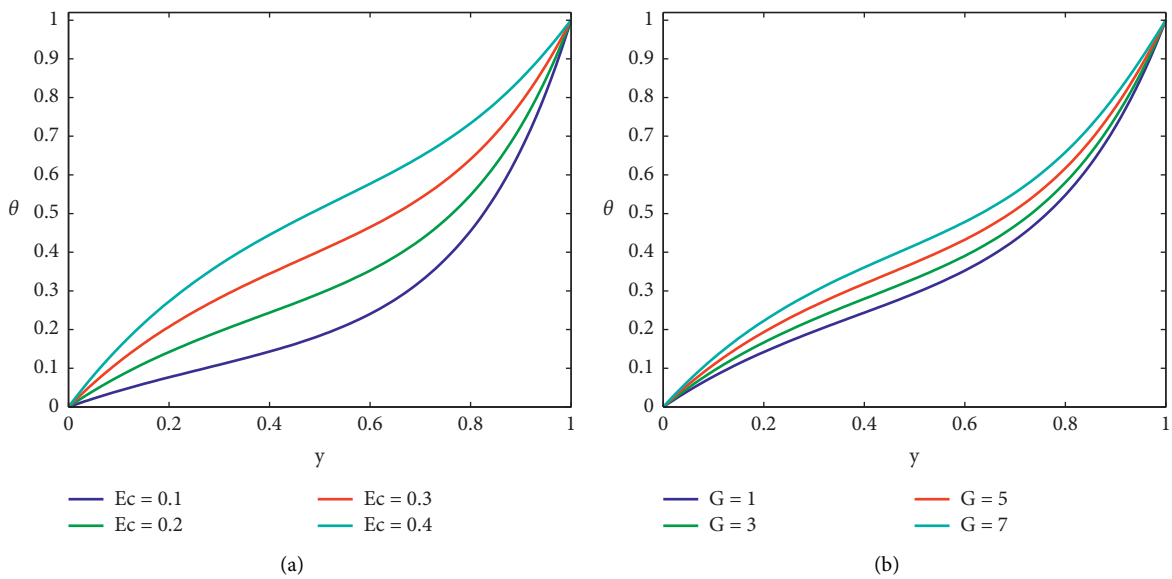

Figure 5: (a) Effect of Ec on the "temperature distribution" when $G = 1$. (b) Effect of G on the "temperature distribution" when Ec = 0.2.

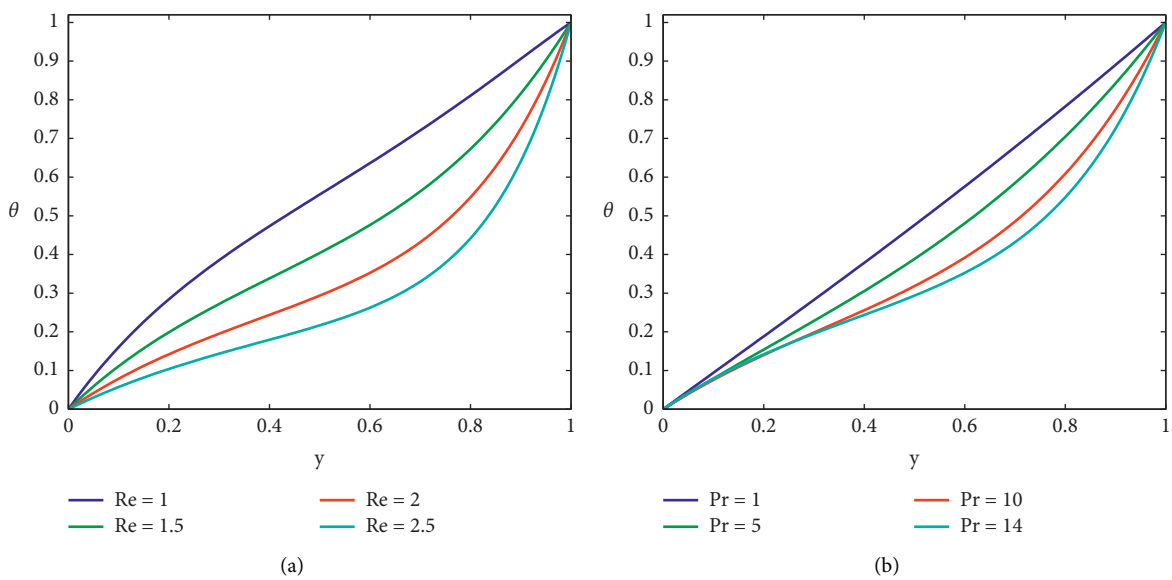

Figure 6: (a) Effect of Re on the "temperature distribution" when Pr = 14. (b) Effect of Pr on the temperature distribution when Re = 2.

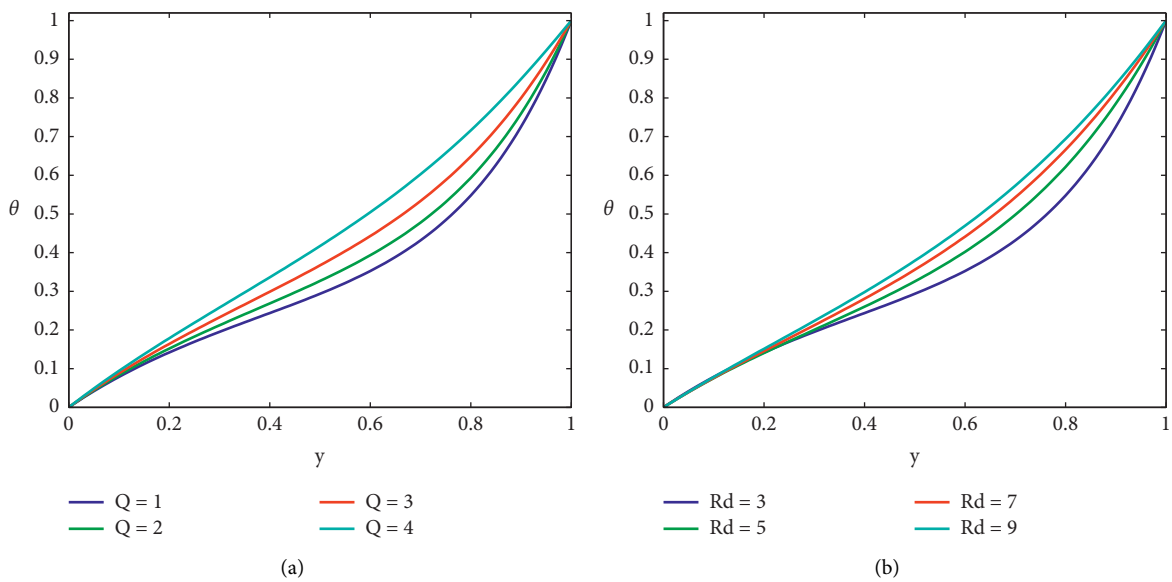

Figure 7: (a) Effect of Q on the "temperature distribution" when Rd = 3. (b) Effect of Rd on the "temperature distribution" when $Q = 0.5$.

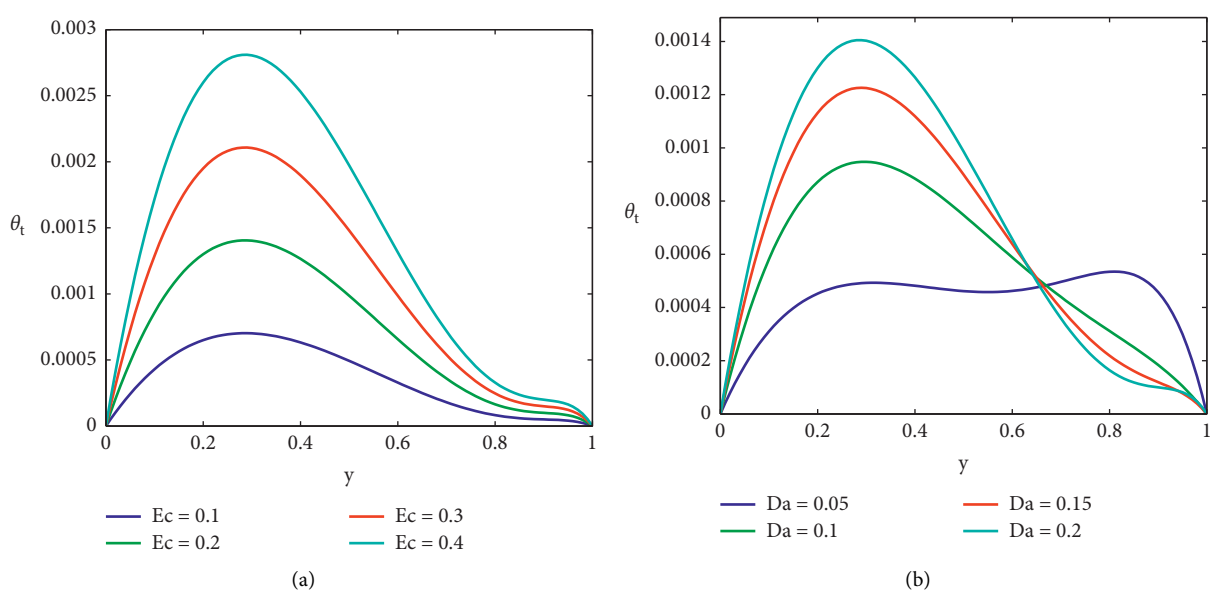

Figure 8: (a) Effect of Ec on "unsteady temperature distribution" for Da = 0.2. (b) Effect of Da on "unsteady temperature distribution" for Ec = 0.2.

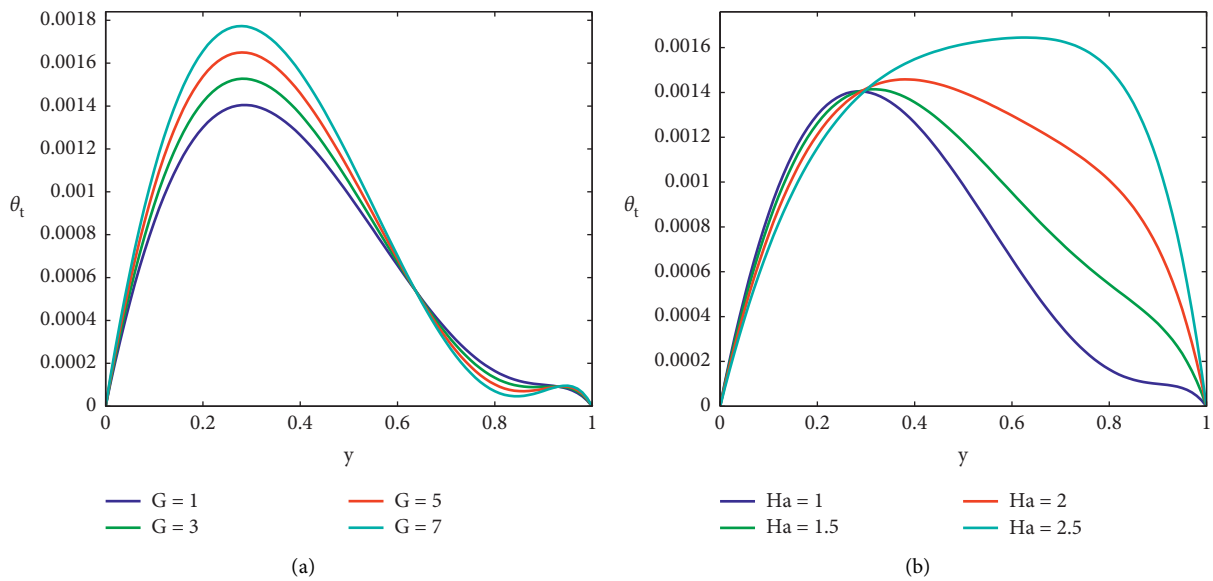

Figure 9: (a) Effect of G on unsteady "temperature distribution" when Ha = 1. (b) Effect of Ha on "unsteady temperature distribution" for $G = 1$.

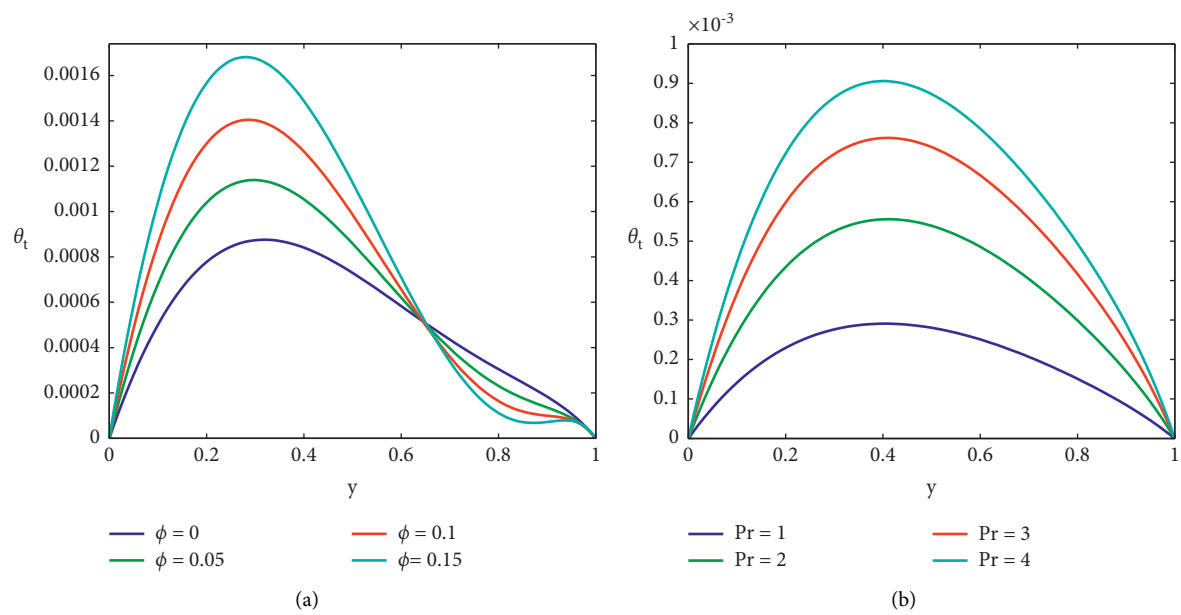

Figure 10: (a) Effect of φ on "unsteady temperature distribution" when Pr = 14. (b) Effect of Pr on "unsteady temperature distribution" for $\varphi = 0.1$.

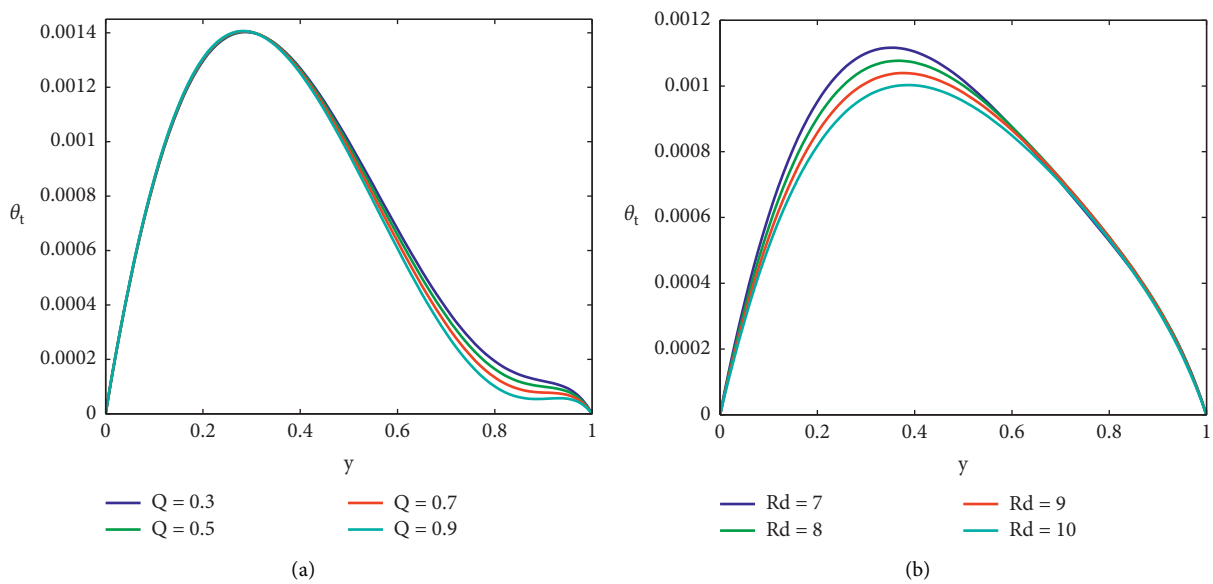

Figure 11: (a) Effect of Q on "unsteady temperature distribution" when Rd = 3. (b) Effect of Rd on "unsteady temperature distribution" for $Q = 0.5$.

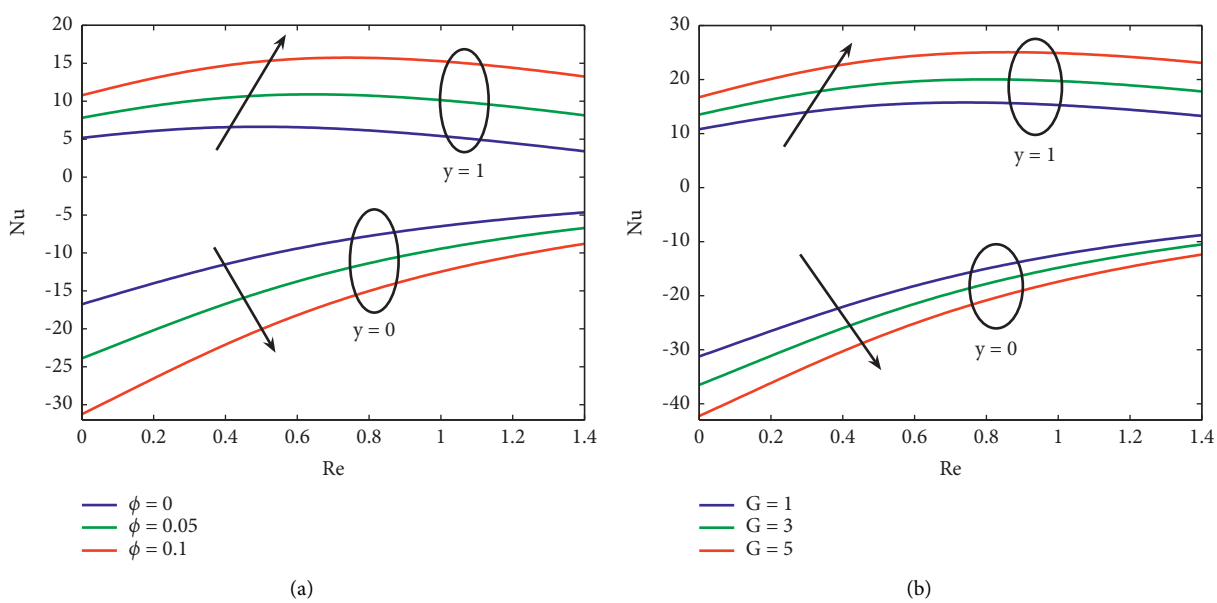

Figure 12: (a) Effect of φ on "Nusselt number distribution" when $G = 1$, $\mathrm{Ec} = 1$, $\mathrm{Ha} = 0.5$, $\mathrm{Rd} = 2$, and $\mathrm{Pr} = 21$. (b) Effect of G on "Nusselt number distribution" for $\varphi = 0.1$, $\mathrm{Ec} = 1$, $\mathrm{Ha} = 0.5$, $\mathrm{Rd} = 2$, and $\mathrm{Pr} = 21$.

at the lower plate. The greatest rate of change for Nu in both the plates was seen near the null values of Rd and Re.

Figure 14 illustrates the variation of the unsteady Nusselt number (Nu_t) for Re with time variation in the upper plate. It is observed that the unsteady Nusselt number upsurges with increasing Re. Thus, the unsteady Nusselt number distribution is a periodic function of "t" with period 2π.

Table 2 shows the variations of the Nusselt number (Nu)for the Casson nanofluid with and without body acceleration. The periodic body acceleration is taken as the body acceleration parameter $G = 1$. From this table,

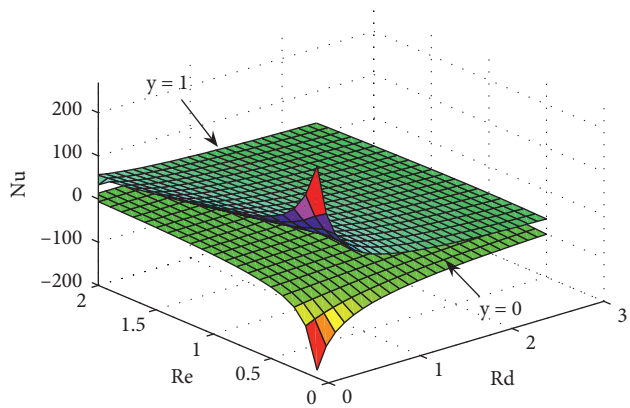

Figure 13: Effect of Rd and Re on "the Nusselt number distribution" when Ec = 1, Ha = 0.5, and Pr = 21.

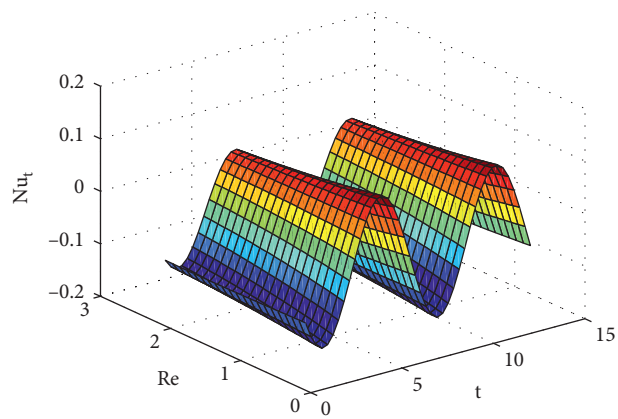

Figure 14: Effect of Re over time variation on the "unsteady Nusselt number distribution" for Ec = 1, Rd = 2, Ha = 0.5, and Pr = 21.

Table 2: Comparison of Nusselt number for channel with and without periodic body acceleration, when $\varepsilon = 0.01, H = 3, \beta = 5$, Ec = 1, Da = 0.2, Pr = 21, and $t = \pi/4$.

Parameter	Values	$\mathrm{Nu} = -(\partial\theta/\partial y)_{y=0}$		$\mathrm{Nu} = -(\partial\theta/\partial y)_{y=1}$	
		Without body acceleration ($G = 0$)	With body acceleration ($G = 1$)	Without body acceleration ($G = 0$)	With body acceleration ($G = 1$)
Ha	0	−5.0478	−5.5719	6.2828	8.1745
	1	−4.7406	−5.2344	8.7987	10.7217
	2	−3.9957	−4.4158	15.0043	16.9792
Re	0	−28.7997	−31.2494	9.6086	10.7870
	2	−4.9676	−5.4839	6.9407	8.8376
	4	−1.4012	−1.5520	−8.8930	−7.7016
Q	0	−4.8737	−5.3805	4.0757	5.7305
	0.5	−4.9676	−5.4839	6.9407	8.8376
	1	−5.0705	−5.5971	10.4949	12.6975
Rd	1	−5.3459	−5.9066	13.2025	16.3828
	2	−4.9676	−5.4839	6.9407	8.8376
	3	−4.6292	−5.1053	4.0732	5.3677

the Nusselt number Nu enhances at the lower plate for both the cases with the higher values of Re and Rd, while the inverse trend is noticed for larger value of Q. However, this behaviour is reversed at the upper plate for Re, Rd, and Q, while it increases for enlarging values of Ha at both the plates. It is also observed that with increasing periodic body acceleration (G), the Nu decreases at the lower plate, while it increases at the upper

plate. Therefore, the body acceleration reduces the heat conduction in lower temperature (T_0), while it is enhanced at higher temperature (T_w).

5. Conclusion

The present study addressed the influence of periodic body acceleration and thermal radiation on the MHD flow of Casson nanofluid through a porous channel. The pulsating flow is included in the flow problem. The analytical technique (perturbation) is utilized to compute the physical system. The considered problem is essential as the study related to periodic body acceleration in the porous channel has enormous applications in industrial and biological sectors. The generalized solutions have been found for the velocity and temperature distributions. Various graphs were depicted to emphasize vivid effects of various parameters, such as Reynolds number, frequency parameter, body acceleration parameter, Casson fluid parameter, radiation parameter, nanoparticle volume fraction, and the Darcy number:

(1) The fluid velocity increased for elevated values of frequency parameter, Casson fluid parameter, body acceleration parameter, nanoparticle volume fraction, and the Darcy number. However, the reverse effect was depicted for growing values of the Hartmann number.

(2) Diminishing behaviour of fluid flow is observed for diverse values of cross Reynolds number and the Prandtl number. Prandtl number has an essential role in the heat transfer process.

(3) The Nusselt number declines at the lower plate and increases at the upper plate with the rise in the nanoparticle volume fraction, Darcy number, and body acceleration parameter.

(4) The unsteady Nusselt number distribution is a periodic function of "t" with period 2π with its lowest values near $2n\pi$ and higher values near $(2n+1)\,\pi$ for all integer values of n.

(5) The body acceleration enhances the velocity at both plates. However, it reduces the heat conduction in lower temperature (T_0), while it increases at higher temperature (T_w).

Appendix

$$\alpha_1 = \frac{((1/\beta)+1)}{\left(1-\varphi+\left(\varphi\rho_n/\rho_f\right)\right)(1-\varphi)^{2.5}},$$

$$\alpha_2 = \frac{1}{\left(1-\varphi+\left(\varphi\rho_n/\rho_f\right)\right)}\left(\mathrm{Ha}^2+\frac{1}{(1-\varphi)^{2.5}\mathrm{Da}}\right),$$

$$A_3 = \frac{H^2+G\cos\psi}{\alpha_2},$$

$$m_{1,2} = \frac{\mathrm{Re}\pm\sqrt{\mathrm{Re}^2+4\alpha_1\alpha_2}}{2\alpha_1},$$

$$A_1 = \frac{A_3\left(e^{m_2}-1\right)+1}{\left(e^{m_1}-e^{m_2}\right)},$$

$$A_2 = \frac{A_3\left(e^{m_1}-1\right)+1}{\left(e^{m_2}-e^{m_1}\right)},$$

$$\alpha_3 = \frac{1}{\left(1-\varphi+\left(\varphi\rho_n/\rho_f\right)\right)}\left(\mathrm{Ha}^2+\frac{1}{(1-\varphi)^{2.5}\mathrm{Da}}\right)+iH^2,$$

$$A_6 = \frac{H^2}{\alpha_3},$$

$$m_{3,4} = \frac{\mathrm{Re}\pm\sqrt{\mathrm{Re}^2+4\alpha_1\alpha_3}}{2\alpha_1},$$

$$A_4 = \frac{A_6\left(e^{m_4}-1\right)+1}{\left(e^{m_3}-e^{m_4}\right)},$$

$$A_5 = \frac{A_6\left(e^{m_3}-1\right)+1}{\left(e^{m_4}-e^{m_3}\right)},$$

$$\alpha_4 = \frac{1}{\left(1-\varphi+\left(\varphi\rho_n/\rho_f\right)\right)}\left(\mathrm{Ha}^2+\frac{1}{(1-\varphi)^{2.5}\mathrm{Da}}\right)+2iH^2,$$

$$A_9 = \frac{H^2}{\alpha_4},$$

$$m_{5,6} = \frac{\mathrm{Re}\pm\sqrt{\mathrm{Re}^2+4\alpha_1\alpha_4}}{2\alpha_1},$$

$$A_7 = \frac{A_9\left(e^{m_6}-1\right)+1}{\left(e^{m_5}-e^{m_6}\right)},$$

$$A_8 = \frac{A_9\left(e^{m_5}-1\right)+1}{\left(e^{m_6}-e^{m_5}\right)},$$

$$\beta_1 = \frac{\left(\left(k_{nf}/k_f\right)+(4/3)\mathrm{Rd}\right)}{\mathrm{Pr}},$$

$$\beta_2 = \mathrm{Re}\left(1-\varphi+\frac{\varphi\left(\rho C_p\right)_n}{\left(\rho C_p\right)_f}\right),$$

$$m_{7,8} = \frac{\beta_2\pm\sqrt{\beta_2^2+4\beta_1\mathrm{Q}}}{2\beta_1},$$

$$\beta_3 = \frac{(1+(1/\beta))}{(1-\varphi)^{2.5}}\mathrm{Ec},$$

$$\beta_4 = \mathrm{Ha}^2\mathrm{Ec},$$

$$B_1 = -\frac{\beta_3 m_1^2 A_1^2 + \beta_4 A_1^2}{4m_1^2\beta_1 - 2m_1\beta_2 + Q},$$

$$B_2 = -\frac{\beta_3 m_2^2 A_2^2 + \beta_4 A_2^2}{4m_2^2\beta_1 - 2m_2\beta_2 + Q},$$

$$B_3 = \frac{2\beta_4 A_1 A_3}{m_1^2\beta_1 - m_1\beta_2 + Q},$$

$$B_4 = \frac{2\beta_4 A_2 A_3}{m_2^2\beta_1 - m_2\beta_2 + Q},$$

$$B_5 = -\frac{2\beta_3 m_1 m_2 A_1 A_2 + 2\beta_4 A_1 A_2}{(m_1+m_2)^2\beta_1 - (m_1+m_2)\beta_2 + Q},$$

$$B_6 = \frac{\beta_4 A_3^2}{Q},$$

$$B_7 = \frac{1}{\left(e^{m_8} - e^{m_7}\right)}\Big(1 + B_1\left(e^{m_7} - e^{2m_1}\right) - B_2\left(e^{m_7} - e^{2m_2}\right) + B_3\left(e^{m_7} - e^{m_1}\right) + B_4\left(e^{m_7} - e^{m_2}\right) + B_5\left(e^{m_7} - e^{(m_1+m_2)}\right) + B_6\left(e^{m_7} - 1\right)\Big),$$

$$B_8 = -\left(B_6 + B_7 + B_5 + B_3 + B_4 + B_2 + B_1\right),$$

$$\beta_5 = Q - i\left(1 - \varphi + \frac{\varphi\left(\rho C_p\right)_n}{\left(\rho C_p\right)_f}\right)H^2,$$

$$m_{9,10} = \frac{\beta_2 \pm \sqrt{\beta_2^2 + 4\beta_1\beta_5}}{2\beta_1},$$

$$B_9 = -\frac{2\beta_3 m_1 m_3 A_1 A_5 + 2\beta_4 A_1 A_5}{(m_1+m_3)^2\beta_1 - (m_1+m_3)\beta_2 + \beta_5},$$

$$B_{10} = -\frac{2\beta_3 m_1 m_4 A_1 A_4 + 2\beta_4 A_1 A_4}{(m_1+m_4)^2\beta_1 - (m_1+m_4)\beta_2 + \beta_5},$$

$$B_{11} = -\frac{2\beta_3 m_2 m_3 A_2 A_5 + 2\beta_4 A_2 A_5}{(m_2+m_3)^2\beta_1 - (m_2+m_3)\beta_2 + \beta_5},$$

$$B_{12} = -\frac{2\beta_3 m_2 m_4 A_2 A_4 + 2\beta_4 A_2 A_4}{(m_2+m_4)^2\beta_1 - (m_2+m_4)\beta_2 + \beta_5},$$

$$B_{13} = \frac{2\beta_4 A_1 A_6}{m_1^2\beta_1 - m_1\beta_2 + \beta_5},$$

$$B_{14} = \frac{2\beta_4 A_2 A_6}{m_2^2\beta_1 - m_2\beta_2 + \beta_5},$$

$$B_{15} = \frac{2\beta_4 A_3 A_5}{m_3^2\beta_1 - m_3\beta_2 + \beta_5},$$

$$B_{16} = \frac{2\beta_4 A_3 A_4}{m_4^2\beta_1 - m_4\beta_2 + \beta_5},$$

$$B_{17} = -\frac{2\beta_4 A_3 A_6}{\beta_5},$$

$$B_{19} = \frac{1}{\left(e^{m_{10}} - e^{m_9}\right)}\Big(B_9\left(e^{m_9} - e^{(m_1+m_3)}\right) + B_{10}\left(e^{m_9} - e^{(m_1+m_4)}\right) - B_{11}\left(e^{m_9} - e^{(m_2+m_3)}\right) + B_{12}\left(e^{m_9} - e^{(m_4+m_2)}\right) + B_{13}\left(e^{m_9} - e^{m_1}\right) + B_{14}\left(e^{m_9} - e^{m_2}\right) + B_{15}\left(e^{m_9} - e^{m_3}\right) + B_{16}\left(e^{m_9} - e^{m_4}\right) + B_{17}\left(e^{m_9} - 1\right),$$

$$B_{18} = -\left(B_{10} + B_9 + B_{11} + B_{13} + B_{12} + B_{14} + B_{16} + B_{15} + B_{17} + B_{19}\right),$$

$$\beta_6 = Q - 2i\left(1 - \varphi + \frac{\varphi\left(\rho C_p\right)_n}{\left(\rho C_p\right)_f}\right)H^2,$$

$$m_{11,12} = \frac{\beta_2 \pm \sqrt{\beta_2^2 + 4\beta_1\beta_6}}{2\beta_1},$$

$$B_{20} = -\frac{\beta_3 m_3^2 A_5^2 + \beta_4 A_5^2}{m_3^2\beta_1 - 2m_3\beta_2 + \beta_6},$$

$$B_{21} = -\frac{\beta_3 m_4^2 A_4^2 + \beta_4 A_4^2}{m_4^2\beta_1 - 2m_4\beta_2 + \beta_6},$$

$$B_{22} = -\frac{2\beta_3 m_3 m_4 A_4 A_5 + 2\beta_4 A_4 A_5}{(m_3+m_4)^2\beta_1 - (m_3+m_4)\beta_2 + \beta_6},$$

$$B_{23} = -\frac{2\beta_3 m_1 m_3 A_1 A_5}{(m_1+m_3)^2\beta_1 - (m_1+m_2)\beta_2 + \beta_6},$$

$$B_{24} = -\frac{2\beta_3 m_1 m_4 A_1 A_4}{(m_1+m_4)^2\beta_1 - (m_1+m_4)\beta_2 + \beta_6},$$

$$B_{25} = -\frac{2\beta_3 m_2 m_3 A_2 A_5}{(m_2+m_3)^2\beta_1 - (m_2+m_3)\beta_2 + \beta_6},$$

$$B_{26} = -\frac{2\beta_3 m_2 m_4 A_2 A_4}{(m_2+m_4)^2\beta_1 - (m_2+m_4)\beta_2 + \beta_6},$$

$$B_{27} = -\frac{2\beta_4 A_1 A_7}{(m_1+m_5)^2\beta_1 - (m_1+m_5)\beta_2 + \beta_6},$$

$$B_{28} = -\frac{2\beta_4 A_1 A_8}{(m_1+m_6)^2\beta_1 - (m_1+m_6)\beta_2 + \beta_6},$$

$$B_{29} = -\frac{2\beta_4 A_2 A_7}{(m_2+m_5)^2\beta_1 - (m_2+m_5)\beta_2 + \beta_6},$$

$$B_{30} = -\frac{2\beta_4 A_2 A_8}{(m_2+m_6)^2\beta_1 - (m_2+m_6)\beta_2 + \beta_6},$$

$$B_{31} = \frac{2\beta_4 A_5 A_6}{m_3^2\beta_1 - m_3\beta_2 + \beta_6},$$

$$B_{32} = \frac{2\beta_4 A_4 A_6}{m_4^2\beta_1 - m_4\beta_2 + \beta_6},$$

$$B_{33} = \frac{2\beta_4 A_3 A_7}{m_5^2\beta_1 - m_5\beta_2 + \beta_6},$$

$$B_{34} = \frac{2\beta_4 A_3 A_8}{m_6^2\beta_1 - m_6\beta_2 + \beta_6},$$

$$B_{35} = \frac{\beta_4 A_6^2}{\beta_6},$$

$$\begin{aligned} B_{36} = {} & \frac{1}{\left(e^{m_{11}} - e^{m_{12}}\right)}\Big(B_{20}\left(e^{m_{11}} - e^{2m_3}\right) + B_{21}\left(e^{m_{11}} - e^{2m_4}\right) \\ & + B_{22}\left(e^{m_{11}} - e^{(m_4+m_3)}\right) + B_{23}\left(e^{m_{11}} - e^{(m_1+m_3)}\right) \\ & + B_{24}\left(e^{m_{11}} - e^{(m_1+m_4)}\right) + B_{25}\left(e^{m_{11}} - e^{(m_2+m_3)}\right) \\ & + B_{26}\left(e^{m_{11}} - e^{(m_4+m_2)}\right) + B_{27}\left(e^{m_{11}} - e^{(m_1+m_5)}\right) \\ & + B_{28}\left(e^{m_{11}} - e^{(m_1+m_6)}\right) \\ & + B_{29}\left(e^{m_{11}} - e^{(m_2+m_5)}\right) + B_{30}\left(e^{m_{11}} - e^{(m_6+m_2)}\right) \\ & + B_{31}\left(e^{m_{11}} - e^{m_3}\right) + B_{32}\left(e^{m_{11}} - e^{m_4}\right) + B_{33}\left(e^{m_{11}} - e^{m_5}\right) \\ & + B_{34}\left(e^{m_{11}} - e^{m_6}\right) + B_{35}\left(e^{m_{11}} - 1\right), \end{aligned}$$

$$\begin{aligned} B_{37} = {} & -\big(B_{21} + B_{22} + B_{28} + B_{26} + B_{29} + B_{27} + B_{31} + B_{34} \\ & + B_{32} + B_{30} + B_{36} + B_{25} + B_{33} + B_{23} + B_{24} + B_{35} + B_{20}\big). \end{aligned} \tag{A.1}$$

Nomencluature

Length:	D, m (meter)
Mass:	M, kg (kilogram)
Temperature:	η, K (Kelvin)
Time:	τ, s (second)
Electric current:	I, A (ampere)

Symbol Physical quantity (Dimension)

A:	Constant defined in equation (1) ($D\ \tau^{-2}$)
B_0:	Uniform magnetic field ($D\ \tau^{-1}\ I^{-1}$)
$C_{p_{nf}}$:	Specific heat at a constant pressure of nanofluid ($D^2\ \tau^{-2}\eta^{-1}$)
κ_{nf}:	Thermal conductivity of the nanofluid ($M\ D\tau^{-3}\eta^{-1}$)
p^*:	Pressure ($M\ D^{-1}\ \tau^{-2}$)
k:	Permeability of the porous media (D^2)
Φ:	Porosity of the porous medium
σ:	Electrical conductivity of the fluid ($M^{-1}\ D^{-3}\ \tau^3\ I^2$)
μ_{nf}:	Dynamic viscosity of the nanofluid ($M\ D^{-1}\ \tau^{-1}$)
ρ_{nf}:	Density of the nanofluid (MD^{-3})
ν_{nf}:	Kinematic viscosity of the nanofluid ($D^2\ \tau^{-1}$)
φ:	Nanoparticle volume fraction
$(\rho C_p)_{nf}$:	Heat capacity of the nanofluid ($M\ D^{-1}\ \tau^{-2}\ \eta^{-1}$)
ω:	Frequency (τ^{-1})
g_0:	Amplitude of the body acceleration ($D\ \tau^{-2}$)
ψ:	Phase difference of the body acceleration
K^*:	Rosseland mean absorption coefficient (D^{-1})
Q_0:	Heat source/sink coefficient ($M\ D^{-1}\ \tau^{-3}\ \eta^{-1}$)
σ^*:	Stefan- Boltzmann constant ($M\ \tau^{-3}\eta^{-4}$)
u^*:	Dimensional velocity in X-direction ($D\ \tau^{-1}$)
T^*:	Temperature of the nanofluid (H)
T_0:	Temperature at the lower wall (H)
T_w:	Temperature at the upper wall (H)
β:	Casson parameter
Da:	Darcy number of the porous media
Ec:	Eckert number
H:	Frequency parameter
Ha:	Hartmann number
Nu:	Nusselt number
Pr:	Prandtl number
Q:	Heat source/sink parameter
Re:	Cross-flow Reynolds number
Rd:	Radiation parameter
G:	Body acceleration parameter

Subscripts

f: Fluid fraction

n: Nanoparticle fraction
nf: Nanofluid.

Data Availability

The raw data supporting the conclusions of this article are available from the corresponding author upon request.

Conflicts of Interest

The authors declare that they have no conflicts of interest.

Acknowledgments

The authors are grateful to Research and Development Wing, Live4Research, Tiruppur, Tamil Nadu, India, for the technical and financial support to this project work.

References

[1] M. Tamoor, M. Waqas, M. I. Khan, A. Alsaedi, and T. Hayat, "Magnetohydrodynamic flow of Casson fluid over a stretching cylinder," *Results in Physics*, vol. 7, pp. 498–502, 2017.

[2] P. B. A. Reddy, "Magnetohydrodynamic flow of a Casson fluid over an exponentially inclined permeable stretching surface with thermal radiation and chemical reaction," *Ain Shams Engineering Journal*, vol. 7, no. 2, pp. 593–602, 2016.

[3] S. Choi, "Enhancing thermal conductivity of fluids with nanoparticles," in *Proceedings of the ASME International Mechanical Engineering Congress & Exposition*, pp. 99–105, San Francisco, CA, USA, January 1995.

[4] N. Sandeep, A. J. Chamkha, and I. L. Animasaun, "Numerical exploration of magnetohydrodynamic nanofluid flow suspended with magnetite nanoparticles," *Journal of the Brazilian Society of Mechanical Sciences and Engineering*, vol. 39, no. 2, pp. 3635–3644, 2017.

[5] K. S. Nisar, U. Khan, A. Zaib, I. Khan, and A. Morsy, "A novel study of radioactive flow involving micropolar nanoliquid from a shrinking/stretching curved surface including blood gold nanoparticles," *The European Physical Journal Plus*, vol. 135, no. 10, pp. 1–19, 2020.

[6] M. H. Abolbashari, N. Freidoonimehr, F. Nazari, and M. M. Rashidi, "Analytical modeling of entropy generation for Casson nano-fluid flow induced by a stretching surface," *Advanced Powder Technology*, vol. 231, no. 2, pp. 542–552, 2015.

[7] A. Tassaddiq, I. Khan, K. Sooppy Nisar, and J. Singh, "MHD flow of a generalized Casson fluid with Newtonian heating: a fractional model with Mittag-Leffler memory," *Alexandria Engineering Journal*, vol. 59, no. 5, pp. 3049–3059, 2020.

[8] Y. Menni, H. Ameur, and M. Inc, "Improvement of the performance of solar channels by using vortex generators and hydrogen fluid," *Journal of Thermal Analysis and Calorimetry*, 2020.

[9] Y. Menni, A. J. Chamkha, M. Ghazvini et al., "Enhancement of the turbulent convective heat transfer in channels through the baffling technique and oil/multiwalled carbon nanotube nanofluids," *Numerical Heat Transfer Applications*, vol. 79, no. 4, pp. 1–41, 2021.

[10] J. A. Khan, M. Mustafa, T. Hayat, M. A. Farooq, A. Alsaedi, and S. J. Liao, "On model for three-dimensional flow of nanofluid: an application to solar energy," *Journal of Molecular Liquids*, vol. 194, pp. 41–47, 2014.

[11] R. Maouedj, Y. Menni, M. Inc, Y.-M. Chu, H. Ameur, and G. Lorenzini, "Simulating the turbulent hydrothermal behavior of oil/MWCNT nanofluid in a Solar channel heat exchanger equipped with vortex generators," *Computer Modeling in Engineering & Sciences*, vol. 126, no. 3, pp. 855–889, 2021.

[12] M. Irfan, M. A. Farooq, A. Mushtaq, and Z. H. Shamsi, "Unsteady MHD bionanofluid flow in a porous medium with thermal radiation near a stretching/shrinking sheet," *Mathematical Problems in Engineering*, vol. 2020, Article ID 8822999, 14 pages, 2020.

[13] N. Vellanki, K. Hemalatha, and G. V. R. Reddy, "Radiation and chemical reaction effects on MHD Casson fluid flow of a porous medium with suction/injection," *International Journal of Mechanical Engineering and Technology*, vol. 11, no. 2, pp. 99–116, 2020.

[14] J. A. Falede and S. O. Adensanya, "MHD oscillatory flow through porous channel saturated with porous media," *Alexandria Engineering Journal*, vol. 56, no. 1, pp. 147–152, 2017.

[15] K. Dwivedi, R. K. Khare, and A. Paul, "MHD flow through a vertical channel with porous medium," *International Journal of Applied Engineering Research*, vol. 13, pp. 11923–11926, 2018.

[16] Y. Peng, A. S. Alsagri, M. Afrand, and R. Moradi, "A numerical simulation for magnetohydrodynamic nanofluid flow and heat transfer in rotating horizontal annulus with thermal radiation," *RSC Advances*, vol. 9, no. 39, pp. 22185–22197, 2019.

[17] A. Sharma and A. V. Dubewar, "MHD flow between two parallel plates under the influence of inclined magnetic field by finite difference method," *International Journal of Innovative Technology and Exploring Engineering*, vol. 8, no. 12, 2019.

[18] K. Loganathan, K. Mohana, M. Mohanraj, P. Sakthivel, and S. Rajan, "Impact of third-grade nanofluid flow across a convective surface in the presence of inclined Lorentz force: an approach to entropy optimization," *Journal of Thermal Analysis and Calorimetry*, vol. 144, no. 5, pp. 1935–1947, 2021.

[19] T. Anwar, P. Kumam, D. Baleanu, I. Khan, and P. Thounthong, "Radiative heat transfer enhancement in MHD porous channel flow of an Oldroyd-B fluid under generalized boundary conditions," *Physica Scripta*, vol. 95, no. 11, 2020.

[20] S. Pramanik, "Casson fluid flow and heat transfer past an exponentially porous stretching surface in presence of thermal radiation," *Ain Shams Engineering Journal*, vol. 5, no. 1, pp. 205–212, 2014.

[21] K. Loganathan, N. Alessa, K. Tamilvanan, and F. S. Alshammari, "Significances of Darcy–Forchheimer porous medium in third-grade nanofluid flow with entropy features," *The European Physical Journal Special Topics*, vol. 230, pp. 1293–1305, 2021.

[22] M. A. A. Hamad, M. J. Uddin, and A. I. M. Ismail, "Radiation effects on heat and mass transfer in MHD stagnation-point flow over a permeable flat plate with thermal convective surface boundary condition, temperature dependent viscosity and thermal conductivity," *Nuclear Engineering and Design*, vol. 242, pp. 194–200, 2012.

[23] K. Loganathan, G. Muhiuddin, A. M. Alanazi, F. S. Alshammari, B. M. Alqurashi, and S. Rajan, "Entropy optimization of third-grade nanofluid slip flow embedded in a porous sheet with zero mass flux and a non-Fourier heat flux model," *Frontiers in Physics*, vol. 8, p. 250.

[24] M. G. Reddy, "Heat generation and thermal radiation effects over a stretching sheet in a micropolar fluid," *International Scholarly Research notices*, vol. 2012, Article ID 795814, 2012.

[25] A. Jamaludin, K. Naganthran, R. Nazar, and L. Pop, "Thermal radiation and MHD effects in the mixed convection flow of Fe_3O_4–water Ferrofluid towards a nonlinearly moving surface," *Process*, vol. 8, no. 1, p. 95, 2020.

[26] K. Loganathan and S. Rajan, "An entropy approach of Williamson nanofluid flow with Joule heating and zero nanoparticle mass flux," *Journal of Thermal Analysis and Calorimetry*, vol. 141, no. 6, pp. 2599–2612, 2020.

[27] M. Sheikholeslami, D. Domiri Ganji, M. Younus Javed, and R. Ellahi, "Effect of thermal radiation on magnetohydrodynamics nanofluid flow and heat transfer by means of two phase model," *Journal of Magnetism and Magnetic Materials*, vol. 374, pp. 36–43, 2015.

[28] K. Loganathan, N. Alessa, and S. Kayikci, "Heat transfer analysis of 3-D viscoelastic nanofluid flow over a convectively heated porous riga plate with Cattaneo-Christov double flux," *Frontiers in Physics*, vol. 9, Article ID 641645, 2021.

[29] S. Srinivas, C. K. Kumar, and A. S. Reddy, "Pulsating flow of Casson fluid in a porous channel with thermal radiation, chemical reaction and applied magnetic field," *Nonlinear Analysis Modelling and Control*, vol. 23, no. 2, pp. 213–233, 2018.

[30] C. K. Kumar, S. Srinivas, and A. S. Reddy, "MHD pulsating flow of Casson nanofluid in a vertical porous space with thermal radiation and joule heating," *Journal of Mechanics*, vol. 36, no. 4, pp. 1–15, 2020.

[31] B. Vishali and G. Sarojamma, "Effect of a periodic body acceleration on fluid flow through a catheterized artery," *International Journal of Scintific and Innovative Mathematical Research*, vol. 3, no. 7, pp. 26–35, 2015.

[32] P. Sulochana, "Unsteady MHD pulsatile flow of couple stress fluid under the influence of periodic body acceleration," *Advances in Applied Science Research*, vol. 5, no. 4, pp. 136–143, 2014.

[33] G. M. Sobamowo, "Perturbation methods to analysis of thermal, fluid flow and dynamics behaviours of engineering systems," *A Collection of Papers on Chaos Theory and its Applications*, 2021, https://www.intechopen.com/chapters/75426.

[34] A. Kumar, "Perturbation technique to unsteady MHD periodic flow of viscous fluid through a planer channel," *Journal of Engineering and Technology Research*, vol. 2, no. 4, pp. 73–81, 2010.

[35] N. Thamaraikannan, S. Karthikeyan, and D. K. Chaudhary, "Significance of MHD radiative non-Newtonian nanofluid flow towards a porous channel: a framework of the Casson fluid model," *Journal of Mathematics*, vol. 2021, Article ID 9912239, 15 pages, 2021.

Hindawi
Complexity
Volume 2021, Article ID 7625031, 21 pages
https://doi.org/10.1155/2021/7625031

Research Article

Dufour Effect on Transient MHD Double Convection Flow of Fractionalized Second-Grade Fluid with Caputo–Fabrizio Derivative

Imran Siddique,[1] Sehrish Ayaz,[1] and Fahd Jarad[2,3]

[1]*Department of Mathematics, University of Management and Technology, Lahore 54770, Pakistan*
[2]*Department of Mathematics, Cankaya University, Etimesgut, Ankara, Turkey*
[3]*Department of Medical Research, China Medical University Hospital, China Medical University, Taichung, Taiwan*

Correspondence should be addressed to Fahd Jarad; fahd@cankaya.edu.tr

Received 3 May 2021; Accepted 25 August 2021; Published 11 September 2021

Academic Editor: Marcus Aguiar

This article presents the problem, in which we study the unsteady double convection flow of a magnetohydrodynamics (MHD) differential-type fluid flow in the presence of heat source, Newtonian heating, and Dufour effect over an infinite vertical plate with fractional mass diffusion and thermal transports. The constitutive equations for the mass flux and thermal flux are modeled for noninteger-order derivative Caputo–Fabrizio (CF) with nonsingular kernel, respectively. The Laplace transform and Laplace inversion numerical algorithms are used to derive the analytical and semianalytical solutions for the dimensionless concentration, temperature, and velocity fields. Expressions for the skin friction and rates of heat and mass transfer from the plate to fluid with noninteger and integer orders, respectively, are also determined. Furthermore, the influence of flow parameters and fractional parameters α and β on the concentration, temperature, and velocity fields are tabularly and graphically underlined and discussed. Furthermore, a comparison between second-grade and viscous fluids for noninteger and integer is also depicted. It is observed that integer-order fluids have greater velocities than noninteger-order fluids. This shows how the fractional parameters affect the fluid flow.

1. Introduction

The interest in fluid mechanics is truly significant within the sight of transport phenomena, which is a critical element in thermal, chemical, and mechanical engineering science. A few actual systems exist which can be utilized to move thermal energy and compound species through a phase and across limits of the phase. The three mechanisms for heat transfer are diffusion, convection, and radiation. The classification of convection of heat transfer into three consequent branches are natural (free), forced, and mixed convection, which is essential for the physical system that takes up the motion of the fluid. Free convection flows ensuing from the heat and mass transfer directed by the combined buoyancy effects because of temperature and concentration variations have been widely studied due to their applications in geotechnical engineering and chemical and bioengineering and in industrial activities [1]. Usually, the mass transfer due to the concentration disparity influences the rate of heat transfer. The driving force for the free convection is buoyancy, so its effects cannot be neglected whether the velocity of the fluid is small and change in temperature between the ambient fluid and surface is large enough [2–4].

Electrically conducting fluids also have accepted enough consideration from the researchers due to their extensive applications in industrial appliances. The MHD has its own practical implication, such as the tumor treating fields and power generation and earthquake assumption [5]. Parvin and Nasrin [6] have presented the analysis of the flow and

heat transfer characteristics for MHD-free convection in inclusion with heated difficulties. They showed that the influence of the magnetic parameter on streamlines and isotherms is significant.

The energy flux which is due to a composition gradient is said to be the Dufour or diffusion-thermo effect. Such influences are significant when density differences occur in the flow regime. Such as when species are introduced at a surface in the fluid domain with different (lower) density than the surrounding fluid, Dufour effects can be beneficial. Also, when heat and mass transfers take place simultaneously in a moving fluid, it has a relationship between the fluxes and the driving potentials are of more twisting nature. It has been analyzed that an energy flux can be generated not only by temperature gradients but also by composition gradients as well. The diffusion-thermo effect was found to be of a considerable magnitude such that it cannot be negligible [7]. Dufour effects are essential in geothermal energy, hydrology, and nuclear waste disposal. In view of the importance of the diffusion-thermo effect, Kafoussias and Williams [8] studied the effect of thermal diffusion and diffusion-thermo on the mixed free forced convective and mass transfer boundary layer flow with temperature-dependent viscosity. Babu et al. [9] studied the diffusion-thermo and radiation effects on MHD-free convective heat and mass transfer flow past an infinite vertical plate in the presence of a chemical reaction of the first order. The dimensionless governing equations were solved with the Laplace transform technique. Rajput and Gupta [10] investigated the diffusion-thermo effect on unsteady free convection MHD flow past an exponentially accelerated plate through porous media with variable temperature and constant mass diffusion in an inclined magnetic field. Sharma and Buragohain [11] examined the Soret and Dufour effects on unsteady flow past an oscillating vertical plate with the help of numerical technique. Postelnicu [12] studied simultaneous heat and mass transfer by natural convection from a vertical plate embedded in an electrically conducting fluid saturated porous medium in the presence of Soret and Dufour effects using the Darcy–Boussinesq model. Gaikwad et al. [13] investigated the onset of double diffusive convection in two component couple of the stress fluid layer with Soret and Dufour effects using both linear and nonlinear stability analysis. Prakash et al. [14] considered the Dufour effects on unsteady MHD natural convection flow past a spontaneously started infinite vertical plate with variable temperature and constant mass diffusion through a permeable medium, and the dimensionless governing equations were solved in a closed form by utilizing the Laplace transform technique. They tracked down that the Dufour impact has critical effect on the velocity and temperature fields.

Numerous fluids in practical developments show non-Newtonian behavior because the consistent Newtonian fluids do not explicitly clarify the attributes of real fluids. Among non-Newtonian fluids, second-grade fluid is one of the viscoelastic fluids which were introduced by Rivlin [15] and Rivlin and Erickson [16]. Beard and Walters [17] are considered the pioneer of viscoelastic fluids. They developed the boundary layer theory for the second-grade fluids. This

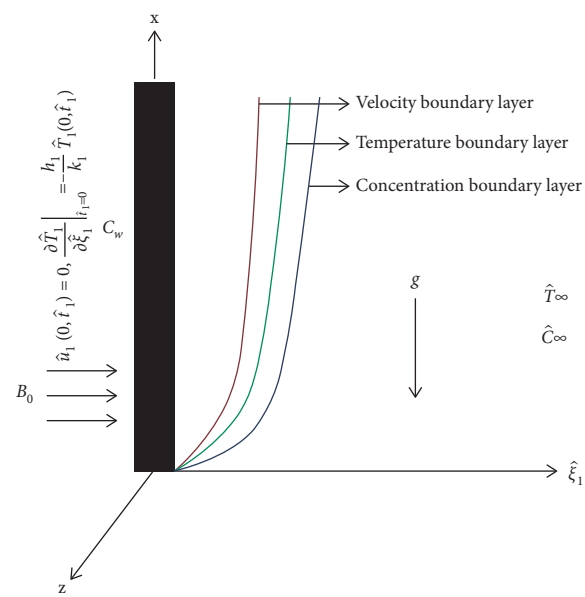

Figure 1: Flow geometry.

boundary layer theory for the second-grade fluids has motivated many researchers to really explore this kind of fluids with various conditions. Ariel [18] attained an interpretive solution for an incompressible laminar second-grade fluid between the plates. Kecebas and Yurusoy [19] analyzed an unsteady two-dimensional power law fluid of the second grade and used a finite difference approach to solve reduced governing equations. Raftari [20] considered the MHD steady flow and heat transfer of a second-grade fluid and obtained an analytical solution. Aman et al. [21] analyzed the unsteady heat and mass transfer in second-grade fluid over a flat plate with wall suction and injection.

Recently, it has progressively been seen as a dynamic tool through which a beneficial generalization of physical ideas can be obtained. Most fractional derivatives used are the Riemann–Liouville (RL) fractional derivative and the Caputo fractional derivative [22, 23]. It is observed that these operators exhibit obstacle in applications, such as the RL derivative of a constant is not zero, and the Laplace transform of the RL derivative involves terms which have no physical signification. The Caputo fractional derivative has excluded these difficulties, but the kernel of the definition is a singular function. Caputo and Fabrizio have introduced recently a new definition of the fractional derivatives with an exponential kernel without singularities [24]. The results that are been analyzed using these operators are expressed in complicated forms involving some generalized functions [25–34].

The innovation of the present paper is to examine the double convection flow of an incompressible differential-type fluid near a vertical plate with heat source, Newtonian heating, and diffusion-thermo effect. Fractional derivative CF with nonsingular kernel is used in the constitutive equations of the mass flux and thermal flux to describe the diffusion and thermal processes, respectively. Semianalytical solutions of the dimensionless problems are established by

virtue of the Laplace inversion numerical algorithm Gaver–Stehfest [35, 36]. Expressions of skin friction, Sherwood and Nusselt numbers with fractional, and ordinary cases, respectively, are also determined. The results which we attained here are new and can be applied to other viscoelastic fluids. Applications of this research would be helpful in magnetic material processing and chemical engineering systems. At the end, the influence of flow parameters and the fractional parameter on the temperature and concentration field as well as on the velocity field are tabularly and graphically analyzed.

2. Mathematical Model

Let us consider the double convection flow of an electrically conducting incompressible differential-type fluid lying over an infinite vertical plate occupying in the $x\,\bar{\xi}_1$-plane with Newtonian heating as shown in Figure 1. Initially, the fluid and the plate are at rest and its temperature is M (ambient fluid temperature) and the concentration level on the plate is $L^{-1}\{1/(s^2+b_1 s+b_2)\} = (2/\sqrt{b_1^2-4b_2})\sinh((\sqrt{b_1^2-4b_2}/2)t)e^{-(b_1/2)t}$ (ambient fluid concentration). After time $\bar{t}_1 = 0^+$, the heat transfer from the plate to the fluid is proportional to the local surface temperature $\bar{T}_1$, and the concentration level on the plate is $\bar{C}_w$ (wall concentration) which is thereafter kept constant. Presume that the influence of double convection and viscous dissipation in momentum and energy equations are insignificant, respectively. Also, the direction of flow has no pressure gradient. We assume that the velocity, temperature, and concentration are functions of $\bar{\xi}_1$ and $\bar{t}_1$ only. For such a flow, the constraint of incompressibility is identically satisfied. Taking the consistent Boussinesq approximation, the convection flow is governed by the following set of partial differential equations [32, 33, 37]:

$$\frac{\partial \bar{u}_1\left(\bar{\xi}_1,\bar{t}_1\right)}{\partial \bar{t}_1} = \nu\frac{\partial^2 \bar{u}_1\left(\bar{\xi}_1,\bar{t}_1\right)}{\partial \bar{\xi}_1^2} + \frac{\alpha_1}{\rho}\frac{\partial^3 \bar{u}_1\left(\bar{\xi}_1,\bar{t}_1\right)}{\partial \bar{\xi}_1^2 \partial \bar{t}_1} + g\beta_T\left(\bar{T}_1\left(\bar{\xi}_1,\bar{t}_1\right)-\bar{T}_\infty\right) + g\beta_C\left(\bar{C}_1\left(\bar{\xi}_1,\bar{t}_1\right)-\bar{C}_\infty\right) - \frac{\sigma B_0^2 \bar{u}_1\left(\bar{\xi}_1,\bar{t}_1\right)}{\rho}, \quad \bar{\xi}_1,\bar{t}_1>0, \tag{1}$$

$$\rho C_P\frac{\partial \bar{T}_1\left(\bar{\xi}_1,\bar{t}_1\right)}{\partial \bar{t}_1} = -\frac{\partial \bar{q}}{\partial \bar{\xi}_1} - Q\left(\bar{T}_1\left(\bar{\xi}_1,\bar{t}_1\right)-\bar{T}_\infty\right) - \frac{D_m K_T \rho}{C_s}\frac{\partial \bar{j}}{\partial \bar{\xi}_1}, \quad \bar{\xi}_1,\bar{t}_1>0, \tag{2}$$

$$\bar{q} = -k_1\frac{\partial \bar{T}_1}{\partial \bar{\xi}_1}, \tag{3}$$

$$\frac{\partial \bar{C}_1\left(\bar{\xi}_1,\bar{t}_1\right)}{\partial \bar{t}_1} = -\frac{\partial \bar{j}}{\partial \bar{\xi}_1}, \quad \bar{\xi}_1,\bar{t}_1>0, \tag{4}$$

$$\bar{j} = -D_m\frac{\partial \bar{C}_1}{\partial \bar{\xi}_1}. \tag{5}$$

The appropriate initial and boundary conditions are as follows:

$$\begin{aligned}
&\bar{u}_1\left(\bar{\xi}_1, 0\right) = 0,\\
&\bar{T}_1\left(\bar{\xi}_1, 0\right) = \bar{T}_\infty,\\
&\bar{C}_1\left(\bar{\xi}_1, 0\right) = \bar{C}_\infty, \quad \bar{\xi}_1 \geq 0,
\end{aligned} \tag{6}$$

$$\begin{aligned}
&\bar{u}_1\left(0, \bar{t}_1\right) = 0,\\
&\frac{\partial \bar{T}_1}{\partial \bar{\xi}_1}\Big|_{\bar{\xi}_1=0} = -\frac{h_1}{k_1}\bar{T}_1\left(0, \bar{t}_1\right),\\
&\bar{C}_1\left(0, \bar{t}_1\right) = \bar{C}_w, \quad \bar{t}_1 > 0,
\end{aligned} \tag{7}$$

$$\begin{aligned}
&\bar{u}_1\left(\bar{\xi}_1, \bar{t}_1\right) \longrightarrow 0,\\
&\bar{T}_1\left(\bar{\xi}_1, \bar{t}_1\right) \longrightarrow \bar{T}_\infty,\\
&\bar{C}_1\left(\bar{\xi}_1, \bar{t}_1\right) \longrightarrow \bar{C}_\infty, \quad \bar{\xi}_1 \longrightarrow 0, \bar{t}_1 > 0.
\end{aligned} \tag{8}$$

On introducing the nondimensional quantities from Appendix A into equations (1)–(8), we get the following nondimensional partial differential equations:

$$\begin{aligned}
\frac{\partial u}{\partial t} = \frac{\partial^2 u(y,t)}{\partial y^2} + \gamma \frac{\partial^3 u(y,t)}{\partial y^2 \partial t} + \mathrm{Gr}\theta(y,t)\\
+ \mathrm{Gm}C(y,t) - \mathrm{Mu}(y,t), \quad y, t > 0,
\end{aligned} \tag{9}$$

$$\mathrm{Pr}\frac{\partial \theta}{\partial t} = -\frac{\partial q}{\partial y} - S\theta(y,t) - \mathrm{PrDu}\frac{\partial j}{\partial y}, \quad y, t > 0, \tag{10}$$

$$q = -\frac{\partial \theta}{\partial y}, \tag{11}$$

$$\frac{\partial C}{\partial t} = -\frac{\partial j}{\partial y}, \quad y, t > 0, \tag{12}$$

$$j = -\frac{1}{\mathrm{Sc}}\frac{\partial C}{\partial y}, \tag{13}$$

with the initial and boundary conditions

$$\begin{aligned}
&u(y,0) = 0,\\
&\theta(y,0) = 0,\\
&C(y,0) = 0, \quad y \geq 0,
\end{aligned} \tag{14}$$

$$\begin{aligned}
&u(0,t) = 0,\\
&\frac{\partial \theta}{\partial y}\Big|_{y=0} = -[\theta(0,t) + 1],\\
&C(0,t) = 1,
\end{aligned} \tag{15}$$

$$\begin{aligned}
&u(y,t) \longrightarrow 0,\\
&\theta(y,t) \longrightarrow 0,\\
&C(y,t) \longrightarrow 0, \quad \text{as } y \longrightarrow \infty, t > 0.
\end{aligned} \tag{16}$$

To establish a model with time-fractional derivatives, we assume a thermal process with memory illustrated by the next generalized fractional constitutive equation for thermal flux and mass diffusion, respectively [38, 39]:

$$j(y,t) = -\frac{1}{\mathrm{Sc}}\,{}^{\mathrm{CF}}D_t^{\alpha}\frac{\partial C(y,t)}{\partial y}, \quad \alpha \in [0,1), \tag{17}$$

$$q(y,t) = -{}^{\mathrm{CF}}D_t^{\beta}\frac{\partial \theta(y,t)}{\partial y}, \quad \beta \in [0,1), \tag{18}$$

where the CF time-fractional derivative ${}^{\mathrm{CF}}D_t^p(\cdot)$ of order p is defined by [24]

$${}^{\mathrm{CF}}D_t^p u(y,t) = \frac{1}{1-p}\int_0^t \exp\left(\frac{-p(t-\tau)}{1-p}\right)\frac{\partial u(y,\tau)}{\partial \tau}\mathrm{d}\tau, \quad p \in [0,1). \tag{19}$$

The Laplace transform of the CF time derivative is as follows:

$$L\left\{{}^{\mathrm{CF}}D_t^p u(y,t)\right\} = \frac{sL\{u(y,t)\} - u(y,0)}{(1-p)s + p}. \tag{20}$$

Remark 1. If $u(y,0) = 0$ and $p \longrightarrow 0$, equation (20) becomes $L\left\{{}^{\mathrm{CF}}D_t^p u(y,t)\right\} = L\{u(y,t)\}$. In this case, the generalized mass flux and thermal flux equations (17) and (18) reduce to the classical Fourier's law and Fick's law equations (11) and (13), respectively. For $p \longrightarrow 1$,

$$\lim_{p\longrightarrow 1} L\left\{{}^{\mathrm{CF}}D_t^p u(y,t)\right\} = sL\{u(y,t)\} - u(y,0) = L\left\{\frac{\partial u(y,t)}{\partial t}\right\}. \tag{21}$$

For the correspondence, it will be as follows:

$$\frac{\partial u(y,t)}{\partial t} = \lim_{p\longrightarrow 1}\,{}^{\mathrm{CF}}D_t^p u(y,t). \tag{22}$$

3. Solution of the Problem

3.1. Concentration Field. Applying the Laplace transform to equations (12), (13), third equation in (15), third equation in (16), and (17), keep in mind the initial condition (third equation in (14)), and after simplification, we obtain the transformed problem:

$$\frac{\partial^2 \overline{C}(y,s)}{\partial y^2} - \mathrm{Sc}[(1-\alpha)s + \alpha]\overline{C}(y,s) = 0, \quad y > 0, \tag{23}$$

$$\begin{aligned}
&\overline{C}(0,s) = \frac{1}{s},\\
&\overline{C}(y,s) \longrightarrow 0, \quad \text{as } y \longrightarrow \infty.
\end{aligned} \tag{24}$$

The differential equation (24) gives the solution with respect to condition (24):

$$\overline{C}(y,s) = \frac{1}{s}e^{-ya_0\sqrt{s+a}}, \tag{25}$$

where $a_0 = \sqrt{\mathrm{Sc}(1-\alpha)}$ and $a = (a/1-\alpha)$.

The inverse Laplace transform of the above equation is perceived using equation (A.3) from Appendix C.

$$C(y,t) = \frac{1}{2}\left[e^{ya_0\sqrt{a}}\,erfc\left(\frac{ya_0}{2\sqrt{t}} + \sqrt{at}\right) + e^{-ya_0\sqrt{a}}\,erfc\left(\frac{ya_0}{2\sqrt{t}} - \sqrt{at}\right)\right]. \tag{26}$$

The local mass transfer coefficient from the plate to the fluid, that is, Sherwood number, is taken by the subsequent relation:

$$\mathrm{Sh}_g = j(0,t) = -\frac{1}{(1-\alpha)\mathrm{Sc}}L^{-1}\left\{\frac{s}{s+a}\frac{\partial\overline{C}(y,s)}{\partial y}\Big|_{y=0}\right\} = \frac{a_0}{(1-\alpha)\mathrm{Sc}}\left\{\frac{e^{-at}}{\sqrt{\pi t}}\right\}. \tag{27}$$

The obtained results in equations (26) and (27) identical results exist in [29] (equations (3.9) and (3.22)).

3.2. Concentration Field for an Ordinary Case ($\alpha \longrightarrow 0$). In special case when $\alpha \longrightarrow 0$, we obtain the ordinary concentration field by means of the equation (A.4) from Appendix C.

$$C(y,t) = erfc\left(\frac{ya_1}{2\sqrt{t}}\right). \tag{28}$$

Similarly, we obtain the expression for the Sherwood number as follows:

$$\mathrm{Sh}_o = \sqrt{\frac{\mathrm{Sc}}{\pi t}}. \tag{29}$$

4. Temperature Field

Applying the Laplace transform to equations (10), (11), second equation in (15), second equation in (16), and (18), using the initial condition (second equation in (14)), after simplification, we get the transformed problem:

$$\frac{\partial^2\overline{\theta}}{\partial y^2} - \frac{b_0\left(s^2 + b_1 s + b_2\right)}{s}\overline{\theta}(y,s) = \frac{b_3(s+b)}{s}e^{-ya_0\sqrt{s+a}}, \tag{30}$$

$$\begin{aligned} &\frac{\partial\overline{\theta}(y,s)}{\partial y}\Big|_{y=0} = -\left[\overline{\theta}(0,s) + \frac{1}{s}\right], \\ &\overline{\theta}(y,s) \longrightarrow 0, \quad \text{as } y \longrightarrow \infty. \end{aligned} \tag{31}$$

Differential equation (30) gives the following solution with the boundary condition (31):

$$\begin{aligned} \overline{\theta}(y,s) = {} & \frac{1}{s}\frac{1}{\sqrt{b_0}}\frac{1}{\sqrt{w_1(s)} + \xi}e^{-y\sqrt{b_0}\sqrt{w_1(s)}} \\ & + \frac{sb_6}{w_2(s)}\left\{\frac{e^{-ya_0\sqrt{s+a}}}{s} + \frac{1}{s}\frac{1}{\sqrt{b_0}}\frac{e^{-y\sqrt{b_0}\sqrt{w_1(s)}}}{\sqrt{w_1(s)} + \xi}\left(1 - a_0 b_6\sqrt{s+a}\right)\right\}, \end{aligned} \tag{32}$$

where $b_i, i = 0, \ldots, 6$ and ξ are constants given in Appendix B

$$b = \frac{\beta}{1-\beta},$$
$$w_1(s) = \frac{b_0\left(s^2 + b_1 s + b_2\right)}{s}, \tag{33}$$
$$w_2(s) = \frac{s^2 + b_4 s + b_5}{s+b}.$$

To find the inverse Laplace transform, equation (34) can be written as follows:

$$\overline{\theta}(y,s) = \overline{\theta}_1(s)\cdot\overline{\theta}_2(y,s) + \overline{\theta}_3(s)\cdot\left[\overline{\theta}_4(y,s) + \overline{\theta}_6(s)\cdot\overline{\theta}_5(y,s)\right], \tag{34}$$

where

$$\overline{\theta}_1(s) = \frac{1}{s}\frac{1}{\sqrt{b_0}}\frac{1}{\sqrt{w_1(s)}+\xi},$$
$$\overline{\theta}_2(y,s) = e^{-y\sqrt{b_0}\sqrt{w_1(s)}},$$
$$\overline{\theta}_3(y,s) = \frac{sb_6}{w_2(s)},$$
$$\overline{\theta}_4(y,s) = \frac{e^{-ya_0\sqrt{s+a}}}{s},$$
$$\overline{\theta}_5(s) = \frac{1}{s}\frac{1}{\sqrt{b_0}}\frac{e^{-y\sqrt{b_0}\sqrt{w_1(s)}}}{\sqrt{w_1(s)}+\xi}, \tag{35}$$
$$\overline{\theta}_6(y,s) = 1 - a_0 b_6\sqrt{s+a}.$$

The inverse Laplace transform of equation (35) is obtained using (A.3), (A.5)–(A.11) from Appendix C, and by taking convolution theorem, we will get the following equation:

$$\theta(y,t) = \theta_1(t) * \theta_2(y,t) + \theta_3(t) * \left[\theta_4(y,t) + \theta_6(t) * \theta_5(y,t)\right], \tag{36}$$

where $*$ denotes the convolution product.

$$\theta_1(t) = -\frac{1}{\sqrt{b_0}} - \frac{1}{b_0}\int_0^t G_2(\tau)\mathrm{d}\tau,$$
$$\theta_2(y,t) = e^{-b_1 t}\frac{e^{-\left(b_0 y^2/4t\right)}}{\sqrt{\pi t}} - \int_0^\infty \frac{e^{-b_1 u - \left(b_0 y^2/4u\right)}}{\sqrt{\pi u}}\sqrt{\frac{b_2 u}{t-u}}J_1\left(2\sqrt{b_2 u(t-u)}\right)\mathrm{d}u,$$
$$\theta_3(t) = \delta(t) + \frac{2(b-b_4)}{\sqrt{b_4^2-4b_5}}\int_0^\infty \delta'(t-\tau)e^{-\left(b_4/2\right)\tau}\sinh\left(\frac{\sqrt{b_4^2-4b_5}}{2}\tau\right)\mathrm{d}\tau$$
$$-\frac{2b_5}{\sqrt{b_4^2-4b_5}}\sinh\left(\frac{\sqrt{b_4^2-4b_5}}{2}t\right)e^{-\left(b_4/2\right)\tau}, \tag{37}$$
$$\theta_4(y,t) = \text{equation}\,(27),$$
$$\theta_5(y,t) = \theta_1(t) * \theta_2(y,t) = \int_0^t \theta_1(t-\tau)\theta_2(y,\tau)\mathrm{d}\tau,$$
$$\theta_6(t) = \delta(t) + a_0 b_6\frac{e^{-at}}{2t\sqrt{\pi t}},$$

here

$$G_2(t) = e^{-b_1 t}\left(\frac{1}{\sqrt{\pi t}} - \xi e^{\xi^2 t}erfc(\xi\sqrt{t})\right) - \int_0^\infty e^{-b_1 u}\left(\frac{1}{\sqrt{\pi u}} - \xi e^{\xi^2 u}erfc(\xi\sqrt{u})\right)\sqrt{\frac{b_2 u}{t-u}}J_1\left(2\sqrt{b_2 u(t-u)}\right)\mathrm{d}u. \tag{38}$$

The local coefficient of heat transfer from the plate to the fluid, in terms of the Nusselt number, is as follows:

$$\begin{aligned}\mathrm{Nu}_g = q(0,t) &= -\frac{1}{1-\beta}L^{-1}\left\{\frac{\partial\overline{\theta}(y,s)}{\partial y}\Big|_{y=0}\right\}\\ &= \frac{1}{1-\beta}L^{-1}\left\{\frac{\sqrt{w_1(s)}}{(s+b)\left(\sqrt{w_1(s)}+\xi\right)}\left(1+\frac{b_6}{w_2(s)}\left(1+a_0b_6\sqrt{s+a}\right)\right)+\frac{a_0b_6}{w_2(s)\sqrt{s+a}}\right\}.\end{aligned} \tag{39}$$

The inverse Laplace transform of equation (39) is established numerically and is described in Section 6 in the tabular form.

4.1. Temperature Field for an Ordinary Case $(\alpha \longrightarrow 0, \beta \longrightarrow 0)$. In special case, that is, $\alpha \longrightarrow 0, \beta \longrightarrow 0$, to obtain the ordinary temperature field by means of equations (A.10) and (A.11) from Appendix C,

$$\begin{aligned}\theta(y,t) = &\frac{1}{\sqrt{\mathrm{Pr}}}\int_0^t \frac{1}{\sqrt{\pi\tau}}e^{-a_1\tau-\left(\mathrm{Pr}y^2/4\tau\right)} - \varsigma e^{\sqrt{\mathrm{Pr}}\varsigma y+\left(\varsigma^2-a_1\right)\tau}erfc\left(\frac{\sqrt{\mathrm{Pr}}\,y}{2\sqrt{\tau}}+\varsigma\sqrt{\tau}\right)\mathrm{d}\tau\\ &+\frac{a_2}{2}\int_0^t\left[e^{-a_3\tau-iy\sqrt{\mathrm{Sc}}\sqrt{a_3}}erfc\left(\frac{y\sqrt{\mathrm{Sc}}}{2\sqrt{\tau}}-i\sqrt{a_3\tau}\right)+e^{-a_3\tau+iy\sqrt{\mathrm{Sc}}\sqrt{a_3}}erfc\left(\frac{y\sqrt{\mathrm{Sc}}}{2\sqrt{\tau}}+i\sqrt{a_3\tau}\right)\right]\mathrm{d}\tau,\end{aligned} \tag{40}$$

where $a_i, i = 1, \ldots, 3$ and ζ are constants given in Appendix B.

The above equation would be expressed as the Nusselt number using (A.12) from Appendix C as follows:

$$\begin{aligned}\mathrm{Nu}_o = 1 &- \frac{\varsigma}{a_1-\varsigma^2}\left[\sqrt{a_1}\,erf\left(\sqrt{a_1t}\right)-\left(e^{-\left(a_1-\xi^2\right)t}erfc\left(\varsigma\sqrt{t}\right)-1\right)\right]\\ &+a_2\sqrt{\mathrm{Sc}}\int_0^\infty\frac{1}{\sqrt{\pi u}}\left(\delta(t-u)-a_3e^{-a_3(t-u)}\right)\mathrm{d}u.\end{aligned} \tag{41}$$

5. Velocity Field

Applying the Laplace transform to equation (9), with the initial condition (first equation in (14)) and using the expressions of equations (25) and (32), we obtain the following Laplace transform velocity:

$$\begin{aligned}\frac{\partial^2\overline{u}}{\partial y^2}-\frac{s+M}{1+\gamma s}\overline{u}(y,s) = &-\frac{G_r}{1+\gamma s}\left[\frac{1}{s}\frac{1}{\sqrt{b_0}}\frac{1}{\sqrt{w_1(s)}+\xi}e^{-y\sqrt{b_0}\sqrt{w_1(s)}}+\frac{sb_6}{w_2(s)}\left\{\frac{e^{-ya_0\sqrt{s+a}}}{s}+\frac{1}{s}\frac{1}{\sqrt{b_0}}\frac{e^{-y\sqrt{b_0}\sqrt{w_1(s)}}}{\sqrt{w_1(s)}+\xi}\left(1-a_0b_6\sqrt{s+a}\right)\right\}\right]\\ &-\frac{G_m}{1+\gamma s}\frac{1}{s}e^{-ya_0\sqrt{s+a}}.\end{aligned} \tag{42}$$

Here, $\overline{u}(y,s)$ represents the function of the Laplace transform and $u(y,t)$ that has to satisfy the conditions.

$$\begin{aligned}&\overline{u}(0,s) = 0,\\ &\overline{u}(y,s) \longrightarrow 0, \quad \text{as } y \longrightarrow \infty.\end{aligned} \tag{43}$$

The ordinary differential equation (42) gives the solution with subject to conditions (43):

$$\begin{aligned}\overline{u}(y,s) &= \frac{1}{s^3+d_0s^2+d_1s+d_2}.\frac{1}{\sqrt{w_1(s)}+\xi}\left\{A_1+A_2\frac{s}{w_2(s)}\right\}\left[\frac{1}{s}e^{-yc_0\sqrt{(s+M)/(s+d_3)}}-e^{-y\sqrt{b_0w_1(s)}}\right]\\ &+\frac{A_2}{s^3+d_0s^2+d_1s+d_2}.\frac{s\sqrt{s+a}}{\sqrt{w_1(s)}+\xi}.\frac{a_0}{w_2(s)}\left[\frac{1}{s}e^{-yc_0\sqrt{(s+M)/(s+d_3)}}+e^{-y\sqrt{b_0w_1(s)}}\right]\\ &+\frac{1}{s^2+a_4s+a_5}\left\{A_3+A_4\frac{1}{w_2(s)}\right\}\left[\frac{1}{s}e^{-yc_0\sqrt{(s+M)/(s+d_3)}}-e^{-ya_0\sqrt{s+a}}\right],\end{aligned} \tag{44}$$

where $c_0 = 1/\sqrt{\gamma}$ $a_i, i = 4, 5,$ $A_j, j = 0, \ldots, 4$ and $d_k, k = 0, \ldots, 3$ are all constants given in Appendix B.

The skin friction coefficient corresponding to this motion is as follows:

$$\begin{aligned}\tau_g &= \frac{\partial u(0,t)}{\partial y} = L^{-1}\left\{\frac{\partial \overline{u}(0,s)}{\partial y}\right\}\\ &= L^{-1}\left[\frac{1}{s^3+d_0s^2+d_1s+d_2}.\frac{1}{\sqrt{w_1(s)}+\xi}\left\{A_1+A_2.\frac{s}{w_2(s)}\right\}\left(\frac{c_0}{s}\sqrt{\frac{s+M}{s+d_3}}-\sqrt{b_0w_1(s)}\right)\right.\\ &+\frac{A_2}{s^3+d_0s^2+d_1s+d_2}\frac{s\sqrt{s+a}}{\sqrt{w_1(s)}+\xi}.\frac{a_0}{w_2(s)}\left(\frac{c_0}{s}\sqrt{\frac{s+M}{s+d_3}}+\sqrt{b_0w_1(s)}\right)\\ &\left.+\frac{1}{s^2+a_4s+a_5}.\left\{\frac{A_3}{w_2(s)}+A_4\right\}\left(\frac{c_0}{s}\sqrt{\frac{s+M}{s+d_3}}-a_0\sqrt{s+a}\right)\right].\end{aligned} \tag{45}$$

The inverse Laplace transform of equations (44) and (45) will be found numerically in Section 6 by applying the Stehfest's algorithm [35].

5.1. Velocity Field for Fractional Viscous Fluid ($\gamma \longrightarrow 0$). In this special case, that is, $\gamma \longrightarrow 0$, we will obtain the velocity field for fractional viscous fluid from equation (44) as follows:

$$\begin{aligned}\overline{u}_2(y,s) &= \frac{1}{s^2+p_1s+p_2}.\frac{1}{\sqrt{w_1(s)}+\xi}\left\{A_5+A_6\frac{s}{w_2(s)}\right\}\left[\frac{1}{s}e^{-y\sqrt{s+M}}-e^{-y\sqrt{b_0w_1(s)}}\right]+\frac{A_6}{s^2+p_1s+p_2}.\\ &\frac{s\sqrt{s+a}}{\sqrt{w_1(s)}+\xi}.\frac{a_0}{w_2(s)}\left[\frac{1}{s}e^{-y\sqrt{s+M}}+e^{-y\sqrt{b_0w_1(s)}}\right]+\frac{1}{s+p_3}\left\{A_7+A_8\frac{1}{w_2(s)}\right\}\left[\frac{1}{s}e^{-y\sqrt{s+M}}-\frac{1}{s}e^{-ya_0\sqrt{s+a}}\right],\end{aligned} \tag{46}$$

where $A_i, i = 5, \ldots, 8$ and $p_j, j = 0, \ldots, 3$ are all constants given in Appendix B.

The Laplace transform of equation (46) is established numerically and described in Section 6.

5.2. Velocity Field for Ordinary Second-Grade Fluid ($\alpha \longrightarrow 0, \beta \longrightarrow 0$). In this ordinary case, where $\alpha \longrightarrow 0$, $\beta \longrightarrow 0$, the expression of flow of velocity for the second-grade fluid given in equation (44) would be illustrated as follows:

$$\overline{u}(y,s)=\frac{A_9}{s^2+p_4s+p_5}.\frac{1}{\sqrt{s+a_1}+\zeta}.\left[\frac{1}{s}e^{-yc_0\sqrt{(s+M)/(s+d_3)}}-\frac{1}{s}e^{-y\sqrt{\Pr}\sqrt{s+a_1}}\right]$$
$$+\frac{1}{s^2+p_4s+p_5}\left\{\frac{A_{10}}{s+a_3}+A_{11}\right\}.\left[\frac{1}{s}e^{-yc_0\sqrt{(s+M)/(s+d_3)}}-\frac{1}{s}e^{-y\sqrt{\mathrm{Sc}}\sqrt{s}}\right], \tag{47}$$

where $A_i, i=9,\ldots,11$ and $p_j, j=4,5$ are constants given in Appendix B.

Equation (47) can be expressed as follows:

$$\overline{u}(y,s)=\overline{u}_1(s)\cdot\left[\overline{u}_2(y,s)-\overline{u}_3(y,s)\right]+\overline{u}_4(s)\cdot\left[\overline{u}_5(y,s)-\overline{u}_6(y,s)\right]. \tag{48}$$

The inverse Laplace transform of equation (48) using equations (A.3), (A.4), (A.7), (A.9), and (A.13) from Appendix C as well as the convolution theorem is given as follows:

$$u(y,t)=u_1(t)*\left[u_2(y,t)-u_3(y,t)\right]+u_4(t)*\left[u_5(y,t)-u_6(y,t)\right], \tag{49}$$

where $*$ denotes the convolution product.

$$\begin{aligned}
u_1(t)&=\frac{2A_9}{\sqrt{p_4^2-4p_5}}e^{-(p_4/2)t}\int_0^t\sinh\left(\frac{\sqrt{p_4^2-4p_5}}{2}(t-\tau)\right)\left\{\frac{1}{\sqrt{\pi\tau}}-\zeta e^{\zeta^2\tau}erfc(\zeta\sqrt{\tau})\right\}e^{((p_4/2)-a_1)\tau}\mathrm{d}\tau,\\
u_2(y,t)&=e^{-yc_0}-\frac{yc_0\sqrt{M-d_3}}{2\sqrt{\pi}}\int_0^\infty\int_0^t\frac{1}{\sqrt{t}}e^{-\left(d_3t-\left((yc_0)^2/4\tau\right)-\tau\right)}I_1\left(2\sqrt{(M-d_3)\tau t}\right)\mathrm{d}t\mathrm{d}\tau,\\
u_3(y,s)&=\frac{1}{2}\left[e^{y\sqrt{\Pr}\sqrt{a_1}}erfc\left(\frac{\sqrt{\Pr}\,y}{2\sqrt{t}}+\sqrt{a_1t}\right)+e^{-y\sqrt{\Pr}\sqrt{a_1}}erfc\left(\frac{\sqrt{\Pr}\,y}{2\sqrt{t}}-\sqrt{a_1t}\right)\right],\\
u_4(y,t)&=\frac{2A_{10}}{\sqrt{p_4^2-4p_5}}e^{-(p_4/2)t}\int_0^t\sinh\left(\frac{\sqrt{p_4^2-4p_5}}{2}(t-\tau)\right)e^{((p_4/2)-a_3)\tau}\mathrm{d}\tau\\
&\quad+A_{11}\frac{2}{\sqrt{p_4^2-4p_5}}\sinh\left(\frac{\sqrt{p_4^2-4p_5}}{2}t\right)e^{-(p_4/2)t},\\
u_5(y,t)&=u_2(y,t),\\
u_6(y,t)&=erfc\left(\frac{y\sqrt{\mathrm{Sc}}}{2\sqrt{t}}\right).
\end{aligned} \tag{50}$$

5.3. Velocity Field for Ordinary Viscous Fluid ($\alpha\longrightarrow 0,\beta\longrightarrow 0,\gamma\longrightarrow 0$). In this special case where $\alpha\longrightarrow 0,\beta\longrightarrow 0$, and $\gamma\longrightarrow 0$, the velocity expression for ordinary viscous given in equation (44), takes a form as follows:

$$u_4(y,s)=\frac{A_{12}}{s+p_6}\frac{1}{\sqrt{s+a_1}+\zeta}\left[\frac{1}{s}e^{-y\sqrt{s+M}}-\frac{1}{s}e^{-y\sqrt{\Pr}\sqrt{s+a_1}}\right]$$
$$+\frac{1}{s+p_7}\left\{\frac{A_{13}}{s+a_3}+A_{14}\right\}\left[\frac{1}{s}e^{-y\sqrt{s+M}}-\frac{1}{s}e^{-y\sqrt{Sc}\sqrt{s}}\right], \tag{51}$$

where $A_i, i = 12, \ldots, 14$ and $p_j, j = 6, 7$ are all constants given in Appendix B.

Equation (51) can be expressed as follows:

$$\overline{u}_4(y,s) = \overline{u}_1(s) \cdot \left[\overline{u}_2(y,s) - \overline{u}_3(y,s)\right] + \overline{u}_4(s) \cdot \left[\overline{u}_5(y,s) - \overline{u}_6(y,s)\right]. \tag{52}$$

The inverse Laplace transform of equation (52), using (A.3), (A.4), and (A.9) from Appendix C, then by the convolution theorem, is given as follows:

$$u(y,t) = u_1(t) * \left[u_2(y,t) - u_3(y,t)\right] + u_4(t) * \left[u_5(y,t) - u_6(y,t)\right], \tag{53}$$

where

$$\begin{aligned}
u_1(t) &= A_{12} e^{-p_6 t} \int_0^t e^{(p_6 - a_1)\tau} \left\{ \frac{1}{\sqrt{\pi\tau}} - \zeta e^{\zeta^2 \tau} erfc(\zeta\sqrt{\tau}) \right\} \mathrm{d}\tau, \\
u_2(y,t) &= \frac{1}{2}\left[e^{y p_0 \sqrt{M}} erfc\left(\frac{y p_0}{2\sqrt{t}} + \sqrt{Mt} \right) + e^{-y p_0 \sqrt{M}} erfc\left(\frac{y p_0}{2\sqrt{t}} - \sqrt{Mt} \right) \right], \\
u_3(y,t) &= \frac{1}{2}\left[e^{y\sqrt{\mathrm{Pr}}\sqrt{a_1}} erfc\left(\frac{y\sqrt{\mathrm{Pr}}}{2\sqrt{t}} + \sqrt{a_1 t} \right) + e^{-y\sqrt{\mathrm{Pr}}\sqrt{a_1}} erfc\left(\frac{y a_2}{2\sqrt{t}} - \sqrt{a_1 t} \right) \right], \\
u_4(t) &= A_{13}\left(\frac{e^{-p_7 t} - e^{-a_5 t}}{a_3 - p_7} \right) + A_{14} e^{-a_3 t}, \\
u_5(y,t) &= u_2(y,t), \\
u_6(y,t) &= erfc\left(\frac{y\sqrt{\mathrm{Sc}}}{2\sqrt{t}} \right).
\end{aligned} \tag{54}$$

6. Numerical Results and Discussion

The MHD second-grade fluid on an infinite vertical plate is considered with Newtonian heating, heat source, and diffusion-thermo effects. Time-fractional derivative CF with a nonsingular kernel is used in the constitutive equations of the mass flux and thermal flux to describe the diffusion and thermal processes, respectively. The magnetic field is introduced in the fluid flow which acts as opposing force to fluid motion. The expressions for dimensionless concentration, temperature, velocity fields, skin friction, and Sherwood and Nusselt numbers are obtained by means of the Laplace transform technique. Solutions for the classical model corresponding to the integer-order derivative are also obtained as limiting cases. All the parameters and profiles which are used here are dimensionless. It is observed initially in a consequence of the fractionalize parameters α and β on the concentration, temperature, and velocity of fluid flow. Along with the effect of the absorption parameter S, the Prandtl number Pr, Dufour number Du, and time t on the temperature as well as the impact of Schmidt number Sc, and Reynolds number Re on the concentration and fluid velocity are studied. The consequence of the thermal and mass Grashof number Gr and Gm second-grade parameter γ and magnetic parameter $M$for velocity is also presented.

Figures 2(a) and 3(a) present the dimensionless temperature and concentration profiles for distinct values of the fractional parameters α and β. As probable, the fluid temperature and concentration are decreasing functions with respect to their fractional parameters. Their values are maximum near the plate and smoothly decrease to zero for increasing y. Figure 4(a) was drawn to interpret the effect of the fractional parameters α and β on the fluid velocity. If we give the same values to fractional parameters, the fluid flow velocity raises by increasing the values of α and β. The influence of the Schmidt number Sc on the fluid concentration is presented in Figure 2(b). It can be clearly seen from the figure that the concentration level of the fluid decreases whenever Sc is increasing. By the increase in time t, we observed from Figure 2(c) that the concentration profile is increasing.

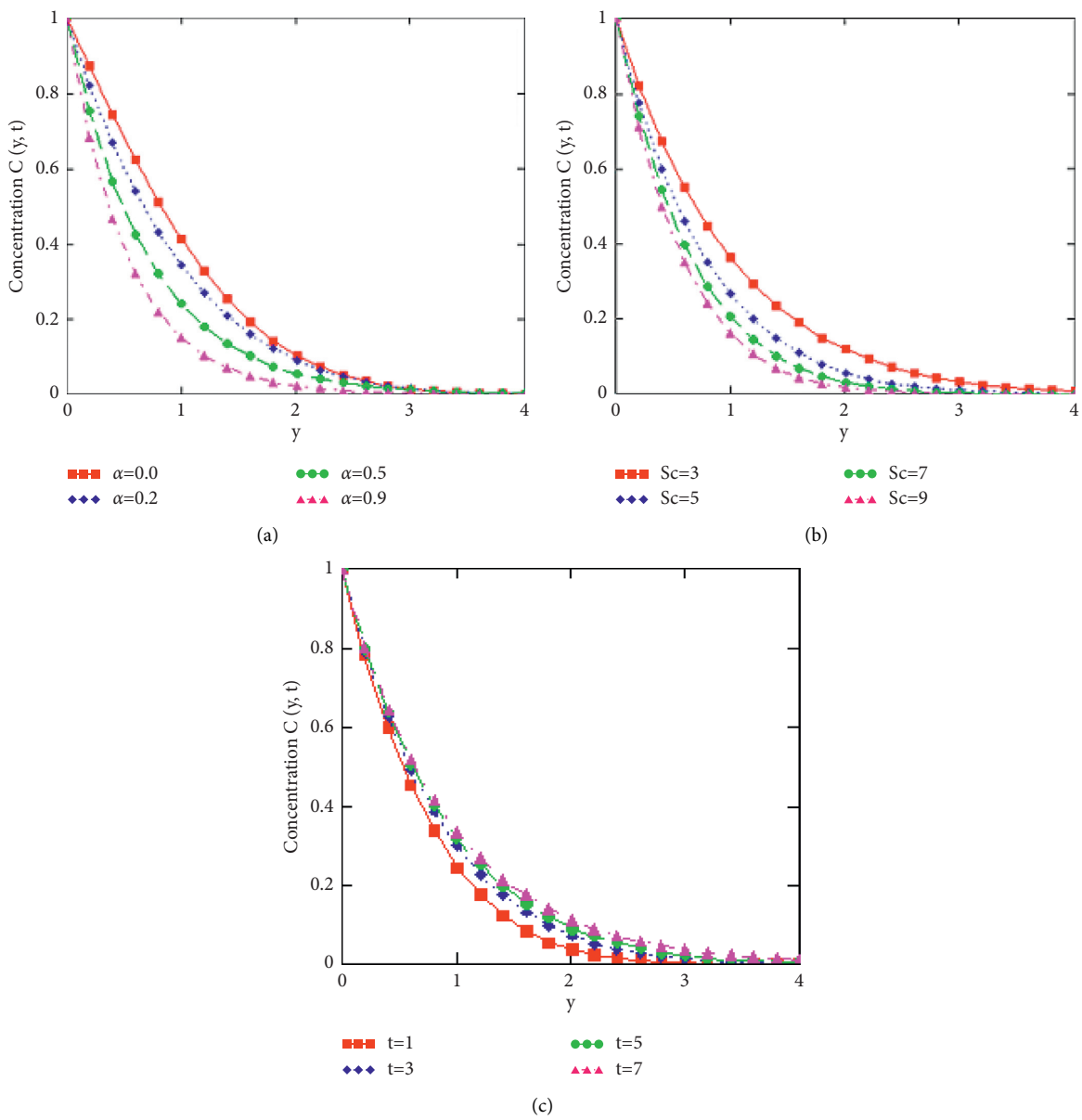

Figure 2: Concentration profiles vs. for y at $\alpha = 0.3, \mathrm{Sc} = 4, t = 3$.

The influence of the Prandtl number Prand absorption parameter S is shown in Figures 3(b) and 3(c). It is noticed that by increasing the values of Pr and S, the temperature profile is decreasing while increasing corresponding to the values of the Schmidt number Sc as presented in Figure 3(d). Figures 3(e) and 4(e) illustrate the temperature and velocity profiles for different values of the Dufour number Du. It is observed that the thermal diffusivity as well as the velocity profile both are increasing and the boundary layer thickness gets maximized. In addition, by increasing in time t, the temperature profile and velocity profile both are increasing as shown in Figures 3(f) and 4(j).

It is seen in Figures 4(b)–4(d) that by assigning the higher values to Pr, S, Sc, and γ, the fluid velocity profile decreases. The MHD principle is used for controlling the flow field in the essential direction by changing the making of the boundary layer. The variation of the velocity profile with different values of the magnetic parameter M is shown in Figure 4(i). Increase in the values of M shows the reduction in velocity. We agree with this result as expected that the magnetic field exerts a retarding effect on the mixed convection flow. Figure 4(g) is plotted to see the impact of thermal Grashof Gr. Gr is the ratio of buoyancy forces to viscous forces on the motion of the fluid, which stimulates free or inner convection. It is found that the fluid flow velocity is increasing by increasing the values of Gr. Figure 4(f) is plotted to allocated the influence of the mass Grashof Gm. It generates due to the change in concentration by a change in the density of a fluid, and it is the ratio of buoyancy forces to viscous forces; we found that by increasing Gm, the velocity profile increases.

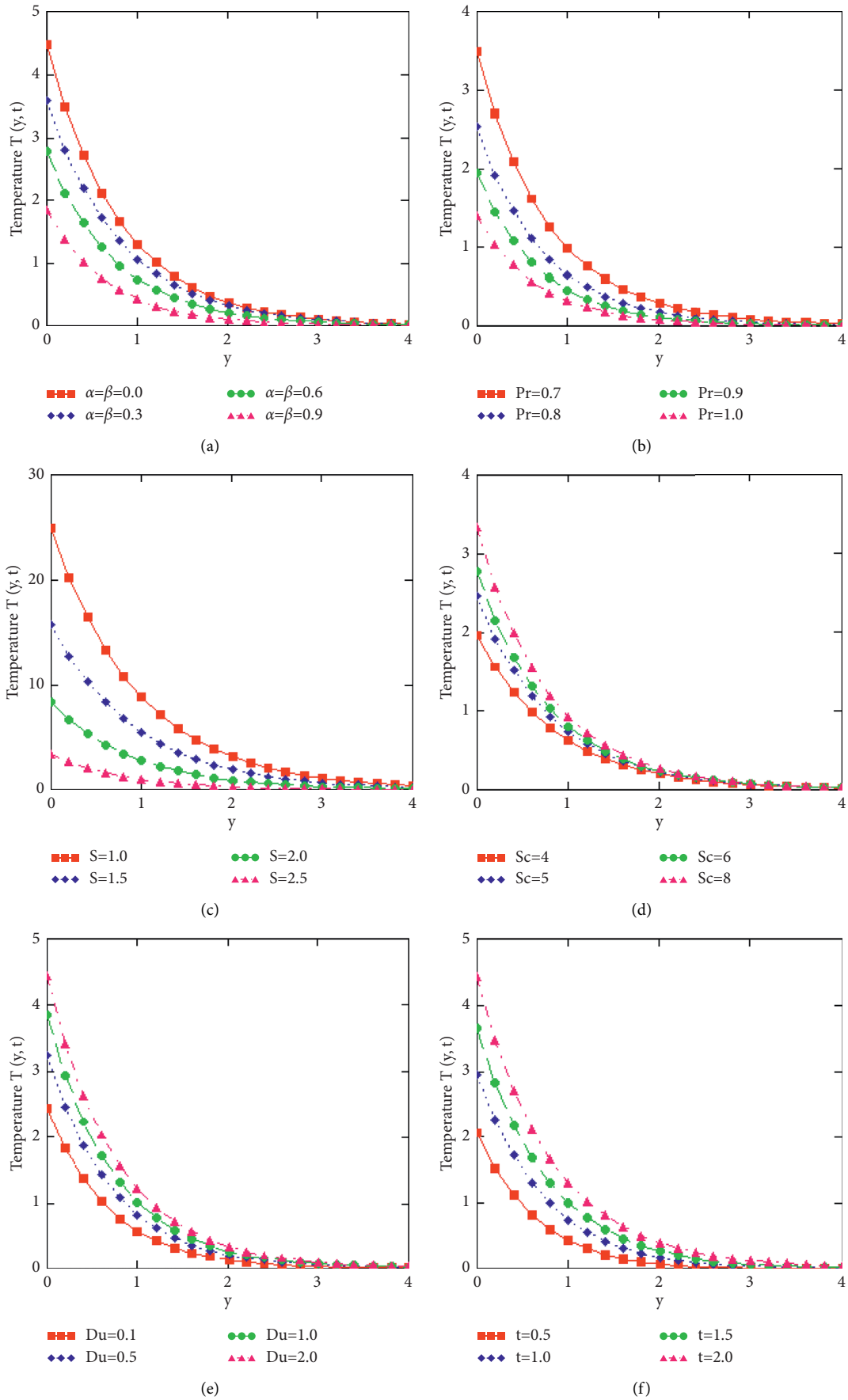

FIGURE 3: Temperature profiles vs. for y at $\alpha = 0.3$, $\beta = 0.3$, Pr = 0.6, $S = 3$,Sc = 4, Du = 0.05, $t = 2$.

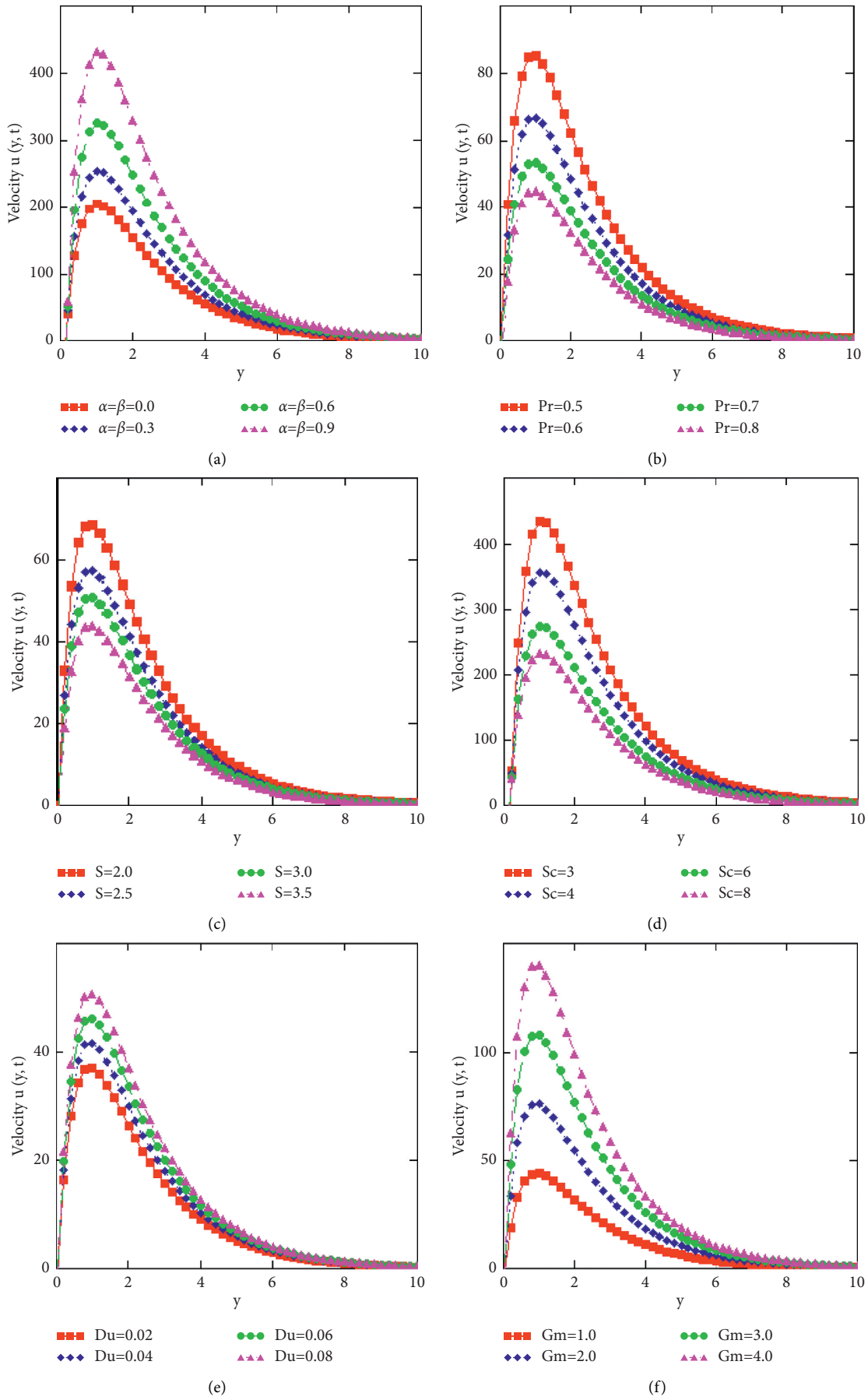

Figure 4: Continued.

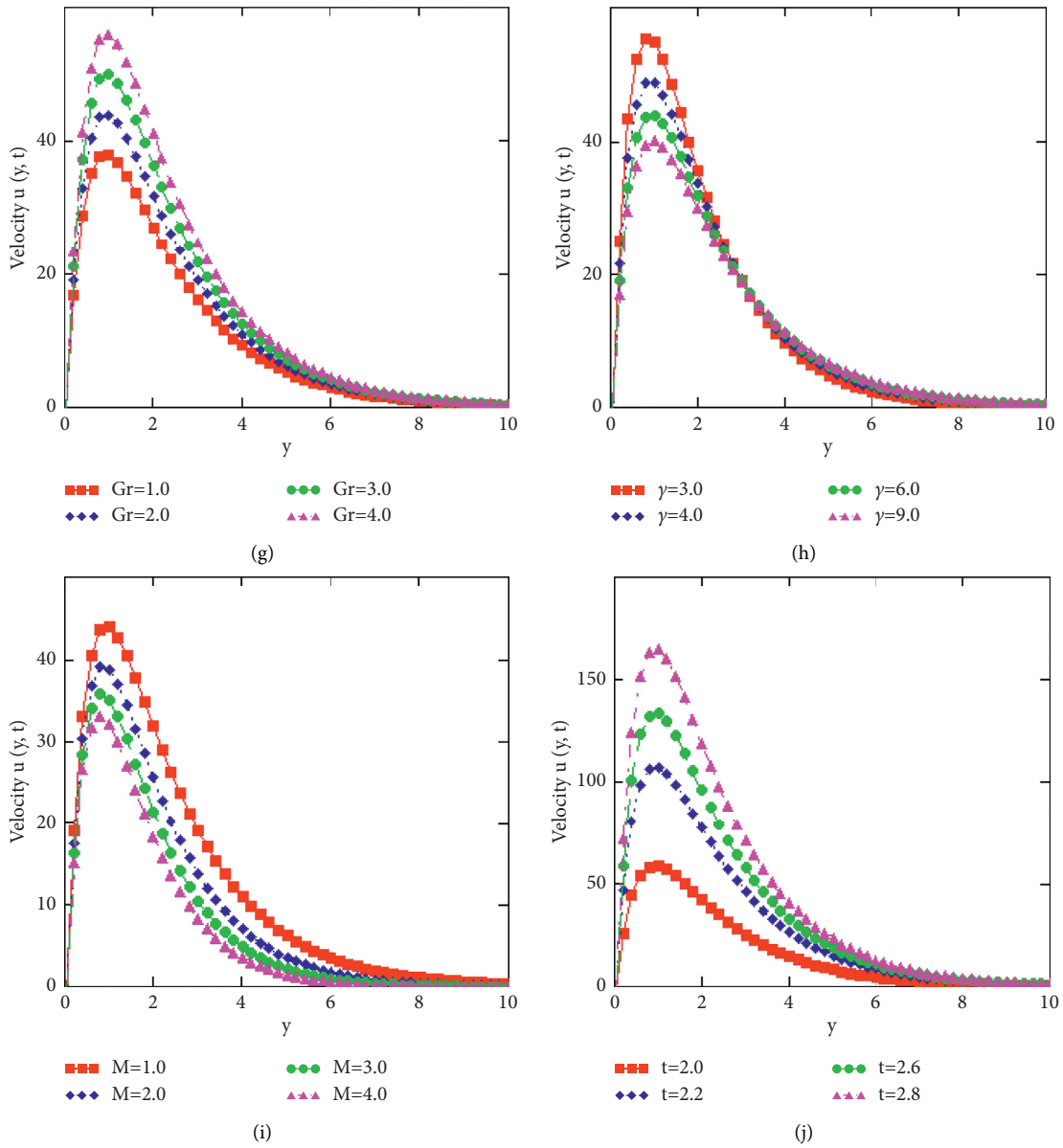

FIGURE 4: Velocity profiles *vs* for y at $\alpha = 0.3, \beta = 0.3, \mathrm{Pr} = 0.6, S = 3, \mathrm{Sc} = 4, \mathrm{Du} = 0.05$ $\mathrm{Du} = 0.05, \mathrm{Gm} = 1,$ $\mathrm{Gr} = 2,$ $\gamma = 5, M = 1, t = 2.$

The impact of fractional parameters α and β is described in Table 1. It is attained that the concentration, rate of mass, temperature, rate of heat transfer, velocity, and skin friction are decreasing for the large variation of fractional parameters α and β.

Furthermore, we have drawn a comparison between fractional second-grade and fractional viscous fluids ordinary fluid models in Figure 5. It is investigated that ordinary fluids have higher velocities as compare to the fractional fluids. It reveals in what way noninteger-order fractional parameters influence the flow of fluid.

Furthermore, to see the validity of our results for concentration, temperature, and velocity profiles graphically, we plotted Figures 6(a)–6(c). It can be seen from these figures that by ignoring the effects of Du and M, our results are identical to those obtained by Vieru et al. [40], Imran et al. [25], and Siddique et al. [33] for fractional fluids.

Table 1: Validation of the model for various values of fractional parameters.

Fractional parameters α and β	Concentration (α)	Sherwood number	Temperature (α and β)	Nusselt number	Velocity (α and β)	Skin friction
0.0	1.000	3.950	4.444	2.459	45.583	1.196
0.1	0.753	1.142	3.468	2.414	155.188	1.010
0.2	0.567	0.757	2.706	2.307	215.824	0.824
0.3	0.426	0.570	2.112	2.153	245.001	0.646
0.4	0.321	0.453	1.648	1.967	254.274	0.482
0.5	0.241	0.371	1.285	1.761	251.246	0.337
0.6	0.181	0.310	1.002	1.548	240.903	0.216
0.7	0.135	0.263	0.782	1.341	226.490	0.121
0.8	0.101	0.225	0.609	1.001	210.100	0.054
0.9	0.075	0.194	0.475	0.829	193.064	0.015

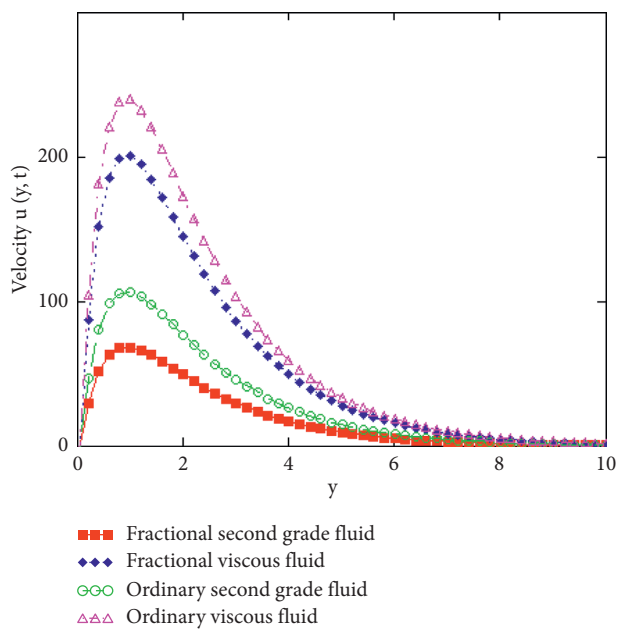

Figure 5: Comparison between ordinary and fractional fluids.

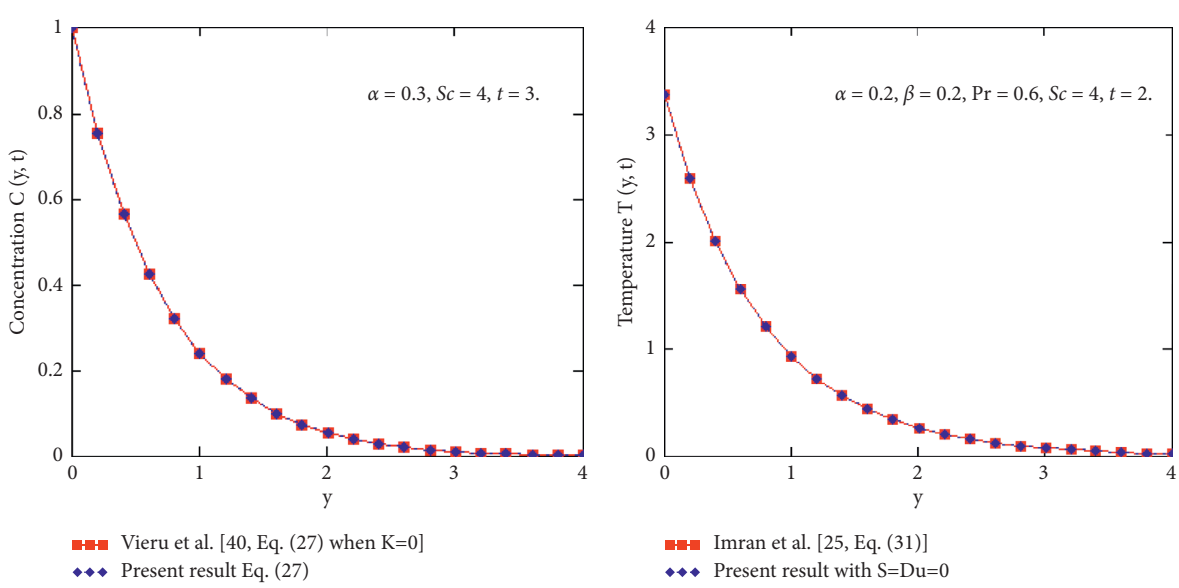

(a) (b)

Figure 6: Continued.

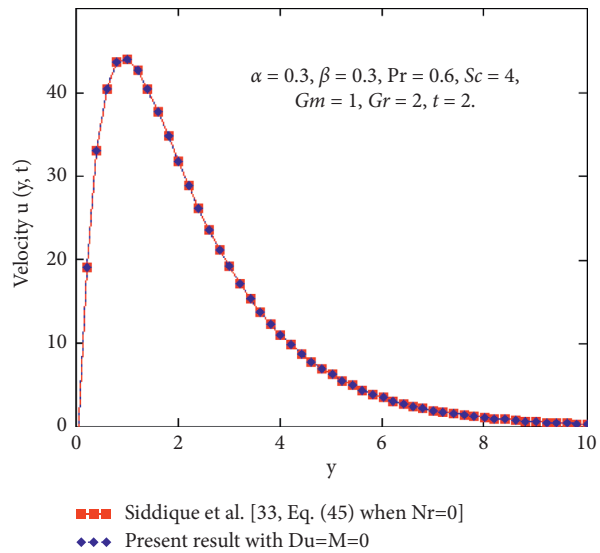

(c)

Figure 6: Comparison between the present results with the concentration, temperature, and velocity profiles of Vieru et al. [40], Imran et al. [25], and Siddique et al. [33], respectively.

7. Conclusion

In this paper, we analyzed the double convective flow of an incompressible differential-type fluid near a vertical plate with heat absorption, Newtonian heating, and diffusion-thermo effect. Time-fractional derivative CF is used in the constitutive equations of the mass flux and thermal flux to describe the diffusion and thermal processes, respectively. Semianalytical solutions of the dimensionless problems are obtained by virtue of the Laplace inversion numerical algorithm Stehfest's. The computations and discussion graphically and numerically have formed to distinguish the effect of CF time-fractional parameters and the second-grade parameter γ. From numerical simulation and graphical interpretation, the findings are summarized as follows:

(i) For greater values of fractional parameter α and flow parameter Sc, the concentration profile decreases, whereas it increases due to the increasing values of time t

(ii) For larger values of fractional parameters α and β and flow parameters Pr and S, the temperature profile decreases, whereas it increases due to increasing values of the Dufour number Du, Sc, and time t

(iii) Fluid velocity increases with the increasing values of fractional and flow parameters α, β, Du, Gm, Gr, and time t, and it is observed that the boundary layer thickness increases and velocity is maximum near the plate

(iv) Velocity field as well as the boundary layer thickness decreases near the plate as we increase the values of flow parameters Pr, S, Sc, M, and γ

(v) Ordinary fluids (Newtonian and second grade) have greater velocities than fractional fluids

(vi) Skin friction, Nusselt numbers, and Sherwood numbers decrease by increasing the fractional parameters α and β

(vii) The solutions obtained by Vieru et al. [40], Imran et al. [25], and Siddique et al. [33] for fractional fluids are the particular case of our general results for fractional second-grade fluid when Du = M = 0, and they are in good agreement graphically

Appendix

A. Nomenclature

$\widehat{u}_1$: velocity field of fluid in the x direction

$\widehat{\xi}_1$: coordinate axis normal to the plate

y: dimensionless coordinate axis normal to the plate

$\widehat{t}_1$: time

$\widehat{C}_\infty$: concentration of the fluid far away from the plate

$\widehat{T}_1$: temperature of the fluid near the plate

$\widehat{T}_\infty$: temperature of the fluid far away from the plate

C_P: specific heat at a constant pressure

$\widehat{j}$: mass flux diffusion

S: dimensionless heat absorption parameter

k_1: thermal conductivity of the fluid

D_m: coefficient of mass diffusivity

Gr: thermal Grashof number

M: magnetic field parameter

Sc: Schmidt number

u: dimensionless velocity

$\widehat{C}_1$: species concentration

$\widehat{C}_w$: concentration of the plate

t: dimensionless time
C: dimensionless concentration
θ: dimensionless temperature
B_0: magnetic field parameter
$\widehat{q}$: heat flux
Q: heat absorption parameter
h_1: heat transfer coefficient
C_s: concentration susceptibility
K_T: thermal diffusion ratio
Gm: mass Grashof number
Pr: Prandtl number
Du: Dufour parameter
Greek symbols
ν: kinematic viscosity
g: acceleration due to gravity
θ: dimensionless temperature
β_T: volumetric coefficient of thermal expansion
β_C: volumetric coefficient of expansion with concentration
μ: dynamic viscosity
ρ: fluid density
σ: electrical conductivity
α_1: second-grade fluid parameter
γ: second-grade coefficient

B. Nondimensional Quantities

$$
\begin{aligned}
y &= \frac{h_1}{k_1}\widehat{\xi}_1, \\
t &= \nu\left(\frac{h_1}{k_1}\right)^2 \widehat{t}_1, \\
u &= \frac{1}{\nu}\left(\frac{k_1}{h_1}\right)\widehat{u}_1, \\
\theta &= \frac{\widehat{T}_1 - \widehat{T}_\infty}{\widehat{T}_\infty}, \\
C &= \frac{\widehat{C}_1 - \widehat{C}_\infty}{\widehat{C}_w - \widehat{C}_\infty}, \\
q &= \frac{\widehat{q}}{h_1\widehat{T}_\infty}, \\
j &= \frac{\widehat{j}k_1}{\nu\left(\widehat{C}_w - \widehat{C}_\infty\right)h_1}, \\
\mathrm{Pr} &= \frac{\mu C_p}{k_1}, \\
\mathrm{Sc} &= \frac{\nu}{D_m}, \\
\gamma &= \frac{h_1^2\alpha_1}{\rho k_1^2}, \\
\mathrm{Gr} &= \frac{g\beta_T k_1^3\widehat{T}_\infty}{\nu^2 h_1^3}, \\
\mathrm{Gm} &= \frac{g\beta_C k_1^3\left(\widehat{C}_w - \widehat{C}_\infty\right)}{\nu^2 h_1^3}, \\
S &= \frac{Q}{k_1}\left(\frac{k_1}{h_1}\right)^2, \\
\mathrm{Du} &= \frac{D_m K_T\left(\widehat{C}_w - \widehat{C}_\infty\right)}{C_s C_p \widehat{T}_\infty}, \\
M &= \frac{\sigma B_0^2 k_1^2}{\mu h_1^2}.
\end{aligned}
\tag{A.1}
$$

C. Some Constants Involved in the Text

$$
\begin{aligned}
a_1 &= \frac{S}{\mathrm{Pr}},\\
a_2 &= -\frac{\mathrm{PrDu}}{(\mathrm{Sc}-\mathrm{Pr})},\\
a_3 &= -\frac{S}{\mathrm{Sc}-\mathrm{Pr}},\\
a_4 &= \frac{a_0^2(1+a\gamma)-1}{a_0^2\gamma},\\
a_5 &= \frac{a_0^2 a - M}{a_0^2\gamma},\\
b_0 &= (1-\beta)\mathrm{Pr},\\
b_1 &= \frac{S+b\mathrm{Pr}}{\mathrm{Pr}},\\
b_2 &= \frac{bS}{\mathrm{Pr}},\\
b_3 &= -\frac{\mathrm{PrDu}a_0^2(1-\beta)}{\mathrm{Sc}(1-\alpha)},\\
b_4 &= \frac{a_0^2 a - b_0 b_1}{a_0^2 - b_0},\\
b_5 &= -\frac{b_0 b_2}{a_0^2 - b_0},\\
b_6 &= \frac{b_3}{a_0^2 - b_0},\\
d_0 &= \frac{b_0 + b_0 b_1 - 1}{b_0\gamma},\\
d_1 &= \frac{b_0 b_1 + b_0 b_2\gamma - M}{b_0\gamma},\\
d_2 &= \frac{b_2}{\gamma},\\
d_3 &= \frac{1}{\gamma},\\
p_1 &= \frac{b_0 b_1 - M}{b_0 - 1},\\
p_2 &= \frac{b_0 b_2}{b_0 - 1},\\
p_3 &= \frac{a a_0^2 - M}{a_0^2 - 1},\\
p_4 &= \frac{(\mathrm{Pr})^{3/2}(1+a_1\gamma)-1}{(\mathrm{Pr})^{3/2}\gamma},\\
p_5 &= \frac{a_1(\mathrm{Pr})^{3/2} - M}{(\mathrm{Pr})^{3/2}\gamma},\\
p_6 &= \frac{\mathrm{Pr}a_1 - M}{\mathrm{Pr}-1},\\
p_7 &= -\frac{M}{\mathrm{Pr}-1},\\
A_1 &= \frac{\mathrm{Gr}}{b_0^{3/2}\gamma},\\
A_2 &= A_1 b_6,\\
A_3 &= \frac{\mathrm{Gr}b_6}{a_0^2\gamma},\\
A_4 &= \frac{\mathrm{Gm}}{a_0^2\gamma},\\
A_5 &= \frac{\mathrm{Gr}}{\sqrt{b_0}(b_0-1)},\\
A_6 &= A_1 b_6,\\
A_7 &= \frac{\mathrm{Gr}\, b_6}{a_0^2 - 1},\\
A_8 &= \frac{\mathrm{Gm}}{a_0^2 - 1},\\
A_9 &= \frac{\mathrm{Gr}}{(\mathrm{Pr})^{3/2}\gamma},\\
A_{10} &= \frac{\mathrm{Gr}a_2}{\mathrm{Sc}\,\gamma},\\
A_{11} &= \frac{\mathrm{Gm}}{\mathrm{Sc}\,\gamma},\\
A_{12} &= A_{13} = \frac{\mathrm{Gr}}{\mathrm{Sc}-1},\\
A_{14} &= \frac{\mathrm{Gm}}{\mathrm{Sc}-1},\\
\xi &= -\frac{1}{\sqrt{b_0}},\\
\zeta &= -\frac{1}{\sqrt{\mathrm{Pr}}}.
\end{aligned}
\tag{A.2}
$$

D. Some Inverse Laplace Formulas

$$L^{-1}\left\{\frac{e^{-a\sqrt{s+b}}}{s}\right\} = \frac{1}{2}\left[e^{a\sqrt{b}}\,erfc\left(\frac{a}{2\sqrt{t}}+\sqrt{bt}\right)+e^{-a\sqrt{b}}\,erfc\left(\frac{a}{2\sqrt{t}}-\sqrt{bt}\right)\right], \tag{A.3}$$

$$L^{-1}\left\{\frac{e^{-a\sqrt{s}}}{s}\right\} = erfc\left(\frac{a}{2\sqrt{t}}\right), \tag{A.4}$$

$$\begin{aligned}&\text{If } g_1(t) = L^{-1}\{G_1(s)\}, \text{ then } L^{-1}\{G_1(\psi(s))\} = \int_0^\infty g_1(r)h_1(r,t)\mathrm{d}r,\\ &\text{where } h_1(r,t) = L^{-1}\{\exp(-r\psi(s))\},\end{aligned} \tag{A.5}$$

$$L^{-1}\left\{e^{-(a/(s+b))}\right\} = e^{-bt}\left\{\delta(t)-\sqrt{\frac{a}{t}}J_1(2\sqrt{at})\right\}, \tag{A.6}$$

$$L^{-1}\left\{\frac{1}{s^2+b_1s+b_2}\right\} = \frac{2}{\sqrt{b_1^2-4b_2}}\sinh\left(\frac{\sqrt{b_1^2-4b_2}}{2}t\right)e^{-(b_1/2)t}, \tag{A.7}$$

$$L^{-1}\{\sqrt{s+a}\} = \frac{e^{-at}}{2t\sqrt{\pi t}}, \tag{A.8}$$

$$L^{-1}\left\{\frac{1}{\sqrt{s+a}+b}\right\} = e^{-at}\left\{\frac{1}{\sqrt{\pi t}}-a_0e^{b^2t}erfc(b\sqrt{t})\right\}, \tag{A.9}$$

$$L^{-1}\left\{\frac{e^{-a\sqrt{s+c}}}{\sqrt{s+c}+b}\right\} = e^{-ct}\left\{\frac{e^{-a^2/4t}}{\sqrt{\pi t}}-be^{ab+b^2t}erfc\left(\frac{a}{2\sqrt{t}}+b\sqrt{t}\right)\right\}, \tag{A.10}$$

$$\int_0^t \xi^{-3/2}\exp\left(u^2\xi-\frac{x^2}{\xi}\right)\mathrm{d}\xi = \frac{\sqrt{\pi}}{2x}\left[e^{-2iux}erfc\left(\frac{x}{\sqrt{t}}-iu\sqrt{t}\right)+e^{2iux}erfc\left(\frac{x}{\sqrt{t}}+iu\sqrt{t}\right)\right], \tag{A.11}$$

$$L^{-1}\left\{\frac{1}{s(\sqrt{s+b}+c)}\right\} = \frac{1}{b-c^2}\left\{\sqrt{b}\,erf(b\sqrt{t})-\left(e^{-(b-c^2)}\right)erfc(c\sqrt{t})-1\right\}, \tag{A.12}$$

$$L^{-1}\left\{\frac{e^{-y\sqrt{(s+b)/(s+c)}}}{s}\right\} = e^{-y}-\frac{y\sqrt{b-c}}{2\sqrt{\pi}}\int_0^\infty\int_0^t\frac{1}{\sqrt{t}}e^{-(ct+(y^2/4u)+u)}I_1(2\sqrt{(b-c)ut})\mathrm{d}t\mathrm{d}u. \tag{A.13}$$

Data Availability

No data were used to support this study.

Conflicts of Interest

The authors declare that they have no conflicts of interest.

References

[1] Y. Jaluria, *Natural Convection Heat and Mass Transfer*, Pergamon Pergamon Press, Oxford, UK, 1980.

[2] P. S. Ghoshdastidar, *Heat Transfer*, Oxford University Press, Oxford, UK, 2004.

[3] M. A. Imran, I. Khan, M. Ahmad, N. A. Shah, and M. Nazar, "Heat and mass transport of differential type fluid with non-integer order time-fractional Caputo derivatives," *Journal of Molecular Liquids*, vol. 229, pp. 67–75, 2017.

[4] C. Fetecau, D. Vieru, C. Fetecau, and I. Pop, "Slip effects on the unsteady radiative MHD free convection flow over a moving plate with mass diffusion and heat source," *The European Physical Journal Plus*, vol. 130, no. 1, p. 6, 2015.

[5] B. R. Sharma and K. Nath, "Effects of magnetic field and variation of viscosity and thermal conductivity on separation of a binary fluid mixture over a continuously moving surface,"

International Journal for Innovative Research in Science, Engineering and Technology, vol. 2, no. 11, pp. 6516–6524, 2013.

[6] S. Parvin and R. Nasrin, "Analysis of the flow and heat transfer characteristics for MHD free convection in an enclosure with a heated obstacle," *Nonlinear Analysis: Modelling and Control*, vol. 16, no. 1, pp. 89–99, 2011.

[7] E. R. G. Eckert and R. M. Drake, *Analysis of Heat and Mass Transfer*, McGraw-Hill Book Co., New York, NY, USA, 1972.

[8] N. G. Kafoussias and E. W. Williams, "Thermal-diffusion and diffusion-thermo effects on mixed free-forced convective and mass transfer boundary layer flow with temperature dependent viscosity," *International Journal of Engineering Science*, vol. 33, no. 9, pp. 1369–1384, 1995.

[9] K. R. Babu, A. G. V. Kumar, and S. V. K. Varma, "Diffusion-thermo and radiation effects on MHD free convective heat and mass transfer flow past an infinite vertical plate in the presence of a chemical reaction of first order," *Advances in Applied Science Research*, vol. 3, no. 4, pp. 2446–2462, 2012.

[10] U. S. Rajput and N. K. Gupta, "Dufour effect on unsteady free convection MHD flow past an exponentially accelerated plate through porous media with variable temperature and constant mass diffusion in an inclined magnetic field," *International Research Journal of Engineering and Technology*, vol. 3, no. 8, pp. 2135–2140, 2016.

[11] B. R. Sharma and B. Buragohain, "Soret and Dufour effects on unsteady flow past an oscillating vertical plate," *International Journal for Innovative Research in Science, Engineering and Technology*, vol. 2, no. 8, pp. 2349–6010, 2016.

[12] A. Postelnicu, "Influence of a magnetic field on heat and mass transfer by natural convection from vertical surfaces in porous media considering Soret and Dufour effects," *International Journal of Heat and Mass Transfer*, vol. 47, no. 6-7, pp. 1467–1472, 2004.

[13] S. N. Gaikwad, M. S. Malashetty, and K. Rama Prasad, "An analytical study of linear and non-linear double diffusive convection with Soret and Dufour effects in couple stress fluid," *International Journal of Non-linear Mechanics*, vol. 42, no. 7, pp. 903–913, 2007.

[14] J. Prakash, D. Bhanumathi, A. G. Vijaya Kumar, and S. V. K. Varma, "Diffusion-thermo and radiation effects on unsteady MHD flow through porous medium past an impulsively started infinite vertical plate with variable temperature and mass diffusion," *Transport in Porous Media*, vol. 96, no. 1, pp. 135–151, 2013.

[15] R. S. Rivlin, "The hydrodynamics of non-Newtonian fluids-I," *Proceedings of the Royal Society of London A*, vol. 193, pp. 260–281, 1948.

[16] R. S. Rivlin and J. L. Ericksen, "Stress deformation relations for isotropic materials," *Journal of Rational Mechanics and Analysis*, vol. 4, no. 21, pp. 323–425, 1955.

[17] D. W. Beard and K. Walters, "Elastico-viscous boundary-layer flows I. Two-dimensional flow near a stagnation point," *Mathematical Proceedings of the Cambridge Philosophical Society*, vol. 60, no. 3, pp. 667–674, 1964.

[18] P. Donald Ariel, "On exact solutions of flow problems of a second grade fluid through two Parallel porous walls," *International Journal of Engineering Science*, vol. 40, pp. 913–941, 2002.

[19] A. Kecebas and M. Yurusoy, "Numerical solutions of unsteady boundary layer equations for a generalized second grade fluid," *Journal of Theoretical and Applied Mechanics*, vol. 49, no. 1, pp. 71–82, 2011.

[20] B. Raftari, F. Parvaneh, and K. Vajravelu, "Homotopy analysis of the magnetohydrodynamic flow and heat transfer of a second grade fluid in a porous channel," *Energy*, vol. 59, no. 15, pp. 625–632, 2013.

[21] S. Aman, Z. Ismail, M. Z. Salleh, and I. Khan, "Flow analysis of second grade fluid with wall suction/injection and convective boundary condition," *Journal of Advanced Research in Fluid Mechanics and Thermal Sciences*, vol. 58, no. 1, pp. 135–143, 2019.

[22] R. Hilfer, *Threefold Introduction to Fractional Derivatives*, Anomalous Transport: Foundations and Applications,, Stuttgart, Germany, 2008.

[23] R. Gorenflo, F. Mainardi, D. Moretti, and P. Paradisi, "Time fractional diffusion: a discret random walk approach," *Nonlinear Dynamics*, vol. 29, pp. 129–143, 2002.

[24] M. Caputo and M. Fabrizio, "A new definition of fractional derivative without singular kernel," *Progress in Fractional Differentiation and Applications*, vol. 1, no. 2, pp. 73–85, 2015.

[25] M. I. Asjad, N. A. Shah, M. Aleem, and I. Khan, "Heat transfer analysis of fractional second-grade fluid subject to Newtonian heating with Caputo and Caputo-Fabrizio fractional derivatives: a comparison," *The European Physical Journal Plus*, vol. 132, p. 340, 2017.

[26] S. Akhter, "Flows between two parallel plates of Couple stress fluids with time-fractional Caputo and Caputo-Fabrizio derivative," *The European Physical Journal Plus*, vol. 131, p. 401, 2016.

[27] S. Ullah, S. Zulfiqar, A. A. Buhader, and N. A. Khan, "Analysis of Caputo-Fabrizio fractional order semi-linear parabolic equations via effective amalgamated technique," *Physica Scripta*, vol. 96, no. 3, p. 035214, 2021.

[28] M. Ali Dokuyucu, "A fractional order alcoholism model via Caputo-Fabrizio derivative," *AIMS Mathematics*, vol. 5, no. 2, pp. 781–797, 2020.

[29] M. Saqib, I. Khan, S. Shafie, and A. Q. Mohamad, "Shape effect on MHD flow of time fractional Ferro-Brinkman type nanofluid with ramped heating," *Scientific Reports*, vol. 11, p. 3725, 2021.

[30] M. Aleem, M. I. Asjad, A. Shaheen, and I. Khan, "MHD influence on different water based nanofluids (TiO_2, Al_2O_3, CuO) in porous medium with chemical reaction and Newtonian heating," *Chaos, Solitons & Fractals*, vol. 130, p. 109437, 2020.

[31] M. B. Riaz and N. Iftikhar, "A comparative study of heat transfer analysis of MHD Maxwell fluid in view of local and nonlocal differential operators," *Chaos, Solitons & Fractals*, vol. 132, p. 109556, 2020.

[32] S. Ul Haq, S. Ullah Jan, S. Inayat Ali Shah, I. Khan, and J. Singh, "Heat and mass transfer of fractional second grade fluid with slippage and ramped wall temperature using Caputo-Fabrizio fractional derivative approach," *AIMS Mathematics*, vol. 5, no. 4, pp. 3056–3088, 2020.

[33] I. Siddique and S. M. Bukhari, "Analysis of the effect of generalized fractional Fourier's and Fick's laws on convective flows of non-Newtonian fluid subject to Newtonian heating," *The European Physical Journal Plus*, vol. 135, no. 1, p. 45, 2020.

[34] I. Siddique, I. Tlili, S. M. Bukhari, and Y. Mahsud, "Heat transfer analysis in convective flows of fractional second grade fluids with Caputo-Fabrizio and Atangana--Baleanu derivative subject to Newtonion heating," *Mechanics of Time-Dependent Materials*, 2020.

[35] H. Stehfest, "Algorithm 368: numerical inversion of Laplace transforms [D5]," *Communications of the ACM*, vol. 13, no. 1, pp. 47–49, 1970.

[36] K. L. Kuhlman, "Review of inverse Laplace transform algorithms for Laplace-space numerical approaches," *Numerical Algorithms*, vol. 63, no. 2, pp. 339–355, 2013.

[37] B. C. Tai and M. I. Char, "Soret and Dufour effects on free convection flow of non-Newtonian fluids along a vertical plate embedded in a porous medium with thermal radiation," *International Communications in Heat and Mass Transfer*, vol. 37, no. 5, pp. 480–483, 2010.

[38] J. Hristove, *Fronttiers in Fractional Calculus*, S. Bhalekar, Ed., pp. 235–295, Bentham Science Publishers, Sharjah, UAE, 1st edition, 2017.

[39] Y. Povstenko, "Fractional thermoelasticity," in *Encyclopedia of Thermal Stresses*, R. B. Hetnarski, Ed., vol. 4, pp. 1778–1787, Springer, New York, NY, USA, 2014.

[40] D. Vieru, C. Fetecau, and C. Fetecau, "Time fractional free convection flow near a vertical plate with Newtonian heating and Mass diffusion," *Thermal Science*, vol. 19, no. 1, pp. S85–S98, 2015.

Hindawi
Complexity
Volume 2021, Article ID 8946459, 21 pages
https://doi.org/10.1155/2021/8946459

Research Article

Functional Application of G-Functions of Lorenzo and Hartley on the Free Convection Flow of Oldroyd-B Fluid with Ordinary and Fractional Techniques

Imran Siddique,[1] **Sehrish Ayaz**,[1] **Dalal Alrowaili**,[2] **and Sohaib Abdal**[3]

[1]*Department of Mathematics, University of Management and Technology, Lahore 54770, Pakistan*
[2]*Mathematics Department, College of Science, Jouf University, P.O. Box: 2014, Sakaka, Saudi Arabia*
[3]*School of Mathematics, Northwest University, No. 229 North Taibai Avenue, Xi'an 710069, Shaanxi Province, China*

Correspondence should be addressed to Imran Siddique; imransmsrazi@gmail.com

Received 6 April 2021; Revised 5 June 2021; Accepted 28 August 2021; Published 8 September 2021

Academic Editor: Sheng Du

In this article, free convection flow of an Oldroyd-B fluid (OBF) through a vertical rectangular channel in the presence of heat generation or absorption subject to generalized boundary conditions is studied. The fractionalized mathematical model is established by Caputo time-fractional derivative through mechanical laws (generalized shear stress constitutive equation and generalized Fourier's law). Closed form solutions for the velocity and temperature profiles are obtained via Laplace coupled with sine-Fourier transforms and have been embedded with regards to the special functions, namely, the generalized G-functions of Lorenzo and Hartley. Solutions of the known results from recently published work (Nehad et al. Chin. J. Phy., 65, (2020) 367–376) are recovered as limiting cases. Finally, the effects of fractional and various physical parameters are graphically underlined. Furthermore, a comparison between Oldroyd-B, Maxwell and viscous fluids (fractional and ordinary) is depicted. It is found that, for short time, ordinary fluids have greater velocity as compared to the fractional fluids.

1. Introduction

Fluids are classified in two categories with respect to the relation of shear stress and rate of deformation called Newtonian and non-Newtonian fluids. In non-Newtonian fluids, this relation is not linear, while in Newtonian fluids the relation of shear stress is linearly related to the rate of deformation. Several fluids have non-Newtonian behavior such as molten, salt solutions, custard, ketchup, blood, toothpaste, paint, and shampoo. A significant class of non-Newtonian fluids is viscoelastic fluids which show both adaptable and viscous property and numerous models of constitutive equations have been proposed to depict the transport conduct of these fluids. Oldroyd-B fluid (OBF) [1] is an exceptional non-Newtonian fluids and its transport conduct cannot be appropriately depicted by the usual relation between the shear rate and shear stress in a straightforward shear flow. Hence, numerous models of constitutive equations have been offered for these fluids in [2–8].

Free convection flows are of incredible viable significance to engineers and researchers on account of its all-inclusive event in various mechanical applications, for example, cooling of electronic equipment's, solar amassers, fiber protection, and geothermal frameworks [9]. Because of its event in many engineering applications, numerous authors deliberate the free convection fluid flow models between two vertical parallel plates. The free convection fluid flow between two infinite vertical parallel plates is examined by Singh et al. [10]. Narahari [11] presented critical solution for the transient free convection flow between two vertical parallel plates within the sight of steady temperature and mass diffusion by using the Laplace transform method. Na et al. [12] found the closed form solutions of Maxwell free-

convection fluid flow between vertical plates with damped shear and thermal flux. Zaib et al. [13] studied the natural convection flow of second-grade fluid with thermal radiation and damped thermal flux between vertical channels. Hajizadeh et al. [14] got the exact solutions for free convection flow of nanofluids between two vertical plates with damped thermal flux. Shao et al. [15] found the semianalytical solutions for hydromagnetic free-convection flow of viscous fluid between vertical parallel plates with damped thermal and mass fluxes. Seth et al. [16] have investigated the unsteady hydromagnetic flow formation with Hall Effect due to time-dependent free stream in a rotating medium. Seth et al. [17] have studied the effect of Hall current on MHD natural convection heat and mass transfer flow of rotating fluid past a vertical plate with ramped wall temperature. The natural convective heat transfer and nanofluid flows through a rectangular vertical channel under Robin-type conditions are concentrated by Ahmed et al. [18].

On the contrart, heat generation/absorption effects become relevant in many processes involving chemical reaction and dissociating fluids, since the flow and thermal fields can be greatly influenced by the heat source/sink term. Jha et al. [19] examined the effect of heat generation/absorption on flow formation in a parallel plate channel with ramped temperatures. In a related work, Jha and Aina [20] obtained the exact solution for heat generating/absorbing fluid in a cylinder under time periodic boundary conditions in the presence of magnetic field. They found out that the rate of heat transfer is significantly declined with increase in heat sink, while the contrast is true in presence of heat source. Jha et al. [21] presented the exact solution responsible for the mixed convection in an annular geometry when the fluid is either heat generating or heat absorbing. In another work, Saba et al. [22] presented a study on thermal analysis of nanofluid in the presence of internal heat generation/absorption. Other related discussion can be found in [23–28].

Fractional calculus [29, 30] has been utilized effectively in the depiction of viscoelasticity. Mostly, these constitutive equations are obtained from known models via substituting time ordinary derivatives of stress and strain by derivatives of fractional order. The generality permits one to express indeed noninteger-order integral or derivatives. Recently, numerous specialists have considered various issues associated to such fluids. Hyder Ali Muttaqi Shah [31] examined the flows of generalized OBF between two side walls perpendicular to the plate. Akgül et al. [32, 33] analyzed the MHD Couette flows by fractal-fractional differential operators. Some accelerated flows of a generalized OBF are discussed by Fetecau et al. [34]. Siddique and Akgül [35] examined the blood liquor model via nonlocal and singular constant proportional Caputo hybrid differential operator. Khan et al. [36] examined the MHD flow of a generalized OBF in a round funnel. Siddique and Sajid [37] founnd the exact solutions for the unsteady axial flow of non-Newtonian fluids through a circular cylinder. MHD OBF through fractional calculus approach under several conditions has been examined by Liu et al. [38]. Solutions for OBF between two oscillating plates with transverse magnetic field have been investigated by Bose and Basu [39]. Zhao et al. [40] carried out numerical solutions for fractional OBF in porous medium under the influence of heat transfer. Zafar et al. [41] contemplated an OBF for circular cylinders with noninteger-order derivatives. Zhang et al. [42] examined the analytical solutions for time-fractional OBF utilizing the definition of Caputo derivative. As of late, Riaz and Saeed [43] evaluated the conduct of MHD OBF under slip condition with the assistance of integer order, Caputo–Fabrizio, and Atangana–Baleanu fractional derivatives. Wang et al. [44] acquired the semianalytical solutions for velocity field and tangential stress correspond to fractional Oldroyd-B fluid in an annulus by Laplace transforms and modified Bessel equation. Kamran et al. [45] find the exact solutions for the unsteady rotational flow of an Oldroyd-B fluid with fractional derivative through an infinite circular cylinder by means of the finite Hankel and Laplace transforms. In all these studies the ordinary derivatives are falsely supplanted by fractional derivatives. Some recent works were done by specialists, and they introduced fractional derivatives through mechanical laws to governing equations [12–15, 46–48].

In the current paper, as uniqueness, we build up a nonlocal mathematical model in which the thermal transport is depicted by the fractional Fourier's law. The new fractional constitutive equations are characterized with the time-fractional Caputo derivative; hence, they give a power-law damping to the temperature and velocity. These realities were the significant reason of the lack of literature on the study of OBFs between two-side walls under general boundary conditions. In this work, we acquire the closed form solutions of the generalized convection flows of OBF between two parallel plates under general boundary conditions by utilizing the Laplace transform coupled with the finite sine-Fourier transform. The solutions are uttered in the form of generalized G-functions of Lorenzo and Hartley [49]. The impacts of fractional and physical parameters are graphically outlined. In addition, the limiting cases of the current outcomes compare to the solutions for fractional Maxwell, ordinary Maxwell, Oldroyd-B, and Newtonian fluids.

2. Mathematical Modeling

Let us consider the unsteady free-convection Oldroyd-B, incompressible, and electrically conducting fluid flow between two infinite nonconducting parallel vertical plates separated by a distance d. The flow geometry in fixed Cartesian coordinate system $x, \zeta_1^{\mp}$ and z is shown in Figure 1. The x–axis is taken along the plates in the direction of fluid flow with the velocity $u^{\mp}$ and the $\zeta_1^{\mp}$-axis is taken perpendicular to the plates.

Since the channel is infinitely extended in the x and z directions, we can assume that all physical entities describing the fluid motion and heat transfer are the functions of $\zeta_1^{\mp}$ and $t_1^{\mp}$ only. At first, both the plates and the enclosed fluid are at rest at the ambient temperature T_a. After this moment, the left and right plates starts to slid in their own planes along x–direction with the velocities $U_0 g_1^{\mp}(t_1^{\mp})$ and $U_0 g_2^{\mp}(t_1^{\mp})$; individually, plates are maintained at temperatures $T_a + (T_b - T_a) f_1^{\mp}(t_1^{\mp})$ and $T_a + (T_b - T_a) f_2^{\mp}(t_1^{\mp})$,

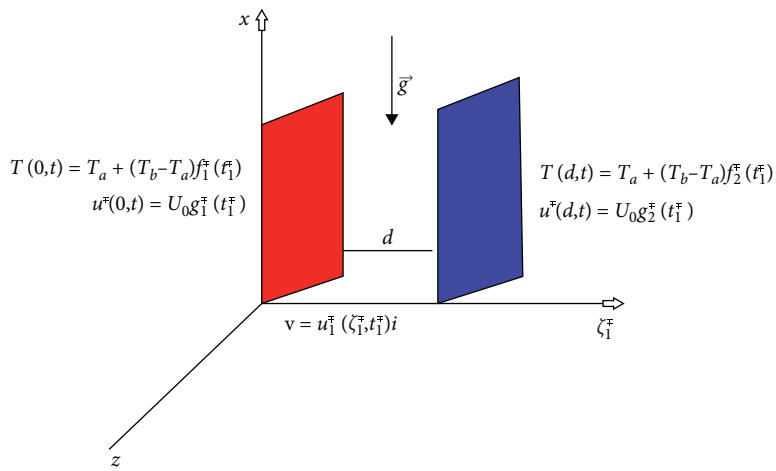

Figure 1: Flow geometry.

respectively, where U_0 is a constant with dimension of velocity; the functions $f_i(\cdot)$ and $g_i(\cdot), i = 1, 2$, are piecewise continuous and exponential order functions at infinity with $f_i(0) = g_i(0) = 0, i = 1, 2$.

We made the following assumptions for the fluid flows:

(i) Velocity is only a function of material coordinate $\zeta_1^{\mp}$ and special coordinate $t_1^{\mp}$, i.e., $\mathbf{v} = (u_1^{\mp}(\zeta_1^{\mp}, t_1^{\mp}), 0, 0)$

(ii) Joule heating and viscous dissipation in energy equations are negligible

In the absence of a pressure gradient in the flow direction and utilizing the typical Boussinesq's approximation, the governing equations for the unsteady free-convection flow of OBF through the vertical channel communicated by the subsequent equations [50, 51] are the linear momentum equation,

$$\rho \frac{\partial u_1^{\mp}(\zeta_1^{\mp}, t_1^{\mp})}{\partial t_1^{\mp}} = \frac{\partial \tau_1^{\mp}(\zeta_1^{\mp}, t_1^{\mp})}{\partial \zeta_1^{\mp}} + g\rho\beta_T \left[T^{\mp}(\zeta_1^{\mp}, t_1^{\mp}) - T_a\right], \quad (1)$$

the constitutive equation,

$$\left(1 + \lambda^{\pm} \frac{\partial}{\partial t_1^{\mp}}\right) \tau_1^{\mp}(\zeta_1^{\mp}, t_1^{\mp}) = \mu \left(1 + \lambda_r^{\mp} \frac{\partial}{\partial t_1^{\mp}}\right) \frac{\partial u_1^{\mp}(\zeta_1^{\mp}, t_1^{\mp})}{\partial \zeta_1^{\mp}}, \quad (2)$$

the thermal balance equation,

$$\rho c_p \frac{\partial T^{\mp}(\zeta_1^{\mp}, t_1^{\mp})}{\partial t_1^{\mp}} = -\frac{\partial q_1(\zeta_1^{\mp}, t_1^{\mp})}{\partial \zeta_1^{\mp}} - Q_0 \left[T^{\pm}(\zeta_1^{\mp}, t_1^{\mp}) - T_a\right], \quad (3)$$

and Fourier's law,

$$q_1(\zeta_1^{\mp}, t_1^{\mp}) = -k \frac{\partial T^{\mp}(\zeta_1^{\mp}, t_1^{\mp})}{\partial \zeta_1^{\mp}}, \quad (4)$$

under corresponding initial and boundary conditions:

$$\begin{aligned} &T^{\mp}(\zeta_1^{\mp}, 0) = T_a, \\ &u_1^{\mp}(\zeta_1^{\mp}, 0) = 0, \quad 0 \le \zeta_1^{\mp} \le d, \end{aligned} \quad (5)$$

$$\begin{aligned} &T^{\mp}(0, t_1^{\mp}) = T_a + (T_b - T_a) f_1^{\mp}(t_1^{\mp}), \\ &T^{\mp}(d, t_1^{\mp}) = T_a + (T_b - T_a) f_2^{\mp}(t_1^{\mp}), \quad t_1^{\mp} \ge 0, \end{aligned} \quad (6)$$

$$\begin{aligned} &u_1^{\mp}(0, t_1^{\mp}) = U_0 g_1^{\mp}(t_1^{\mp}), \\ &u_1^{\mp}(d, t_1^{\mp}) = U_0 g_2^{\mp}(t_1^{\mp}), \quad t_1^{\mp} \ge 0. \end{aligned} \quad (7)$$

Introducing the following nondimensionless variables, functions, and parameters,

$$\left.\begin{aligned}
y &= \frac{\zeta_1^{\mp}}{d},\\
t &= \frac{\nu t_1^{\mp}}{d^2},\\
u &= \frac{u_1^{\mp}}{U_0},\\
T &= \frac{T^{\mp}-T_a}{T_b-T_a},\\
q &= \frac{q_1 d}{k(T_b-T_a)},\\
\tau &= \frac{\tau_1^{\mp} d}{\mu U_0},\\
\lambda &= \frac{\nu\lambda^{\mp}}{d^2},\\
\lambda_r &= \frac{\nu\lambda_r^{\mp}}{d^2},\\
\mathrm{Q}_0 &= \frac{Qd^2}{k},\\
\mathrm{Pr} &= \frac{\mu c_p}{k},\\
\mathrm{Gr} &= \frac{g\beta_T(T_b-T_a)d^2}{\nu U_0},\\
f_j^{\mp}(t_1^{\mp}) &= f_j\left(\frac{\mathrm{d}^2 t}{\nu}\right),\\
g_j^{\mp}(t_1^{\mp}) &= g_j\left(\frac{\mathrm{d}^2 t}{\nu}\right), \quad j=1,2,
\end{aligned}\right\}, \tag{8}$$

into equations (1)–(7), we have

$$\frac{\partial u(y,t)}{\partial t} = \frac{\partial \tau(y,t)}{\partial y} + \mathrm{Gr}T(y,t), \tag{9}$$

$$\left(1+\lambda\frac{\partial}{\partial t}\right)\tau(y,t) = \left(1+\lambda_r\frac{\partial}{\partial t}\right)\frac{\partial u(y,t)}{\partial y}, \tag{10}$$

$$\frac{\partial T(y,t)}{\partial t} = -\frac{1}{\mathrm{Pr}}\frac{\partial q(y,t)}{\partial y} - QT(y,t), \tag{11}$$

$$q(y,t) = -\frac{\partial T(y,t)}{\partial y}. \tag{12}$$

The partial differential equations (9)–(12) are taken along with the following dimensionless initial and boundary conditions:

$$\begin{aligned}
&u(y,0) = 0,\\
&T(y,0) = 0, \quad 0 \le y \le 1,
\end{aligned} \tag{13}$$

$$\begin{aligned}
&T(0,t) = f_1(t),\\
&T(1,t) = f_2(t), \quad t \ge 0,
\end{aligned} \tag{14}$$

$$\begin{aligned}
&u(0,t) = g_1(t),\\
&u(1,t) = g_2(t), \quad t \ge 0.
\end{aligned} \tag{15}$$

In the following, we develop a fractional model in which the classical constitutive equations (10) and (12) are generalized by using the constitutive shear stress equation:

$$\left(1+\lambda\frac{\partial}{\partial t}\right)\tau(y,t) = \left(1+\lambda_r\frac{\partial}{\partial t}\right){}^{C}D_t^{1-\alpha}\left(\frac{\partial u(y,t)}{\partial y}\right), \quad 0<\alpha\le 1, \tag{16}$$

proposed by Scott-Blair [52], respectively, and the generalized Fourier's law,

$$q(y,t) = -{}^{C}D_t^{1-\beta}\left(\frac{\partial T(y,t)}{\partial y}\right), \quad 0<\beta\le 1, \tag{17}$$

proposed by Povstenko [53] and Hristov [54], respectively. In the above constitutive equations, ${}^{C}D_t^{\alpha}(\cdot)$ denotes the time-fractional Caputo derivative defined by [55, 56]. Hence,

$$\begin{aligned}
{}^{C}D_t^{\alpha}u(y,t) &= \frac{1}{\Gamma(1-\alpha)}\int_0^t \dot{u}(y,s)(t-s)^{-\alpha}\mathrm{d}s\\
&= \left(h_\alpha(t) * \dot{u}(y,t)\right), \quad 0\le\alpha\le 1,
\end{aligned} \tag{18}$$

where $h_\alpha(t) = (t^{-\alpha}/\Gamma(1-\alpha))$ is the singular power-law kernel for $\dot{u}(y,s) = (\partial u(y,t)/\partial t)|_{t=s}$.

Furthermore, using the second form of the time-fractional Caputo derivative from equation (18) and one of the following properties of $h_\alpha(\cdot)$ is defined as

$$\begin{aligned}
&L\{h_\alpha(t)\} = \frac{1}{s^{1-\alpha}},\\
&\left(h_{1-\alpha} * h_\alpha\right)(t) = 1,\\
&h_0(t) = L^{-1}\left\{\frac{1}{s}\right\} = 1,\\
&h_1(t) = L^{-1}\{1\} = \delta(t),
\end{aligned} \tag{19}$$

where $L\{\cdot\}$ denotes the Laplace transform, $\delta(\cdot)$ is Dirac's distribution, and s is the transform parameter, and it is easy to show that

$$
\begin{aligned}
&{}^{C}D_{t}^{0} f(y,t) = f(y,t) - f(y,0),\\
&\left({}^{C}D_{t}^{0} f(y,t) = f(y,t), \text{if } f(y,0) = 0\right),\\
&{}^{C}D_{t}^{1} f(y,t) = \frac{\partial f(y,t)}{\partial t}.
\end{aligned}
\tag{20}
$$

Using properties (20), for $\alpha = \beta = 1$, equations (16) and (17) reduce to the classical forms (10) and (12).

It is important to specify that the models based on fractional constitutive equations are more general than those described by constitutive equations with integer derivatives.

For this, let us analyze the constitutive equations for the thermal flux (12) and (17). Equation (12) corresponding to Fourier's law is a local form in time and space. Indeed, the value of the heat flux in a position y at time t is determined by the value of the temperature gradient in the same spatial position and at the same time.

The generalized constitutive equation (17), written in the equivalent form $q(y,t) = -(1/\Gamma(\beta))(\partial/\partial y)\int_0^t (t-s)^{\beta-1} \partial T(y,t)/\partial t|_{t=s} \mathrm{d}s$, shows that the value of the thermal flux in position y at time t is influenced by the temperature history; therefore, the values of the time derivative of temperature for all past and present times determine the thermal flux at the moment t. Such types of constitutive equations describe the thermal processes with time nonlocality. The function $h_{1-\beta}(t) = (t^{\beta-1}/\Gamma(\beta))$ is the time-nonlocality kernel (the weight function).

The processes with time nonlocality are called processes with memory. The classical Fourier's law describes processes with "instantaneous memory" whose time nonlocality kernel being Dirac's distribution. If the weight function is constant, the process is called the "full memory" process, i.e., there is no fading of memory.

A similar discussion can be made regarding the generalized constitutive equation (16). The difference, in this case, is about the memory of the material deformation. It can be seen from equation (16) that the history of the strain rate influences the stress at the moment t.

Eliminating τ from equations (9) and (16) and q from equations (11) and (17), we obtain

$$
\left(1 + \lambda \frac{\partial}{\partial t}\right) \frac{\partial u(y,t)}{\partial t} = \left(1 + \lambda_r \frac{\partial}{\partial t}\right) {}^{C}D_{t}^{1-\alpha} \left(\frac{\partial^2 u(y,t)}{\partial y^2}\right) + \mathrm{Gr}\left(1 + \lambda \frac{\partial}{\partial t}\right) T(y,t),
\tag{21}
$$

$$
\frac{\partial T(y,t)}{\partial t} = \frac{1}{\mathrm{Pr}} {}^{C}D_{t}^{1-\beta} \left(\frac{\partial^2 T(y,t)}{\partial y^2}\right) - QT(y,t).
\tag{22}
$$

In order to obtain the equivalent forms of equations (21) and (22), we recall the time-fractional integral operator:

$$
J_t^{\alpha} f(y,t) = \left(h_{1-\alpha} * f\right)(t) = \frac{1}{\Gamma(\alpha)} \int_0^t f(y,s)(t-s)^{\alpha-1} \mathrm{d}s,
\tag{23}
$$

which is the left-inverse operator of the derivative operator ${}^{C}D_t^{\alpha}(\cdot)$. Indeed, using equations (18), (19), and (23), we obtain that

$$
\begin{aligned}
\left(J_t^{\alpha} \circ {}^{C}D_t^{\alpha}\right) f(y,t) &= J_t^{\alpha}\left({}^{C}D_t^{\alpha} f(y,t)\right) = \left[h_{1-\alpha} * \left(h_{\alpha} * \dot{f}\right)\right](t)\\
&= \left[\left(h_{1-\alpha} * h_{\alpha}\right) * \dot{f}\right](t) = [1 * \dot{f}](t) = f(y,t) - f(y,0),
\end{aligned}
\tag{24}
$$

which implies

$$
\left(J_t^{\alpha} \circ {}^{C}D_t^{\alpha}\right) f(y,t) = f(y,t), \quad \text{if } f(y,0) = 0.
\tag{25}
$$

Moreover, using equations (18) and (23), it results that

$$
J_t^{1-\alpha} \dot{f}(y,t) = \left(h_{\alpha} * \dot{f}\right)(t) = {}^{C}D_t^{\alpha} f(y,t).
\tag{26}
$$

Now, applying the fractional integral operators $J_t^{1-\alpha}$ and $J_t^{1-\beta}$ to equations (21) and (22) and using properties (24)–(26) together with the initial condition, we obtain the following fractional differential equations:

$$\left(1+\lambda\frac{\partial}{\partial t}\right){}^{C}D_t^{\alpha}u(y,t)=\left(1+\lambda_r\frac{\partial}{\partial t}\right)\frac{\partial^2 u(y,t)}{\partial y^2}+\mathrm{Gr}J_t^{1-\alpha}\left(1+\lambda\frac{\partial}{\partial t}\right)T(y,t), \tag{27}$$

$${}^{C}D_t^{\beta}T(y,t)=\frac{1}{\mathrm{Pr}}\frac{\partial^2 T(y,t)}{\partial y^2}-QJ_t^{1-\beta}T(y,t). \tag{28}$$

To determine the solutions of equations (27) and (28), we will employ the Laplace and finite Fourier transform.

The mathematical models considered in this paper describe real problems of fluid flow and heat transfer in a rectangular channel. Therefore, we consider for the study problems in which the temperature and velocity fields are functions that are at least twice differentiable in relation to the variables on which they depend. It is also considered that the functions that describe the movement and heat transfer have additional properties so that the existence of the Laplace and Fourier transforms to be provided.

Therefore, for the studied problems, we search solutions in the class of functions that satisfy the above properties.

3. Solution of the Problem

3.1. Temperature Distribution. Applying the Laplace transform to equations (28) and (14), using initial condition (13), we obtain

$$s^{\beta}\overline{T}(y,s)=\frac{1}{\mathrm{Pr}}\frac{\partial^2\overline{T}(y,s)}{\partial y^2}-Qs^{\beta-1}\overline{T}(y,s), \tag{29}$$

$$\begin{aligned}\overline{T}(0,s)&=F_1(s),\\ \overline{T}(1,s)&=F_2(s),\end{aligned} \tag{30}$$

where $\overline{T}(y,s)=\int_0^{\infty}\overline{T}(y,t)e^{-st}\mathrm{d}t$, s is Laplace transform parameter, and $L\{f_i(t)\}=F_i(s); i=1,2$.

Applying the finite sine-Fourier transform to differential equation (29) subject to the conditions in equation (30), we obtain

$$\widetilde{\overline{T}}_s(n,s)=\frac{(n\pi)\left(F_1(s)+(-1)^{n+1}F_2(s)\right)}{\mathrm{Pr}s^{\beta}+Qs^{\beta-1}+(n\pi)}, \tag{31}$$

where $\widetilde{\overline{T}}_s(n,s)=\int_0^1\overline{T}(y,s)\sin(n\pi y)\mathrm{d}y, n=1,2,\ldots$.

Equation (31) can be written in the following equivalent form:

$$\widetilde{\overline{T}}_s(n,p)=\frac{F_1(s)}{n\pi}+\frac{(-1)^{n+1}F_2(s)}{n\pi}-\frac{\left[F_1(s)+(-1)^{n+1}F_2(s)\right]}{n\pi}\times\left[1-\frac{(n\pi)^2}{\mathrm{Pr}}\frac{1}{\left(s^{\beta}+\left((n\pi)^2/\mathrm{Pr}\right)\right)+Q\mathrm{Pr}^{-1}s^{\beta-1}}\right]. \tag{32}$$

Taking inverse Laplace transform of equation (32), we obtain

$$\widetilde{T}_s(n,t)=\frac{f_1(t)}{n\pi}+\frac{(-1)^{n+1}f_2(t)}{n\pi}-\frac{\left[f_1(t)+(-1)^{n+1}f_2(t)\right]}{n\pi}*\left[\delta(t)-(n\pi)^2\sum_{m=0}^{\infty}\frac{(-Q)^m}{\mathrm{Pr}^{m+1}}G_{\beta,(\beta-1)m,m+1}\left(-\frac{(n\pi)^2}{\mathrm{Pr}},t\right)\right], \tag{33}$$

where " $*$ " represents the convolution product, $\delta(t)$ is the direct delta function, and $G_{a,b,c}(\cdot)$ is the generalized G-function of Lorenzo and Hartley [49] defined as

$$G_{a,b,c}(d,t)=L^{-1}\left\{\frac{p^b}{(p^a-d)^c}\right\},\quad R(p)>0, R(ac-b)>0, \left|\frac{d}{p^a}\right|<1. \tag{34}$$

Taking the inverse sine-Fourier transform of equation (33), we obtain the temperature field

$$T(y,t)=f_1(t)(1-y)+f_2(t)y-2\sum_{n=1}^{\infty}\frac{1}{n\pi}\left[f_1(t)+(-1)^{n+1}f_2(t)\right]*\left[\delta(t)-(n\pi)^2\sum_{m=0}^{\infty}\frac{(-Q)^m}{\mathrm{Pr}^{m+1}}G_{\beta,(\beta-1)m,m+1}\left(-\frac{(n\pi)^2}{\mathrm{Pr}},t\right)\right]\sin(n\pi y). \tag{35}$$

For the ordinary case when $\beta=1$, we have

$$T(y,t) = f_1(t)(1-y) + f_2(t)y - 2\sum_{n=1}^{\infty}\frac{1}{n\pi}\left[f_1(t) + (-1)^{n+1}f_2(t)\right] * \left[\delta(t) - \frac{(n\pi)^2}{\mathrm{Pr}}\exp\left(-\frac{(n\pi)^2 + Q}{\mathrm{Pr}}t\right)\right]\sin(n\pi y). \tag{36}$$

For the special case, when $Q = 0$, the similar solution is recovered as obtained in equation (35) in [12].

3.2. Velocity Field. Applying the Laplace transform to equations (27) and (15), using initial condition (13), we obtain

$$(1+\lambda s)s^{\alpha}\overline{u}(y,s) = (1+\lambda_r s)\frac{\partial^2\overline{u}(y,s)}{\partial y^2} + \mathrm{Gr}(1+\lambda s)s^{\alpha-1}\overline{T}(y,s), \tag{37}$$

$$\begin{aligned}\overline{u}(0,s) &= G_1(s),\\ \overline{u}(1,s) &= G_2(s).\end{aligned} \tag{38}$$

Applying the finite sine-Fourier transform to differential equation (37) subject to the conditions in equation (38), we obtain

$$\begin{aligned}&\left[s^{\alpha} + \lambda s^{\alpha+1} + (1+\lambda_r s)(n\pi)^2\right]\widetilde{\overline{u}}_s(n,s)\\ &\quad = (n\pi)(1+\lambda_r s)\left[G_1(s) + (-1)^{n+1}G_2(s)\right] + \mathrm{Gr}\left[s^{\alpha-1} + \lambda s^{\alpha}\right]\widetilde{\overline{T}}_s(n,s).\end{aligned} \tag{39}$$

Using equation (31) in equation (39), we write the expression in suitable form as

$$\begin{aligned}\widetilde{\overline{u}}_s(n,s) &= \frac{(n\pi)(1+\lambda_r s)\left[G_1(s) + (-1)^{n+1}G_2(s)\right]}{\left(s^{\alpha} + \lambda s^{\alpha+1} + (1+\lambda_r s)(n\pi)^2\right)}\\ &\quad + \frac{\mathrm{Gr}(n\pi)}{\mathrm{Pr}}\frac{\left(s^{\alpha-1} + \lambda s^{\alpha}\right)\left[F_1(s) + (-1)^{n+1}F_2(s)\right]}{\left(s^{\alpha} + \lambda s^{\alpha+1} + (1+\lambda_r s)(n\pi)^2\right)}\frac{1}{\left(s^{\beta} + \left((n\pi)^2/\mathrm{Pr}\right)\right) + Q\mathrm{Pr}^{-1}s^{\beta-1}}.\end{aligned} \tag{40}$$

Equation (40) can be written in the following equivalent form by using the series formula $(1/(z_1+b)) = \sum_{k=0}^{\infty}((-1)^k z_1^k/b^{k+1}), |z_1/b| < 1$ as

$$\begin{aligned}\widetilde{\overline{u}}_s(n,s) &= \frac{G_1(s)}{n\pi} + \frac{(-1)^{n+1}G_2(s)}{n\pi} - \frac{\left[G_1(s) + (-1)^{n+1}G_2(s)\right]}{n\pi}\\ &\quad \times \sum_{l=0}^{\infty}\frac{(-1)^l}{\lambda^{l+1}}\sum_{k=0}^{l}\frac{l!(n\pi)^{2(l-k)}}{k!(l-k)!}\left[\frac{s^{(\alpha+1)k-l-1}}{\left(s^{\alpha} + \left(\lambda_r(n\pi)^2/\lambda\right)\right)^{l+1}} + \frac{\lambda s^{(\alpha+1)k-l}}{\left(s^{\alpha} + \left(\lambda_r(n\pi)^2/\lambda\right)\right)^{l+1}}\right]\\ &\quad + \mathrm{Gr}(n\pi)\left[F_1(s) + (-1)^{n+1}F_2(s)\right]\\ &\quad \times \sum_{n=0}^{\infty}\frac{(-1)^n}{\lambda^{l+1}}\sum_{k=0}^{n}\frac{l!(n\pi)^{2(l-k)}}{k!(l-k)!}\left[\frac{s^{(\alpha+1)k-l-2}}{\left(s^{\alpha} + \left(\lambda_r(n\pi)^2/\lambda\right)\right)^{l+1}} + \frac{\lambda s^{(\alpha+1)k-l-1}}{\left(s^{\alpha} + \left(\lambda_r(n\pi)^2/\lambda\right)\right)^{l+1}}\right]\\ &\quad \sum_{m=0}^{\infty}\frac{(-Q)^m}{\mathrm{Pr}^{m+1}}\frac{s^{(\beta-1)m}}{\left(s^{\beta} + \left((n\pi)^2/\mathrm{Pr}\right)\right)^{m+1}}.\end{aligned} \tag{41}$$

Taking the inverse Laplace transform of equation (41), we obtain

$$\begin{aligned}\tilde{u}_s(n,t) &= \frac{g_1(t)}{n\pi} + \frac{(-1)^{n+1} g_2(t)}{n\pi} - \frac{1}{n\pi}\left[g_1(t) + (-1)^{n+1} g_2(t)\right] \\ &* \sum_{l=0}^{\infty} \frac{(-1)^l}{\lambda^{l+1}} \sum_{k=0}^{l} \frac{l!\,(n\pi)^{2(l-k)}}{k!\,(l-k)!} \left[G_{\alpha,(\alpha+1)k-l-1,l+1}\left(-\frac{\lambda_r (n\pi)^2}{\lambda}, t\right) + \lambda G_{\alpha,(\alpha+1)k-l,l+1}\left(-\frac{\lambda_r (n\pi)^2}{\lambda}, t\right)\right] \\ &+ \mathrm{Gr}(n\pi)\left[f_1(t) + (-1)^{n+1} f_2(t)\right] \\ &* \sum_{l=0}^{\infty} \frac{(-1)^l}{\lambda^{l+1}} \sum_{k=0}^{l} \frac{l!\,(n\pi)^{2(l-k)}}{k!\,(l-k)!} \left[G_{\alpha,(\alpha+1)k-l-2,n+1}\left(-\frac{\lambda_r (n\pi)^2}{\lambda}, t\right) + \lambda G_{\alpha,(\alpha+1)k-l-1,m+1}\left(-\frac{\lambda_r (n\pi)^2}{\lambda}, t\right)\right] \\ &* \sum_{m=0}^{\infty} \frac{(-Q)^m}{\mathrm{Pr}^{m+1}} G_{\beta,(\beta-1)m,m+1}\left(-\frac{(n\pi)^2}{\mathrm{Pr}}, t\right).\end{aligned} \tag{42}$$

Taking the inverse sine-Fourier transform of equation (42), we have

$$\begin{aligned}u(y,t) &= g_1(t)(1-y) + g_2(t)y - 2\sum_{n=1}^{\infty} \frac{1}{n\pi}\left[g_1(t) + (-1)^{n+1} g_2(t)\right] * \sum_{l=0}^{\infty} \frac{(-1)^l}{\lambda^{l+1}} \sum_{k=0}^{l} \frac{l!\,(n\pi)^{2(l-k)}}{k!\,(l-k)!} \\ &\cdot \left[G_{\alpha,(\alpha+1)k-l-1,l+1}\left(-\frac{\lambda_r (n\pi)^2}{\lambda}, t\right) + \lambda G_{\alpha,(\alpha+1)k-l,l+1}\left(-\frac{\lambda_r (n\pi)^2}{\lambda}, t\right)\right] \sin(n\pi y) \\ &+ 2\mathrm{Gr}\sum_{n=1}^{\infty}\left[f_1(t) + (-1)^{n+1} f_2(t)\right] * \sum_{l=0}^{\infty} \frac{(-1)^l}{\lambda^{l+1}} \sum_{k=0}^{n} \frac{l!\,(n\pi)^{2(l-k)+1}}{k!\,(l-k)!} \times \\ &\cdot \left[G_{\alpha,(\alpha+1)k-l-2,n+1}\left(-\frac{\lambda_r (n\pi)^2}{\lambda}, t\right) + \lambda G_{\alpha,(\alpha+1)k-l-1,l+1}\left(-\frac{\lambda_r (n\pi)^2}{\lambda}, t\right)\right] \\ &* \sum_{m=0}^{\infty} \frac{(-Q)^m}{\mathrm{Pr}^{m+1}} G_{\beta,(\beta-1)m,m+1}\left(-\frac{(n\pi)^2}{\mathrm{Pr}}, t\right) \sin(n\pi y).\end{aligned} \tag{43}$$

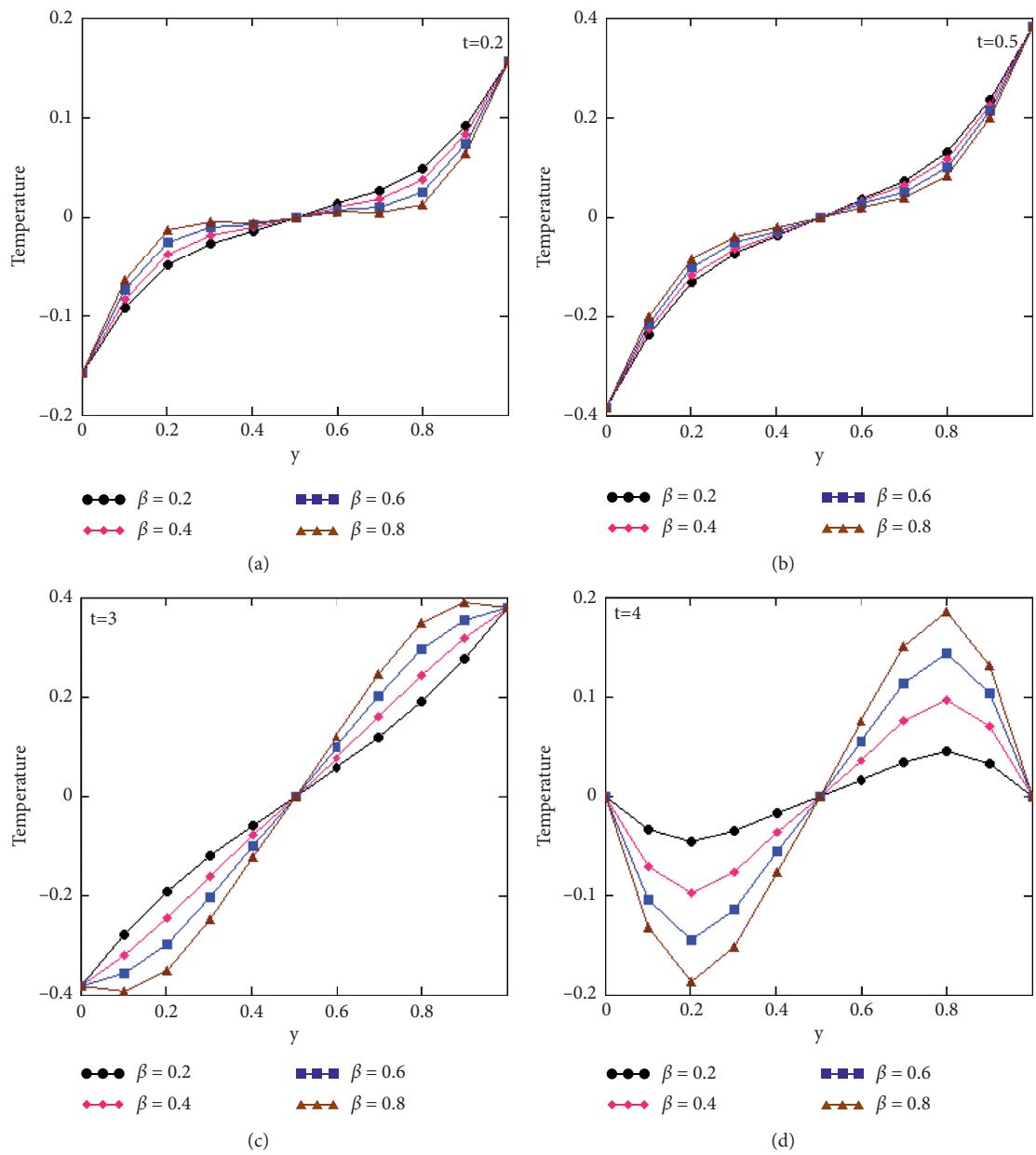

Figure 2: Profiles of dimensionless temperature versus y for variation of β at altered values of time t, $\Pr = 20$ and $Q = 0.5$, and $f_1(t) = -\sin(\pi t/4)$ and $f_2(t) = \sin(\pi t/4)$.

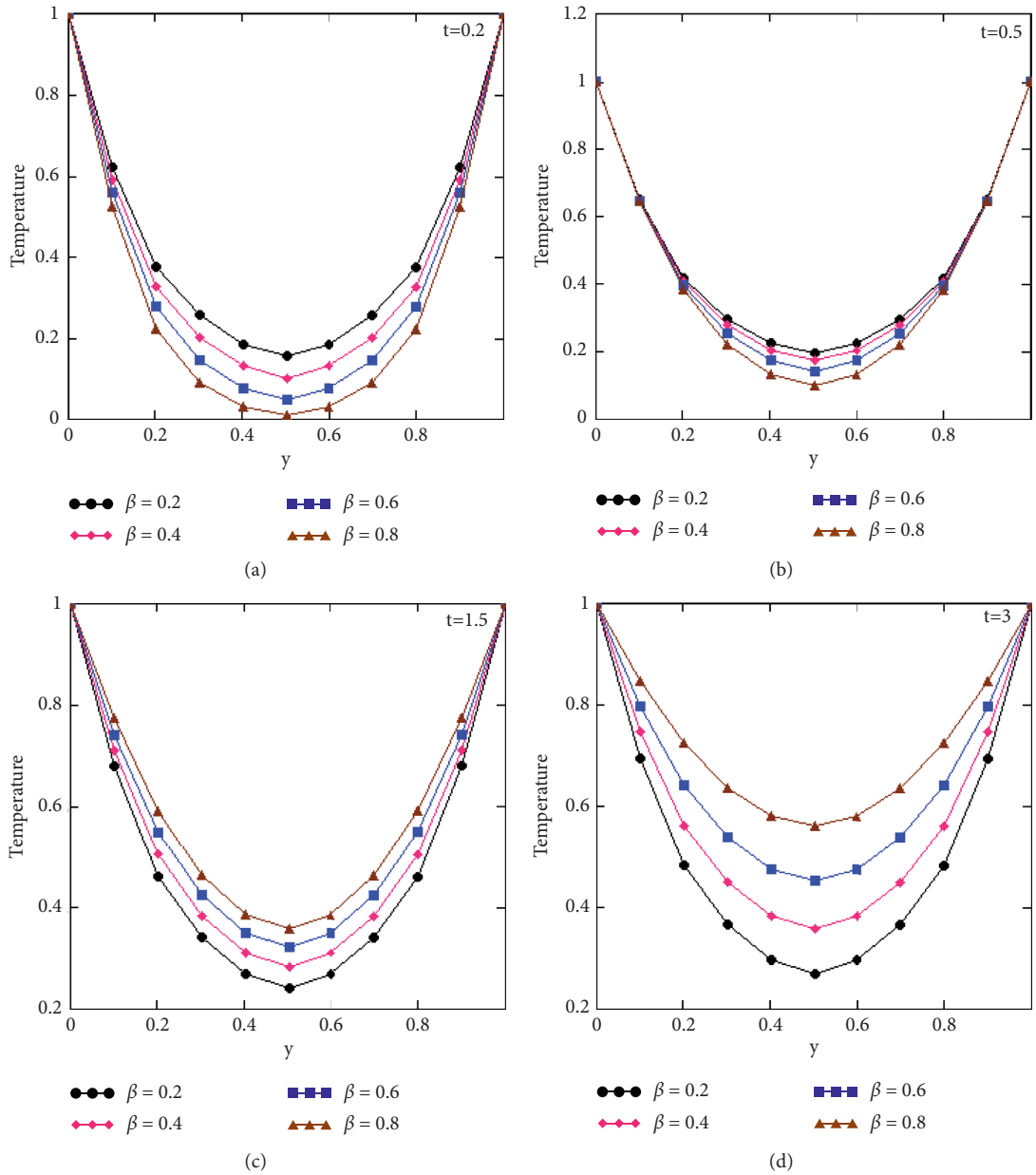

Figure 3: Profiles of dimensionless temperature versus y for variation of β at altered values of time t, $\Pr = 20$ and $Q = 0.5$, and $f_1(t) = H(t) = f_2(t)$.

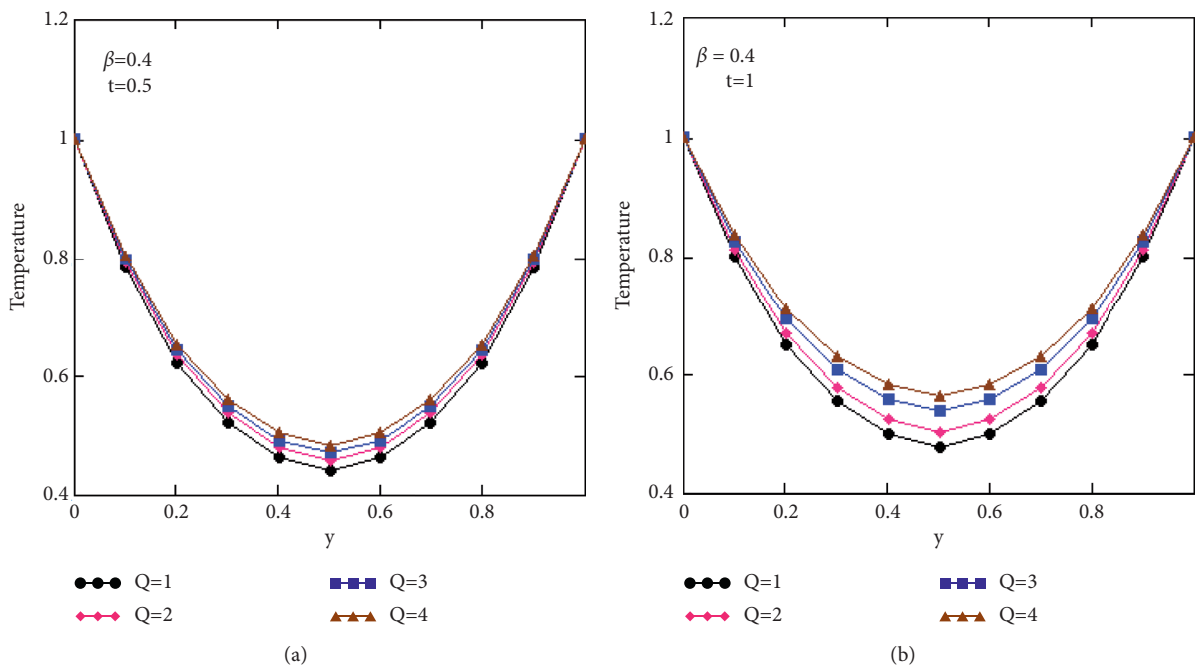

Figure 4: Profiles of dimensionless temperature versus y for variation of Q at altered values of time t, Pr = 20, and $f_1(t) = H(t) = f_2(t)$.

Remarks 1

(i) For the classical case corresponding to $\alpha = \beta = 1$, we have the ordinary velocity field of the OBF from equation (43):

$$\begin{aligned} u(y,t) = {} & g_1(t)(1-y) + g_2(t)y - 2\sum_{n=1}^{\infty}\frac{1}{n\pi}\left[g_1(t) + (-1)^{n+1}g_2(t)\right] * \\ & \sum_{l=0}^{\infty}\frac{(-1)^l}{\lambda^{l+1}}\sum_{k=0}^{l}\frac{l!\,(n\pi)^{2(l-k)}}{k!\,(l-k)!}\left[G_{1,2k-l-1,l+1}\left(-\frac{\lambda_r(n\pi)^2}{\lambda},t\right) + \lambda G_{1,2k-l,l+1}\left(-\frac{\lambda_r(n\pi)^2}{\lambda},t\right)\right]\sin(n\pi y) \\ & + 2\frac{\mathrm{Gr}(n\pi)}{\mathrm{Pr}}\sum_{n=1}^{\infty}\left[f_1(q) + (-1)^{n+1}f_2(q)\right] \\ & * \sum_{l=0}^{\infty}\frac{(-1)^l}{\lambda^{l+1}}\sum_{k=0}^{n}\frac{l!\,(n\pi)^{2(l-k)}}{k!\,(l-k)!}\left[G_{1,2k-l-2,n+1}\left(-\frac{\lambda_r(n\pi)^2}{\lambda},t\right) + \lambda G_{1,2k-l-1,l+1}\left(-\frac{\lambda_r(n\pi)^2}{\lambda},t\right)\right] * \\ & \sum_{m=0}^{\infty}\frac{(-Q)^m}{\mathrm{Pr}^{m+1}}G_{1,0,m+1}\left(-\frac{(n\pi)^2}{\mathrm{Pr}},t\right)\sin(n\pi y). \end{aligned} \tag{44}$$

(ii) For fractional and classical Maxwell fluid when $\lambda_r \longrightarrow 0$ and $Q = 0$ in equation (44), the similar solution is recovered as obtained in equations (43) and (44) in [12], respectively.

(iii) For fractional and classical viscous fluid when $\lambda \longrightarrow 0, \lambda_r \longrightarrow 0$, and $Q = 0$ in equation (44), w the similar solution is recovered as obtained in equation (45) and (46) in [12], respectively.

4. Numerical Results and Discussion

In order to examine the communicative changes on the thermal transport and flow profiles arising due to change of physical parameters, numerical estimations of the fluid temperature and velocity are figured and shown graphically in Figures 2–14.

In Figure 2, we exposed the effect of fractional parameter β at different values of time t and considering the functions $f_1(t) = -\sin(\pi t/4)$ and $f_2(t) = \sin(\pi t/4)$ at left and right plates, respectively. It is pointed out that, for small values of time t, the temperature is decreasing by increasing the values of fractional parameter β; after critical point, the influence becomes reversed for the large value of time. In Figure 3, we presented the effect of fractional parameter β at different values of time t and considering constant temperature at both plates. It has the similar influence like Figure 2. Also, we observed from this figure that the value of temperature at the

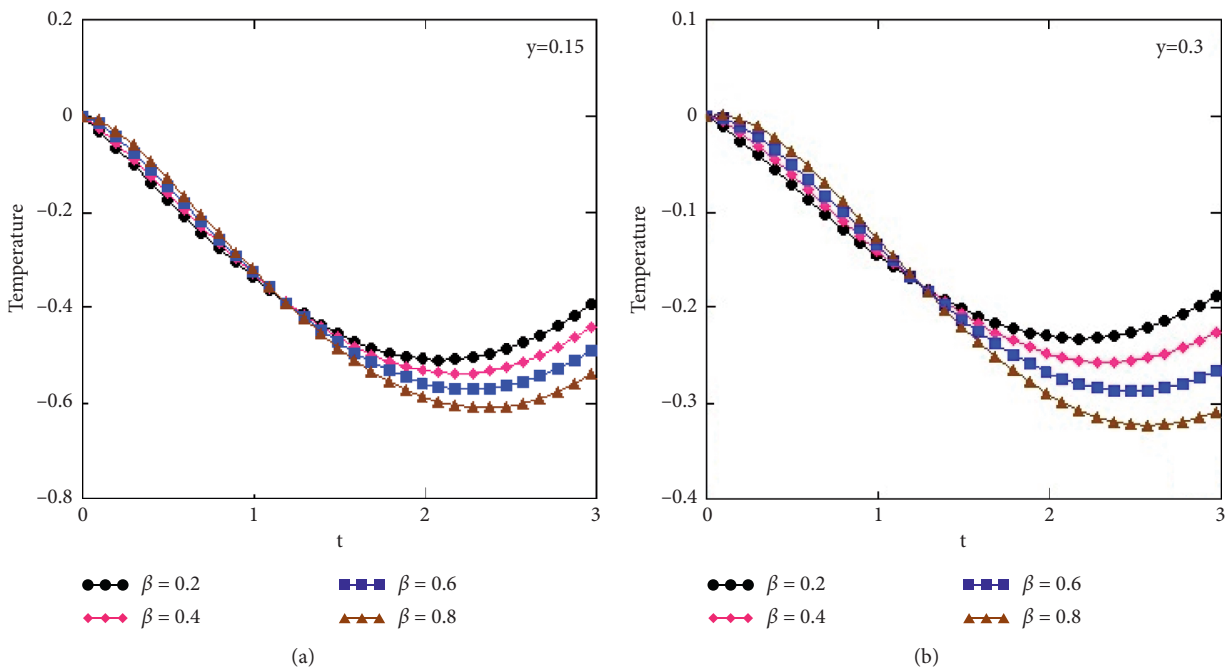

Figure 5: Profiles of dimensionless temperature verses t for β at two values of y for $\Pr = 20$ and $Q = 0.5$ and $f_1(t) = -\sin(\pi t/4)$ and $f_2(t) = \sin(\pi t/4)$.

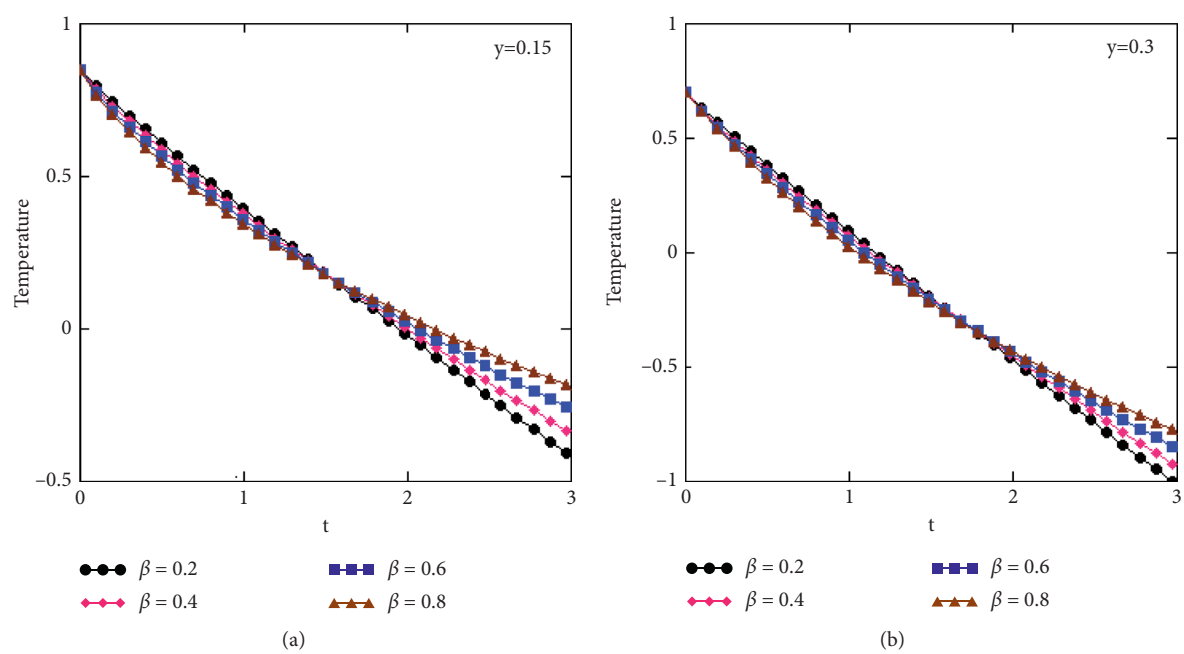

Figure 6: Profiles of dimensionless temperature verses t for β at two values of y for $\Pr = 20, Q = 0.5$, and $f_1(t) = H(t) = f_2(t)$.

middle of the channel is low. The impact of absorption coefficient Q on temperature profile is presented in Figure 4. We observed that temperature is an increasing function of Q for small and large values of time t.

Figures 5 and 6 are presented to show the critical point for Figures 2 and 3, respectively.

In Figure 7, we presented the effect of fractional parameter α at different values of time t, and $f_1(t) = H(t)$, $f_2(t) = e^{-5t}$, and $g_1(t) = H(t) = g_2(t)$. From Figures 7(a) and 7(b), we observed that velocity profile increasing for small time t corresponds to the large values of α, while velocity profile increasing for large values of time t corresponds to small values of α. The effect of fractional parameter β at different values of time t, $f_1(t) = f_1(t) = H(t) = g_1(t) = g_2(t)$ and $f_1(t) = -H(t)$, and $f_2(t) = H(t) = g_1(t) = g_2(t)$ is presented in Figures 8 and 9, respectively.

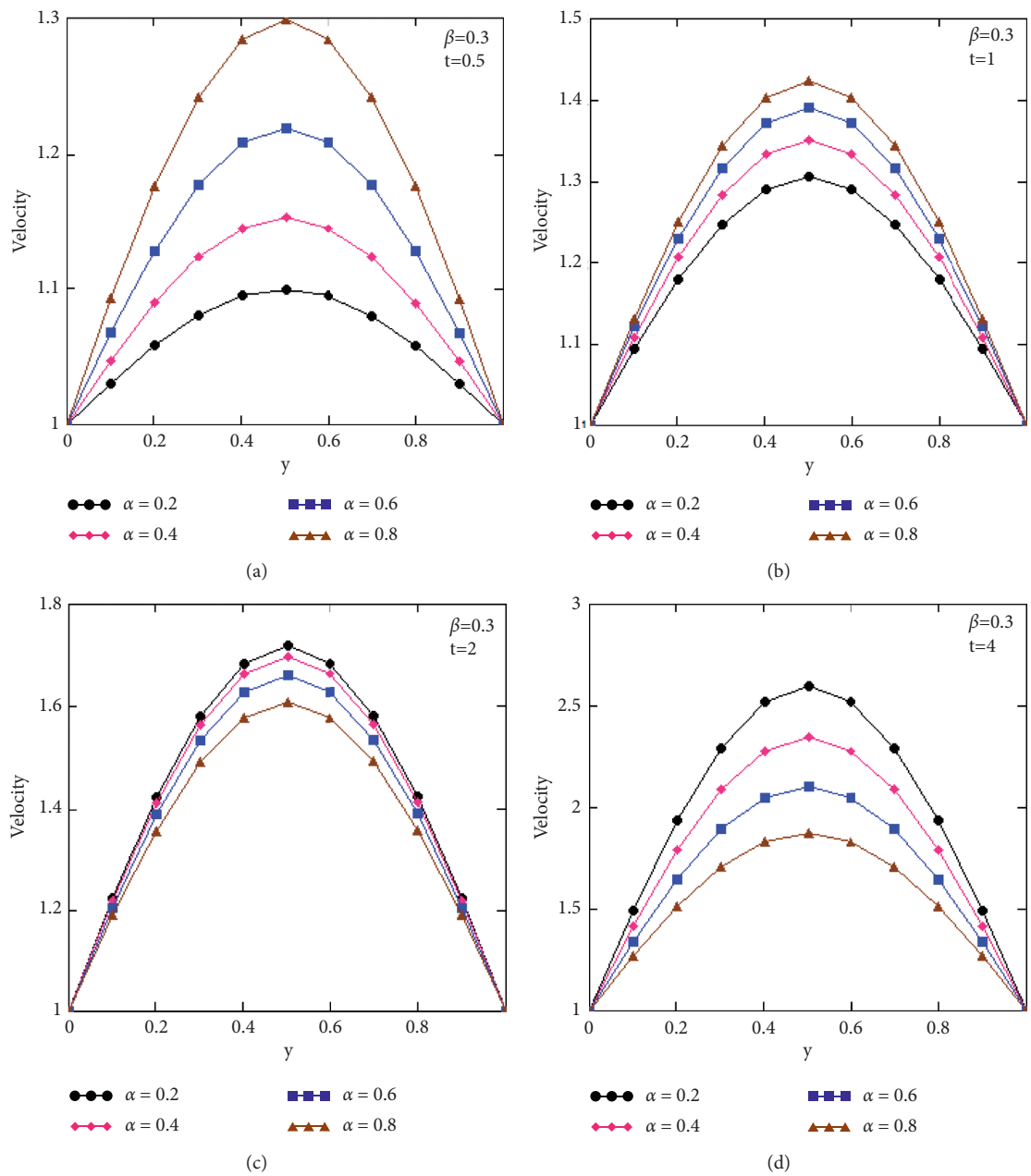

FIGURE 7: Profiles of dimensionless velocity versus y for variation of α at altered values of time t, Gr = 5, $\lambda = 2, \lambda_r = 3$, Pr = 20, and $Q = 0.5$, and $f_1(t) = H(t)$, $f_2(t) = e^{-5t}$, and $g_1(t) = H(t) = g_2(t)$.

From Figures 7–9, it is observed that, for small values of time velocity decreases by increasing the values of fractional parameters α, while the influence is opposite for large values of time.

In order to find the critical value of time at which the influence becomes reversed, it is presented in Figure 10. The effects of relaxation and retardation parameters λ and λ_r and absorption coefficient Q on velocity profile are presented in Figures 11–13. We observed that the velocity is an increasing function of λ for small and large values of time t because the relaxation time is the time needed by the fluid particles to adjust the flow motion of the fluid, while velocity is a decreasing function of λ_r and Q for small and large values of time t. The comparison between fractional Oldroyd-B, ordinary Oldroyd-B, fractional Maxwell, ordinary Maxwell, fractional viscous, and ordinary viscous fluids is presented in Figure 14. It is investigated that, for small time, ordinary fluids have greater velocity as compared to fractional fluids while for large time vice versa. Figures 15 and 16 are plotted to see the validity of our obtained results for temperature and velocity profiles by comparing to the Na et al. [12] outcomes. It can be seen from these figures that, by ignoring

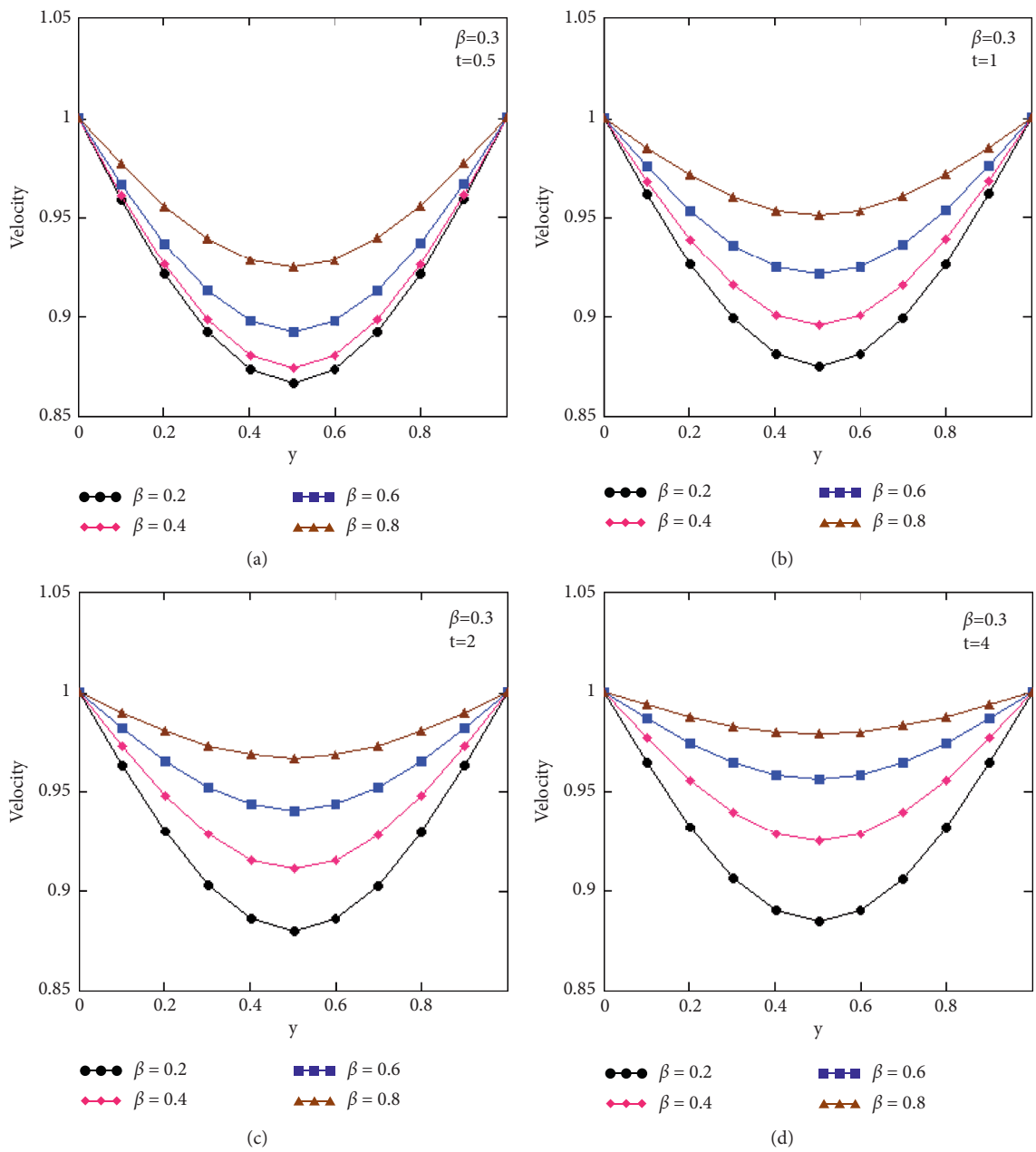

FIGURE 8: Profiles of dimensionless velocity versus y for variation of α at altered values of time t, $\mathrm{Gr} = 5, \lambda = 2, \lambda_r = 3, \mathrm{Pr} = 20,$ and $Q = 0.5$, and $f_1(t) = -H(t)$ and $f_2(t) = H(t) = g_1(t) = g_2(t)$.

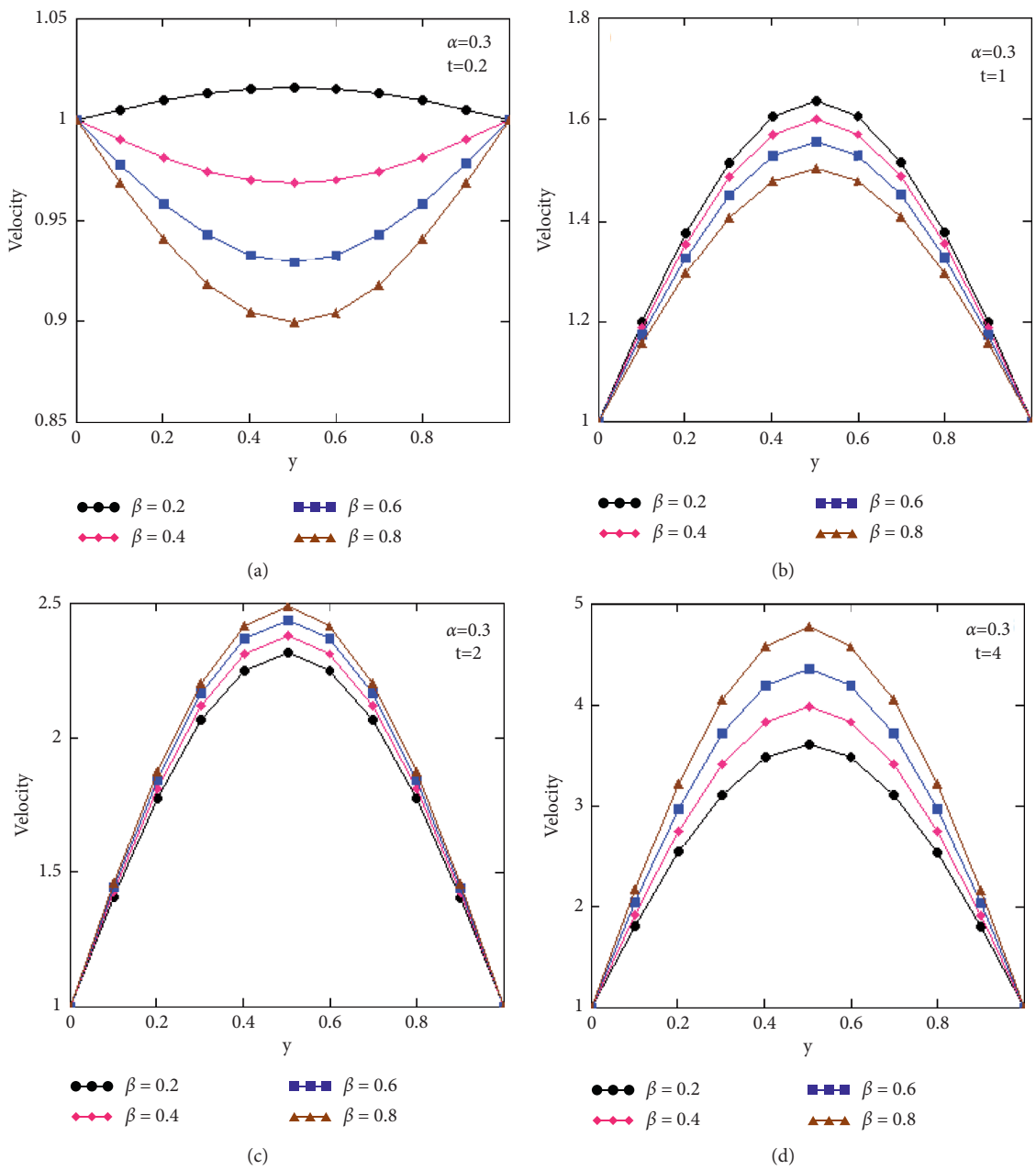

FIGURE 9: Profiles of dimensionless velocity versus y for variation of β at altered values of time t, $\mathrm{Gr} = 5, \lambda = 2, \lambda_r = 3, \mathrm{Pr} = 20, Q = 0.5$, and $f_1(t) = f_1(t) = H(t) = g_1(t) = g_2(t)$.

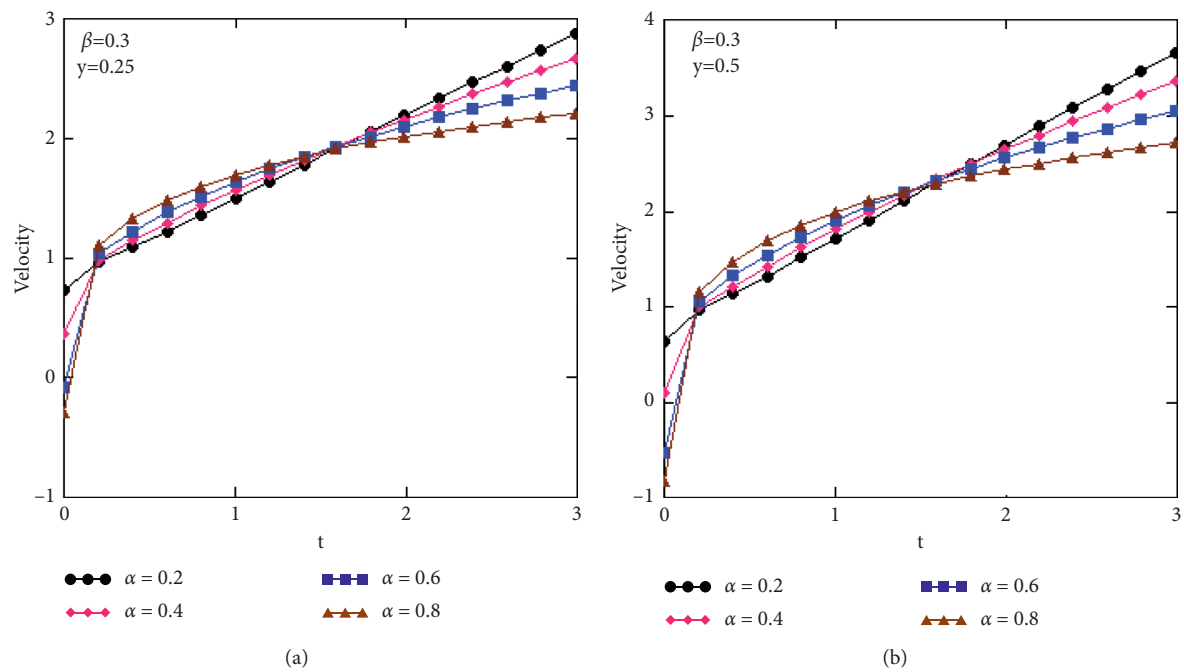

FIGURE 10: Profiles of dimensionless velocity versus y for variation of α at altered values of time t, $\mathrm{Gr} = 5, \lambda = 2, \lambda_r = 3, \mathrm{Pr} = 20, Q = 0.5$, and $f_1(t) = f_1(t) = H(t) = g_1(t) = g_2(t)$.

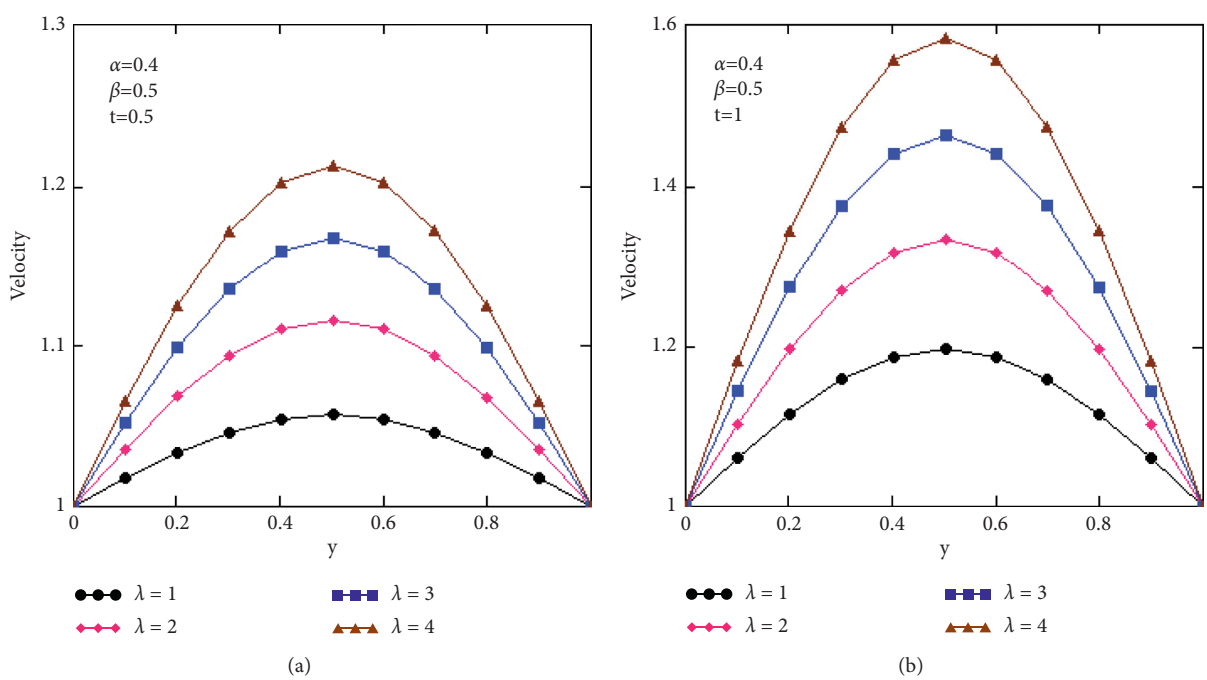

FIGURE 11: Profiles of dimensionless velocity versus y for variation of λ at altered values of time t, $\mathrm{Gr} = 5, \lambda_r = 3, \mathrm{Pr} = 20, Q = 0.5$, and $f_1(t) = f_1(t) = H(t) = g_1(t) = g_2(t)$.

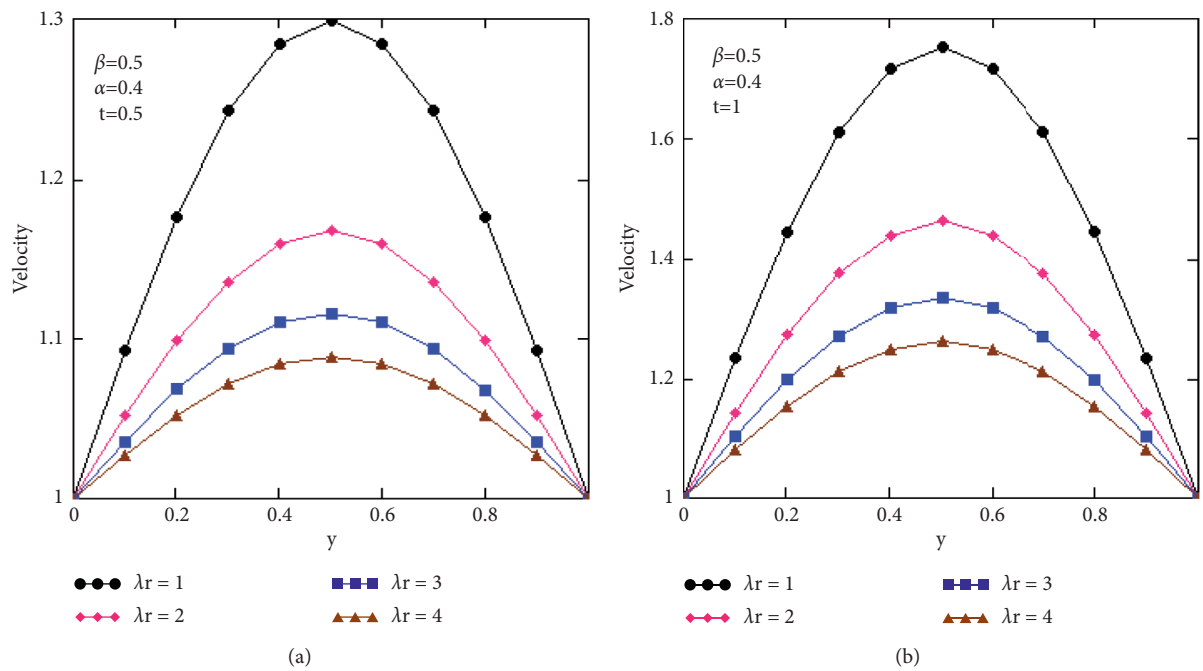

Figure 12: Profiles of dimensionless velocity versus y for variation of λ at altered values of time t, $\mathrm{Gr} = 5, \lambda = 2, \mathrm{Pr} = 20, Q = 0.5$, and $f_1(t) = f_1(t) = H(t) = g_1(t) = g_2(t)$.

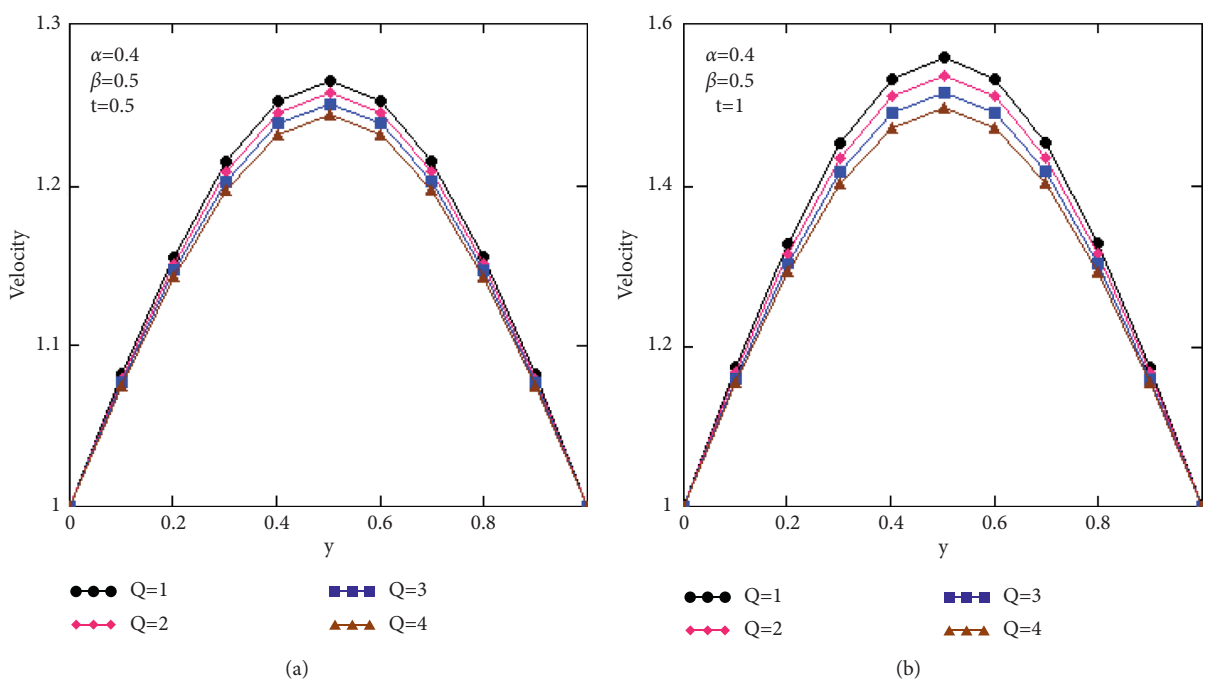

Figure 13: Profiles of dimensionless velocity versus y for variation of Q at altered values of time t, $\mathrm{Gr} = 5, \lambda = 2, \lambda_r = 3, \mathrm{Pr} = 20$, and $f_1(t) = f_1(t) = H(t) = g_1(t) = g_2(t)$.

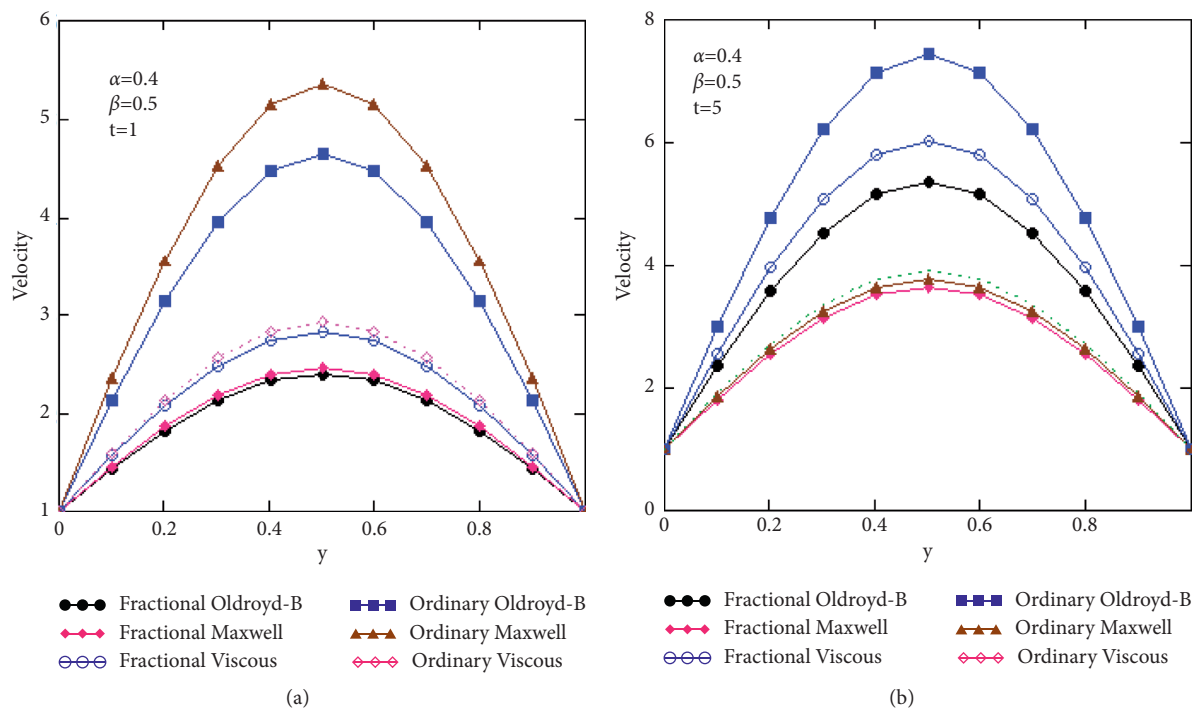

Figure 14: Comparisons between fractional Oldroy-B, ordinary Oldroyd-B, fractional Maxwell, ordinary Maxwell, fractional viscous, and ordinary viscous fluids at $\mathrm{Gr} = 5, \mathrm{Pr} = 20, Q = 0.5$, and $f_1(t) = f_1(t) = H(t) = g_1(t) = g_2(t)$.

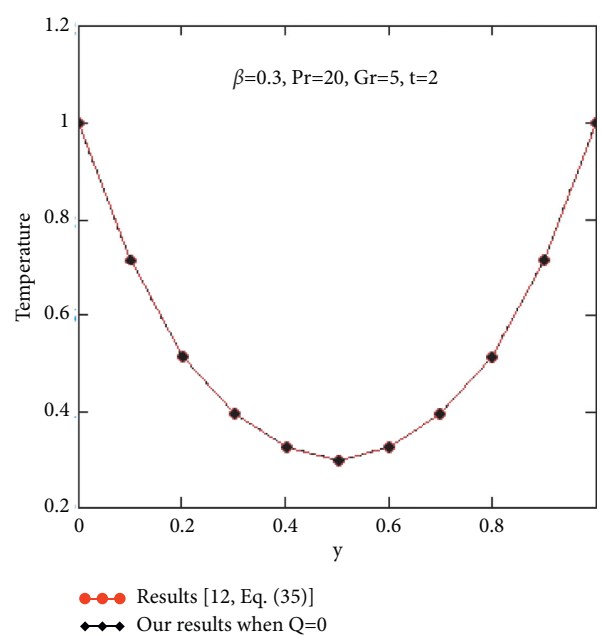

Figure 15: Temperature profiles of our models compared with the temperature profile of [12] $f_1(t) = f_1(t) = H(t) = g_1(t) = g_2(t)$.

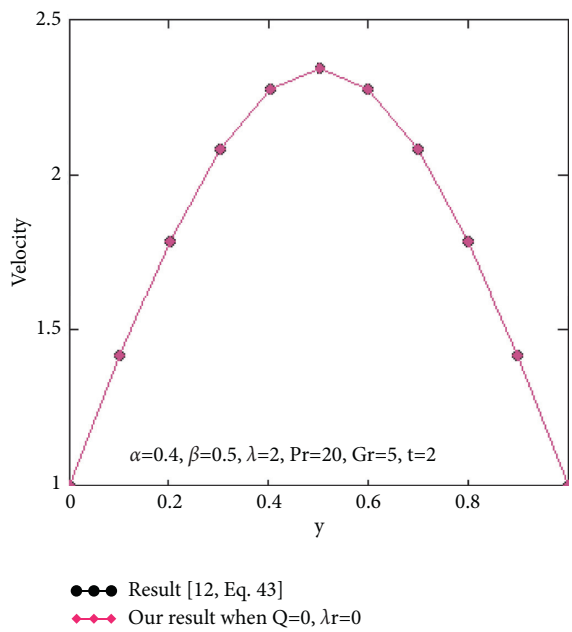

Figure 16: Velocity profiles of our models compared with the velocity profile of [12] $f_1(t) = f_1(t) = H(t) = g_1(t) = g_2(t)$.

the effects of Q and λ_r, our results are identical to those obtained by [12].

5. Conclusions

The aim of this work is to study the free-convection flow of an OBF between two vertical parallel plates in the presence of heat generation or absorption subject to generalized boundary conditions. The Caputo time-fractional derivative is introduced by means of the generalized constitutive shear stress and damped thermal flux by using generalized Fourier's law. Closed form solutions of fractional differential equations are found by employing the Laplace and sine-Fourier transforms which are suitable for the boundary conditions. The obtained solutions are expressed in the form of generalized G-functions of Lorenzo and Hartley. The effects of fractional and physical parameters are graphically presented in Figures 2–14. Some key findings of our work are

(i) For small values of time, temperature is decreasing by increasing the values of fractional parameter and vice versa

(ii) Velocity decreases by increasing the values of fractional parameters for small values of time and vice versa

(iii) Velocity is an increasing and decreasing functions of λ and λ_r for small and large values of time t, respectively

(iv) Velocity is a decreasing functions of absorption coefficient Q for small and large values of time t

(v) Velocity of Maxwell ordinary fluid is higher as compared to ordinary viscous and ordinary OBF for small times, while for large times velocity of fractional Maxwell fluid is higher as compared to fractional viscous and fractional OBF

(vi) Our obtained results for temperature and velocity profiles are identical to those obtained by [12]

Nomenclature

$u_1^{\mp}$: Velocity (m/s)
$T^{\mp}$: Temperature (K)
$t^{\mp}$: Time (sec)
g: Gravitational acceleration (m/s^2)
k: Thermal conductivity (W/mK)
c_p: Specific heat (J/kgK)
Q_0: Heat absorption coefficient (W/m^{3}K)
Gr: Thermal Grash of number
Pr: Prandtl number
$\lambda^{\mp}$: Relaxation time (sec)
$\lambda_r^{\mp}$: Retardation time (sec)
$\tau^{\mp}$: Shear stress (kg/ms^2)
μ: Dynamic viscosity (kg/ms)
ρ: Density (kg/m^3)
ν: Kinematic viscosity (m^2/s)
β_T: Thermal expansion coefficient (K^{-1}).

Data Availability

No data were used to support this study.

Conflicts of Interest

The authors declare that there are no conflicts of interest regarding the publication of this paper.

References

[1] J. G. Oldroyd, "On the formulation of rheological equations of state," *Proceedings of the Royal Society of London - Series A: Mathematical and Physical Sciences*, vol. 200, no. 1063, pp. 523–541, 1950.

[2] K. R. Rajagopal and R. K. Bhatnagar, "Exact solutions for some simple flows of an Oldroyd-B fluid," *Acta Mechanica*, vol. 113, no. 1-4, pp. 233–239, 1995.

[3] T. Hayat, A. M. Siddiqui, and S. Asghar, "Some simple flows of an Oldroyd-B fluid," *International Journal of Engineering Science*, vol. 39, no. 2, pp. 135–147, 2001.

[4] C. Fetecau and C. Fetecau, "The first problem of Stokes for an Oldroyd-B fluid," *International Journal of Non-linear Mechanics*, vol. 38, no. 10, pp. 1539–1544, 2003.

[5] C. Fetecau and C. Fetecau, "Unsteady flows of Oldroyd-B fluids in a channel of rectangular cross-section," *International Journal of Non-linear Mechanics*, vol. 40, no. 9, pp. 1214–1219, 2005.

[6] C. Fetecau, S. C. Prasad, and K. R. Rajagopal, "A note on the flow induced by a constantly accelerating plate in an Oldroyd-B fluid," *Applied Mathematical Modelling*, vol. 31, no. 4, pp. 647–654, 2007.

[7] H. Qi and M. Xu, "Stokes' first problem for a viscoelastic fluid with the generalized Oldroyd-B model," *Acta Mechanica Sinica*, vol. 23, no. 5, pp. 463–469, 2007.

[8] M. Khan, "The Rayleigh-Stokes problem for an edge in a viscoelastic fluid with a fractional derivative model," *Nonlinear Analysis: Real World Applications*, vol. 10, no. 5, pp. 3190–3195, 2009.

[9] S. Kakac, M. Aung, and R. Viskanta, *Natural Convection: Fundamentals and Applications*, Hemisphere Publishing Corporation, Washington, DC, USA, 1985.

[10] A. K. Singh, H. R. Gholami, and V. M. Soundalgekar, "Transient free convection flow between two vertical parallel plates," *Heat and Mass Transfer*, vol. 31, no. 5, pp. 329–331, 1996.

[11] M. Narahari, *Transient Free Convection Flow between Two Long Vertical Parallel Plates with Constant Temperature and Mass Diffusion*, Proceedings of the World Congress on Engineering, London, UK, 2008.

[12] W. Na, N. A. Shah, I. Tlili, and I. Siddique, "Maxwell fluid flow between vertical plates with damped shear and thermal flux: free convection," *Chinese Journal of Physics*, vol. 65, pp. 367–376, 2020.

[13] U. N. Zaib, N. A. Shah, I. Tlili, S. Ullah, and M. Nazar, "Natural convection flow of second grade fluid with thermal radiation and damped thermal flux between vertical channels," *Alexandria Engineering Journal*, vol. 58, no. 4, pp. 1119–1125, 2019.

[14] A. Hajizadeh, N. A. Shah, S. I. A. Shah, I. L. Animasaun, M. Rahimi-Gorji, and I. M. Alarifi, "Free convection flow of nanofluids between two vertical plates with damped thermal flux," *Journal of Molecular Liquids*, vol. 289, Article ID 110964, 2019.

[15] Z. Shao, N. A. Shah, I. Tlili, U. Afzal, and M. S. Khan, "Hydromagnetic free convection flow of viscous fluid between vertical parallel plates with damped thermal and mass fluxes," *Alexandria Engineering Journal*, vol. 58, no. 3, pp. 989–1000, 2019.

[16] G. S. Seth, N. Mahto, R. Tripathi, and A. Bhattacharyya, "Unsteady hydromagnetic flow formation with Hall effect due to time-dependent free stream in a rotating medium," *Journal of Nature Science and Sustainable Technology*, vol. 11, no. 3, pp. 197–211, 2018.

[17] G. S. Seth, A. Bhattacharyya, and R. Tripathi, "Effect of Hall current on MHD natural convection heat and mass transfer flow of rotating fluid past a vertical plate with ramped wall temperature," *Frontiers in Heat and Mass Transfer*, vol. 9, no. 21, 2017.

[18] N. Ahmed, D. Vieru, C. Fetecau, and N. A. Shah, "Convective flows of generalized time-nonlocal nanofluids through a vertical rectangular channel," *Physics of Fluids*, vol. 30, no. 5, Article ID 52002, 2018.

[19] B. K. Jha, K. A. Samaila, and A. O. Ajibade, "Natural convection flow of heat generating/absorbing fluid near a vertical plate with ramped temperature," *Journal of Encapsulation and Adsorption Sciences*, vol. 2, no. 4, pp. 61–68, 2012.

[20] B. K. Jha and B. Aina, "Impact of Heat generation/absorption on MHD mixed convection flow in a vertical tube having time periodic boundary condition: steady-periodic regime," *Heat Pipe Science and Technology, An International Journal*, vol. 7, no. 1-2, pp. 123–147, 2016.

[21] B. K. Jha, M. O. Oni, and B. Aina, "Steady fully developed mixed convection flow in a vertical micro-concentric-annulus with heat generating/absorbing fluid: an exact solution," *Ain Shams Engineering Journal*, vol. 9, no. 4, pp. 1289–1301, 2018.

[22] F. Saba, N. Ahmed, S. Hussain, U. Khan, S. Mohyud-Din, and M. Darus, "Thermal analysis of nanofluid flow over a curved stretching surface suspended by carbon nanotubes with internal heat generation," *Applied Sciences*, vol. 8, no. 3, p. 395, 2018.

[23] M. Aleem, M. I. ASjad, A. Shaheen, and I. Khan, "MHD Influence on different water based nanofluids (TiO2, Al2O3, CuO) in porous medium with chemical reaction and Newtonian heating," *Chaos, Solitons & Fractals*, vol. 130, Article ID 109437, 2020.

[24] N. A. Shah, A. H. Seikh, I. Tlili et al., "Natural convection of bio-nanofluid between two vertical parallel plates with damped shear and thermal flux," *Journal of Molecular Liquids*, vol. 296, no. 15, p. 111575, 2019.

[25] M. Ramzan, Z. Un Nisa, M. Ahmad, and M. Nazar, "Unsteady free convective magnetohydrohynamics flow of a casson fluid through a channel with double diffusion and ramp temperature and concentration," *Mathematical Methods and Applied Sciences*, vol. 2021, pp. 1–11, 2021.

[26] I. Siddique, N. A. Shah, and K. A. Abro, "Thermography of ferromagnetic Walter's-B fluid through varying thermal stratification," *South African Journal of Chemical Engineering*, vol. 36, pp. 118–126, 2021.

[27] I. Siddique, K. Sadiq, I. Khan, and K. S. Nisar, "Nanomaterials in convection flow of nanofluid in upright channel with gradients," *Journal of Materials Research and Technology*, vol. 11, pp. 1411–1423, 2021.

[28] X. Qiang, I. Siddique, K. Sadiq, and N. A. Shah, "Double diffusive MHD convective flows of a viscous fluid under influence of the inclined magnetic field, source/sink and chemical reaction," *Alexandria Engineering Journal*, vol. 6, no. 59, pp. 4171–4181, 2020.

[29] J. Hristov, "A transient flow of a non-Newtonian fluid modelled by a mixed time-space derivative: an improved integral-balance approach," in *Mathematical Methods in Engineering—Theory*, K. Tas, D. Baleanu, and J. A. T. Machado, Eds., Springer International Publishing, Berlin, Germany, 2018.

[30] I. Podlubny, *Fractional Differential Equations*, Academic, San Diego, CA, USA, 1999.

[31] S. Hyder Ali Muttaqi Shah, "Some accelerated flows of generalized Oldroyd-B fluid between two side walls perpendicular to the plate," *Nonlinear Analysis: Real World Applications*, vol. 10, no. 4, pp. 2146–2150, 2009.

[32] A. Akgül and I. Siddique, "Analysis of MHD Couette flow by fractal-fractional differential operators," *Chaos, Solitons & Fractals*, vol. 146, Article ID 110893, 2021.

[33] A. Akgül and I. Siddique, "Novel applications of the magnetohydrodynamics couple stress fluid flows between two plates with fractal-fractional derivatives," *Numerical Methods for Partial Differential Equations*, vol. 37, no. 3, pp. 2178–2189, 2021.

[34] C. Fetecau, C. Fetecau, M. Kamran, and D. Vieru, "Exact solutions for the flow of a generalized Oldroyd-B fluid induced by a constantly accelerating plate between two side walls perpendicular to the plate," *Journal of Non-newtonian Fluid Mechanics*, vol. 156, no. 3, pp. 189–201, 2009.

[35] I. Siddique and A. Akgül, "Analysis of blood liquor model via nonlocal and singular constant proportional Caputo hybrid differential operator," *Mathematical Methods in the Applied Sciences*, vol. 66, 2021.

[36] M. Khan, T. Hayat, and S. Asghar, "Exact solution for MHD flow of a generalized Oldroyd-B fluid with modified Darcy's law," *International Journal of Engineering Science*, vol. 44, no. 5-6, pp. 333–339, 2006.

[37] I. Siddique and Z. Sajid, "Exact solutions for the unsteady axial flow of non-Newtonian fluids through a circular cylinder," *Communications in Nonlinear Science and Numerical Simulation*, vol. 16, no. 1, pp. 226–238, 2011.

[38] Y. Liu, L. Zheng, and X. Zhang, "Unsteady MHD Couette flow of a generalized Oldroyd-B fluid with fractional derivative," *Computers & Mathematics with Applications*, vol. 61, no. 2, pp. 443–450, 2011.

[39] D. Bose and U. Basu, "Unsteady incompressible flow of a generalized Oldroyd-B fluid between two oscillating infinite parallel plates in presence of a transverse magnetic field," *Applied Mathematics*, vol. 6, no. 1, pp. 106–115, 2015.

[40] J. Zhao, L. Zheng, X. Zhang, F. Liu, and X. Chen, "Unsteady natural convection heat transfer past a vertical flat plate embedded in a porous medium saturated with fractional Oldroyd-B fluid," *Journal of Heat Transfer*, vol. 1, Article ID 12501, 2017.

[41] A. A. Zafar, M. B. Riaz, N. A. Shah, and M. A. Imran, "Influence of non-integer-order derivatives on unsteady unidirectional motions of an Oldroyd-B fluid with generalized boundary conditions," *The European Physical Journal Plus*, vol. 133, no. 3, p. 127, 2018.

[42] J. Zhang, F. Liu, and V. V. Anh, "Analytical and numerical solutions of a two-dimensional multi-term time-fractional Oldroyd-B model," *Numerical Methods for Partial Differential Equations*, vol. 35, no. 3, pp. 875–893, 2019.

[43] M. B. Riaz and S. T. Saeed, "Comprehensive analysis of integer-order, Caputo-Fabrizio (CF) and Atangana-Baleanu (ABC) fractional time derivative for MHD Oldroyd-B fluid with slip effect and time dependent boundary condition," *Discrete & Continuous Dynamical Systems - S*, vol. 14, no. 10, p. 3719, 2021.

[44] B. O. Wang, M. Javaid, M. Imran, M. Tahir, and C. Y. Jung, "Semi Analytical solutions for fractional Oldroyd-B fluid through rotating annulus," *IEEE Access*, vol. 7, 2019.

[45] M. Kamran, M. Imran, and M. Athar, "Exact solutions for the unsteady rotational flow of an Oldroyd-B fluid with fractional derivatives induced by a circular cylinder," *Meccanica*, vol. 48, no. 5, pp. 1215–1226, 2013.

[46] I. Siddique and S. M. Bukhari, "Analysis of the effect of generalized fractional Fourier's and Fick's laws on convective flows of non-Newtonian fluid subject to Newtonian heating," *The European Physical Journal Plus*, vol. 135, no. 1, p. 45, 2020.

[47] I. Siddique, I. Tlili, S. M. Bukhari, and Y. Mahsud, "Heat transfer analysis in convective flows of fractional second grade fluids with caputo–fabrizio and atangana–baleanu derivative subject to newtonion heating," *Mechanics of Time-Dependent Materials*, vol. 32, pp. 1–21, 2020.

[48] K. Sadiq, F. Jarad, I. Siddique, and B. Ali, "Soret and radiation effects on mixture of ethylene glycol-water (50%-50%) based Maxwell nanofluid flow in an upright channel," *Complexity*, vol. 2021, Article ID 5927070, 12 pages, 2021.

[49] C. F. Lorenzo and T. T. Hartley, "Generalized functions for fractional calculus," ResearchGate, Berlin, Germany, NASA/TP-1999-209424, 1999.

[50] J. Zhao, L. Zheng, X. Zhang, and F. Liu, "Unsteady convection heat and mass transfer of a fractional oldroyd-b fluid with chemical reaction and heat source/sink effect," *Heat Transfer Research*, vol. 49, no. 13, pp. 1231–1246, 2018.

[51] M. B. Riaz, A. Atangana, and T. Abdeljawad, "Local and nonlocal differential operators: a comparative study of heat and mass transfers in mhd oldroyd-b fluid with ramped wall temperature," *Fractals*, vol. 28, no. 8, Article ID 2040033, 2020.

[52] J. E. Caffyn and G. W. S. Blair, "Significance of power-law relations in rheology," *Nature*, vol. 155, pp. 171-172, 1955.

[53] Y. Povstenko, *Fractional Thermoelasticity, Solid Mechanics and its Applications*, Springer International Publishing, Cham, Switzerland, 2015.

[54] J. Hristov, "Derivatives with non-singular kernels. from the CaputoFabrizio definition and beyond: appraising analysis with emphasis on diffusion models," in *Frontiers in Fractional Calculus*, S. Bhalekar, Ed., pp. 269–340, Bentham Science Publishers, Sharjah, UAE, 1st edition, 2017.

[55] M. Caputo, "Linear models of dissipation whose Q is almost frequency independent--II," *Geophysical Journal International*, vol. 13, no. 5, pp. 529–539, 1967.

[56] T. M. Atanackovic´, S. Pilipovic´, B. Stankovic´, and D. Zorica, "Fractional calculus with applications in mechanics: vibrations and diffusion processes," in *Applied Mathematics*, N. Challamel, Ed., ISTE Ltd., John Wiley & Sons, Inc., London, UK, 2014.

Hindawi
Complexity
Volume 2021, Article ID 9260828, 30 pages
https://doi.org/10.1155/2021/9260828

Research Article

Fractional Hermite–Jensen–Mercer Integral Inequalities with respect to Another Function and Application

Saad Ihsan Butt,[1] **Muhammad Umar**,[2] **Khuram Ali Khan**,[3] **Artion Kashuri**,[4] **and Homan Emadifar**[5]

[1]*COMSATs University Islamabad, Lahore Campus, Lahore, Pakistan*
[2]*Afro-Asian Institute, Lahore, Pakistan*
[3]*Department of Mathematics, University of Sargdha, Sargodha 40100, Pakistan*
[4]*Department of Mathematics, Faculty of Technical Science, University "Ismail Qemali", 9400 Vlorë, Albania*
[5]*Department of Mathematics, Islamic Azad University, Hamedan Branch, Hamedan, Iran*

Correspondence should be addressed to Homan Emadifar; homan_emadi@yahoo.com

Received 18 June 2021; Accepted 18 August 2021; Published 6 September 2021

Academic Editor: Muhammad Imran Asjad

In this paper, authors prove new variants of Hermite–Jensen–Mercer type inequalities using ψ–Riemann–Liouville fractional integrals with respect to another function via convexity. We establish generalized identities involving ψ–Riemann–Liouville fractional integral pertaining first and twice differentiable convex function λ, and these will be used to derive novel estimates for some fractional Hermite–Jensen–Mercer type inequalities. Some known results are recaptured from our results as special cases. Finally, an application from our results using the modified Bessel function of the first kind is established as well.

1. Introduction and Preliminaries

The theory of fractional integrals and derivatives has occurred in many fields and directions such as partial differential equations, difference equations, probability, and stochastic processes (see [1–6]). Behind it, the theory of convex functions with integral inequalities is also useful.

Definition 1. A function $\lambda: J \subset \mathfrak{R} \longrightarrow \mathfrak{R}$ is said to be convex on J if

$$\lambda((1-\zeta)y_1 + \zeta y_2) \leq (1-\zeta)\lambda(y_1) + \zeta\lambda(y_2), \tag{1}$$

holds for every $y_1, y_2 \in J$ and $\zeta \in [0,1]$.

One of the best-known inequalities for convex functions is the following Hermite–Hadamard's inequality: if $\lambda: J \subseteq \mathfrak{R} \longrightarrow \mathfrak{R}$ is a convex function in J, where $y_1, y_2 \in J$ and $y_1 < y_2$, then

$$\lambda\left(\frac{y_1+y_2}{2}\right) \leq \frac{1}{y_2-y_1}\int_{y_1}^{y_2}\lambda(\zeta)\mathrm{d}\zeta \leq \frac{\lambda(y_1)+\lambda(y_2)}{2} \quad (\mathrm{H}-\mathrm{H}). \tag{2}$$

It is also known as classical (H – H) inequality. A number of mathematicians in the field of applied and pure mathematics have dedicated their efforts to extend, generalize, counterpart, and refine Hermite–Hadamard's inequality (H – H) for different classes of convex functions. For more recent results obtained on inequality (H – H), we refer the reader to references [7–10].

Let $\sigma_i \in [0,1]$ be nonnegative weights such that $\sum_{i=1}^{n}\sigma_i = 1$. The Jensen inequality states that, if λ is convex function on $[y_1, y_2]$, then

$$\lambda\left(\sum_{i=1}^{n}\sigma_i\ell_i\right) \leq \sum_{i=1}^{n}\sigma_i\lambda(\ell_i), \tag{3}$$

holds for all $\ell_i \in [y_1, y_2]$ and all $i = 1, 2, \ldots, n$, see [11].

In the literature, Jensen's inequality and Hermite–Hadamard's inequality are highly familiar results pertaining convex functions. One of the well-known and most significant inequalities in mathematical analysis is Jensen's and related inequalities. Jensen's inequality for differentiable convex functions plays a significant role in the field of inequalities as several other inequalities can be seen as special cases of it. It is used in order to make claims regarding the function while just a little is known or is needed to be known about the distribution. Furthermore, this inequality has been used in various areas of sciences and technology to solve several problems, such as engineering, mathematical statistics, financial economics, and computer science. Some recent results can be seen in [12–14].

Jensen's inequality has a following variant gave by Mercer (see [15]).

Theorem 1. *Let λ be a convex function on $[y_1, y_2]$, then*

$$\lambda\left(y_1 + y_2 - \sum_{i=1}^{n} \sigma_i \ell_i\right) \leq \lambda(y_1) + \lambda(y_2) - \sum_{i=1}^{n} \sigma_i \lambda(\ell_i), \quad (4)$$

holds for all $\ell_i \in [y_1, y_2]$ and all $\sigma_i \in [0, 1]$, $(i = 1, 2, \ldots, n)$.

Jensen–Mercer's type inequality is a topic of supreme interest as it gives more information with explicit boundary conditions. It is quite effective for applications in operator analysis in higher dimensions [16–18]. Moradi et al. established some new improvements and generalization of Jensen–Mercer's type inequalities [19]. Recently, in [20], Adil et al. gave applications of Jensen–Mercer's inequality in information theory. They computed new estimates for Csiszár and related divergences. Taking into consideration the wonderful packages of Jensen's and associated inequalities in diverse fields of mathematics and engineering sciences, their generalizations and upgrades were a subject of an excellent hobby for the researchers in the last few years as obvious from a massive variety of investigation on it (see [21–24]).

In [25], Vanterler da Costa Sousa and Capelas de Oliveira introduced ψ–fractional integrals and ψ–Hilfer fractional derivative with respect to another function. They also studied Gronwall inequalities using ψ–Hilfer operator (see [26]).

Definition 2 (see [23]). Suppose that (y_1, y_2) $(-\infty \leq y_1 < y_2 \leq \infty)$ and $\alpha > 0$. Also let ψ be an increasing and positive monotone function on $(y_1, y_2]$, having a continuous derivative ψ' on (y_1, y_2). Then, the left-sided and right-sided ψ–Riemann–Liouville fractional integrals of a function λ with respect to another function ψ on $[y_1, y_2]$ are defined as follows:

$$\begin{aligned}
\left(I_{y_1+}^{\alpha:\psi}\right)\lambda(\ell) &= \frac{1}{\Gamma(\alpha)} \int_{y_1}^{\ell} \psi'(\zeta)(\psi(\ell) - \psi(\zeta))^{\alpha-1} \lambda(\zeta) \mathrm{d}\zeta, \quad y_1 < \ell, \\
\left(I_{y_2-}^{\alpha:\psi}\right)\lambda(\ell) &= \frac{1}{\Gamma(\alpha)} \int_{\ell}^{y_2} \psi'(\zeta)(\psi(\zeta) - \psi(\ell))^{\alpha-1} \lambda(\zeta) \mathrm{d}\zeta, \quad \ell < y_2,
\end{aligned} \quad (5)$$

respectively.

If we choose $\psi(\zeta) = \zeta$ and $\psi(\zeta) = \ln\zeta$, then we get, respectively, Riemann–Liouville and Hadamard fractional integrals.

Motivated by previous results, we will establish several new Hermite–Hadamard–Mercer type inequalities involving ψ–Riemann–Liouville fractional integrals (i.e., Riemann–Liouville fractional integral of any function with respect to another function). Moreover, our results recover several known results. Finally, an application using the modified Bessel function of the first kind will be established as well.

2. Hermite–Jensen–Mercer Type Inequalities

Throughout the paper, the following assumption will be used in the sequel.

(A_1): Let $0 \leq y_1 < y_2$, λ: $[y_1, y_2] \longrightarrow \mathfrak{R}$ be a positive function and $\lambda \in L_1[y_1, y_2]$. Also suppose, $\psi(\cdot)$ is an increasing and positive monotone function on $(y_1, y_2]$, having a continuous derivative ψ' on (y_1, y_2) and $\alpha > 0$.

Theorem 2. *If (A_1) is satisfied and λ is a convex function on $[y_1, y_2]$, then*

$$\begin{aligned}
\lambda\left(y_1 + y_2 - \frac{\ell_1}{+}\ell_2 2\right) &\leq [\lambda(y_1) + \lambda(y_2)] - \frac{\Gamma(\alpha+1)}{2(\ell_2 - \ell_1)^{\alpha}} \\
&\quad \times \left\{\left(I_{\psi^{-1}(\ell_1)^+}^{\alpha:\psi}\right)(\lambda \circ \psi)\left(\psi^{-1}(\ell_2)\right) + \left(I_{\psi^{-1}(\ell_2)^-}^{\alpha:\psi}\right)(\lambda \circ \psi)\left(\psi^{-1}(\ell_1)\right)\right\} \\
&\leq [\lambda(y_1) + \lambda(y_2)] - \lambda\left(\frac{\ell_1 + \ell_2}{2}\right),
\end{aligned} \quad (6)$$

$$\lambda\left(y_1+y_2-\frac{\ell_1+\ell_2}{2}\right)\le\frac{2^{\alpha-1}\Gamma(\alpha+1)}{(\ell_2-\ell_1)^{\alpha}}\times\left\{\left(I^{\alpha:\psi}_{\psi^{-1}(y_1+y_2-\ell_2)^+}\right)(\lambda\circ\psi)\left(\psi^{-1}(y_1+y_2-\ell_1)\right)+\left(I^{\alpha:\psi}_{\psi^{-1}(y_1+y_2-\ell_1)^-}\right)(\lambda\circ\psi)\left(\psi^{-1}(y_1+y_2-\ell_2)\right)\right\}\le\lambda(y_1)+\lambda(y_2)-\left(\frac{\lambda(\ell_1)+\lambda(\ell_2)}{2}\right), \tag{7}$$

for all $\ell_1,\ell_2\in[y_1,y_2]$, where $\Gamma(\cdot)$ is the gamma function.

Proof. Using Jensen–Mercer's inequality, we have

$$\lambda\left(y_1+y_2-\frac{x+z}{2}\right)\le\lambda(y_1)+\lambda(y_2)-\frac{\lambda(x)+\lambda(z)}{2}, \tag{8}$$

for all $x,z\in[y_1,y_2]$.

Now, by change of variables $x=\zeta\ell_1+(1-\zeta)\ell_2$ and $z=(1-\zeta)\ell_1+\zeta\ell_2$, for all $\ell_1,\ell_2\in[y_1,y_2]$ and $\zeta\in[0,1]$ in (8), we get

$$\lambda\left(y_1+y_2-\frac{\ell_1+\ell_2}{2}\right)\le\lambda(y_1)+\lambda(y_2)-\frac{\lambda(\zeta\ell_1+(1-\zeta)\ell_2)+\lambda((1-\zeta)\ell_1+\zeta\ell_2)}{2}. \tag{9}$$

Multiplying the above inequality by $\zeta^{\alpha-1}$ on both sides and integrating with respect to ζ on $[0,1]$, we obtain

$$\frac{1}{\alpha}\lambda\left(y_1+y_2-\frac{\ell_1+\ell_2}{2}\right)\le\frac{1}{\alpha}\{\lambda(y_1)+\lambda(y_2)\}-\frac{1}{2}\left\{\int_0^1\zeta^{\alpha-1}(\lambda(\zeta\ell_1+(1-\zeta)\ell_2)+\lambda((1-\zeta)\ell_1+\zeta\ell_2))\mathrm{d}\zeta\right\}, \tag{10}$$

where

$$\frac{\alpha}{2}\left\{\int_0^1\zeta^{\alpha-1}(\lambda(\zeta\ell_1+(1-\zeta)y_2)+\lambda((1-\zeta)y_1+\zeta y_2))\mathrm{d}\zeta\right\}=\frac{\alpha}{2}\int_0^1\zeta^{\alpha-1}\lambda(\zeta\ell_1+(1-\zeta)\ell_2)\mathrm{d}\zeta+\frac{\alpha}{2}\int_0^1\zeta^{\alpha-1}\lambda((1-\zeta)\ell_1+\zeta\ell_2)\mathrm{d}\zeta. \tag{11}$$

Now, let $\zeta=(\psi(\gamma)-\ell_1)/(\ell_2-\ell_1)$, then $\mathrm{d}\zeta=(\psi'(\gamma)\mathrm{d}\gamma)/(\ell_2-\ell_1)$. Using the above equality, we obtain

$$
\begin{aligned}
&= \frac{\alpha}{2}\int_{\psi^{-1}(\ell_1)}^{\psi^{-1}(\ell_2)}\left(\frac{\ell_2-\psi(\gamma)}{\ell_2-\ell_1}\right)^{\alpha-1}\lambda(\psi(\gamma))\frac{\psi'(\gamma)}{\ell_2-\ell_1}\mathrm{d}\gamma \\
&\quad+\frac{\alpha}{2}\int_{\psi^{-1}(\ell_1)}^{\Psi^{-1}(\ell_2)}\left(\frac{\psi(\gamma)-\ell_1}{\ell_2-\ell_1}\right)^{\alpha-1}\lambda(\psi(\gamma))\frac{\psi'(\gamma)}{\ell_2-\ell_1}\mathrm{d}\gamma \\
&= \frac{\Gamma(\alpha+1)}{2(\ell_2-\ell_1)^{\alpha}}\frac{1}{\Gamma(\alpha)}\left\{\int_{\psi^{-1}(\ell_1)}^{\psi^{-1}(\ell_2)}\psi'(\gamma)(\ell_2-\psi(\gamma))^{\alpha-1}(\lambda\circ\psi)(\gamma)\mathrm{d}\gamma\right\} \\
&\quad+\frac{\Gamma(\alpha+1)}{2(\ell_2-\ell_1)^{\alpha}}\frac{1}{\Gamma(\alpha)}\left\{\int_{\psi^{-1}(\ell_1)}^{\psi^{-1}(\ell_2)}\psi'(\gamma)(\psi(\gamma)-\ell_1)^{\alpha-1}(\lambda\circ\psi)(\gamma)\mathrm{d}\gamma\right\}.
\end{aligned}
\tag{12}
$$

So, the final form will be of this type as follows:

$$
\begin{aligned}
&= \frac{\Gamma(\alpha+1)}{2(\ell_2-\ell_1)^{\alpha}} \\
&\quad\times\left\{\left(I^{\alpha:\psi}_{\psi^{-1}(\ell_1)^+}\right)(\lambda\circ\psi)\left(\psi^{-1}(\ell_2)\right)+\left(I^{\alpha:\psi}_{\psi^{-1}(\ell_2)^-}\right)(\lambda\circ\psi)\left(\psi^{-1}(\ell_1)\right)\right\},
\end{aligned}
\tag{13}
$$

and so the first inequality of (6) is proved.

Regarding the second inequality of (6), since λ is convex function, then for $\zeta\in[0,1]$, we have

$$
\begin{aligned}
\lambda\left(\frac{\ell_1+\ell_2}{2}\right) &= \lambda\left(\frac{\zeta\ell_1+(1-\zeta)\ell_2+(1-\zeta)\ell_1+\zeta\ell_2}{2}\right) \\
&\le \frac{\lambda(\zeta\ell_1+(1-\zeta)\ell_2)+\lambda((1-\zeta)\ell_1+\zeta\ell_2)}{2}.
\end{aligned}
\tag{14}
$$

Multiplying the above inequality by $\zeta^{\alpha-1}$ on both sides and integrating with respect to ζ on $[0,1]$, we get

$$
\frac{1}{\alpha}\lambda\left(\frac{\ell_1+\ell_2}{2}\right)\le\frac{1}{2}\left\{\int_0^1\zeta^{\alpha-1}\left(\lambda(\zeta\ell_1+(1-\zeta)\ell_2)+\lambda((1-\zeta)\ell_1+\zeta\ell_2)\right)\right\}.
\tag{15}
$$

Let $\psi(\gamma)=\zeta\ell_1+(1-\zeta)\ell_2$ and $\psi(\beta)=(1-\zeta)\ell_1+\zeta\ell_2$. Then, we have

$$
\lambda\left(\frac{\ell_1+\ell_2}{2}\right)\le\frac{\Gamma(\alpha+1)}{2(\ell_2-\ell_1)^{\alpha}}\left\{\left(I^{\alpha:\psi}_{\psi^{-1}(\ell_1)^+}\right)(\lambda\circ\psi)\left(\psi^{-1}(\ell_2)\right)+\left(I^{\alpha:\psi}_{\psi^{-1}(\ell_2)^-}\right)(\lambda\circ\psi)\left(\psi^{-1}(\ell_1)\right)\right\}.
\tag{16}
$$

Multiplying by (-1), we will get

$$
-\frac{\Gamma(\alpha+1)}{2(\ell_2-\ell_1)^{\alpha}}\left\{\left(I^{\alpha:\psi}_{\psi^{-1}(\ell_1)^+}\right)(\lambda\circ\psi)\left(\psi^{-1}(\ell_2)\right)+\left(I^{\alpha:\psi}_{\psi^{-1}(\ell_2)^-}\right)(\lambda\circ\psi)\left(\psi^{-1}(\ell_1)\right)\right\}\le-\lambda\left(\frac{\ell_1+\ell_2}{2}\right).
\tag{17}
$$

Adding $\lambda(y_1)+\lambda(y_2)$ both sides in (17), we obtain our second inequality of (6).

To prove the first inequality of (7) by using the convexity of λ, we have

$$2\lambda\left(y_1+y_2-\frac{x+z}{2}\right)\leq\lambda\left(y_1+y_2-x\right)+\lambda\left(y_1+y_2-z\right), \tag{18}$$

for all $x, z \in [y_1, y_2]$. By change of variables $x = \zeta\ell_1 + (1-\zeta)\ell_2$ and $z = (1-\zeta)\ell_1 + \zeta\ell_2$, $\zeta \in [0,1]$, we get

$$2\lambda\left(y_1+y_2-\frac{\ell_1+\ell_2}{2}\right)\leq\lambda\left(y_1+y_2-\left(\zeta\ell_1+(1-\zeta)\ell_2\right)\right)+\lambda\left(y_1+y_2-\left((1-\zeta)\ell_1+\zeta\ell_2\right)\right). \tag{19}$$

Multiplying the above inequality by $\zeta^{\alpha-1}$ on both sides and integrating with respect to ζ over $[0,1]$, we get

$$\frac{2}{\alpha}\lambda\left(y_1+y_2-\frac{\ell_1+\ell_2}{2}\right)\leq\int_0^1\zeta^{\alpha-1}\left(\lambda\left(y_1+y_2-\left(\zeta\ell_1+(1-\zeta)\ell_2\right)\right)+\lambda\left(y_1+y_2-\left((1-\zeta)\ell_1+\zeta\ell_2\right)\right)\right)\mathrm{d}\zeta. \tag{20}$$

Hence, by change of variables, we obtain

$$\lambda\left(y_1+y_2-\frac{\ell_1+\ell_2}{2}\right)\leq\frac{2^{\alpha-1}\Gamma(\alpha+1)}{(\ell_2-\ell_1)^{\alpha}}\times\left\{\left(I^{\alpha:\psi}_{\psi^{-1}(y_1+y_2-\ell_2)^+}\right)(\lambda\circ\Psi)\left(\psi^{-1}(y_1+y_2-\ell_1)\right)+\left(I^{\alpha:\psi}_{\psi^{-1}(y_1+y_2-\ell_1)^-}\right)(\lambda\circ\psi)\left(\psi^{-1}(y_1+y_2-\ell_2)\right)\right\}, \tag{21}$$

and so the first inequality of (7) is proved.

About the second inequality of (7), since λ is convex function, then for $\zeta \in [0,1]$, we obtain

$$\lambda\left(y_1+y_2-\left(\zeta\ell_1+(1-\zeta)\ell_2\right)\right)\leq\lambda\left(y_1\right)+\lambda\left(y_2\right)-\left[\zeta\lambda\left(\ell_1\right)+(1-\zeta)\lambda\left(\ell_2\right)\right], \tag{22}$$

$$\lambda\left(y_1+y_2-\left((1-\zeta)\ell_1+\zeta\ell_2\right)\right)\leq\lambda\left(y_1\right)+\lambda\left(y_2\right)-\left[(1-\zeta)\lambda\left(\ell_1\right)+\zeta\lambda\left(\ell_2\right)\right]. \tag{23}$$

By adding inequalities (22) and (23), we have

$$\lambda\left(y_1+y_2-\left(\zeta\ell_1+(1-\zeta)\ell_2\right)\right)+\lambda\left(y_1+y_2-\left((1-\zeta)\ell_1+\zeta\ell_2\right)\right)\leq 2\left(\lambda\left(y_1\right)+\lambda\left(y_2\right)\right)-\left(\lambda\left(\ell_1\right)+\lambda\left(\ell_2\right)\right). \tag{24}$$

Multiplying the above inequality by $\zeta^{\alpha-1}$ on both sides and integrating with respect to ζ on $[0,1]$, we get

$$\frac{2^{\alpha}\Gamma(\alpha)}{(\ell_2-\ell_1)^{\alpha}}\left\{\left(I^{\alpha:\psi}_{\psi^{-1}(y_1+y_2-\ell_2)^+}\right)(\lambda\circ\psi)\left(\psi^{-1}(y_1+y_2-\ell_1)\right)+\left(I^{\alpha:\psi}_{\psi^{-1}(y_1+y_2-\ell_1)^-}\right)(\lambda\circ\psi)\left(\psi^{-1}(y_1+y_2-\ell_2)\right)\right\}\leq\left\{2\left(\lambda\left(y_1\right)+\lambda\left(y_2\right)\right)-\left(\lambda\left(\ell_1\right)+\lambda\left(\ell_2\right)\right)\right\}\cdot\frac{1}{\alpha}. \tag{25}$$

Multiplying by $\alpha/2$, we will get

$$\frac{2^{\alpha-1}\Gamma(\alpha+1)}{(\ell_2-\ell_1)^{\alpha}}\left\{\left(I^{\alpha:\psi}_{\psi^{-1}(y_1+y_2-\ell_2)^+}\right)(\lambda\circ\psi)\left(\psi^{-1}(y_1+y_2-\ell_1)\right)+\left(I^{\alpha:\psi}_{\psi^{-1}(y_1+y_2-\ell_1)^-}\right)(\lambda\circ\psi)\left(\psi^{-1}(y_1+y_2-\ell_2)\right)\right\}$$
$$\leq(\lambda(y_1)+\lambda(y_2))-\frac{\lambda(\ell_1)+\lambda(\ell_2)}{2}. \tag{26}$$

From inequalities (21) and (26), we get the desired double inequality (7). □

Remark 1. Taking $\psi(\gamma)=\gamma$ in Theorem 2, we will get Theorem 2 proved in [27].

Remark 2. Taking $\psi(\gamma)=\gamma$ and $\alpha=1$ in Theorem 2, we will obtain Theorem 2 proved by Kian and Moslehian in [28].

Theorem 3. *If (A_1) is satisfied and λ is a convex function on $[y_1,y_2]$, then*

$$\lambda\left(y_1+y_2-\frac{\ell_1+\ell_2}{2}\right)\leq\frac{2^{\alpha-1}\Gamma(\alpha+1)}{(\ell_2-\ell_1)^{\alpha}}$$
$$\times\left\{\left(I^{\alpha:\psi}_{\psi^{-1}(y_1+y_2-((\ell_1+\ell_2)/2))^+}\right)(\lambda\circ\psi)\left(\psi^{-1}(y_1+y_2-\ell_1)\right)\right.$$
$$\left.+\left(I^{\alpha:\psi}_{\psi^{-1}(y_1+y_2-((\ell_1+\ell_2)/2))^-}\right)(\lambda\circ\psi)\left(\psi^{-1}(y_1+y_2-\ell_2)\right)\right\}$$
$$\leq\lambda(y_1)+\lambda(y_2)-\left(\frac{\lambda(\ell_1)+\lambda(\ell_2)}{2}\right), \tag{27}$$

for all $\ell_1,\ell_2\in[y_1,y_2]$.

Proof. About the first inequality (27) by using the convexity of λ, we have

$$2\lambda\left(y_1+y_2-\frac{x+z}{2}\right)\leq\lambda(y_1+y_2-x)+\lambda(y_1+y_2-z), \tag{28}$$

for all $x,z\in[y_1,y_2]$. By change of variables $x=(\zeta/2)\ell_1+((2-\zeta)/2)\ell_2$ and $z=((2-\zeta)/2)\ell_1+(\zeta/2)\ell_2$, $\zeta\in[0,1]$, we get

$$2\lambda\left(y_1+y_2-\frac{\ell_1+\ell_2}{2}\right)\leq\lambda\left(y_1+y_2-\left(\frac{\zeta}{2}\ell_1+\frac{2-\zeta}{2}\ell_2\right)\right)$$
$$+\lambda\left(y_1+y_2-\left(\frac{2-\zeta}{2}\ell_1+\frac{\zeta}{2}\ell_2\right)\right). \tag{29}$$

Multiplying the above inequality by $\zeta^{\alpha-1}$ on both sides and integrating with respect to ζ over $[0,1]$, we have

$$\frac{2}{\alpha}\lambda\left(y_1+y_2-\frac{\ell_1+\ell_2}{2}\right)$$
$$\leq\int_0^1\zeta^{\alpha-1}\left(\lambda\left(y_1+y_2-\left(\frac{\zeta}{2}\ell_1+\frac{2-\zeta}{2}\ell_2\right)\right)+\lambda\left(y_1+y_2-\left(\frac{2-\zeta}{2}\ell_1+\frac{\zeta}{2}\ell_2\right)\right)\right)d\zeta. \tag{30}$$

Hence, by change of variables, we obtain

$$\lambda\left(y_1+y_2-\frac{\ell_1+\ell_2}{2}\right)\leq\frac{2^{\alpha-1}\Gamma(\alpha+1)}{(\ell_2-\ell_1)^{\alpha}}$$
$$\times\left\{\left(I^{\alpha:\psi}_{\psi^{-1}(y_1+y_2-((\ell_1+\ell_2)/2))^+}\right)(\lambda\circ\Psi)\left(\psi^{-1}(y_1+y_2-\ell_1)\right)+\left(I^{\alpha:\psi}_{\psi^{-1}(y_1+y_2-((\ell_1+\ell_2)/2))^-}\right)(\lambda\circ\psi)\left(\psi^{-1}(y_1+y_2-\ell_2)\right)\right\}, \tag{31}$$

which proved the first inequality of (27).

Regarding the second inequality of (27), since λ is convex function, then for $\zeta\in[0,1]$, we have

$$\lambda\left(y_1+y_2-\left(\frac{\zeta}{2}\ell_1+\frac{2-\zeta}{2}\ell_2\right)\right)\leq\lambda(y_1)+\lambda(y_2)-\left[\frac{\zeta}{2}\lambda(\ell_1)+\frac{2-\zeta}{2}\lambda(\ell_2)\right], \tag{32}$$

$$\lambda\left(y_1+y_2-\left(\frac{2-\zeta}{2}\ell_1+\frac{\zeta}{2}\ell_2\right)\right)\leq\lambda(y_1)+\lambda(y_2)-\left[\frac{2-\zeta}{2}\lambda(\ell_1)+\frac{\zeta}{2}\lambda(\ell_2)\right]. \tag{33}$$

By adding inequalities (32) and (33), we get

$$\begin{aligned}&\lambda\left(y_1+y_2-\left(\frac{\zeta}{2}\ell_1+\frac{2-\zeta}{2}\ell_2\right)\right)+\lambda\left(y_1+y_2-\left(\frac{2-\zeta}{2}\ell_1+\frac{\zeta}{2}\ell_2\right)\right)\\&\leq 2(\lambda(y_1)+\lambda(y_2))-(\lambda(\ell_1)+\lambda(\ell_2)).\end{aligned} \tag{34}$$

Multiplying the above inequality by $\zeta^{\alpha-1}$ on both sides and integrating with respect to ζ on $[0,1]$, we obtain

$$\begin{aligned}&\int_0^1\zeta^{\alpha-1}\left(\lambda\left(y_1+y_2-\left(\frac{\zeta}{2}\ell_1+\frac{2-\zeta}{2}\ell_2\right)\right)+\lambda\left(y_1+y_2-\left(\frac{2-\zeta}{2}\ell_1+\frac{\zeta}{2}\ell_2\right)\right)\right)\mathrm{d}\zeta\\&\leq(2(\lambda(y_1)+\lambda(y_2))-(\lambda(\ell_1)+\lambda(\ell_2)))\int_0^1\zeta^{\alpha-1}\mathrm{d}\zeta.\end{aligned} \tag{35}$$

Then, we have the following inequality:

$$\begin{aligned}&\frac{2^\alpha\Gamma(\alpha)}{(\ell_2-\ell_1)^\alpha}\left\{\left(I^{\alpha:\psi}_{\psi^{-1}(y_1+y_2-((\ell_1+\ell_2)/2))^+}\right)(\lambda\circ\psi)\left(\psi^{-1}(y_1+y_2-\ell_1)\right)+\left(I^{\alpha:\psi}_{\psi^{-1}(y_1+y_2-((\ell_1+\ell_2)/2))^-}\right)(\lambda\circ\psi)\left(\psi^{-1}(y_1+y_2-\ell_2)\right)\right\}\\&\leq(2(\lambda(y_1)+\lambda(y_2))-(\lambda(\ell_1)+\lambda(\ell_2)))\cdot\frac{1}{\alpha}.\end{aligned} \tag{36}$$

Multiplying by $\alpha/2$, we will get

$$\begin{aligned}&\frac{2^{\alpha-1}\Gamma(\alpha+1)}{(\ell_2-\ell_1)^\alpha}\left\{\left(I^{\alpha:\psi}_{\psi^{-1}(y_1+y_2-((\ell_1+\ell_2)/2))^+}\right)(\lambda\circ\psi)\left(\psi^{-1}(y_1+y_2-\ell_1)\right)+\left(I^{\alpha:\psi}_{\psi^{-1}(y_1+y_2-((\ell_1+\ell_2)/2))^-}\right)(\lambda\circ\psi)\left(\psi^{-1}(y_1+y_2-\ell_2)\right)\right\}\\&\leq(\lambda(y_1)+\lambda(y_2))-\frac{\lambda(\ell_1)+\lambda(\ell_2)}{2}.\end{aligned} \tag{37}$$

From inequalities (31) and (37), we get the desired double inequality (27). □

Remark 3. Taking $\psi(\gamma)=\gamma$ in Theorem 3, we will get Theorem 3 proved in [27].

Remark 4. Taking $\psi(\gamma)=\gamma$ and $\alpha=1$ in Theorem 3, we will obtain Theorem 2.1 proved by Kian and Moslehian in [28].

Theorem 4. *If (A_1) is satisfied and λ is a convex function on $[y_1,y_2]$, then*

$$\lambda\left(y_1+y_2-\frac{\ell_1+\ell_2}{2}\right)\leq\frac{2^{\alpha-1}\Gamma(\alpha+1)}{(\ell_2-\ell_1)^{\alpha}}$$
$$\times\left\{\left(I^{\alpha:\psi}_{\psi^{-1}(y_1+y_2-\ell_2)^+}\right)(\lambda\circ\psi)\left(\psi^{-1}\left(y_1+y_2-\frac{\ell_1+\ell_2}{2}\right)\right)+\left(I^{\alpha:\psi}_{\psi^{-1}(y_1+y_2-\ell_1)^-}\right)(\lambda\circ\psi)\left(\psi^{-1}\left(y_1+y_2-\frac{\ell_1+\ell_2}{2}\right)\right)\right\} \tag{38}$$
$$\leq\lambda(y_1)+\lambda(y_2)-\left(\frac{\lambda(\ell_1)+\lambda(\ell_2)}{2}\right),$$

for all $\ell_1,\ell_2\in[y_1,y_2]$.

Proof. Regarding the first part of inequality (38) by using the convexity of λ, we have

$$2\lambda\left(y_1+y_2-\frac{x+z}{2}\right)\leq\lambda(y_1+y_2-x)+\lambda(y_1+y_2-z), \tag{39}$$

for all $x,z\in[y_1,y_2]$. By change of variables $x=((1+\zeta)/2)\ell_1+((1-\zeta)/2)\ell_2$ and $z=((1-\zeta)/2)\ell_1+((1+\zeta)/2)\ell_2$, $\zeta\in[0,1]$, we get

$$2\lambda\left(y_1+y_2-\frac{\ell_1+\ell_2}{2}\right)\leq\lambda\left(y_1+y_2-\left(\frac{1+\zeta}{2}\ell_1+\frac{1-\zeta}{2}\ell_2\right)\right)$$
$$+\lambda\left(y_1+y_2-\left(\frac{1-\zeta}{2}\ell_1+\frac{1+\zeta}{2}\ell_2\right)\right). \tag{40}$$

Multiplying the above inequality by $\zeta^{\alpha-1}$ on both sides and integrating with respect to $\zeta\in[0,1]$, we obtain

$$\frac{2}{\alpha}\lambda\left(y_1+y_2-\frac{\ell_1+\ell_2}{2}\right)$$
$$\leq\int_0^1\zeta^{\alpha-1}\left(\lambda\left(y_1+y_2-\left(\frac{1+\zeta}{2}\ell_1+\frac{1-\zeta}{2}\ell_2\right)\right)+\lambda\left(y_1+y_2-\left(\frac{1-\zeta}{2}\ell_1+\frac{1+\zeta}{2}\ell_2\right)\right)\right)d\zeta. \tag{41}$$

Hence, by change of variables, we have

$$\lambda\left(y_1+y_2-\frac{\ell_1+\ell_2}{2}\right)\leq\frac{2^{\alpha-1}\Gamma(\alpha+1)}{(\ell_2-\ell_1)^{\alpha}}\times\left\{\left(I^{\alpha:\psi}_{\psi^{-1}(y_1+y_2-\ell_2)^+}\right)(\lambda\circ\psi)\left(\psi^{-1}\left(y_1+y_2-\frac{\ell_1+\ell_2}{2}\right)\right)\right.$$
$$\left.+\left(I^{\alpha:\psi}_{\psi^{-1}(y_1+y_2-\ell_1)^-}\right)(\lambda\circ\psi)\left(\psi^{-1}\left(y_1+y_2-\frac{\ell_1+\ell_2}{2}\right)\right)\right\}, \tag{42}$$

which concludes the first inequality of (38).

About the second inequality of (38), since λ is convex function, then for $\zeta\in[0,1]$, we get

$$\lambda\left(y_1+y_2-\left(\frac{1+\zeta}{2}\ell_1+\frac{1-\zeta}{2}\ell_2\right)\right)\leq\lambda(y_1)+\lambda(y_2)-\left[\frac{1+\zeta}{2}\lambda(\ell_1)+\frac{1-\zeta}{2}\lambda(\ell_2)\right], \tag{43}$$

$$\lambda\left(y_1+y_2-\left(\frac{1-\zeta}{2}\ell_1+\frac{1+\zeta}{2}\ell_2\right)\right)\leq\lambda(y_1)+\lambda(y_2)-\left[\frac{1-\zeta}{2}\lambda(\ell_1)+\frac{1+\zeta}{2}\lambda(\ell_2)\right]. \tag{44}$$

By adding inequalities (43) and (44), we have

$$\lambda\left(y_1+y_2-\left(\frac{1+\zeta}{2}\ell_1+\frac{1-\zeta}{2}\ell_2\right)\right)+\lambda\left(y_1+y_2-\left(\frac{1-\zeta}{2}\ell_1+\frac{1+\zeta}{2}\ell_2\right)\right)$$
$$\leq 2(\lambda(y_1)+\lambda(y_2))-(\lambda(\ell_1)+\lambda(\ell_2)). \tag{45}$$

Multiplying the above inequality by $\zeta^{\alpha-1}$ on both sides and integrating with respect to ζ over $[0,1]$, we obtain

$$\int_0^1 \zeta^{\alpha-1}\left(\lambda\left(y_1+y_2-\left(\frac{1+\zeta}{2}\ell_1+\frac{1-\zeta}{2}\ell_2\right)\right)+\lambda\left(y_1+y_2-\left(\frac{1-\zeta}{2}\ell_1+\frac{1+\zeta}{2}\ell_2\right)\right)\right)\mathrm{d}\zeta$$
$$\leq (2(\lambda(y_1)+\lambda(y_2))-(\lambda(\ell_1)+\lambda(\ell_2)))\int_0^1 \zeta^{\alpha-1}\mathrm{d}\zeta. \tag{46}$$

Then, we have the following inequality:

$$\frac{2^\alpha\Gamma(\alpha)}{(\ell_2-\ell_1)^\alpha}$$
$$\times\left\{\left(I^{\alpha:\psi}_{\psi^{-1}(y_1+y_2-\ell_2)^+}\right)(\lambda\circ\psi)\left(\psi^{-1}\left(y_1+y_2-\frac{\ell_1+\ell_2}{2}\right)\right)+\left(I^{\alpha:\psi}_{\psi^{-1}(y_1+y_2-\ell_1)^-}\right)(\lambda\circ\psi)\left(\psi^{-1}\left(y_1+y_2-\frac{\ell_1+\ell_2}{2}\right)\right)\right\} \tag{47}$$
$$\leq (2(\lambda(y_1)+\lambda(y_2))-(\lambda(\ell_2)+\lambda(\ell_2)))\cdot\frac{1}{\alpha}.$$

Multiplying by $\alpha/2$, we will get

$$\frac{2^{\alpha-1}\Gamma(\alpha+1)}{(\ell_2-\ell_1)^\alpha}\times\left\{\left(I^{\alpha:\psi}_{\psi^{-1}(y_1+y_2-\ell_2)^+}\right)(\lambda\circ\psi)\left(\psi^{-1}\left(y_1+y_2-\frac{\ell_1+\ell_2}{2}\right)\right)+\left(I^{\alpha:\psi}_{\psi^{-1}(y_1+y_2-\ell_1)^-}\right)(\lambda\circ\psi)\left(\psi^{-1}\left(y_1+y_2-\frac{\ell_1+\ell_2}{2}\right)\right)\right\}$$
$$\leq (\lambda(y_1)+\lambda(y_2))-\frac{\lambda(\ell_1)+\lambda(\ell_2)}{2}. \tag{48}$$

So, the second inequality of (38) holds. □

Remark 5. Taking $\psi(\gamma)=\gamma$ in Theorem 4, we will get Theorem 2 proved in [29].

Remark 6. Taking $\psi(\gamma)=\gamma$ and $\alpha=1$ in Theorem 4, we will obtain Theorem 2.1 proved by Kian and Moslehian in [28].

3. New Generalized Identities and Their Integral Inequalities

In this section, the following lemmas will play a basic role in our next results.

Lemma 1. *If (A_1) is satisfied and λ: $[y_1,y_2]\longrightarrow\mathfrak{R}$ is a differentiable function on $L_1[y_1,y_2]$, then*

$$\begin{aligned}
&\frac{\lambda(y_1+y_2-\ell_1)+\lambda(y_1+y_2-\ell_2)}{2}-\frac{\Gamma(\alpha+1)}{2(\ell_2-\ell_1)^{\alpha}}\\
&\quad\times\left\{\left(I^{\alpha:\psi}_{\psi^{-1}(y_1+y_2-\ell_2)^{+}}\right)(\lambda\circ\psi)\left(\psi^{-1}(y_1+y_2-\ell_1)\right)+\left(I^{\alpha:\psi}_{\psi^{-1}(y_1+y_2-\ell_1)^{-}}\right)(\lambda\circ\psi)\left(\psi^{-1}(y_1+y_2-\ell_2)\right)\right\}\\
&=\frac{1}{2(\ell_2-\ell_1)^{\alpha}}\\
&\quad\times\int_{\psi^{-1}(y_1+y_2-\ell_2)}^{\psi^{-1}(y_1+y_2-\ell_1)}\left((\psi(\gamma)-(y_1+y_2-\ell_2))^{\alpha}-((y_1+y_2-\ell_1)-\psi(\gamma))^{\alpha}\right)\times(\lambda'\circ\psi)(\gamma)\psi'(\gamma)\mathrm{d}\gamma,
\end{aligned}\tag{49}$$

for all $\ell_1,\ell_2\in[y_1,y_2]$.

Proof. It suffices to note that

$$I=\frac{\lambda(y_1+y_2-\ell_1)-\lambda(y_1+y_2-\ell_2)}{2}-\{I_1+I_2\},\tag{50}$$

where

$$\begin{aligned}
I_1&=\frac{\Gamma(\alpha+1)}{2(\ell_2-\ell_1)^{\alpha}}\left[I^{\alpha:\psi}_{\Psi^{-1}(y_1+y_2-\ell_2)^{+}}(\lambda\circ\psi)\left(\psi^{-1}(y_1+y_2-\ell_1)\right)\right]\\
&=\frac{\alpha}{2(\ell_2-\ell_1)^{\alpha}}\int_{\psi^{-1}(y_1+y_2-\ell_2)}^{\psi^{-1}(y_1+y_2-\ell_1)}\psi'(\gamma)((y_1+y_2-\ell_1)-\psi(\gamma))^{\alpha-1}(\lambda\circ\psi)(\gamma)\mathrm{d}\gamma\\
&=\frac{-1}{2(\ell_2-\ell_1)^{\alpha}}\int_{\psi^{-1}(y_1+y_2-\ell_1)}^{\psi^{-1}(y_1+y_2-\ell_2)}\mathrm{d}((y_1+y_2-\ell_1)-\psi(\gamma))^{\alpha}(\lambda\circ\psi)(\gamma)\\
&=\frac{1}{2(\ell_2-\ell_1)^{\alpha}}\left[\lambda(y_1+y_2-\ell_2)(\ell_2-\ell_1)^{\alpha}\right]\\
&\quad+\int_{\psi^{-1}(y_1+y_2-\ell_2)}^{\psi^{-1}(y_1+y_2-\ell_1)}\psi'(\gamma)((y_1+y_2-\ell_1)-\psi(\gamma))^{\alpha}(\lambda'\circ\psi)(\gamma)\mathrm{d}\gamma,
\end{aligned}\tag{51}$$

$$\begin{aligned}
I_2&=\frac{\Gamma(\alpha+1)}{2(\ell_2-\ell_1)^{\alpha}}\left[I^{\alpha:\psi}_{\psi^{-1}(y_1+y_2-\ell_1)^{-}}(\lambda\circ\psi)\left(\psi^{-1}(y_1+y_2-\ell_2)\right)\right]\\
&=\frac{\alpha}{2(\ell_2-\ell_1)^{\alpha}}\int_{\psi^{-1}(y_1+y_2-\ell_2)}^{\psi^{-1}(y_1+y_2-\ell_1)}\psi'(\gamma)(-(y_1+y_2-\ell_2)+\psi(\gamma))^{\alpha-1}(\lambda\circ\psi)(\gamma)\mathrm{d}\gamma\\
&=\frac{1}{2(\ell_2-\ell_1)^{\alpha}}\int_{\psi^{-1}(y_1+y_2-\ell_2)}^{\psi^{-1}(y_1+y_2-\ell_1)}\mathrm{d}(-(y_1+y_2-\ell_2)+\psi(\gamma))^{\alpha}(\lambda\circ\psi)(\gamma)\\
&=\frac{1}{2(\ell_2-\ell_1)^{\alpha}}\left[\lambda(y_1+y_2-\ell_1)(\ell_2-\ell_1)^{\alpha}\right]\\
&\quad-\int_{\psi^{-1}(y_1+y_2-\ell_2)}^{\psi^{-1}(y_1+y_2-\ell_1)}\psi'(\gamma)(-(y_1+y_2-\ell_2)+\psi(\gamma))^{\alpha}(\lambda'\circ\psi)(\gamma)\mathrm{d}\gamma.
\end{aligned}\tag{52}$$

Substituting (51) and (52) in (50), we get the desired equality (49). □

Remark 7. For $\ell_1=y_1$ and $\ell_2=y_2$ in Lemma 1, we will get Lemma 3.1 proved in [30].

Theorem 5. *If (A_1) is satisfied and $|\lambda'|$ is a convex function on $[y_1, y_2]$, then*

$$\begin{aligned}&\left|\frac{\lambda(y_1+y_2-\ell_1)+\lambda(y_1+y_2-\ell_2)}{2}-\frac{\Gamma(\alpha+1)}{2(\ell_2-\ell_1)^{\alpha}}\left(\left(I^{\alpha:\psi}_{\psi^{-1}(y_1+y_2-\ell_2)^{+}}\right)\lambda(y_1+y_2-\ell_1)\right.\right.\\&\left.\left.+\left(I^{\alpha:\psi}_{\psi^{-1}(y_1+y_2-\ell_1)^{-}}\right)\lambda(y_1+y_2-\ell_2)\right)\right|\\&\leq\frac{(\ell_2-\ell_1)}{\alpha+1}\left(1-\frac{1}{2^{\alpha}}\right)\left\{|\lambda'(y_1)|+|\lambda'(y_2)|-\left(\frac{|\lambda'(\ell_1)|+|\lambda'(\ell_2)|}{2}\right)\right\}.\end{aligned}\tag{53}$$

for all $\ell_1, \ell_2 \in [y_1, y_2]$.

Proof. Here, we will use Lemma 1, properties of modulus, and Jensen–Mercer's inequality.

For every $\gamma \in (\psi^{-1}(y_1+y_2-\ell_2), \psi^{-1}(y_1+y_2-\ell_1))$, we have $(y_1+y_2-\ell_2) < \psi(\gamma) < (y_1+y_2-\ell_1)$.

Let $\zeta = ((y_1+y_2-\ell_1)-\psi(\gamma))/(\ell_2-\ell_1)$, and then $\psi(\gamma) = y_1+y_2-(\zeta\ell_1+(1-\zeta)\ell_2)$. So, we get

$$\begin{aligned}&\left|\frac{\lambda(y_1+y_2-\ell_1)+\lambda(y_1+y_2-\ell_2)}{2}-\frac{\Gamma(\alpha+1)}{2(\ell_2-\ell_1)^{\alpha}}\left(\left(I^{\alpha:\psi}_{(y_1+y_2-\ell_2)^{+}}\right)\lambda(y_1+y_2-\ell_1)\right.\right.\\&\left.\left.+\left(I^{\alpha:\psi}_{(y_1+y_2-\ell_1)^{-}}\right)\lambda(y_1+y_2-\ell_2)\right)\right|\\&\leq\frac{1}{2(\ell_2-\ell_1)^{\alpha}}\int_{\psi^{-1}(y_1+y_2-\ell_2)}^{\psi^{-1}(y_1+y_2-\ell_1)}\left|(\psi(\gamma)-(y_1+y_2-\ell_2))^{\alpha}-((y_1+y_2-\ell_1)-\psi(\gamma))^{\alpha}\right|\times\left|(\lambda'\circ\psi)(\gamma)\right|\psi'(\gamma)\mathrm{d}\gamma\\&=\frac{(\ell_2-\ell_1)}{2}\int_0^1\left|\zeta^{\alpha}-(1-\zeta)^{\alpha}\right|\left|\lambda'(y_1+y_2-(\zeta\ell_1+(1-\zeta)\ell_2))\right|\mathrm{d}\zeta\\&\leq\frac{(\ell_2-\ell_1)}{2}\int_0^1\left|\zeta^{\alpha}-(1-\zeta)^{\alpha}\right|\left\{|\lambda'(y_1)|+|\lambda'(y_2)|-\left(\zeta|\lambda'(\ell_1)|+(1-\zeta)|\lambda'(\ell_2)|\right)\right\}\mathrm{d}\zeta\\&=\frac{(\ell_2-\ell_1)}{2}[I_1+I_2],\end{aligned}\tag{54}$$

where

$$\begin{aligned}I_1&=\int_0^{1/2}\left((1-\zeta)^{\alpha}-\zeta^{\alpha}\right)\left\{|\lambda'(y_1)|+|\lambda'(y_2)|-\left(\zeta|\lambda'(\ell_1)|+(1-\zeta)|\lambda'(\ell_2)|\right)\right\}\mathrm{d}\zeta\\&=\left(|\lambda'(y_1)|+|\lambda'(y_2)|\right)\left(\frac{1}{(\alpha+1)}-\frac{2^{-\alpha}}{(\alpha+1)}\right)\\&\quad-\left\{|\lambda'(\ell_1)|\left(\frac{1}{(\alpha+1)(\alpha+2)}-\frac{2^{-\alpha-1}}{(\alpha+1)}\right)+|\lambda'(\ell_2)|\left(\frac{1}{(\alpha+2)}-\frac{2^{-\alpha-1}}{(\alpha+1)}\right)\right\},\end{aligned}\tag{55}$$

$$\begin{aligned}I_2&=\int_{1/2}^{1}\left(\zeta^{\alpha}-(1-\zeta)^{\alpha}\right)\left\{|\lambda'(y_1)|+|\lambda'(y_2)|-\left(\zeta|\lambda'(\ell_1)|+(1-\zeta)|\lambda'(\ell_2)|\right)\right\}\mathrm{d}\zeta\\&=\left(|\lambda'(y_1)|+|\lambda'(y_2)|\right)\left(\frac{1}{(\alpha+1)}-\frac{2^{-\alpha}}{(\alpha+1)}\right)\\&\quad-\left\{|\lambda'(\ell_1)|\left(\frac{1}{(\alpha+2)}-\frac{2^{-\alpha-1}}{(\alpha+1)}\right)+|\lambda'(\ell_2)|\left(\frac{1}{(\alpha+1)(\alpha+2)}-\frac{2^{-\alpha-1}}{(\alpha+1)}\right)\right\}.\end{aligned}\tag{56}$$

Substituting (55) and (56) in (54), we get (53). □

Remark 8. For $\ell_1 = y_1$ and $\ell_2 = y_2$ in Theorem 5, we will get Theorem 3.4 proved in [30].

Remark 9. Taking $\psi(\gamma) = \gamma$ in Theorem 5, we will get Theorem 4 proved in [27].

Lemma 2. *If (A_1) is satisfied and λ: $[y_1, y_2] \longrightarrow \mathfrak{R}$ is a differentiable function on $L_1[y_1, y_2]$, then*

$$\begin{aligned}
&\frac{\lambda(y_1+y_2-\ell_1)+\lambda(y_1+y_2-\ell_2)}{2}-\frac{2^{\alpha-1}\Gamma(\alpha+1)}{(\ell_2-\ell_1)^{\alpha}}\\
&\times\left\{\left(I^{\alpha:\psi}_{\psi^{-1}(y_1+y_2-\ell_2)^+}\right)\left[\lambda\circ\psi\left(\psi^{-1}\left(y_1+y_2-\frac{\ell_1+\ell_2}{2}\right)\right)\right]\right.\\
&\left.+\left(I^{\alpha:\psi}_{\psi^{-1}(y_1+y_2-\ell_1)^-}\right)\left[\lambda\circ\psi\left(\psi^{-1}\left(y_1+y_2-\frac{\ell_1+\ell_2}{2}\right)\right)\right]\right\}\\
&=\frac{(\ell_2-\ell_1)}{4}\left[\int_0^1\zeta^{\alpha}\lambda'\left(y_1+y_2-\left(\frac{1+\zeta}{2}\ell_1+\frac{1-\zeta}{2}\ell_2\right)\right)\mathrm{d}\zeta\right.\\
&\left.-\int_0^1\zeta^{\alpha}\lambda'\left(y_1+y_2-\left(\frac{1-\zeta}{2}\ell_1+\frac{1+\zeta}{2}\ell_2\right)\right)\mathrm{d}\zeta\right].
\end{aligned}\tag{57}$$

Proof. It suffices to note that

$$I=\frac{(\ell_2-\ell_1)}{4}\{I_1-I_2\},\tag{58}$$

where

$$\begin{aligned}
I_1&=\int_0^1\zeta^{\alpha}\lambda'\left(y_1+y_2-\left(\frac{1+\zeta}{2}\ell_1+\frac{1-\zeta}{2}\ell_2\right)\right)\mathrm{d}\zeta\\
&=\frac{2}{(\ell_2-\ell_1)}\lambda(y_1+y_2-\ell_1)-\frac{2^{\alpha}}{\ell_2-\ell_1}\int_0^1\zeta^{\alpha-1}\lambda\left(y_1+y_2-\left(\frac{1+\zeta}{2}\ell_1+\frac{1-\zeta}{2}\ell_2\right)\right)\mathrm{d}\zeta\\
&=\frac{2}{(\ell_2-\ell_1)}\lambda(y_1+y_2-\ell_1)\\
&\quad-\frac{2^{\alpha+1}\Gamma(\alpha+1)}{(\ell_2-\ell_1)^{\alpha+1}}\left(I^{\alpha:\psi}_{\psi^{-1}(y_1+y_2-\ell_1)^-}\right)\left[\lambda\circ\psi\left(\psi^{-1}\left(y_1+y_2-\frac{\ell_1+\ell_2}{2}\right)\right)\right],
\end{aligned}\tag{59}$$

$$\begin{aligned}
I_2&=\int_0^1\zeta^{\alpha}\lambda\left(y_1+y_2-\left(\frac{1-\zeta}{2}\ell_1+\frac{1+\zeta}{2}\ell_2\right)\right)\mathrm{d}\zeta\\
&=-\frac{2}{(\ell_2-\ell_1)}\lambda(y_1+y_2-\ell_2)-\frac{2^{\alpha}}{\ell_2-\ell_1}\int_0^1\zeta^{\alpha-1}\lambda\left(y_1+y_2-\left(\frac{1-\zeta}{2}\ell_1+\frac{1+\zeta}{2}\ell_2\right)\right)\mathrm{d}\zeta\\
&=-\frac{2}{(\ell_2-\ell_1)}\lambda(y_1+y_2-\ell_2)\\
&\quad-\frac{2^{\alpha+1}\Gamma(\alpha+1)}{(\ell_2-\ell_1)^{\alpha+1}}\left(I^{\alpha:\psi}_{\psi^{-1}(y_1+y_2-\ell_2)^+}\right)\left[\lambda\circ\psi\left(\psi^{-1}\left(y_1+y_2-\frac{\ell_1+\ell_2}{2}\right)\right)\right].
\end{aligned}\tag{60}$$

Substituting (59) and (60) in (58), we get (57). □

Remark 10. Taking $\psi(\gamma) = \gamma$ in Lemma 2, we will get Lemma 1 proved in [29].

Theorem 6. *If (A_1) is satisfied and λ' is a convex function on $[y_1, y_2]$, then*

$$\begin{aligned}&\Bigg|\frac{\lambda(y_1+y_2-\ell_1)+\lambda(y_1+y_2-\ell_2)}{2}-\frac{2^{\alpha-1}\Gamma(\alpha+1)}{(\ell_2-\ell_1)^{\alpha}}\\&\quad\times\Bigg\{\left(I^{\alpha:\psi}_{\psi^{-1}(y_1+y_2-\ell_2)^+}\right)\left[\lambda\circ\psi\left(\psi^{-1}\left(y_1+y_2-\frac{\ell_1+\ell_2}{2}\right)\right)\right]\\&\quad+\left(I^{\alpha:\psi}_{\psi^{-1}(y_1+y_2-\ell_1)^-}\right)\left[\lambda\circ\psi\left(\psi^{-1}\left(y_1+y_2-\frac{\ell_1+\ell_2}{2}\right)\right)\right]\Bigg\}\Bigg|\\&\le\frac{(\ell_2-\ell_1)}{4(\alpha+2)}\sup_{\xi\in[y_1,y_2]}\left|\lambda''(\xi)\right|,\end{aligned}\tag{61}$$

for all $\ell_1, \ell_2 \in [y_1, y_2]$.

Proof. From Lemma 2 and using mean value theorem for λ', we have

$$\begin{aligned}&\frac{\lambda(y_1+y_2-\ell_1)+\lambda(y_1+y_2-\ell_2)}{2}-\frac{2^{\alpha-1}\Gamma(\alpha+1)}{(\ell_2-\ell_1)^{\alpha}}\\&\quad\times\Bigg\{\left(I^{\alpha:\psi}_{\psi^{-1}(y_1+y_2-\ell_2)^+}\right)\left[\lambda\circ\psi\left(\psi^{-1}\left(y_1+y_2-\frac{\ell_1+\ell_2}{2}\right)\right)\right]\\&\quad+\left(I^{\alpha:\psi}_{\psi^{-1}(y_1+y_2-\ell_1)^-}\right)\left[\lambda\circ\psi\left(\psi^{-1}\left(y_1+y_2-\frac{\ell_1+\ell_2}{2}\right)\right)\right]\Bigg\}\\&=\frac{(\ell_2-\ell_1)^2}{4}\int_0^1\zeta^{\alpha+1}\lambda''(\xi)\mathrm{d}\zeta,\end{aligned}\tag{62}$$

where $\xi \in [y_1, y_2]$. This leads us to

$$\begin{aligned}&\Bigg|\frac{\lambda(y_1+y_2-\ell_1)+\lambda(y_1+y_2-\ell_2)}{2}-\frac{2^{\alpha-1}\Gamma(\alpha+1)}{(\ell_2-\ell_1)^{\alpha}}\\&\quad\times\Bigg\{\left(I^{\alpha:\psi}_{\psi^{-1}(y_1+y_2-\ell_2)^+}\right)\left[\lambda\circ\psi\left(\psi^{-1}\left(y_1+y_2-\frac{\ell_1+\ell_2}{2}\right)\right)\right]\\&\quad+\left(I^{\alpha:\psi}_{\psi^{-1}(y_1+y_2-\ell_1)^-}\right)\left[\lambda\circ\psi\left(\psi^{-1}\left(y_1+y_2-\frac{\ell_1+\ell_2}{2}\right)\right)\right]\Bigg\}\Bigg|\\&\le\frac{(\ell_2-\ell_1)^2}{4}\int_0^1\left|\zeta^{\alpha+1}\right|\left|\lambda''(\xi)\right|\mathrm{d}\zeta\\&\le\frac{(\ell_2-\ell_1)^2}{4}\sup_{\xi\in[y_1,y_2]}\left|\lambda''(\xi)\right|\left\{\int_0^1\zeta^{\alpha+1}\mathrm{d}\zeta\right\}\\&=\frac{(\ell_2-\ell_1)^2}{4(\alpha+2)}\sup_{\xi\in[y_1,y_2]}\left|\lambda''(\xi)\right|.\end{aligned}\tag{63}$$

□

Remark 11. For $\psi(\gamma) = \gamma$ in Theorem 6, we will get Theorem 3 proved in [29].

Theorem 7. *If (A_1) is satisfied and $|\lambda'|$ is a convex function on $[y_1, y_2]$, then*

$$\begin{aligned}
&\left|\frac{\lambda(y_1+y_2-\ell_1)+\lambda(y_1+y_2-\ell_2)}{2}-\frac{2^{\alpha-1}\Gamma(\alpha+1)}{(\ell_2-\ell_1)^{\alpha}}\right.\\
&\times\left\{\left(I^{\alpha:\psi}_{\psi^{-1}(y_1+y_2-\ell_2)^{+}}\right)\left[\lambda\circ\psi\left(\psi^{-1}\left(y_1+y_2-\frac{\ell_1+\ell_2}{2}\right)\right)\right]\right.\\
&\left.\left.+\left(I^{\alpha:\psi}_{\psi^{-1}(y_1+y_2-\ell_1)^{-}}\right)\left[\lambda\circ\psi\left(\psi^{-1}\left(y_1+y_2-\frac{\ell_1+\ell_2}{2}\right)\right)\right]\right\}\right|\\
&\leq\frac{(\ell_2-\ell_1)}{2(\alpha+1)}\left\{|\lambda'(y_1)|+|\lambda'(y_2)|-\left(\frac{|\lambda'(\ell_1)|+|\lambda'(\ell_2)|}{2}\right)\right\},
\end{aligned}\tag{64}$$

for all $\ell_1, \ell_2 \in [y_1, y_2]$.

Proof. By using Lemma 2, properties of modulus, and Jensen–Mercer inequality, we have

$$\begin{aligned}
&\left|\frac{\lambda(y_1+y_2-\ell_1)+\lambda(y_1+y_2-\ell_2)}{2}-\frac{2^{\alpha-1}\Gamma(\alpha+1)}{(\ell_2-\ell_1)^{\alpha}}\right.\\
&\times\left\{\left(I^{\alpha:\psi}_{\psi^{-1}(y_1+y_2-\ell_2)^{+}}\right)\left[\lambda\circ\psi\left(\psi^{-1}\left(y_1+y_2-\frac{\ell_1+\ell_2}{2}\right)\right)\right]\right.\\
&\left.\left.+\left(I^{\alpha:\psi}_{\psi^{-1}(y_1+y_2-\ell_1)^{-}}\right)\left[\lambda\circ\psi\left(\psi^{-1}\left(y_1+y_2-\frac{\ell_1+\ell_2}{2}\right)\right)\right]\right\}\right|\\
&\leq\frac{(\ell_2-\ell_1)}{4}\left[\int_0^1\zeta^{\alpha}\left|\lambda'\left(y_1+y_2-\left(\frac{1+\zeta}{2}\ell_1+\frac{1-\zeta}{2}\ell_2\right)\right)\right|d\zeta\right.\\
&\left.+\int_0^1\zeta^{\alpha}\left|\lambda'\left(y_1+y_2-\left(\frac{1-\zeta}{2}\ell_1+\frac{1+\zeta}{2}\ell_2\right)\right)\right|d\zeta\right]\\
&\leq\frac{(\ell_2-\ell_1)}{4}\left[\int_0^1\zeta^{\alpha}\left\{|\lambda'(y_1)|+|\lambda'(y_2)|-\left(\frac{(1+\zeta)}{2}|\lambda'(\ell_1)|+\frac{(1-\zeta)}{2}|\lambda'(\ell_2)|\right)\right\}d\zeta\right.\\
&\left.+\int_0^1\zeta^{\alpha}\left\{|\lambda'(y_1)|+|\lambda'(y_2)|-\left(\frac{(1-\zeta)}{2}|\lambda'(\ell_1)|+\frac{(1+\zeta)}{2}|\lambda'(\ell_2)|\right)\right\}d\zeta\right],
\end{aligned}\tag{65}$$

and after integration, we get required result. □

Remark 12. For $\psi(\gamma)=\gamma$ in Theorem 7, we will get Theorem 4 proved in [29].

Lemma 3. *If (A_1) is satisfied and $\lambda\colon [y_1,y_2]\longrightarrow\Re$ is a differentiable function on $L_1[y_1,y_2]$, then*

$$\begin{aligned}&\lambda\left(y_1+y_2-\frac{\ell_1+\ell_2}{2}\right)-\frac{2^{\alpha-1}\Gamma(\alpha+1)}{(\ell_2-\ell_1)^{\alpha}}\\&\quad\times\left\{\left(I^{\alpha:\psi}_{\psi^{-1}(y_1+y_2-((\ell_1+\ell_2)/2))^{+}}\right)(\lambda\circ\psi)\left(\psi^{-1}(y_1+y_2-\ell_1)\right)\right.\\&\quad\left.+\left(I^{\alpha:\psi}_{\psi^{-1}(y_1+y_2-((\ell_1+\ell_2)/2))^{-}}\right)(\lambda\circ\psi)\left(\psi^{-1}(y_1+y_2-\ell_2)\right)\right\}\\&=\frac{(\ell_2-\ell_1)}{4}\left[\int_0^1\zeta^{\alpha}\lambda'\left(y_1+y_2-\left(\frac{\zeta}{2}\ell_1+\frac{2-\zeta}{2}\ell_2\right)\right)\mathrm{d}\zeta\right.\\&\quad\left.-\int_0^1\zeta^{\alpha}\lambda'\left(y_1+y_2-\left(\frac{2-\zeta}{2}\ell_1+\frac{\zeta}{2}\ell_2\right)\right)\mathrm{d}\zeta\right].\end{aligned}\tag{66}$$

Proof. See the proof of Lemma 2. □

Remark 13. For $\psi(\gamma)=\gamma$, $\ell_1=y_1$, and $\ell_2=y_1$ in Lemma 3, we will get Lemma 3 proved in [31].

Remark 14. For $\psi(\gamma)=\gamma$ in Lemma 3, we will get Lemma 2 proved in [27].

Theorem 8. *If (A_1) is satisfied and $|\lambda'|$ is a convex function on $[y_1,y_2]$, then*

$$\begin{aligned}&\left|\lambda\left(y_1+y_2-\frac{\ell_1+\ell_2}{2}\right)-\frac{2^{\alpha-1}\Gamma(\alpha+1)}{(\ell_2-\ell_1)^{\alpha}}\right.\\&\quad\times\left\{\left(I^{\alpha:\psi}_{\psi^{-1}(y_1+y_2-((\ell_1+\ell_2)/2))^{+}}\right)(\lambda\circ\psi)\left(\psi^{-1}(y_1+y_2-\ell_1)\right)\right.\\&\quad\left.\left.+\left(I^{\alpha:\psi}_{\psi^{-1}(y_1+y_2-((\ell_1+\ell_2)/2))^{-}}\right)(\lambda\circ\psi)\left(\psi^{-1}(y_1+y_2-\ell_2)\right)\right\}\right|\\&\le\frac{(\ell_2-\ell_1)}{2(\alpha+1)}\left\{|\lambda'(y_1)|+|\lambda'(y_2)|-\left(\frac{|\lambda'(\ell_1)|+|\lambda'(\ell_2)|}{2}\right)\right\},\end{aligned}\tag{67}$$

for all $\ell_1,\ell_2\in[y_1,y_2]$.

Proof. By using Lemma 3, properties of modulus, and Jensen–Mercer inequality, we have

$$\begin{aligned}&\left|\lambda\left(y_1+y_2-\frac{\ell_1+\ell_2}{2}\right)-\frac{2^{\alpha-1}\Gamma(\alpha+1)}{(\ell_2-\ell_1)^{\alpha}}\right.\\&\quad\times\left\{\left(I^{\alpha:\psi}_{\psi^{-1}(y_1+y_2-((\ell_1+\ell_2)/2))^{+}}\right)(\lambda\circ\psi)\left(\psi^{-1}(y_1+y_2-\ell_1)\right)\right.\\&\quad\left.\left.+\left(I^{\alpha:\psi}_{\psi^{-1}(y_1+y_2-((\ell_1+\ell_2)/2))^{-}}\right)(\lambda\circ\psi)\left(\psi^{-1}(y_1+y_2-\ell_2)\right)\right\}\right|\\&\le\frac{(\ell_2-\ell_1)}{4}\left[\int_0^1\zeta^{\alpha}\left|\lambda'\left(y_1+y_2-\left(\frac{\zeta}{2}\ell_1+\frac{2-\zeta}{2}\ell_2\right)\right)\right|\mathrm{d}\zeta\right.\\&\quad\left.+\int_0^1\zeta^{\alpha}\left|\lambda'\left(y_1+y_2-\left(\frac{2-\zeta}{2}\ell_1+\frac{\zeta}{2}\ell_2\right)\right)\right|\mathrm{d}\zeta\right]\\&\le\frac{(\ell_2-\ell_1)}{4}\left[\int_0^1\zeta^{\alpha}\left\{|\lambda'(y_1)|+|\lambda'(y_2)|-\left(\frac{\zeta}{2}|\lambda'(\ell_1)|+\frac{(2-\zeta)}{2}|\lambda'(\ell_2)|\right)\right\}\mathrm{d}\zeta\right.\\&\quad\left.+\int_0^1\zeta^{\alpha}\left\{|\lambda'(y_1)|+|\lambda'(y_2)|-\left(\frac{(2-\zeta)}{2}|\lambda'(\ell_1)|+\frac{\zeta}{2}|\lambda'(\ell_2)|\right)\right\}\mathrm{d}\zeta\right].\end{aligned}\tag{68}$$

After integration, we get required result. □

Remark 15. Taking $\psi(\gamma)=\gamma$ in Theorem 8, we will get Theorem 5 proved in [27].

Theorem 9. *If (A_1) is satisfied and $|\lambda'|^q$ is convex function, then*

$$\begin{aligned}
&\Bigg|\lambda\left(y_1+y_2-\frac{\ell_1+\ell_2}{2}\right)-\frac{2^{\alpha-1}\Gamma(\alpha+1)}{(\ell_2-\ell_1)^{\alpha}}\\
&\quad\times\left\{\left(I^{\alpha:\psi}_{\psi^{-1}(y_1+y_2-((\ell_1+\ell_2)/2))^{+}}\right)(\lambda\circ\psi)\left(\psi^{-1}(y_1+y_2-\ell_1)\right)\right.\\
&\quad\left.+\left(I^{\alpha:\psi}_{\psi^{-1}(y_1+y_2-((\ell_1+\ell_2)/2))^{-}}\right)(\lambda\circ\psi)\left(\psi^{-1}(y_1+y_2-\ell_2)\right)\right\}\Bigg|\\
&\le\frac{(\ell_2-\ell_1)}{4}\left(\frac{1}{p\alpha+1}\right)^{1/p}\left[\left(|\lambda'(y_1)|^q+|\lambda'(y_2)|^q-\left(\frac{1}{4}|\lambda'(\ell_1)|^q+\frac{3}{4}|\lambda'(\ell_2)|^q\right)\right)^{1/q}\right.\\
&\quad\left.+\left(|\lambda'(y_1)|^q+|\lambda'(y_2)|^q-\left(\frac{3}{4}|\lambda'(\ell_1)|^q+\frac{1}{4}|\lambda'(\ell_2)|^q\right)\right)^{1/q}\right],
\end{aligned}\tag{69}$$

where $q>1$ and $(1/p)+(1/q)=1$ for all $\ell_1,\ell_2\in[y_1,y_2]$.

Proof. Applying Lemma 3, Hölder and Jensen–Mercer inequalities, the fact that $|\lambda'|^q$ is convex function, and properties of modulus, we have

$$\begin{aligned}
&\Bigg|\lambda\left(y_1+y_2-\frac{\ell_1+\ell_2}{2}\right)-\frac{2^{\alpha-1}\Gamma(\alpha+1)}{(\ell_2-\ell_1)^{\alpha}}\\
&\quad\times\left\{\left(I^{\alpha:\psi}_{\psi^{-1}(y_1+y_2-((\ell_1+\ell_2)/2))^{+}}\right)(\lambda\circ\psi)\left(\psi^{-1}(y_1+y_2-\ell_1)\right)\right.\\
&\quad\left.+\left(I^{\alpha:\psi}_{\psi^{-1}(y_1+y_2-((\ell_1+\ell_2)/2))^{-}}\right)(\lambda^{\circ}\psi)\left(\psi^{-1}(y_1+y_2-\ell_2)\right)\right\}\Bigg|\\
&\le\frac{(\ell_2-\ell_1)}{4}\int_0^1\zeta^{\alpha}\left|\lambda'\left(y_1+y_2-\left(\frac{\zeta}{2}\ell_1+\frac{(2-\zeta)}{2}\ell_2\right)\right)\right|\mathrm{d}\zeta\\
&\quad+\frac{(\ell_2-\ell_1)}{4}\int_0^1\zeta^{\alpha}\left|\lambda'\left(y_1+y_2-\left(\frac{(2-\zeta)}{2}\ell_1+\frac{\zeta}{2}\ell_2\right)\right)\right|\mathrm{d}\zeta\\
&\le\frac{(\ell_2-\ell_1)}{4}\left(\int_0^1\zeta^{p\alpha}\mathrm{d}\zeta\right)^{1/p}\left(\int_0^1\left|\lambda'\left(y_1+y_2-\left(\frac{\zeta}{2}\ell_1+\frac{(2-\zeta)}{2}\ell_2\right)\right)\right|^q\mathrm{d}\zeta\right)^{1/q}\\
&\quad+\frac{(\ell_2-\ell_1)}{4}\left(\int_0^1\zeta^{p\alpha}\mathrm{d}\zeta\right)^{1/p}\left(\int_0^1\left|\lambda'\left(y_1+y_2-\left(\frac{(2-\zeta)}{2}\ell_1+\frac{\zeta}{2}\lambda'\ell_2\right)\right)\right|^q\mathrm{d}\zeta\right)^{1/q}\\
&\le\frac{(\ell_2-\ell_1)}{4}\left(\frac{1}{p\alpha+1}\right)^{1/p}\left(|\lambda'(y_1)|^q+|\lambda'(y_2)|^q-\left(\frac{1}{4}|\lambda'(\ell_1)|^q+\frac{3}{4}|\lambda'(\ell_2)|^q\right)\right)^{1/q}\\
&\quad+\frac{(\ell_2-\ell_1)}{4}\left(\frac{1}{p\alpha+1}\right)^{1/p}\left(|\lambda'(y_1)|^q+|\lambda'(y_2)|^q-\left(\frac{3}{4}|\lambda'(\ell_1)|^q+\frac{1}{4}|\lambda'(\ell_2)|^q\right)\right)^{1/q}.
\end{aligned}\tag{70}$$

After further simplifications, we get required result. □

Remark 16. For $\psi(\gamma)=\gamma$ in Theorem 9, we will get Theorem 6 proved in [27].

Lemma 4. *If (A_1) is satisfied and $\lambda\colon [y_1,y_2]\longrightarrow \mathfrak{R}$ is a twice differentiable function on $L_1[y_1,y_2]$, then*

$$\begin{aligned}
&\frac{2^{\alpha-1}\Gamma(\alpha+1)}{(\ell_2-\ell_1)^{\alpha}}\left\{\left(I^{\alpha:\psi}_{\psi^{-1}(y_1+y_2-((\ell_1+\ell_2)/2))^{+}}\right)\left(\lambda\circ\psi\left(\psi^{-1}(y_1+y_2-\ell_1)\right)\right)\right.\\
&\left.+\left(I^{\alpha:\psi}_{\psi^{-1}(y_1+y_2-((\ell_1+\ell_2)/2))^{-}}\right)\left(\lambda\circ\psi\left(\psi^{-1}(y_1+y_2-\ell_2)\right)\right)\right\}-\lambda\left(y_1+y_2-\frac{\ell_1+\ell_2}{2}\right)\\
&=\frac{(\ell_2-\ell_1)^2}{8(\alpha+1)}\left[\int_0^1(1-\zeta)^{\alpha+1}\lambda''\left(y_1+y_2-\left(\frac{1+\zeta}{2}\ell_1+\frac{1-\zeta}{2}\ell_2\right)\right)\mathrm{d}\zeta\right.\\
&\left.+\int_0^1(1-\zeta)^{\alpha+1}\lambda''\left(y_1+y_2-\left(\frac{1-\zeta}{2}\ell_1+\frac{1+\zeta}{2}\ell_2\right)\right)\mathrm{d}\zeta\right].
\end{aligned}\tag{71}$$

Proof. It suffices to note that

$$I=\frac{(\ell_2-\ell_1)^2}{8(\alpha+1)}\{I_1+I_2\},\tag{72}$$

where

$$\begin{aligned}
I_1&=\int_0^1(1-\zeta)^{\alpha+1}\lambda''\left(y_1+y_2-\left(\frac{1+\zeta}{2}\ell_1+\frac{1-\zeta}{2}\ell_2\right)\right)\mathrm{d}\zeta\\
&=-\frac{2}{(\ell_2-\ell_1)}\lambda'\left(y_1+y_2-\frac{\ell_1+\ell_2}{2}\right)\\
&\quad+\frac{2(\alpha+1)}{\ell_2-\ell_1}\int_0^1(1-\zeta)^{\alpha}\lambda'\left(y_1+y_2-\left(\frac{1+\zeta}{2}\ell_1+\frac{1-\zeta}{2}\ell_2\right)\right)\mathrm{d}\zeta\\
&=-\frac{2}{(\ell_2-\ell_1)}\lambda'\left(y_1+y_2-\frac{\ell_1+\ell_2}{2}\right)-\frac{4(\alpha+1)}{(\ell_2-\ell_1)^2}\lambda\left(y_1+y_2-\frac{\ell_1+\ell_2}{2}\right)\\
&\quad+\frac{4\alpha(\alpha+1)}{(\ell_2-\ell_1)^2}\int_0^1(1-\zeta)^{\alpha-1}\lambda\left(y_1+y_2-\left(\frac{1+\zeta}{2}\ell_1+\frac{1-\zeta}{2}\ell_2\right)\right)\mathrm{d}\zeta\\
&=-\frac{2}{(\ell_2-\ell_1)}\lambda'\left(y_1+y_2-\frac{\ell_1+\ell_2}{2}\right)-\frac{4(\alpha+1)}{(\ell_2-\ell_1)^2}\lambda\left(y_1+y_2-\frac{\ell_1+\ell_2}{2}\right)\\
&\quad+\frac{2^{\alpha+2}\Gamma(\alpha+2)}{(\ell_2-\ell_1)^{\alpha+2}}\left(I^{\alpha:\psi}_{\psi^{-1}(y_1+y_2-((\ell_1+\ell_2)/2))^{+}}\right)\left[\lambda\circ\psi\left(\psi^{-1}(y_1+y_2-\ell_1)\right)\right],\\
I_2&=\int_0^1(1-\zeta)^{\alpha+1}\lambda''\left(y_1+y_2-\left(\frac{1-\zeta}{2}\ell_1+\frac{1+\zeta}{2}\ell_2\right)\right)\mathrm{d}\zeta\\
&=\frac{2}{(\ell_2-\ell_1)}\lambda'\left(y_1+y_2-\frac{\ell_1+\ell_2}{2}\right)\\
&\quad-\frac{2(\alpha+1)}{\ell_2-\ell_1}\int_0^1(1-\zeta)^{\alpha}\lambda'\left(y_1+y_2-\left(\frac{1-\zeta}{2}\ell_1+\frac{1+\zeta}{2}\ell_2\right)\right)\mathrm{d}\zeta
\end{aligned}\tag{73}$$

$$
\begin{aligned}
&= \frac{2}{(\ell_2-\ell_1)}\lambda'\left(y_1+y_2-\frac{\ell_1+\ell_2}{2}\right)-\frac{4(\alpha+1)}{(\ell_2-\ell_1)^2}\lambda\left(y_1+y_2-\frac{\ell_1+\ell_2}{2}\right)\\
&\quad+\frac{4\alpha(\alpha+1)}{(\ell_2-\ell_1)^2}\int_0^1(1-\zeta)^{\alpha-1}\lambda\left(y_1+y_2-\left(\frac{1-\zeta}{2}\ell_1+\frac{1+\zeta}{2}\ell_2\right)\right)\mathrm{d}\zeta\\
&= \frac{2}{(\ell_2-\ell_1)}\lambda'\left(y_1+y_2-\frac{\ell_1+\ell_2}{2}\right)-\frac{4(\alpha+1)}{(\ell_2-\ell_1)^2}\lambda\left(y_1+y_2-\frac{\ell_1+\ell_2}{2}\right)\\
&\quad+\frac{2^{\alpha+2}\Gamma(\alpha+2)}{(\ell_2-\ell_1)^{\alpha+2}}\left(I^{\alpha:\psi}_{\psi^{-1}(y_1+y_2-((\ell_1+\ell_2)/2))^-}\right)\left[\lambda\circ\psi\left(\psi^{-1}(y_1+y_2-\ell_2)\right)\right].
\end{aligned}
\tag{74}
$$

Substituting (73) and (74) in (72), we get (71). □

Corollary 1. *If we set $\ell_1 = y_1$ and $\ell_2 = y_2$, we get*

$$
\begin{aligned}
&\frac{2^{\alpha-1}\Gamma(\alpha+1)}{(y_2-y_1)^\alpha}\left\{\left(I^{\alpha:\psi}_{\psi^{-1}((y_1+y_2)/2)^+}\right)\left(\lambda\circ\psi\left(\psi^{-1}(y_2)\right)\right)\right.\\
&\quad\left.+\left(I^{\alpha:\psi}_{\psi^{-1}((y_1+y_2)/2)^-}\right)\left(\lambda\circ\psi\left(\psi^{-1}(y_1)\right)\right)\right\}-\lambda\left(\frac{y_1+y_2}{2}\right)\\
&=\frac{(y_2-y_1)^2}{8(\alpha+1)}\left[\int_0^1(1-\zeta)^{\alpha+1}\lambda''\left(\frac{1+\zeta}{2}y_1+\frac{1-\zeta}{2}y_2\right)\mathrm{d}\zeta\right.\\
&\quad\left.+\int_0^1(1-\zeta)^{\alpha+1}\lambda''\left(\frac{1-\zeta}{2}y_1+\frac{1+\zeta}{2}y_2\right)\mathrm{d}\zeta\right].
\end{aligned}
\tag{75}
$$

Remark 17. If we set $\psi(\gamma)=\gamma$ in Lemma 4, we get Lemma 2 of [29].

Moreover, if we set $\ell_1 = y_1$ and $\ell_2 = y_2$, we obtain Lemma 1 of [32].

Remark 18. For $\psi(\gamma)=\gamma$, $\alpha=1$, $\ell_1=y_1$, and $\ell_2=y_2$ in Lemma 4, it reduces to Lemma 2 proved in [32].

Theorem 10. *If (A_1) is satisfied and $|\lambda''|$ is a convex function on $[y_1, y_2]$, then*

$$
\begin{aligned}
&\left|\frac{2^{\alpha-1}\Gamma(\alpha+1)}{(\ell_2-\ell_1)^\alpha}\left\{\left(I^{\alpha:\psi}_{\psi^{-1}(y_1+y_2-((\ell_1+\ell_2)/2))^+}\right)\left(\lambda\circ\psi\left(\psi^{-1}(y_1+y_2-\ell_1)\right)\right)\right.\right.\\
&\quad\left.\left.+\left(I^{\alpha:\psi}_{\psi^{-1}(y_1+y_2-((\ell_1+\ell_2)/2))^-}\right)\left(\lambda\circ\psi\left(\psi^{-1}(y_1+y_2-\ell_2)\right)\right)\right\}-\lambda\left(y_1+y_2-\frac{\ell_1+\ell_2}{2}\right)\right|\\
&\le\frac{(\ell_2-\ell_1)^2}{4(\alpha+1)(\alpha+2)}\left\{|\lambda''(y_1)|+|\lambda''(y_2)|-\left(\frac{|\lambda''(\ell_1)|+|\lambda''(\ell_2)|}{2}\right)\right\}.
\end{aligned}
\tag{76}
$$

Proof. By using Lemma 4, properties of modulus, and Jensen–Mercer inequality, we have

$$\begin{aligned}
&\left|\frac{2^{\alpha-1}\Gamma(\alpha+1)}{(\ell_2-\ell_1)^{\alpha}}\left\{\left(I^{\alpha:\psi}_{\psi^{-1}(y_1+y_2-((\ell_1+\ell_2)/2))^{+}}\right)\left(\lambda\circ\psi\left(\psi^{-1}(y_1+y_2-\ell_1)\right)\right)\right.\right.\\
&\quad\left.\left.+\left(I^{\alpha:\psi}_{\psi^{-1}(y_1+y_2-((\ell_1+\ell_2)/2))^{-}}\right)\left(\lambda\circ\psi\left(\psi^{-1}(y_1+y_2-\ell_2)\right)\right)\right\}-\lambda\left(y_1+y_2-\frac{\ell_1+\ell_2}{2}\right)\right|\\
&\le\frac{(\ell_2-\ell_1)^2}{8(\alpha+1)}\left[\int_0^1(1-\zeta)^{\alpha+1}\left|\lambda''\left(y_1+y_2-\left(\frac{1+\zeta}{2}\ell_1+\frac{1-\zeta}{2}\ell_2\right)\right)\right|\mathrm{d}\zeta\right.\\
&\quad\left.+\int_0^1(1-\zeta)^{\alpha+1}\left|\lambda''\left(y_1+y_2-\left(\frac{1-\zeta}{2}\ell_1+\frac{1+\zeta}{2}\ell_2\right)\right)\right|\mathrm{d}\zeta\right]\\
&\le\frac{(\ell_2-\ell_1)^2}{8(\alpha+1)}\left[\int_0^1(1-\zeta)^{\alpha+1}\left\{\left|\lambda''(y_1)\right|+\left|\lambda''(y_2)\right|-\left(\frac{1+\zeta}{2}\left|\lambda''(\ell_1)\right|+\frac{1-\zeta}{2}\left|\lambda''(\ell_2)\right|\right)\right\}\mathrm{d}\zeta\right.\\
&\quad\left.+\int_0^1(1-\zeta)^{\alpha+1}\left\{\left|\lambda''(y_1)\right|+\left|\lambda''(y_2)\right|-\left(\frac{1-\zeta}{2}\left|\lambda''(\ell_1)\right|+\frac{1+\zeta}{2}\left|\lambda''(\ell_2)\right|\right)\right\}\mathrm{d}\zeta\right],
\end{aligned}\tag{77}$$

and after integration, we get required result. □

Corollary 2. *If we set $\ell_1 = y_1$ and $\ell_2 = y_2$ in Theorem 10, we get*

$$\begin{aligned}
&\left|\frac{2^{\alpha-1}\Gamma(\alpha+1)}{(y_2-y_1)^{\alpha}}\left\{\left(I^{\alpha:\psi}_{\psi^{-1}((y_1+y_2)/2)^{+}}\right)\left(\lambda\circ\psi\left(\psi^{-1}(y_2)\right)\right)\right.\right.\\
&\quad\left.\left.+\left(I^{\alpha:\psi}_{\psi^{-1}((y_1+y_2)/2)^{-}}\right)\left(\lambda\circ\psi\left(\psi^{-1}(y_1)\right)\right)\right\}-\lambda\left(\frac{y_1+y_2}{2}\right)\right|\\
&\le\frac{(y_2-y_1)^2}{4(\alpha+1)(\alpha+2)}\left\{\left(\frac{\left|\lambda''(y_1)\right|+\left|\lambda''(y_2)\right|}{2}\right)\right\}.
\end{aligned}\tag{78}$$

Remark 19. If we set $\psi(\gamma)=\gamma$ in Theorem 10, we obtain Theorem 5 of [29].

Moreover, if we set $\ell_1 = y_1$ and $\ell_2 = y_2$, we get Theorem 5 of [32].

Corollary 3. *If we set $\psi(\gamma)=\gamma$, $\ell_1 = y_1$, $\ell_2 = y_2$, and $\alpha = 1$ in Theorem 10, we get Proposition 1 of [33]:*

$$\left|\frac{1}{y_2-y_1}\int_{y_1}^{y_2}\lambda(x)\mathrm{d}x-\lambda\left(\frac{y_1+y_2}{2}\right)\right|\le\frac{(y_2-y_1)^2}{24}\left\{\left(\frac{\left|\lambda''(y_1)\right|+\left|\lambda''(y_2)\right|}{2}\right)\right\}.\tag{79}$$

Theorem 11. *If (A_1) is satisfied and $|\lambda''|^q$ is convex function, then*

$$\begin{aligned}
&\left|\frac{2^{\alpha-1}\Gamma(\alpha+1)}{(\ell_2-\ell_1)^{\alpha}}\left\{\left(I^{\alpha:\psi}_{\psi^{-1}(y_1+y_2-((\ell_1+\ell_2)/2))^{+}}\right)\left(\lambda\circ\psi\left(\psi^{-1}(y_1+y_2-\ell_1)\right)\right)\right.\right.\\
&\quad\left.\left.+\left(I^{\alpha:\psi}_{\psi^{-1}(y_1+y_2-((\ell_1+\ell_2)/2))^{-}}\right)\left(\lambda\circ\psi\left(\psi^{-1}(y_1+y_2-\ell_2)\right)\right)\right\}-\lambda\left(y_1+y_2-\frac{\ell_1+\ell_2}{2}\right)\right|\\
&\le\frac{(\ell_2-\ell_1)^2}{8(\alpha+1)}\left(\frac{1}{p(\alpha+1)+1}\right)^{1/p}\left[\left(\left|\lambda''(y_1)\right|^q+\left|\lambda''(y_2)\right|^q-\frac{\left|3\lambda''(\ell_1)\right|^q+\left|\lambda''(\ell_2)\right|^q}{4}\right)^{1/q}\right.\\
&\quad\left.+\left(\left|\lambda''(y_1)\right|^q+\left|\lambda''(y_2)\right|^q-\frac{\left|\lambda''(\ell_1)\right|^q+3\left|\lambda''(\ell_2)\right|^q}{4}\right)^{1/q}\right],
\end{aligned}\tag{80}$$

where $q > 1$ *and* $(1/p) + (1/q) = 1$ *for all* $\ell_1, \ell_2 \in [y_1, y_2]$.

Proof. From Lemma 4, Hölder and Jensen–Mercer inequalities, the fact that $|\lambda''|^q$ is convex function, and properties of modulus, we have

$$
\begin{aligned}
&\left|\frac{2^{\alpha-1}\Gamma(\alpha+1)}{(\ell_2-\ell_1)^{\alpha}}\left\{\left(I^{\alpha:\psi}_{\psi^{-1}\left(y_1+y_2-\frac{\ell_1+\ell_2}{2}\right)^{+}}\right)\left(\lambda\circ\psi\left(\psi^{-1}(y_1+y_2-\ell_1)\right)\right)\right.\right.\\
&\quad\left.\left.+\left(I^{\alpha:\psi}_{\psi^{-1}(y_1+y_2-((\ell_1+\ell_2)/2))^{-}}\right)\left(\lambda\circ\psi\left(\psi^{-1}(y_1+y_2-\ell_2)\right)\right)\right\}-\lambda\left(y_1+y_2-\frac{\ell_1+\ell_2}{2}\right)\right|\\
&\le\frac{(\ell_2-\ell_1)^2}{8(\alpha+1)}\left[\int_0^1(1-\zeta)^{\alpha+1}\left|\lambda''\left(y_1+y_2-\left(\frac{1+\zeta}{2}\ell_1+\frac{1-\zeta}{2}\ell_2\right)\right)\right|\mathrm{d}\zeta\right.\\
&\quad\left.+\int_0^1(1-\zeta)^{\alpha+1}\left|\lambda''\left(y_1+y_2-\left(\frac{1-\zeta}{2}\ell_1+\frac{1+\zeta}{2}\ell_2\right)\right)\right|\mathrm{d}\zeta\right]\\
&\le\frac{(\ell_2-\ell_1)^2}{8(\alpha+1)}\left[\left(\int_0^1(1-\zeta)^{p(\alpha+1)}\mathrm{d}\zeta\right)^{1/p}\left(\int_0^1\left|\lambda''\left(y_1+y_2-\left(\frac{1+\zeta}{2}\ell_1+\frac{1-\zeta}{2}\ell_2\right)\right)\right|^q\mathrm{d}\zeta\right)^{1/q}\right.\\
&\quad\left.+\left(\int_0^1(1-\zeta)^{p(\alpha+1)}\mathrm{d}\zeta\right)^{1/p}\left(\int_0^1\left|\lambda''\left(y_1+y_2-\left(\frac{1-\zeta}{2}\ell_1+\frac{1+\zeta}{2}\ell_2\right)\right)\right|^q\mathrm{d}\zeta\right)^{1/q}\right]\\
&\le\frac{(\ell_2-\ell_1)^2}{8(\alpha+1)}\left(\int_0^1(1-\zeta)^{p(\alpha+1)}\mathrm{d}\zeta\right)^{1/p}\\
&\quad\times\left[\left(\int_0^1\left(|\lambda''(y_1)|^q+|\lambda''(y_2)|^q-\frac{1+\zeta}{2}|\lambda''(\ell_1)|^q-\frac{1-\zeta}{2}|\lambda''(\ell_2)|^q\right)\mathrm{d}\zeta\right)^{1/q}\right.\\
&\quad\left.+\left(\int_0^1\left(|\lambda''(y_1)|^q+|\lambda''(y_2)|^q-\frac{1-\zeta}{2}|\lambda''(\ell_1)|^q-\frac{1+\zeta}{2}|\lambda''(\ell_2)|^q\right)\mathrm{d}\zeta\right)^{1/q}\right]\\
&=\frac{(\ell_2-\ell_1)^2}{8(\alpha+1)}\left(\frac{1}{p(\alpha+1)+1}\right)^{1/p}\left[\left(|\lambda''(y_1)|^q+|\lambda''(y_2)|^q-\frac{|3\lambda''(\ell_1)|^q+|\lambda''(\ell_2)|^q}{4}\right)^{1/q}\right.\\
&\quad\left.+\left(\left|\lambda''(y_1)|^q+|\lambda''(y_2)|^q-\frac{|\lambda''(\ell_1)|^q+3|\lambda''(\ell_2)|^q}{4}\right|^q\right)\right)^{1/q}\right].
\end{aligned}
\tag{81}
$$

□

Remark 20. If we set $\psi(\gamma) = \gamma$ in Theorem 11, we get Theorem 6 of [29].

Lemma 5. *If* (A_1) *satisfied and* λ: $[y_1, y_2] \longrightarrow \mathfrak{R}$ *is a twice differentiable function on* $L_1[y_1, y_2]$, *then*

$$\begin{aligned}
&\frac{2^{\alpha-1}\Gamma(\alpha+1)}{(\ell_2-\ell_1)^{\alpha}}\left\{\left(I^{\alpha:\psi}_{\psi^{-1}(y_1+y_2-((\ell_1+\ell_2)/2))^{+}}\right)\left(\lambda\circ\psi\left(\psi^{-1}(y_1+y_2-\ell_1)\right)\right)\right.\\
&\quad\left.+\left(I^{\alpha:\psi}_{\psi^{-1}(y_1+y_2-((\ell_1+\ell_2)/2))^{-}}\right)\left(\lambda\circ\psi\left(\psi^{-1}(y_1+y_2-\ell_2)\right)\right)\right\}-\lambda\left(y_1+y_2-\frac{\ell_1+\ell_2}{2}\right)\\
&=\frac{(\ell_2-\ell_1)^2}{8(\alpha+1)}\left[\int_0^1\zeta^{\alpha+1}\lambda''\left(y_1+y_2-\left(\frac{2-\zeta}{2}\ell_1+\frac{\zeta}{2}\ell_2\right)\right)\mathrm{d}\zeta\right.\\
&\quad\left.+\int_0^1\zeta^{\alpha+1}\lambda''\left(y_1+y_2-\left(\frac{\zeta}{2}\ell_1+\frac{2-\zeta}{2}\ell_2\right)\right)\mathrm{d}\zeta\right].
\end{aligned}\tag{82}$$

Proof. It suffices to note that

$$I=\frac{(\ell_2-\ell_1)^2}{8(\alpha+1)}\{I_1+I_2\},\tag{83}$$

where

$$\begin{aligned}
I_1&=\int_0^1\zeta^{\alpha+1}\lambda''\left(y_1+y_2-\left(\frac{2-\zeta}{2}\ell_1+\frac{\zeta}{2}\ell_2\right)\right)\mathrm{d}\zeta\\
&=-\frac{2}{(\ell_2-\ell_1)}\lambda'\left(y_1+y_2-\frac{\ell_1+\ell_2}{2}\right)\\
&\quad+\frac{2(\alpha+1)}{\ell_2-\ell_1}\int_0^1\zeta^{\alpha}\lambda'\left(y_1+y_2-\left(\frac{2-\zeta}{2}\ell_1+\frac{\zeta}{2}\ell_2\right)\right)\mathrm{d}\zeta\\
&=-\frac{2}{(\ell_2-\ell_1)}\lambda'\left(y_1+y_2-\frac{\ell_1+\ell_2}{2}\right)-\frac{4(\alpha+1)}{(\ell_2-\ell_1)^2}\lambda\left(y_1+y_2-\frac{\ell_1+\ell_2}{2}\right)\\
&\quad+\frac{4\alpha(\alpha+1)}{(\ell_2-\ell_1)^2}\int_0^1\zeta^{\alpha-1}\lambda\left(y_1+y_2-\left(\frac{2-\zeta}{2}\ell_1+\frac{\zeta}{2}\ell_2\right)\right)\mathrm{d}\zeta\\
&=-\frac{2}{(\ell_2-\ell_1)}\lambda'\left(y_1+y_2-\frac{\ell_1+\ell_2}{2}\right)-\frac{4(\alpha+1)}{(\ell_2-\ell_1)^2}\lambda\left(y_1+y_2-\frac{\ell_1+\ell_2}{2}\right)\\
&\quad+\frac{2^{\alpha+2}\Gamma(\alpha+2)}{(\ell_2-\ell_1)^{\alpha+2}}\left(I^{\alpha:\psi}_{\psi^{-1}(y_1+y_2-((\ell_1+\ell_2)/2))^{+}}\right)\left[\lambda\circ\psi\left(\psi^{-1}(y_1+y_2-\ell_1)\right)\right],
\end{aligned}\tag{84}$$

$$\begin{aligned}
I_2&=\int_0^1\zeta^{\alpha+1}\lambda''\left(y_1+y_2-\left(\frac{\zeta}{2}\ell_1+\frac{2-\zeta}{2}\ell_2\right)\right)\mathrm{d}\zeta\\
&=\frac{2}{(\ell_2-\ell_1)}\lambda'\left(y_1+y_2-\frac{\ell_1+\ell_2}{2}\right)\\
&\quad-\frac{2(\alpha+1)}{\ell_2-\ell_1}\int_0^1\zeta^{\alpha}\lambda'\left(y_1+y_2-\left(\frac{\zeta}{2}\ell_1+\frac{2-\zeta}{2}\ell_2\right)\right)\mathrm{d}\zeta\\
&=\frac{2}{(\ell_2-\ell_1)}\lambda'\left(y_1+y_2-\frac{\ell_1+\ell_2}{2}\right)-\frac{4(\alpha+1)}{(\ell_2-\ell_1)^2}\lambda\left(y_1+y_2-\frac{\ell_1+\ell_2}{2}\right)\\
&\quad+\frac{4\alpha(\alpha+1)}{(\ell_2-\ell_1)^2}\int_0^1\zeta^{\alpha-1}\lambda\left(y_1+y_2-\left(\frac{\zeta}{2}\ell_1+\frac{2-\zeta}{2}\ell_2\right)\right)\mathrm{d}\zeta\\
&=\frac{2}{(\ell_2-\ell_1)}\lambda'\left(y_1+y_2-\frac{\ell_1+\ell_2}{2}\right)-\frac{4(\alpha+1)}{(\ell_2-\ell_1)^2}\lambda\left(y_1+y_2-\frac{\ell_1+\ell_2}{2}\right)\\
&\quad+\frac{2^{\alpha+2}\Gamma(\alpha+2)}{(\ell_2-\ell_1)^{\alpha+2}}\left(I^{\alpha:\psi}_{\psi^{-1}(y_1+y_2-((\ell_1+\ell_2)/2))^{-}}\right)\left[\lambda\circ\psi\left(\psi^{-1}(y_1+y_2-\ell_2)\right)\right].
\end{aligned}\tag{85}$$

Substituting (84) and (85) in (83), we get (82). □

Corollary 4. *If we set $\ell_1 = y_1$ and $\ell_2 = y_2$, we get*

$$\begin{aligned}&\frac{2^{\alpha-1}\Gamma(\alpha+1)}{(y_2-y_1)^{\alpha}}\left\{\left(I^{\alpha:\psi}_{\psi^{-1}((y_1+y_2)/2)^{+}}\right)\left(\lambda\circ\psi\left(\psi^{-1}(y_2)\right)\right)\right.\\&\left.+\left(I^{\alpha:\psi}_{\psi^{-1}((y_1+y_2)/2)^{-}}\right)\left(\lambda\circ\psi\left(\psi^{-1}(y_1)\right)\right)\right\}-\lambda\left(\frac{y_1+y_2}{2}\right)\\&=\frac{(y_2-y_1)^2}{8(\alpha+1)}\left[\int_0^1\zeta^{\alpha+1}\lambda''\left(\frac{2-\zeta}{2}y_1+\frac{\zeta}{2}y_2\right)\mathrm{d}\zeta+\int_0^1\zeta^{\alpha+1}\lambda''\left(\frac{\zeta}{2}y_1+\frac{2-\zeta}{2}y_2\right)\mathrm{d}\zeta\right].\end{aligned}\tag{86}$$

Corollary 5. *If we set $\psi(\gamma)=\gamma$, we get*

$$\begin{aligned}&\frac{2^{\alpha-1}\Gamma(\alpha+1)}{(\ell_2-\ell_1)^{\alpha}}\left\{\left(I^{\alpha}_{(y_1+y_2-((\ell_1+\ell_2)/2))^{+}}\right)(\lambda(y_1+y_2-\ell_1))\right.\\&\left.+\left(I^{\alpha}_{(y_1+y_2-((\ell_1+\ell_2)/2))^{-}}\right)(\lambda(y_1+y_2-\ell_2))\right\}-\lambda\left(y_1+y_2-\frac{\ell_1+\ell_2}{2}\right)\\&=\frac{(\ell_2-\ell_1)^2}{8(\alpha+1)}\left[\int_0^1\zeta^{\alpha+1}\lambda''\left(y_1+y_2-\left(\frac{2-\zeta}{2}\ell_1+\frac{\zeta}{2}\ell_2\right)\right)\mathrm{d}\zeta\right.\\&\left.+\int_0^1\zeta^{\alpha+1}\lambda''\left(y_1+y_2-\left(\frac{\zeta}{2}\ell_1+\frac{2-\zeta}{2}\ell_2\right)\right)\mathrm{d}\zeta\right].\end{aligned}\tag{87}$$

Moreover, if we set $\ell_1 = y_1$ and $\ell_2 = y_2$, we get

$$\begin{aligned}&\frac{2^{\alpha-1}\Gamma(\alpha+1)}{(y_2-y_1)^{\alpha}}\left\{I^{\alpha}_{((y_1+y_2)/2)^{+}}\lambda(y_2)+I^{\alpha}_{((y_1+y_2)/2)^{-}}\lambda(y_1)\right\}-\lambda\left(\frac{y_1+y_2}{2}\right)\\&=\frac{(y_2-y_1)^2}{8(\alpha+1)}\left[\int_0^1\zeta^{\alpha+1}\lambda''\left(\frac{2-\zeta}{2}y_1+\frac{\zeta}{2}y_2\right)\mathrm{d}\zeta+\int_0^1\zeta^{\alpha+1}\lambda''\left(\frac{\zeta}{2}y_1+\frac{2-\zeta}{2}y_2\right)\mathrm{d}\zeta\right].\end{aligned}\tag{88}$$

Remark 21. By using Lemma 5, we can get the same results of Theorems 10 and 11, so we omit their proof here.

Lemma 6. *If (A_1) is satisfied and λ: $[y_1, y_2] \longrightarrow \mathfrak{R}$ is a twice differentiable function on $L_1[y_1, y_2]$, then*

$$\begin{aligned}&\frac{2^{\alpha-2}\Gamma(\alpha)}{(\ell_2-\ell_1)^{\alpha-1}}\left\{\left(I^{\alpha-1:\psi}_{\psi^{-1}(y_1+y_2-((\ell_1+\ell_2)/2))^{+}}\right)\left(\lambda\circ\psi\left(\psi^{-1}(y_1+y_2-\ell_1)\right)\right)\right.\\&\left.+\left(I^{\alpha-1:\psi}_{\psi^{-1}(y_1+y_2-((\ell_1+\ell_2)/2))^{-}}\right)\left(\lambda\circ\psi\left(\psi^{-1}(y_1+y_2-\ell_2)\right)\right)\right\}-\lambda\left(y_1+y_2-\frac{\ell_1+\ell_2}{2}\right)\\&=\frac{(\ell_2-\ell_1)^2}{\alpha\cdot 2^{2-\alpha}}\left[\int_0^{1/2}\zeta^{\alpha}\lambda''(y_1+y_2-(\zeta\ell_2+(1-\zeta)\ell_1))\mathrm{d}\zeta\right.\\&\left.+\int_{1/2}^1(1-\zeta)^{\alpha}\lambda''(y_1+y_2-(\zeta\ell_2+(1-\zeta)\ell_1))\mathrm{d}\zeta\right].\end{aligned}\tag{89}$$

Proof. It suffices to note that

$$I = \frac{(\ell_2 - \ell_1)^2}{\alpha \cdot 2^{1-\alpha}} \{I_1 + I_2\}, \tag{90}$$

where

$$\begin{aligned}
I_1 &= \int_0^{1/2} \zeta^\alpha \lambda''(y_1 + y_2 - (\zeta\ell_2 + (1-\zeta)\ell_1))\mathrm{d}\zeta \\
&= -\frac{1}{2^\alpha(\ell_2 - \ell_1)}\lambda'\left(y_1 + y_2 - \frac{\ell_1 + \ell_2}{2}\right) \\
&\quad + \frac{\alpha}{\ell_2 - \ell_1}\int_0^{1/2} \zeta^{\alpha-1}\lambda'(y_1 + y_2 - ((1-\zeta)\ell_1 + \zeta\ell_2))\mathrm{d}\zeta \\
&= -\frac{1}{2^\alpha(\ell_2 - \ell_1)}\lambda'\left(y_1 + y_2 - \frac{\ell_1 + \ell_2}{2}\right) - \frac{\alpha}{2^{\alpha-1}(\ell_2 - \ell_1)^2}\lambda\left(y_1 + y_2 - \frac{\ell_1 + \ell_2}{2}\right) \\
&\quad + \frac{\alpha(\alpha-1)}{(\ell_2 - \ell_1)^2}\int_0^{1/2} \zeta^{\alpha-2}\lambda(y_1 + y_2 - ((1-\zeta)\ell_1 + \zeta\ell_2))\mathrm{d}\zeta \\
&= -\frac{1}{2^\alpha(\ell_2 - \ell_1)}\lambda'\left(y_1 + y_2 - \frac{\ell_1 + \ell_2}{2}\right) - \frac{\alpha}{2^{\alpha-1}(\ell_2 - \ell_1)^2}\lambda\left(y_1 + y_2 - \frac{\ell_1 + \ell_2}{2}\right) \\
&\quad + \frac{\Gamma(\alpha+1)}{(\ell_2 - \ell_1)^{\alpha+1}}\left(I^{\alpha-1:\,\psi}_{\psi^{-1}(y_1+y_2-((\ell_1+\ell_2)/2))^+}\right)\left[\lambda\circ\psi\left(\psi^{-1}(y_1 + y_2 - \ell_1)\right)\right],
\end{aligned} \tag{91}$$

$$\begin{aligned}
I_2 &= \int_{1/2}^1 (1-\zeta)^\alpha \lambda''(y_1 + y_2 - (\zeta\ell_2 + (1-\zeta)\ell_1))\mathrm{d}\zeta \\
&= \frac{1}{2^\alpha(\ell_2 - \ell_1)}\lambda'\left(y_1 + y_2 - \frac{\ell_1 + \ell_2}{2}\right) \\
&\quad - \frac{\alpha}{\ell_2 - \ell_1}\int_{1/2}^1 (1-\zeta)^{\alpha-1}\lambda'(y_1 + y_2 - ((1-\zeta)\ell_1 + \zeta\ell_2))\mathrm{d}\zeta \\
&= \frac{1}{2^\alpha(\ell_2 - \ell_1)}\lambda'\left(y_1 + y_2 - \frac{\ell_1 + \ell_2}{2}\right) + \frac{\alpha}{2^{\alpha-1}(\ell_2 - \ell_1)^2}\lambda\left(y_1 + y_2 - \frac{\ell_1 + \ell_2}{2}\right) \\
&\quad + \frac{\alpha(\alpha-1)}{(\ell_2 - \ell_1)^2}\int_{1/2}^1 (1-\zeta)^{\alpha-2}\lambda(y_1 + y_2 - ((1-\zeta)\ell_1 + \zeta\ell_2))\mathrm{d}\zeta \\
&= \frac{1}{2^\alpha(\ell_2 - \ell_1)}\lambda'\left(y_1 + y_2 - \frac{\ell_1 + \ell_2}{2}\right) - \frac{\alpha}{2^{\alpha-1}(\ell_2 - \ell_1)^2}\lambda\left(y_1 + y_2 - \frac{\ell_1 + \ell_2}{2}\right) \\
&\quad + \frac{\Gamma(\alpha+1)}{(\ell_2 - \ell_1)^{\alpha+1}}\left(I^{\alpha-1:\,\psi}_{\psi^{-1}(y_1+y_2-((\ell_1+\ell_2)/2))^-}\right)\left[\lambda\circ\psi\left(\psi^{-1}(y_1 + y_2 - \ell_2)\right)\right].
\end{aligned} \tag{92}$$

Substituting (91) and (92) in (90), we get (89). □

Corollary 6. *If we set $\ell_1 = y_1$ and $\ell_2 = y_2$ in Lemma 6, we get*

$$\frac{2^{\alpha-2}\Gamma(\alpha)}{(y_2-y_1)^{\alpha-1}}\left\{\left(I^{\alpha:\psi}_{\psi^{-1}((y_1+y_2)/2)^+}\right)\left(\lambda\circ\psi\left(\psi^{-1}(y_2)\right)\right)\right.$$
$$\left.+\left(I^{\alpha:\psi}_{\psi^{-1}((y_1+y_2)/2)^-}\right)\left(\lambda\circ\psi\left(\psi^{-1}(y_1)\right)\right)\right\}-\lambda\left(\frac{y_1+y_2}{2}\right) \tag{93}$$
$$=\frac{(y_2-y_1)^2}{\alpha\cdot 2^{2-\alpha}}\left[\int_0^{1/2}\zeta^\alpha\lambda''(\zeta y_1+(1-\zeta)y_2)\mathrm{d}\zeta+\int_{1/2}^1(1-\zeta)^\alpha\lambda''(\zeta y_1+(1-\zeta)y_2)\mathrm{d}\zeta\right].$$

Corollary 7. *If we set $\psi(\gamma)=\gamma$ in Lemma 6, we get*

$$\frac{2^{\alpha-2}\Gamma(\alpha)}{(\ell_2-\ell_1)^{\alpha-1}}\left\{\left(J^\alpha_{(y_1+y_2-((\ell_1+\ell_2)/2))^+}\right)(\lambda(y_1+y_2-\ell_1))\right.$$
$$\left.+\left(J^\alpha_{(y_1+y_2-((\ell_1+\ell_2)/2))^-}\right)(\lambda(y_1+y_2-\ell_2))\right\}-\lambda\left(y_1+y_2-\frac{\ell_1+\ell_2}{2}\right)$$
$$=\frac{(\ell_2-\ell_1)^2}{\alpha\cdot 2^{2-\alpha}}\left[\int_0^{1/2}\zeta^\alpha\lambda''(y_1+y_2-(\zeta\ell_2+(1-\zeta)\ell_1))\mathrm{d}\zeta\right. \tag{94}$$
$$\left.+\int_{1/2}^1(1-\zeta)^\alpha\lambda''(y_1+y_2-(\zeta\ell_2+(1-\zeta)\ell_1))\mathrm{d}\zeta\right].$$

Moreover, if we set $\ell_1=y_1$ and $\ell_2=y_2$, we obtain Lemma 2.1 of [34] for $m=1$.

Theorem 12. *If (A_1) is satisfied and $|\lambda''|$ is a convex function on $[y_1,y_2]$, then*

$$\left|\frac{2^{\alpha-2}\Gamma(\alpha)}{(\ell_2-\ell_1)^{\alpha-1}}\left\{\left(I^{\alpha-1:\psi}_{\psi^{-1}(y_1+y_2-((\ell_1+\ell_2)/2))^+}\right)\left(\lambda\circ\psi\left(\psi^{-1}(y_1+y_2-\ell_1)\right)\right)\right.\right.$$
$$\left.\left.+\left(I^{\alpha-1:\psi}_{\psi^{-1}(y_1+y_2-((\ell_1+\ell_2)/2))^-}\right)\left(\lambda\circ\psi\left(\psi^{-1}(y_1+y_2-\ell_2)\right)\right)\right\}-\lambda\left(y_1+y_2-\frac{\ell_1+\ell_2}{2}\right)\right| \tag{95}$$
$$\le\frac{(\ell_2-\ell_1)^2}{4\alpha(\alpha+1)}\left\{|\lambda''(y_1)|+|\lambda''(y_2)|-\frac{|\lambda''(\ell_1)|+|\lambda''(\ell_2)|}{2}\right\}.$$

Proof. By using Lemma 6, properties of modulus, and Jensen–Mercer inequality, we have

$$\begin{aligned}
&\left|\frac{2^{\alpha-2}\Gamma(\alpha)}{(\ell_2-\ell_1)^{\alpha-1}}\left\{\left(I^{\alpha-1:\,\psi}_{\psi^{-1}(y_1+y_2-((\ell_1+\ell_2)/2))^+}\right)\left(\lambda\circ\psi\left(\psi^{-1}(y_1+y_2-\ell_1)\right)\right)\right.\right.\\
&\quad\left.\left.+\left(I^{\alpha-1:\,\psi}_{\psi^{-1}(y_1+y_2-((\ell_1+\ell_2)/2))^-}\right)\left(\lambda\circ\psi\left(\psi^{-1}(y_1+y_2-\ell_2)\right)\right)\right\}-\lambda\left(y_1+y_2-\frac{\ell_1+\ell_2}{2}\right)\right|\\
&\le\frac{(\ell_2-\ell_1)^2}{\alpha\cdot 2^{2-\alpha}}\left[\int_0^{1/2}\zeta^\alpha\left|\lambda''(y_1+y_2-((1-\zeta)\ell_1+\zeta\ell_2))\right|\mathrm{d}\zeta\right.\\
&\quad\left.+\int_{1/2}^1(1-\zeta)^\alpha\left|\lambda''(y_1+y_2-((1-\zeta)\ell_1+\zeta\ell_2))\right|\mathrm{d}\zeta\right]\\
&\le\frac{(\ell_2-\ell_1)^2}{\alpha\cdot 2^{2-\alpha}}\left[\int_0^{1/2}\zeta^\alpha\left\{\left|\lambda''(y_1)\right|+\left|\lambda''(y_2)\right|-\left((1-\zeta)\left|\lambda''(\ell_1)\right|+\zeta\left|\lambda''(\ell_2)\right|\right)\right\}\mathrm{d}\zeta\right.\\
&\quad\left.+\int_{1/2}^1(1-\zeta)^\alpha\left\{\left|\lambda''(y_1)\right|+\left|\lambda''(y_2)\right|-\left((1-\zeta)\left|\lambda''(\ell_1)\right|+\zeta\left|\lambda''(\ell_2)\right|\right)\right\}\mathrm{d}\zeta\right],
\end{aligned}\tag{96}$$

and after integration, we get required result. □

Corollary 8. *If we set $\ell_1 = y_1$ and $\ell_2 = y_2$ in Theorem 12, we get*

$$\begin{aligned}
&\left|\frac{2^{\alpha-2}\Gamma(\alpha)}{(y_2-y_1)^{\alpha-1}}\left\{\left(I^{\alpha-1:\,\psi}_{\psi^{-1}((y_1+y_2)/2)^+}\right)\left(\lambda\circ\psi\left(\psi^{-1}(y_2)\right)\right)\right.\right.\\
&\quad\left.\left.+\left(I^{\alpha-1:\,\psi}_{\psi^{-1}((y_1+y_2)/2)^-}\right)\left(\lambda\circ\psi\left(\psi^{-1}(y_1)\right)\right)-\lambda\left(\frac{y_1+y_2}{2}\right)\right|\\
&\le\frac{(y_2-y_1)^2}{8\alpha(\alpha+1)}\left(\left|\lambda''(y_1)\right|+\left|\lambda''(y_2)\right|\right).
\end{aligned}\tag{97}$$

Corollary 9. *If we set $\psi(\gamma) = \gamma$ in Theorem 12, we get*

$$\begin{aligned}
&\left|\frac{2^{\alpha-2}\Gamma(\alpha)}{(\ell_2-\ell_1)^{\alpha-1}}\left\{\left(J^{\alpha-1}_{(y_1+y_2-((\ell_1+\ell_2)/2))^+}\right)(\lambda(y_1+y_2-\ell_1))\right.\right.\\
&\quad\left.\left.+\left(J^{\alpha-1}_{(y_1+y_2-((\ell_1+\ell_2)/2))^-}\right)(\lambda(y_1+y_2-\ell_2))-\lambda\left(y_1+y_2-\frac{\ell_1+\ell_2}{2}\right)\right|\right.\\
&\le\frac{(\ell_2-\ell_1)^2}{4\alpha(\alpha+1)}\left\{\left|\lambda''(y_1)\right|+\left|\lambda''(y_2)\right|-\left(\frac{\left|\lambda''(\ell_1)\right|+\left|\lambda''(\ell_2)\right|}{2}\right)\right\}.
\end{aligned}\tag{98}$$

Remark 22. If we set $\psi(\gamma) = \gamma$, $\ell_1 = y_1$, and $\ell_2 = y_2$ in Theorem 12, we get Theorem 2.1 of [34].

Moreover, if we set $\alpha = 2$, we obtain Proposition 1 of [33].

Theorem 13. *If (A_1) is satisfied and $|\lambda''|^q$ is convex function, then*

$$\begin{aligned}
&\left|\frac{2^{\alpha-2}\Gamma(\alpha)}{(\ell_2-\ell_1)^{\alpha-1}}\left(\left(I^{\alpha-1:\,\psi}_{\psi^{-1}(y_1+y_2-((\ell_1+\ell_2)/2))^+}\right)\left(\lambda\circ\psi\left(\psi^{-1}(y_1+y_2-\ell_1)\right)\right)\right)\right.\\
&\quad\left.+\left(I^{\alpha-1:\,\psi}_{\psi^{-1}(y_1+y_2-((\ell_1+\ell_2)/2))^-}\right)\left(\lambda\circ\psi\left(\psi^{-1}(y_1+y_2-\ell_2)\right)\right)-\lambda\left(y_1+y_2-\frac{\ell_1+\ell_2}{2}\right)\right|\\
&\le\frac{(\ell_2-\ell_1)^2}{\alpha\cdot 2^{2-\alpha}}\left(\frac{1}{2^{p\alpha+1}(p\alpha+1)}\right)^{1/p}\left[\left(\frac{|\lambda''(y_1)|^q+|\lambda''(y_2)|^q}{2}-\frac{3|\lambda''(\ell_1)|^q+|\lambda''(\ell_2)|^q}{8}\right)^{1/q}\right.\\
&\quad\left.+\left(\frac{|\lambda''(y_1)|^q+|\lambda''(y_2)|^q}{2}-\frac{|\lambda''(\ell_1)|^q+3|\lambda''(\ell_2)|^q}{8}\right)^{1/q}\right.,
\end{aligned}\tag{99}$$

where $q>1$ and $(1/p)+(1/q)=1$ for all $\ell_1,\ell_2\in[y_1,y_2]$.

Proof. Applying Lemma 6, Hölder and Jensen–Mercer inequalities, the fact that $|\lambda''|^q$ is convex function, and properties of modulus, we have

$$\begin{aligned}
&\left|\frac{2^{\alpha-2}\Gamma(\alpha)}{(\ell_2-\ell_1)^{\alpha-1}}\left(\left(I^{\alpha-1:\,\psi}_{\psi^{-1}(y_1+y_2-((\ell_1+\ell_2)/2))^+}\right)\left(\lambda\circ\psi\left(\psi^{-1}(y_1+y_2-\ell_1)\right)\right)\right)\right.\\
&\quad\left.+\left(I^{\alpha-1:\,\psi}_{\psi^{-1}(y_1+y_2-((\ell_1+\ell_2)/2))^-}\right)\left(\lambda\circ\psi\left(\psi^{-1}(y_1+y_2-\ell_2)\right)\right)-\lambda\left(y_1+y_2-\frac{\ell_1+\ell_2}{2}\right)\right|\\
&\le\frac{(\ell_2-\ell_1)^2}{\alpha\cdot 2^{2-\alpha}}\left[\int_0^{1/2}\zeta^\alpha\left|\lambda''(y_1+y_2-((1-\zeta)\ell_1+\zeta\ell_2))\right|d\zeta\right.\\
&\quad\left.+\int_{1/2}^1(1-\zeta)^\alpha\left|\lambda''(y_1+y_2-((1-\zeta)\ell_1+\zeta\ell_2))\right|d\zeta\right.\\
&\le\frac{(\ell_2-\ell_1)^2}{\alpha\cdot 2^{2-\alpha}}\left[\left(\int_0^{1/2}\zeta^{p\alpha}d\zeta\right)^{1/p}\left(\int_0^{1/2}\left|\lambda''(y_1+y_2-((1-\zeta)\ell_1+\zeta\ell_2))\right|^q d\zeta\right)^{1/q}\right.\\
&\quad\left.+\left(\int_{1/2}^1(1-\zeta)^{p\alpha}d\zeta\right)^{1/p}\left(\int_{1/2}^1\left|\lambda''(y_1+y_2-((1-\zeta)\ell_1+\zeta\ell_2))\right|^q d\zeta\right)^{1/q}\right.\\
&\le\frac{(\ell_2-\ell_1)^2}{\alpha\cdot 2^{2-\alpha}}\left(\frac{1}{2^{p\alpha+1}(p\alpha+1)}\right)^{1/p}\\
&\quad\times\left[\left(\int_0^{1/2}\left(|\lambda''(y_1)|^q+|\lambda''(y_2)|^q-(1-\zeta)|\lambda''(\ell_1)|^q-\zeta|\lambda''(\ell_2)|^q\right)d\zeta\right)^{1/q}\right.\\
&\quad\left.+\left(\int_{1/2}^1\left(|\lambda''(y_1)|^q+|\lambda''(y_2)|^q-(1-\zeta)|\lambda''(\ell_1)|^q-\zeta|\lambda''(\ell_2)|^q\right)d\zeta\right)^{1/q}\right.\\
&=\frac{(\ell_2-\ell_1)^2}{\alpha\cdot 2^{2-\alpha}}\left(\frac{1}{2^{p\alpha+1}(p\alpha+1)}\right)^{1/p}\left[\left(\frac{|\lambda''(y_1)|^q+|\lambda''(y_2)|^q}{2}-\frac{3|\lambda''(\ell_1)|^q+|\lambda''(\ell_2)|^q}{8}\right)^{1/q}\right.\\
&\quad\left.+\left(\frac{|\lambda''(y_1)|^q+|\lambda''(y_2)|^q}{2}-\frac{|\lambda''(\ell_1)|^q+3|\lambda''(\ell_2)|^q}{8}\right)^{1/q}\right..
\end{aligned}\tag{100}$$

□

Corollary 10. *If we set $\ell_1 = y_1$ and $\ell_2 = y_2$ in Theorem 12, we get*

$$\begin{aligned}
&\left|\frac{2^{\alpha-2}\Gamma(\alpha)}{(y_2-y_1)^{\alpha-1}}\left(\left(I^{\alpha-1:\,\psi}_{\psi^{-1}((y_1+y_2)/2)^+}\right)\left(\lambda\circ\psi\left(\psi^{-1}(y_2)\right)\right)\right)\right.\\
&\quad\left.+\left(I^{\alpha-1:\,\psi}_{\psi^{-1}((y_1+y_2)/2)^-}\right)\left(\lambda\circ\psi\left(\psi^{-1}(y_1)\right)\right)-\lambda\left(\frac{y_1+y_2}{2}\right)\right|\\
&\le\frac{(\ell_2-\ell_1)^2}{\alpha\cdot 2^{2-\alpha}}\left(\frac{1}{2^{p\alpha+1}(p\alpha+1)}\right)^{1/p}\left[\left(\frac{|\lambda''(y_1)|^q+3|\lambda''(y_2)|^q}{8}\right)^{1/q}\right.\\
&\quad\left.+\left(\frac{3|\lambda''(y_1)|^q+|\lambda''(y_2)|^q}{8}\right)^{1/q}\right.
\end{aligned}\tag{101}$$

Corollary 11. *If we set $\psi(\gamma) = \gamma$ in Theorem 12, we get*

$$\begin{aligned}
&\left|\frac{2^{\alpha-2}\Gamma(\alpha)}{(\ell_2-\ell_1)^{\alpha-1}}\left(\left(J^{\alpha-1}_{(y_1+y_2-((\ell_1+\ell_2)/2))^+}\right)(\lambda(y_1+y_2-\ell_1))\right)\right.\\
&\quad+\left(J^{\alpha-1}_{(y_1+y_2-((\ell_1+\ell_2)/2))^-}\right)(\lambda(y_1+y_2-\ell_2))\\
&\quad\left.-\lambda\left(y_1+y_2-\frac{\ell_1+\ell_2}{2}\right)\right|\\
&\le\frac{(\ell_2-\ell_1)^2}{\alpha\cdot 2^{2-\alpha}}\left(\frac{1}{2^{p\alpha+1}(p\alpha+1)}\right)^{1/p}\left[\left(\frac{|\lambda''(y_1)|^q+|\lambda''(y_2)|^q}{2}-\frac{3|\lambda''(\ell_1)|^q+|\lambda''(\ell_2)|^q}{8}\right)^{1/q}\right.\\
&\quad\left.+\left(\frac{|\lambda''(y_1)|^q+|\lambda''(y_2)|^q}{2}-\frac{|\lambda''(\ell_1)|^q+3|\lambda''(\ell_2)|^q}{8}\right)^{1/q}\right.
\end{aligned}\tag{102}$$

Theorem 14. *If (A_1) is satisfied and $|\lambda''|^q$ is convex function, then*

$$\begin{aligned}
&\left|\frac{2^{\alpha-2}\Gamma(\alpha)}{(\ell_2-\ell_1)^{\alpha-1}}\left(\left(I^{\alpha-1:\,\psi}_{\psi^{-1}(y_1+y_2-((\ell_1+\ell_2)/2))^+}\right)\left(\lambda\circ\psi\left(\psi^{-1}(y_1+y_2-\ell_1)\right)\right)\right)\right.\\
&\quad\left.+\left(I^{\alpha-1:\,\psi}_{\psi^{-1}(y_1+y_2-((\ell_1+\ell_2)/2))^-}\right)\left(\lambda\circ\psi\left(\psi^{-1}(y_1+y_2-\ell_2)\right)\right)-\lambda\left(y_1+y_2-\frac{\ell_1+\ell_2}{2}\right)\right|\\
&\le\frac{(\ell_2-\ell_1)^2}{\alpha\cdot 2^{2-\alpha}}\left(\frac{1}{2^{\alpha+1}(\alpha+1)}\right)^{1-(1/q)}\\
&\quad\times\left[\left(\frac{|\lambda''(y_1)|^q+|\lambda''(y_2)|^q}{2^{\alpha+1}(\alpha+1)}-\frac{(\alpha+3)|\lambda''(\ell_1)|^q}{2^{\alpha+2}(\alpha+1)(\alpha+2)}-\frac{|\lambda''(\ell_2)|^q}{2^{\alpha+2}(\alpha+2)}\right)^{1/q}\right.\\
&\quad\left.+\left(\frac{|\lambda''(y_1)|^q+|\lambda''(y_2)|^q}{2^{\alpha+1}(\alpha+1)}-\frac{|\lambda''(\ell_1)|^q}{2^{\alpha+2}(\alpha+2)}-\frac{(\alpha+3)|\lambda''(\ell_2)|^q}{2^{\alpha+2}(\alpha+1)(\alpha+2)}\right)^{1/q}\right.,
\end{aligned}\tag{103}$$

where $q \geq 1$ for all $\ell_1, \ell_2 \in [y_1, y_2]$.

Proof. From Lemma 2, power-mean and Jensen–Mercer inequalities, the fact that $|\lambda''|^q$ is convex function, and properties of modulus, we have

$$\begin{aligned}
&\left|\frac{2^{\alpha-2}\Gamma(\alpha)}{(\ell_2-\ell_1)^{\alpha-1}}\left(\left(I^{\alpha-1:\,\psi}_{\psi^{-1}(y_1+y_2-((\ell_1+\ell_2)/2))^+}\right)\left(\lambda\circ\psi\left(\psi^{-1}(y_1+y_2-\ell_1)\right)\right)\right)\right.\\
&\quad\left.+\left(I^{\alpha-1:\,\psi}_{\psi^{-1}(y_1+y_2-((\ell_1+\ell_2)/2))^-}\right)\left(\lambda\circ\psi\left(\psi^{-1}(y_1+y_2-\ell_2)\right)\right)-\lambda\left(y_1+y_2-\frac{\ell_1+\ell_2}{2}\right)\right|\\
&\leq\frac{(\ell_2-\ell_1)^2}{\alpha\cdot 2^{2-\alpha}}\left[\int_0^{1/2}\zeta^\alpha\left|\lambda''\left(y_1+y_2-((1-\zeta)\ell_1+\zeta\ell_2)\right)\right|\mathrm{d}\zeta\right.\\
&\quad\left.+\int_{1/2}^{1}(1-\zeta)^\alpha\left|\lambda''\left(y_1+y_2-((1-\zeta)\ell_1+\zeta\ell_2)\right)\right|\mathrm{d}\zeta\right.\\
&\leq\frac{(\ell_2-\ell_1)^2}{\alpha\cdot 2^{2-\alpha}}\left[\left(\int_0^{1/2}\zeta^\alpha\mathrm{d}\zeta\right)^{1-(1/q)}\right.\\
&\quad\times\left(\left(|\lambda''(y_1)|^q+|\lambda''(y_2)|^q\right)\int_0^{1/2}\zeta^\alpha\mathrm{d}\zeta-|\lambda''(\ell_1)|^q\int_0^{1/2}\zeta^\alpha(1-\zeta)\mathrm{d}\zeta-|\lambda''(\ell_2)|^q\int_0^{1/2}\zeta^{\alpha+1}\mathrm{d}\zeta\right)^{1/q}\\
&\quad+\left(\int_{1/2}^{1}(1-\zeta)^\alpha\mathrm{d}\zeta\right)^{1-(1/q)}\\
&\quad\times\left(\left(|\lambda''(y_1)|^q+|\lambda''(y_2)|^q\right)\int_{1/2}^{1}(1-\zeta)^\alpha\mathrm{d}\zeta-|\lambda''(\ell_1)|^q\int_{1/2}^{1}\zeta(1-\zeta)^\alpha\mathrm{d}\zeta-|\lambda''(\ell_2)|^q\int_{1/2}^{1}(1-\zeta)^{\alpha+1}\mathrm{d}\zeta\right)^{1/q}\\
&=\frac{(\ell_2-\ell_1)^2}{\alpha\cdot 2^{2-\alpha}}\left(\frac{1}{2^{\alpha+1}(\alpha+1)}\right)^{1-(1/q)}\\
&\quad\times\left[\left(\frac{|\lambda''(y_1)|^q+|\lambda''(y_2)|^q}{2^{\alpha+1}(\alpha+1)}-\frac{(\alpha+3)|\lambda''(\ell_1)|^q}{2^{\alpha+2}(\alpha+1)(\alpha+2)}-\frac{|\lambda''(\ell_2)|^q}{2^{\alpha+2}(\alpha+2)}\right)^{1/q}\right.\\
&\quad\left.+\left(\frac{|\lambda''(y_1)|^q+|\lambda''(y_2)|^q}{2^{\alpha+1}(\alpha+1)}-\frac{|\lambda''(\ell_1)|^q}{2^{\alpha+2}(\alpha+2)}-\frac{(\alpha+3)|\lambda''(\ell_2)|^q}{2^{\alpha+2}(\alpha+1)(\alpha+2)}\right)^{1/q}\right.
\end{aligned}\tag{104}$$

□

Remark 23. If we set $\psi(\gamma)=\gamma$, $\ell_1=y_1$, and $\ell_2=y_2$ in Theorem 14, we get Theorem 2.2 of [34] for $m=s=1$.

Moreover, if we set $\alpha=2$, we obtain Proposition 5 of [33].

4. Application

In this last section, we will give an application of our results using modified Bessel function of the first kind.

Let the function $\mathfrak{I}_p\colon \mathfrak{R}\longrightarrow[1,+\infty)$ be defined by

$$\mathfrak{I}_p(\ell_1)=2^p\Gamma(p+1)\ell_1^{-\nu}I_p(\ell_1),\quad p>1,\ell_1\in\mathfrak{R}.\tag{105}$$

For this, we recall the modified Bessel function of the first kind $\mathfrak{I}_p$ which is defined as follows [35]:

$$\mathfrak{I}_p(\ell_1)=\sum_{n\geq 0}\frac{(\ell_1/2)^{p+2n}}{n!\Gamma(p+n+1)}.\tag{106}$$

The first and the n th order derivative formula of $\mathfrak{I}_p$ is, respectively, given by the following [36]:

$$\mathfrak{I}_p'(\ell_1) = \frac{\ell_1}{2(p+1)}\mathfrak{I}_{p+1}(\ell_1), \tag{107}$$

$$\begin{aligned}\frac{\mathrm{d}^n\mathfrak{I}_p(\ell_1)}{\mathrm{d}\ell_1^n} &= 2^{n-2p}\sqrt{\pi}\ell_1^{p-n}\Gamma(p+1)\\ &\quad\times {}_2F_3\left(\frac{p+1}{2},\frac{p+2}{2};\frac{p+1-n}{2},\frac{p+2-n}{2},p+1;\frac{\ell_1^2}{4}\right),\end{aligned} \tag{108}$$

where ${}_2F_3(\cdot,\cdot;\cdot,\cdot,\cdot;\cdot)$ is the hypergeometric function defined by the following [36]:

$$\begin{aligned}&{}_2F_3\left(\frac{p+1}{2},\frac{p+2}{2};\frac{p+1-n}{2},\frac{p+2-n}{2},p+1;\frac{\ell_1^2}{4}\right)\\ &= \sum_{k=0}^{\infty}\frac{((p+1)/2)_k((p+2)/2)_k}{((p-1)/2)_k((p-2)/2)_k(p+1)_k}\cdot\frac{\ell_1^{2k}}{4^k\cdot k!},\end{aligned} \tag{109}$$

and for some parameter v, the Pochhammer symbol $(v)_k$ is defined as

$$\begin{aligned}&(v)_0 = 1,\\ &(v)_k = v(v+1)\cdots(v+k+1), \quad k = 1,2,3,\ldots.\end{aligned} \tag{110}$$

Proposition 1. *Let $0 < y_1 < y_2$ be real numbers and $p > -1$, then*

$$\begin{aligned}&\left|\frac{\mathfrak{I}_p(y_2)-\mathfrak{I}_p(y_1)}{y_2-y_1} - \frac{y_1+y_2}{4(p+1)}\mathfrak{I}_{p+1}\left(\frac{y_1+y_2}{2}\right)\right|\\ &\le \frac{(y_2-y_1)^2}{48}2^{3-2p}\sqrt{\pi}\Gamma(p+1)\\ &\quad\times\left\{y_1^{p-3}\cdot{}_2F_3\left(\frac{p+1}{2},\frac{p+2}{2};\frac{p-2}{2},\frac{p-1}{2},p+1;\frac{y_1^2}{4}\right)\right.\\ &\quad\left.+\, y_2^{p-3}\cdot{}_2F_3\left(\frac{p+1}{2},\frac{p+2}{2};\frac{p-2}{2},\frac{p-1}{2},p+1;\frac{y_2^2}{4}\right)\right.\\ &\le \frac{(y_2-y_1)^2}{48}2^{3-2p}\sqrt{\pi}\Gamma(p+1)\\ &\quad\times\left\{y_1^{p-3}\cdot{}_2F_3\left(\frac{p+1}{2},\frac{p+2}{2};\frac{p-2}{2},\frac{p-1}{2},p+1;\frac{y_1^2}{4}\right)\right.\\ &\quad\left.+\, y_2^{p-3}\cdot{}_2F_3\left(\frac{p+1}{2},\frac{p+2}{2};\frac{p-2}{2},\frac{p-1}{2},p+1;\frac{y_2^2}{4}\right)\right.\end{aligned} \tag{111}$$

Proof. Let $\lambda(\ell_1) = \mathfrak{I}_p'(\ell_1)$. Note that the function $\ell_1 \longrightarrow \mathfrak{I}'''(\ell_1)$ is convex on the interval $[0,+\infty)$ for each $p > -1$. Using Corollary 3 and relations (107) and (108), we obtain the desired inequality (111). □

Remark 24. Using the same technique like Proposition 1, we can obtain some new interesting inequalities pertaining modified Bessel function of the first kind or the well-known q–digamma function for $q \in (0,1)$ from our generic results. We omit here their proofs, and the details are left to the interested reader.

5. Conclusion

In this article, some new Hermite–Jensen–Mercer type inequalities involving ψ–Riemann–Liouville fractional integrals are found. Several ψ–Riemann–Liouville fractional integral inequalities using identities as auxiliary results are provided, and the known results are recaptured as special cases as well. Finally, the efficiency of our results is showed with an application via modified Bessel function of the first kind. We hope that current work using our idea and technique will attract the attention of researchers working in mathematical analysis and other related fields in pure and applied sciences.

Data Availability

No data were used to support this study.

Conflicts of Interest

The authors declare that they have no conflicts of interest.

References

[1] R. Hilfer, *Applications of Fractional Calculus in Physics*, World Scientific, vol. 35, pp. 87–130, Singapore, 2000.

[2] C. Cesarano, N. Pierpaolo, and E. R. Paolo, "Pseudo–Lucas functions of fractional degree and applications," *Axioms*, vol. 10, p. 51, 2021.

[3] J. Sabatier, O. P. Agrawal, and J. A. T. Machado, *Advances in Fractional Calculus*, Springer, Dordrecht, The Netherlands, 2007.

[4] M. S. Al-Luhaibi, "An analytical treatment to fractional Fornberg-Whitham equation," *Mathematical Sciences*, vol. 11, no. 1, pp. 1–6, 2017.

[5] S. Rashid, M. A. Latif, Z. Hammouch, and Y.-M. Chu, "Fractional integral inequalities for strongly h -preinvex functions for a kth order differentiable functions," *Symmetry*, vol. 11, no. 12, p. 1448, 2019.

[6] T. Abdeljawad, S. Rashid, Z. Hammouch, İ. İşcan, and Y.-M. Chu, "Some new Simpson-type inequalities for generalized p-convex function on fractal sets with applications," *Advances in Difference Equations*, vol. 2020, Article ID 2955-9, 1 page, 2020.

[7] S. Rashid, M. A. Noor, K. I. Noor, F. Safdar, and Y.-M. Chu, "Hermite-hadamard type inequalities for the class of convex functions on time scale," *Mathematics*, vol. 7, no. 10, p. 956, 2019.

[8] S. I. Butt, M. Umar, S. Rashid, A. O. Akdemir, and Y.-M. Chu, "New Hermite-Jensen-Mercer-type inequalities via k-fractional integrals," *Advances in Difference Equations*, vol. 2020, Article ID 03093-y, 1 page, 2020.

[9] S. Ihsan Butt, A. Kashuri, A. Kashuri, A. Aslam, and W. Gao, "Hermite-Jensen-Mercer type inequalities via Ψ-Riemann-Liouville k-fractional integrals," *AIMS Mathematics*, vol. 5, no. 5, pp. 5193–5220, 2020.

[10] S. Zhao, S. I. Butt, W. Nazeer, J. Nasir, M. Umar, and Y. Liu, "Some Hermite-Jensen-Mercer type inequalities for k-Caputo-fractional derivatives and related results," *Advances in Difference Equations*, vol. 2020, Article ID 2693-y, 1 page, 2020.

[11] J. Pečarić, D. S. Mitrinovic, and A. M. Fink, *Classical and New Inequalities in Analysis*, pp. 1-2, Springer, Berlin, Germany, 1993.

[12] M. Adil Khan, S. Khan, I. Ullah, K. Ali Khan, and Y. M. Chu, "A novel approach to the Jensen gap through Taylor's theorem," *Mathematical Methods in the Applied Sciences*, vol. 44, no. 5, pp. 3324–3333, 2021.

[13] S. I. Butt, M. Klaričić Bakula, Đ. Pečarić, and J. Pečarić, "Jensen-grüss inequality and its applications for the zipf-mandelbrot law," *Mathematical Methods in the Applied Sciences*, vol. 44, no. 2, pp. 1664–1673, 2021.

[14] N. Mehmood, S. I. Butt, D. Pečarić, and J. Pečarić, "Generalizations of cyclic refinements of Jensen's inequality by Lidstone's polynomial with applications in information theory," *Journal of Mathematical Inequalities*, vol. 14, no. 1, pp. 249–271, 2019.

[15] A. McD. Mercer, "A variant of Jensen's inequality," *Journal of Inequalities in Pure and Applied Mathematics*, vol. 4, no. 4, Article ID 23792-8_7, 2003.

[16] A. Matkovic, J. Pečarić, and I. Perić, "A variant of Jensens inequality of Mercer's type for operators with applications," *Linear Algebra and Its Applications*, vol. 418, pp. 551–564, 2006.

[17] M. Niezgoda, "A generalization of Mercer's result on convex functions," *Nonlinear Analysis Forum*, vol. 71, 2009.

[18] E. Anjidani and M. R. Changalvaiy, "Reverse jensen-mercer type operator inequalities," *The Electronic Journal of Linear Algebra*, vol. 31, pp. 87–99, 2016.

[19] H. R. Moradi and S. Furuichi, "Improvement and generalization of some Jensen-Mercer-type inequalities," *Journal of Mathematical Inequalities*, vol. 14, no. 2, pp. 377–383, 2020.

[20] M. A. Khan, Z. Husain, and Y. M. Chu, "New estimates for Csiszár divergence and zipf–mandelbrot entropy via jensen–mercer's inequality," *Complexity*, vol. 2020, Article ID 8928691, 8 pages, 2020.

[21] R. Khalil, M. Al Horani, A. Yousef, and M. Sababheh, "A new definition of fractional derivative," *Journal of Computational and Applied Mathematics*, vol. 264, pp. 65–70, 2014.

[22] R. Almeida, M. Guzowska, and T. Odzijewicz, "A remark on local fractional calculus and ordinary derivatives," *Open Mathematics*, vol. 14, no. 1, pp. 1122–1124, 2016.

[23] A. A. Kilbas, H. M. Srivastava, and J. J. Trujillo, "Theory and applications of fractional differential equations," *Math. Studies*, North-Holland, New York, NY, USA, 2006.

[24] K. S. Miller and B. Ross, *An Introduction to Fractional Calculus and Fractional Differential Equations*, A Wiley-Interscience Publication, John Wiley and Sons, Inc., New York, NY, USA, 1993.

[25] E. Capelas de Oliveira and E. C. Oliveira, "On the ψ -Hilfer fractional derivative," *Communications in Nonlinear Science and Numerical Simulation*, vol. 60, pp. 72–91, 2018.

[26] J. Vanterler da Costa Sousa and E. Capelas de Oliveira, "A Gronwall inequality and the Cauchy-type problem by means of ψ-Hilfer operator," *Differential Equations & Applications*, vol. 11, no. 1, pp. 87–106, 2019.

[27] H. Öğülmüş and M. Z. Sarikaya, "Hermite–Hadamard–Mercer type inequalities for fractional integrals," 2019, https://www.researchgate.net/publication/337682540.

[28] M. Kian and M. S. Moslehian, "Refinements of the operator jensen–mercer inequality," *The Electronic Journal of Linear Algebra*, vol. 26, pp. 742–753, 2013.

[29] Q. Kang, S. I. Butt, W. Nazeer, M. Nadeem, J. Nasir, and H. Yang, "New variant of Hermite–Jensen–Mercer type inequalities via Riemann–Liouville fractional integral operators," *Jurnal Matematika*, vol. 2020, Article ID 4303727, 14 pages, 2020.

[30] K. Liu, J. R. Wang, and D. O'Regan, "On the Hermite–Hadamard type inequality for ψ–Riemann–Liouville fractional integrals via convex functions," *Journal of Inequalities and Applications*, vol. 2019, Article ID 19-1982-1, 27 pages, 2019.

[31] M. Z. Sarikaya and H. Yildirim, "On Hermite–Hadamard type inequalities for Riemann–Liouville fractional integrals," *Miskolc Mathematical Notes*, vol. 17, no. 2, pp. 1049–1059, 2016.

[32] M. A. Noor and M. U. Awan, "Some integral inequalities for two kinds of convexities via fractional integrals," *Transylvanian Journals of Mathematics and Mechanics*, vol. 5, no. 2, pp. 129–136, 2013.

[33] M. Z. Sarikaya and N. Aktan, "On the generalization of some integral inequalities and their applications," *Mathematical and Computer Modelling*, vol. 54, no. 9-10, pp. 2175–2182, 2011.

[34] B. Bayraktar, "Some integral inequalities of Hermite–Hadamard type for differentable (s, m)–convex functions via fractional integrals," *TWMS Journal of Applied and Engineering Mathematics*, vol. 10, no. 3, pp. 625–637, 2020.

[35] G. N. Watson, *A Treatise on the Theory of Bessel Functions*, Cambridge University Press, Cambridge, UK, 1944.

[36] Y. L. Luke, *The Special Functions and Their Approximations*, vol. 1, Academic Press, Cambridge, MA, USA, 1969.

Hindawi
Complexity
Volume 2021, Article ID 9401655, 16 pages
https://doi.org/10.1155/2021/9401655

Research Article

A Comparative Study of Natural Convection Flow of Fractional Maxwell Fluid with Uniform Heat Flux and Radiation

Ruihua Tang,[1] **Sadique Rehman**,[2] **Aamir Farooq**,[3] **Muhammad Kamran**,[4] **Muhammad Imran Qureshi**,[5] **Asfand Fahad**,[5] **and Jia-Bao Liu**[6]

[1]*College of Electronic Engineering, Chaohu University, Hefei 238024, China*
[2]*Department of Mathematics, Islamia College Peshawar, Peshawar 25000, Pakistan*
[3]*Department of Mathematics, Abbottabad University of Science and Technology, Abbottabad, Pakistan*
[4]*Department of Mathematics, COMSATS University Islamabad, Wah Campus, Wah Cantt 47040, Pakistan*
[5]*Department of Mathematics, COMSATS University Islamabad, Vehari Campus, Vehari 61100, Pakistan*
[6]*School of Mathematics and Physics, Anhui Jianzhu University, Hefei 230601, China*

Correspondence should be addressed to Muhammad Kamran; getkamran@gmail.com

Received 17 June 2021; Accepted 13 August 2021; Published 31 August 2021

Academic Editor: Atila Madureira Bueno

This paper focuses on the comparative study of natural convection flow of fractional Maxwell fluid having uniform heat flux and radiation. The well-known Maxwell fluid equation with an integer-order derivative has been extended to a non-integer-order derivative, i.e., fractional derivative. The explicit expression for the temperature and velocity is acquired by utilizing the Laplace transform (LT) technique. The two fractional derivative concepts are used (Caputo and Caputo–Fabrizio derivatives) in the formulation of the problem. Utilizing the Mathcad programming, the effect of certain embedded factors and fractional parameters on temperature and velocity profile is graphically presented.

1. Introduction

To specify the performance of non-Newtonian fluids, numerous models have been applied. The Maxwell fluid is the first viscoelastic rate type fluid, which is also extensively utilized. The differential form and rate type models have gotten a lot of attention among them. In recent years, this model has shown some achievements in portraying the reactions of some polymeric liquids. In industry and engineering, viscoelastic fluids pass through many processes, such as synthetic propellants and so on. Because of the simplicity of the Maxwell fluid, many investigators are paying particular attention to it [1–4]. Khan et al. [5] researched on heat transfer of Maxwell fluid through an infinite vertical plate. In this study, they obtained the analytical solutions for temperature and velocity via LT. Such a model was studied by Khan et al. [6] using fractional CF derivative.

The subject of fractional calculus is as old as standard calculus. Fractional calculus began when L' Hospital wrote to Leibnitz about the significance of $\mathrm{d}^n y/\mathrm{d}x^n$ when $n = 1/2$. Leibnitz replied in 1695 saying that it might be an apparent paradox from which one day useful repercussions would be drawn. Between the 17th century and the early 20th century, the subject of fractional calculus stayed more or less dormant. The subject matter has been found in applications in all kinds of problems in various fields over the last few years, like fluid flow, reaction, diffusion, relaxation, rheology, reaction-diffusion, oscillation, anomalous diffusion, physics, electrical network, chemistry, dynamical problems, and so on. Nowadays, many researchers are using the concept of fractional derivative because fractional-order differential equation solutions define real-life situations effectively than the solution obtained through the corresponding integer-order differential equations. Aman et al. [7] discussed about heat, velocity, and shear stress of fractional Maxwell model in a flexible medium using numerical LT. The semianalytical solutions for Maxwell fluid with fractional derivative were discussed in [8, 9]. The solutions for generalized Maxwell

fluid using Fourier and Laplace transform can be determined by Fetecau et al. [10]. Maxwell nanofluids were examined by Aman et al. [11] using four distinct molecular liquids. The impact of second-order fractional Maxwell (MHD) fluid was investigated by Liu and Guo [12].The flow of Maxwell fluid with MHD effects flowing over a stretching sheet was investigated numerically by Shateyi and Marewo [13]. Mohi [14] discussed the closed-form solution of fractional Maxwell of MHD effects using Laplace and Fourier transform. The comparative research was performed in [15] on MHD Maxwell fluid with Newtonian heating on a boundary layer. Abro and Shaikh [16] investigated the analytical solutions for Maxwell fluid over a vibratory plane. Asjad et al. [17] presented the comparisons between Caputo and Caputo–Fabrizio fractional derivatives on second-grade fluid over Newtonian heating. Raza and Ullah [18] used the fractional Maxwell fluid to compare the fractional derivatives of C and CF using the Laplace transformation. Maxwell fluid's natural convection between two parallel plates was discussed by Wang et al. [19]. The exact solution for Maxwell MHD fluid in a perforated medium was obtained by Khan et al. [20]. Zheng et al. [21] investigated extended Maxwell flow due to a vibratory and uniform moving plate. Fetecau et al. [22] used the LT to solve the second problem of Stokes for Maxwell fluids. Farooq et al. [23] presented the MHD Maxwell flow through the infinitely stretched surface of nanomaterials. Many interesting and very useful results related to the cylindrical Maxwell model can be found in [24–27]. The analytical and semianalytical solutions for Maxwell fluid between two moving plates were obtained by Hisham et al. [28]. Free convection flow has many applications in science and engineering like determining heat losses or heat load for heating, ventilating, air conditioning, and so on. Azhar et al. [29] considered the mixed convection flow of fractional nanofluids with uniform heat flux and heat source. Toki [30] examined the natural convection flow of unsteady MHD fluid and found the exact solutions of flow parameters. Fetecau et al. [31] studied the influence of radiation and permeability on MHD flow moving via an oscillating vertical plate with uniform heat flux.

The above literature motivates us to work on the natural convection flow of the fractional Maxwell model. The Caputo and CF fractional derivative approaches are used to determine the solutions. The numerical Laplace transform is utilized for the solutions of velocity and temperature. We see the comparisons between standard-order derivative and fractional-order derivative. Finally, we observe the graphical representation of various embedded parameters like Maxwell fluid factor, fractional parameter, and Grashof and Prandtl numbers.

2. Mathematical Statement

Here, we will assume the unsteady oscillatory natural convection flow of Maxwell fluid under the effects of radiation and uniform heat flux. Initially, with the uniform temperature T_∞, the fluid and the plate are at rest. After some time, at $t = 0^+$, the plate begins to oscillate in x-direction, and its velocity is given by

$$v = UH(t)\mathrm{Cos}(\omega t)i, \quad t > 0. \tag{1}$$

Following are the governing equations for the flow model:

$$\left(1 + \lambda_1 \frac{\partial}{\partial t}\right)\frac{\partial u}{\partial t} = \nu \frac{\partial^2 u}{\partial y^2} + \left(1 + \lambda_1 \frac{\partial}{\partial t}\right) g\beta (T - T_\infty), \tag{2}$$

$$\frac{\partial T}{\partial t} = \frac{k}{\rho c_p}\frac{\partial^2 T}{\partial y^2} - \frac{1}{\rho c_p}\frac{\partial q_r}{\partial y}, \tag{3}$$

$$\left(1 + \lambda_1 \frac{\partial}{\partial t}\right)\tau(y,t) = \mu \frac{\partial^2 u}{\partial y^2}. \tag{4}$$

Appropriate initial-boundary conditions are

$$\begin{aligned} &u(y,0) = 0, \quad T(y,0) = T_\infty, y > 0, \\ &u(0,t) = UH(t)\mathrm{Cos}(\omega t), \quad \frac{\partial T(0,t)}{\partial y} = -\frac{q_1}{k}, t > 0, \\ &u(\infty,t) = 0, \quad T(\infty,t) = T_\infty, t > 0. \end{aligned} \tag{5}$$

Using Rosseland approximations [22, 30–32] and accepting the small temperature variation among the temperature T_∞ of the free stream and the fluid temperature T, utilizing the Taylor theorem on T^4 at T_∞, and ignoring the second- and higher-order terms, we obtain

$$q_r = -\frac{4\sigma^*}{3\kappa^*}\frac{\partial T^4}{\partial y}, \tag{6}$$

and

$$T^4 \cong 4T_\infty^3 T - 3T_\infty^4, \tag{7}$$

where $\sigma^*, \kappa^*$are, respectively, the Stefan Boltzman constant and the mean absorption coefficient.

Substituting (7) into (6) and then into (3), we obtain (see [30, 32]) the following form:

$$\rho c_p \frac{\partial T}{\partial t} = k\frac{\partial^2 T}{\partial y^2} + \frac{16\sigma^* T_\infty^3}{3\kappa^*}\frac{\partial^2 T}{\partial y^2}. \tag{8}$$

Now, we will make use of the following similarity transformations in order to reduce equations (2), (4), and (8) into the dimensionless form

$$\begin{aligned} u^* &= \frac{u}{U}, \\ t^* &= \frac{U^2}{\nu}t, \\ \omega^* &= \frac{\nu}{U^2}\omega, \\ \zeta^* &= \frac{U}{\nu}y, \\ \lambda &= \frac{U^2}{\nu}\lambda_1, \end{aligned}$$

$$S = \frac{Uk}{\nu q_1}(T - T_\infty),$$
$$\Pr = \frac{\mu c_p}{k},$$
$$Gr = \left(\frac{\nu}{U^2}\right)^2 \frac{g\beta q_1}{k},$$
$$Nr = \frac{16\sigma^* T_\infty^3}{3k\kappa^*},$$
$$\psi^* = \frac{\nu}{\mu U^2}\tau. \tag{9}$$

Substituting the above dimensionless parameters into equations (2), (4), and (8) and removing * from u, t, ω, ψ, and ζ, we get the following forms:

$$\left(1 + \lambda\frac{\partial}{\partial t}\right)\frac{\partial u(\zeta,t)}{\partial t} = \frac{\partial^2 u(\zeta,t)}{\partial \zeta^2} + \left(1 + \lambda\frac{\partial}{\partial t}\right)GrS(\zeta,t), \tag{10}$$

$$\Pr\frac{\partial S}{\partial t} = (1 + Nr)\frac{\partial^2 S(y,t)}{\partial \zeta^2}, \quad \zeta, t > 0, \tag{11}$$

$$\left(1 + \lambda\frac{\partial}{\partial t}\right)\psi(\zeta,t) = \frac{\partial u(\zeta,t)}{\partial \zeta}. \tag{12}$$

To obtain the fractional model, we replace the inner time derivative by the time fractional derivative and we acquire a set of fractional PDEs as follows:

$$(1 + \lambda D_t^\alpha)\frac{\partial u(\zeta,t)}{\partial t} = \frac{\partial^2 u(\zeta,t)}{\partial \zeta^2} + (1 + \lambda D_t^\alpha)GrS(\zeta,t), \tag{13}$$

$$\Pr D_t^\alpha S = (1 + Nr)\frac{\partial^2 S(\zeta,t)}{\partial \zeta^2}, \quad \zeta, t > 0, \tag{14}$$

$$(1 + \lambda D_t^\alpha)\psi(\zeta,t) = \frac{\partial u(\zeta,t)}{\partial \zeta}. \tag{15}$$

By neglecting the $*$ sign and utilizing equation (9), we will get the following initial and boundary conditions:

$$\begin{aligned} &u(\zeta,0) = 0,\\ &\theta(\zeta,0) = 0,\\ &u(0,t) = H(t)\mathrm{Cos}(\omega t),\\ &\frac{\partial S(0,t)}{\partial \zeta} = -1,\\ &u(\zeta,t) = 0,\\ &S(\zeta,t) = 0, \quad \zeta \longrightarrow \infty. \end{aligned} \tag{16}$$

3. Preliminaries

3.1. Caputo Fractional Derivative. The Caputo fractional derivative is given by

$$^C D_t^\chi f(y,t) = \begin{cases} \dfrac{1}{\Gamma(1-\chi)}\displaystyle\int_0^t (t-\nu)^{-\chi} f'(y,\nu)\mathrm{d}\nu, & 0 \le \chi < 1,\\ \dfrac{\partial f(y,t)}{\partial t} & \chi = 1. \end{cases} \tag{17}$$

The LT of Caputo fractional derivative is given by

$$L\left\{^C D_t^\chi g(y,t)\right\} = q^\chi L\{g(y,t)\} - q^{\chi-1} g(y,0). \tag{18}$$

3.2. Caputo–Fabrizio Fractional Derivative. The Caputo–Fabrizio fractional derivative is given by

$$^{CF} D_t^\chi g(y,t) = \begin{cases} \dfrac{1}{(1-\chi)}\displaystyle\int_0^t e^{(-\chi(t-\nu)/(1-\chi))} g\prime(y,\nu)\mathrm{d}\nu, & 0 \le \chi < 1,\\ \dfrac{\partial g(y,t)}{\partial t} & \chi = 1. \end{cases} \tag{19}$$

The LT of Caputo–Fabrizio fractional derivative is defined by the following formula:

$$L\left\{^{CF} D_t^\chi g(y,t)\right\} = \frac{qL\{g(y,t)\} - g(y,0)}{(1-\chi)q + \chi}. \tag{20}$$

Remark. If $\chi \longrightarrow 1$, then we obtain

$$\lim_{\chi\longrightarrow 1} L\left\{^C D_t^\chi g(y,t)\right\} = \lim_{\chi\longrightarrow 1} L\left\{^{CF} D_t^\chi g(y,t)\right\} = qL\{g(y,t)\} - g(y,0) = L\left\{\frac{\partial g(y,t)}{\partial t}\right\}. \tag{21}$$

4. Temperature Profile with Caputo Derivative

Taking the LT of equation (14) and utilizing the corresponding ICs and BCs, we obtain the following form:

$$\overline{S}(\zeta,q) = \frac{1}{q\sqrt{q^\alpha \Pr_{\mathrm{eff}}}} e^{-y\sqrt{q^\alpha \Pr_{\mathrm{eff}}}}, \quad \text{where } \Pr_{\mathrm{eff}} = \frac{\Pr}{1 + Nr}. \tag{22}$$

The inverse LT of equation (22) is given by convolution product:

$$S(\zeta,t)=\frac{1}{\sqrt{\mathrm{Pr}_{\mathrm{eff}}}}\int_0^t\left[\theta_1(t-\psi)*\theta_2(\zeta,\psi)\right]\mathrm{d}\psi, \tag{23}$$

where

$$\theta_1(t)=L^{-1}\left\{\frac{1}{\sqrt{q^\alpha}}\right\}=\frac{t^{-1+(\alpha/2)}}{\Gamma(\alpha/2)},$$

$$\theta_2(\zeta,t)=L^{-1}\left\{\frac{e^{-y\sqrt{\mathrm{Pr}_{\mathrm{eff}}}q^{\alpha/2}}}{q}\right\}=\varphi\left(1,-\frac{\alpha}{2},-y\sqrt{\mathrm{Pr}_{\mathrm{eff}}}\,t^{-\alpha/2}\right), \tag{24}$$

where $\varphi(x,y,z)=\sum_{n=0}^{\infty}z^n/(\Gamma(n+1)\Gamma(x+ny));\ 0<\alpha<1$.

5. Temperature Profile with CF Derivative

Applying LT to equation (14) and introducing equations (19) and (20), we get

$$\overline{S}(\zeta,q)=\frac{1}{q\sqrt{\mathrm{Pr}_{\mathrm{eff}}\left(m_0q/(q+\alpha m_0)\right)}}e^{-y\sqrt{\mathrm{Pr}_{\mathrm{eff}}m_0q/(q+\alpha m_0)}},\quad \text{where } m_0=\frac{1}{1-\alpha}. \tag{25}$$

Inverse Laplace of equation (25) is obtained through the Faltung theorem, and we have

$$S(\zeta,t)=\int_0^t\left[g(t-\xi)*h(\zeta,\xi)\right]\mathrm{d}\xi, \tag{26}$$

where $g(t)=L^{-1}\{g(q)\}=(1/\mathrm{Pr}_{\mathrm{eff}}m_0)[\delta(t)+m_0\alpha]$ and

$$h(\zeta,t)=L^{-1}\{H(\zeta,q)\}$$
$$=\frac{1}{\pi}H(t)\int_0^{\alpha m_0}\sqrt{\frac{\alpha m_0}{\mathrm{Pr}_{\mathrm{eff}}m_0-v}}e^{-vt}\mathrm{Cos}\left(y\frac{\alpha m_0}{\mathrm{Pr}_{\mathrm{eff}}m_0-v}\right)\mathrm{d}v. \tag{27}$$

6. Nusselt Number

The Nusselt number Nu measures the rate of heat transfer at the plate. The Nusselt number for both equations (22) and (25) is constant:

$$Nu(t)=1. \tag{28}$$

7. Temperature Profile in Ordinary Case $\alpha\longrightarrow 1$

Taking LT on equation (11) and utilizing the related initial-boundary conditions, we get

$$\overline{S}(\zeta,q)=\frac{1}{\sqrt{\mathrm{Pr}_{\mathrm{eff}}}q^{3/2}}e^{-\zeta\sqrt{q\mathrm{Pr}_{\mathrm{eff}}}}. \tag{29}$$

The inverse LT of equation (29) is

$$S(\zeta,t)=\frac{2\sqrt{t}}{\sqrt{\mathrm{Pr}_{\mathrm{eff}}}}\left[\frac{1}{\sqrt{\pi}}e^{\left(-\zeta^2\frac{\mathrm{Pr}_{\mathrm{eff}}}{4t}\right)}-\frac{\zeta\sqrt{\mathrm{Pr}_{\mathrm{eff}}}}{2\sqrt{t}}erfc\left(\frac{\zeta\sqrt{\mathrm{Pr}_{\mathrm{eff}}}}{2\sqrt{t}}\right)\right], \tag{30}$$

and such solution was obtained by Abro and Shaikh [16].

8. Velocity Profile with Caputo Derivative

Taking LT on equation (13) and related initial-boundary conditions and substituting equation (22) for $\overline{S}(\zeta,q)$, we find that

$$\overline{u}(\zeta,q)=\left[\frac{q}{q^2+\omega^2}+\frac{Gr}{\sqrt{\mathrm{Pr}_{\mathrm{eff}}}}\frac{(1+\lambda q^\alpha)}{q\sqrt{q^\alpha}\left[q^\alpha\mathrm{Pr}_{\mathrm{eff}}-(1+\lambda q^\alpha)q\right]}\right]e^{-\zeta\sqrt{(1+\lambda q^\alpha)q}}$$
$$-\left[\frac{Gr}{\sqrt{\mathrm{Pr}_{\mathrm{eff}}}}\frac{(1+\lambda q^\alpha)}{q\sqrt{q^\alpha}\left[q^\alpha\mathrm{Pr}_{\mathrm{eff}}-(1+\lambda q^\alpha)q\right]}\right]e^{-\zeta\sqrt{\mathrm{Pr}_{\mathrm{eff}}q^\alpha}}. \tag{31}$$

9. Velocity Profile with CF Derivative

Taking the LT on equation (13) and related initial-boundary conditions and substituting equation (25) for $\overline{S}(\zeta,q)$, we have

$$\overline{u}(\zeta,q)=\left[\frac{q}{q^2+\omega^2}+\frac{Gr}{\sqrt{\mathrm{Pr}_{\mathrm{eff}}m_0}}\frac{(q+m_0\alpha+\lambda qm_0)}{q\sqrt{(q/(q+m_0\alpha))}\left[qm_0\mathrm{Pr}_{\mathrm{eff}}-(q+m_0\alpha+\lambda qm_0)q\right]}\right]e^{-\zeta\sqrt{(q+m_0\alpha+\lambda qm_0)q/(q+m_0\alpha)}}$$

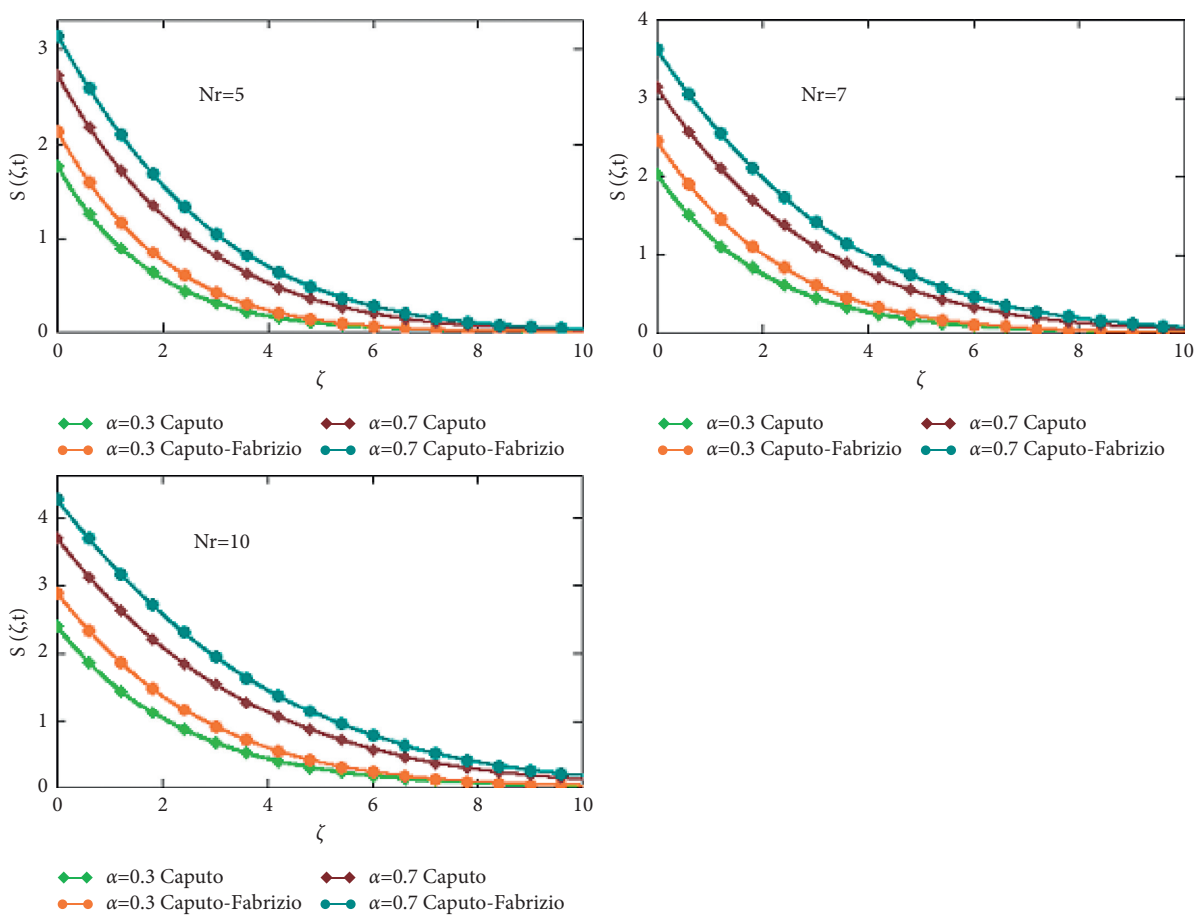

Figure 1: Variation of Nr with $\Pr = 4$ and $t = 7$.

$$-\left[\frac{Gr}{\sqrt{\Pr_{\text{eff}} m_0}} \frac{(q + m_0\alpha + \lambda q m_0)}{q\sqrt{(q/(q+m_0\alpha))}\,[q m_0 \Pr_{\text{eff}} - (q + m_0\alpha + \lambda q m_0)q]}\right] e^{-\zeta\sqrt{\Pr_{\text{eff}} m_0 q/(q+m_0\alpha)}}. \tag{32}$$

10. Velocity Profile in Ordinary Case $\alpha \longrightarrow 1$

Now taking the Laplace transform on equation (10) and related initial and boundary conditions and also substituting equation (29) for $\overline{S}(\zeta, q)$, we obtain

$$\frac{\partial^2 \overline{u}(\zeta,q)}{\partial \zeta^2} - (1+\lambda q) q \overline{u}(\zeta,q) = -Gr(1+\lambda q)\frac{1}{\sqrt{\Pr_{\text{eff}}}\, q^{3/2}} e^{-\zeta\sqrt{q \Pr_{\text{eff}}}}. \tag{33}$$

On solving the ODE (33), then we acquire

$$\overline{u}(\zeta,q) = \left[\frac{q}{q^2+\omega^2} + \frac{Gr(1+\lambda q)}{q^2\sqrt{q}\,\sqrt{\Pr_{\text{eff}}}\,[\Pr_{\text{eff}} - (1+\lambda q)]}\right] e^{-\zeta\sqrt{q(1+\lambda q)}} - \left[\frac{Gr(1+\lambda q)}{q^2\sqrt{q}\,\sqrt{\Pr_{\text{eff}}}\,[\Pr_{\text{eff}} - (1+\lambda q)]}\right] e^{-\zeta\sqrt{q \Pr_{\text{eff}}}}. \tag{34}$$

We can write equation (34) into the following equivalent form:

$$\begin{aligned}\overline{u}(\zeta,q) = {} & \frac{q}{q^2+\omega^2} e^{-\zeta\sqrt{q(1+\lambda q)}} - \frac{Gr}{\sqrt{\Pr_{\text{eff}}}}\left[\frac{m_1 - m_2}{m_1^2}\frac{1}{q\sqrt{q}} + \frac{m_2}{m_1}\frac{1}{q^2\sqrt{q}} + \frac{m_2 - m_1}{m_1^2 m_3}\left(\frac{m_3}{\sqrt{q}\left(q - (\sqrt{m_3})^2\right)}\right)\right] e^{-\zeta\sqrt{q(1+\lambda q)}} \\ & + \frac{Gr}{\sqrt{\Pr_{\text{eff}}}}\left[\frac{m_1 - m_2}{m_1^2}\frac{1}{q\sqrt{q}} + \frac{m_2}{m_1}\frac{1}{q^2\sqrt{q}} + \frac{m_2 - m_1}{m_1^2 m_3}\left(\frac{m_3}{\sqrt{q}\left(q - (\sqrt{m_3})^2\right)}\right)\right] e^{-\zeta\sqrt{q}\sqrt{\Pr_{\text{eff}}}},\end{aligned} \tag{35}$$

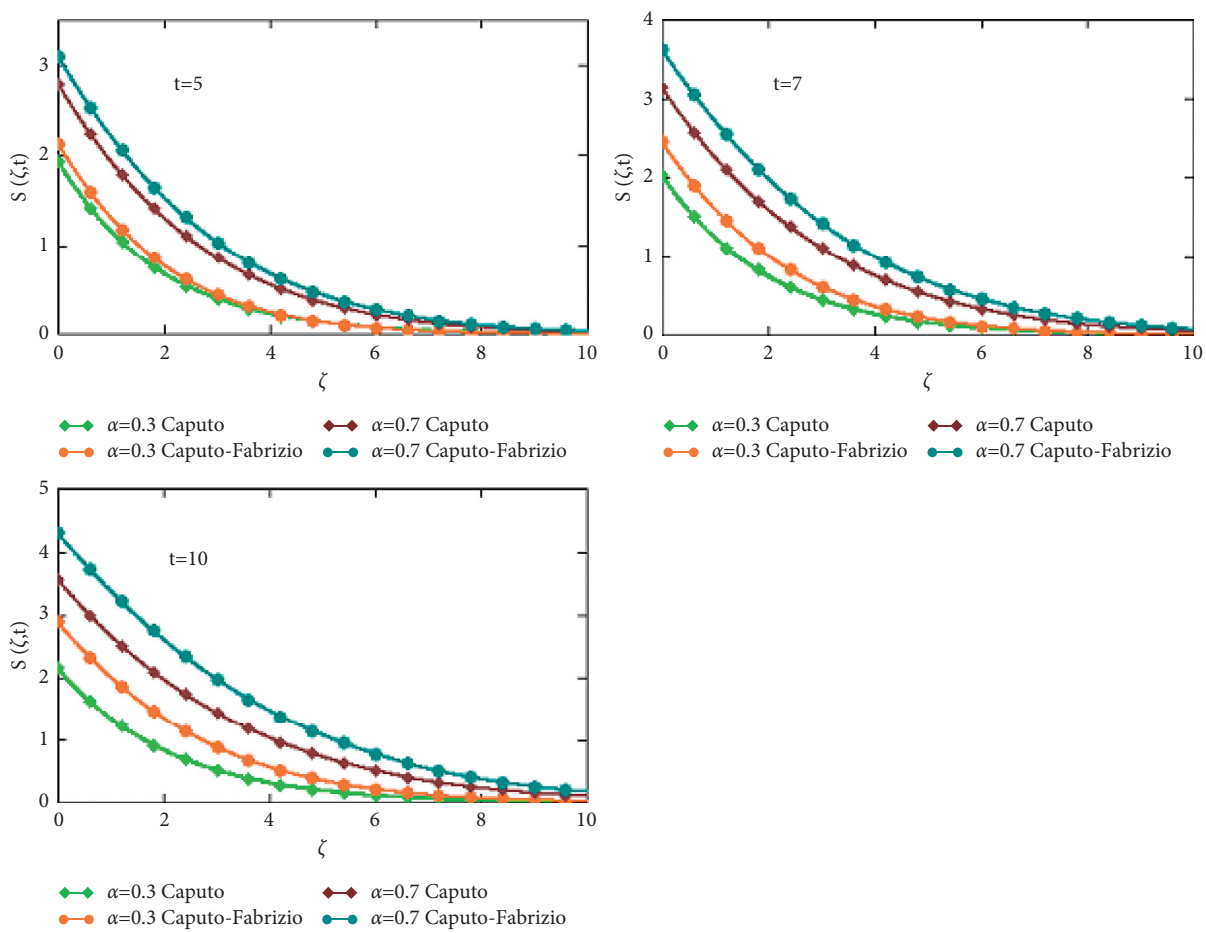

Figure 2: Variation of t with $\Pr = 4$ and $Nr = 7$.

where $m_1 = (1 - \Pr_{\text{eff}})/\lambda, m_2 = 1/\lambda, m_3 = (\Pr_{\text{eff}} - 1)/\lambda$.

Let

$$M_1(\zeta, q) = e^{-\zeta\sqrt{\Pr_{\text{eff}}}\sqrt{q}}. \tag{36}$$

The Laplace inverse of (36) is

$$m(\zeta, t) = L^{-1}\{M_1(\zeta, q)\} = \begin{cases} \dfrac{\zeta\sqrt{\Pr_{eff}}\, e^{-\zeta^2(\Pr_{\text{eff}}/4t)}}{2t\sqrt{\pi t}}; & \zeta > 0, \\ \delta(t); & \zeta = 0. \end{cases} \tag{37}$$

$$F(\zeta, q) = e^{-\zeta\sqrt{\lambda}\sqrt{(q+(m_2/2))^2-(m_2/2)^2}}. \tag{38}$$

Now applying the inverse LT of equation (38), we get

$$\begin{aligned} f_1(\zeta, t) &= \left[m(\zeta, t) + \frac{1}{2\lambda}\int_0^t m(\zeta, w)\frac{w}{\sqrt{t^2 - w^2}} I_1\left(\frac{1}{2\lambda}\sqrt{t^2 - w^2}\right)\mathrm{d}w\right]e^{-(1/2\lambda)t} \\ &= \frac{\zeta\sqrt{t}}{2t\sqrt{\pi t}} e^{\left(-\left(\zeta^2\lambda/4t\right)-(1/2\lambda)t\right)} + \frac{1}{2\lambda}e^{-(1/2\lambda)t}\int_0^t \frac{\zeta\sqrt{\lambda}}{2w\sqrt{\pi w}} e^{\left(-\zeta^2\lambda/4w\right)}\frac{w}{\sqrt{t^2 - w^2}} I_1\left(\frac{1}{2\lambda}\sqrt{t^2 - w^2}\right)\mathrm{d}w, \end{aligned} \tag{39}$$

$$f(\zeta, t) = L^{-1}\{F(\zeta, q)\} = \begin{cases} f_1(\zeta, t); & \zeta > 0, \\ \delta(t); & \zeta = 0, \end{cases}$$

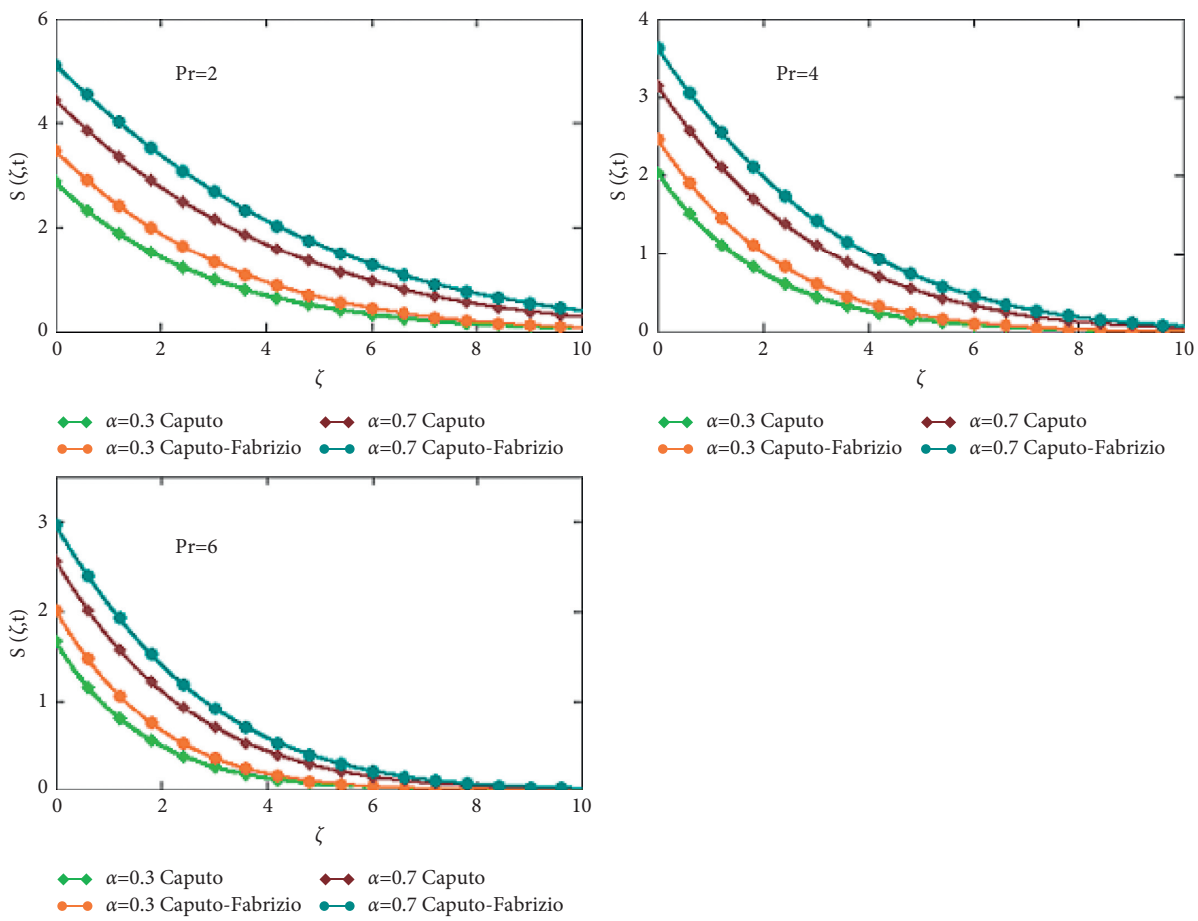

Figure 3: Variation of Pr with $Nr = 7$ and $t = 7$.

Let

$$P(q) = \frac{m_1 - m_2}{m_1^2}\frac{1}{q\sqrt{q}} + \frac{m_2}{m_1}\frac{1}{q^2\sqrt{q}} + \frac{m_2 - m_1}{m_1^2 m_3}\left(\frac{m_3}{\sqrt{q}\left\{q - \left(\sqrt{m_3}\right)^2\right\}}\right). \tag{40}$$

Applying the inverse LT of equation (40), we get

$$p(t) = \left[\frac{m_1 - m_2}{m_1^2} 2\sqrt{\frac{t}{\pi}} + \frac{m_2}{m_1}\frac{4t}{3}\sqrt{\frac{t}{\pi}} + \frac{m_2 - a_1}{m_1^2 m_3} e^{m_3 t} erf\left(\sqrt{m_3 t}\right)\right]. \tag{41}$$

Taking the inverse LT on equation (35) and by the convolution theorem, we get

$$\begin{aligned} u(\zeta, t) = &\int_0^t \mathrm{Cos}\omega(t-u) f(\zeta, u)\mathrm{d}u \\ &- \frac{Gr}{\sqrt{\mathrm{Pr}_{\mathrm{eff}}}}\int_0^t p(t-u) f(\zeta, u)\mathrm{d}u \\ &+ \frac{Gr}{\sqrt{\mathrm{Pr}_{\mathrm{eff}}}}\int_0^t p(t-u) m(y, u)\mathrm{d}u. \end{aligned} \tag{42}$$

11. Shear Stress with Caputo Time Fractional Derivative

Taking Laplace transform on (15), we acquire

$$\overline{\psi}(\zeta, q) = \frac{1}{(1+\lambda q^\alpha)}\frac{\partial \overline{u}(\zeta, q)}{\partial \zeta}. \tag{43}$$

Differentiating (31) w. r. t ζ, we get

$$\begin{aligned} \frac{\partial \overline{u}(\zeta, q)}{\partial \zeta} = &\left[\frac{Gr}{\sqrt{\mathrm{Pr}_{\mathrm{eff}}}}\frac{(1+\lambda q^\alpha)\sqrt{\mathrm{Pr}_{\mathrm{eff}} q^\alpha}}{q\sqrt{q^\alpha}\left[q^\alpha \mathrm{Pr}_{\mathrm{eff}} - (1+\lambda q^\alpha) q\right]}\right] e^{-\zeta\sqrt{\mathrm{Pr}_{\mathrm{eff}} q^\alpha}} \\ &- \left[\frac{q\sqrt{(1+\lambda q^\alpha) q}}{q^2 + \omega^2}\right. \\ &+ \left.\frac{Gr}{\sqrt{\mathrm{Pr}_{\mathrm{eff}}}}\frac{(1+\lambda q^\alpha)\sqrt{(1+\lambda q^\alpha) q}}{q\sqrt{q^\alpha}\left[q^\alpha \mathrm{Pr}_{\mathrm{eff}} - (1+\lambda q^\alpha) q\right]}\right] e^{-\zeta\sqrt{(1+\lambda q^\alpha) q}}. \end{aligned} \tag{44}$$

Substituting (44) into (43), we obtain

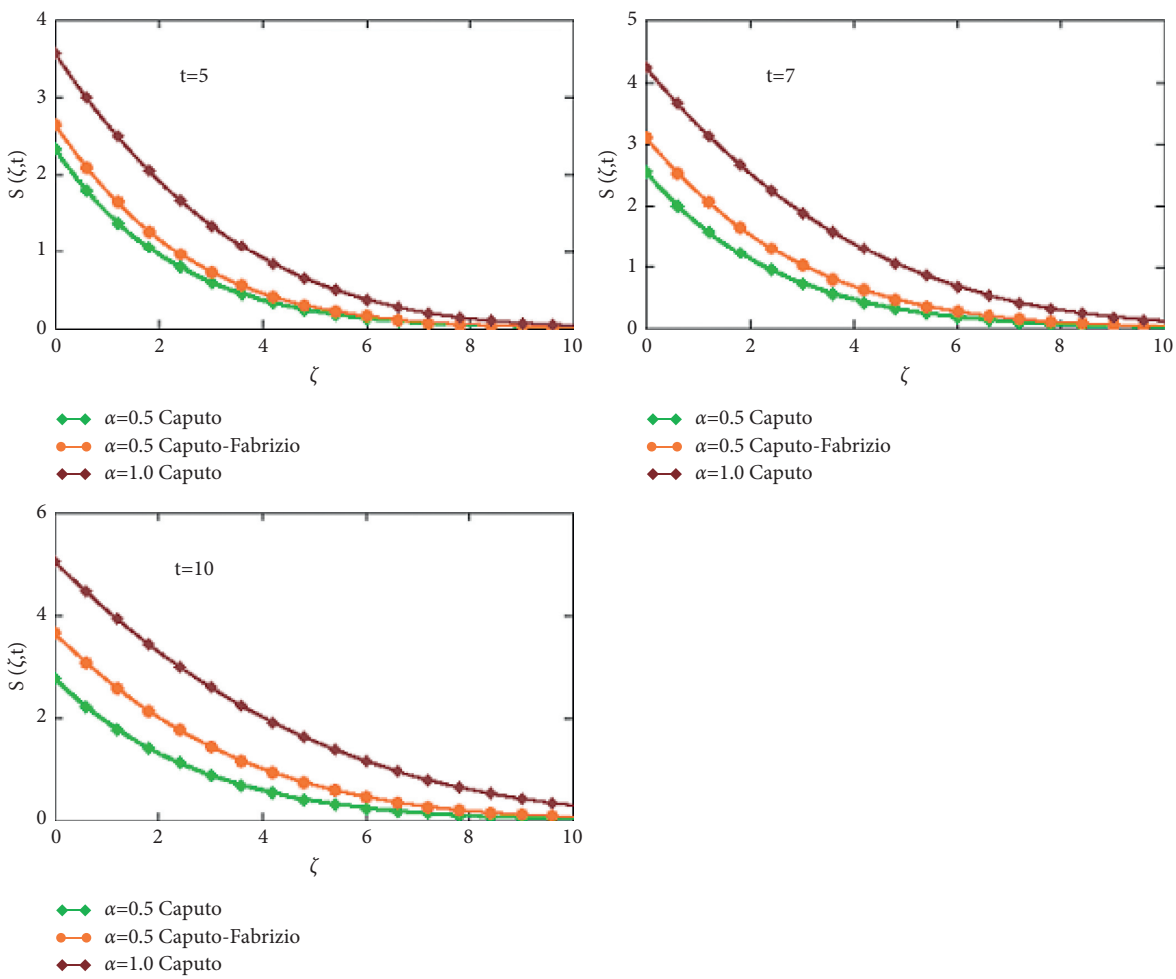

Figure 4: Comparison between fractional model and ordinary model, i.e., $\alpha \longrightarrow 1$.

$$\overline{\psi}(\zeta,q)=\frac{1}{(1+\lambda q^{\alpha})}\left[\frac{Gr}{\sqrt{\mathrm{Pr}_{\mathrm{eff}}}}\frac{(1+\lambda q^{\alpha})\sqrt{\mathrm{Pr}_{\mathrm{eff}}q^{\alpha}}}{q\sqrt{q^{\alpha}}\left[q^{\alpha}\mathrm{Pr}_{\mathrm{eff}}-(1+\lambda q^{\alpha})q\right]}\right]e^{-\zeta\sqrt{\mathrm{Pr}_{\mathrm{eff}}q^{\alpha}}}$$
$$-\frac{1}{(1+\lambda q^{\alpha})}\left[\frac{q\sqrt{(1+\lambda q^{\alpha})q}}{q^{2}+\omega^{2}}+\frac{Gr}{\sqrt{\mathrm{Pr}_{\mathrm{eff}}}}\frac{(1+\lambda q^{\alpha})\sqrt{(1+\lambda q^{\alpha})q}}{q\sqrt{q^{\alpha}}\left[q^{\alpha}\mathrm{Pr}_{\mathrm{eff}}-(1+\lambda q^{\alpha})q\right]}\right]e^{-\zeta\sqrt{(1+\lambda q^{\alpha})q}}. \tag{45}$$

12. Shear Stress with Caputo–Fabrizio Time Fractional Derivative

Taking LT of Caputo–Fabrizio fractional derivative on (15), we get

$$\overline{\psi}(\zeta,q)=\left(\frac{(q+\alpha m_{0})}{q+\alpha m_{0}+\lambda q m_{0}}\right)\frac{\partial\overline{u}(\zeta,q)}{\partial\zeta}. \tag{46}$$

Differentiating (32) w. r. t ζ, we have

$$\frac{\partial\overline{u}(\zeta,q)}{\partial\zeta}=\left[Gr\frac{(q+m_{0}\alpha+\lambda q m_{0})}{q\left[q m_{0}\mathrm{Pr}_{\mathrm{eff}}-(q+m_{0}\alpha+\lambda q m_{0})q\right]}\right]e^{-\zeta\sqrt{\mathrm{Pr}_{\mathrm{eff}}m_{0}q/(q+m_{0}\alpha)}}$$
$$-\left[\frac{q\sqrt{(q+m_{0}\alpha+\lambda q m_{0})q/(q+m_{0}\alpha)}}{q^{2}+\omega^{2}}+\frac{Gr}{\sqrt{\mathrm{Pr}_{\mathrm{eff}}m_{0}}}\frac{(q+m_{0}\alpha+\lambda q m_{0})\sqrt{(q+m_{0}\alpha+\lambda q m_{0})q/(q+m_{0}\alpha)}}{q\sqrt{q/(q+m_{0}\alpha)}\left[q m_{0}\mathrm{Pr}_{\mathrm{eff}}-(q+m_{0}\alpha+\lambda q m_{0})q\right]}\right]e^{-\zeta\sqrt{(q+m_{0}\alpha+\lambda q m_{0})q/q+m_{0}\alpha}}. \tag{47}$$

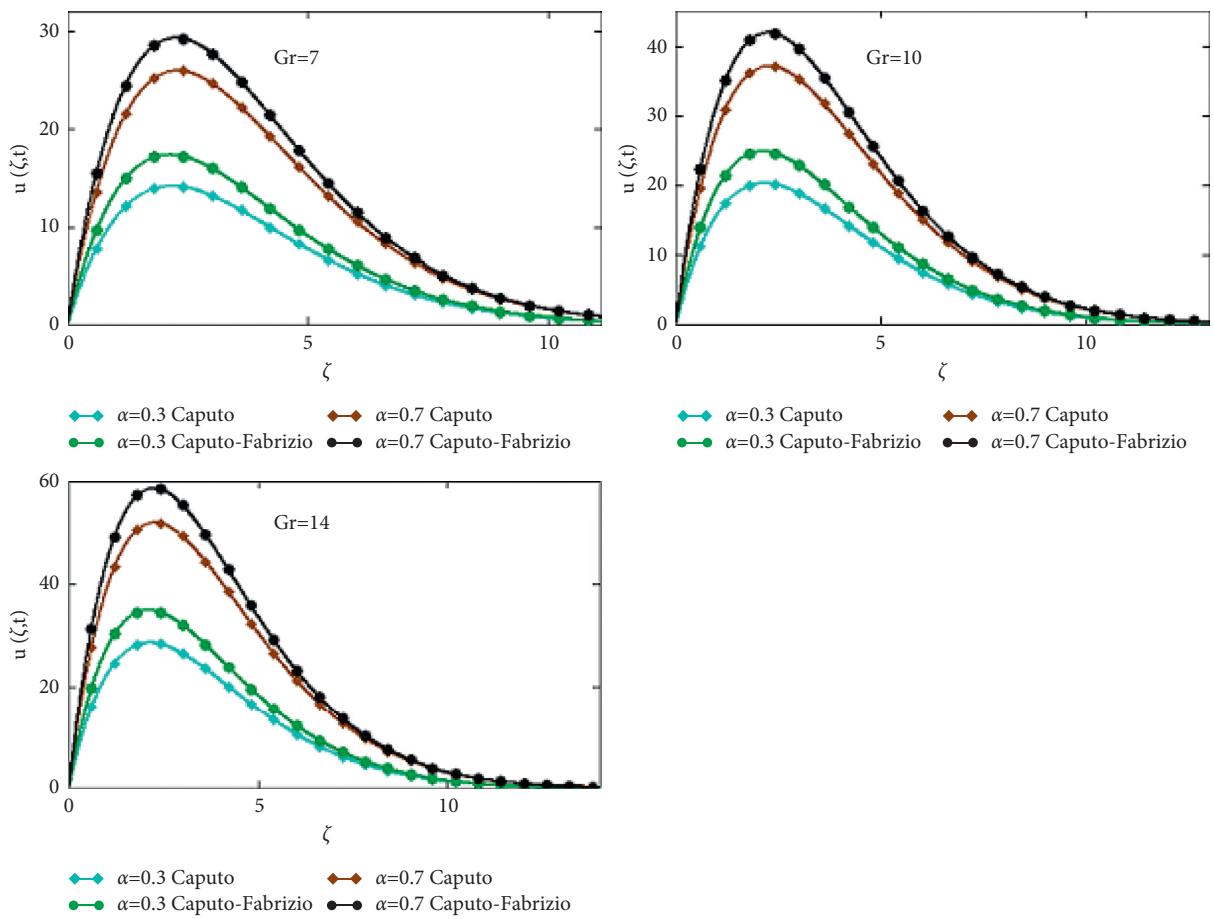

Figure 5: Variation of Gr with $Nr = 7, \lambda = 0.1$, and $\Pr = 4$.

Table 1: Effects of fractional factor α on temperature and velocity profile for CF and C fractional models with $\lambda = 0.1, Gr = 7, Nr = 7, Pr = 4, t = 7$, and $\omega = \pi/2$.

Parameter α	$S(\zeta,t)$ (CF)	$S(\zeta,t)$ (Caputo)	$u(\zeta,t)$ (CF)	$u(\zeta,t)$ (Caputo)
0.0	0.993	0.993	4.237	4.237
0.1	1.43	1.171	5.749	5.050
0.2	1.732	1.368	7.197	5.954
0.3	2.034	1.585	8.585	6.952
0.4	2.350	1.821	9.915	8.049
0.5	2.622	2.080	11.193	9.250
0.6	2.874	2.362	12.423	10.557
0.7	3.110	2.667	13.608	11.976
0.8	3.331	2.998	14.753	13.510
0.9	3.541	3.356	15.863	15.163
1.0	3.741	3.741	16.939	16.939

Table 2: Effects of ζ on temperature and velocity profile for CF and Caputo fractional models with $\lambda = 0.1, Gr = 7, Nr = 5, Pr = 4, t = 10, \alpha = 0.5$, and $\omega = \pi/2$.

ζ	$S(\zeta,t)$ (Stehfest)	$S(\zeta,t)$ (Tzou)	$S(\zeta,t)$ (Zakian)	$u(\zeta,t)$ (Stehfest)	$u(\zeta,t)$ (Tzou)	$u(\zeta,t)$ (Zakian)
0.2	2.973	2.961	2.973	5.743	4.551	4.965
0.4	2.785	2.768	2.785	10.628	9.427	10.035
0.6	2.607	2.586	2.607	14.765	13.696	14.326
0.8	2.436	2.415	2.436	18.224	17.356	17.918
1.0	2.274	2.253	2.274	21.070	20.418	20.875
1.2	2.119	2.100	2.119	23.362	22.910	23.259

Table 3: Numerical values of temperature profile, velocity profile, and shear stress subjected to various physical factors.

t	Gr	Pr	Nr	λ	$S(\zeta,t)$ (CF)	$u(\zeta,t)$ (CF)	$\psi(\zeta,t)$ (CF)
5	—	—	—	—	2.187	8.250	12.634
7	—	—	—	—	2.622	11.193	17.950
10	—	—	—	—	3.182	16.078	26.449
—	7	—	—	—	—	11.193	17.950
—	10	—	—	—	—	16.032	25.628
—	14	—	—	—	—	22.483	35.866
—	—	2	—	—	3.896	19.035	31.548
—	—	4	—	—	2.622	11.193	17.950
—	—	6	—	—	2.060	8.039	12.571
—	—	—	5	—	2.212	8.865	13.972
—	—	—	7	—	2.622	11.193	17.950
—	—	—	10	—	3.182	14.360	23.413
—	—	—	-	0.1	—	11.193	17.950
—	—	—	-	0.3	—	11.639	18.700
—	—	—	—	0.7	—	12.531	20.197
t	Gr	Pr	Nr	λ	$S(\zeta,t)$ CF	$u(\zeta,t)$ CF	$\psi(\zeta,t)$ CF
5	—	—	—	—	1.879	7.491	11.555
7	—	—	—	—	2.080	9.250	14.874
10	—	—	—	—	2.313	11.915	19.479
-	7	—	—	—	—	9.250	14.874
—	10	—	—	—	—	13.255	21.234
—	14	—	—	—	—	18.596	29.715
—	—	2	—	—	3.119	15.992	26.596
—	—	4	—	—	2.080	9.250	14.874
—	—	6	—	—	1.623	6.572	10.302
—	—	—	5	—	1.746	7.271	11.488
—	—	—	7	—	2.080	9.250	14.874
—	—	—	10	—	2.512	11.960	19.560
—	—	—	—	0.1	—	9.250	14.874
—	—	—	—	0.3	—	9.745	15.656
—	—	—	—	0.7	—	10.714	17.172

Table 4: Nomenclature.

u	Velocity of the fluid	S	Temperature of the fluid
U	Amplitude of the fluid	$H(t)$	Heaviside step function
ω	Frequency of oscillation	q_r	Radiative heat flux
g	Gravitational acceleration	λ_1	Maxwell fluid coefficient
c_p	Specific heat at constant pressure	k	Thermal conductivity
β	Volumetric coefficient of thermal expansion	ρ	Fluid density
v	Kinematic viscosity	μ	Absolute viscosity
Pr	Prandtl number	Gr	Grashof number
Nr	Radiation parameter	ψ	Shear stress
C	Caputo	CF	Caputo–Fabrizio
LT	Laplace transform	q	Laplace transform parameter
α	Fractional parameter	t	Time
q_1	Constant heat flux	i	Unit vector in direction of y

Substituting (47) into (46), we obtain the following form:

$$\overline{\psi}(\zeta,q)=\left[Gr\frac{(q+\alpha m_0)}{q\left[qm_0\mathrm{Pr}_{eff}-(q+m_0\alpha+\lambda qm_0)q\right]}\right]e^{-\zeta\sqrt{\mathrm{Pr}_{\mathrm{eff}}m_0q/(q+m_0\alpha)}}$$
$$-\left[\frac{q(q+\alpha m_0)\sqrt{(q+m_0\alpha+\lambda qm_0)q/(q+m_0\alpha)}}{(q^2+\omega^2)(q+m_0\alpha+\lambda qm_0)}+\frac{Gr}{\sqrt{\mathrm{Pr}_{\mathrm{eff}}m_0}}\frac{(q+\alpha m_0)\sqrt{(q+m_0\alpha+\lambda qm_0)q/(q+m_0\alpha)}}{q\sqrt{q/(q+m_0\alpha)}\left[qm_0\mathrm{Pr}_{\mathrm{eff}}-(q+m_0\alpha+\lambda qm_0)q\right]}\right]$$
$$\cdot e^{-\zeta\sqrt{(q+m_0\alpha+\lambda qm_0)q/(q+m_0\alpha)}}. \tag{48}$$

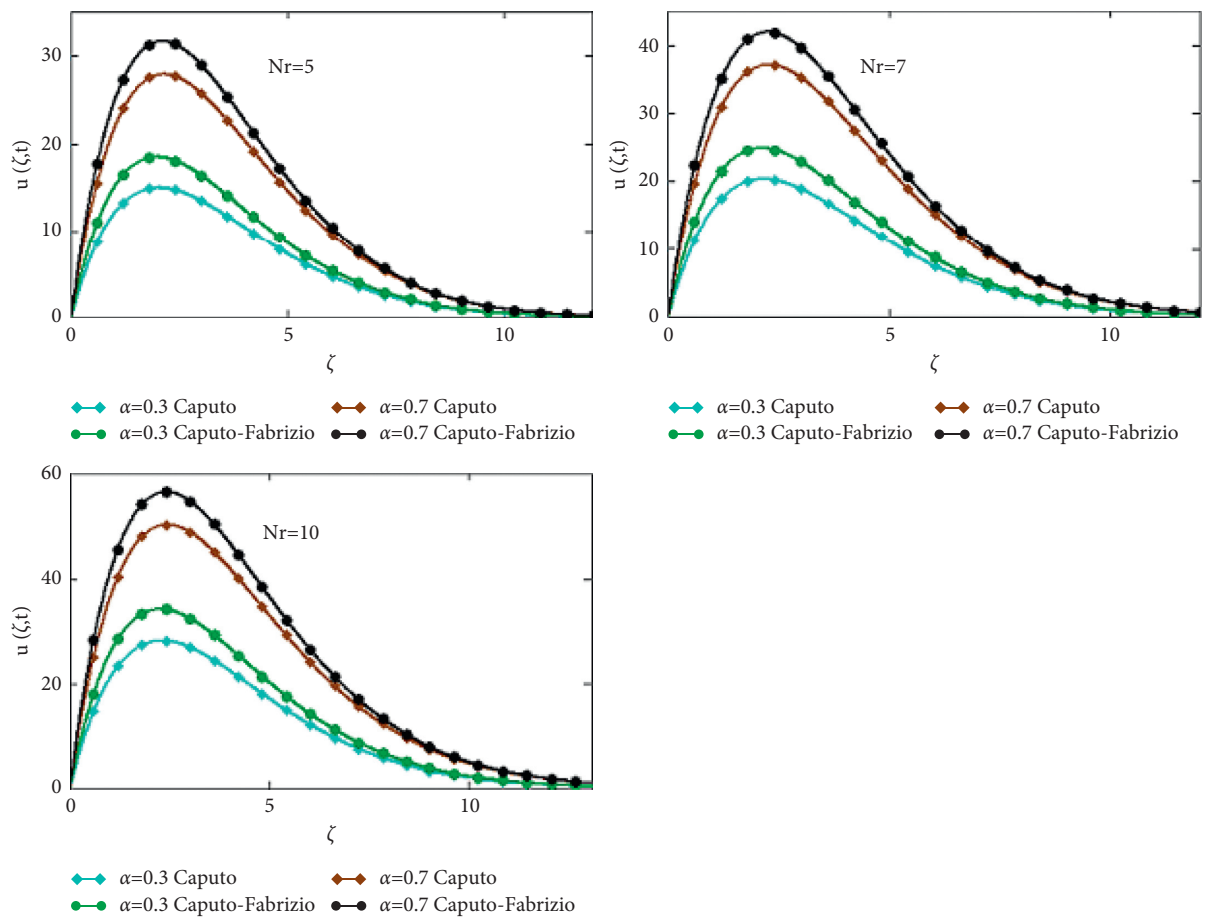

Figure 6: Variation of Nr with $Gr = 10, \lambda = 0.1$, $t = 7$, $\Pr = 4$, and $t = 7$.

13. Shear Stress in Ordinary Case $\alpha \longrightarrow 1$

Taking Laplace transform on equation (12), we get

$$\overline{\psi}(\zeta, q) = \frac{1}{(1+\lambda q)} \frac{\partial \overline{u}(\zeta, q)}{\partial \zeta}. \tag{49}$$

Differentiating equation (34) w. r. t ζ, we get

$$\frac{\partial \overline{u}(\zeta, q)}{\partial \zeta} = \left[\frac{-q\sqrt{q(1+\lambda q)}}{q^2+\omega^2} - \frac{Gr(1+\lambda q)\sqrt{q(1+\lambda q)}}{q^2\sqrt{q}\sqrt{\Pr_{\text{eff}}}\left[\Pr_{\text{eff}} - (1+\lambda q)\right]}\right] e^{-\zeta\sqrt{q(1+\lambda q)}} + \left[\frac{Gr(1+\lambda q)\sqrt{s\Pr_{\text{eff}}}}{q^2\sqrt{q}\sqrt{\Pr_{\text{eff}}}\left[\Pr_{\text{eff}} - (1+\lambda q)\right]}\right] e^{-\zeta\sqrt{q\Pr_{\text{eff}}}}. \tag{50}$$

The above equation can be written as

$$\begin{aligned}\frac{\partial \overline{u}(\zeta, q)}{\partial \zeta} = &-\frac{q\sqrt{q(1+\lambda q)}}{q^2+\omega^2} e^{-\zeta\sqrt{q(1+\lambda q)}} \\ &- \frac{Gr\sqrt{q(1+\lambda q)}}{\sqrt{\Pr_{\text{eff}}}}\left[\frac{m_1-m_2}{m_1^2}\frac{1}{q\sqrt{q}} + \frac{m_2}{m_1}\frac{1}{q^2\sqrt{q}} + \frac{m_2-m_1}{m_1^2 m_3}\left(\frac{m_3}{\sqrt{q}\left(q-\left(\sqrt{m_3}\right)^2\right)}\right)\right] e^{-\zeta\sqrt{q(1+\lambda q)}} \\ &+ \frac{Gr\sqrt{q\Pr_{\text{eff}}}}{\sqrt{\Pr_{\text{eff}}}}\left[\frac{m_1-m_2}{m_1^2}\frac{1}{q\sqrt{q}} + \frac{m_2}{m_1}\frac{1}{q^2\sqrt{q}} + \frac{m_2-m_1}{m_1^2 m_3}\left(\frac{m_3}{\sqrt{q}\left(q-\left(\sqrt{m_3}\right)^2\right)}\right)\right] e^{-\zeta\sqrt{q}\sqrt{\Pr_{\text{eff}}}}.\end{aligned} \tag{51}$$

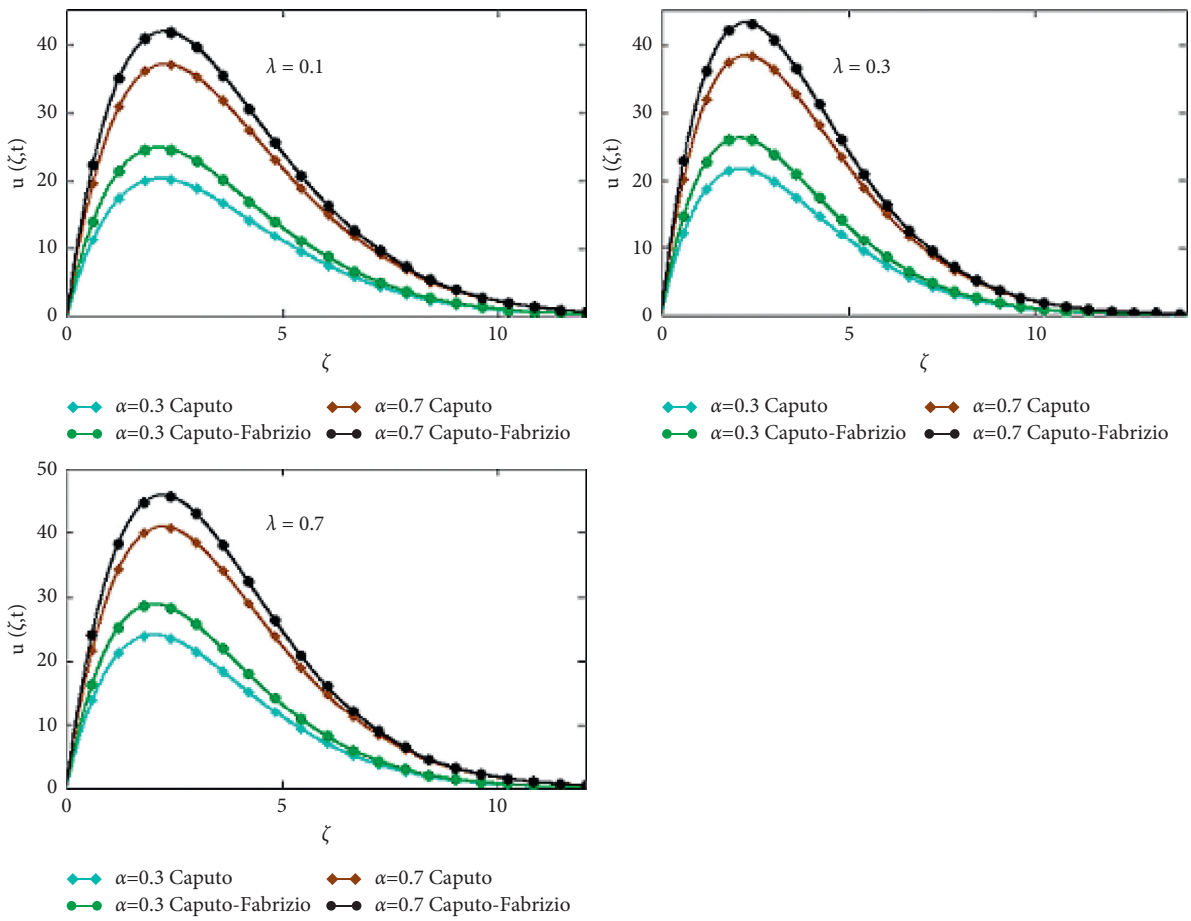

Figure 7: Variation of λ with $Nr = 7, Gr = 10$, and $\Pr = 4$.

Substituting equation (51) into equation (49), we have

$$\overline{\psi}(\zeta,q) = D(q)F(\zeta,q) - \frac{Gr}{\sqrt{\Pr_{\text{eff}}}}E(q)F(\zeta,q) + \frac{Gr}{\sqrt{\Pr_{\text{eff}}}}K(q)M(\zeta,q), \tag{52}$$

where

$$D(q) = -\frac{q\sqrt{q(1+\lambda q)}}{(1+\lambda q)\left(q^2+\omega^2\right)},$$
$$E(q) = \frac{P(q)\sqrt{q(1+\lambda q)}}{(1+\lambda q)}, \tag{53}$$
$$K(q) = \frac{G(q)\sqrt{\Pr_{\text{eff}}q}}{(1+\lambda q)}.$$

Taking the inverse LT on equation (52) and utilizing Faltung theorem, we get

$$\psi(\zeta,t) = D(\zeta,t) * F(\zeta,t) - \frac{Gr}{\sqrt{\Pr_{\text{eff}}}}E(t) * F(\zeta,t) + \frac{Gr}{\sqrt{\Pr_{\text{eff}}}}K(t) * m(\zeta,t). \tag{54}$$

Taking Laplace inverse transform on equation (53), we get

$$D(t) = \frac{\omega}{\lambda}\int_0^t \text{Sin}[\omega(t-h)]e^{(-h/2\lambda)}I_0\left(\frac{h}{2\lambda}\right)\text{d}h,$$
$$E(t) = g(t) * \left[\frac{1}{m_1\lambda\sqrt{\lambda}}\int_0^t I_0\left(\frac{h}{2\lambda}\right)e^{-(-h/2\lambda)}\text{d}h - \frac{1-m_1\lambda}{m_1\lambda\sqrt{\lambda}}\int_0^t I_1\left(\frac{h}{2\lambda}\right)e^{\left(-(-h/2\lambda)-m_1(t-h)\right)}\text{d}h\right],$$

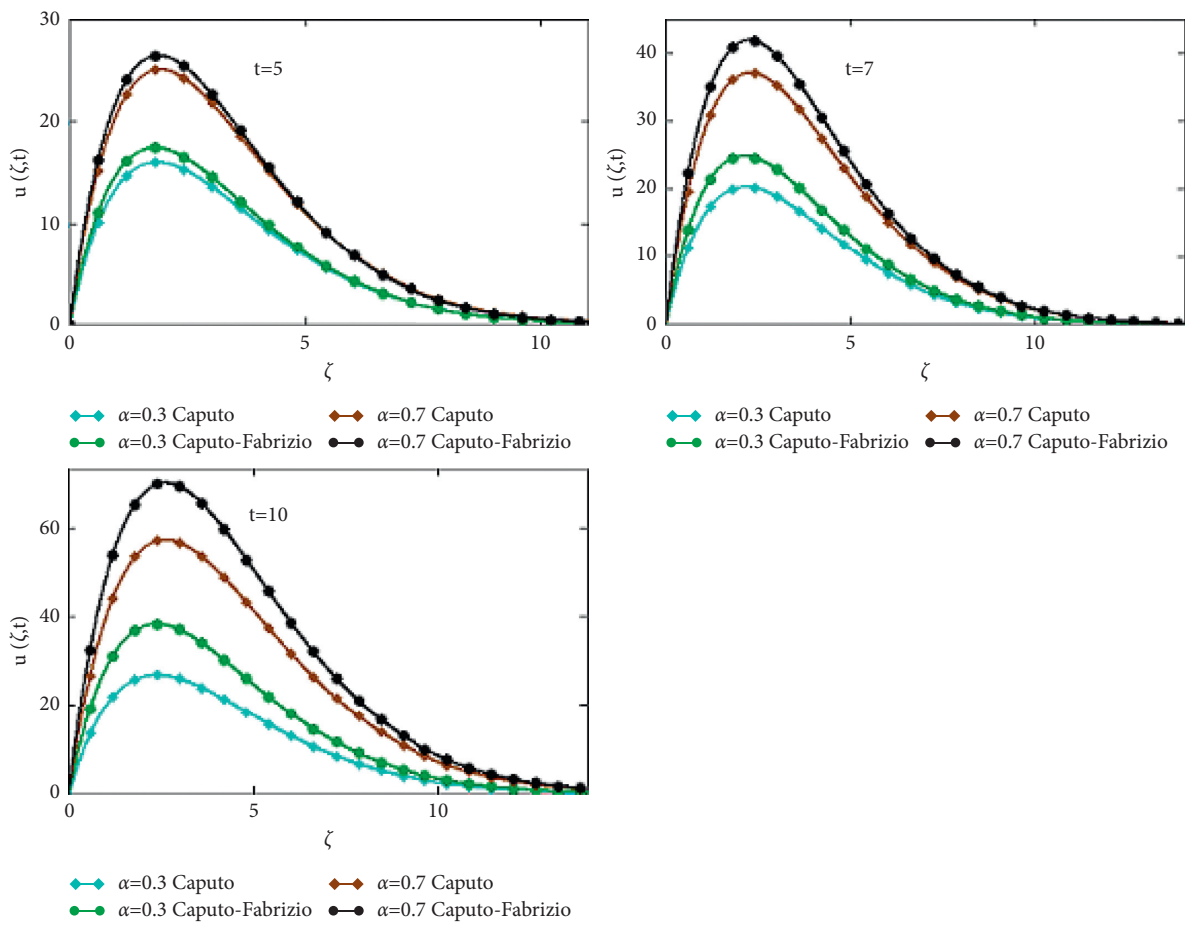

Figure 8: Variation of t with $Gr = 10, \lambda = 0.1$, $t = 7$, $Nr = 7$, and $\Pr = 4$.

$$K(t) = g(t) * \left[\frac{m_1\lambda - 1}{m_1^2\lambda} n(t) + \frac{1}{m_1\lambda}\int_0^t n(x)\mathrm{d}x + \frac{m_1\lambda - 1}{m_1^2\lambda}\left[n(t) - m_1\int_0^t e^{[-m_1(t-x)]} n(x)\mathrm{d}x\right]\right]. \tag{55}$$

Due to the complex combination of Laplace transform in equations (32), (33), (47), and (50), analytical LP inversion is very difficult, so for the Laplace inversion, we use different numerical LP inversion methods like Stehfest's numerical method, Tzou's algorithms, and Zakian's algorithms.

14. Numerical Discussion and Graphs

The aim of this research is to study the Maxwell fluid's natural convection flow with radiation and consistent heat flow. The differential model is developed into fractional order. There are two fractional derivative concepts that we used (Caputo and Caputo–Fabrizio derivatives). Solutions for temperature and velocity are extended to Caputo and Caputo–Fabrizio derivatives. Solutions are obtained through the Laplace transform method. The effect of various embedded factors on temperature and velocity is a key feature of the model. We are also interested in comparing the Caputo and Caputo–Fabrizio derivative results. Figure 1 shows the behavior of radiation parameter Nr on temperature. The Caputo fractional model has a smaller temperature as compared to Caputo–Fabrizio. The enhancement of radiation parameter Nrenhances the fluid temperature. The variation of time t on temperature is shown in Figure 2. Figure 2 presents the same behavior of fractional models like Figure 1. The fluid temperature increases with increasing time. Due to this, the boundary layer increases with increasing time. The impact of Pr is indicated in Figure 3. It is stated that incrementing the Prandtl number Pr decrements the temperature. Physically, the higher the value of Pr, the higher the fluid viscosity and the lower the thermal conductivity. Because of this, the thickness of the boundary layer falls. Figure 4 shows the comparison between the fractional model and ordinary model, i.e., $\alpha \longrightarrow 1$. The temperature of the ordinary model is higher than that of the fractional model.

Tables 1–3 show some basic findings of the given work. Table 4 depicts a numerical solution for temperature and velocity profiles calculated using the CF and Caputo time derivatives for different values of fractional factor α. It indicates that increasing the fractional factor's value enhances the fluid's temperature and velocity. It suggests that

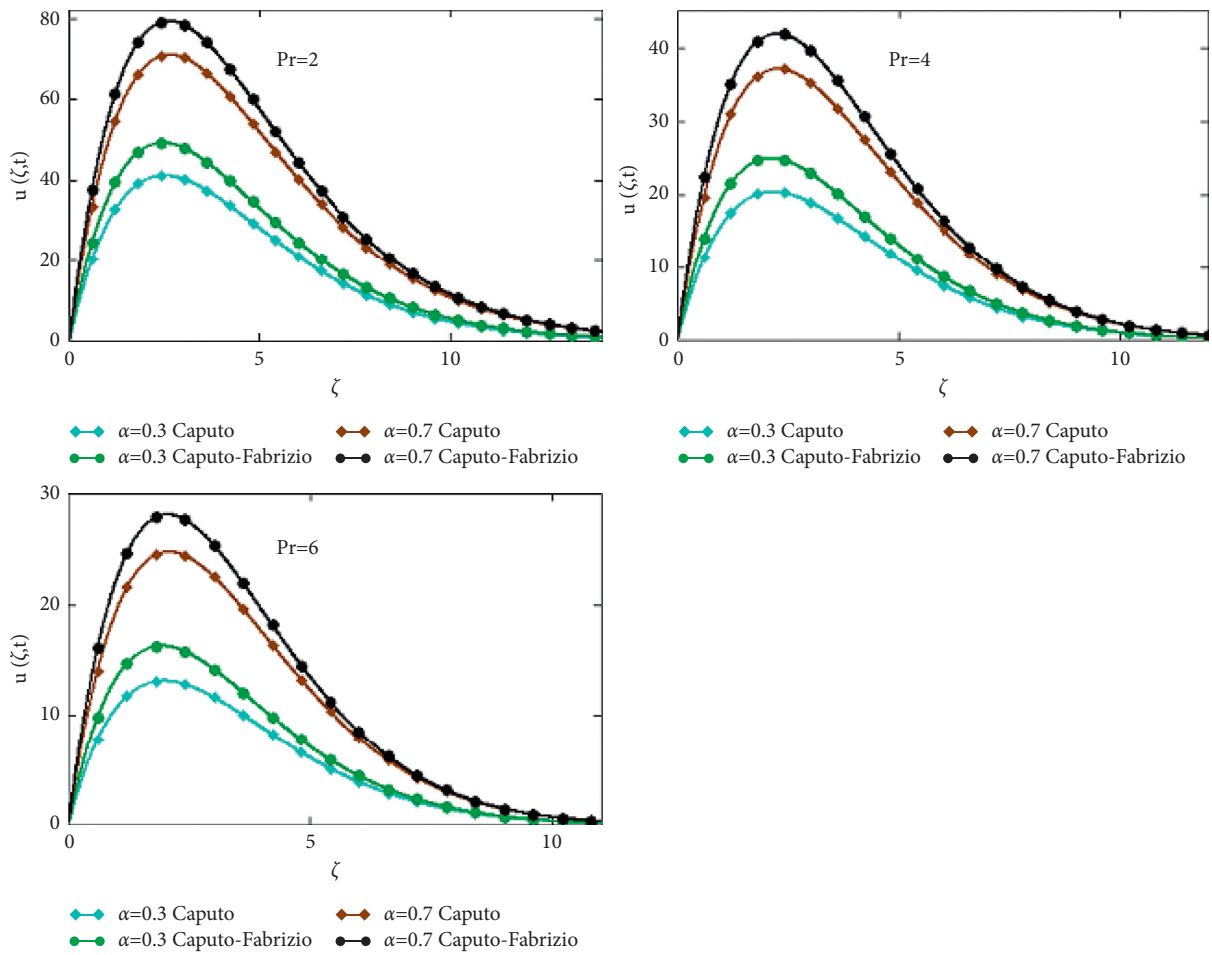

Figure 9: Variation of Pr with $Nr = 7, Gr = 10, t = 7$, and $\lambda = 0.1$.

CF has a greater velocity and temperature than Caputo. Table 2 shows the comparisons between various numerical inverse LT algorithms like Stehfest's algorithm and Tzou's algorithm with the exact solution. It verifies the validity and correctness of solutions up to the desired level of precision. Table 3 presents the relationships between the solutions obtained for temperature, velocity, and shear stress using various embedded factors. From this, we can see that the increase of various embedded parameters increases the fluid temperature, velocity, and shear stress except for the Prandtl number which shows the inverse effects from other parameters.

The effect of the velocity curve for the Grashof number is presented in Figure 5. It shows that the enhancement of the value of Gr enhances the velocity of both the models. This behavior is due to the rise in buoyancy force because of temperature gradient. Figure 6 shows the influence of radiation factor Nr on velocity. Clearly, Figure 6 shows that the velocity of fluid with C and CF variants of fractional derivatives increases due to increasing value of the radiation factor. Figure 7 portrays the behavior of Maxwell fluid factor on velocity field. It shows the same effect as Figure 6. Incrementing the value of the Maxwell fluid factor increments the velocity of the Caputo and Caputo–Fabrizio models. In Figure 8, the impact of time is shown for velocity. It is noted that the fluid velocity increases with the increase in time. The temperature is greater near the plate and decreases as we go away from the plate and finally becomes zero in the free stream region. From Figure 9, we can see that the fluid velocity decreases when the value of Prandtl number Pr increases. Moreover, the enhancement of Pr decreases the thickness of the boundary layer. Figure 10 shows the comparison between the fractional model and ordinary fluid model. It shows that the velocity of the ordinary fluid model, i.e., $\alpha \longrightarrow 1$, is greater than the velocity of the fractional model.

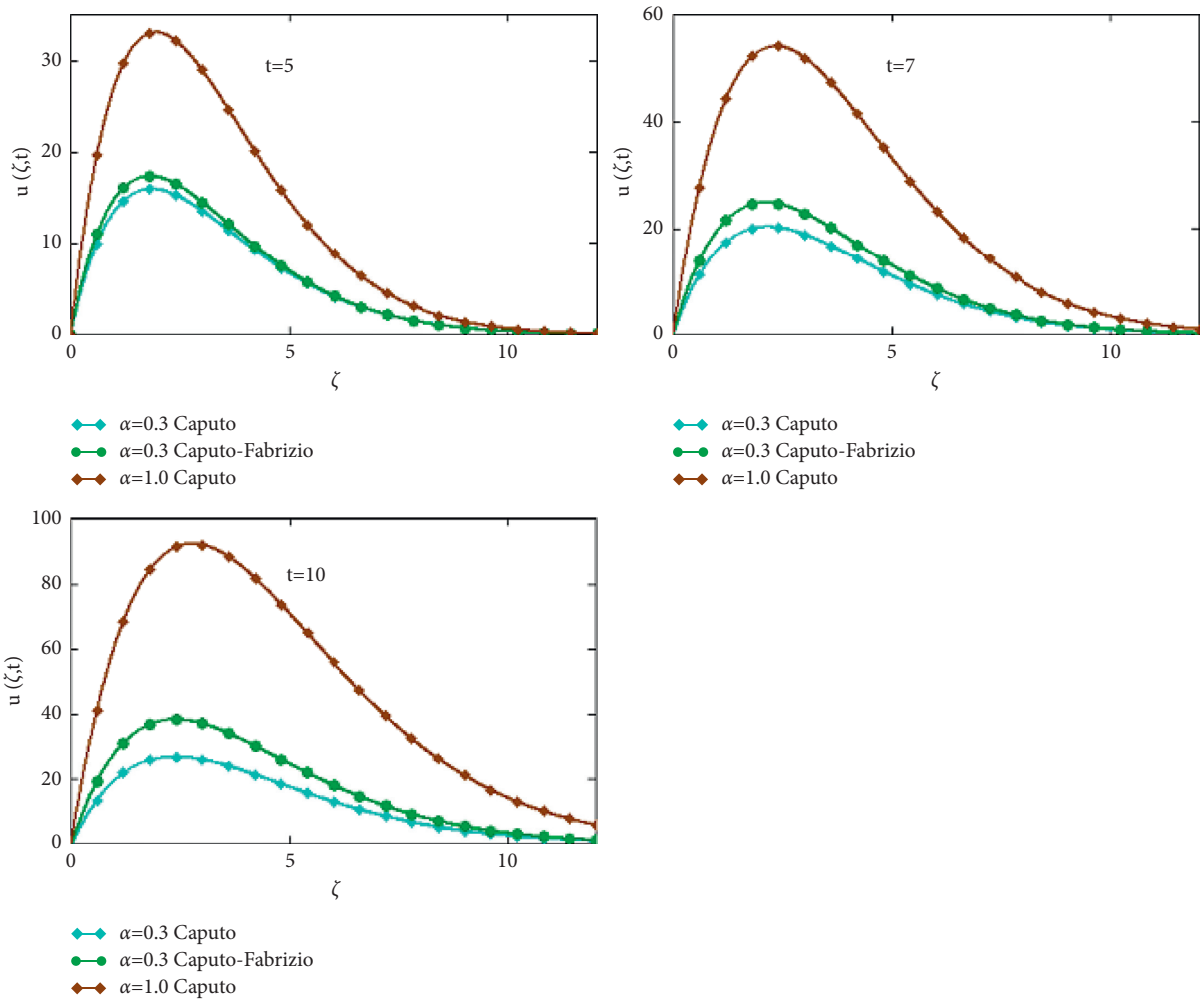

Figure 10: Comparison between fractional model ($t = 7$ and $\lambda = 0.1$) and ordinary model, i.e., $\alpha \longrightarrow 1$.

15. Conclusion

The objective of the present work is to conduct a comparative study of the natural convection flow of fractional Maxwell fluid in the presence of radiation and uniform heat flux. The two fractional derivative definitions are used (C and CF) in the formulation of the problem. The solutions for heat and velocity are obtained through the Laplace transform method. The following are the study's key findings:

(i) The temperature of the fluid increases with increase in the embedded factors like Nr and t.

(ii) Increasing the Prandtl number reduces the fluid's temperature.

(iii) The enhancement of the fluid parameters like Gr, Nr, λ, and t enhances the fluid's velocity for both models, while the Prandtl number shows the adverse effects from other factors.

(iv) Increasing the value of Gr, Nr, and λ increases the shear stress of the fluid, while the Prandtl number has the opposite effect.

Data Availability

No data were used to support this study.

Conflicts of Interest

The authors declare that there are no conflicts of interest.

Acknowledgments

This study was supported by the Key Scientific Research Projects of Chaohu University (subject nos. XLZ-201804 and XLZ-201808) and the Industry University Research Project of Chaohu University (subject nos. hxkt20200013 and hxkt20200059).

References

[1] M. Sheikholeslami, T. Hayat, and A. Alsaedi, "MHD free convection of Al_2O_3-water nanofluid considering thermal radiation: a numerical study," *International Journal of Heat and Mass Transfer*, vol. 96, pp. 513–524, 2016.

[2] M. Sheikholeslami and D. D. Ganji, "CVFEM for free convective heat transfer of CuO-water nanofluid in a tilted semi annulus," *Alexandria Engineering Journal*, vol. 56, no. 4, pp. 635–645, 2017.

[3] M. Sheikholeslami and M. M. Rashidi, "Effect of space dependent magnetic field on free convection of Fe_3O_4-water nanofluid," *Journal of the Taiwan Institute of Chemical Engineers*, vol. 56, pp. 6–15, 2015.

[4] M. Sheikholeslami, K. Vajravelu, and M. M. Rashidi, "Forced convection heat transfer in a semi annulus under the influence of a variable magnetic field," *International Journal of Heat and Mass Transfer*, vol. 92, pp. 339–348, 2016.

[5] I. Khan, N. A. Shah, and L. C. Dennis, "A scientific report on heat transfer analysis in mixed convection flow of Maxwell fluid over an oscillating vertical plate," *Scientific Reports*, vol. 7, no. 1, pp. 40147–40211, 2017.

[6] I. Khan, N. A. Shah, Y. Mahsud, and D. Vieru, "Heat transfer analysis in a Maxwell fluid over an oscillating vertical plate using fractional Caputo-Fabrizio derivatives," *The European Physical Journal Plus*, vol. 132, no. 4, pp. 1–12, 2017.

[7] S. Aman, Q. Al-Mdallal, and I. Khan, "Heat transfer and second order slip effect on MHD flow of fractional Maxwell fluid in a porous medium," *Journal of King Saud University Science*, vol. 32, no. 1, pp. 450–458, 2020.

[8] E. U. Haque, A. U. Awan, N. Raza, M. Abdullah, and M. A. Chaudhry, "A computational approach for the unsteady flow of Maxwell fluid with Caputo fractional derivatives," *Alexandria engineering journal*, vol. 57, no. 4, pp. 2601–2608, 2018.

[9] M. B. Riaz, A. Atangana, and N. Iftikhar, "Heat and mass transfer in Maxwell fluid in view of local and non-local differential operators," *Journal of Thermal Analysis and Calorimetry*, vol. 143, no. 1, pp. 1–17, 2020.

[10] C. Fetecau, M. Athar, and C. Fetecau, "Unsteady flow of a generalized Maxwell fluid with fractional derivative due to a constantly accelerating plate," *Computers & Mathematics with Applications*, vol. 57, no. 4, pp. 596–603, 2009.

[11] S. Aman, I. Khan, Z. Ismail, M. Z. Salleh, and Q. M. Al-Mdallal, "Heat transfer enhancement in free convection flow of CNTs Maxwell nanofluids with four different types of molecular liquids," *Scientific Reports*, vol. 7, no. 1, pp. 2445–2513, 2017.

[12] Y. Liu and B. Guo, "Effects of second-order slip on the flow of a fractional Maxwell MHD fluid," *Journal of the Association of Arab Universities for Basic and Applied Sciences*, vol. 24, no. 1, pp. 232–241, 2017.

[13] S. Shateyi and G. T. Marewo, "A new numerical approach of MHD flow with heat and mass transfer for the UCM fluid over a stretching surface in the presence of thermal radiation," *Mathematical Problems in Engineering*, vol. 2013, Article ID 670205, 8 pages, 2013.

[14] A. Mohi, "Effect of MHD on unsteady flow with fractional maxwell model," *Journal of Al-Nahrain University-Science*, vol. 19, no. 2, pp. 130–136, 2016.

[15] M. B. Riaz and N. Iftikhar, "A comparative study of heat transfer analysis of MHD Maxwell fluid in view of local and nonlocal differential operators," *Chaos, Solitons & Fractals*, vol. 132, Article ID 109556, 2020.

[16] K. A. Abro and A. A. Shaikh, "Exact analytical solutions for Maxwell fluid over an oscillating plane," *Science International (Lahore) ISSN*, vol. 27, pp. 923–929, 2015.

[17] M. I. Asjad, N. A. Shah, M. Aleem, and I. Khan, "Heat transfer analysis of fractional second-grade fluid subject to Newtonian heating with Caputo and Caputo-Fabrizio fractional derivatives: a comparison," *The European Physical Journal Plus*, vol. 132, no. 8, pp. 1–19, 2017.

[18] N. Raza and M. A. Ullah, "A comparative study of heat transfer analysis of fractional Maxwell fluid by using Caputo and Caputo-Fabrizio derivatives," *Canadian Journal of Physics*, vol. 98, no. 1, pp. 89–101, 2020.

[19] N. Wang, N. A. Shah, I. Tlili, and I. Siddique, "Maxwell fluid flow between vertical plates with damped shear and thermal flux: free convection," *Chinese Journal of Physics*, vol. 65, pp. 367–376, 2020.

[20] I. Khan, F. Ali, and S. Shafie, "Exact solutions for unsteady magnetohydrodynamic oscillatory flow of a Maxwell fluid in a porous medium," *Zeitschrift für Naturforschung A*, vol. 68, no. 10-11, pp. 635–645, 2013.

[21] L. Zheng, F. Zhao, and X. Zhang, "Exact solutions for generalized Maxwell fluid flow due to oscillatory and constantly accelerating plate," *Nonlinear Analysis: Real World Applications*, vol. 11, no. 5, pp. 3744–3751, 2010.

[22] C. Fetecau, M. Jamil, C. Fetecau, and I. Siddique, "A note on the second problem of Stokes for Maxwell fluids," *International Journal of Non-linear Mechanics*, vol. 44, no. 10, pp. 1085–1090, 2009.

[23] U. Farooq, D. Lu, S. Munir, M. Ramzan, M. Suleman, and S. Hussain, "MHD flow of Maxwell fluid with nanomaterials due to an exponentially stretching surface," *Scientific Reports*, vol. 9, no. 1, pp. 7312–7411, 2019.

[24] M. Jamil, C. Fetecau, and C. Fetecau, "Unsteady flow of viscoelastic fluid between two cylinders using fractional Maxwell model," *Acta Mechanica Sinica*, vol. 28, no. 2, pp. 274–280, 2012.

[25] A. A. Zafar, N. A. Shah, N. Nigar, and N. Nigar, "On some rotational flows of non-integer order rate type fluids with shear stress on the boundary," *Ain Shams Engineering Journal*, vol. 9, no. 4, pp. 1865–1876, 2018.

[26] M. Jamil, K. A. Abro, and N. A. Khan, "Helices of fractionalized Maxwell fluid," *Nonlinear Engineering*, vol. 9, no. 4, p. 191, 2015.

[27] T. Hayat, M. Rashid, A. Alsaedi, and S. Asghar, "Nonlinear convective flow of Maxwell nanofluid past a stretching cylinder with thermal radiation and chemical reaction," *Journal of the Brazilian Society of Mechanical Sciences and Engineering*, vol. 41, no. 2, p. 86, 2019.

[28] M. D. Hisham, A. Rauf, D. Vieru, and A. U. Awan, "Analytical and semi-analytical solutions to flows of two immiscible Maxwell fluids between moving plates," *Chinese Journal of Physics*, vol. 56, no. 6, pp. 3020–3032, 2018.

[29] W. A. Azhar, D. Vieru, and C. Fetecau, "Free convection flow of some fractional nanofluids over a moving vertical plate with uniform heat flux and heat source," *Physics of Fluids*, vol. 29, no. 8, 2017.

[30] J. N. Tokis, "A class of exact solutions of the unsteady magnetohydrodynamic free-convection flows," *Astrophysics and Space Science*, vol. 112, no. 2, pp. 413–422, 1985.

[31] C. Fetecau, S. Akhtar, I. Pop, and C. Fetecau, "Unsteady general solution for MHD natural convection flow with radiative effects, heat source and shear stress on the boundary," *International Journal of Numerical Methods for Heat & Fluid Flow*, vol. 27, no. 6, pp. 1266–1281, 2017.

[32] Samiulhaq, C. Fetecau, I. Khan, F. Ali, and S. Shafie, "Radiation and porosity effects on the magnetohydrodynamic flow past an oscillating vertical plate with uniform heat flux," *Zeitschrift für Naturforschung A*, vol. 67, no. 10-11, pp. 572–580, 2012.

Hindawi
Complexity
Volume 2021, Article ID 5757991, 11 pages
https://doi.org/10.1155/2021/5757991

Research Article

Flow of Brinkman Fluid with Heat Generation and Chemical Reaction

M. Ramzan,[1] Zaib Un Nisa,[2] M. Ahmad,[1] and M. Nazar[1,3]

[1]*Centre for Advanced Studies in Pure and Applied Mathematics, Bahauddin Zakariya University, Multan, Pakistan*
[2]*Department of Mathematics, University of Education Lahore, Multan Campus, Multan, Pakistan*
[3]*School of Mathematical Sciences, University of Science and Technology of China, Hefei, Anhui, China*

Correspondence should be addressed to M. Nazar; mudassar_666@yahoo.com

Received 8 June 2021; Accepted 7 August 2021; Published 25 August 2021

Academic Editor: Ali Akgül

Unsteady magnetohydrodynamics (MHD) flow of fractionalized Brinkman-type fluid over a vertical plate is discussed. In the model of problem, additional effects such as heat generation/absorption and chemical reaction are also considered. The model is solved by using the Caputo fractional derivative. The governing dimensionless equations for velocity, concentration, and temperature profiles are solved using the Laplace transform method and compared graphically. The effects of different parameters like fractional parameter, heat generation/absorption Q, chemical reaction R, and magnetic parameter M are discussed through numerous graphs. Furthermore, comparison among ordinary and fractionalized velocity fields are also drawn. From the figures, it is observed that chemical reaction and magnetic field have decreasing effect on velocity profile, whereas thermal radiation and mass Grashof numbers have increasing effect on the velocity of the fluid.

1. Introduction

The important significance of non-Newtonian fluids can be seen in applied mathematics, engineering, and physics. It has various significances in many areas, such as uses of lubricants, biological fluid food processing, or plastic manufacturing. Some commonly examples of non-Newtonian fluids are custard, colloids, melted butter, paint, ketchup, starch suspensions, blood, toothpaste, gels, shampoo, and corn starch.

Mass transfer and heat transfer occurs mostly in nature due to temperature and concentration differences, respectively. Today, research work in magnetohydrodynamics (MHD) has substantial significance as these flows are absolutely prevailing in nature.

Convection flow with porous media has numerous applications such as flows in soils, solar power collectors, heat transfer correlated with geothermal systems, heat source in the field of agricultural storage system, heat transfer in nuclear reactors, heat transfer in aerobic and anaerobic reactions, heat evacuation from nuclear fuel detritus, and heat exchangers for porous material.

MHD fluid has many implementations in meteorology, distillation of gasoline, energy generators, geophysics, accelerators, petroleum industry, astrophysics, polymer technology, aerodynamics, and boundary layer control and in material processes such as glass fiber drawing, extrusion, and casting wire. The flow of viscous fluid through a perpendicular plate is analyzed by Swamy et al. [1]. The effect of mass diffusion on MHD fluid with porosity has been observed by Chaudhary et al. [2]. Exact solution for magnetohydrodynamics flow through a perpendicular plate in the existence of porosity is obtained by Sivaiah et al. [3]. The solution for unsteady flow of viscous fluid with porosity is obtained by Das and Jana [4].

Furthermore, convection flow in the existence of porosity has wide applications such as ground water hydrology, oil extraction, geothermal systems, cooling systems, storage of nuclear waste materials, energy-efficient drying processes, solid matrix heat exchangers, and wall-cooled catalytic reactors. Kataria and Patel [5] analyzed the impact of magnetic field with heat transfer over a plate. The authors of [6] discussed the solution of viscous fluid flow with thermal

radiation. Chamkha [7] discussed the effect of heat source on MHD fluid through a moving plate.

The authors of [8] studied the flow of polar fluid through a plate. Rahman and Sattar [9] studied the flow of fluid with a heat source. Rajesh and Varma [10] studied the influence of mass diffusion on magnetohydrodynamic fluid flow. The authors of [11] analyzed the solution of convection flow through a vertical plate. They also discussed the solution for time-dependent concentration and temperature. Convection flow immersed in a porous media through a surface is discussed in [12–14].

The impact of conjugate flow of MHD fluid is discussed by Khan et al. [15]. Rajesh et al. [16] discussed the MHD flow through a moving plate. MHD flow through an accelerated surface in the existence of porous media is discussed by Chaudhary et al. [17]. The authors also analyzed the solution of velocity field graphically. Das [18] analyzed the solution of magnetohydrodynamics of convection flow through a plate. Pal et al. [19] examined the solution of viscous fluid with thermal radiation on magnetohydrodynamics flow, whereas the solution for convection flow with nonuniform temperature through a moving plate is obtained by Seth et al. [20]. The solution of nanofluid with ramped temperature is studied by Khalid et al. [21].

The discussion of mass diffusion has empirical use in numerous areas of engineering and applied sciences. These phenomena play a vital role in cooling of a nuclear reactor and tabular reactor, chemical industry, mixture of terracotta material, petroleum industry, and decomposition of rigid materials. Seddeek et al. [22] examined the MHD fluid flow with thermal radiation. An intensive study of chemical reaction with heat source/sink is studied by Shah et al. [23]. Seth et al. [24] obtained the solution of unsteady magnetohydrodynamic flow of the fluid over a plate with ramped condition. The solution of convection flow of MHD fluid over a plate with heat generation/absorption is obtained by Shateyi and Motsa[25]. MHD fluid flow with Ohmic heating and heat generation is analyzed by Kasim et al. [26]. The exact solution of MHD fluid with mass transfer immersed in a porous media is discussed by Ali et al. [27]. The exact solution of magnetohydrodynamic flow of a Brinkman fluid perpendicular to the plate is analyzed by Khan et al. [28]. The analytical investigation of Brinkman fluid flow with variable concentration, temperature, and velocity is obtained by Ali et al. [29]. The flow of nanofluid with thermal radiation is studied in [30–35]. Patel et al. [36] studied the effect of Joule's heating on ferrofluid. The influence of Brownian motion and thermophoresis is studied by Mittal and Kataria [37]. Kataria [38] studied the effect of radiation and magnetic field on Casson fluid. Hashemi et al. [39] analyzed the solution of a circular rod. Some flows of fluids with numerical and computational methods are discussed in [40–42].

In this problem, the model of unsteady magnetohydrodynamic free convection flow of Brinkman fluid through a plate is considered. The impact of chemical reaction and heat absorption/generation is added into account. Firstly, the governing equations have been made nondimensional and then solved semianalytically. The results for velocity profile, temperature profile, and concentration profile are obtained and then analyzed graphically. Various graphs are plotted and discussed for different parameters, which are used in the flow model. The comparison between ordinary and fractionalized fluid is drawn graphically and shows that Caputo fractional derivative is the best choice for controlled fluid velocity.

2. Mathematical Description of the Model

The magnetohydrodynamic flow of Brinkman fluid through a plate with mass and heat transfer is considered. The fluid is flowing along the $x^{\cdot}$ axis. The motion of fluid depends on $y^{\cdot}$-axis and time $t_1^{\cdot}$. The plate and fluid have concentration $C_\infty^{\cdot}$ and temperature $T_\infty^{\cdot}$ at constant $t_1^{\cdot} = 0$ with zero velocity. But, for $t_1^{\cdot} > 0$, the plate starts to move in the plane with uniform velocity $U_1 e^{at_1}$. The concentration and temperature of the plate increased linearly to $C_w^{\cdot}$ and $T_w^{\cdot}$ with time $t^{\cdot}$. A constant strength β_0 of magnetic field is applied normally. In view of the above assumption and using Boussinesq's approximation, the convection flow of Brinkman fluid with chemical reaction, and magnetic field through a plate, the linear momentum equation is

$$\rho \frac{\partial u_1(y^{\cdot}, t_1^{\cdot})}{\partial t_1^{\cdot}} + B_1 u_1(y^{\cdot}, t_1^{\cdot}) = \frac{\partial \tau(y^{\cdot}, t_1^{\cdot})}{\partial y^{\cdot}} + g\beta_{T^{\cdot}}(T^{\cdot} - T_\infty^{\cdot}) - \sigma\beta_0^2 u_1(y^{\cdot}, t_1^{\cdot}) + g\beta_{C^{\cdot}}(C^{\cdot} - C_\infty^{\cdot}). \tag{1}$$

Shear stress τ is

$$\tau = \mu \frac{\partial u_1(y^{\cdot}, t_1^{\cdot})}{\partial y^{\cdot}}. \tag{2}$$

Thermal equation is

$$\rho C_p \frac{\partial T^{\cdot}(y^{\cdot}, t_1^{\cdot})}{\partial t_1^{\cdot}} = -\frac{\partial q_1(y^{\cdot}, t_1^{\cdot})}{\partial y^{\cdot}} + Q_1(T^{\cdot} - T_\infty^{\cdot}). \tag{3}$$

According to Fourier's Law, $q_1(y^{\cdot}, t_1^{\cdot})$ is given by

$$q_1(y^{\cdot}, t_1^{\cdot}) = -\alpha_0 \frac{\partial T^{\cdot}(y^{\cdot}, t_1^{\cdot})}{\partial y^{\cdot}}. \tag{4}$$

Diffusion equation is

$$\frac{\partial C^{\cdot}(y^{\cdot}, t_1^{\cdot})}{\partial t_1^{\cdot}} = -\frac{\partial J_1(y^{\cdot}, t_1^{\cdot})}{\partial y^{\cdot}} - R_1(C^{\cdot} - C_\infty^{\cdot}). \tag{5}$$

According to Fick's Law, $J_1(y^{\cdot}, t_1^{\cdot})$ is given by

$$J_1(y^{\cdot}, t_1^{\cdot}) = -D_m \frac{\partial C^{\cdot}(y^{\cdot}, t_1^{\cdot})}{\partial y^{\cdot}}. \tag{6}$$

The boundary conditions for the flow model are

$$\begin{aligned} u_1(y', t_1') &= 0, \\ T'(y', t_1') &= T'_\infty, \\ C'(y', t_1') &= C'_\infty, \\ y' > 0, t_1' &= 0. \end{aligned} \tag{7}$$

$$\begin{aligned} u_1(0, t_1') &= U_1 f(t_1') = U_1 e^{at_1'}, \\ T'(0, t_1') &= T'_w, \\ C'(0, t_1') &= C'_w, \\ t_1' &> 0, \end{aligned} \tag{8}$$

$$\begin{aligned} u_1(y', t_1') &\longrightarrow 0, \\ T'(y', t_1') &\longrightarrow 0, \\ C'(y', t_1') &\longrightarrow 0, \\ y' &\longrightarrow \infty, t_1' > 0. \end{aligned} \tag{9}$$

To write the flow model in dimensionless form, we used the following dimensionless variables:

$$\begin{aligned} y^* &= \frac{Uy'}{\nu}, \\ t^* &= \frac{U^2 t_1'}{\nu}, \\ \mathrm{Pr}^* &= \frac{\rho \nu C_p}{\alpha_0}, \\ v^* &= \frac{u_1}{U'}, \\ \mathrm{Gr}^* &= \frac{\rho \nu \beta_{T'} (T'_w - T'_\infty)}{U^3}, \\ M^* &= \frac{\beta_0^2 \sigma}{\rho U^2}, \\ Q^* &= \frac{Q_1 \nu}{U^2 \rho C_p}, \\ R^* &= \frac{R_1 \nu}{U^2}, \\ C^* &= \frac{C' - C'_\infty}{C'_w - C'_\infty}, \\ \mathrm{Sc}^* &= \frac{\nu}{D_1} \mathrm{Gm}^* = \frac{\rho \nu \beta_{C'} (C'_w - C'_\infty)}{U^3}. \end{aligned} \tag{10}$$

Using nondimensional variables from equations in (10) into the equations (1)–(9), we have

$$\left(\frac{\partial}{\partial t} + B\right) v(y,t) = K_1 \frac{\partial \tau}{\partial y} - M v(y,t) + \mathrm{Gr} T(y,t) + \mathrm{Gm} C(y,t), \tag{11}$$

$$\tau = L_1 \frac{\partial v(y,t)}{\partial y}, \tag{12}$$

$$\frac{\partial T(y,t)}{\partial t} + K_2 \frac{\partial q}{\partial y} - Q T(y,t) = 0, \tag{13}$$

$$q = -m_1 \frac{\partial T(y,t)}{\partial y}, \tag{14}$$

$$\frac{\partial C(y,t)}{\partial t} + K_3 \frac{\partial J}{\partial y} + R C(y,t) = 0, \tag{15}$$

$$J = -n_1 \frac{\partial C(y,t)}{\partial y}, \tag{16}$$

with boundary conditions as

$$\begin{aligned} v(y,0) = T(y,0) = C(y,0) = 0, &\quad y > 0, t = 0, \\ v(y,t) = e^{at}, T(y,t) = 1, C(y,t) = 1, &\quad t > 0, \\ v(\infty,t) = T(\infty,t) = C(\infty,t) \longrightarrow 0, &\quad t > 0, \end{aligned} \tag{17}$$

where

$$\begin{aligned} K_1 &= \frac{\tau}{U^2 \rho}, \\ K_2 &= \frac{q}{U \rho C_p (T_w - T_\infty)}, \\ K_3 &= \frac{J_1}{(C_w - C_\infty) U}, \\ L_1 &= \frac{U^2 \mu}{q_1 \nu}, \\ m_1 &= \frac{\alpha_0 (T_w - T_\infty) U}{q \nu}, \\ n_1 &= \frac{D_m (C_w - C_\infty) U}{J \nu}, \end{aligned} \tag{18}$$

where Gr, B, Sc, Q, M, Pr, Gm, and v represent the Grashof number for heat transfer, Brinkman parameter, Schmidt number, nondimensional heat source, magnetic field, Prandtl number, mass Grashof number, and velocity of the fluid, respectively.

3. Generalized Model

Equation (12) is frictionally generalized by Blair and Caffyn [43]:

$$\tau = L_{1-\beta} D_t^{1-\beta} \frac{\partial u(y,t)}{\partial y}, \quad 1 \geq \beta > 0. \tag{19}$$

Equation (14) is generalized by using Fourier Law defined by Povstenko and Hristov [44, 45]:

$$q = -m_{1-\gamma} D_t^{1-\gamma} \frac{\partial T(y,t)}{\partial y}, \quad 1 \geq \gamma > 0. \tag{20}$$

By using Fick's Law, equation (16) is generalized as

$$J = -n_{1-\alpha} D_t^{1-\alpha} \frac{\partial C(y,t)}{\partial y}, \quad 1 \geq \alpha > 0. \tag{21}$$

Using equation (19) into equation (11), equation (20) into equation (13), and equation (21) into equation (15), we have

$$\left[\frac{\partial}{\partial t} + B\right] v(y,t) = K_1 \frac{\partial}{\partial y}\left[L_{1-\beta} D_t^{1-\beta} \frac{\partial v(y,t)}{\partial y}\right] - Mv(y,t) + \mathrm{Gr}T(y,t) + \mathrm{Gm}C(y,t), \tag{22}$$

$$\frac{\partial T(y,t)}{\partial t} = K_2 \frac{\partial}{\partial y}\left[m_{1-\gamma} D_t^{1-\gamma} \frac{\partial T(y,t)}{\partial y}\right] + QT(y,t), \tag{23}$$

$$\frac{\partial C(y,t)}{\partial t} = K_3 \frac{\partial}{\partial y}\left[n_{1-\alpha} D_t^{1-\alpha} \frac{\partial C(y,t)}{\partial y}\right] - RC(y,t). \tag{24}$$

Taking inversion left operator in equations (22)–(24), we obtain

$$\left[I_t^{1-\beta} \frac{\partial}{\partial t} + BI_t^{1-\beta}\right] v(y,t) = \left[D_t^{\beta} + BI_t^{1-\beta}\right] v(y,t) = P_1 \frac{\partial^2 v(y,t)}{\partial y^2} - I_t^{1-\beta} Mv(y,t) + I_t^{1-\beta}\mathrm{Gr}T(y,t) + I_t^{1-\beta}\mathrm{Gm}C(y,t), \tag{25}$$

$$I_t^{1-\gamma} \frac{\partial T(y,t)}{\partial t} = D_t^{\gamma} T(y,t) = P_2 \frac{\partial^2 T(y,t)}{\partial y^2} + QI_t^{1-\gamma} T(y,t), \tag{26}$$

$$I_t^{1-\alpha} \frac{\partial C(y,t)}{\partial t} = D_t^{\alpha} C(y,t) = P_3 \frac{\partial^2 C(y,t)}{\partial y^2} - RI_t^{1-\alpha} C(y,t), \tag{27}$$

where $P_1 = K_1 L_{1-\beta} = 1$ when $\beta \longrightarrow 1$, $P_2 = K_2 m_{1-\gamma} = 1/\mathrm{Pr}$ when $\gamma \longrightarrow 1$, $P_3 = K_3 n_{1-\alpha} = 1/\mathrm{Sc}$ when $\alpha \longrightarrow 1$, and $D_t^{\alpha} v(y,t)$ represents the Caputo fractional derivative of $v(y,t)$ as

$$D_t^{\alpha} v(y,t) = \begin{cases} \dfrac{1}{\Gamma(1-\alpha)} \displaystyle\int_0^t \frac{1}{(t-q)^{\alpha}} \frac{\partial v(y,q)}{\partial q} \mathrm{d}q, & 0 \leq \alpha < 1, \\ \dfrac{\partial v(y,t)}{\partial t}, & \alpha = 1, \end{cases} \tag{28}$$

and the left inverse operator of the derivative operator is

$$I_t^{\alpha} g(y,t) = \frac{1}{\Gamma(\alpha)} \int_0^t g(y,s)(t-s)^{\alpha-1} \mathrm{d}s, \tag{29}$$

with

$$I_t^{1-\alpha} \frac{\partial g(y,t)}{\partial t} = D_t^{\alpha} g(y,t). \tag{30}$$

4. Solution of the Problem

Equations (25)–(27) with initial and boundary conditions are solved semianalytically.

4.1. Calculation of Concentration. Solution of equation (27) is

$$s^{\alpha} \overline{C}(y,s) = P_3 \frac{\partial^2 \overline{C}(y,s)}{\partial y^2} - R \frac{\overline{C}(y,s)}{s^{1-\alpha}}. \tag{31}$$

Boundary conditions satisfying equation (31) are

$$\begin{aligned} \overline{C}(0,s) &= s^{-1}, \\ \overline{C}(y,s) &\longrightarrow 0, \\ y &\longrightarrow \infty. \end{aligned} \tag{32}$$

Equation (31) is solved by using conditions given in equation (32), and we have

$$\overline{C}(y,s) = s^{-1} e^{-y\sqrt{(1/P_3)((s+R)/s^{1-\alpha})}}, \tag{33}$$

which is complicated and cannot be solved analytically. The numerical result of equation (33) is obtained by using the algorithm in [46, 47].

4.2. Calculation of Temperature. Solution of equation (26) is

$$s^{\gamma} \overline{T}(y,s) = P_2 \frac{\partial^2 \overline{T}(y,s)}{\partial y^2} + Q \frac{\overline{T}(y,s)}{s^{1-\gamma}}. \tag{34}$$

Boundary conditions satisfying equation (34) are

$$\begin{aligned} \overline{T}(0,s) &= s^{-1}, \\ \overline{T}(y,s) &\longrightarrow 0, \\ y &\longrightarrow \infty. \end{aligned} \tag{35}$$

Equation (34) is solved by using conditions given in equation (35), which results in

$$\overline{T}(y,s) = \frac{1}{s} e^{-y\sqrt{(1/P_2)((s-Q)/s^{1-\gamma})}}, \tag{36}$$

which is complicated one and cannot be solved analytically. The numerical result of equation (36) is obtained by using the algorithm in [46, 47].

4.3. Calculation of Velocity. Solution of equation (25) is

$$\left[s^{\beta} + \frac{B}{s^{1-\beta}}\right] v(y,t) = P_1 \frac{\partial^2 v(y,t)}{\partial y^2} - \frac{1}{s^{1-\beta}} M v(y,t) + \frac{1}{s^{1-\beta}} \mathrm{Gr} T(y,t) + \frac{1}{s^{1-\beta}} \mathrm{Gm} C(y,t). \tag{37}$$

Boundary conditions satisfying equation (37) are

$$\begin{aligned} \overline{v}(0,s) &= \frac{1}{s-a}, \\ \overline{v}(y,s) &\longrightarrow 0, \\ y &\longrightarrow \infty. \end{aligned} \tag{38}$$

Equation (37) is solved by using conditions given in equation (38), and we obtain

$$\begin{aligned} \overline{v}(y,s) = {} & \frac{1}{s-a} e^{-y\sqrt{(1/P_1)((s+H)/s^{1-\beta})}} + \frac{\mathrm{Gr}}{s\left(s^{1-\beta}\right)\left[(P_1/P_2)\left((s-Q)/s^{1-\gamma}\right) - \left((s+H)/s^{1-\beta}\right)\right]} \\ & \left[e^{-y\sqrt{(1/P_1)((s+H)/s^{1-\beta})}} - e^{-y\sqrt{(1/P_2)((s-Q)/s^{1-\gamma})}}\right] + \frac{\mathrm{Gm}}{s\left(s^{1-\beta}\right)\left[(P_1/P_3)\left((s+R)/s^{1-\alpha}\right) - \left((s+H)/s^{1-\beta}\right)\right]} \\ & \left[e^{-y\sqrt{(1/P_1)((s+H)/s^{1-\beta})}} - e^{-y\sqrt{(1/P_3)((s+R)/s^{1-\alpha})}}\right], \end{aligned} \tag{39}$$

which is much complicated, so it cannot be solved analytically. Numerical result of equation (39) will be obtained by using the algorithm in [46, 47].

5. Results and Discussion

Semianalytical solution for MHD flow of Brinkman fluid with a combined concentration and temperature gradient over a plate is obtained. The generalized model is solved with a Caputo fractional derivative. The graph of concentration profile, temperature profile, and velocity profile are plotted for different parameters.

Figure 1 represents the effect of B on $v(y,t)$. It is noted that the $v(y,t)$ decreases with increasing values of the Brinkman parameter. Physically, Brinkman is the relation between drag force and density; therefore, drag force increases with increasing values of the Brinkman parameter which decays down the fluid motion. The behavior of Gm is reported in Figure 2. From this graph, it is concluded that the magnitude of fluid velocity rises by raising the values of Gm. Gm is the relative strength of viscous force and concentration buoyancy force. As Gm increases, the motion of fluid is accelerated due to an increment of buoyancy force. Figure 3 represents the impact of different values of Gr on $v(y,t)$. From this graph, it is noted that velocity distribution is directly proportional with Gr. Physically, Gr is a relation between viscous force and buoyancy force. Therefore, with an increment in the values of Gr, buoyancy force is increased which raises the magnitude of $v(y,t)$.

Figure 4 displays the behavior of M and Q on fluid motion. The speed of fluid layer is reduced for raising values of M as shown in the graph. Physically, the Lorentz force creates the low resistivity which increases the thickness or width of momentum boundary layer in the solution. The impact of Q on fluid velocity is displayed in Figure 4. The $v(y,t)$ is increased by increasing values of Q as depicted in the figure. Physically, when the values of heat generation parameter are increased, the thermal conductivity becomes dominant. Fluid particles attract each other weakly which improve the fluid motion.

Figure 5 represents the behavior of R and Pr on the $v(y,t)$. The graph shows that $v(y,t)$ falls down for larger values of R. The impact of various values of Pr on $v(y,t)$ is displayed in Figure 5. Pr represents the ratio of momentum (product of mass and velocity) diffusion to thermal diffusion. In the problems of heat transfer, Pr manages the thickness of boundary layer and momentum (velocity). For larger value of Pr, diffusion of heat becomes slow as compared to the fluid momentum (velocity) which decreases the thermal conductivity (thickness) and raises the boundary layer momentum. The influence of R on fluid motion is shown in Figure 5. From the figure, it is concluded that fluid motion decays by increasing the values of R. Physically, boundary layer thickness is increased by increasing values of

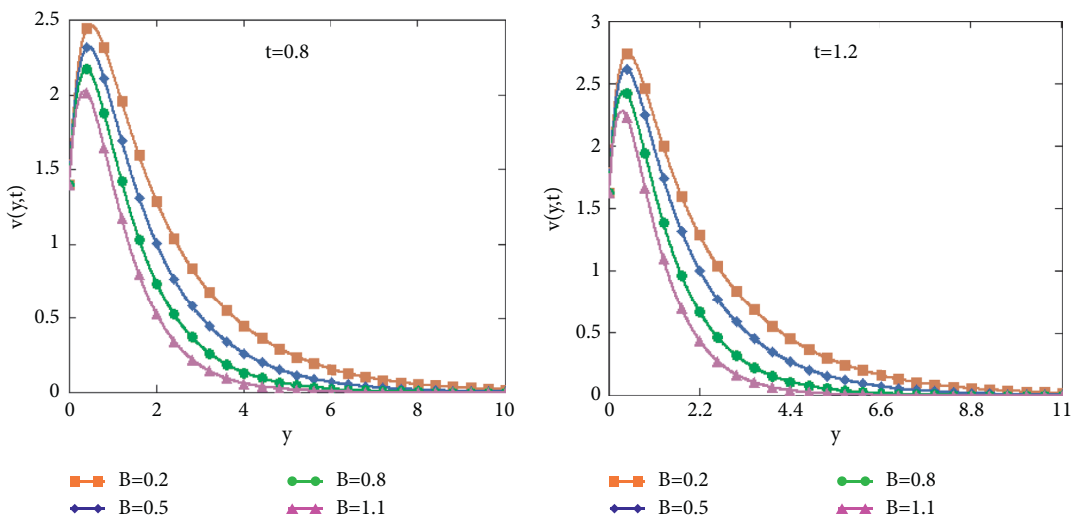

FIGURE 1: Velocity diagram $v(y,t)$ for various values of Brinkman parameter B at $R = 1.4, Q = 0.4, \mathrm{Gr} = 9, \mathrm{Gm} = 6, M = .85$, $\alpha = \beta = \gamma = 0.5, \mathrm{Sc} = 4.5$, and $\mathrm{Pr} = 4.0$.

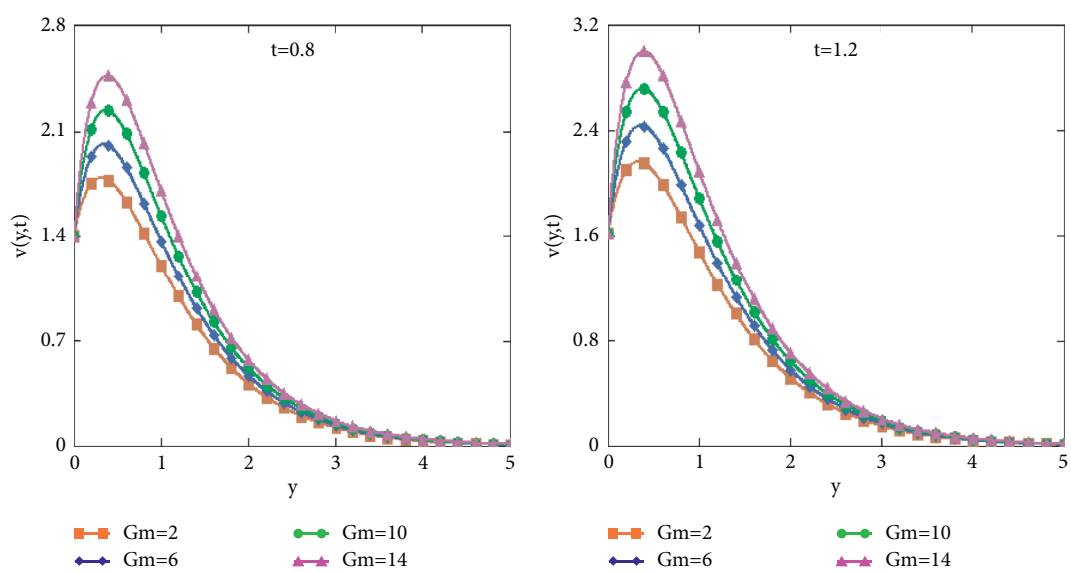

FIGURE 2: Profiles of velocity $v(y,t)$ for various values of the mass Grashof number Gm at $R = 1.4, Q = 0.4, \mathrm{Gr} = 9, M = .85, \mathrm{Sc} = 4.5$, $\alpha = \beta = \gamma = 0.5, B = 0.2$, and $\mathrm{Pr} = 4.0$.

R which slows down the velocity distribution. Figure 6 shows the influence of Sc and α, β, and γ on $v(y,t)$. The graph shows that for increasing values of Sc, the diffusion of the molecule increases which reduces the fluid level. However, fluid velocity rises with increasing values of fractional parameters.

The behavior of heat generation Q and Pr on $T(y,t)$ is displayed in Figure 7. This figure shows that temperature increases with increment in the values of Q. Figure 7 indicates the influence of Pr on temperature $T(y,t)$. Temperature distribution is accelerated with decreasing values of Pr as shown in the graph. Physically, the increase in Pr minimizes viscosity which reduces the thermal boundary layer.

The behavior of chemical reaction R and Sc on $C(y,t)$ is shown in Figure 8. The concentration level is accelerated with decreasing R as depicted in the graph. Physically, boundary layer thickness is increased by increasing values of R which slows down the concentration distribution. Figure 8 shows the influence of Sc on $C(y,t)$. The concentration level increases with reducing values of Sc as highlighted in the figure. The graph shows that for increasing values of Sc, the diffusion of molecule increases which reduces the fluid level. Figure 9 shows the comparison of Brinkman-type fractional fluid with Olisa [48]. From the figure, it is concluded that fractional derivative is the best choice to enhance the fluid motion. Figure 9(b) represents that if we take fractional parameters $\beta = \gamma = \alpha \longrightarrow 1$, $\mathrm{Gm} = F(s) = 0$, and $B = 0$, the

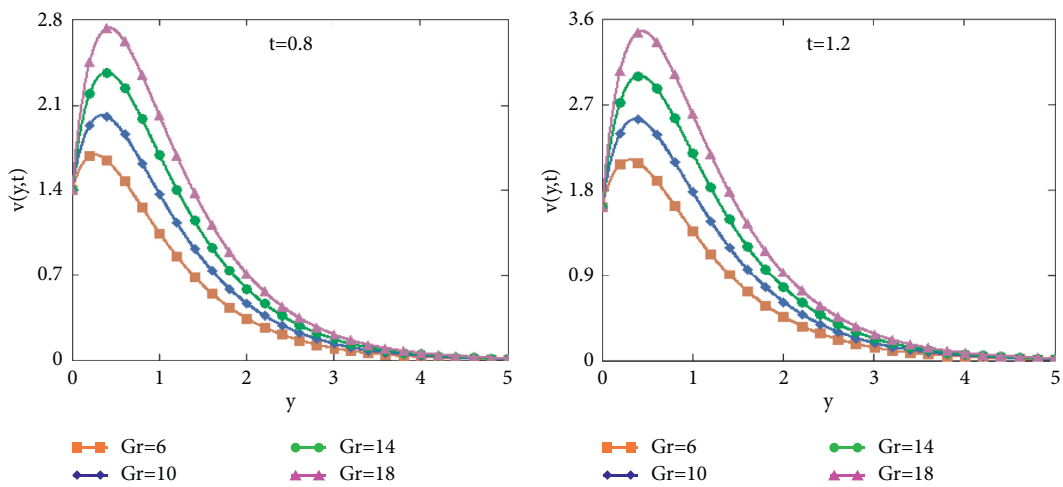

FIGURE 3: Velocity profile $v(y,t)$ for various values of Gr at $R = 1.4, Q = 0.4, \mathrm{Gm} = 6, M = .85, \mathrm{Sc} = 4.5, \alpha = \beta = \gamma = 0.5, B = 0.2,$ and $\mathrm{Pr} = 4.0$.

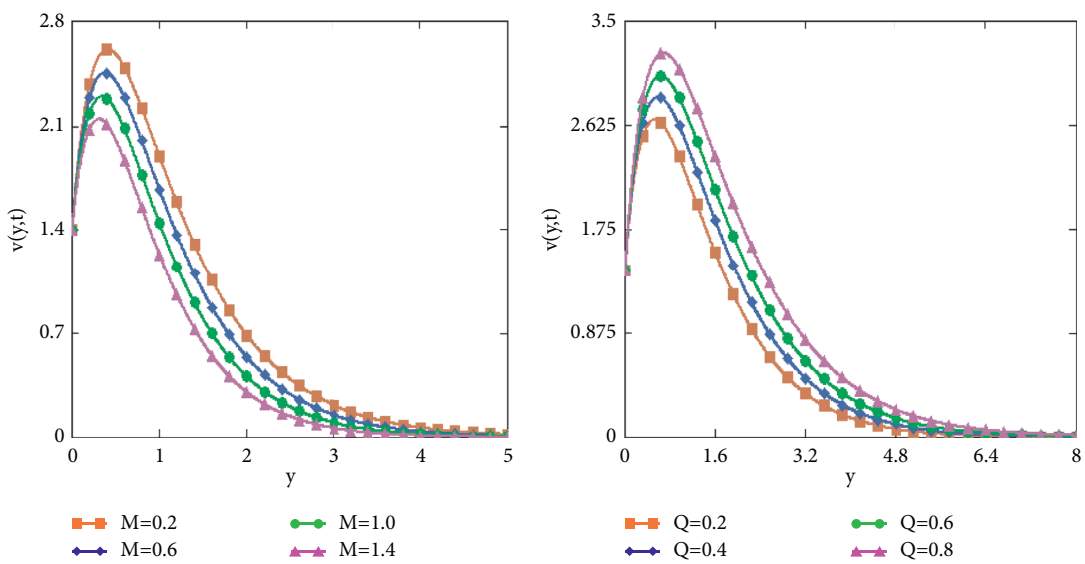

FIGURE 4: Velocity distribution $v(y,t)$ for distinct values of M and heat generation parameter Q at $R = 1.4, \mathrm{Gr} = 9, \mathrm{Gm} = 6, \mathrm{Sc} = 4.5, \alpha = \beta = \gamma = 0.5, B = 0.2,$ and $\mathrm{Pr} = 4.0$.

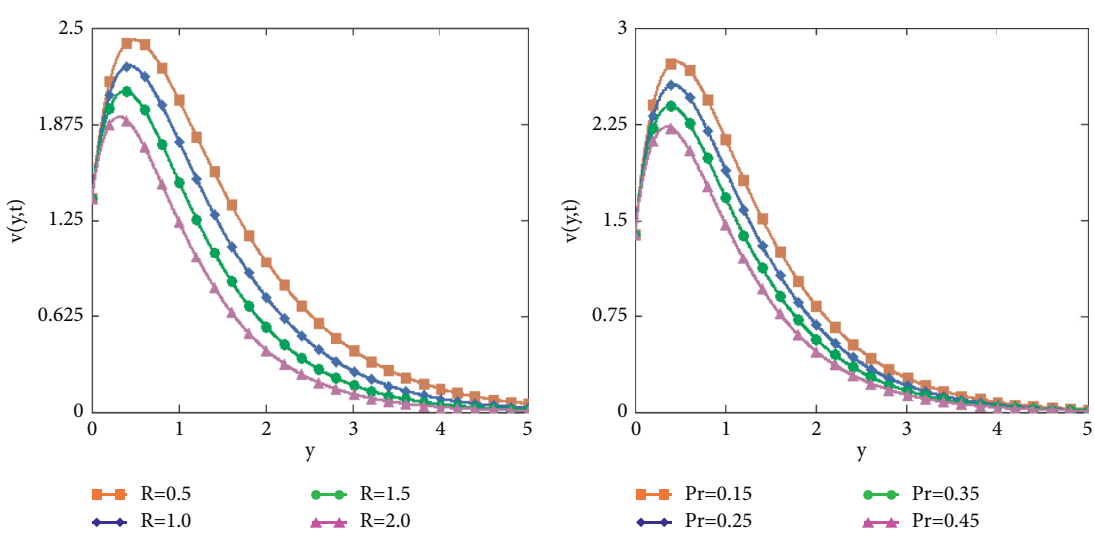

FIGURE 5: Velocity diagram $v(y,t)$ for distinct values of chemical reaction parameter R and Pr at $Q = 0.4, \mathrm{Gr} = 9, \mathrm{Gm} = 6, M = .85, \mathrm{Sc} = 4.5,$ $\alpha = \beta = \gamma = 0.5,$ and $B = 0.2$.

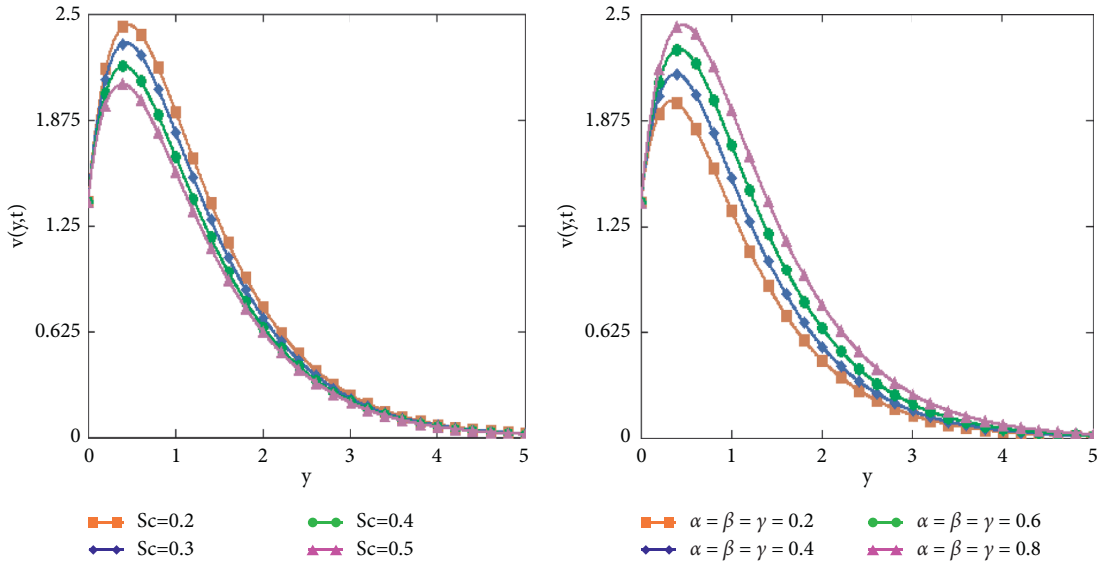

Figure 6: $v(y,t)$ for distinct values of Sc and fractional parameters at $R = 1.4, Q = 0.4, \mathrm{Gr} = 9, \mathrm{Gm} = 6, M = .85, B = 0.2$, and $\mathrm{Pr} = 4.0$.

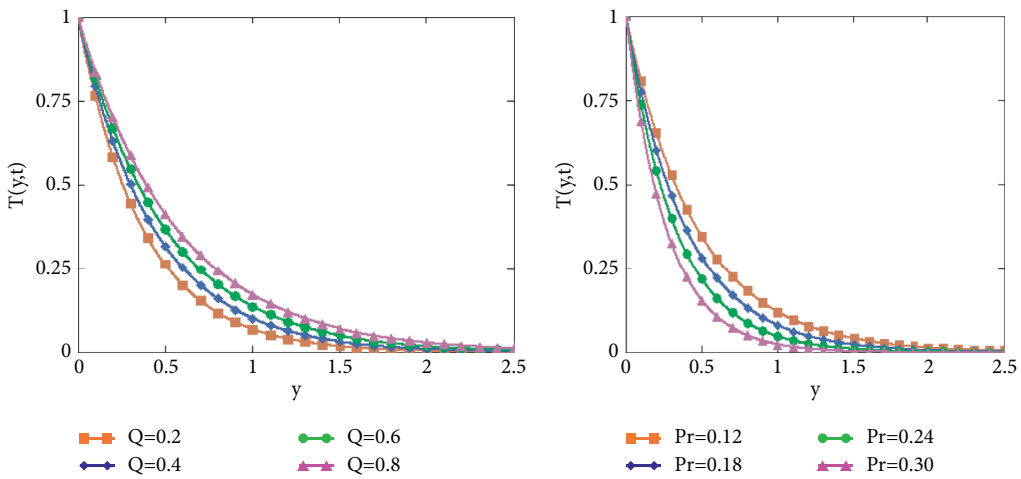

Figure 7: Variation in temperature profile $T(y,t)$ for various values of heat generation parameter Q and Pr at $\gamma = 0.5$.

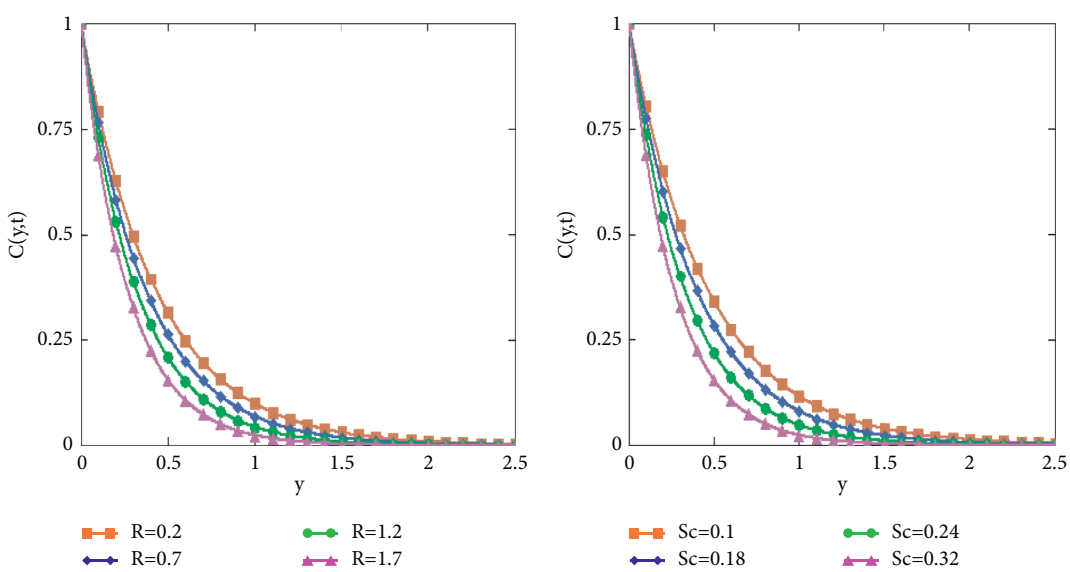

Figure 8: $C(y,t)$ for distinct values of chemical reaction parameter R and Sc at $\alpha = 0.5$.

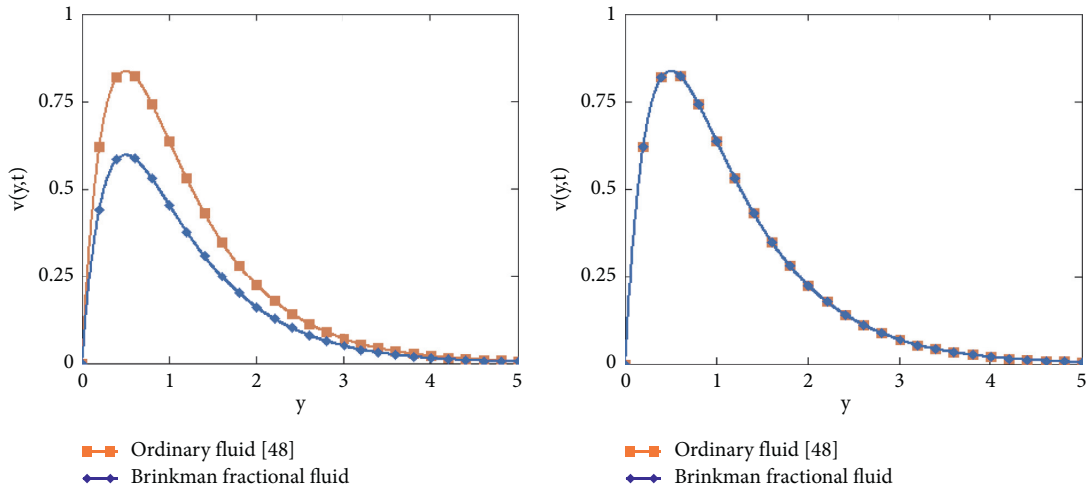

Figure 9: Velocity distribution for comparison of our work with Olisa [48].

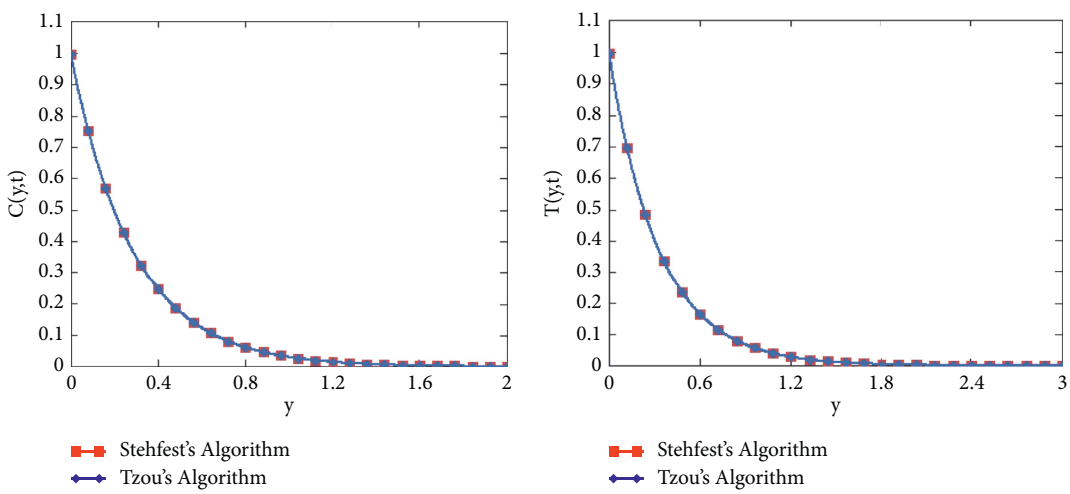

Figure 10: Concentrations and temperatures obtained by Stehfest's and Tzou's algorithms.

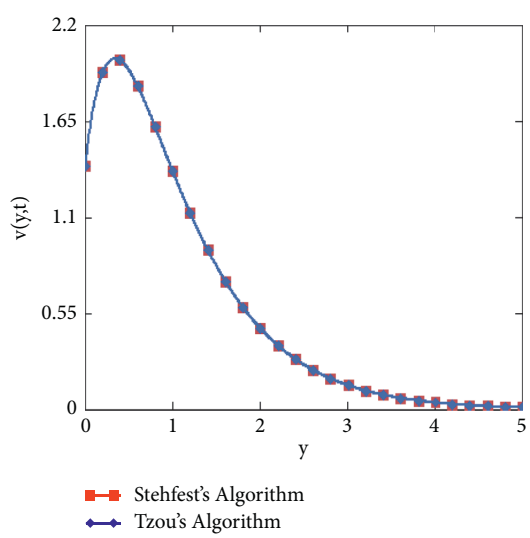

Figure 11: Velocity profile obtained by Stehfest's and Tzou's algorithms.

fluid profiles are identical which shows the authenticity of the present work. Figure 10 represents the validity of inversion algorithms for concentration and temperature profiles. The overlapping velocity profiles show the validity of inversion algorithms as shown in Figure 11.

6. Conclusion

Solution of free convection magnetohydrodynamic flow of Brinkman-type fluid has been obtained via Laplace transform. Different parameters used in the model are plotted and discussed. The model is solved with a fractional derivative known as Caputo fractional derivative.

Here are the main points which have been summarized for this model:

(i) Velocity distribution retards with decreasing values of fractional parameter

(ii) Thermal buoyancy forces lead to accelerate the $v(y,t)$

(iii) The $v(y,t)$ decreases as magnetic parameter, chemical reaction parameter, Prandtl number, and Sc increases

(iv) The Brinkman parameter is a decreasing function of velocity field

(v) The larger values of Q increased the $T(y,t)$

(vi) The larger values of Pr reduced the $T(y,t)$

(vii) The concentration level is a decreasing function of Sc

(viii) The smaller values of R reduce the concentration profile

(ix) Caputo fractional derivative is the best choice to enhance the fluid motion as compared to ordinary fluid

Data Availability

All used data are included within the manuscript.

Conflicts of Interest

The authors declare that they have no conflicts of interest.

References

[1] R. M. Swamy, P. Ganesan, and V. M. Soundalgekar, "Heat and mass transfer effects on flow past an impulsively started vertical plate," *Acta Mechanica*, vol. 146, no. 1-2, pp. 1–8, 2001.

[2] R. C. Chaudhary and A. Jain, "Combined heat and mass transfer effects on MHD free convection flow past an oscillating plate embedded in porous medium," *Romanian Journal of Physics*, vol. 52, no. 5–7, pp. 505–524, 2007.

[3] M. Sivaiah, A. S. Nagarajan, and P. S. Reddy, "Heat and mass transfer effects on MHD free convective flow past a vertical porous plate," *Journal of Computational Mathematics*, vol. 2, no. 2, pp. 14–21, 2009.

[4] K. Das and S. Jana, "Heat and mass transfer effects on unsteady MHD free convection flow near a moving vertical plate in porous medium," *Bulletin of Society of Mathematicians Banja Luka*, vol. 17, no. 10, pp. 15–32, 2010.

[5] H. R. Kataria and H. R. Patel, "Radiation and chemical reaction effects on MHD Casson fluid flow past an oscillating vertical plate embedded in porous medium," *Alexandria Engineering Journal*, vol. 55, no. 1, pp. 583–595, 2016.

[6] A. J. Chamkha, "Thermal radiation and buoyancy effects on hydromagnetic flow over an accelerating permeable surface with heat source or sink," *International Journal of Engineering Science*, vol. 38, no. 15, pp. 1699–1712, 2000.

[7] A. J. Chamkha, "Unsteady MHD convective heat and mass transfer past a semi-infinite vertical permeable moving plate with heat absorption," *International Journal of Engineering Science*, vol. 42, no. 2, pp. 217–230, 2004.

[8] Y. J. Kim, "Unsteady MHD convection flow of polar fluids past a vertical moving porous plate in a porous medium," *International Journal of Heat and Mass Transfer*, vol. 44, no. 15, pp. 2791–2799, 2001.

[9] M. M. Rahman and M. A. Sattar, "Magnetohydrodynamic convective flow of a micropolar fluid past a continuously moving vertical porous plate in the presence of heat generation/absorption," *Journal of Heat Transfer*, vol. 128, no. 2, pp. 142–152, 2006.

[10] V. Rajesh and S. V. K. Varma, "Radiation effects on MHD flow through a porous medium with variable temperature or variable mass diffusion," *International Journal of Applied Mathematics and Mechanics*, vol. 6, no. 1, pp. 39–57, 2010.

[11] M. A. Sattar, "Free convection and mass transfer flow through a porous medium past an infinite vertical porous plate with time dependent temperature and concentration," *International Journal of Pure and Applied Mathematics*, vol. 23, pp. 759–766, 1994.

[12] D. A. S. Rees and I. Pop, "Free convection induced by a vertical wavy surface with uniform heat flux in a porous medium," *Journal of Heat Transfer*, vol. 117, no. 2, pp. 547–550, 1995.

[13] M. Acharya, G. C. Dash, and I. P. Singh, "Magnetic field effects on the free convection and mass transfer flow through porous medium with constant suction and constant heat flux," *Indian Journal of Pure and Applied Mathematics*, vol. 31, no. 1, pp. 1–18, 2000.

[14] C. Y. Ching-Yang Cheng, "Natural convection heat and mass transfer near a vertical wavy surface with constant wall temperature and concentration in a porous medium," *International Communications in Heat and Mass Transfer*, vol. 27, no. 8, pp. 1143–1154, 2000.

[15] A. Khan, I. Khan, F. Ali, and S. Shafie, "Effects of wall shear stress MHD conjugate flow over an inclined plate in a porous medium with ramped wall temperature," *Mathematical Problems in Engineering*, vol. 4, pp. 62–73, 2014.

[16] V. Rajesh and S. V. K. Varma, "Heat source effects on MHD flow past an exponentially accelerated vertical plate with variable temperature through a porous medium," *International Journal of Applied Mathematics and Mechanics*, vol. 6, no. 12, pp. 68–78, 2010.

[17] R. C. Chaudhary and A. Jain, "An exact solution of magnetohydrodynamic convection flow past an accelerated surface embedded in a porous medium," *International Journal of Heat and Mass Transfer*, vol. 53, no. 7, pp. 1609–1611, 2010.

[18] K. Das, "Exact solution of MHD free convection flow and mass transfer near a moving vertical plate in presence of thermal radiation," *African Journal of Mathematical Physics*, vol. 8, pp. 29–41, 2010.

[19] D. Pal and B. Talukdar, "Buoyancy and chemical reaction effects on MHD mixed convection heat and mass transfer in a porous medium with thermal radiation and ohmic heating," *Communications in Nonlinear Science and Numerical Simulation*, vol. 15, no. 10, pp. 2878–2893, 2010.

[20] G. S. Seth, M. S. Ansari, and R. Nandkeolyar, "MHD natural convection flow with radiative heat transfer past an impulsively moving plate with ramped wall temperature," *Heat and Mass Transfer*, vol. 47, no. 5, pp. 551–561, 2011.

[21] A. Khalid, I. Khan, and S. Shafie, "Exact solutions for free convection flow of nano fluids with ramped wall temperature," *European Physical Journal Plus*, vol. 130, pp. 243–255, 2015.

[22] M. A. Seddeek, A. A. Darwish, and M. S. Abdelmeguid, "Effects of chemical reaction and variable viscosity on hydromagnetic mixed convection heat and mass transfer for hiemenz flow through porous media with radiation," *Communications in Nonlinear Science and Numerical Simulation*, vol. 12, no. 2, pp. 195–213, 2007.

[23] N. A. Shah, A. A. Zafar, and S. Akhtar, "General solution for MHD-free convection flow over a vertical plate with ramped wall temperature and chemical reaction," *Arabian Journal of Mathematics*, vol. 7, no. 1, pp. 49–60, 2018.

[24] G. S. Seth, A. K. Singha, and R. Sharma, "MHD natural convection flow with hall effects, radiation and heat absorption over an exponentially accelerated vertical plate with ramped temperature," *Indian Journal of Scientific Research and Technology*, vol. 5, pp. 10–22, 2015.

[25] S. Shateyi and S. Motsa, "Unsteady magnetohydrodynamic convective heat and mass transfer past an infinite vertical plate in a porous medium with thermal radiation, heat generation/absorption and chemical reaction," *Advanced Topics in Mass Transfer*, vol. 1, pp. 145–162, 2011.

[26] A. R. M. Kasim, N. F. Mohammad, and S. Shafie, "Unsteady MHD mixed convection flow with heat and mass transfer over a vertical plate in a micropolar fluid-saturated porous medium," *Journal of Applied Science and Engineering*, vol. 16, no. 2, pp. 141–150, 2013.

[27] F. Ali, I. Khan, S. Shafie, and N. Musthapa, "Heat and mass transfer with free convection MHD flow past a vertical plate embedded in a porous medium," *Mathematical Problems in Engineering*, vol. 2013, pp. 1–13, 2013.

[28] Z. A. Khan, S. U. Haq, T. S. Khan, I. Khan, and I. Tlili, "Unsteady MHD flow of a Brinkman type fluid between two side walls perpendicular to an infinite plate," *Results in Physics*, vol. 9, pp. 1602–1608, 2018.

[29] F. Ali, M. Gohar, and I. Khan, "MHD flow of water-based Brinkman type nanofluid over a vertical plate embedded in a porous medium with variable surface velocity, temperature and concentration," *Journal of Molecular Liquids*, vol. 223, pp. 412–419, 2016.

[30] M. Sheikholeslami, H. R. Kataria, and A. S. Mittal, "Effect of thermal diffusion and heat-generation on MHD nanofluid flow past an oscillating vertical plate through porous medium," *Journal of Molecular Liquids*, vol. 257, pp. 12–25, 2018.

[31] H. R. Kataria and A. S. Mittal, "Velocity, mass and temperature analysis of gravity-driven convection nanofluid flow past an oscillating vertical plate in the presence of magnetic field in a porous medium," *Applied Thermal Engineering*, vol. 110, pp. 864–874, 2017.

[32] H. R. Patel, A. S. Mittal, and R. R. Darji, "MHD flow of micropolar nanofluid over a streching/shrinking sheet considering radiation," *Journal Comunication in heat and mass transfer*, vol. 51, pp. 45–69, 2019.

[33] H. R. Kataria and A. S. Mittal, "Mathematical model for velocity and temperature of gravity-driven convective optically thick nanofluid flow past an oscillating vertical plate in presence of magnetic field and radiation," *Journal of the Nigerian Mathematical Society*, vol. 34, no. 3, pp. 303–317, 2015.

[34] A. S. Mittal and H. R. Kataria, "Three dimensional Cuo-Water nanofluid flow considering Brownian motion in presence of radiation," *Karbala International Journal of Modern Science*, vol. 4, no. 3, pp. 275–286, 2018.

[35] M. Sheikholeslami, H. R. Kataria, and A. S. Mittal, "Radiation effects on heat transfer of three dimensional nanofluid flow considering thermal interfacial resistance and micro mixing in suspensions," *Chinese Journal of Physics*, vol. 55, no. 6, pp. 2254–2272, 2017.

[36] H. R. Patel, A. S. Mittal, and R. R. Darji, "Mixed convection micropolar ferrofluid flow with viscous dissipation, joule heating and convective boundary conditions," *Journal Comunication in heat and mass transfer*, vol. 110, pp. 864–874, 2017.

[37] A. S. Mittal and H. R. Kataria, "Infulence of thermophoresis and Brownian motion on mixed convection two dimensional MHD Casson fluid flow with non linear radiation and heat generation," *Physica A: Statistical Mechanics and its Applications*, vol. 537, 2020.

[38] H. R. Kataria, "Analysis of casson nanofluid flow in presence of magnetic field and radiation," *Journal of mathematics today*, vol. 33, pp. 99–120, 2017.

[39] M. S. Hashemi, M. Inc, B. Kilic, and A. Akgül, "On solitons and invariant solutions of the Magneto-electro-elastic circular rod," *Waves in Random and Complex Media*, vol. 26, no. 3, pp. 259–271, 2016.

[40] M. S. Hashemi, "Constructing a new geometric numerical integration method to the nonlinear heat transfer equations," *Communications in Nonlinear Science and Numerical Simulation*, vol. 22, no. 1–3, pp. 990–1001, 2015.

[41] M. S. Hashemi, A. Atangana, and S. Hajikhah, "Solving fractional pantograph delay equations by an effective computational method," *Mathematics and Computers in Simulation*, vol. 177, pp. 295–305, 2020.

[42] M. S. Hashemi, M. Inc, and A. Yusuf, "On three dimensional variable order time fractional chaotic system with nonsingular Kernal," *Journal of Chaos, Solitons and Fractals*, vol. 133, 2020.

[43] G. S. Blair and J. Caffyn, "Significance of power law relation in rheology," *Nature*, vol. 155, pp. 171-172, 1955.

[44] Y. Povstenko, *Fractional Thermoelasticity, Solid Mechanics and its Applications*, Springer International Publishing, Berlin, Germany, 2015.

[45] J. Hristov, *Derivatives with Non-Singular Kernals, from the Caputo-Fabrizo Definition and Beyond, Appraising Analysis with Emphasis on Diffusion Model, Frontiers in Fractional Calculas*, Bentham Science Publishers, Sharjah, UAE, 1st edition, 2017.

[46] D. Y. Tzou, *Macro to Microscale Heat transfer: the Lagging Behavior*, pp. 01–339, Taylor and Francis, Washington, DC, USA, 1997.

[47] H. Stehfest, "Algorithm 368: numerical inversion of Laplace transforms [D5]," *Communications of the ACM*, vol. 13, no. 1, pp. 47–49, 1970.

[48] J. D. Olisa, "Transient laminar MHD free convective heat transfer past a vertical plate with heat generation," *International Journal of Engineering Science*, vol. 6, no. 4, pp. 08–13, 2017.

Hindawi
Complexity
Volume 2021, Article ID 1904067, 12 pages
https://doi.org/10.1155/2021/1904067

Research Article

Study of HIV Disease and Its Association with Immune Cells under Nonsingular and Nonlocal Fractal-Fractional Operator

Shabir Ahmad,[1] **Aman Ullah**,[1] **Ali Akgül**,[2] **and Manuel De la Sen**[3]

[1]*Department of Mathematics, University of Malakand, Dir (L), Khyber Pakhtunkhwa, Pakistan*
[2]*Art and Science Faculty, Department of Mathematics, Siirt University, TR-56100 Siirt, Turkey*
[3]*Institute of Research and Development of Processes Faculty of Science and Technology, University of the Basque Country, Campus of Leioa (Bizkaia), 644-Leioa, Biscay, Spain*

Correspondence should be addressed to Shabir Ahmad; shabirahmad2232@gmail.com

Received 18 May 2021; Revised 3 August 2021; Accepted 10 August 2021; Published 20 August 2021

Academic Editor: Ning Cai

HIV, like many other infections, is a severe and lethal infection. Fractal-fractional operators are frequently used in modeling numerous physical processes in the current decade. These operators provide better dynamics of a mathematical model because these are the generalization of integer and fractional-order operators. This paper aims to study the dynamics of the HIV model during primary infection by fractal-fractional Atangana–Baleanu (AB) operators. The sufficient conditions for the existence and uniqueness of the solution of the proposed model under the AB operator are derived via fixed point theory. The numerical scheme is presented by using the Adams–Bashforth method. Numerical results are demonstrated for different fractal and fractional orders to see the effect of fractional order and fractal dimension on the dynamics of HIV and CD4+ T-cells during primary infection.

1. Introduction

Over the past few decades, the field of mathematical modeling of the physical process has gained considerable attention from scientists and investigators. We point out that mathematical models are important tools for studying many physical and biological science dynamic problems [1, 2]. Bernoulli has initiated this concept in 1776. Mathematical models of the biological problem have become important means for understanding the many infectious diseases and choosing the appropriate technique for controlling the disease or reducing its social transmission. In this respect, many mathematical models were built to study the understanding of many infectious diseases and to follow certain precautions to save a community from excessive loss. HIV is one of the most severe and dangerous illnesses of the last decades. Many people all over the world have died because of the disease. According to UNAIDS, about 690,000 people died from AIDS-related illnesses in 2019. The aforementioned infections target the largest WBCs in the immune system (IS) during HIV disease, called CD4 + T-cells [3]. In this way, HIV infection affects human IS. It has detrimental impacts on the CD4 + T-cells and other cells. A body becomes susceptible to diseases because the number of CD4 + T-cells falls below the amount needed, and thus the IS begins to weaken. Several countries, particularly in Africa, have recently been infected with HIV for up to 35% of the population aged 15–50 years. Usually, differential equations are commonly used during mathematical models. A basic model for primary HIV infection was first developed in 1989 by Perelson [4]. In 1993, Perelson et al. [5] expanded the model and further addressed some of the behavior of the models. For examination of the HIV infection, the two cells model was established in [6]. A simple general model in [7] was considered. In this regard, numerous models have been further developed and to explain the dynamics of HIV decay observed and studied for local and global stability [8, 9]. Further, Arafa et al. [10] have proposed the following model:

$$\begin{cases} \dfrac{\mathrm{d}X}{\mathrm{d}t} = \mu - k^* XZ - d^* X + b^* Y, \\ \dfrac{\mathrm{d}Y}{\mathrm{d}t} = k^* XZ - (b^* + \delta)Y, \\ \dfrac{\mathrm{d}Z}{\mathrm{d}t} = N^* \delta Y - c^* Z. \end{cases} \tag{1}$$

The symbol X denotes the concentration of susceptible $CD4^+$ T-cells, Y represents concentration of infected CD4 + T-cells, and free HIV virus particles in the blood cells are denoted by Z. The parameter μ represents new T-cells supply rate. The rate of natural death is denoted by d^*, k^* is the rate of infection T-cell, δ is the death rate of infected T-cells, b^* represents the rate of return of infected cells to uninfected class, c^* is the death rate of virus, and N^* is average number of particles infected by an uninfected cell.

Fractional calculus theory has been a hot topic of the twenty-first century due to its applications in various fields of science. Different fractional operators have been implemented in many mathematical models, and they have yielded a lot of success. Different forms of operators exist in fractional calculus, depending on the kernels involved. The three major operators, which are widely used by researchers, are briefly discussed here. The Caputo operator, which is built on the power law kernel, is the first. This operator has a problem with the singularity of the kernel involved in it. The second operator is the Caputo–Fabrizio fractional derivative, which is based on an exponential-decay kernel but has a locality problem. The third operator is the AB fractional derivative which is based on the Mittag-Leffler kernel. Because of its nonlocal and nonsingular kernel, this derivative gives superior results as compared with Caputo and Caputo–Fabrizio. The FDEs had a significant impact on modeling and simulation using these three types of kernels [11, 12]. In literature [1], computational solutions of the HIV-1 infection of the CD4+ T-cells fractional mathematical model that causes acquired immunodeficiency syndrome (AIDS) with the effect of antiviral drug therapy are presented. Khater et al. analyzed abundant stable computational solutions of Atangana–Baleanu fractional nonlinear HIV-1 infection of CD4+ T-cells of immunodeficiency syndrome [2]. In comparison to the classical model, the model involving FDEs is more accurate [13]. Various methods are used by researchers for solving linear and nonlinear fractional DEs [14, 15]. Many problems in nature are solved by the concept of fractal derivatives. Atangana [16] recently proposed new kinds of general operators called fractal-fractional operators, which combine fractional and fractal derivatives. The newly proposed operators have been implemented by many scientists to investigate the dynamics of different models. Ahmad et al. studied the model describing the tumor and its relation with immune cells under the AB fractal-fractional operators [17]. Literature [18] has demonstrated the dynamics of the dengue infection model via fractal-fractional operators which are best fitted with real data. For more applications of fractional-fractal calculus, see [19, 20]. We will investigate the above model using the AB fractal-fractional operator, as suggested by the literature. We extend the above model as follows:

$$\begin{cases} \mathscr{D}_{0,t}^{\alpha,\tau} X = \mu - k^* XZ - d^* X + b^* Y, \\ \mathscr{D}_{0,t}^{\alpha,\tau} Y = k^* XZ - (b^* + \delta)Y, \\ \mathscr{D}_{0,t}^{\alpha,\tau} Z = N^* \delta Y - c^* Z, \end{cases} \tag{2}$$

along with the following initial conditions:

$$\begin{aligned} X(0) &= X_0, \\ Y(0) &= Y_0, \\ Z(0) &= Z_0. \end{aligned} \tag{3}$$

Here, we use more generalized operators to model HIV infections and their association with immune cells. We explore the existence theory under AB fractal-fractional derivative through fixed point theory. Our proposed model is nonlinear. One common obstacle is determining the exact solution to a nonlinear problem. Due to the complexity, we will find a numerical solution to the model. The Adam Bashforth methodology is an efficient and stable numerical method. We use this method to determine the solution to the given model. We obtain the numerical scheme for the Mittag-Leffler law via the Adams–Bashforth technique. To present the effect of fractal dimension on fractional order, we simulate the proposed model for various values of fractal values. We find out that the AB operator provides better dynamics of the disease due to nonsingular kernel. We show the impact of fractal and fractional order on the dynamics of HIV infection and its association with immune cells.

The paper is structured as follows. The introduction and motivation part is presented in Section 1. The basic definitions of AB fractal-fractional operators are given in Section 2. The existence theory under AB fractal-fractional derivative is explored in Section 3. Section 4 is devoted to the numerical scheme for the proposed model. Numerical results are simulated in Section 5, whereas the manuscript is concluded in Section 6.

2. Preliminaries

Let $\mathscr{G}(t)$ be continuous and fractal differentiable on (m, n). Let $0 \le \alpha, \tau \le 1$, where α and τ represent fractional and fractal order, respectively.

Definition 1 (see [16]). The AB fractal-fractional derivative of $\mathscr{G}(t)$ is defined as follows:

$$^{\mathscr{FFM}}\mathscr{D}_{0,t}^{\alpha,\tau}(\mathscr{G}(t)) = \frac{\mathscr{AB}(\alpha)}{1-\alpha} \frac{\mathrm{d}}{\mathrm{d}t^{\tau}} \int_0^t E_\alpha\left[-\frac{\alpha}{1-\alpha}(t-\xi)^\alpha\right]\mathscr{G}(\xi)\mathrm{d}\xi, \tag{4}$$

where $\mathscr{AB}(\alpha) = 1 - \alpha + (\alpha/\Gamma(\alpha))$.

Definition 2 (see [16]). The AB fractal-fractional integral of $\mathscr{G}(t)$ is defined as follows:

$$ {}^{\mathcal{FFM}}\mathcal{J}_{0,t}^{\alpha,\tau}\mathcal{G}(t) = \frac{\tau(1-\alpha)t^{\tau-1}\mathcal{G}(t)}{\mathcal{AB}(\alpha)} + \frac{\alpha\tau}{\mathcal{AB}(\alpha)}\int_0^t \xi^{\alpha-1}(t-\xi)^{\alpha-1}\mathcal{G}(\xi)\mathrm{d}\xi. \tag{5} $$

3. Existence and Uniqueness

In this section, we present the existence and uniqueness of the solution of the proposed model under AB fractal-fractional derivative via fixed point theory.

$$ \left\{ {}^{\mathcal{FFM}}\mathcal{D}_{0,t}^{\alpha,\tau}(\mathcal{X}(t)) = \mathcal{H}_1(t,\mathcal{X},Y,Z), {}^{\mathcal{FFM}}\mathcal{D}_{0,t}^{\alpha,\tau}(Y(t)) = \mathcal{H}_2(t,\mathcal{X},Y,Z), {}^{\mathcal{FFM}}\mathcal{D}_{0,t}^{\alpha,\tau}(Z(t)) = \mathcal{H}_3(t,\mathcal{X},Y,Z), \right. \tag{6} $$

where

$$ \begin{cases} \mathcal{H}_1(\xi,\mathcal{X},Y,Z) = \mu - k^*XZ - d^*X + b^*Y, \\ \mathcal{H}_2(\xi,\mathcal{X},Y,Z) = k^*XZ - (b^* + \delta)Y, \\ \mathcal{H}_3(\xi,\mathcal{X},Y,Z) = N^*\delta Y - c^*Z. \end{cases} \tag{7} $$

For this, we can write system (6) as follows:

$$ {}^{\mathcal{FFM}}\mathcal{D}_{0,t}^{\alpha,\tau}[\Omega(t)] = \Xi(t,\Omega(t)), \tag{8} $$

where $\Omega(t) = \begin{cases} \mathcal{X}(t) \\ Y(t) \\ \mathcal{Z}(t) \end{cases}$ and $\Xi(t,\Omega(t)) = \begin{cases} \mathcal{H}_1(t,\mathcal{X},Y,Z) \\ \mathcal{H}_2(t,\mathcal{X},Y,Z) \\ \mathcal{H}_3(t,\mathcal{X},Y,Z). \end{cases}$

Since by definition ${}^{\mathcal{FFM}}\mathcal{D}_{0,t}^{\alpha}[\Omega(t)] = (\mathcal{AB}(\alpha)/1-\alpha)\mathrm{d}/\mathrm{d}t^{\tau}\int_0^t \Xi(\vartheta,\Omega(\vartheta))E_{\alpha}(-\alpha/1-\alpha(t-\xi)^{\alpha})\mathrm{d}\xi$ and integral is differentiable, we can write the above expression as follows:

$$ {}^{\mathcal{FFM}}\mathcal{D}_{0,t}^{\alpha}[\Omega(t)] = \frac{1}{\tau t^{\tau-1}}\frac{\mathcal{AB}(\alpha)}{1-\alpha}\frac{\mathrm{d}}{\mathrm{d}t}\int_0^t \Xi(\vartheta,\Omega(\vartheta))E_{\alpha}\left(-\frac{\alpha}{1-\alpha}(t-\xi)^{\alpha}\right)\mathrm{d}\xi. \tag{9} $$

Therefore, system (8) can be expressed as follows:

$$ \frac{\mathcal{AB}(\alpha)}{1-\alpha}\frac{\mathrm{d}}{\mathrm{d}t}\int_0^t \Xi(\vartheta,\Omega(\vartheta))E_{\alpha}\left(-\frac{\alpha}{1-\alpha}(t-\xi)^{\alpha}\right)\mathrm{d}\xi = \tau t^{\tau-1}\Xi(t,\Omega(t)). \tag{10} $$

Substituting the right hand side by Caputo and implementing the fractional integral, we get

$$ \Omega(t) = \Omega(0) + \frac{1-\alpha}{\mathcal{AB}(\alpha)}\tau t^{\tau-1}\Xi(t,\Omega(t)) + \frac{\alpha\tau}{\mathcal{AB}(\alpha)\Omega(\alpha)}\int_0^t (t-\xi)^{\alpha-1}\Xi(\xi,\Omega(\xi))\xi^{\tau-1}\mathrm{d}\xi. \tag{11} $$

Here, also like Picard Lindlof theorem, we let

$$ \prod_a^b = \mathcal{I}_n(t_n) \times \overline{\mathcal{A}_0(\Omega_0)}, \tag{12} $$

where $\mathcal{I}_n(t_n) = [t_{n-a}, t_{n+a}]$ and $\overline{\mathcal{A}_0(\Omega_0)} = [t_0 - b, t_0 + b]$. Also, let $\sup_{t\in\prod_a^b}\|\Xi\| = \mathcal{K}$; now, we define the norm as follows:

$$\|\Psi\|_\infty = \sup_{t\in\prod_a^b |\Psi(t)|.} \tag{13}$$

Next, we define the operator $\mathcal{O}\colon \mathcal{C}[\mathcal{J}_n(t_n), \mathcal{A}_b(t_n)] \longrightarrow \mathcal{C}[\mathcal{J}_n(b), \mathcal{A}_b(t_n)]$ as

$$\mathcal{O}\Omega(t) = \Omega_0 + \frac{1-\alpha}{\mathcal{AB}(\alpha)}\tau t^{\tau-1}\Xi(t,\Omega(t)) + \frac{\alpha\tau}{\mathcal{AB}(\alpha)\Gamma(\alpha)}\int_0^t \xi^{\tau-1}(t-\xi)^{\alpha-1}\Xi(\xi,\Omega(\xi))\mathrm{d}\xi. \tag{14}$$

The goal is to show that the defined operator is a contraction mapping that translates a complete norm empty metric space Y into itself. First, we need to show that $\|\mathcal{O}\Omega(t) - \Omega_0\| \le b$. For this, consider

$$\begin{aligned}\left\|\mathcal{O}\Omega(t) - \Omega_0\right\| &\le \frac{1-\alpha}{\mathcal{AB}(\alpha)}\tau t^{\xi-1}\|\Xi(t,\Omega(t))\|_\infty \\ &+ \frac{\alpha\tau}{\mathcal{AB}(\alpha)\Omega(\alpha)}\int_0^t (t-\xi)^{\alpha-1}\|\Xi(\xi,\Omega(\xi))\|\xi^{\tau-1}\mathrm{d}\xi \\ &\le \frac{1-\alpha}{\mathcal{AB}(\alpha)}\tau t^{\tau-1}\mathcal{K} + \frac{\alpha\tau}{\mathcal{AB}(\alpha)\Gamma(\alpha)}\mathcal{K}\int_0^t (t-\xi)^{\alpha-1}\xi^{\tau-1}\mathrm{d}\xi.\end{aligned} \tag{15}$$

Let $\xi = ty$, expression (15) becomes

$$\left\|\mathcal{O}\Omega(t) - \Omega_0\right\| \le \frac{1-\alpha}{\mathcal{AB}(\alpha)}\tau t^{\xi-1}\mathcal{K} + \frac{\alpha\tau\mathcal{K}}{\mathcal{AB}(\alpha)\Gamma(\alpha)}t^{\alpha+\tau-1}\mathcal{B}(\alpha,\tau), \tag{16}$$

where $\mathcal{B}(\alpha,\tau)$ represents beta function; thus,

$$\left\|\mathcal{O}\Omega(t) - \Omega_0\right\| \le b \longrightarrow \mathcal{K} < \frac{b\mathcal{B}(\alpha,\tau)}{\Gamma(\alpha)(1-\alpha)\tau t^{\tau-1} + \alpha\tau t^{\tau+\alpha-1}/\mathcal{AB}(\alpha)\Gamma(\alpha)}. \tag{17}$$

Now, for any $\Omega_1, \Omega_2 \in \mathcal{C}[\mathcal{J}_n(t_n), \mathcal{A}_b(t_n)]$, we have

$$\begin{aligned}\left\|\mathcal{O}\Omega_1 - \mathcal{O}\Omega_2\right\| &\le \frac{1-\alpha}{\mathcal{AB}(\alpha)}\tau t^{\tau-1}\left\|\Xi(t,\Omega_1(t)) - \Xi(t,\Omega_2(t))\right\| \\ &+ \frac{\alpha\tau}{\mathcal{AB}(\alpha)\Gamma(\alpha)}\int_0^t (t-\xi)^{\alpha-1}\xi^{\tau-1}\left\|\Xi(t,\Omega_1(t)) - \Xi(t,\Omega_2(t))\right\|\mathrm{d}\xi.\end{aligned} \tag{18}$$

Since Ξ being a contraction, we have

$$\begin{aligned}\left\|\mathcal{O}\Omega_1 - \mathcal{O}\Omega_2\right\| &\le \frac{1-\alpha}{\mathcal{AB}(\alpha)}\tau t^{\tau-1}\mathfrak{L}\left\|\Omega_1 - \Omega_2\right\|_\infty \\ &+ \frac{\alpha\tau\mathfrak{L}}{\mathcal{AB}(\alpha)\Gamma(\alpha)}\left\|\Omega_1 - \Omega_2\right\|_\infty\int_0^t (t-\xi)^{\alpha-1}\xi^{\tau-1}\mathrm{d}\xi \le \frac{1-\alpha}{\mathcal{AB}(\alpha)}\tau t^{\tau-1}\mathfrak{L}\left\|\Omega_1 - \Omega_2\right\|_\infty \\ &+ \frac{\alpha\tau\mathfrak{L}}{\mathcal{AB}(\alpha)\Gamma(\alpha)}\left\|\Omega_1 - \Omega_2\right\|_\infty t^{\alpha+\tau-1}\mathcal{B}(\alpha,\tau).\end{aligned} \tag{19}$$

It follows that

$$\left\|\mathcal{O}\Omega_1 - \mathcal{O}\Omega_2\right\| \leq \left[\frac{1-\alpha}{\mathcal{AB}(\alpha)}\tau t^{\tau-1}\mathfrak{L} + \frac{\alpha\tau\mathfrak{L}}{\mathcal{AB}(\alpha)\Gamma(\alpha)}t^{\alpha+\tau-1}\mathcal{B}(\alpha,\tau)\right]\left\|\Omega_1 - \Omega_2\right\|_\infty. \tag{20}$$

Now, since

$$\begin{aligned}&\frac{1-\alpha}{\mathcal{AB}(\alpha)}\tau t^{\tau-1}\mathfrak{L} + \frac{\alpha\tau\mathfrak{L}}{\mathcal{AB}(\alpha)\Gamma(\alpha)}t^{\alpha+\tau-1}\mathcal{B}(\alpha,\tau)\\ &< \frac{1-\alpha}{\mathcal{AB}(\alpha)}\tau a^{\tau-1}\mathfrak{L} + \frac{\alpha\tau\mathfrak{L}}{\mathcal{AB}(\alpha)\Gamma(\alpha)}a^{\alpha+\tau-1}\mathcal{B}(\alpha,\tau).\end{aligned} \tag{21}$$

Thus, $\mathcal{O}$ is a contraction if

$$\left\|\mathcal{O}\Omega_1 - \mathcal{O}\Omega_2\right\|_\infty < \left\|\Omega_1 - \Omega_2\right\|. \tag{22}$$

For this, we have

$$\mathfrak{L} < \frac{1}{(1-\alpha/\mathcal{AB}(\alpha))\tau a^{\tau-1} + (\alpha\tau/\mathcal{AB}(\alpha)\Gamma(\alpha))a^{\alpha+\tau-1}\mathcal{B}(\alpha,\tau)}, \tag{23}$$

so

$$\mathcal{K} < \frac{1}{(1-\alpha/\mathcal{AB}(\alpha))\tau a^{\tau-1} + (\alpha\tau/\mathcal{AB}(\alpha)\Gamma(\alpha))a^{\alpha+\tau-1}\mathcal{B}(\alpha,\tau)}. \tag{24}$$

Thus, a unique solution of the proposed model exists.

4. Numerical Scheme with Mittag-Leffler Type Kernel

Consider model (2) as follows:

$$\left\{{}^{\mathcal{BR}}\mathcal{D}_{0,t}^{\alpha}(\mathcal{X}(t)) = \tau t^{\tau-1}\mathcal{H}_1(t,\mathcal{X},Y,Z), {}^{\mathcal{BR}}\mathcal{D}_{0,t}^{\alpha}(Y(t)) = \tau t^{\tau-1}\mathcal{H}_2(t,\mathcal{X},Y,Z), {}^{\mathcal{BR}}\mathcal{D}_{0,t}^{\alpha}(Z(t)) = \tau t^{\tau-1}\mathcal{H}_3(t,\mathcal{X},Y,Z).\right. \tag{25}$$

Then, we reach

$$\begin{cases} X(t) = \mathcal{X}(0) + \dfrac{\tau t^{\tau-1}(1-\alpha)}{\mathcal{AB}(\alpha)}\mathcal{H}_1(t,\mathcal{X},Y,Z) \\ +\dfrac{\alpha\tau}{\mathcal{AB}(\alpha)\Gamma(\alpha)}\displaystyle\int_0^t \xi^{\tau-1}(t-\xi)^{\alpha-1}\mathcal{H}_1(\xi,\mathcal{X},Y,Z)\mathrm{d}\xi, \\ Y(t) = Y(0) + \dfrac{\tau t^{\tau-1}(1-\alpha)}{\mathcal{AB}(\alpha)}\mathcal{H}_2(t,\mathcal{X},Y,Z) \\ +\dfrac{\alpha\tau}{\mathcal{AB}(\alpha)\Gamma(\alpha)}\displaystyle\int_0^t \xi^{\tau-1}(t-\xi)^{\alpha-1}\mathcal{H}_2(\xi,\mathcal{X},Y,Z)\mathrm{d}\xi, \\ \mathcal{Z}(t) = Z(0) + \dfrac{\tau t^{\tau-1}(1-\alpha)}{\mathcal{AB}(\alpha)}\mathcal{H}_3(t,\mathcal{X},Y,Z) \\ +\dfrac{\alpha\tau}{\mathcal{AB}(\alpha)\Gamma(\alpha)}\displaystyle\int_0^t \xi^{\tau-1}(t-\xi)^{\alpha-1}\mathcal{H}_3(\xi,\mathcal{X},Y,Z)\mathrm{d}\xi. \end{cases} \tag{26}$$

Now, at $t = t_{n+1}$, we have

$$\begin{cases} \mathcal{X}^{n+1} = \mathcal{X}^0 + \dfrac{\tau t_n^{\tau-1}(1-\alpha)}{\mathcal{AB}(\alpha)}\mathcal{H}_1(t_n,\mathcal{X}^n,Y^n,Z^n) \\ +\dfrac{\alpha\tau}{\mathcal{AB}(\alpha)\Gamma(\alpha)}\displaystyle\int_0^{t_{n+1}} \xi^{\tau-1}(t_{n+1}-\xi)^{\alpha-1}\mathcal{H}_1(\xi,\mathcal{X},Y,Z)\mathrm{d}\xi, \\ \mathcal{Y}^{n+1} = \mathcal{Y}^0 + \dfrac{\tau t_n^{\tau-1}(1-\alpha)}{\mathcal{AB}(\alpha)}\mathcal{H}_2(t_n,\mathcal{X}^n,Y^n,Z^n) \\ +\dfrac{\alpha\tau}{\mathcal{AB}(\alpha)\Gamma(\alpha)}\displaystyle\int_0^{t_{n+1}} \xi^{\tau-1}(t_{n+1}-\xi)^{\alpha-1}\mathcal{H}_2(\xi,\mathcal{X},Y,Z)\mathrm{d}\xi, \\ \mathcal{Z}^{n+1} = \mathcal{Z}^0 + \dfrac{\tau t_n^{\tau-1}(1-\alpha)}{\mathcal{AB}(\alpha)}\mathcal{H}_2(t_n,\mathcal{X}^n,Y^n,Z^n) \\ +\dfrac{\alpha\tau}{\mathcal{AB}(\alpha)\Gamma(\alpha)}\displaystyle\int_0^{t_{n+1}} \xi^{\tau-1}(t_{n+1}-\xi)^{\alpha-1}\mathcal{H}_2(\xi,\mathcal{X},Y,Z)\mathrm{d}\xi. \end{cases} \tag{27}$$

Using the approximation of the integrals in (27), we get

$$\begin{cases} \mathscr{X}^{n+1} = \mathscr{X}^{0} + \dfrac{\tau t_n^{\tau-1}(1-\alpha)}{\mathscr{AB}(\alpha)}\mathscr{H}_1\left(t_n, \mathscr{X}^n, Y^n, Z^n\right) \\ \\ +\dfrac{\alpha\tau}{\mathscr{AB}(\alpha)\Gamma(\alpha)}\displaystyle\sum_{f=0}^{p}\int_{t_f}^{t_{f+1}} \xi^{\tau-1}\left(t_{n+1}-\xi\right)^{\alpha-1}\mathscr{H}_1(\xi, \mathscr{X}, Y, Z)\mathrm{d}\xi, \\ \\ \mathscr{Y}^{n+1} = \mathscr{Y}^{0} + \dfrac{\tau t_n^{\tau-1}(1-\alpha)}{\mathscr{AB}(\alpha)}\mathscr{H}_2\left(t_n, \mathscr{X}^n, Y^n, Z^n\right) \\ \\ +\dfrac{\alpha\tau}{\mathscr{AB}(\alpha)\Gamma(\alpha)}\displaystyle\sum_{f=0}^{p}\int_{t_f}^{t_{f+1}} \xi^{\tau-1}\left(t_{n+1}-\xi\right)^{\alpha-1}\mathscr{H}_2(\xi, \mathscr{X}, Y, Z)\mathrm{d}\xi, \\ \\ \mathscr{Z}^{n+1} = \mathscr{Z}^{0} + \dfrac{\tau t_n^{\tau-1}(1-\alpha)}{\mathscr{AB}(\alpha)}\mathscr{H}_2\left(t_n, \mathscr{X}^n, Y^n, Z^n\right) \\ \\ +\dfrac{\alpha\tau}{\mathscr{AB}(\alpha)\Gamma(\alpha)}\displaystyle\sum_{f=0}^{p}\int_{t_f}^{t_{f+1}} \xi^{\tau-1}\left(t_{n+1}-\xi\right)^{\alpha-1}\mathscr{H}_2(\xi, \mathscr{X}, Y, Z)\mathrm{d}\xi. \end{cases} \tag{28}$$

Now, utilizing the Lagrangian polynomial piecewise interpolation, one can get

$$\begin{cases} X^{n+1} = X^{0} + \dfrac{\tau t_n^{\tau-1}(1-\alpha)}{\mathscr{AB}(\alpha)}\mathscr{H}_1\left(t_n, X^n, Y^n, Z^n\right) + \dfrac{\tau(\Delta t)^{\alpha}}{\mathscr{AB}(\alpha)\Gamma(\alpha+2)} \\ \\ \times\displaystyle\sum_{f=0}^{p}\begin{bmatrix} t_f^{\tau-1}\mathscr{H}_1\left(t_f, X^f, Y^f, Z^f\right)\times\left((p+1-f)^{\alpha}(p-f+2+\alpha)-(p-f)^{\alpha}(p-f+2+2\alpha)\right) \\ -t_{f-1}^{\tau-1}\mathscr{H}_1\left(t_{f-1}, X^{f-1}, Y^{f-1}, Z^{f-1}\right)\times\left((p-f+1)^{\alpha+1}-(p-f)^{\alpha}(p-f+1+\alpha)\right) \end{bmatrix}, \\ \\ Y^{n+1} = Y^{0} + \dfrac{\tau t_n^{\tau-1}(1-\alpha)}{\mathscr{AB}(\alpha)}\mathscr{H}_2\left(t_n, X^n, Y^n, Z^n\right) + \dfrac{\tau(\Delta t)^{\alpha}}{\mathscr{AB}(\alpha)\Gamma(\alpha+2)} \\ \\ \times\displaystyle\sum_{f=0}^{p}\begin{bmatrix} t_f^{\tau-1}\mathscr{H}_1\left(t_f, X^f, Y^f, Z^f\right)\times\left((p+1-f)^{\alpha}(p-f+2+\alpha)-(p-f)^{\alpha}(p-f+2+2\alpha)\right) \\ -t_{f-1}^{\tau-1}\mathscr{H}_1\left(t_{f-1}, X^{f-1}, Y^{f-1}, Z^{f-1}\right)\times\left((p-f+1)^{\alpha+1}-(p-f)^{\alpha}(p-f+1+\alpha)\right) \end{bmatrix}, \\ \\ Z^{n+1} = Z^{0} + \dfrac{\tau t_n^{\tau-1}(1-\alpha)}{\mathscr{AB}(\alpha)}\mathscr{H}_3\left(t_n, X^n, Y^n, Z^n\right) + \dfrac{\tau(\Delta t)^{\alpha}}{\mathscr{AB}(\alpha)\Gamma(\alpha+2)} \\ \\ \times\displaystyle\sum_{f=0}^{p}\begin{bmatrix} t_f^{\tau-1}\mathscr{H}_1\left(t_f, X^f, Y^f, Z^f\right)\times\left((p+1-f)^{\alpha}(p-f+2+\alpha)-(p-f)^{\alpha}(p-f+2+2\alpha)\right) \\ -t_{f-1}^{\tau-1}\mathscr{H}_1\left(t_{f-1}, X^{f-1}, Y^{f-1}, Z^{f-1}\right)\times\left((p-f+1)^{\alpha+1}-(p-f)^{\alpha}(p-f+1+\alpha)\right) \end{bmatrix}. \end{cases} \tag{29}$$

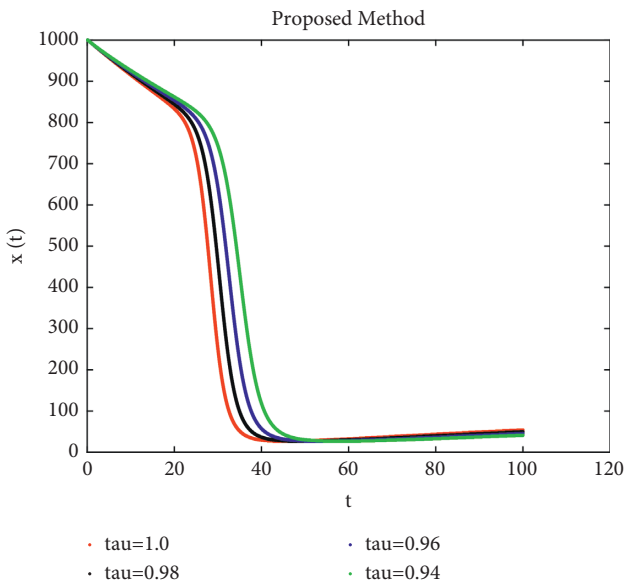

Figure 1: Dynamical behavior of concentration of uninfected (susceptible) cells at $\alpha = 1$ and various fractal order under power law kernel.

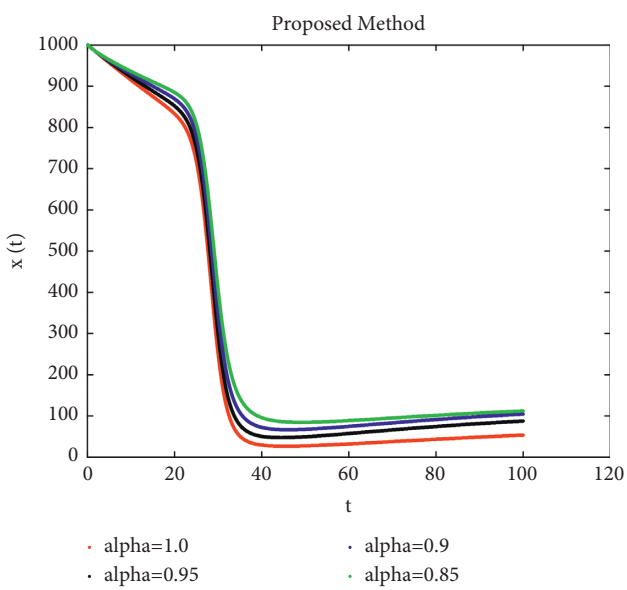

Figure 2: Dynamical behavior of concentration of uninfected (susceptible) cells at $\tau = 1$ and various fractional order under power law kernel.

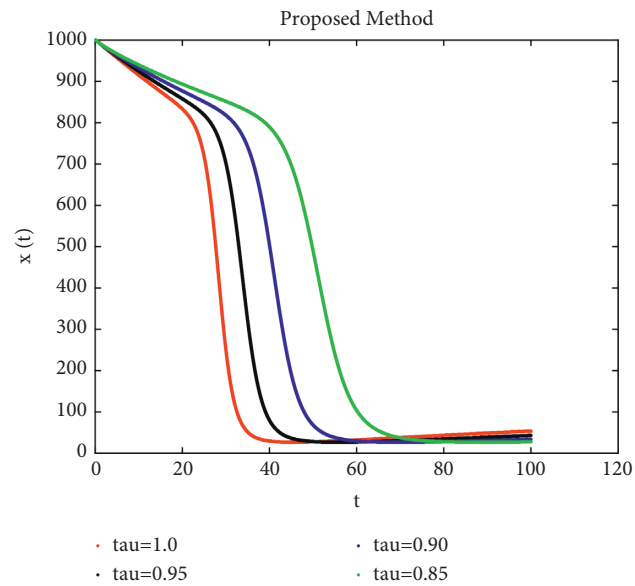

Figure 3: Dynamical behavior of concentration of uninfected (susceptible) cells at $\alpha = 1$ and various fractal order = 0.85, 0.9, 0.95, 1 under power law kernel.

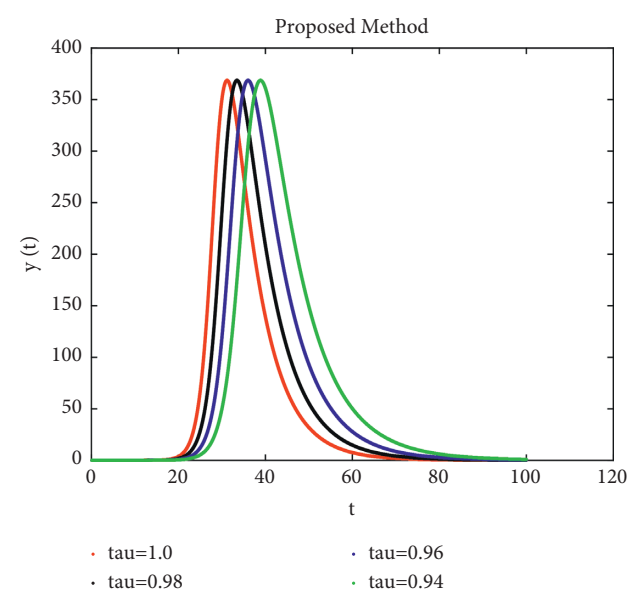

Figure 4: Dynamical behavior infected cells at $\alpha = 1$ and fractal order under power law kernel.

5. Numerical Simulations

In this section, we discuss the numerical simulations of the proposed model. For the desired simulation, we take $X_0 = 1000$ (millions), $Y_0 = 0$, and $Z_0 = 0.001$ (millions). The parameter values are as follows: $\mu = 10$, $d^* = 0.01$, $k^* = 0.000024$, $\delta = 0.16$, $b^* = 0.02$, $c^* = 3.4$, and $N^* = 1000$. Via MATLAB, we graphically present the different compartments of the model against the various fractional and fractal orders. Figures 1–9 represent the dynamics of the proposed model for the Caputo fractal-fractional operator, and Figures 10–18 represent the dynamics suggested for the Atangana–Baleanu fractal-fractional operator. It is observed in Figures 1–3 and 10–12, which is the primary stage of HIV infection, the concentration level of uninfected CD4+ T-cells

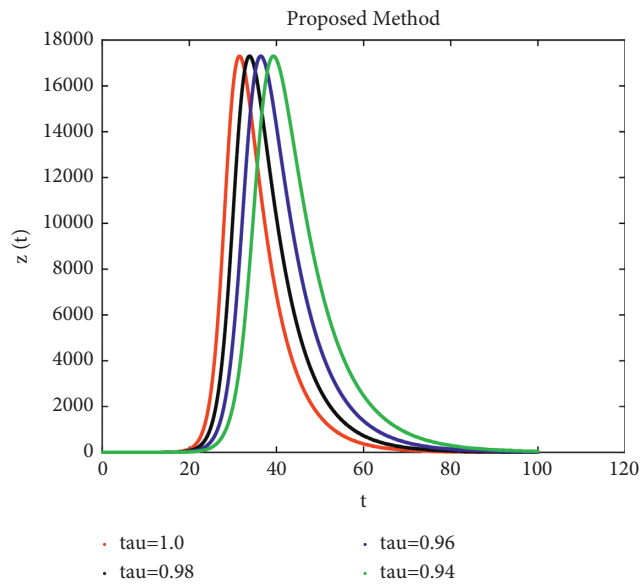

Figure 5: Dynamical behavior of free HIV virus particles at $\alpha = 1$ and various fractal order under power law kernel.

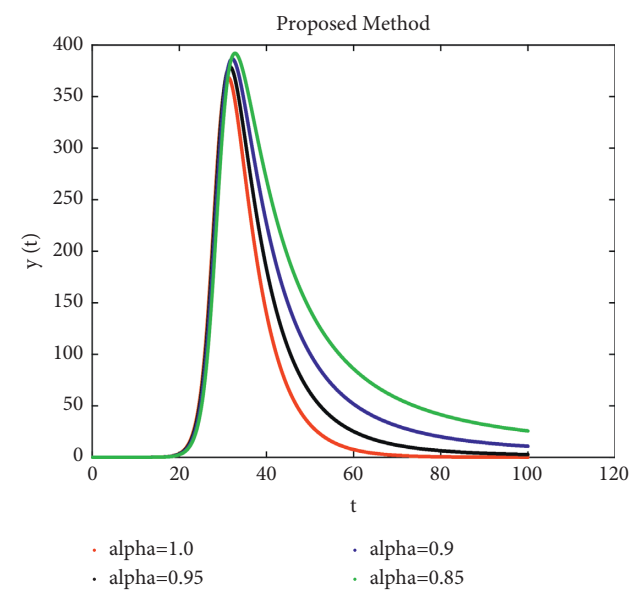

Figure 6: Dynamical behavior infected cells at $\tau = 1$ and various fractional order under power law kernel.

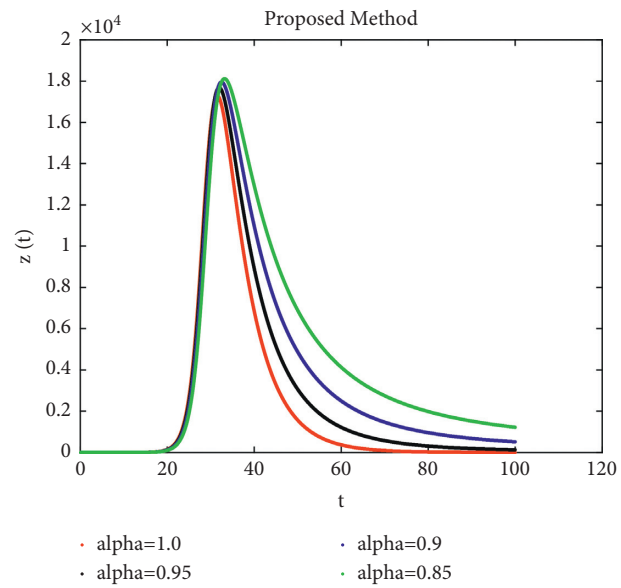

Figure 7: Dynamical behavior of free HIV virus particles at $\tau = 1$ and various fractional order under power law kernel.

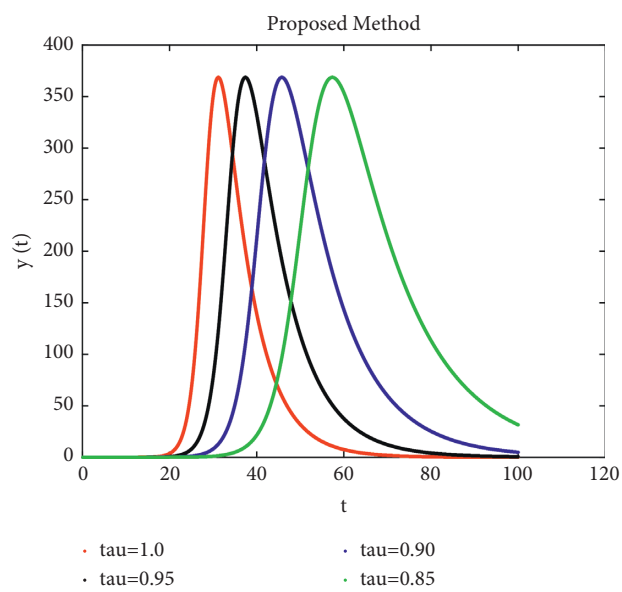

Figure 8: Dynamical behavior infected cells at $\alpha = 1$ and various fractal order = 0.85, 0.9, 0.95, 1 under power law kernel.

is significantly decreased. It is because such infected cells have died. This decrease occurs mainly due to fractal and fractional order, with different rates. The smaller the order, the faster the decay, and thus the stability takes place before the highest order. On the other hand, we analyze from Figures 4–8 that the amount of infected CD4+ T-cells and free HIV particles is increasing. This rapid increase is also different in different fractal and fractional orders, and in smaller orders, it is faster, and as the order increases, the growth rate becomes slower. From these graphic representations, it is clear that the development of healthy T-cells slows during HIV infection. We conclude from the figures that the use of fractal-fractional to solve an epidemic model gives the best results relative to fractional systems. We provide numerical simulations with different sets of fractal and fractional order for the proposed model. We observe the effect of the fractal dimension on the dynamics of the model.

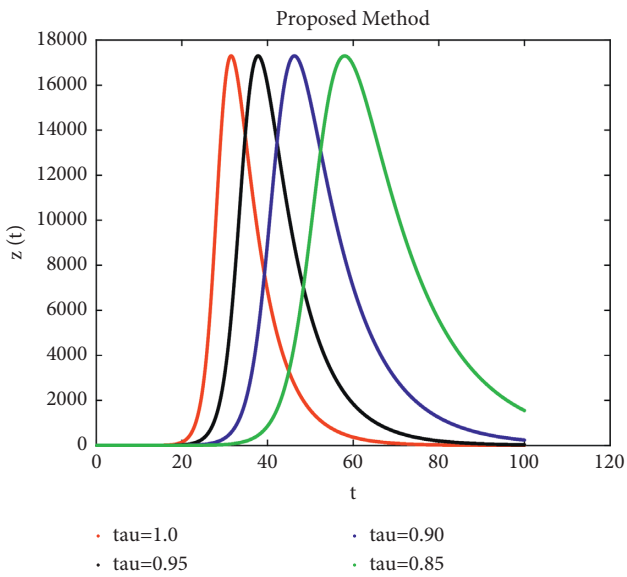

Figure 9: Dynamical behavior of free HIV virus particles at $\alpha = 1$ and various fractal order = 0.85, 0.9, 0.95, 1 under power law kernel.

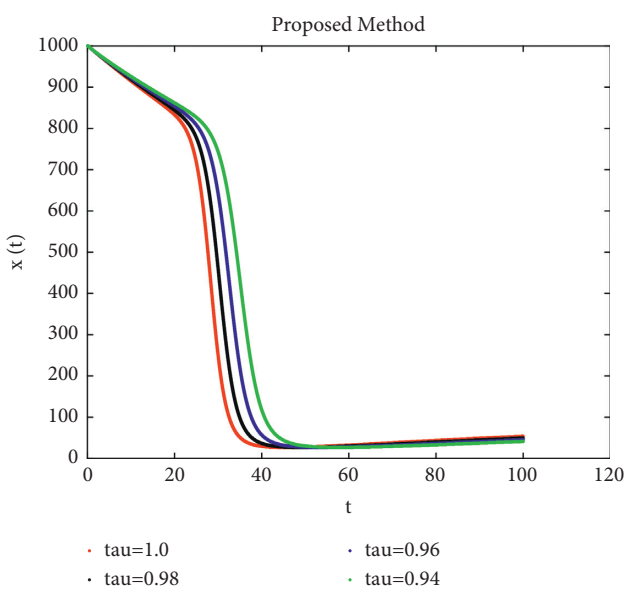

Figure 10: Dynamical behavior of concentration of uninfected (susceptible) cells at $\alpha = 1$ and various fractal order under Mittag-Leffler kernel.

Also, we provide a comparison between Caputo and Atangana–Beleanu operators via numerical simulations. We have almost same result for the both operators for $\alpha = 1$ and $\tau = 0.85, 0.9, 0.95, 1$ (see Figures 1, 4, 5, 10, 13, and 14). However, by changing fractional order and keeping fractal dimension fix, Atangana–Baleanu gives better dynamics of the proposed model. From Figures 2, 6, and 7, one can easily observe that there is no clear information about the population class for up to 40 days when changing the fractional

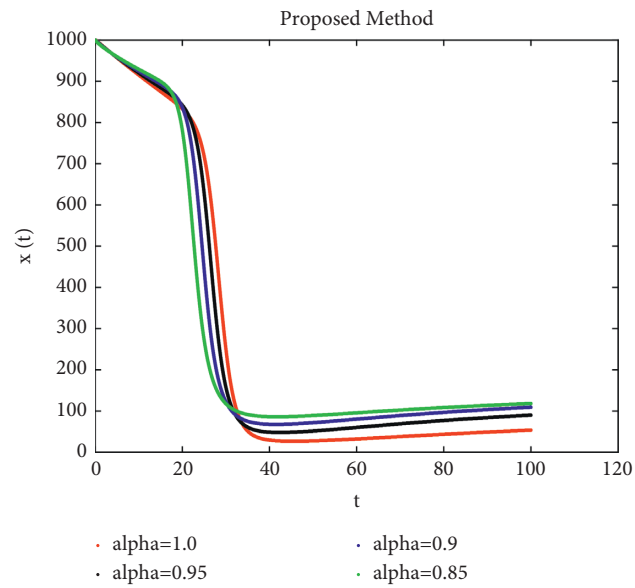

Figure 11: Dynamical behavior of concentration of uninfected (susceptible) cells at $\tau = 1$ and various fractional order under Mittag-Leffler kernel.

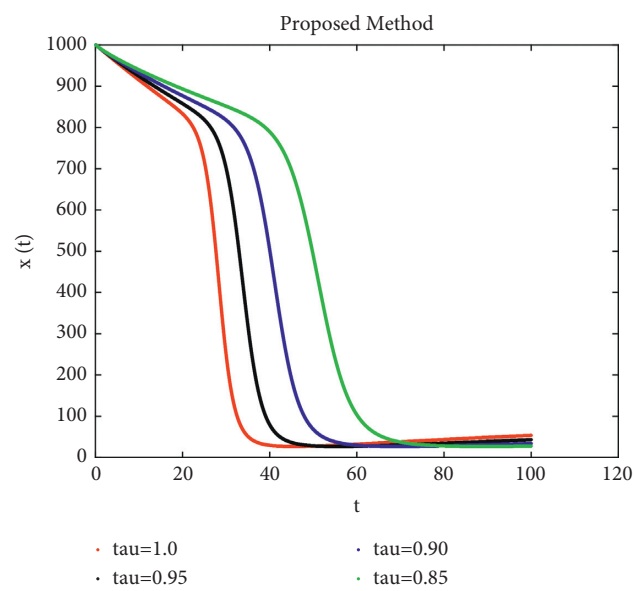

Figure 12: Dynamical behavior of concentration of uninfected (susceptible) cells at $\alpha = 1$ and various fractal order = 0.85, 0.9, 0.95, 1 under Mittag-Leffler kernel.

order. However, from Figures 11, 15, and 16, the effect of fractional order on the dynamics of the proposed model is much more clear. There is clear information of memory property about population class up to 40 days when changing the fractional order. It provides all previous history of the diseases, which is the main function of fractional order. Further, in Figure 19, we compare our simulated

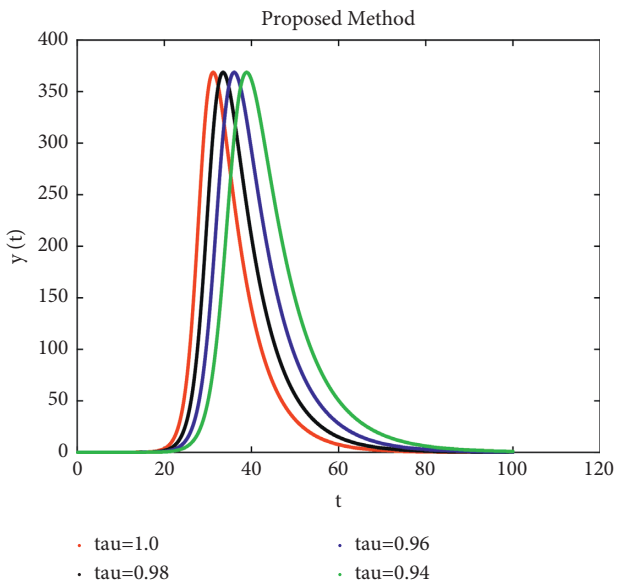

Figure 13: Dynamical behavior of infected cells at $\alpha = 1$ and various fractal order under Mittag-Leffler kernel.

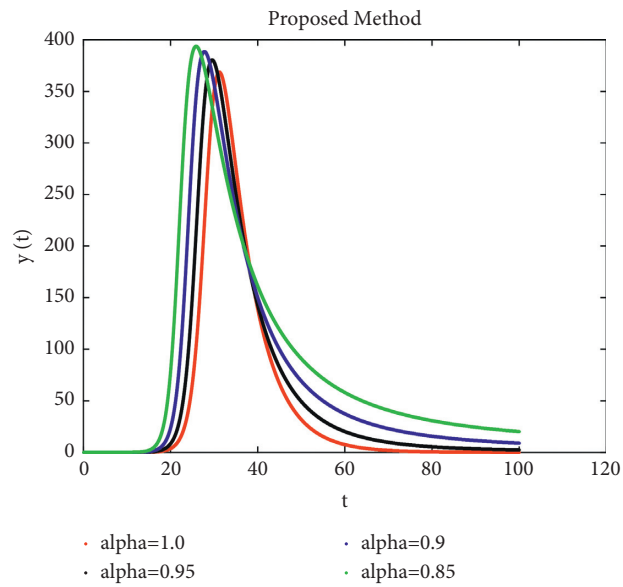

Figure 15: Dynamics of infected cells at $\tau = 1$ and various fractional order under Mittag-Leffler kernel.

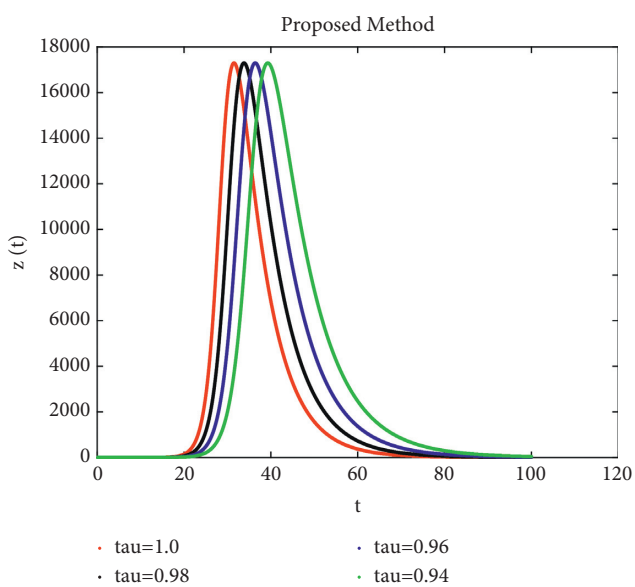

Figure 14: Dynamical behavior of free HIV virus particles at $\alpha = 1$ and various fractal order under Mittag-Leffler kernel.

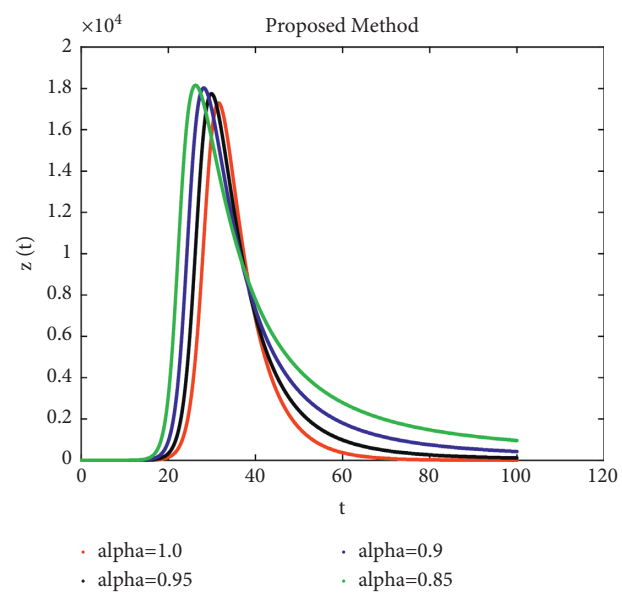

Figure 16: Dynamical behavior of free HIV virus particles at $\tau = 1$ and various fractional order under Mittag-Leffler kernel.

results in the case of Atangana–Baleanu operator with the actual data for the country of Brazil. We have taken the data of HIV-infected people for 15 years from [21]. The red dots represent actual data, and the green curve represents the dynamics of infected HIV cells under the Atangana–Baleanu operator at fractional order 0.94. We see that the graph of simulated data and actual data is very close to each other at the order of 0.94. On this basis, we conclude that fractal-fractional operator in Atangana–Baleanu sense provides a clear understanding of an epidemic model's dynamics and can be applied successfully to several other problems.

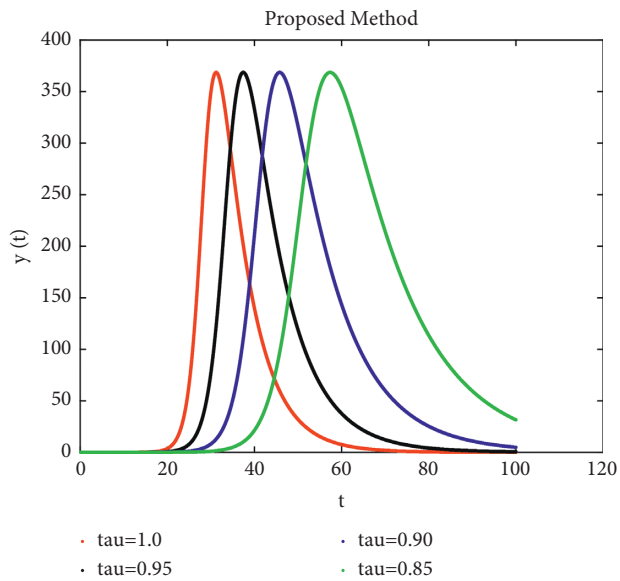

Figure 17: Dynamical behavior of infected cells at $\alpha = 1$ and various fractal order = 0.85, 0.9, 0.95, 1 under Mittag-Leffler kernel.

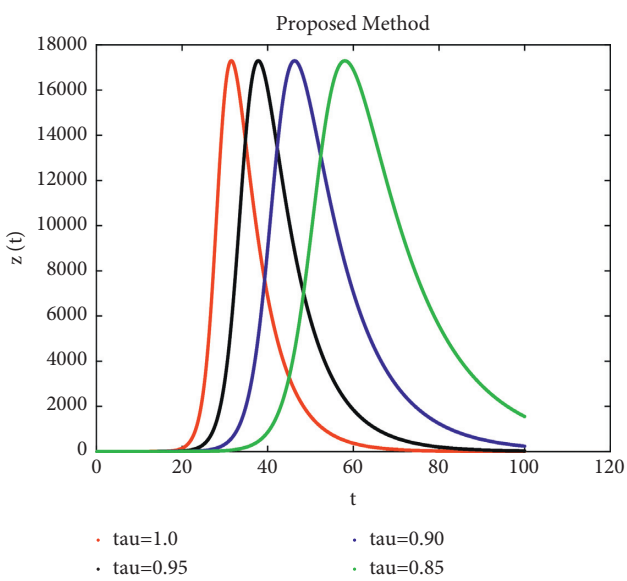

Figure 18: Dynamical behavior of free HIV virus particles at $\alpha = 1$ and various fractal order = 0.85, 0.9, 0.95, 1 under Mittag-Leffler kernel.

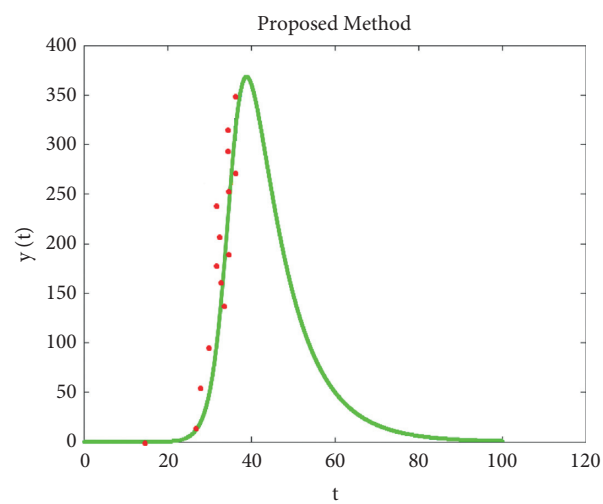

Figure 19: Comparison of simulated result with real data.

6. Conclusion

In the current manuscript, we have applied the more generalized operators to study the relationship between HIV infection and its relation with CD4+ T-cells during primary infection. We have derived the results of the existence and uniqueness of the proposed fractal-fractional HIV model described by the operator in the Atangana–Baleanu sense. We have obtained numerical results through the Adams–Bashforth method. To visualize the dynamics of considered, we have simulated the obtained results through MATLAB-18. We have observed the impact of fractal dimension on the fractional order through graphs. The increase and decrease in fractal dimension affect the dynamics of the different compartments of the model. From the numerical simulations, we have observed that the fractal-fractional idea produces better results in the sense of Atangana–Baleanu operators. So, we recommend that the Atangana–Baleanu fractal-fractional model gives the best results and may be more valuable to scientists and researchers. It is also observable from the numerical simulations that fractal-fractional order can capture more complexities than usual fractional derivatives. We keep hoping that this work may assist young researchers in a different direction of applied mathematics.

Data Availability

No data were used to support this study

Conflicts of Interest

The authors declare that there are no conflicts of interest in this research study.

Authors' Contributions

All the authors contributed equally to this study.

Acknowledgments

The authors are grateful to the Basque Government (IT1207-19).

References

[1] A.-H. Abdel-Aty, M. M. A. Khater, H. Dutta, J. Bouslimi, and M. Omri, "Computational solutions of the HIV-1 infection of CD4+ T-cells fractional mathematical model that causes acquired immunodeficiency syndrome (AIDS) with the effect of antiviral drug therapy," *Chaos, Solitons & Fractals*, vol. 139, Article ID 110092, 2020.

[2] M. M. A. Khater, A. E.-S. Ahmed, and M. A. El-Shorbagy, "Abundant stable computational solutions of Atangana-Baleanu fractional nonlinear HIV-1 infection of CD4+ T-cells of immunodeficiency syndrome," *Results in Physics*, vol. 22, Article ID 103890, 2021.

[3] L. Wang and M. Y. Li, "Mathematical analysis of the global dynamics of a model for HIV infection of CD4+ T cells," *Mathematical Biosciences*, vol. 20, no. 1, pp. 44–57, 2004.

[4] A. S. Perelson, "Modeling the interaction of the immune system with HIV," *Lecture Notes in Biomathematics*, vol. 83, pp. 350–370, 1989.

[5] A. S. Perelson, D. E. Kirschner, and R. D. Boer, "Dynamics of HIV infection of CD4+ T cells," *Mathematical Biosciences*, vol. 114, no. 81, pp. 81–125, 1993.

[6] T. CHenry and Y. M. W. Frederic, "On the behavior of solutions in viral dynamical models," *BioSystems*, vol. 73, pp. 157–161, 2004.

[7] A. S. Perelson, A. U. Neumann, M. Markowitz, J. M. Leonard, and D. D. Ho, "HIV-1 dynamics in vivo: virion clearance rate, infected cell life-span, and viral generation time," *Science*, vol. 271, no. 5255, pp. 1582–1586, 1996.

[8] Y. Ding and H. Ye, "A fractional-order differential equation model of HIV infection of CD4+ T-cells," *Mathematical and Computer Modelling*, vol. 50, no. 3-4, pp. 386–392, 2009.

[9] G. Nazir, K. Shah, A. Debbouche, and R. A. Khan, "Study of HIV mathematical model under nonsingular kernel type derivative of fractional order," *Chaos, Solitons & Fractals*, vol. 139, Article ID 110095, 2020.

[10] A. A. M. Arafa, S. Z. Rida, and M. Khalil, "Fractional modeling dynamics of HIV and CD4+ T-cells during primary infection," *Nonlinear Biomedical Physics*, vol. 6, no. 1, p. 7, 2012.

[11] S. Ahmad, A. Ullah, M. Arfan, and K. Shah, "On analysis of the fractional mathematical model of rotavirus epidemic with the effects of breastfeeding and vaccination under Atangana-Baleanu (AB) derivative," *Chaos, Solitons & Fractals*, vol. 140, Article ID 110233, 2020.

[12] A. Ullah, T. Abdeljawad, S. Ahmad, and K. Shah, "Study of a fractional-order epidemic model of childhood diseases," *Journal of Function Spaces*, vol. 2020, Article ID 5895310, 8 pages, 2020.

[13] K. S. Nisar, S. Ahmad, A. Ullah, K. Shah, H. Alrabaiah, and M. Arfan, "Mathematical analysis of SIRD model of COVID-19 with Caputo fractional derivative based on real data," *Results in Physics*, vol. 21, Article ID 103772, 2021.

[14] A. M. A. El-Sayed, H. M. Nour, W. E. Raslan, and E. S. El-Shazly, "A study of projectile motion in a quadratic resistant medium via fractional differential transform method," *Applied Mathematical Modelling*, vol. 39, no. 10-11, pp. 2829–2835, 2015.

[15] S. Ahmad, A. Ullah, K. Shah, and A. Akgül, "Computational analysis of the third order dispersive fractional PDE under exponential-decay and Mittag-Leffler type kernels," *Numerical Methods for Partial Differential Equations*, vol. 16, p. 1, 2020.

[16] A. Atangana, "Fractal-fractional differentiation and integration: connecting fractal calculus and fractional calculus to predict complex system," *Chaos, Solitons & Fractals*, vol. 102, no. 396, pp. 396–406, 2017.

[17] S. Ahmad, A. Ullah, T. Abdeljawad, A. Akgül, and N. Mlaiki, "Analysis of fractal-fractional model of tumor-immune interaction," *Results in Physics*, vol. 25, Article ID 104178, 2021.

[18] Fatmawati and M. A. Khan, "The dynamics of dengue infection through fractal-fractional operator with real statistical data," *Alexandria Engineering Journal*, vol. 60, no. 1, pp. 321–336, 2021.

[19] K. M. Owolabi, A. Atangana, and A. Akgül, "Modelling and analysis of fractal-fractional partial differential equations: application to reaction-diffusion model," *Alexandria Engineering Journal*, vol. 59, no. 4, pp. 2477–2490, 2020.

[20] S. Ahmad, A. Ullah, and A. Akgül, "Investigating the complex behaviour of multi-scroll chaotic system with Caputo fractal-fractional operator," *Chaos, Solitons & Fractals*, vol. 146, Article ID 110900, 2021.

[21] https://www.unaids.org/en/resources/fact-sheet.

Hindawi
Complexity
Volume 2021, Article ID 9915551, 9 pages
https://doi.org/10.1155/2021/9915551

Research Article

A New Scheme for Solving Multiorder Fractional Differential Equations Based on Müntz–Legendre Wavelets

Haifa Bin Jebreen and Fairouz Tchier

Department of Mathematics, College of Science, King Saud University, Riyadh, Saudi Arabia

Correspondence should be addressed to Haifa Bin Jebreen; hjebreen@ksu.edu.sa

Received 12 March 2021; Revised 4 April 2021; Accepted 20 July 2021; Published 31 July 2021

Academic Editor: Átila Madureira Bueno

In this study, we apply the pseudospectral method based on Müntz–Legendre wavelets to solve the multiorder fractional differential equations with Caputo fractional derivative. Using the operational matrix for the Caputo derivative operator and applying the Chebyshev and Legendre zeros, the problem is reduced to a system of linear algebraic equations. We illustrate the reliability, efficiency, and accuracy of the method by some numerical examples. We also compare the proposed method with others and show that the proposed method gives better results.

1. Introduction

This paper is dedicated to the numerical solution of the multiorder fractional differential equation with Caputo fractional derivative based on Müntz–Legendre wavelets. Let $\alpha \in \mathbb{R}_+$, $\mathbb{N} \ni n := [-\alpha]$, for $\alpha \notin \mathbb{N}$. Further, let $\alpha_j \in \mathbb{R}_+ (j = 1, \ldots, \sigma \in \mathbb{N})$ which satisfies

$$0 = \alpha_0 < \alpha_1 < \cdots < \alpha_\sigma < \alpha. \tag{1}$$

We aim to compute the approximate solution of the linear or nonlinear fractional differential equation

$$\begin{aligned} {}^c\mathscr{D}_0^\alpha (y)(x) &= f\left[x, y(x), {}^c\mathscr{D}_0^{\alpha_1}(y)(x), \ldots, {}^c\mathscr{D}_0^{\alpha_\sigma}(y)(x)\right], \quad x \in [0,1], \\ y^{(\eta)}(0) &= q_\eta, \quad q_\eta \in \mathbb{R}, \eta = 0, 1, \ldots, n-1, \end{aligned} \tag{2}$$

where ${}^c\mathscr{D}_0^\alpha$ is the Caputo fractional differential operator [1] and the function $f[x, y, y_1, \ldots, y_\sigma] \in C[0,1]$ with $y_1, \ldots, y_\sigma \in \mathscr{G}$ ($\mathscr{G} \subset \mathbb{C}$ is an open set) satisfies the Lipschitz condition

$$\left| f[x, y, y_1, \ldots, y_\sigma](x) - f[x, u, u_1, \ldots, u_\sigma](x) \right| \le \mathscr{L}_\sigma \sum_{j=0}^{\sigma} \left| y_j - u_j \right|, \quad y_j, u_j \in G, \tag{3}$$

where $\mathscr{L}_\sigma > 0$ is independent of x. We also assume for simplicity that

$$f_{\alpha_0,\ldots,\alpha_\sigma}[t,y] := f\left[x, y(x), {}^c\mathscr{D}_0^{\alpha_1}(y)(x), \ldots, {}^c\mathscr{D}_0^{\alpha_\sigma}(y)(x)\right]. \tag{4}$$

The existence and uniqueness of L_1 solution of the multiorder fractional differential equation with the Riemann–Liouville and Caputo fractional derivatives under the assumption that $f(x,t) \in L_1[0,1]$ satisfies the Lipschitz condition with respect to the second variable are investigated by Kilbas et al. [1]. The previous investigation is based on converting equation (2) into the equivalent Volterra integral equation and then solving it. But in this study, we solve the problem directly.

There exist some numerical methods that solve the desired problem. Laksetani et al. [2] introduced an operational method using B-spline functions to solve the multiorder fractional differential equation

$$F\left(u(x), {}^cD_0^{\beta_1}, \ldots, {}^cD_0^{\beta_m}\right) = g(x), \quad \beta_i \in \mathbb{R}. \tag{5}$$

In this paper, the operational matrix of the Caputo fractional derivative has been constructed directly, and then using the collocation method, the problem is solved. In [3], the authors applied the collocation method to solve the fractional differential equation

$${}^cD^\alpha y(t) = f(t, y(t)), \quad \alpha \in (0,1]. \tag{6}$$

Their investigation is based on the collocation method using the Chebyshev–Gauss–Lobatto collocation points. The main advantage of this method is its superior accuracy. We can point out its exponential convergence too. But solving this problem is not a big challenge because it lacks multiorder fractional derivatives. Dehestani et al. [4] applied the fractional-Lucas optimization method to solve the multidimensional and multiorder fractional differential equation with Caputo fractional derivative. To this end, they used the operational matrix of fractional derivative for Lucas functions and reduced the problem into a linear or nonlinear system. The result shows the accuracy and efficiency of the method. A special type of equation (2) is considered by Bhrawy et al. [5] as

$${}^cD^\alpha y(t) + \gamma y(t) = f(t). \tag{7}$$

To solve this equation, they utilized the Laguerre tau technique. To this end, firstly fractional-order generalized Laguerre functions are introduced and Caputo fractional-order derivative is represented by these bases. In [6], after introducing the fractional-order Legendre functions and the operational matrix of Caputo derivative, the multiorder fractional differential equation is solved. For more details, we refer the readers to [7–10].

The fractional differential equations are applied to model various physical phenomena, such as heat conduction, viscoelasticity, dynamical behavior of quantum particles, and laxation and diffusion problems [11–16].

This paper is organized as follows. In Section 2, we introduce the Müntz–Legendre wavelets, and we construct the operational matrix of fractional integration and Caputo fractional derivative. In Section 3, the pseudospectral method is applied to solve the generalized Cauchy-type problems with Caputo fractional differentiation based on Müntz–Legendre wavelets, and then the error analysis is investigated. Section 4 is devoted to some numerical examples to illustrate the accuracy and efficiency of the proposed method.

2. Müntz–Legendre Wavelets

In the last decade, wavelets have been able to get a special place in numerical analysis and especially in the numerical solution of equations [17–22]. As you know, one of the ways to get wavelets is to use multiresolution analysis (MRA). MRA is a family of nested spaces that satisfies certain circumstances [23], namely,

$$\{0\} \subset \cdots \subset V_{-1} \subset V_0 \subset V_1 \subset \cdots \subset L^2(\Omega), \tag{8}$$

where Ω is a bounded interval or is equal to $\mathbb{R}$.

In this paper, we apply Müntz–Legendre wavelets to solve the multiorder fractional differential equations. To this end, we give a brief introduction to Müntz–Legendre wavelets. Assume that the space V_J ($J \in \mathbb{Z}^+ \cup \{0\}$) is spanned by a set of bases which are called multiscaling functions or mother wavelets, i.e.,

$$V_J = \operatorname{span}\left\{\psi_{J,b}^m : b \in \mathscr{B}, m \in \mathscr{M}\right\}, \tag{9}$$

where $\mathscr{B} := \{0, 1, \ldots, 2^J - 1\}$ and $\mathscr{M} := \{0, 1, \ldots, r-1\}$, $r \in \mathbb{N}$. The parameter r is called the multiplicity parameter, and J is the refinement level. In the following, we introduce the functions $\psi_{J,b}^m$.

Assume that $\lambda_k := k\mu$ where μ is a real constant. Denote by $L_m(x)$ the Müntz–Legendre polynomials [24] which are defined on $\Omega := [0,1]$ as

$$L_m(x) = \sum_{k=0}^{m} l_{k,m} x^{\lambda_k}, \quad x \in \Omega, \tag{10}$$

where the coefficient $l_{k,m}$ is defined by [24]

$$l_{k,m} := \frac{\prod_{i=0}^{m-1}(\lambda_k + \lambda_i + 1)}{\prod_{i=0, i\neq k}^{m}(\lambda_k - \lambda_i)}. \tag{11}$$

Among the properties of these functions, we can mention their orthogonality. These polynomials form an orthogonal system that satisfies the following relation:

$$\langle L_{m'}(x), L_m(x)\rangle = \int_0^1 L_{m'}(x) L_m(x) \mathrm{d}x = \frac{\delta_{m',m}}{2\lambda_m + 1}, \quad m \geq m', \tag{12}$$

where $\delta_{m',m}$ is used for the Kronecker symbol and is given by

$$\delta_{m',m} := \begin{cases} 1, & m = m', \\ 0, & m \geq m'. \end{cases} \tag{13}$$

Now we are ready to introduce the functions $\psi_{J,b}^m$. The Müntz–Legendre wavelets on the interval $[0,1]$ are defined as follows [24]:

$$\psi_{J,b}^{m} = \begin{cases} 2^{J/2}\sqrt{2\lambda_m + 1}\, L_m\left(2^J x - b\right), & \dfrac{b}{2^J} \le x \le \dfrac{b+1}{2^J}, \\ 0, & \text{otherwise.} \end{cases} \tag{14}$$

Let $\mathscr{P}_J$ be an operator that projects any function $f(x) \in L^2[0,1]$ onto the subspace V_J as follows:

$$f(x) \approx \mathscr{P}_J(f)(x) = \sum_{b=0}^{2^J-1}\sum_{m=0}^{r-1} f_{b,m}\psi_{J,b}^{m}(x), \tag{15}$$

where the coefficients $\{f_{b,m}\}$ are evaluated by

$$f_{b,m} = \langle f, \psi_{J,b}^{m}\rangle = \int_0^1 f(x)\psi_{J,b}^{m}(x)\mathrm{d}x. \tag{16}$$

Let F and $\Psi(x)$ be vectors of dimension $N = 2^J r$ whose $(br + m + 1)$-th element is $f_{b,m}$ and $\psi_{J,b}^{m}(x)$, respectively. Hence, it follows from equation (15) that

$$f(x) \approx \mathscr{P}_J(f)(x) = F^T\Psi(x), \tag{17}$$

where the superscript T is used for the matrix transpose.

It follows from [24] that there are some error estimates in the sense of Sobolev norms.

Lemma 1 (see [24]). *Let $n \ge 0$ and $r > n$. If $f \in H^n[0,1]$, then*

$$\left\|f - \mathscr{P}_J(f)\right\|_{L_2(0,1)} \le c(r-1)^{-n}\left(2^{J-1}\right)^{-n}\left\|f^{(n)}\right\|_{L_2(0,1)}, \tag{18}$$

and for $s \ge 1$, we have

$$\left\|f - \mathscr{P}_J(f)\right\|_{H^s(0,1)} \le c(r-1)^{2s-(1/2)-n}\left(2^{J-1}\right)^{s-n}\left\|f^{(n)}\right\|_{L_2(0,1)}, \tag{19}$$

where $H^n(0,1)$ is the Sobolev space and

$$\|f\|_{H^n(0,1)} = \left(\sum_{j=0}^{n}\left\|f^{(j)}\right\|_{L_2(0,1)}^2\right)^{1/2}. \tag{20}$$

2.1. Representation of the Caputo Fractional Derivative Operator in Müntz–Legendre Wavelets. Recall that the Riemann–Liouville fractional integral operator $\mathscr{I}_0^{\alpha}$ $(\alpha \in \mathbb{R}^+)$ is determined by

$$\mathscr{I}_a^{\alpha} f(x) := \frac{1}{\Gamma(\alpha)}\int_a^x (x-s)^{\alpha-1} f(s)\mathrm{d}s, \quad x \in [a,b]. \tag{21}$$

Note that if $f \in L_1[a,b]$, then the function $\mathscr{I}_a^{\alpha} f \in L_1[a,b]$. We know that there is an operator that satisfies the relation

$${}^{RL}\mathscr{D}_a^{\alpha} = \mathscr{D}^n\mathscr{I}_a^{n-\alpha}, \tag{22}$$

where $\mathscr{D} := (\mathrm{d}/\mathrm{d}x)$ and ${}^{RL}\mathscr{D}_a^{\alpha}$ is called the Riemann–Liouville fractional derivative operator. There is also another fractional derivative operator that satisfies the relation ${}^{c}\mathscr{D}_a^{\alpha} f(x) := \mathscr{I}_a^{n-\alpha}\mathscr{D}^n(f)(x)$ and is called the Caputo fractional derivative.

In this section, we would like to represent the Caputo fractional derivative operator in Müntz–Legendre wavelets. To this end, we first construct the operational matrix for fractional integral operator $\mathscr{I}_0^{\alpha}$. Then, applying the operational matrix of derivative D for Müntz–Legendre wavelets [25] and relation ${}^{c}\mathscr{D}_a^{\alpha} f(x) := \mathscr{I}_a^{n-\alpha}\mathscr{D}^n(f)(x)$, we can find the operational matrix of fractional derivative for Müntz–Legendre wavelets.

Applying the projection operator $\mathscr{P}$, the fractional integral operator $\mathscr{I}_0^{\alpha}$ acting on the vector function $\Psi(x)$ can be approximated by

$$\mathscr{P}\left(\mathscr{I}_0^{\alpha}\right)(\Psi(x)) = I_{\alpha}(x)\Psi(x), \quad \alpha \in (0,1), \tag{23}$$

where $I_{\alpha}(x)$ is the operational matrix of integral for the Müntz–Legendre wavelets.

To facilitate the evaluation of the operational matrix elements of fractional integration for the Müntz–Legendre wavelets, it is necessary to introduce the piecewise fractional-order Taylor functions. For a fixed $J \in \mathbb{Z}^+ \cup \{0\}$, these functions are constructed as

$$\phi_{J,b}^{m} = \begin{cases} t^{\lambda_m}, & \dfrac{b}{2^J} \le x \le \dfrac{b+1}{2^J}, \\ 0, & \text{otherwise,} \end{cases} \tag{24}$$

$$b \in \mathscr{B}, m \in \mathscr{M}.$$

Let $\Phi(x)$ be a vector of dimension N whose $(br + m + 1)$-th element is $\phi_{J,b}^{m}(x)$.

To derive matrix $I_{\alpha}(x)$, we first introduce a matrix of dimension $N \times N$ that is used to transfer the Müntz–Legendre wavelets $\Psi(x)$ to the piecewise fractional-order Taylor functions $\Phi(x)$. Assume that there is a matrix of dimension $N \times N$ such that

$$\Psi(x) = T^{-1}\Phi(x), \tag{25}$$

where T_J^{-1} stands for the inverse of the matrix T. The matrix T is called the transformation matrix whose (i,j)-th element is evaluated by

$$T_{i,j} = \langle \Phi_i(x), \Psi_j(x)\rangle = \int_0^1 \Phi_i(x)\Psi_j(x)\mathrm{d}x, \quad i,j = 1,\ldots,N. \tag{26}$$

Let Λ be a vector of dimension r whose i-th element is x^{λ_i}, and thus it follows from equation (24) that

$$\Phi(x) = [\Lambda,\ldots,\Lambda]^T. \tag{27}$$

It is easy to verify that the Riemann–Liouville fractional integration of the power functions x^{κ} is equal to power functions of the same form, i.e.,

$$\mathscr{I}_0^{\alpha}\left(x^{\kappa}\right) = \frac{\Gamma(\kappa+1)}{\Gamma(\kappa+\alpha+1)}x^{\kappa+\alpha}. \tag{28}$$

This gives rise to find the i-th element of $\mathscr{I}_0^{\alpha}(\Phi)(x)$, via

$$\mathcal{J}_0^\alpha(\Phi_i)(x) = \frac{\Gamma(\lambda_i+1)}{\Gamma(\lambda_i+\alpha+1)} x^{\lambda_i+\alpha}. \tag{29}$$

Thus, there exists a diagonal matrix $I_{\Phi,\alpha}(x)$ of dimension $N \times N$ such that

$$\mathcal{J}_0^\alpha(\Phi)(x) = I_{\Phi,\alpha}(x)\Phi(x). \tag{30}$$

The matrix $I_{\Phi,\alpha}(x)$ elements are obtain as follows:

$$I_{\Phi,\alpha}(x) = \operatorname{diag}\left[I_{T,\alpha}(x), \ldots, I_{T,\alpha}(x)\right], \tag{31}$$

where $I_{T,\alpha}(x) := x^\alpha G\,(\mathcal{J}_0^\alpha(\Lambda)(x) = I_{T,\alpha}(x)\Lambda(x))$ and G is a diagonal matrix of the form

$$(G)_{i,i} = \frac{\Gamma(\lambda_i+1)}{\Gamma(\lambda_i+\alpha+1)}. \tag{32}$$

To derive the operational matrix of integral for the Müntz–Legendre wavelets, it follows from equation (25) that

$$\begin{aligned}\mathcal{P}(\mathcal{J}_0^\alpha)(\Psi(x)) &= \mathcal{P}(\mathcal{J}_0^\alpha)\left(T^{-1}\Phi(x)\right)\\ &= T^{-1}I_{\Phi,\alpha}(x)\Phi(x)\\ &= T^{-1}I_{\Phi,\alpha}(x)T\Psi(x).\end{aligned} \tag{33}$$

This gives rise to

$$I_\alpha(x) := T^{-1}I_{\Phi,\alpha}(x)T. \tag{34}$$

Now using ${}^c\mathcal{D}_a^\alpha := \mathcal{J}_a^{n-\alpha}\mathcal{D}^n$, we can introduce the operational matrix for the Caputo fractional derivative

$$D_\alpha(x) := D^n I_{n-\alpha}(x). \tag{35}$$

3. Pseudospectral Method

To derive the numerical solution of equation (2), the approximate solution can be approximated by Müntz–Legendre wavelets as follows:

$$y \approx \mathcal{P}(y)(x) = Y^T\Psi(x), \tag{36}$$

where Y is a vector of dimension N that should be determined. A similar expression is valid for $F_{\alpha_0,\ldots,\alpha_\sigma}[x, \mathcal{P}(y)(x)] \in C_\gamma([0,1])$ where $C_\gamma([0,1])$ is the space of functions that satisfies $(x-a)^\gamma f(x) \in C([0,1])$ for $0 \le \gamma < 1$.

$$\mathcal{P}\left(f_{\alpha_0,\ldots,\alpha_\sigma}[x, \mathcal{P}(y)(x)]\right)(x) = F^T\Psi(x). \tag{37}$$

To compute the elements of matrix F, let $y_J = \mathcal{P}(y)$; then, using ${}^c\mathcal{D}_a^\alpha := \mathcal{J}_a^{n-\alpha}\mathcal{D}^n$,

$$\begin{aligned}\mathcal{P}\left(f_{\alpha_0,\ldots,\alpha_\sigma}\left[x, y_J(x)\right]\right)(x) &= f\left[x, y_J(x), {}^c\mathcal{D}_a^{\alpha_1}\left(y_J\right)(x), \ldots, {}^c\mathcal{D}_a^{\alpha_\sigma}\left(y_J\right)(x)\right]\\ &= f\left[x, y_J(x), \mathcal{J}_0^{n_1-\alpha_1}\mathcal{D}^{n_1}\left(y_J\right)(x), \ldots, \mathcal{J}_0^{n_\sigma-\alpha_\sigma}\mathcal{D}^{n_\sigma}\left(y_J\right)(x)\right],\\ \mathcal{J}_0^{n_j-\alpha_j}\mathcal{D}^{n_j}\left(y_J\right)(x) &:= Y^T\mathcal{J}_0^{n_j-\alpha_j}\mathcal{D}^{n_j}(\Psi)(x) = Y^T\mathcal{J}_0^{n_j-\alpha_j}\mathcal{D}^{n_j}(\Psi)(x)\\ &= Y^T\mathcal{D}^{n_j}I_{n_j-\alpha_j}(x)\Psi(x), \quad j = 1, \ldots, \sigma.\end{aligned} \tag{38}$$

It follows from equations (36) and (38) that we can compute the residual in approximating equation (2) as follows:

$$r_J(x) = \left(D_\alpha Y^T - F^T\right)(x)\Psi(x). \tag{39}$$

We aim to reduce the residual to zero. One of the available methods is to use the pseudospectral method such that $r_J(x_i) = 0$ where x_i are the collocation points. In this paper, we use the shifted Legendre and Chebyshev polynomial zeros. This gives rise to a system of linear or nonlinear algebraic equations that should be solved to find the unknown coefficients Y. To apply the initial conditions (2), we replace the first n equations of the obtained system of the pseudospectral method with them.

$$\left[r_J(x_i)\right]_\eta := Y^T\mathcal{D}^\eta\Psi(0) - q_\eta, \quad \eta = 0, \ldots, n-1. \tag{40}$$

3.1. Convergence Analysis. It follows from [1] that the fractional integration operators $\mathcal{J}_0^\alpha$ is bounded in $L_p[0,1]$ (see [1] Lemma 1(a))

$$\begin{aligned}\left\|\mathcal{J}_0^\alpha y\right\|_{L_p(0,1)} &\le \mathcal{C}_\alpha\|y\|_{L_p(0,1)},\\ \mathcal{C}_\alpha &= \frac{1}{\Gamma(\alpha+1)}.\end{aligned} \tag{41}$$

Also there is an optimal error estimate in term of error between the Müntz–Legendre polynomials derivative $\mathcal{D}y$ and the exact derivative $\mathcal{P}(\mathcal{D}y)$, via

$$\|\mathcal{D}y - \mathcal{P}(\mathcal{D}y)\|_{L_2(0,1)} \le C_D(r-1)^{1-n}|y|_{H^{n,r-1}(0,1)}, \tag{42}$$

where C_D is a constant and

$$|g|^2_{H^{n,r-1}(0,1)} = \sum_{l=\min\{n,r-1\}}^{r-1}\left\|g^{(l)}(t)\right\|^2_{L^2(0,1)} \tag{43}$$

is a seminorm.

Theorem 1. *Let $n = [-\alpha]$ and $\alpha \in \mathbb{R}_+$. Assume that $f_{\alpha_0,\ldots,\alpha_\sigma}[t, y] \in H^n[0,1]$ and satisfies the Lipschitz condition (3). Also, assume that y and y_J are the exact and the approximate solutions (39) of equation (2), respectively.*

If y is a sufficiently smooth function, then the overall error

$$e(x) = {}^{c}\mathscr{D}_0^{\alpha}(y)(x) - \mathscr{P}\left({}^{c}\mathscr{D}_0^{\alpha}(y)\right)(x) - f_{\alpha_0,\ldots,\alpha_\sigma}[t,y] + \mathscr{P}\left(f_{\alpha_0,\ldots,\alpha_\sigma}\left[t,y_J\right]\right) \tag{44}$$

satisfies

$$\|e(x)\|_{L_2(0,1)} \longrightarrow 0, \quad \text{as } r \longrightarrow \infty, \text{ or } J \longrightarrow \infty. \tag{45}$$

Proof. If $f_{\alpha_0,\ldots,\alpha_\sigma}[t,y] \in H^n[0,1]$, then by Lemma 1, we can write

$$\left\|f_{\alpha_0,\ldots,\alpha_\sigma}\left[t,y_J\right] - \mathscr{P}_J\left(f_{\alpha_0,\ldots,\alpha_\sigma}\left[t,y_J\right]\right)\right\|_{L_2(0,1)} \le c_1(r-1)^{-n}\left(2^{J-1}\right)^{-n}\left\|f^{(n)}_{\alpha_0,\ldots,\alpha_\sigma}\left[t,y_J\right]\right\|_{L_2(0,1)}. \tag{46}$$

Using the Lipschitz conditions (3) and (41), we can write the following bound:

$$\begin{aligned}\left\|f_{\alpha_0,\ldots,\alpha_\sigma}[t,y] - f_{\alpha_0,\ldots,\alpha_\sigma}\left[t,y_J\right]\right\|_{L_2(0,1)} &\le \left|\mathscr{L}_\sigma\right|\left\|\sum_{j=0}^{\sigma} {}^{c}\mathscr{D}_0^{\alpha_j}\left(y-y_J\right)\right\|_{L_2(0,1)} \\ &= \left|\mathscr{L}_\sigma\right|\left\|\sum_{j=0}^{\sigma} \mathscr{I}_0^{n_j-\alpha_j}\mathscr{D}^{n_j}\left(y-y_J\right)\right\|_{L_2(0,1)} \\ &\le \left|\mathscr{L}_\sigma\right|\sum_{j=0}^{\sigma}\mathscr{C}_{n_j-\alpha_j}\left\|\mathscr{D}^{n_j}\left(y-y_J\right)\right\|_{L_2(0,1)}.\end{aligned} \tag{47}$$

Now, applying equation (41) and Theorem 2 [24], we have

$$\begin{aligned}\left\|f_{\alpha_0,\ldots,\alpha_\sigma}[t,y] - f_{\alpha_0,\ldots,\alpha_\sigma}\left[t,y_J\right]\right\|_{L_2(0,1)} &\le \left|\mathscr{L}_\sigma\right|\sum_{j=0}^{\sigma}\mathscr{C}_{n_j-\alpha_j}C_{D^{n_j}}(r-1)^{1-n}\left|y^{\left(n_j-1\right)}\right|_{H^{n,r-1}(0,1)} \\ &\le \left|\mathscr{L}_\sigma\right|\sum_{j=0}^{\sigma}\mathscr{C}_{n_j-\alpha_j}C_{D^{n_j}}(r-1)^{1-n}\left(2^{J-1}\right)^{-n}\left\|y^{\left(n+n_j-1\right)}\right\|_{L_2(0,1)}.\end{aligned} \tag{48}$$

Also, using Lemma 1 and equation (41), we have

$$\begin{aligned}\left\|{}^{c}\mathscr{D}_0^{\alpha}(y)(x) - \mathscr{P}\left({}^{c}\mathscr{D}_0^{\alpha}(y)\right)(x)\right\|_{L_2(0,1)} &\le c_2(r-1)^{-n}\left(2^{J-1}\right)^{-n}\left\|{}^{c}\mathscr{D}_0^{\alpha}y\right\|_{L_2(0,1)} \\ &= \le c_2(r-1)^{-n}\left(2^{J-1}\right)^{-n}\left\|\mathscr{I}_0^{n-\alpha}\mathscr{D}^{n}(y)\right\|_{L_2(0,1)} \\ &\le C_{n-\alpha}c_2(r-1)^{-n}\left(2^{J-1}\right)^{-n}\left\|y^{n}\right\|_{L_2(0,1)}.\end{aligned} \tag{49}$$

Subtracting equation (2) from equation (39), one can write

$$e(x) = {}^{c}\mathscr{D}_0^{\alpha}(y)(x) - \mathscr{P}\left({}^{c}\mathscr{D}_0^{\alpha}(y)\right)(x) - f_{\alpha_0,\ldots,\alpha_\sigma}[t,y] + \mathscr{P}\left(f_{\alpha_0,\ldots,\alpha_\sigma}\left[t,y_J\right]\right) + f_{\alpha_0,\ldots,\alpha_\sigma}\left[t,y_J\right] - f_{\alpha_0,\ldots,\alpha_\sigma}\left[t,y_J\right]. \tag{50}$$

Taking norms from both sides of equation (50) and using equations (46)–(49), we end up with

$$\begin{aligned}\|e(x)\|_{L_2(0,1)} \le & \left\|{}^c\mathscr{D}_0^\alpha(y)(x) - \mathscr{P}\left({}^c\mathscr{D}_0^\alpha(y)\right)(x)\right\|_{L_2(0,1)} + \left\|f_{\alpha_0,\ldots,\alpha_\sigma}[t,y] - f_{\alpha_0,\ldots,\alpha_\sigma}\left[t,y_J\right]\right\|_{L_2(0,1)} \\ & + \left\|f_{\alpha_0,\ldots,\alpha_\sigma}\left[t,y_J\right] - \mathscr{P}\left(f_{\alpha_0,\ldots,\alpha_\sigma}\left[t,y_J\right]\right)\right\|_{L_2(0,1)} \\ \le & C_{n-\alpha}c_2(r-1)^{-n}\left(2^{J-1}\right)^{-n}\left\|y^n\right\|_{L_2(0,1)} \\ & + \left|\mathscr{L}_\sigma\right|\sum_{j=0}^{\sigma}\mathscr{C}_{n_j-\alpha_j}C_{D^{n_j}}(r-1)^{1-n}\left(2^{J-1}\right)^{-n}\left\|y^{\left(n+n_j-1\right)}\right\|_{L_2(0,1)} \\ & + c_1(r-1)^{-n}\left(2^{J-1}\right)^{-n}\left\|f^{(n)}_{\alpha_0,\ldots,\alpha_\sigma}\left[t,y_J\right]\right\|_{L_2(0,1)}.\end{aligned} \tag{51}$$

Suppose that $C_1 := \max\{\mathscr{C}_{n_j-\alpha_j}C_{D^{n_j}}\}$ $(j = 0,\ldots,\sigma)$ and $C := \max\{C_{n-\alpha}c_2, C_1, c_1\}$; then, we can obtain the following from equation (51):

$$\|e(x)\|_{L_2(0,1)} \le C(r-1)^{-n}\left(2^{J-1}\right)^{-n}\left(\left\|y^n\right\|_{L_2(0,1)} + \left|\mathscr{L}_\sigma\right|\sum_{j=0}^{\sigma}\left\|y^{\left(n+n_j-1\right)}\right\|_{L_2(0,1)} + \left\|f^{(n)}_{\alpha_0,\ldots,\alpha_\sigma}\left[t,y_J\right]\right\|_{L_2(0,1)}\right). \tag{52}$$

It is easy to show that $\|e(x)\|_{L_2(0,1)} \longrightarrow 0$ as $r \longrightarrow \infty$ or $J \longrightarrow \infty$. □

4. Numerical Implementation

In this section, we reported the numerical results for some examples to show the accuracy and efficiency of the method. To this end, we have performed all numerical computations in Maple and Matlab simultaneously. Wherever collocation nodes have not been reported, we have used Legendre nodes.

Example 1. Let us dedicate the first example to the following one.

$$\begin{aligned}{}^c\mathscr{D}_0^\alpha(y)(x) + {}^c\mathscr{D}_0^{\alpha_1}(y)(x) + [y(x)]^2 &= \left(x^2 - x\right)^2 + \frac{2x^{2-\alpha}}{\Gamma(3-\alpha)} + \frac{2x^{2-\alpha_1}}{\Gamma(3-\alpha_1)} - \frac{2x^{1-\alpha_1}}{\Gamma(2-\alpha_1)}, \\ y(0) = 0, y'(0) &= -1.\end{aligned} \tag{53}$$

The exact solution is reported in [4] as follows:

$$y(x) = x^2 - x. \tag{54}$$

To show the ability and efficiency of the proposed method, Tables 1 and 2 are reported. The absolute error for proposed method is compared with the fractional-Lucas optimization method [4] and Chebyshev wavelet method [26] in Table 1. The results illustrate that the proposed method is flexible against other methods and gives a better approximation. We show L_2–error, L_∞–error, and CPU time for different values of α and α_1 taking $\mu = 0.5$ in Table 2.

Example 2. The second example is dedicated to the following equation:

$$\begin{aligned}{}^c\mathscr{D}_0^\alpha(y)(x) + [y(x)]^2 &= x + \left(\frac{x^{\alpha+1}}{\Gamma(\alpha+2)}\right)^2, \\ y(0) = 0 y'(0) &= -1.\end{aligned} \tag{55}$$

The exact solution is reported in [5] as follows:

$$y(x) = \frac{x^{\alpha+1}}{\Gamma(\alpha+2)}, \quad 0 < \alpha \le 2. \tag{56}$$

In Table 3, we compare the maximum of absolute value error of our method with fractional-order generalized Laguerre functions (FGLFs) [5]. In this example, we set the value of μ equal to α. L^2–errors taking different vales for r and absolute value of error for different values of α are plotted in Figure 1.

Table 1: Comparison of the absolute error for Example 1.

x	Our method: Chebyshev nodes ($r = 5, J = 1, \mu = 0.5$)	Our method: Legendre nodes ($r = 5, J = 1, \mu = 0.5$)	Fractional-Lucas optimization method [4] ($\mathfrak{m} = 2$)	Chebyshev wavelet method [26] ($M = 6, k = 4$)
0.1	1.3620×10^{-49}	2.0240×10^{-49}	2.8022×10^{-17}	8.8658×10^{-6}
0.2	6.2780×10^{-49}	5.2750×10^{-49}	1.1208×10^{-14}	8.5359×10^{-6}
0.3	1.3344×10^{-48}	9.4020×10^{-49}	2.5219×10^{-14}	8.1318×10^{-6}
0.4	2.1909×10^{-48}	1.4212×10^{-48}	4.4835×10^{-14}	7.6897×10^{-6}
0.5	3.1020×10^{-48}	1.9086×10^{-48}	7.0055×10^{-14}	7.1843×10^{-6}
0.6	4.0646×10^{-48}	2.4139×10^{-48}	1.0087×10^{-13}	6.7665×10^{-6}
0.7	4.9381×10^{-48}	2.8187×10^{-48}	1.3730×10^{-13}	6.3058×10^{-6}
0.8	5.8985×10^{-48}	3.3089×10^{-48}	1.7934×10^{-13}	5.8497×10^{-6}
0.9	6.8068×10^{-48}	3.7540×10^{-48}	2.2697×10^{-13}	5.4018×10^{-6}

Table 2: L_2–error, L_∞–error, and CPU time taking different values for α and α_1 for Example 1.

	$\alpha = 1.75$			$\alpha = 1.80$		
	$\alpha_1 = 0.2$	$\alpha_1 = 0.5$	$\alpha_1 = 0.8$	$\alpha_1 = 0.2$	$\alpha_1 = 0.5$	$\alpha_1 = 0.8$
L_2–error	5.52×10^{-49}	2.41×10^{-48}	2.76×10^{-48}	1.35×10^{-47}	1.16×10^{-47}	1.33×10^{-47}
L_∞–error	8.92×10^{-49}	3.66×10^{-48}	4.24×10^{-48}	2.10×10^{-47}	1.78×10^{-47}	2.07×10^{-47}
CPU time	0.906	0.969	1.031	0.953	0.985	0.968

Table 3: The maximum of absolute value error taking different values for r and α for Example 2.

	$r = 8$			$r = 12$		
	$\alpha = 0.5$	$\alpha = 0.7$	$\alpha = 0.8$	$\alpha = 0.5$	$\alpha = 0.7$	$\alpha = 0.8$
Our method	8.31×10^{-46}	9.72×10^{-5}	1.56×10^{-4}	7.55×10^{-46}	1.89×10^{-5}	3.32×10^{-5}
FGLFs [5]	1.42×10^{-14}	4.28×10^{-3}	6.08×10^{-3}	1.42×10^{-14}	1.74×10^{-3}	1.87×10^{-3}

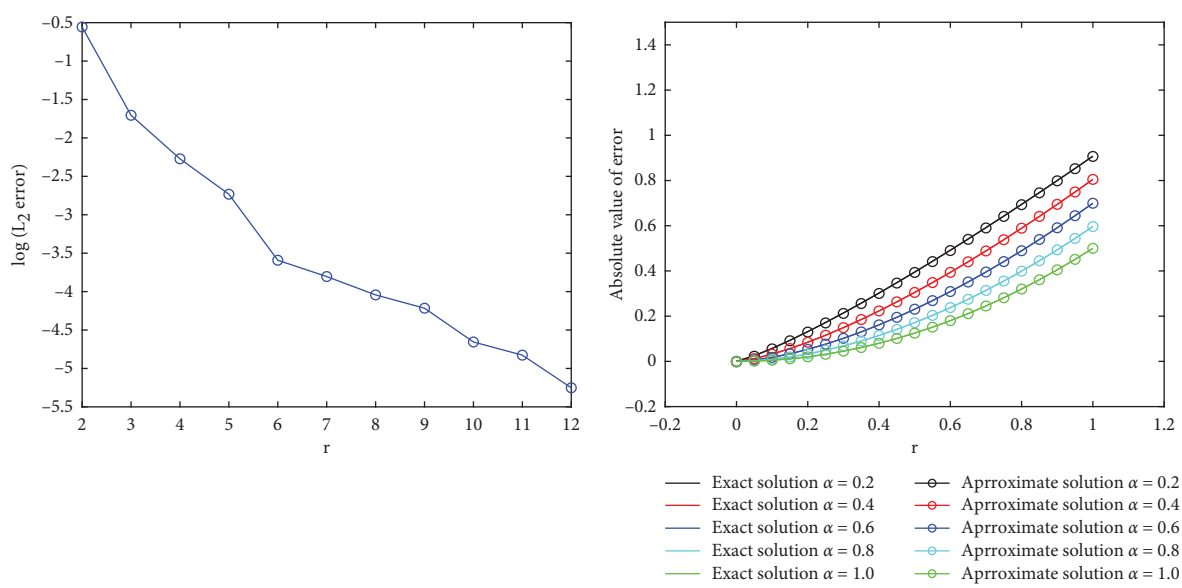

(a) (b)

Figure 1: Plot of L^2–errors taking different vales for r (a) and absolute value of error for different values of α (b) for Example 2.

Example 3. We dedicated this example to the Bagley–Torvik equation [27, 28]:

$$\mathscr{D}^2 y(x) + {}^c\mathscr{D}_0^{3/2}(y)(x) + y(x) = 1 + x, \quad y(0) = 1, y'(0) = 1. \tag{57}$$

The exact solution can be found in [27, 28], which is $y(x) = x + 1$.

In Figure 2, we plot the exact solution along with the approximate solution. Also, in this figure, the absolute value of error is reported for $\mu = 0.5$, $r = 3$, and $J = 1$. In Table 4, we compare the proposed method with the Bessel

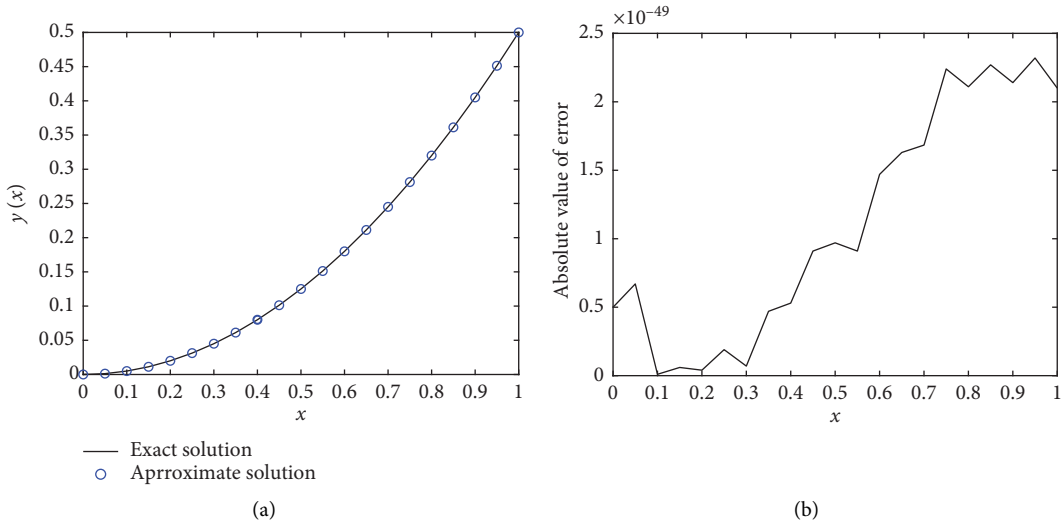

(a) (b)

Figure 2: Plot of the exact solution along with the approximate solution (a) and absolute value of error (b) for Example 3.

Table 4: Comparison of the absolute error for Example 3.

	Our method	Bessel collocation method [28]	
	$r = 3$	$N = 6$	$N = 9$
0.1	1.0×10^{-51}	6.1919×10^{-16}	9.3742×10^{-16}
0.2	4.0×10^{-51}	1.0292×10^{-15}	3.9634×10^{-15}
0.3	7.0×10^{-51}	1.4779×10^{-15}	4.2834×10^{-15}
0.4	5.3×10^{-50}	1.9697×10^{-15}	3.2975×10^{-15}
0.5	9.7×10^{-50}	2.4941×10^{-15}	2.0455×10^{-15}
0.6	1.47×10^{-49}	3.0365×10^{-15}	1.0277×10^{-15}
0.7	1.68×10^{-49}	3.5805×10^{-15}	3.4773×10^{-16}
0.8	2.11×10^{-49}	4.1090×10^{-15}	6.9289×10^{-17}
0.9	2.14×10^{-49}	4.6047×10^{-15}	2.3947×10^{-16}
1.0	2.10×10^{-49}	5.0500×10^{-15}	1.2006×10^{-16}

collocation method [28]. We observe that our method gives a better result than [28]. In this example, we put $\mu = 0.5$.

5. Conclusion

In this paper, we apply the pseudospectral method based on Müntz–Legendre wavelets to solve the multiorder fractional differential equations with Caputo fractional derivative. To this end, we represent the Caputo fractional derivative operator in the Müntz–Legendre wavelets. The results illustrate that by selecting the proper value for μ, the proposed method gives better results than others. The most important advantage of this method over other methods is its flexibility and ease of use. In most cases, the approximate solution is very close to the exact solution and we can almost say that the exact solution is obtained.

Data Availability

The data used to support this study are included within this article.

Conflicts of Interest

The authors declare that they have no conflicts of interest.

Authors' Contributions

All authors contributed equally and significantly in writing this paper. All authors read and approved the final manuscript.

Acknowledgments

The authors extend their appreciation to the Deanship of Scientific Research at King Saud University for funding this work through Research Group no. RG-1441-326.

References

[1] A. Kilbas, H. M. Srivastava, and J. J. Trujillo, *Theory and Applications of Fractional Differential Equations*, Elsevier, Amsterdam, Netherlands, 2006.

[2] M. Lakestani, M. Dehghan, and S. Irandoust-Pakchin, "The construction of operational matrix of fractional derivatives using B-spline functions," *Communications in Nonlinear Science and Numerical Simulation*, vol. 17, no. 3, pp. 1149–1162, 2012.

[3] S. Esmaeili, M. Luchko, and Y. Luchkob, "Numerical solution of fractional differential equations with a collocation method based on Müntz polynomials," *Computers & Mathematics with Applications*, vol. 62, no. 3, pp. 918–929, 2011.

[4] H. Dehestani, Y. Ordokhani, and M. Razzaghi, "Fractional-lucas optimization method for evaluating the approximate solution of the multi-dimensional fractional differential equations," *Engineering with Computers*, pp. 1–17, 2020.

[5] A. Bhrawy, Y. Alhamed, D. Baleanu, and A. Al-Zahrani, "New spectral techniques for systems of fractional differential equations using fractional-order generalized Laguerre orthogonal functions," *Fractional Calculus and Applied Analysis*, vol. 17, no. 4, pp. 1137–1157, 2014.

[6] S. Kazem, S. Abbasbandy, and S. Kumar, "Fractional-order Legendre functions for solving fractional-order differential equations," *Applied Mathematical Modelling*, vol. 37, no. 7, pp. 5498–5510, 2013.

[7] I. Hashim, O. Abdulaziz, and S. Momani, "Homotopy analysis method for fractional IVPs," *Communications in Nonlinear Science and Numerical Simulation*, vol. 14, no. 3, pp. 674–684, 2009.

[8] P. Kumar and O. P. Agrawal, "An approximate method for numerical solution of fractional differential equations," *Signal Processing*, vol. 86, no. 10, pp. 2602–2610, 2006.

[9] Z. Odibat and S. Momani, "An algorithm for the numerical solution of differential equations of fractional order," *Journal of Applied Mathematics and Informatics*, vol. 26, pp. 15–27, 2008.

[10] A. Saadatmandi and M. Dehghan, "A new operational matrix for solving fractional-order differential equations," *Computers & Mathematics with Applications*, vol. 59, no. 3, pp. 1326–1336, 2010.

[11] F. Ben Adda and J. Cresson, "Fractional differential equations and the Schrödinger equation," *Applied Mathematics and Computation*, vol. 161, no. 1, pp. 323–345, 2005.

[12] J. F. Douglas, "Some applications of fractional calculus to polymer science," *Advances in Chemical Physics*, vol. 102, pp. 121–191, John Wiley & Sons, Inc, Hoboken, NJ, USA, 2007.

[13] M. Inc, M. N. Khan, I. Ahmad, S.-W. Yao, H. Ahmad, and P. Thounthong, "Analysing time-fractional exotic options via efficient local meshless method," *Results in Physics*, vol. 19, Article ID 103385, 2020.

[14] J.-F. Li, I. Ahmad, H. Ahmad et al., "Numerical solution of two-term time-fractional PDE models arising in mathematical physics using local meshless method," *Open Physics*, vol. 18, no. 1, pp. 1063–1072, 2020.

[15] S. Qureshi, A. Yusuf, A. A. Shaikh, and M. Inc, "Transmission dynamics of varicella zoster virus modeled by classical and novel fractional operators using real statistical data," *Physica A: Statistical Mechanics and its Applications*, vol. 534, Article ID 122149, 2019.

[16] L. Zada, R. Nawaz, M. Ayaz, H. Ahmad, H. Alrabaiah, and Y. M. Chu, "New algorithm for the approximate solution of generalized seventh order Korteweg-Devries equation arising in shallow water waves," *Results in Physics*, vol. 20, Article ID 103744, 2021.

[17] B. K. Alpert, "A class of bases in L^2 for the sparse representation of integral operators," *SIAM Journal on Mathematical Analysis*, vol. 24, no. 1, pp. 246–262, 1993.

[18] B. Alpert, G. Beylkin, R. Coifman, and V. Rokhlin, "Wavelet-like bases for the fast solution of second-kind integral equations," *SIAM Journal on Scientific Computing*, vol. 14, no. 1, pp. 159–184, 1993.

[19] B. Alpert, G. Beylkin, D. Gines, and L. Vozovoi, "Adaptive solution of partial differential equations in multiwavelet bases," *Journal of Computational Physics*, vol. 182, no. 1, pp. 149–190, 2002.

[20] B. N. Saray, "Abel's integral operator: sparse representation based on multiwavelets," *Bit Numerical Mathematics*, vol. 61, no. 1, 2021.

[21] M. Shahriari, B. N. Saray, M. Lakestani, and J. Manafian, "Numerical treatment of the Benjamin-Bona-Mahony equation using Alpert multiwavelets," *The European Physical Journal Plus*, vol. 133, no. 5, pp. 1–12, 2018.

[22] S. H. Seyedi, B. Nemati Saray, and A. Ramazani, "On the multiscale simulation of squeezing nanofluid flow by a highprecision scheme," *Powder Technology*, vol. 340, pp. 264–273, 2018.

[23] S. G. Mallat, *A Wavelet Tour of Signal Processing*, Academic Press, Cambridge, MA, USA, 1999.

[24] P. Rahimkhani, Y. Ordokhani, and E. Babolian, "Müntz-Legendre wavelet operational matrix of fractional-order integration and its applications for solving the fractional pantograph differential equations," *Numerical Algorithms*, vol. 77, no. 4, pp. 1283–1305, 2018.

[25] S. Sabermahani and Y. Ordokhani, "A new operational matrix of Müntz-Legendre polynomials and Petrov-Galerkin method for solving fractional Volterra-Fredholm integrodifferential equations," *Computational Methods for Differential Equations*, vol. 8, no. 3, pp. 408–423, 2020.

[26] L. Yuanlu, "Solving a nonlinear fractional differential equation using Chebyshev wavelets," *Communications in Nonlinear Science and Numerical Simulation*, vol. 15, no. 9, pp. 2284–2292, 2010.

[27] V. S. Krishnasamy and M. Razzaghi, "The numerical solution of the bagley–torvik equation with fractional taylor method," *Journal of Computational and Nonlinear Dynamics*, vol. 11, no. 5, Article ID 051010, 2016.

[28] S. Yüzbaşi, "Numerical solution of the Bagley-Torvik equation by the bessel collocation method," *Mathematical Methods in Applied Sciences*, vol. 36, no. 3, pp. 300–312, 2013.

Hindawi
Complexity
Volume 2021, Article ID 9921642, 11 pages
https://doi.org/10.1155/2021/9921642

Research Article

An Analytical Approach to Study the Blood Flow over a Nonlinear Tapering Stenosed Artery in Flow of Carreau Fluid Model

Riaz Ahmad,[1] Asma Farooqi,[1] Rashada Farooqi,[2] Nawaf N. Hamadneh,[3] Md Fayz-Al-Asad,[4] Ilyas Khan,[5] Muhammad Sajid,[6] Ghulam Bary,[1] and Muhammad Farooq Saleem Khan[7,8]

[1]*Faculty of Science, Yibin University, Yibin 644000, Sichuan, China*
[2]*Wah Medical College POF Hospital, Wah Cantt 47040, Pakistan*
[3]*Department of Basic Sciences, College of Science and Theoretical Studies, Saudi Electronic University, Riyadh 11673, Saudi Arabia*
[4]*Department of Mathematics, Bangladesh University of Engineering and Technology, Dhaka 1000, Bangladesh*
[5]*Department of Mathematics, College of Science Al-Zulfi, Majmaah University, Al-Majmaah, Majmaah 11952, Saudi Arabia*
[6]*Faculty of Materials and Chemical Engineering, Yibin University, Yibin 644000, Sichuan, China*
[7]*Faculty of International Applied Technology, Yibin University, Yibin 644000, Sichuan, China*
[8]*School of Environmental Science and Technology, Tsinghua University, Haidian, Beijing, China*

Correspondence should be addressed to Riaz Ahmad; riazgill2007@gmail.com, Md Fayz-Al-Asad; fayzmath.buet@gmail.com, and Ilyas Khan; i.said@mu.edu.sa

Received 15 March 2021; Accepted 18 July 2021; Published 29 July 2021

Academic Editor: Dan Selisteanu

The current study provides an analytical approach to analyze the blood flow through a stenosed artery by using the Carreau fluid model. The flow governing equations are derived under the consideration of mild stenosis. Mathematical analysis has been carried out by considering the blood as non-Newtonian nature. Then, the analytical solution has been investigated by using the regular perturbation technique. The solutions obtained by this perturbation are up to the second-order in dimensionless Weissenberg number (We). The performed computations of various parameter values such as velocity, wall shear stress, shear stress, and resistance impedance at the stenotic throat are discussed in detail for different values of Weissenberg number (We). The obtained results demonstrate that for shear-thinning fluid, the fluid velocity increases with the increasing parameter m while opposite behavior is observed with the increase in We. Hence, the presented numerical analysis reveals many aspects of the flow by considering the blood as a non-Newtonian Carreau fluid model, and the presented model can be equally applicable to other bio-mathematical studies.

1. Introduction

The study of artery constriction due to the development of stenosis has attained prime importance in fluid dynamics [1–4]. The blood flow in the vessels is a result of the delicate relationship between pressure and area of the fluid. The size of the stenosis determines the flow type. Three types of flow have been studied: mild stenosis as the flow is laminar, moderate stenosis as the flow is a combination of turbulent and laminar, and thirdly the flow depicts turbulent nature when the size of the stenosis is increased. The characteristics of the blood flow depend on the shape and size of the stenosis. Many researchers have analyzed this biomechanical aspect of the flow theoretically and experimentally in recent years. Tang et al. [5] propounded that when the blood pressure is low, stenotic vessels get collapsed and the perfusion of the area beyond stenosis is highly compromised leading to ischemia/infarct. Applications of micropolar fluids in biomedical sciences have received attention for blood flow in arteries [6–8].

In the literature, numerous analytical studies related to blood flow through stenosed arteries have been extensively performed [9–13]. In most of these studies, the flow is considered as laminar with mild stenosis [14]. Considerable work has been done for non-Newtonian fluid models. The Carreau fluid model is one of the generalized Newtonian fluid models which is also considered as a viscosity model. This model helps us to explain the behavior of fluid flow in high shear regions and modeling blood at narrow arteries with low shear rates. Firstly, this model was presented by Carreau [15] in his molecular network theories. Then, Siska et al. [16] have proposed a procedure for the terminal velocity of nonspherical particles by using Carreau fluid in transient flow regions. Such regions are responsible for the development of stenosis in the arteries that could lead to stroke, nausea, back pain, etc., specifically with regard to malfunction of the cardiovascular structures. Therefore, the study of blood vessels especially in stenotic arteries has also attained importance in the fluid dynamics field [17].

The shear-thinning and shear-thickening processes of the fluid are well explained by the Carreau fluid model [18, 19]. This method is a mixture of power-law and Newtonian fluid models. Chhabra and Uhlherr [20] have analyzed the Carreau viscosity equations for shear-thinning elastic liquids. Theoretical analysis of the Carreau fluid model is studied by Bush and Phan-Thein [21]. Later on, Lee [22] discussed the Carreau generalized Newtonian model for error estimations. Tabakova et al. [23] analyzed the flow dynamics in blood vessels by using the Carreau model. They have studied the oscillatory and steady flows and approximated their numerical solutions. Liu and Liu [24] investigated the quantitative analysis of blood flow in tapered stenosed arteries. Their main concern is the heat and mass transfer effect on the fluid. Irfan et al. [25] gave a numerical analysis of the unsteady Carreau fluid model. The flow of blood in the arteries is highly pulsatile with unequal velocity distribution which is the cause of many cardiovascular diseases [26]. Ismail et al. [9] constructed a mathematical model to study the generalized Newtonian blood flow through a tapered artery. Liu et al. [27] considered the effects of tapering and stenosis over the blood flow. Moreover, a numerous range of blood flow phenomena, such as hemodynamics behavior [28], axisymmetric micropolar model [10], heat and mass transfer effects [29], Eyring–Prandtl fluid model [30], and the micropolar fluid model for composite stenosis behavior [31], have been analyzed comprehensively. Flow of blood-based nanofluids by using the generalized differential quadrature method and other epidemiological models is carried out by many researchers [32–40].

This study aims to investigate the blood flow through a stenosed artery by using the Carreau fluid model. The analytical solution of the governing equations with boundary conditions of the stenotic artery is derived. The perturbation solution is obtained by removing the nonlinearity in the governing equation. Then, the obtained results of the velocity profile, resistance impedance, shear stress, and shear wall stress are shown with rheological parameters of the Carreau fluid model, i.e., We and m. Eventually, the graphical results are presented with different values of parameters of interest.

2. Problem Formulation

The fundamental equations used in the derivation of the governing equations for the problem considered are

$$\frac{\partial u}{\partial r}+\frac{u}{r}+\frac{\partial w}{\partial z}=0, \tag{1}$$

$$\rho\left(u\frac{\partial}{\partial r}+w\frac{\partial}{\partial z}\right)u=-\frac{\partial p}{\partial r}+\frac{1}{r}\frac{\partial}{\partial r}\left(rS_{rr}\right)+\frac{\partial}{\partial z}\left(S_{rz}\right)-\frac{S_{\theta\theta}}{r}, \tag{2}$$

$$\rho\left(u\frac{\partial}{\partial r}+w\frac{\partial}{\partial z}\right)w=-\frac{\partial p}{\partial z}+\frac{1}{r}\frac{\partial}{\partial r}\left(rS_{rz}\right)+\frac{\partial}{\partial z}\left(S_{zz}\right). \tag{3}$$

It is assumed that the properties of blood flowing the cylindrical tube are described by the constitute relation Carreau model given as [41]

$$\mathbf{S}=\mu\left[1+(\Gamma\dot{\gamma})^2\right]^{(m-1)/2}\dot{\gamma}. \tag{4}$$

Assuming $\Gamma\dot{\gamma}\ll 1$, we can write

$$\mathbf{S}=\mu\left[1+\left(\frac{m-1}{2}\right)(\Gamma\dot{\gamma})^2\right]\dot{\gamma}, \tag{5}$$

where Γ is a time constant of the fluid. The geometrical representation of the constricted portion is shown in Figure 1 and defined as

$$\begin{aligned} h(z)&=d(z)\left[1-\eta\left(b^{n-1}(z-1)-(z-a)^n\right)\right], \quad a\le z\le (a+b)\\ &=d(z), \quad \text{otherwise}, \end{aligned} \tag{6}$$

with

$$d(z)=d_0+\xi^* Z. \tag{7}$$

In the above equation, $\xi^*=\tan\phi$ is called the tapering parameter; a is the length of the nonstenotic part, and b is the length of the stenotic section; the radius of the nontapered artery in the nonstenotic section is d_0; and shape parameter is n which defined the constriction shape, $n=2$ gives the stenosis symmetric behavior. The parameter η is written as

$$\eta=\frac{\delta n^{n/(n-1)}}{d_0 b^n(n-1)}, \tag{8}$$

where δ is the maximum height of the stenosis defined as

$$z=a+\frac{b}{\left(1/n^{(n-1)}\right)}. \tag{9}$$

The detailed derivation of the presenting problem is given here

$$\mathbf{V}=[u(r,z),0,w(r,z)]. \tag{10}$$

Thus

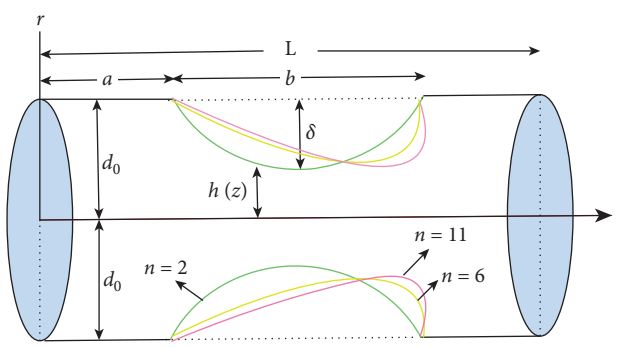

Figure 1: Diagram of axially nonsymmetric stenosis in the artery.

$$\mathbf{L} = \nabla \mathbf{V} = \begin{bmatrix} \frac{\partial u}{\partial r} & 0 & \frac{\partial u}{\partial z} \\ 0 & \frac{u}{r} & 0 \\ \frac{\partial w}{\partial r} & 0 & \frac{\partial w}{\partial z} \end{bmatrix}, \quad \mathbf{L}^T = \begin{bmatrix} \frac{\partial u}{\partial r} & 0 & \frac{\partial w}{\partial r} \\ 0 & \frac{u}{r} & 0 \\ \frac{\partial u}{\partial z} & 0 & \frac{\partial w}{\partial z} \end{bmatrix}. \tag{11}$$

Here we defined the rate of strain tensor as given

$$\dot{\gamma} = \mathbf{L} + \mathbf{L}^T = \begin{bmatrix} u_r & 0 & u_z \\ 0 & \frac{u}{r} & 0 \\ w_r & 0 & w_z \end{bmatrix} + \begin{bmatrix} u_r & 0 & w_r \\ 0 & \frac{u}{r} & 0 \\ u_z & 0 & w_z \end{bmatrix}, \tag{12}$$

$$\text{or } \dot{\gamma} = \begin{bmatrix} 2u_r & 0 & u_z + w_r \\ 0 & 2\frac{u}{r} & 0 \\ w_r + u_z & 0 & 2w_z \end{bmatrix}, \tag{13}$$

now

$$\dot{\gamma} = |\dot{\gamma}| = \sqrt{\frac{1}{2} \sum_i \sum_j \dot{\gamma}_{ij} \dot{\gamma}_{ji}}. \tag{14}$$

Expanding the double sum, we get

$$\dot{\gamma} = \left[\frac{1}{2}\left(\dot{\gamma}_{11}\dot{\gamma}_{11} + \dot{\gamma}_{12}\dot{\gamma}_{12} + \dot{\gamma}_{13}\dot{\gamma}_{13} + \dot{\gamma}_{21}\dot{\gamma}_{21} + \dot{\gamma}_{22}\dot{\gamma}_{22} + \dot{\gamma}_{23}\dot{\gamma}_{23} + \dot{\gamma}_{31}\dot{\gamma}_{31} + \dot{\gamma}_{32}\dot{\gamma}_{32} + \dot{\gamma}_{33}\dot{\gamma}_{33}\right)\right]^{(1/2)}. \tag{15}$$

By choosing the values of the component of $\dot{\gamma}$ from equation (13), we get

$$\dot{\gamma} = \left[\frac{1}{2} 4u_r u_r + (u_z + w_r)(u_z + w_r) + 4\frac{u}{r}\frac{u}{r} + (w_r + u_z)(w_r + u_z) + 4w_z w_z\right]^{(1/2)}. \tag{16}$$

Simplification of the above expression yields

$$\dot{\gamma} = \left[\frac{1}{2}\left(4u_r^2 + 2(u_z + w_r)^2 + 4\frac{u^2}{r^2} + 4w_z^2\right)\right]^{(1/2)}, \tag{17}$$

$$\text{or } \dot{\gamma} = \left[2u_r^2 + (u_z + w_r)^2 + 2\frac{u^2}{r^2} + 2w_z^2\right]^{(1/2)}, \tag{18}$$

by assuming

$$M = (\Gamma\dot{\gamma})^2, \tag{19}$$

we get the following components of the extra stress tensor for the Carreau model:

$$\left.\begin{aligned} S_{rr} &= 2\mu\left[1 + \left(\frac{m-1}{2}\right)M\right]u_r \\ S_{rz} &= \mu\left[1 + \left(\frac{m-1}{2}\right)M\right](u_z + w_z) = S_{zr} \\ S_{\theta\theta} &= 2\mu\left[1 + \left(\frac{m-1}{2}\right)M\right]\frac{u}{r} \end{aligned}\right\}. \tag{20}$$

Applying the mild stenotic conditions, we get

$$\begin{aligned} M &= \Gamma^2 w_r^2, \\ S_{rr} &= 0, \\ S_{\theta\theta} &= 0, \\ S_{zz} &= 0, \\ S_{rz} &= \mu\left[1+\left(\frac{m-1}{2}\right)\Gamma^2\left(w_r\right)^2\right]w_r = S_{zr}. \end{aligned} \tag{21}$$

Given the above results, the governing equations (1)–(3) can be rewritten as

$$\begin{aligned} \frac{\partial p}{\partial r} &= 0, \\ \frac{\partial u}{\partial r}+\frac{u}{r}+\frac{\partial w}{\partial z} &= 0, \\ \frac{\partial p}{\partial z} &= \frac{\mu}{r}\frac{\partial}{\partial r}\left[r\left[\left[1+\left(\frac{m-1}{2}\right)\Gamma^2\left(w_r\right)^2\right]\left(w_r\right)\right]\right]. \end{aligned} \tag{22}$$

Dimensionless variables are defined as

$$\left.\begin{aligned} &\overline{r}=\frac{r}{d_0}, \overline{z}=\frac{z}{b}, \overline{w}=\frac{w}{u_0}, \overline{h}=\frac{h}{d_0}, \overline{u}=\frac{bu}{u_0\delta} \\ &\overline{p}=\frac{d_0^{m+1}p}{u_0^m b\mu}R_e=\frac{\rho d_0^{m+1}}{u_0^{m-2}\mu b}, \overline{S}_{rr}=\frac{bS_{rr}}{u_0^m\mu} \\ &\overline{S}_{rz}=\frac{d_0^m S_{rz}}{u_0^m\mu}, \overline{h}=\frac{h}{d_0}, \overline{S}_{zz}=\frac{bS_{zz}}{u_0^m\mu}, \overline{S}_{\theta\theta}=\frac{bS_{\theta\theta}}{u_0^m\mu} \end{aligned}\right\}, \tag{23}$$

and get the following dimensionless governing equation after dropping the bars for simplicity

$$\frac{\partial p}{\partial r} = 0, \tag{24}$$

$$\frac{\partial u}{\partial r}+\frac{u}{r}+\frac{\partial w}{\partial z} = 0, \tag{25}$$

$$\frac{\partial p}{\partial z} = \frac{1}{r}\frac{\partial}{\partial r}\left[r\left[\frac{\partial w}{\partial r}+\frac{m-1}{2}\mathrm{We}^2\left(\frac{\partial w}{\partial r}\right)^3\right]\right], \tag{26}$$

where $\mathrm{We}=\Gamma u_0/d_0$ is the dimensionless Weissenberg number.

2.1. Boundary Conditions. The following boundary conditions are applied along with geometrical interpretation:

$$w = 0, \quad \text{at } r = h(z), \tag{27}$$

$$\frac{\partial w}{\partial r} = 0, \quad \text{at } r = 0, \tag{28}$$

where $h(z)$ is already defined in equation (6).

3. Employing Perturbation Approach

To get the perturbation solution for the above defined mathematical model, equation (26) can be rearranged as

$$\frac{\partial p}{\partial z} = \frac{1}{r}\frac{\partial}{\partial r}\left[r\left[1+\mathrm{We}^2\frac{(m-1)}{2}\left(\frac{\partial w}{\partial r}\right)^2\right]\frac{\partial w}{\partial r}\right], \tag{29}$$

and by integrating equation (29), we get

$$\frac{r^2}{2}\frac{\partial p}{\partial z}+C_1 = \left[r\left[1+\frac{(m-1)}{2}\mathrm{We}^2\left(\frac{\partial w}{\partial r}\right)^2\right]\frac{\partial w}{\partial r}\right]. \tag{30}$$

The symmetry condition at the center line $r = 0$ yields $C_1 = 0$, and thus we can write equation (30) as

$$\frac{r}{2}\frac{\partial p}{\partial z} = \left[1+\frac{(m-1)}{2}\mathrm{We}^2\left(\frac{\partial w}{\partial r}\right)^2\right]\frac{\partial w}{\partial r}. \tag{31}$$

Due to nonlinearity arising in equation (31), we opt perturbation technique to solve it. We assume

$$w = w_0 + \mathrm{We}^2 w_1 + \cdots, \tag{32}$$

$$p = p_0 + \mathrm{We}^2 p_1 + \cdots, \tag{33}$$

$$F = F_0 + \mathrm{We}^2 F_1 + \cdots. \tag{34}$$

Substituting equations (32) and (33) into equations (27) and (34), we find that

$$\frac{r}{2}\left(\frac{\partial p_0}{\partial z}+\mathrm{We}^2\frac{\partial p_1}{\partial z}\right)=\frac{\partial w_0}{\partial r}+\mathrm{We}^2\left[\frac{\partial w_1}{\partial r}+\frac{m-1}{2}\left(\frac{\partial w_0}{\partial r}\right)^3\right]$$
$$+\mathrm{We}^4\left[\frac{m-1}{2}\left(\frac{\partial w_0}{\partial r}\right)^2\frac{\partial w_1}{\partial r}+2\left(\frac{m-1}{2}\right)\frac{\partial w_1}{\partial r}\left(\frac{\partial w_0}{\partial r}\right)^2\right]$$
$$+\mathrm{We}^6\left[\frac{m-1}{2}\left(\frac{\partial w_1}{\partial r}\right)^4\frac{\partial w_0}{\partial r}+2\left(\frac{m-1}{2}\right)\frac{\partial w_0}{\partial r}\left(\frac{\partial w_1}{\partial r}\right)^2\right]$$
$$+\mathrm{We}^8\frac{m-1}{2}\left(\frac{\partial w_1}{\partial r}\right)^5, \tag{35}$$

$$w_0+\mathrm{We}^2 w_1=0,\quad \text{at } r=h(z). \tag{36}$$

Now comparing the coefficients of various powers of We in equations (35) and (36), the following systems can be obtained.

System of order We^0:

$$\frac{r}{2}\frac{\partial p_0}{\partial z}=\frac{\partial w_0}{\partial r},\qquad w_0=0,\quad \text{at } r=h(z). \tag{37}$$

System of order We^2:

$$\frac{r}{2}\frac{\partial p_0}{\partial z}=\frac{\partial w_1}{\partial r}+\left(\frac{m-1}{2}\right)\left(\frac{\partial w_0}{\partial r}\right)^3,\qquad w_1=0,\quad \text{at } r=h(z). \tag{38}$$

Solving these system results in the following values of w_0 and w_1:

$$w_0=\frac{1}{4}\frac{\partial p_0}{\partial z}\left[r^2-h^2\right], \tag{39}$$

$$w_1=\frac{1}{4}\frac{\partial p_1}{\partial z}\left[r^2-h^2\right]+\frac{(m-1)}{64}\left(\frac{\partial p_0}{\partial z}\right)^3\left[h^4-r^4\right]. \tag{40}$$

The definition of flow rate allows us to write

$$F_0=2\pi\int_0^h r w_0\,\mathrm{d}r, \tag{41}$$

inserting the value w_0 from equation (39) leads to the following expression:

$$\frac{\partial p_0}{\partial z}=-\frac{8}{\pi h^4}F_0, \tag{42}$$

similarly, we can write

$$F_1=2\pi\int_0^h r w_1\,\mathrm{d}r, \tag{43}$$

and thus,

$$\frac{\partial p_1}{\partial z}=-\frac{8F_1}{h^4\pi}-(m-1)\frac{16\times 8}{3\pi^3h^{10}}(F_0)^3. \tag{44}$$

We summarize the results of the perturbation series through an order We^2. By substituting equations (39)–(44), we get

$$w=-\frac{2}{\pi h^4}F_0\left[r^2-h^2\right]+\frac{\mathrm{We}^2}{4}\left[r^2-h^2\right]\left[-\frac{8F_1}{h^4\pi}-(m-1)\frac{128}{3\pi^3h^{10}}(F_0)^3\right]$$
$$-\frac{8\mathrm{We}^2}{\pi^3h^{12}}(m-1)\left[h^4-r^4\right](F_0)^3, \tag{45}$$

$$\frac{\partial p}{\partial z}=-\frac{8}{\pi h^4}F_0-\mathrm{We}^2\left[\frac{8F_1}{h^4\pi}+(m-1)\frac{16\times 8}{3\pi^3h^{10}}(F_0)^3\right]. \tag{46}$$

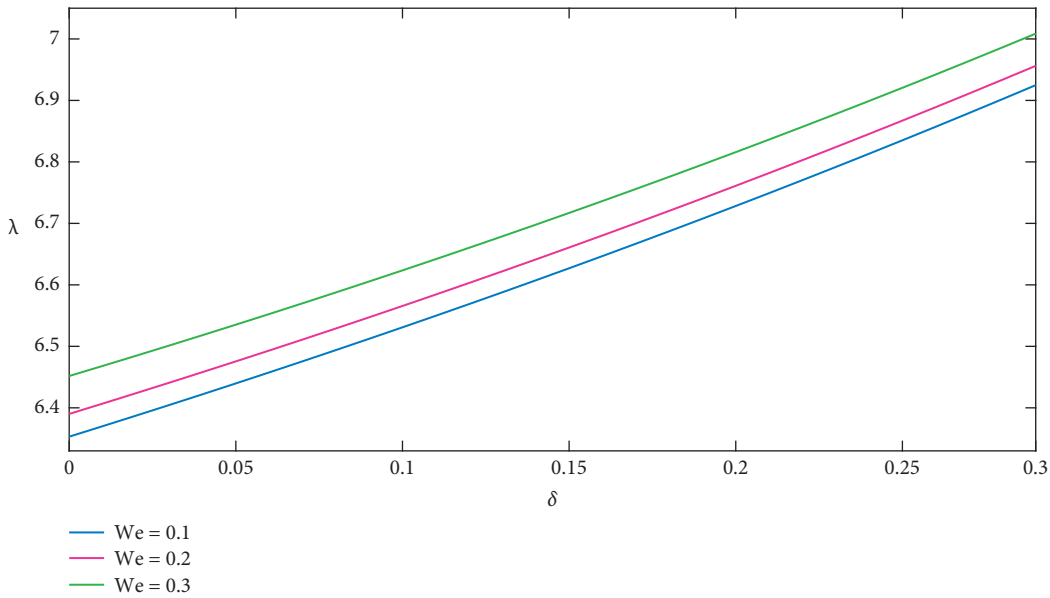

Figure 2: Variation of resistance for the Carreau model for $m = 2, n = 2, L = 1$, and $F = 0.6$.

If we define

$$F^{(2)} = F_0 + \mathrm{We}^2 F_1, \qquad F_0 = F^{(2)} - \mathrm{We}^2 F_1. \tag{47}$$

On substituting these expressions into equations (45) and (46) and retaining only terms up to $O(\mathrm{We}^2)$, we obtain

$$\frac{\partial p}{\partial z} = -\frac{8F}{\pi h^4} - \mathrm{We}^2 (m-1) \frac{16 \times 8}{3\pi^3 h^{10}} F^3, \tag{48}$$

$$w = -\frac{2F}{\pi h^4}\left[r^2 - h^2\right] - \frac{32\mathrm{We}^2}{3\pi^3 h^{10}} F^3 \left[r^2 - h^2\right](m-1) - \frac{8\mathrm{We}^2}{\pi^3 h^{12}} F^3 (m-1)\left[h^4 - r^4\right]. \tag{49}$$

Now the pressure drop is

$$\Delta p = \int_0^{(L/b)} \left(-\frac{\mathrm{d}p}{\mathrm{d}z}\right) \mathrm{d}z, \tag{50}$$

and on substituting the value of $(\mathrm{d}p/\mathrm{d}z)$ from equation (48), we derive

$$\Delta p = \int_0^{(L/b)} \left(\frac{8F}{\pi h^4} + \mathrm{We}^2 (m-1) \frac{128}{3\pi^3 h^{10}} F^3\right) \mathrm{d}z, \tag{51}$$

and similarly, the resistance impedance is defined by the given expression:

$$\lambda = \frac{\Delta p}{F} = \int_0^{(a/b)} R(z)|_{h=1+\xi z} \mathrm{d}z + \int_{(a/b)}^{(a/b)+1} R(z) \mathrm{d}z + \int_{(a/b)+1}^{(L/b)} R(z)|_{h=1+\xi z} \mathrm{d}z, \tag{52}$$

and the nondimensional shear stress for the Carreau law model is given as

$$S_{rz} = \frac{\partial w}{\partial r} + \mathrm{We}^2 \left(\frac{m-1}{2}\right)\left(\frac{\partial w}{\partial r}\right)^3, \tag{53}$$

since

$$w = -\frac{2F}{\pi h^4}\left[r^2 - h^2\right] - \frac{32\mathrm{We}^2}{3\pi^3 h^{10}} F^3 \left[r^2 - h^2\right](m-1) - \frac{8\mathrm{We}^2}{\pi^3 h^{12}} F^3 (m-1)\left[h^4 - r^4\right], \tag{54}$$

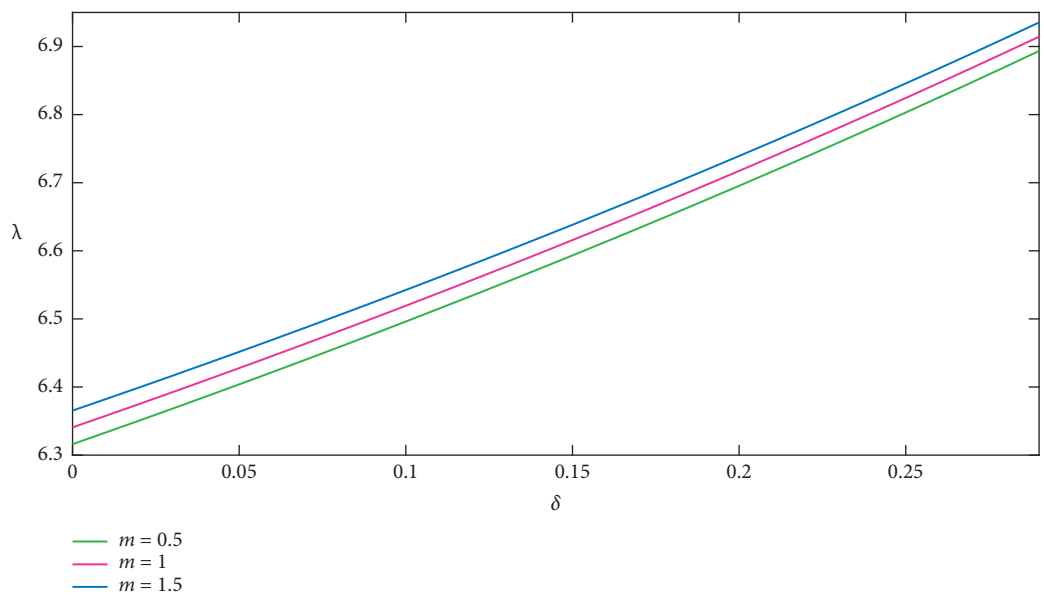

Figure 3: Variation of resistance for the Carreau model for We = 0.2, $n = 2$, $L = 1$, and $F = 0.6$.

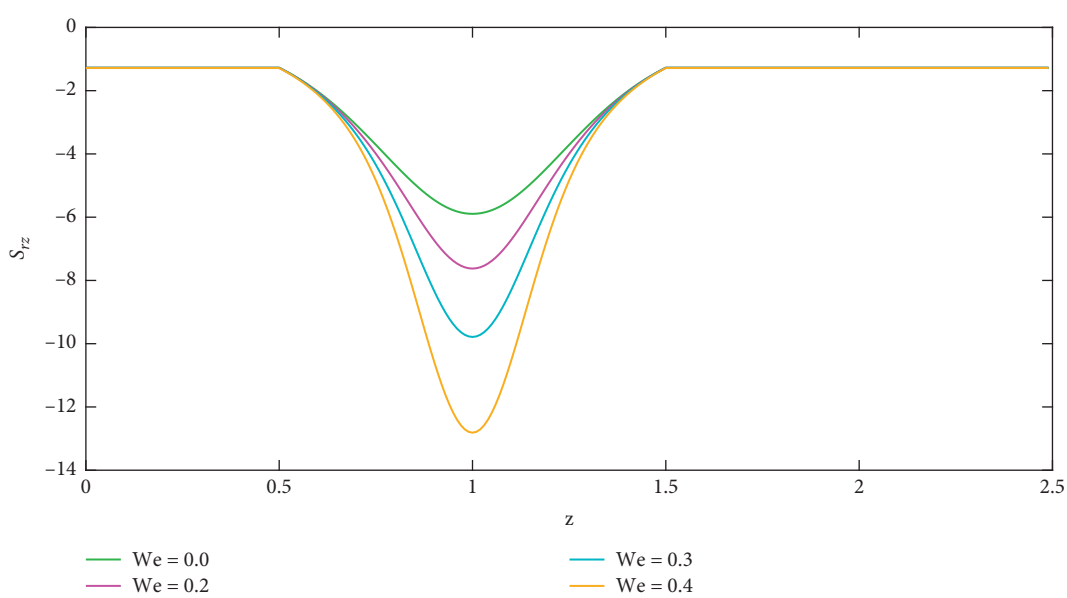

Figure 4: Wall shear stress variation for the Carreau model for $n = 2$, $L = 1$, $F = 1$, and $m = 0.8$.

we obtain

$$\frac{\partial w}{\partial r} = -\frac{4Fr}{\pi h^4} - \frac{64\mathrm{We}^2 F^3 (m-1) r}{3\pi^3 h^{10}} + \frac{32 r^3 \mathrm{We}^2}{\pi^3 h^{12}} F^3 (m-1), \tag{55}$$

and thus equation (53) gives

$$S_{rz} = -\frac{4Fr}{\pi h^4} - \frac{64\mathrm{We}^2 F^3 (m-1) r}{3\pi^3 h^{10}} + \frac{32 r^3 \mathrm{We}^2}{\pi^3 h^{12}} F^3 (m-1) + \mathrm{We}^2 \left(\frac{m-1}{2}\right)\left(-\frac{4Fr}{\pi h^4} - \frac{64\mathrm{We}^2 F^3 (m-1) r}{3\pi^3 h^{10}} + \frac{32 r^3 \mathrm{We}^2}{\pi^3 h^{12}} F^3 (m-1)\right)^3. \tag{56}$$

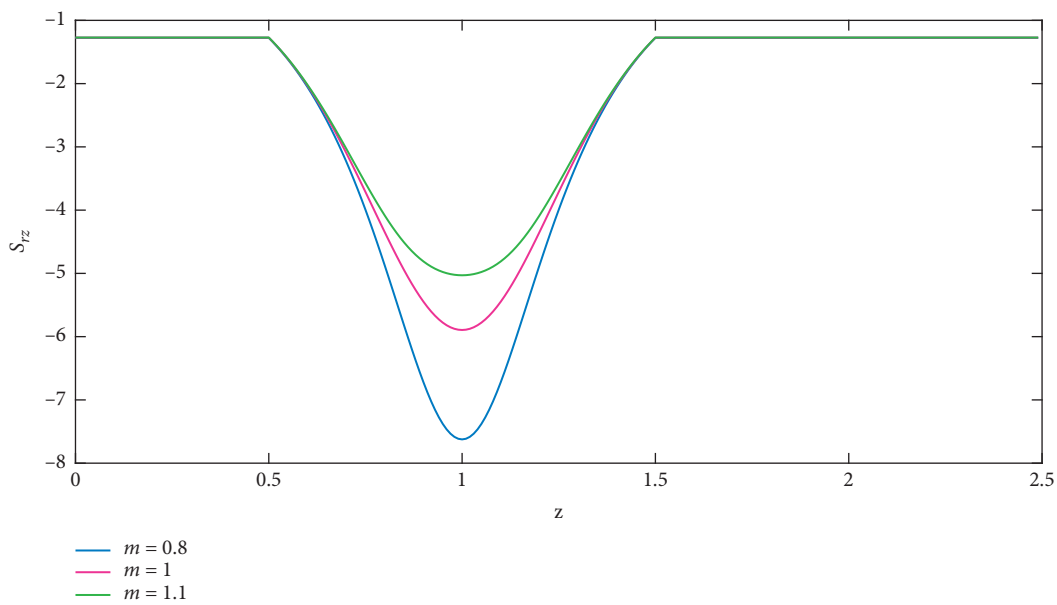

Figure 5: Wall shear stress variation for the Carreau model for $n = 2, L = 1, F = 1$, and $\mathrm{We} = 0.2$.

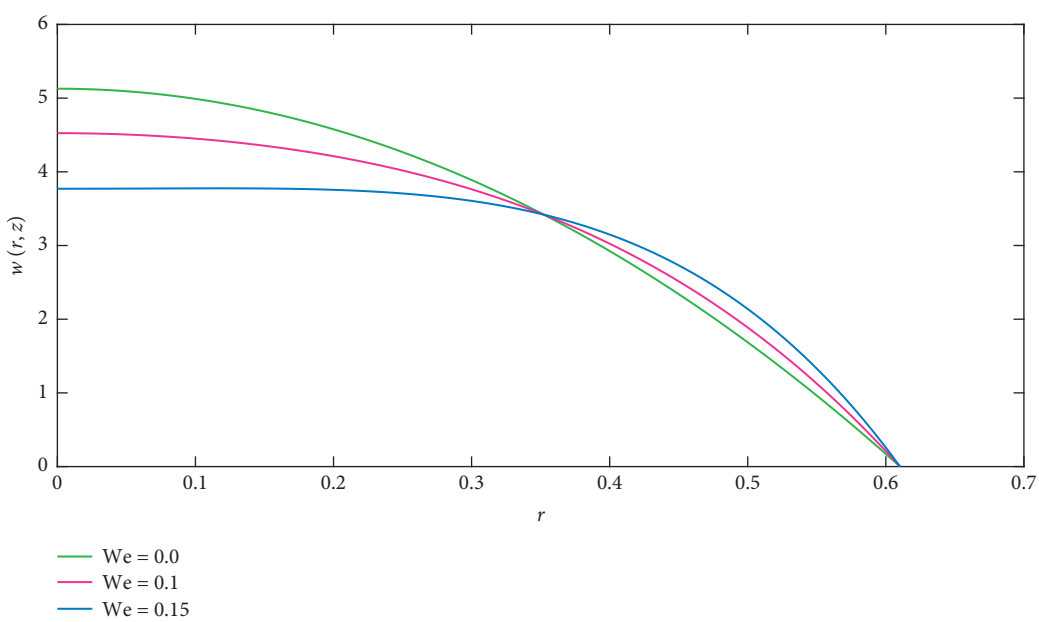

Figure 6: Velocity variation for the Carreau model for $n = 2, L = 1, F = 3$, and $m = 0.5$.

Finally, at maximum height, i.e., $h = 1 - \delta$, the wall shear stress of the stenosis can be written as

$$\tau_s = S_{rz}|_{h=1-\delta} = \frac{4}{\pi(1-\delta)^3}\left[-F - \frac{16\mathrm{We}^2}{3\pi^2(1-\delta)^6}(m-1)F^3 + \frac{8\mathrm{We}^2(m-1)}{\pi^2(1-\delta)^8}F^3\right]. \tag{57}$$

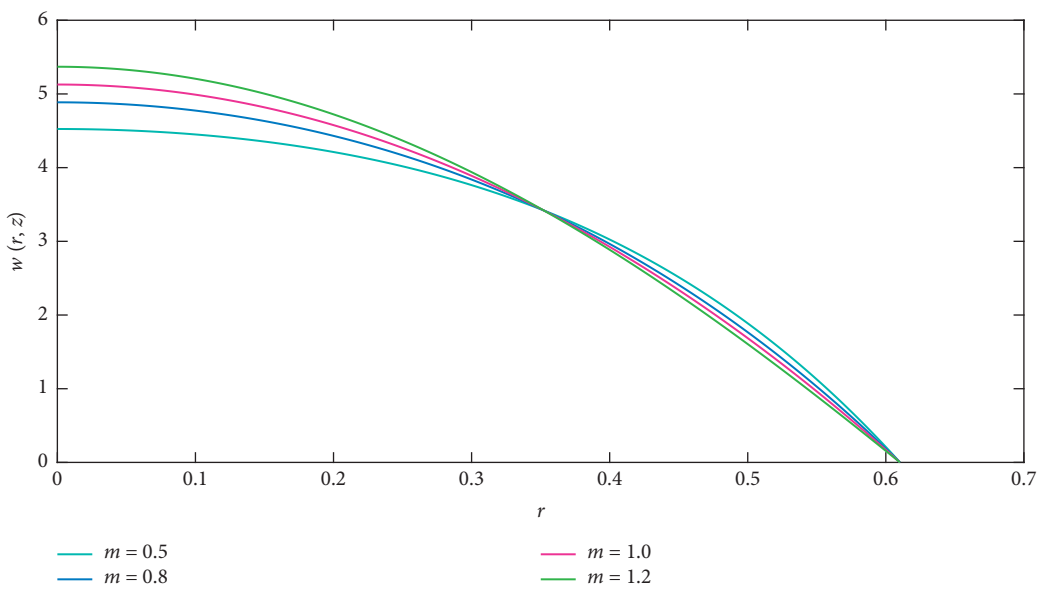

Figure 7: Velocity variation for the Carreau model for $n = 3, L = 1, F = 3$, and We = 0.1.

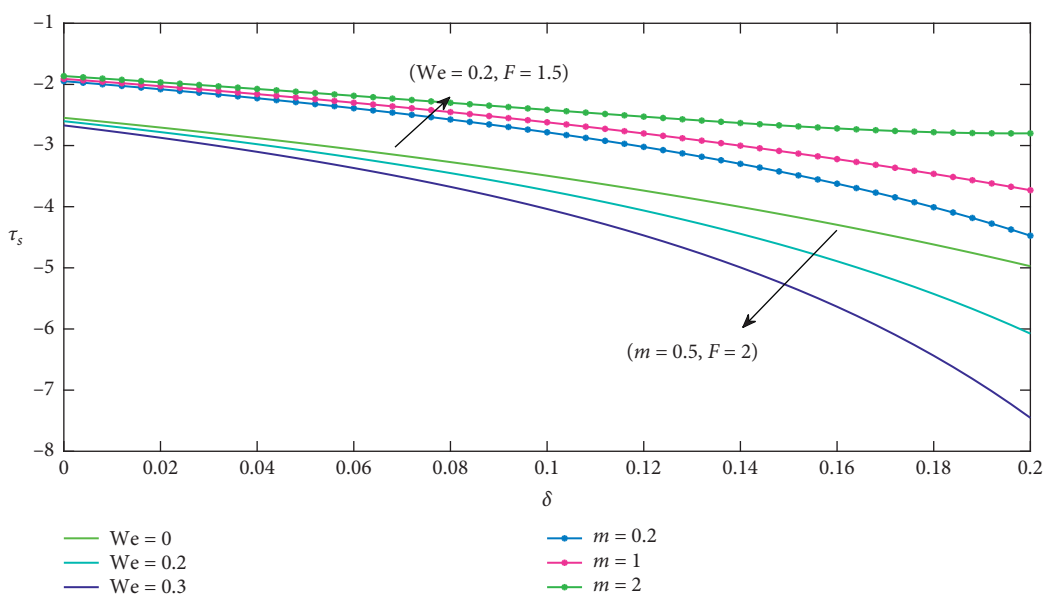

Figure 8: Variation of shear stress at the stenotic throat.

4. Graphical Results and Discussion

In this section, the effect of rheological parameters of the Carreau fluid model, i.e., We and m on velocity profile, resistance impedance, wall shear stress, and shear stress at the stenotic throat, is graphically performed and discussed. The Weissenberg number is the ratio of the relaxation time of the fluid and a specific process time. Relaxation time increases when we increase the Weissenberg number and velocity field easily increases and skin friction decreases. Another aspect of increasing the Weissenberg number is that it reduces the magnitude of the fluid velocity for shear-thinning fluid, while it arises for the shear-thickening fluid. Figure 2 shows that resistance impedance is an increasing function of the Weissenberg number We.

In Figure 3, it is observed that the resistance impedance increases as there is an increase in power-law index m. It explains the the fluid shear-thinning behavior ($m < 1$) slowly compared to Newtonian ($m = 1$) and shear-thickening ($m > 1$) fluids.

The behavior of shear stress for We and m is shown in Figures 4 and 5. It is observed that the magnitude of wall shear stress increases by increasing We as shown in Figure 4. The opposite behavior is observed when m is increased as seen in Figure 5.

The effect of the severity of stenosis on the velocity profile w is shown in Figures 6 and 7. In Figure 6, the velocity profile increases at the center of the channel by increasing m.

And in Figure 7, an increase in We decreases the velocity at the channel center. It can be seen that for a fixed value of prescribed flux F, the velocity profile w increases near the center, while it decreases near the wall with an increase in the severity of stenosis.

In Figure 8, we noticed that the shear stress at the maximum height of stenosis behaves differently by increasing We and m. It is analyzed that shear stress by fixing Weissenberg number We and flow rate F at the stenosis throat increases with an increase in m. While shear stress decreases with an increase in We with defined values of power-law index m and flow rate F.

5. Conclusion

In this study, we have analyzed the numerical solution of the blood flow with its non-Newtonian nature. Analytical solutions are derived from the given governing equations. The presented computation results of various parameter values, namely, velocity, wall shear stress, shear stress, and resistance impedance at the stenotic throat, are studied in detail for different values of Weissenberg number (We) and power-law index m. From the analysis of the related facts and figures, the following results are concluded:

(1) The velocity profile increases at the center of the channel by increasing m. However, an increase in We decreases the velocity at the channel center.

(2) Resistance impedance is an increasing function of We and m.

(3) The magnitude of shear stress increases by increasing We, while it shows the opposite behavior when m is increased.

(4) Shear stress at the maximum height of stenosis behaves differently by increasing We and m.

Conclusively, the present work may be an improvement in the analysis of pulsatile blood flow through a mild stenotic tapering artery.

Nomenclature

We: Weissenberg number
Γ: Time constant of the fluid
ξ^*: Tapering parameter
a: Length of the nonstenotic part
b: Length of the stenotic section
d_0: Radius of the nontapered artery in the nonstenotic section
n: Shape parameter
δ: Maximum height of the stenosis
τ_s: Wall shear stress
Δp: Pressure drop
λ: Resistance impedance
m: Power-law index
w: Velocity profile
F: Flow rate
S_{rz}: Shear stress
$\mathbf{S}$: Extra stress tensor
θ: Tapering angle.

Data Availability

No data were required to perform this research.

Conflicts of Interest

The authors declare that there are no conflicts of interest.

References

[1] R. Nasrin, A. Hossain, and I. Zahan, "Blood flow analysis inside a stenotic artery using power-law fluid model," *Research and Development in Material Science*, vol. 13, no. 1, pp. 1360–1368, 2020.

[2] R. Ahmad, A. Farooqi, J. Zhang, and N. Ali, "Steady flow of a power law fluid through a tapered non-symmetric stenotic tube," *Applied Mathematics and Nonlinear Sciences*, vol. 4, no. 1, pp. 249–260, 2019.

[3] Y. Pratumwal, W. Limtrakarn, S. Muengtaweepongsa et al., "Whole blood viscosity modeling using power law, Casson, and Carreau Yasuda models integrated with image scanning U-tube viscometer technique," *Songklanakarin Journal of Science and Technology*, vol. 39, no. 5, pp. 625–631, 2018.

[4] M. Y. A. Jamalabadi, M. Daqiqshirazi, H. Nasiri, M. R. Safaei, and T. K. Nguyen, "Modeling and analysis of biomagnetic blood Carreau fluid flow through a stenosis artery with magnetic heat transfer: a transient study," *PLoS One*, vol. 13, no. 2, pp. 1–32, 2018.

[5] D. Tang, C. Yang, S. Kobayashic, and D. N. Ku, "Generalized finite difference method for 3-D viscous flow in stenotic tubes with large wall deformation and collapse," *Applied Numerical Mathematics*, vol. 38, no. 2, pp. 49–68, 2001.

[6] T. Elnaqeeb, "Modeling of Au(NPs)-blood flow through a catheterized multiple stenosed artery under radial magnetic field," *The European Physical Journal Special Topics*, vol. 228, no. 12, pp. 2695–2712, 2019.

[7] K. S. Mekheimer, T. Elnaqeeb, M. A. El Kot, and F. Alghamdi, "Simultaneous effect of magnetic field and metallic nanoparticles on a micropolar fluid through an overlapping stenotic artery: blood flow model," *Physics Essays*, vol. 29, no. 2, pp. 272–283, 2016.

[8] T. Elnaqeeb, N. A. Shah, and K. S. Mekheimer, "Hemodynamic characteristics of gold nanoparticle blood flow through a tapered stenosed vessel with variable nanofluid viscosity," *BioNanoScience*, vol. 9, no. 2, pp. 245–255, 2019.

[9] Z. Ismail, I. Abdullah, N. Mustapha, and N. Amin, "A power-law model of blood flow through a tapered overlapping stenosed artery," *Applied Mathematics and Computation*, vol. 195, no. 2, pp. 669–680, 2008.

[10] K. S. Mekheimer and M. A. E. Kot, "The micropolar fluid model for blood flow through a tapered artery with a stenosis," *Acta Mechanica Sinica*, vol. 24, no. 6, pp. 637–644, 2008.

[11] I. Abdullah and N. Amin, "A micropolar fluid model of blood flow through a tapered artery with a stenosis," *Mathematical Methods in the Applied Sciences*, vol. 33, no. 16, pp. 1910–1923, 2010.

[12] K. S. Mekheimer and M. A. El Kot, "Mathematical modelling of unsteady flow of a Sisko fluid through an anisotropically

tapered elastic arteries with time-variant overlapping stenosis," *Applied Mathematical Modelling*, vol. 36, no. 11, pp. 5393–5407, 2012.

[13] D. S. Sankar and U. Lee, "Mathematical modeling of pulsatile flow of non-Newtonian fluid in stenosed arteries," *Communications in Nonlinear Science and Numerical Simulation*, vol. 14, no. 7, pp. 2971–2981, 2009.

[14] K. W. Lee and X. Y. Xu, "Modelling of flow and wall behaviour in a mildly stenosed tube," *Medical Engineering & Physics*, vol. 24, no. 9, pp. 575–586, 2002.

[15] P. J. Carreau, "Rheological equations from molecular network theories," *Transactions of the Society of Rheology*, vol. 16, no. 1, pp. 99–127, 1972.

[16] B. Šiška, H. Bendova, and I. MacHac, "Terminal velocity of non-spherical particles falling through a Carreau model fluid," *Chemical Engineering and Processing*, vol. 44, no. 12, pp. 1312–1319, 2005.

[17] N. Kutev, S. Tabakova, and S. Radev, "Approximation of the oscillatory blood flow using the Carreau viscosity model," in *Proceedings of the International Conference on Mechanics—Seventh Polyakhov's Reading*, pp. 1–4, Saint Petersburg, Russia, Feburary 2015.

[18] A. G. Usman and S. Kausar, "Numerical solution of the partial differential equations that model the steady three-dimensional flow and heat transfer of Carreau fluid between two stretchable rotatory disks," *Numerical Methods for Partial Differential Equations*, pp. 1–29, 2020.

[19] M. I. Khan, S. Qayyum, M. Nigar, Y. Chu, and S. Kadry, "Dynamics of Arrhenius activation energy in flow of Carreau fluid subject to Brownian motion diffusion," *Numerical Methods for Partial Differential Equations*, pp. 1–21, 2020.

[20] R. P. Chhabra and P. H. T. Uhlherr, "Creeping motion of spheres through shear-thinning elastic fluids described by the Carreau viscosity equation," *Rheologica Acta*, vol. 19, no. 2, pp. 187–195, 1980.

[21] M. B. Bush and N. Phan-Thien, "Drag force on a sphere in creeping motion throug a carreau model fluid," *Journal of Non-newtonian Fluid Mechanics*, vol. 16, no. 3, pp. 303–313, 1984.

[22] H. C. Lee, "An adaptively refined least-squares finite element method for generalized Newtonian fluid flows using the Carreau model," *SIAM Journal on Scientific Computing*, vol. 36, no. 1, pp. 193–218, 2014.

[23] S. Tabakova, E. Nikolova, and S. Radev, "Carreau model for oscillatory blood flow in a tube," *American Institute of Physics*, vol. 336, pp. 336–343, 2014.

[24] Y. Liu and W. Liu, "Blood flow analysis in tapered stenosed arteries with the influence of heat and mass transfer," *Journal of Applied Mathematics and Computing*, vol. 63, no. 1-2, pp. 523–541, 2020.

[25] M. Irfan, K. Rafiq, W. A. Khan, and M. Khan, "Numerical analysis of unsteady Carreau nanofluid flow with variable conductivity," *Applied Nanoscience*, vol. 10, no. 8, pp. 3075–3084, 2020.

[26] D. S. Sankar and K. Hemalatha, "Pulsatile flow of Herschel-Bulkley fluid through stenosed arteries-a mathematical model," *International Journal of Non-Linear Mechanics*, vol. 41, no. 8, pp. 979–990, 2006.

[27] G. T. Liu, X. J. Wang, B. Q. Ai, and L. G. Liu, "Numerical study of pulsating flow through a tapered artery with stenosis," *Chinese Journal of Physics*, vol. 42, no. 4, pp. 401–409, 2004.

[28] J. Hun, C. J. Wook, and P. C. Guk, "Asymmetric flows of non-Newtonian fluids in symmetric stenosed artery," *Korea-Australia Rheology Journal*, vol. 16, no. 2, pp. 101–108, 2004.

[29] N. S. Akbar, "Heat and mass transfer effects on Carreau fluid model for blood flow through a tapered artery with a stenosis," *International Journal of Biomathematics*, vol. 7, no. 1, pp. 1–21, 2014.

[30] N. S. Akbar, "Eyring Prandtl fluid flow with convective boundary conditions in small intestines," *International Journal of Biomathematics*, vol. 6, no. 5, pp. 1–13, 2013.

[31] R. Ellahi, S. U. Rahman, M. M. Mudassar Gulzar, S. Nadeem, and K. Vafai, "A mathematical study of non-Newtonian micropolar fluid in arterial blood flow through composite stenosis," *Applied Mathematics & Information Sciences*, vol. 8, no. 4, pp. 1567–1573, 2014.

[32] A. Wakif, "A novel numerical procedure for simulating steady MHD convective flows of radiative casson fluids over a horizontal stretching sheet with irregular geometry under the combined influence of temperature-dependent viscosity and thermal conductivity," *Mathematical Problems in Engineering*, vol. 2020, Article ID 1675350, 20 pages, 2020.

[33] M. Qasim, Z. Ali, A. Wakif, and Z. Boulahia, "Numerical simulation of MHD peristaltic flow with variable electrical conductivity and Joule dissipation using generalized differential quadrature method," *Communications in Theoretical Physics*, vol. 71, no. 509, pp. 509–518, 2019.

[34] M. Ashraf, M. Qasim, A. Wakif, M. Afridi, and I. Animasaun, "A generalized differential quadrature algorithm for simulating magnetohydrodynamic peristaltic flow of blood-based nanofluid containing magnetite nanoparticles: a physiological application," *Numerical Methods for Partial Differential Equations*, vol. 20, pp. 1–27, 2020.

[35] R. Ahmad, A. Farooqi, J. Zhang, I. Khan, and E.-S. M. Sherif, "Analysis of transport and mixing phenomenon to invariant manifolds using LCS and KAM theory approach in unsteady dynamical systems," *IEEE Access*, vol. 8, pp. 141057–141065, 2020.

[36] A. Farooqi, R. Ahmad, H. Alotaibi, T. Nofal, R. Farooqi, and I. Khan, "A comparative epidemiological stability analysis of predictor corrector type non-standard finite difference scheme for the transmissibility of measles," *Results in Physics*, vol. 21, Article ID 103756, 2021.

[37] A. Farooqi, R. Ahmad, R. Farooqi et al., "An accurate predictor-corrector-type nonstandard finite difference scheme for an SEIR epidemic model," *Journal of Mathematics*, vol. 2020, Article ID 8830829, 18 pages, 2020.

[38] G. Bary, W. Zhang, P. Ru, and J. Yang, "Analyses of multi-pion Bose-Einstein correlations for granular sources with coherent pion-emission droplets," *Chinese Physics C*, vol. 21, Article ID 024106, 2021.

[39] G. Bary, P. Ru, and W. Zhang, "Analyses of multi-pion Hanbury Brown-Twiss correlations for the pion-emitting sources with Bose-Einstein condensation," *Journal of Physics G: Nuclear and Particle Physics*, vol. 45, Article ID 065102, 2018.

[40] G. Bary, P. Ru, and W. Zhang, "Normalized multi-pion Hanbury–Brown– Twiss correlation functions of pion-emitting sources with Bose–Einstein condensation," *Journal of Physics G: Nuclear and Particle Physics*, vol. 46, Article ID 115107, 2019.

[41] A. El Hakeem Abd El Naby, A. E. M. Abd El Kareem, and M. F. Kareem, "Separation in the flow through peristaltic motion of a Carreau fluid in uniform tube," *Physica A: Statistical Mechanics and Its Applications*, vol. 343, pp. 1–14, 2004.

Hindawi
Complexity
Volume 2021, Article ID 9962732, 11 pages
https://doi.org/10.1155/2021/9962732

Research Article

Heat Transfer Analysis for Viscous Fluid Flow with the Newtonian Heating and Effect of Magnetic Force in a Rotating Regime

Rashid Ayub,[1] Shahzad Ahmad,[1] Muhammad Imran Asjad,[2] and Mushtaq Ahmad[1]

[1]*Centre for Advanced Studies in Pure and Applied Mathematics, Bahauddin Zakariya University, Multan, Pakistan*
[2]*Department of Mathematics, University of Management and Technology, Lahore, Pakistan*

Correspondence should be addressed to Muhammad Imran Asjad; imran.asjad@umt.edu.pk

Received 24 March 2021; Revised 8 May 2021; Accepted 12 July 2021; Published 27 July 2021

Academic Editor: Atila Bueno

In this article, an unsteady free convection flow of MHD viscous fluid over a vertical rotating plate with Newtonian heating and heat generation is analyzed. The dimensionless governing equations for temperature and velocity fields are solved using the Laplace transform technique. Analytical solutions are obtained for the temperature and components of velocity fields. The obtained solutions satisfy the initial and boundary conditions. Some physical aspects of flow parameters on the fluid motion are presented graphically.

1. Introduction

Free convection flow of Newtonian and non-Newtonian fluids has many applicable usages in processing industry and heat transfer processes. A number of such investigations have been contributed by many researchers of the respective subject. Uddin et al. [1] discussed the free convection flow of fluid over the moving plate. Mahapart et al. [2] considered the effect of magnetic field over the natural convection flow past a horizonal plate. Babaelahi et al. [3] established analytical results for mixed convection flow. Farhad et al. [4] considered MHD rotating flow by imposing slip condition and Hall current through a porous medium. Jana et al. [5] analyzed flow of viscous fluid through a porous medium in a rotating system. Mohammad et al. [6] investigated the results for flow of nanofluid over rotating plates. Hussain et al. [7] discussed heat and mass transfers at the boundary of flow domain for free convection flow of viscous fluid. Islam et al. [8] discussed free convection flow with variable properties in steady-state situation. Alam et al. [9] analyzed the free convection flow by considering Joule heating and heat generation. Mohamed et al. [10] discussed the unsteady free convection flow of second-grade fluid in rotating frame with ramped wall temperature. Krishna and Reddy [11] considered the chemical reaction and Hall current effect for the free convection flow and established analytical results for concentration, temperature, and velocity fields.

Rotational flow is an essential aspect in several physical flow phenomena and has useful applications in many fields of engineering. Raghunath et al. [12] investigated the free convection flow over the rotating surface. Sharma et al. [13] discussed the effect of chemical reaction and magnetic field on the rotating fluid flow. Vasu et al. [14] explained heat and mass transfer flow by imposing the constant thermal and chemical conditions on boundary. Muthucumarasway et al. [15] discussed the free convection flow of fluid with isothermal conditions. Some other studies regarding rotating fluid flow with heat and mass transfers flow are presented in [16–19]. In the present article, it is assumed that heat transfer from the surface is proportional to the local surface temperature; formally this concept is known as Newtonian heating and was intimated by Merkin [20]. Some more investigations regarding Newtonian heating are found in [21–26].

Our focal intension of present study is to construct a flow model of rotating viscous fluid over a moving flat plate in the presence of magnetic field with the effect of

heat generation subject to Newtonian heating. The prescribed rotating flow model is described by the set of partial differential equations as the governing equations. The nondimensional governing equations are solved by the Laplace transform method, and transformed explicit expressions for temperature and velocity components are established. Moreover, the influence of parameters of interest is highlighted in the graphical form. Heat transfer at boundary is quantified in terms of Nusselt number and presented in the tabular form.

2. Mathematical Formulation of Problem

Consider an incompressible viscous fluid lying near the vertical rotating plate. The plate is situated in the xy-plane and z-axis is normal to the plane of plate. Initially, plate and fluid both are at rest with the constant temperature T_∞. A magnetic field of constant magnitude β_0 is applied normally to the xy-plane as shown in Figure 1. And the fluid and the plate rotate with a constant angular velocity $\Omega\hat{k}$ about z-axis taken normal to the plate. Initially, the plate and the fluid are at rest with constant temperature. After passing some time, plate starts to move with time depending on velocity and temperature is raised directly proportional to the temperature at the wall. Heat transfer takes place from plate to fluid according to the Newtonian heating. Under the usual Boussinesq approximation, the governing equations of flow model take the following form [19]:

$$\frac{\partial u(z,t)}{\partial t} - 2\Omega v(z,t) = g\beta_T\left(T - T_\infty\right) + \nu\frac{\partial^2 u(z,t)}{\partial z^2} - \frac{\sigma\beta_0^2 u(z,t)}{\rho}, \tag{1}$$

$$\frac{\partial v(z,t)}{\partial t} + 2\Omega u(z,t) = \nu\frac{\partial^2 v(z,t)}{\partial z^2} - \frac{\sigma\beta_0^2 v(z,t)}{\rho}, \tag{2}$$

$$\frac{\partial T(z,t)}{\partial t} = \frac{k}{\rho c_p}\frac{\partial^2 T(z,t)}{\partial z^2} + Q_0\left(T - T_\infty\right), \tag{3}$$

with suitable initial and boundary conditions

$$\begin{gathered} u(z,0) = 0, v(z,0) = 0, T(z,0) = T_\infty, \quad z \geq 0, \\ u(0,t) = U_0 f(t), v(0,t) = 0, \left.\frac{\partial T(z,t)}{\partial z}\right|_{z=0} = -\frac{h}{k}T(0,t), \\ u(\infty,t) = 0, v(\infty,t) = 0, T(\infty,t) = T_\infty, \quad t > 0, \end{gathered} \tag{4}$$

where Ω is the angular velocity of the fluid, ν is the kinematic viscosity, $u(z,t)$ is the velocity component along x-axis and $v(z,t)$ is the velocity component along y-axis, ρ is the density of the fluid, T is the temperature of the fluid, β is the coefficient of volume expansion, g is the gravitational acceleration, T_∞ is the temperature at infinity, Q_0 is the heat generation parameter, k is the thermal conductivity, β_0 is the external magnetic field, and σ is the current density.

Now, introducing the following nondimensional variables and parameters:

$$\begin{aligned} u &= U_0 u^\bullet, \\ v &= U_0 v^\bullet, \\ t^\bullet &= \frac{tU_0^2}{\nu}, \\ T^\bullet &= \frac{T - T_\infty}{T_\infty}, \\ z^\bullet &= \frac{zU_0}{\nu}, \end{aligned} \tag{5}$$

into equations (1)–(4) after dropping dot notation, we obtain the following dimensionless model:

$$\frac{\partial u(z,t)}{\partial t} - 2\mathrm{Ek}v(z,t) = \mathrm{Gr}T + \frac{\partial^2 u(z,t)}{\partial z^2} - \mathrm{M}u(z,t), \tag{6}$$

$$\frac{\partial v(z,t)}{\partial t} + 2\mathrm{Ek}u(z,t) = \frac{\partial^2 v(z,t)}{\partial z^2} - Mv, \tag{7}$$

$$\frac{\partial T(z,t)}{\partial t} = \frac{1}{\mathrm{Pr}}\frac{\partial^2 T(z,t)}{\partial z^2} - QT(z,t), \tag{8}$$

with nondimensional initial and boundary conditions

$$\begin{gathered} u(z,0) = 0, v(z,0) = 0, T(z,0) = 0, \quad z \geq 0, \\ u(0,t) = f(t), v(0,t) = 0, \left.\frac{\partial T(z,t)}{\partial z}\right|_{z=0} = -\mathrm{hs}\left(T(0,t) + 1\right), \\ u(\infty,t) = 0, v(\infty,t) = 0, T(\infty,t) = 0, \end{gathered} \tag{9}$$

where

$$\begin{aligned} \mathrm{Ek} &= \frac{\nu\Omega}{U_0^2}, \\ \mathrm{Pr} &= \frac{C_p\mu}{k}, \\ Q &= \frac{\nu Q_0}{U_0^2}, \\ M &= \frac{\beta_0^2\sigma\nu}{\rho U_0^2}, \\ \mathrm{Gr} &= \frac{\nu g\beta_T T_\infty}{U_0^3}, \\ \mathrm{hs} &= \frac{\nu h}{U_0 k}, \end{aligned} \tag{10}$$

are Ekman number, Prandtl number, heat absorption parameter, magnetic field parameter, Grashof number, and Newtonian heating parameter, respectively.

Introduce the complex velocity field $F(z,t) = u + \imath v$, where the function $F(z,t)$ is the solution of the following problem:

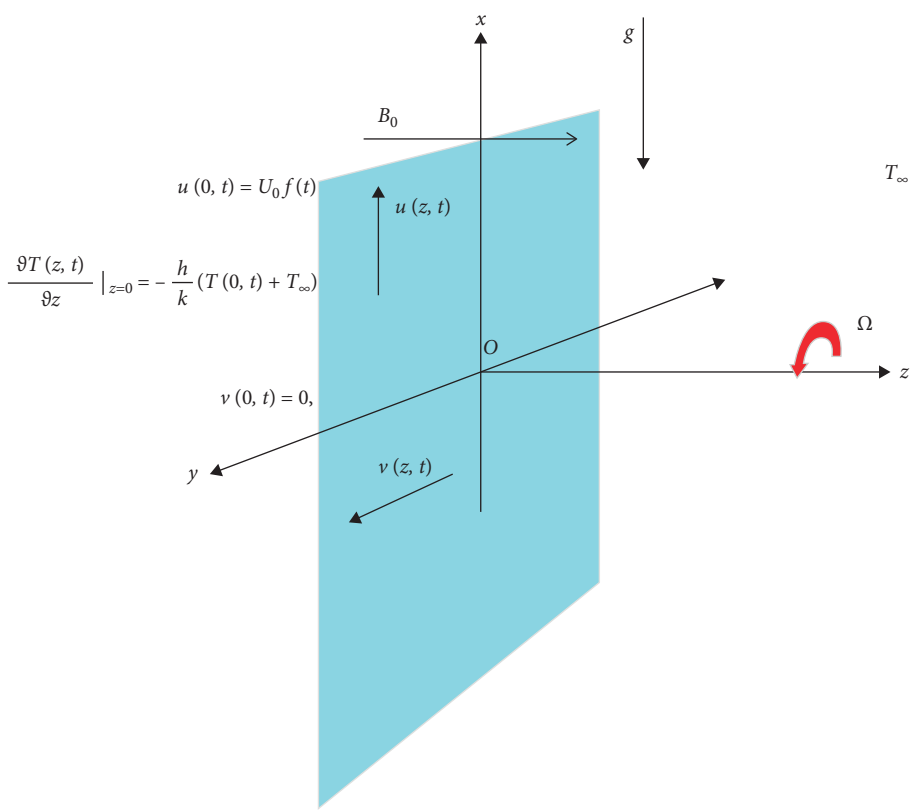

Figure 1: Coordinate system and flow geometry.

$$\frac{\partial F(z,t)}{\partial t} + 2\mathrm{Ek}F(z,t) = \frac{\partial^2 F(z,t)}{\partial z^2} - MF(z,t) + \mathrm{Gr}T(z,t), \tag{11}$$

$$F(z,0) = 0, F(0,t) = f(t), F(\infty,t) = 0. \tag{12}$$

3. Solution of Problem

We solve the dimensionless model of equations (6)–(12) by Laplace transform.

3.1. Calculation of Temperature. Applying Laplace transform to equation (8) and keeping in mind the conditions of equation (9), we get

$$\frac{\partial^2 \overline{T}(z,q)}{\partial z^2} + \mathrm{Pr}Q\overline{T}(z,q) - \mathrm{Pr}q\overline{T}(z,q) = 0. \tag{13}$$

Equation (13) satisfies the following transformed conditions:

$$\frac{\partial \overline{T}(z,q)}{\partial z}\bigg|_{z=0} = -\mathrm{hs}\left[\overline{T}(0,q) + \frac{1}{q}\right], \quad \overline{T}(\infty,q) = 0. \tag{14}$$

Solution of equation (13) subject to the boundary conditions (14) is obtained as follows:

$$\overline{T}(z,q) = \frac{\mathrm{hs}}{q(\sqrt{\mathrm{Pr}(q-Q)} - \mathrm{hs})} e^{-z\sqrt{\mathrm{Pr}(q-Q)}}. \tag{15}$$

In order to invert the Laplace transform, equation (15) can be written in suitable form as

$$\overline{T}(z,q) = \frac{\mathrm{hs}}{\sqrt{\mathrm{Pr}}} \frac{1}{(q-Q)(\sqrt{(q-Q)} - (\mathrm{hs}/\mathrm{Pr}))} e^{-z\sqrt{\mathrm{Pr}}\sqrt{(q-Q)}}$$
$$-Q\frac{1}{q}\frac{\mathrm{hs}}{\sqrt{\mathrm{Pr}}} \frac{1}{(q-Q)(\sqrt{(q-Q)} - (\mathrm{hs}/\mathrm{Pr}))} e^{-z\sqrt{\mathrm{Pr}}\sqrt{(q-Q)}}. \tag{16}$$

Applying the inverse Laplace transform to equation (16), we obtain the following velocity in t-domain:

$$T(z,t) = \mathrm{erfc}\left(\frac{z\sqrt{\mathrm{Pr}}}{2\sqrt{t}}\right)e^{Q} - \mathrm{erfc}\left(\frac{\mathrm{hs}}{\sqrt{\mathrm{Pr}}}\sqrt{t} + \frac{z\sqrt{\mathrm{Pr}}}{2\sqrt{t}}\right)e^{-z\mathrm{hs}+((\mathrm{hs})^2 t)/\mathrm{Pr})+Qt}$$
$$-Q\int_0^t \left[\mathrm{erfc}\left(\frac{z\sqrt{\mathrm{Pr}}}{2\sqrt{\tau}}\right)e^{Q} - \mathrm{erfc}\left(\frac{\mathrm{hs}}{\sqrt{\mathrm{Pr}}}\sqrt{\tau} + \frac{z\sqrt{\mathrm{Pr}}}{2\sqrt{\tau}}\right)e^{-z\mathrm{hs}+((\mathrm{hs})^2 t)/\mathrm{Pr})+Q\tau}\right]d\tau. \tag{17}$$

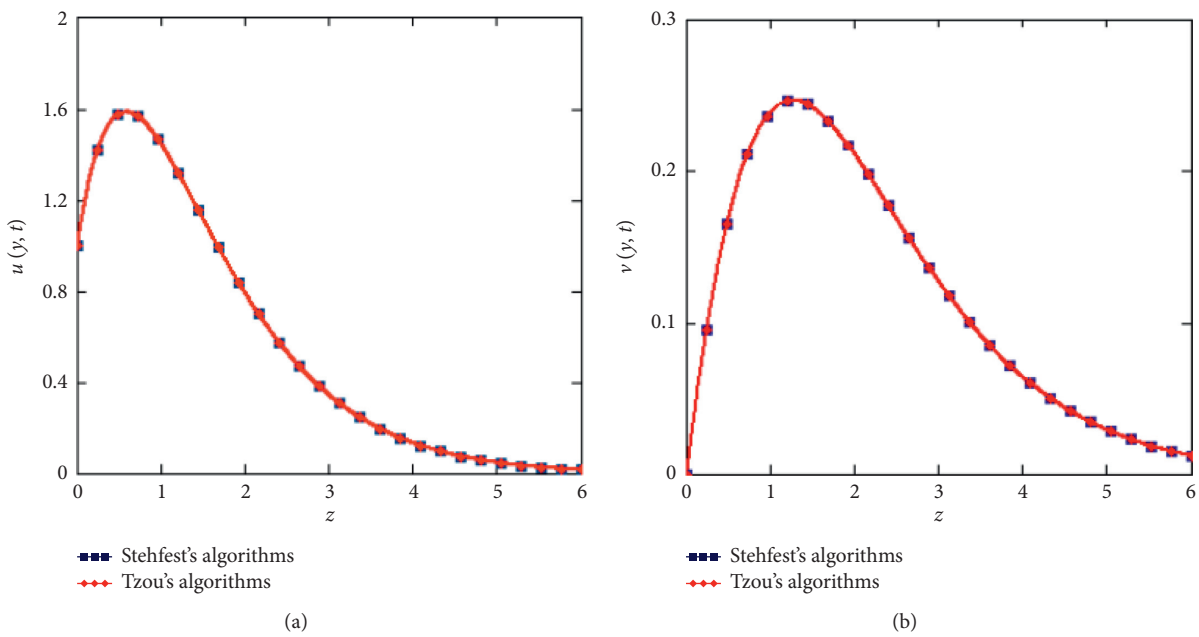

Figure 2: Inversion of real and imaginary components of velocity.

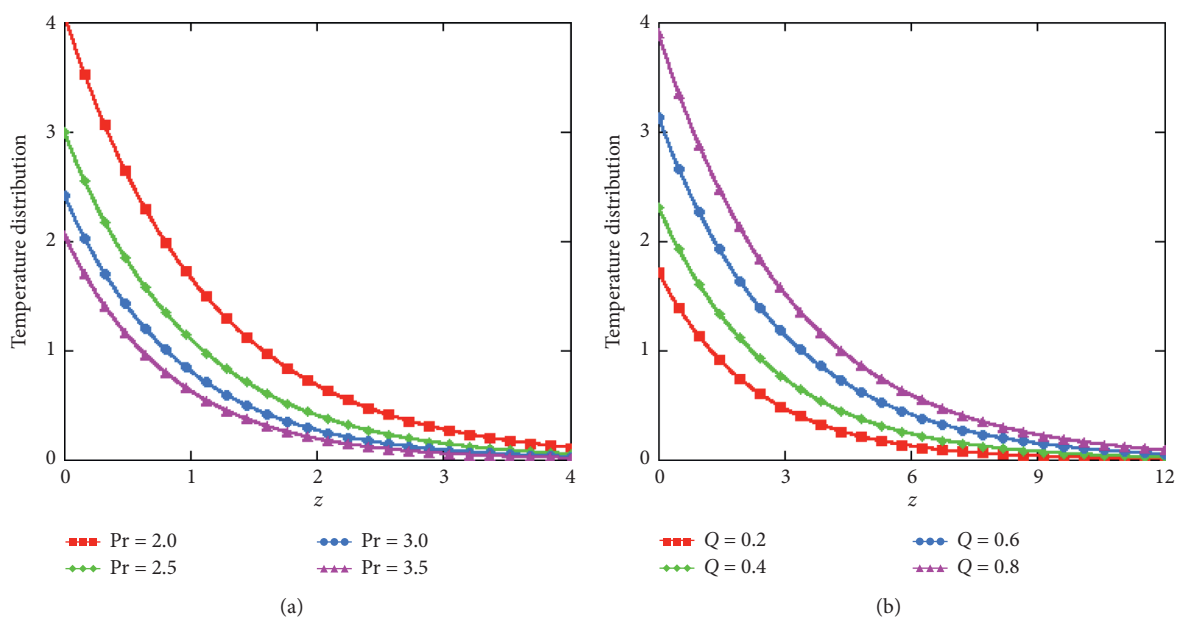

Figure 3: Temperature profiles versus z subject to variation of Pr and Q.

3.2. Nusselt Number. The local coefficient of the rate of heat transfer is defined in terms of Nusselt number and defined by the following relation:

$$\mathrm{Nu} = -\frac{\partial T(z,t)}{\partial z}\bigg|_{y=0} = -\frac{\partial}{\partial y}L^{-1}[\overline{T}(y,q)] = -L^{-1}\left[\frac{\partial \overline{T}(y,q)}{\partial y}\right],$$

$$\mathrm{Nu} = -\frac{\mathrm{hs}\sqrt{\mathrm{Pr}(q-Q)}}{q(\sqrt{\mathrm{Pr}(q-Q)}-\mathrm{hs})}. \tag{18}$$

3.3. Velocity Calculation. Applying Laplace transform to equation (11) and keeping in mind the condition of equation (12), we get

$$\frac{\partial^2 \overline{F}(z,q)}{\partial z^2} - (q + M - 2l\mathrm{Ek})\overline{F}(z,q) = -\mathrm{Gr}\,T(z,q). \tag{19}$$

Equation (19) satisfies the following transformed conditions:

$$\overline{F}(0,q) = f(q), \overline{F}(\infty,q) = 0. \tag{20}$$

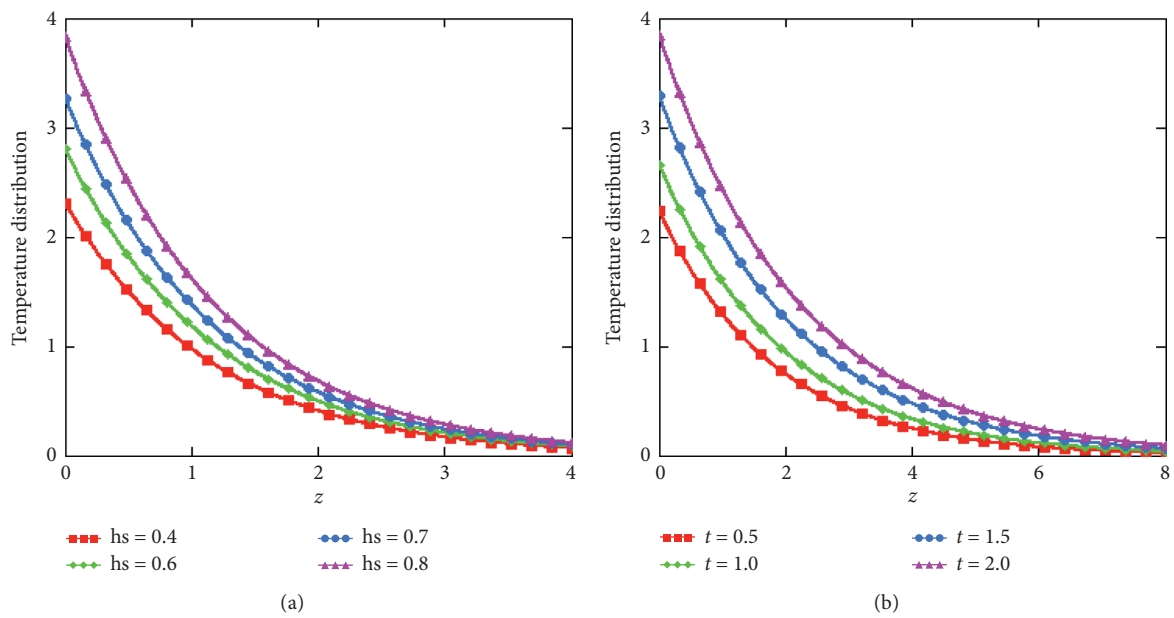

Figure 4: Temperature profiles versus z subject to variation of hs and t.

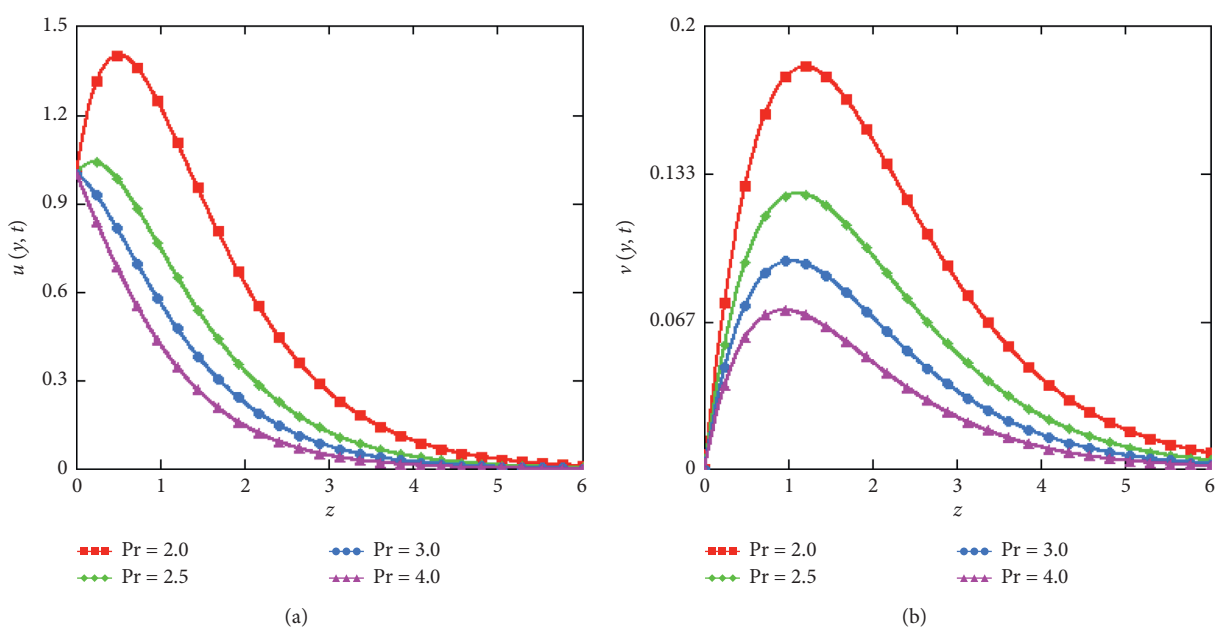

Figure 5: Velocity profiles versus z subject to variation of Pr.

Solution of equation (19) subject to transformed conditions (20) is

$$\overline{F}(z,q) = f(q)e^{-z\sqrt{q+M-2l\mathrm{Ek}}} + \frac{\mathrm{hsGr}\left(e^{-z\sqrt{q+M-2l\mathrm{Ek}}} - e^{-z\sqrt{\mathrm{Pr}(q-\mathrm{Q})}}\right)}{(\mathrm{Pr}-1)(q-((\mathrm{PrQ}+M-2l\mathrm{Ek})/(\mathrm{Pr}-1)))(\sqrt{\mathrm{Pr}(q-\mathrm{Q})}-\mathrm{hs})(q)}. \tag{21}$$

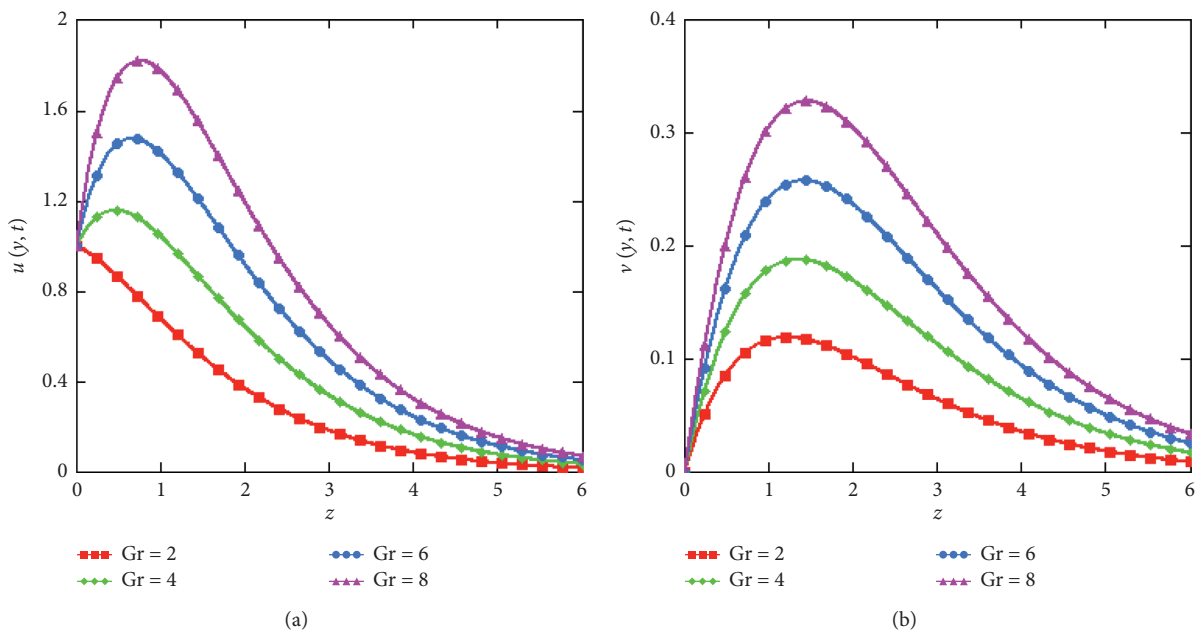

Figure 6: Velocity profiles versus z subject to variation of Gr.

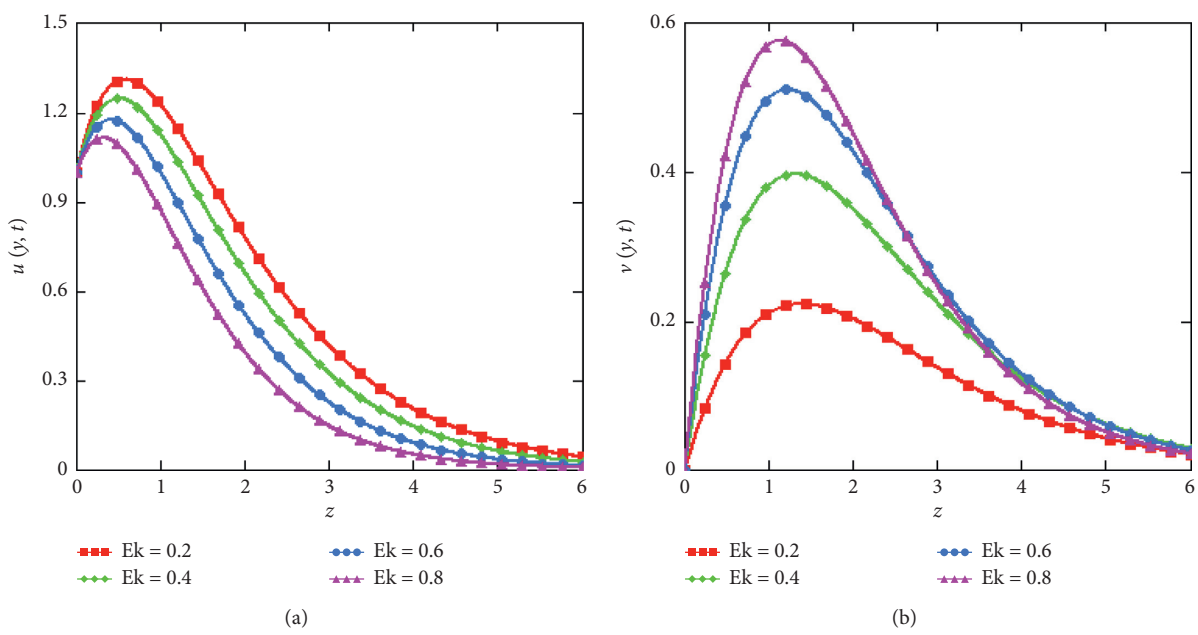

Figure 7: Velocity profiles versus z subject to variation of Ek.

Real and imaginary parts are follows:

$$u(z,q) = f(q)e^{-zl}\cos zm + \frac{z_1z_3 + z_2z_4}{z_3^2 + z_4^2}, \tag{22}$$

$$v(z,q) = -f(q)e^{-zl}\cos zm + \frac{z_2z_3 - z_1z_4}{z_3^2 + z_4^2}, \tag{23}$$

where

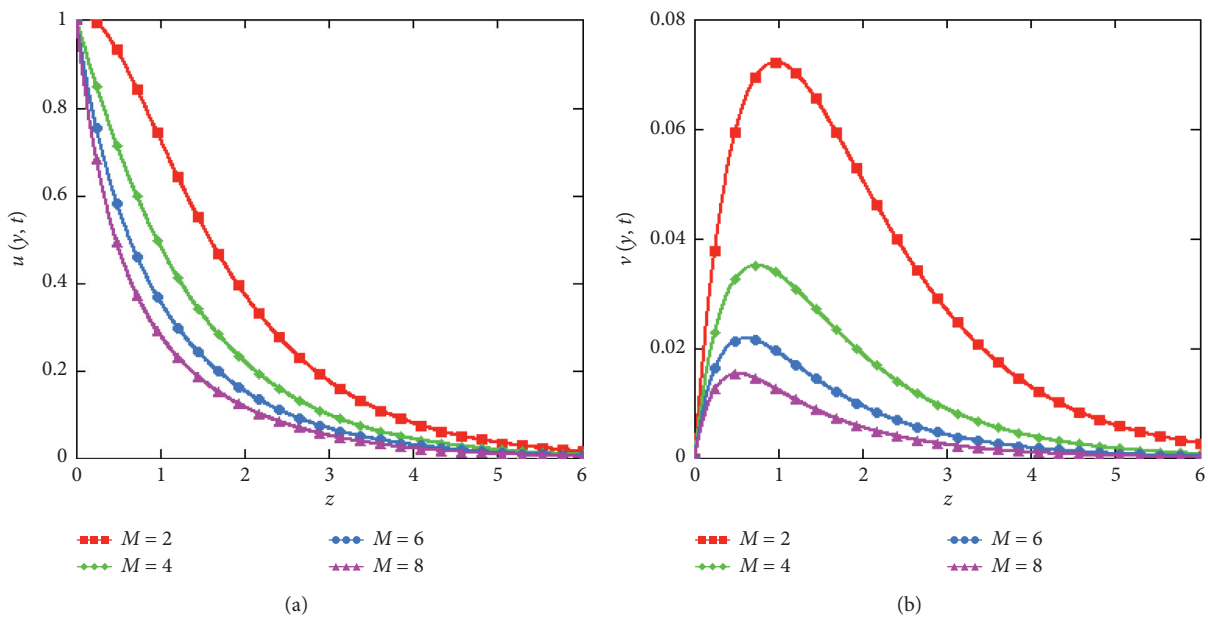

Figure 8: Velocity profiles versus z subject to variation of M.

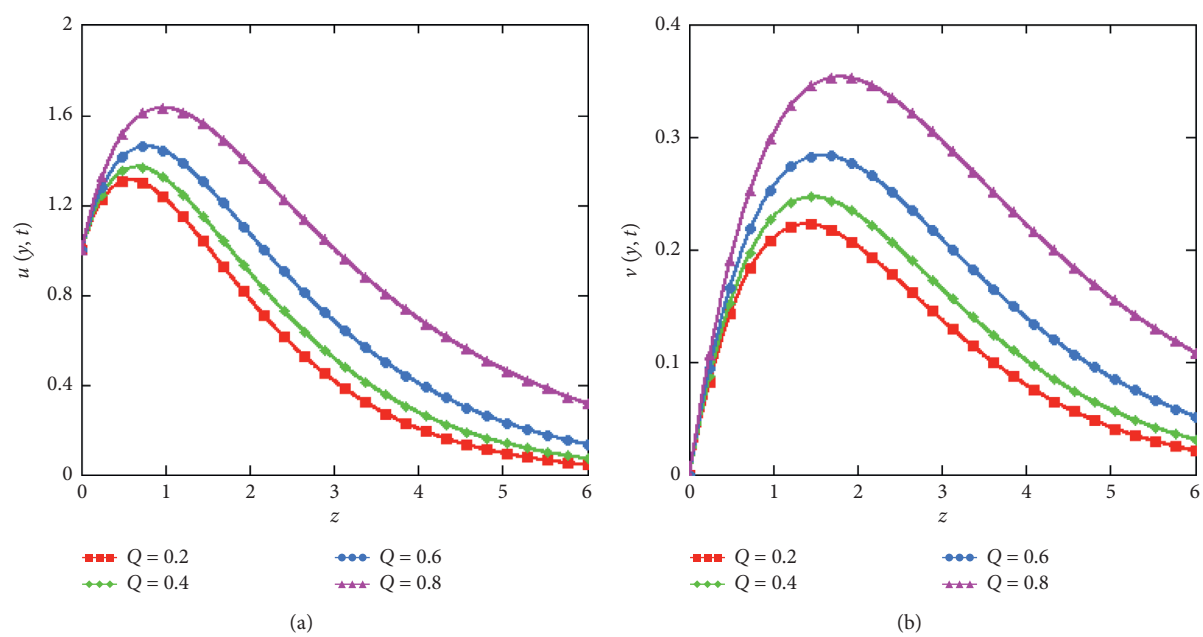

Figure 9: Velocity profiles versus z subject to variation of Q.

$$l = \pm\sqrt{\frac{(q+m) \pm \sqrt{(q+m)^2 + 4\mathrm{Ek}^2}}{2}}, m = \pm\frac{\sqrt{2}\mathrm{Ek}}{\sqrt{(q+m) \pm \sqrt{(q+m)^2 + 4\mathrm{Ek}^2}}}, z_1 = e^{-zl}\cos zm - e^{-z\sqrt{\mathrm{Pr}(q-Q)}},$$
$$z_2 = -\mathrm{hsGr}(\sin zm)e^{-zl}, z_3 = (\mathrm{Pr}(q-Q) - q - M)(\sqrt{\mathrm{Pr}(q-Q)} - \mathrm{hs})(q), z_4 = 2\mathrm{Ek}(\sqrt{\mathrm{Pr}(q-Q)} - \mathrm{hs})(q). \tag{24}$$

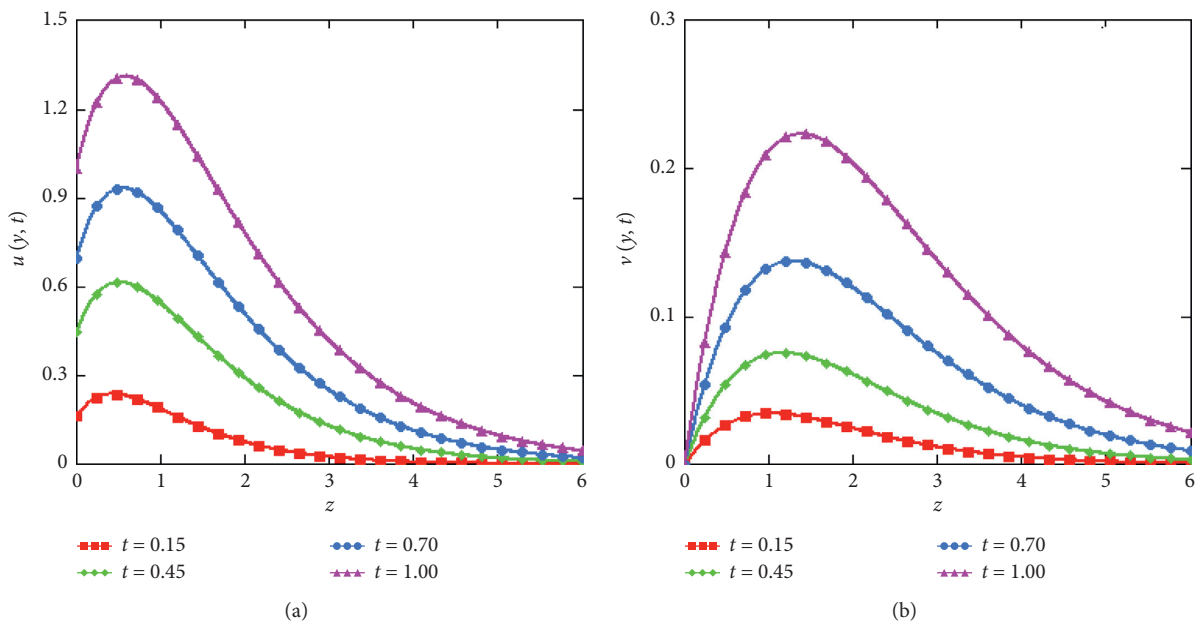

Figure 10: Velocity profiles versus z subject to variation of t.

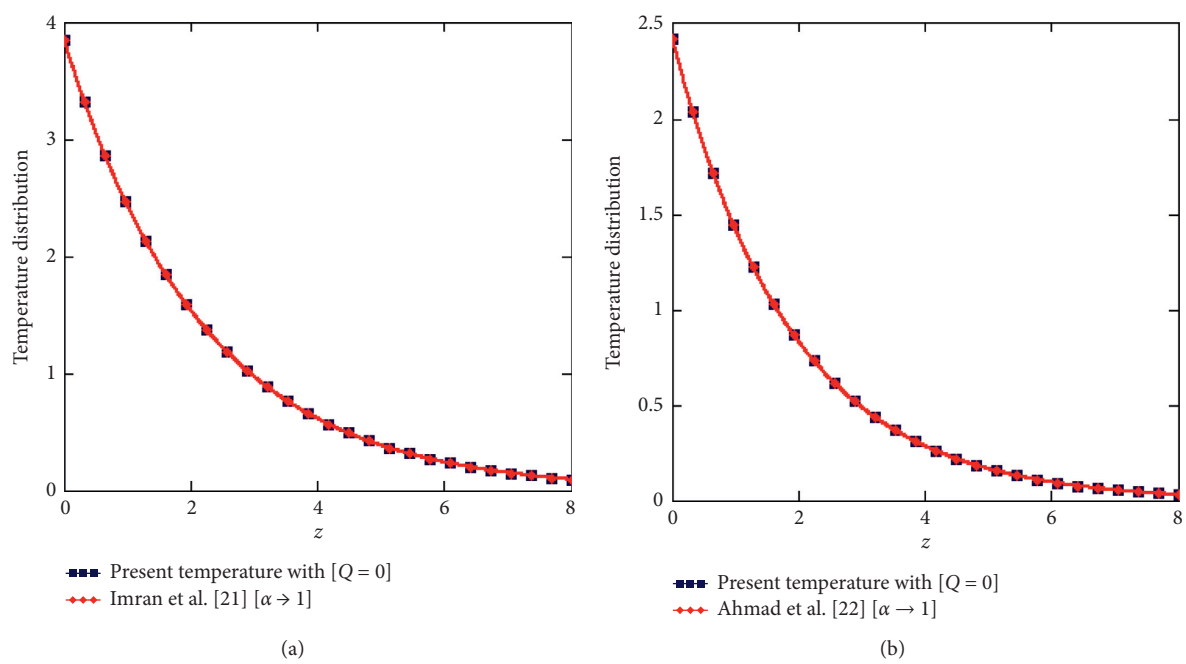

Figure 11: Comparison of temperature.

Equations (22) and (23) are complex relations and cannot be inverted by ordinary inverse relation of Laplace transform. Stehfest's and Tzou's algorithms are utilized for detransformation of velocity components and presented in Figure 2.

4. Results and Discussion

In this paper, the rotational flow of viscous fluid over a flat plate with the Newtonian heating is discussed. Analytical results for temperature and components of velocity fields are established with the help of Laplace transform. Some graphs of velocity against special variable z are sketched to see the physical effect of involved parameters. Figure 3 is plotted to see the effect of Pr and Q over the thermal profile, and it is noted that with the increasing values of Pr, fluid cools down and consequently thermal profile lowers down while it is raised with increasing value of Q. The effect of Newtonian heating and time over the temperature profile is presented in Figure 4. From the figure, it is clear that temperature profiles rise with increasing value of Newtonian heating parameter hs and time t. The effect of Pr over the velocity components is discussed in Figure 5, and it is observed that with the

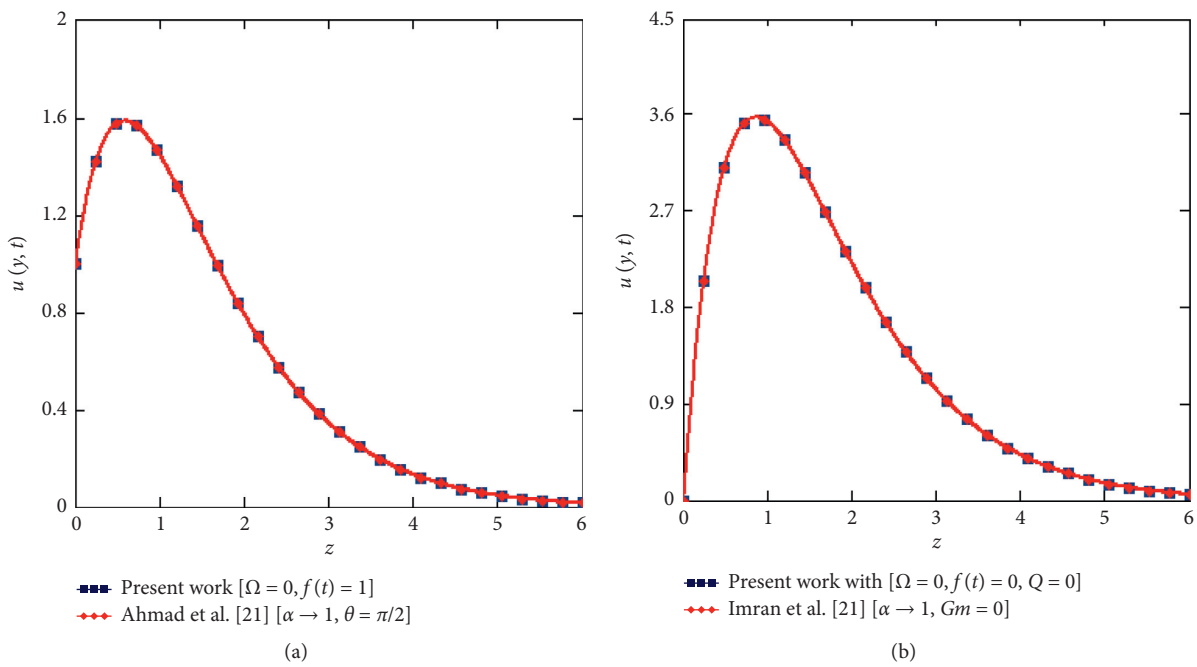

Figure 12: Comparison of velocity.

Table 1: Subjectivity of Nusselt number due to α for different values of Pr and S.

t	Pr = 1.5	Pr = 2	Pr = 2.5	$Q = 0.3$	$Q = 0.5$	$Q = 0.7$
0.1	1.45893971	1.36332825	1.29323441	1.28798185	1.21272314	1.17518651
0.2	1.46973354	1.37659053	1.30680985	1.28874896	1.21304572	1.17537098
0.3	1.48081222	1.38991945	1.32027242	1.28957462	1.21339402	1.17557059
0.4	1.49221241	1.40339890	1.33369919	1.29044904	1.21376360	1.17578257
0.5	1.50398704	1.41712090	1.34716076	1.29136149	1.21414937	1.17600370
0.6	1.51620697	1.43118859	1.36072051	1.29229999	1.21454580	1.17623089
0.7	1.52897061	1.44571909	1.37443112	1.29325166	1.21494653	1.17646033
0.8	1.54241361	1.46084228	1.38832548	1.29420241	1.21534522	1.17668814
0.9	1.55673282	1.47669347	1.40240685	1.29513598	1.21573466	1.17691038
1.0	1.57222017	1.49339487	1.41663477	1.29603494	1.21610801	1.17712268

increasing value of Pr, the fluid's velocity components decreased. The influence of Gr over the fluid's motion is highlighted in Figure 6, and profiles of velocity increased with the increasing value of Gr. Larger value of Gr is referred to the more bouncy effect that is why more fluid currents are generated for increasing values of Gr. The effect of Ekman number Ek over the velocity components is explained in Figure 7, and it is observed that both real and imaginary velocity components speed up with the increasing value of Ek. The subjectivity of magnetic parameter M can be seen in Figure 8, and it is noted that fluid slows down with the enhancing value of M. In the presence of magnetic field, there is some retarding force which creates some hindrance to fluid motion and consequently fluid slows down. The effect of heat generation parameter Q is studied in Figure 9, and it is concluded that fluid speeds up with the increasing value of Q, due to heat generation, there is more heat transfer; therefore, fluid velocity components are increased with the increasing value of Q of Q. The effect of the time over the velocity components is discussed in Figure 10, and it is clear that with the elapsed time, fluid increases, and it is a natural aspect of velocity with the elapsed time. Figure 11 presents a comparison of present temperature for $Q = 0$ with the temperature obtained by Imran et al. [21] and Ahmad et al. [22], and overlapping profile shows the validity of our result for temperature. The real and imaginary components of present velocity are also compared with the velocities obtained in [22, 23], and its overlapping profiles are presented in Figure 12. The heat transfer at boundary is discussed in terms of Nusselt number; moreover the effect of Pr and Q over the Nusselt number is presented in Table 1. Q, heat transfer is presented in Table 1, and from the tabular data, it is clear that Nusselt number increases with the increasing time, but it is reduced with the increasing value of Pr and Q.

5. Conclusion

In this article, rotational flow of viscous fluid over a flat plate with Newtonian heating is discussed for analytical result of temperature field and transformed result for velocity field is

established with the help of Laplace transform. Some key findings of this study are listed below.

(i) Temperature lowers down with the increasing values of Pr while it is raised with increasing values of hs, Q, and time t. Heat transfer coefficient is enhanced with increasing time while it is reduced with increasing values of Pr and Q.

(ii) Velocity components decrease with increasing Pr and M, while they increase with the increasing value of Gr, Ek, Q, and time t.

(iii) Thermal boundary layer declines with greater values of Pr and enhances with increasing values Q, hs, and t, respectively.

(iv) Momentum boundary layer is reduced with increasing values of Pr, Ek, and M while it is enhanced with the increasing values of Gr, Q, and t.

(v) Our obtained results for temperature and velocity have a good agreement with the corresponding results of existing literature.

Data Availability

No datasets were generated or analyzed during the current study.

Conflicts of Interest

The authors declare that they have no conflicts of interest.

References

[1] J. Uddin, W. Khan, and A. Ismail, "Similarity solution of double diffusive free convective flow over a moving vertical flat plate with convective boundary condition," *Ain Shams Engineering Journal*, vol. 6, no. 3, pp. 1–8, 2015.

[2] R. Mahaparta, S. Sidui, and S. K. Nandy, "Effect of magnetic field on indirect natural convection flow above a Horizontal hot flat plate," *Frontiers in Heat and Mass Transfer*, vol. 5, no. 15, pp. 1–6, 2014.

[3] M. Babaelahi, D. Ganji, and A. Joneidi, "Analytical treatment of mixed convection flow past vertical flat plate," *Thermal Science*, vol. 14, no. 2, pp. 409–416, 2010.

[4] A. Farhad, M. Norzieha, S. Sharidan, and I. Khan, "Hydromagnetic rotating flow in a porous medium with slip condition and Hall current," *International Journal of Physical Sciences*, vol. 7, no. 10, pp. 1540–1548, 2012.

[5] M. Jana, S. L. Maji, S. Das, and R. N. Jana, "Unsteady flow of viscous fluid through a porous medium bounded by a porous plate in a rotating system," *Journal of Porous Media*, vol. 13, no. 7, pp. 645–653, 2010.

[6] H. Mohammad, M. Sobhan, and J. Dengwei, "Nanofluid condensation and MHD flow modeling over rotating plates using least square method," *Iranian Journal of Chemical and Chemical Engineering*, vol. 37, no. 4, pp. 193–203, 2018.

[7] S. Hussain, N. C. Roy, M. A. Hossain, and S. C. Saha, "Effect of fluctuating surface heat and mass flux on natural convection flow along a vertical flat plate," *Mathematical Problems in Engineering*, vol. 2015, Article ID 258016, 15 pages, 2015.

[8] R. Islam, M. G. M. Al Faruque, and S. Islam, "Variable fluid properties of MHD steady Natural convection flow over a vertical flat plate," *Journal of Enviromental Sciences*, vol. 1, no. 2, pp. 1–6, 2019.

[9] M. Alam, M. Hossain, M. Parvez, and I. Rahman, "The coupling conduction effects on natural convection flow along a vertical flat plate with joule heating and heat generation," *Current Journal of Applied Science and Technology*, vol. 27, no. 1, pp. 1–12, 2018.

[10] A. Q. Mohamed, I. Khan, Z. Ismail, and S. Shafie, "The unsteady free convection flow of second grade fluid in rotating frame with ramped wall temperature," *AIP Proceedings*, vol. 1605, pp. 398–403, 2014.

[11] M. V. Krishna and M. G. Reddy, "MHD convective rotating flow past an oscillating porous plate with chemical reaction and Hall effects," in *Proceedings of International Conference on Advances in Materials and Manufacturing Applications (IConAMMA-2016), IOP Conference Series: Materials Science and Engineering*, vol. 149, pp. 1–14, Bangalore, India, July 2016.

[12] K. Raghunath, R. S. Prasad, R. S. Prasad, and G. S. S. Raju, "Hall effects on MHD convective rotating flow of through a porous mediumpast infinite vertical plate," *Annals of Pure and Applied Mathematics*, vol. 16, no. 2, pp. 353–363, 2018.

[13] R. P. Sharma, M. C. Raju, O. D. Makinde, P. R. K. Reddy, and P. C. Reddy, "Buoyancy effects on unsteady MHD chemically reacting and rotating fluid flow past a plate in a porous medium," *Defect and Diffusion Forum*, vol. 392, pp. 1–9, 2019.

[14] B. Vasu, V. R. Prasad, and N. B. Reddy, "Radiation and mass Transfer effects on transient free convection flow of a dispative fluid past semi-infinite vertical plate with uniform heat and mass fluxes," *Journal of Applied Fluid Mechanics*, vol. 4, no. 1, pp. 15–26, 2011.

[15] R. Muthucumarasway, N. Dhanasekar, and G. E. Prasad, "Rotation effects on flow past an accelerated isothermal vertical plate with chemical reaction of first order," *International Journal of Mathematical Archive*, vol. 3, no. 5, pp. 2122–2129, 2012.

[16] R. Muthucumarasway, N. Dhanasekar, and G. E. Prasad, "MHD and Rotation effects on flow past an accelerated and mass diffusion in the presence of chemical reaction," *International Journal of Applied Mechanics and Engineering*, vol. 18, no. 4, pp. 1087–1097, 2014.

[17] R. Muthucumarasway, T. Lal, and D. Ranganayakulu, "Rotation effects on MHD flow past an accelerated vertical plate with variable temperature and uniform mass diffusion," *Annals of Faculty Engineering Hunedoara, International Journal of Engineering*, vol. 9, no. 1, pp. 229–234, 2011.

[18] R. Muthucumarasway, T. Lal, and D. Ranganayakulu, "MHD flow past an accelerated vertical plate with variable heat and mass diffusion in the presnce of rotation," *International Journal of Innovative Research in Science Engineering and Technology*, vol. 2, no. 10, pp. 5671–5681, 2013.

[19] A. K. Singh, "MHD free-convection flow past an accelerated vertical porous plate in a rotating fluid," *Astrophysics and Space Science*, vol. 103, no. 1, pp. 155–163, 1984.

[20] J. H. Merkin, "Natural-convection boundary-layer flow on a vertical surface with Newtonian heating," *International Journal of Heat and Fluid Flow*, vol. 15, no. 5, pp. 392–398, 1994.

[21] M. A. Imran, I. Khan, M. Ahmad, N. A. Shah, and M. Nazar, "Heat and mass transport of differential type fluid with non-integer order time-fractional Caputo derivatives," *Journal of Molecular Liquids*, vol. 229, pp. 67–75, 2017.

[22] M. Ahmad, M. A. Imran, and J. Singh, "Application of novel fractional derivative to heat and mass transfer analysis for the

slippage flow of viscous fluid with SWCNT's subject to Newtonian heating," *Mathematical Methods in the Applied Sciences*, pp. 1–27, 2021.

[23] M. Ahmad, M. A. Imran, M. D. Ikram, D. Baleanu, and A. S. Alshomrani, "Thermal analysis of MHD viscous fluid with innovative fractional derivative," *Thermal Sience*, vol. 24, no. 1, pp. 351–360, 2020.

[24] D. Vieru, C. Fetecau, C. Fetecau, and N. Nigar, "Magneto-hydrodynamic natural convection flow with Newtonian heating and mass diffusion over an infinite plate that applies shear stress to a viscous fluid," *Zeitschrift für Naturforschung A*, vol. 69, no. 12, pp. 714–724, 2014.

[25] A. Hussanan, M. I. Anwar, F. Ali, I. Khan, and S. Shafie, "Natural convection flow past an oscillating plate with Newtonian heating," *Heat Transfer Research*, vol. 45, no. 2, pp. 119–135, 2014.

[26] D. Vieru and C. Fetecau, "Corina Fetecau, Time-fractional free convection flow near a vertical plate with Newtonian heating and mass diffusion," *Thermal Science*, vol. 19, pp. S85–S98, 2015.

Hindawi
Complexity
Volume 2021, Article ID 7979365, 21 pages
https://doi.org/10.1155/2021/7979365

Research Article

Numerical Investigation of the Time-Fractional Whitham–Broer–Kaup Equation Involving without Singular Kernel Operators

Kamsing Nonlaopon,[1] Muhammad Naeem,[2] Ahmed M. Zidan,[3,4] Rasool Shah,[5] Ahmed Alsanad,[6] and Abdu Gumaei[6,7]

[1]*Department of Mathematics, Faculty of Science, Khon Kaen University, Khon Kaen 40002, Thailand*
[2]*Deanship of Joint First Year Umm Al-Qura University, Makkah, Saudi Arabia*
[3]*Department of Mathematics, College of Science, King Khalid University, Abha 9004, Saudi Arabia*
[4]*Department of Mathematics, Faculty of Science, Al-Azhar University, Assiut 71524, Egypt*
[5]*Department of Mathematics, Abdul Wali University Mardan, Mardan, Pakistan*
[6]*STC's Artificial Intelligent Chair, Department of Information Systems, College of Computer and Information Sciences, King Saud University, Riyadh 11451, Saudi Arabia*
[7]*Computer Science Department, Faculty of Applied Sciences, Taiz University, Taiz 6803, Yemen*

Correspondence should be addressed to Rasool Shah; rasoolshah@awkum.edu.pk and Ahmed Alsanad; aasanad@ksu.edu.sa

Received 6 May 2021; Revised 15 June 2021; Accepted 13 July 2021; Published 22 July 2021

Academic Editor: Muhammad Imran Asjad

This paper aims to implement an analytical method, known as the Laplace homotopy perturbation transform technique, for the result of fractional-order Whitham–Broer–Kaup equations. The technique is a mixture of the Laplace transformation and homotopy perturbation technique. Fractional derivatives with Mittag-Leffler and exponential laws in sense of Caputo are considered. Moreover, this paper aims to show the Whitham–Broer–Kaup equations with both derivatives to see their difference in a real-world problem. The efficiency of both operators is confirmed by the outcome of the actual results of the Whitham–Broer–Kaup equations. Some problems have been presented to compare the solutions achieved with both fractional-order derivatives.

1. Introduction

In engineering and applied sciences and technology, fractional partial differential equations (FPDEs) containing nonlinearities define many phenomena, ranging from gravitation to dynamics. The nonlinear FPDEs are significant tools analyzed to model nonlinear dynamical behaviour in many areas such as plasma physics, mathematical biology, fluid dynamics, and solid-state physics. The widely held dynamical schemes can be denoted by an appropriate set of FPDEs. Moreover, it is well identified that FPDEs solve mathematical models, such as Poincare conjecture and Calabi conjecture models [1–12].

It has been determined that the nonlinear development of shallow-water waves in fluid mechanics is described by a coupled system of Whitham–Broer–Kaup (WBK) equations [13]. Whitham [14], Broer [15], and Kaup [16] proposed the coupled scheme of the aforementioned equations. The aforementioned equations define shallow-water wave propagation with various spreading relations, as shown in [17]. The governing equations for the respective phenomena in classic order are provided by

$$D_{\mathfrak{I}}^{\beta}\mu(\varphi,\mathfrak{I})+\mu(\varphi,\mathfrak{I})\frac{\partial\mu(\varphi,\mathfrak{I})}{\partial\varphi}+\frac{\partial\mu(\varphi,\mathfrak{I})}{\partial\varphi}+g\frac{\partial\nu(\varphi,\mathfrak{I})}{\partial\varphi}=0,$$
$$D_{\mathfrak{I}}^{\beta}\nu(\varphi,\mathfrak{I})+\mu(\varphi,\mathfrak{I})\frac{\partial\nu(\varphi,\mathfrak{I})}{\partial\varphi}+\nu(\varphi,\mathfrak{I})\frac{\partial\mu(\varphi,\mathfrak{I})}{\partial\varphi}+p\frac{\partial^3\mu(\varphi,\mathfrak{I})}{\partial\varphi^3}-g\frac{\partial^2\nu(\varphi,\mathfrak{I})}{\partial\varphi^2}=0,\quad 0<\beta\leq 1, \tag{1}$$

where $\mu(\varphi,\mathfrak{I})$ and $\nu(\varphi,\mathfrak{I})$ show the height and horizontal velocity that diverges from the liquid's equilibrium position, respectively, and pg are constant, signified in different diffusion powers. Over the last few decades, there has been a lot of research into solutions to such nonlinear PDEs. So, many researchers have created a variety of mathematical methods to investigate the analytical results of nonlinear PDEs. The HPM was used by Biazar and Khah [18] to solve the coupled schemes of the Burger and Brusselator problems. Amjad et al. [19] applied the solution of standard order coupled with fractional-order Whitham–Broer–Kaup equation by Laplace decomposition technique. Noor et al. [20] used the homotopy perturbation technique to investigate the results of much classical order of PDEs. Whitham–Broer–Kaup equations are used by other scholars who implemented several numerical techniques, such as residual power series technique [4], reduced differential transformation technique [21], Adomian decomposition technique [7], homotopy perturbation technique [22, 23], Lie symmetry analysis [24, 25], exp-function technique [26], G'/G-expansion technique [27], and homotopy analysis technique [28].

Fractional calculus (FC) is a new mathematical approach for describing models of nonlocal behaviour. Fractional derivatives have mathematically described many other physical problems in recent years; these representations have yielded excellent outcomes in the simulation of real-world issues. Some basic definitions of fractional operators were given by Riesz, Coimbra, Hadamard, Riemann–Liouville, Grunwald–Letnikov, Weyl, Caputo, Fabrizio, and Atangana Baleanu, among others [29–31]. To investigate the solutions of nonlinear FPDEs, some well-known techniques for finding actual results have been develop, for example, the homotopy perturbation transform technique [32, 33], the invariant subspace technique [34], the Hermite colocation technique [35], the q-homotopy analysis transform method [36], the optimal homotopy asymptotic technique [37], the homotopy analysis Sumudu transform technique [38], the Adomian decomposition technique [39], the Pade approximation and homotopy-Pade method [39], and the Sumudu transform series expansion technique [40]. The Laplace homotopy perturbation transform technique is a mixture of the homotopy perturbation technique introduced by Liao [41] and of the Laplace transformation [42].

The rest of the paper is arranged as follows. Section 2 discusses the basic definitions from fractional calculus. Section 3 is introduced to the fundamental methodology of HPTM. Sections 4 and 5 are the implementations of the techniques for the CF and AN operators. The conclusion of the work is written in Section 6.

2. Fractional Calculus

This section provides some fundamental concepts of fractional calculus.

Definition 1 (see [42]). The Liouville–Caputo operator is given by

$$D_{\mathfrak{I}}^{\beta}u(\varphi,\mathfrak{I})=\frac{1}{\Gamma(n-\beta)}\int_0^{\mathfrak{I}}(\mathfrak{I}-\theta)^{n-1}u^{(n)}(\varphi,\theta)\mathrm{d}\theta,\quad n-1<\beta<n, \tag{2}$$

where $u^{(n)}(\varphi,\theta)$ is the derivative of integer nth order of $u(\varphi,\theta)$, $n\in\mathbb{N}$ and $n-1<\beta\leq n$. If $0<\beta\leq 1$, then we defined the Laplace transformation for the Caputo fractional derivative as follows:

$$\mathscr{L}\left[D_{\mathfrak{I}}^{\beta}u(\varphi,\mathfrak{I})\right](s)=s^{\beta}\mathscr{L}[u(\varphi,\mathfrak{I})](s)-s^{\beta-1}[u(\varphi,0)]. \tag{3}$$

Definition 2 (see [42]). The Caputo–Fabrizio operator (CF) is defined by

$$D_{\mathfrak{I}}^{\beta}u(\varphi,\mathfrak{I})=\frac{(2-\beta)M(\beta)}{2(n-\beta)}\int_0^{\mathfrak{I}}\exp\left(-\beta\frac{(\mathfrak{I}-\theta)}{n-\beta}\right)u^{(n)}(\varphi,\theta)\mathrm{d}\theta, \tag{4}$$

where $M(\beta)$ is a normalization form and $M(0)=M(1)=1$. The exponential law is used as the nonsingular kernel in this fractional operator.

If $0<\beta\leq 1$, then we define the Caputo–Fabrizio of Laplace transformation for the fractional derivative is given as

$$\mathscr{L}\left[D_{\mathfrak{I}}^{\beta}u(\varphi,\mathfrak{I})\right](s)=\left(\frac{s\mathscr{L}[u(\varphi,\mathfrak{I})](s)-u(\varphi,0)}{s+\beta(1-s)}\right). \tag{5}$$

Definition 3 (see [42]). The fractional generalized Mittag-Leffler law with the sense of Atangana–Baleanu operator is defined as follows:

$$D_{\mathfrak{I}}^{\beta}u(\varphi,\mathfrak{I})=\frac{B(\beta)}{1-\beta}\int_0^{\mathfrak{I}}E_{\beta}\left[-\beta\frac{(\mathfrak{I}-\theta)^{\beta}}{n-\beta}\right]u^{(n)}(\varphi,\theta)\mathrm{d}\theta, \tag{6}$$

where $B(\beta)$ is a normalization function with $B(0)=B(1)=1$. The Mittag-Leffler law is used as a nonsingular and nonlocal kernel in this fractional operator.

If $0 < \beta \leq 1$, then we express the Laplace transformation for the Atangana–Baleanu operator fractional derivative as

$$\mathscr{L}\left[D_{\mathfrak{I}}^{\beta} u(\varphi, \mathfrak{I})\right](s) = \left(\frac{s\mathscr{L}[u(\varphi, \mathfrak{I})](s) - u(\varphi, 0)}{s^{\beta}(1-\beta)+\beta}\right). \quad (7)$$

3. Implementation of the LHPTM for the Solution of Fractional Partial Differential Equation

The LHPTM is general methodology and can be written as follows.

The main procedure of this technique is defined as follows:

Step 1: let us consider the following equation:

$$\frac{\partial^{\beta}}{\partial \mathfrak{I}^{\beta}} F(\varphi, \mathfrak{I}) = \Lambda(F(\varphi, \mathfrak{I})) + \Xi(F(\varphi, \mathfrak{I})) + u(\varphi, \mathfrak{I}), \quad \beta = 1, 2, 3, \ldots, \quad (8)$$

under the initial condition

$$\frac{\partial^{i}}{\partial \mathfrak{I}^{i}} F(\varphi, 0) = z_i(\varphi), \qquad \frac{\partial^{\beta-1}}{\partial \mathfrak{I}^{\beta-1}} F(\varphi, 0) = 0, \quad i = 0, 1, 2, 3, \ldots, \beta - 2, \quad (9)$$

where $u(\varphi, \mathfrak{I})$ is a known function, β is the order of the derivative, Λ represents a linear differential operator, and Ξ is the general nonlinear differential operator.

Step 2: using both sides Laplace transformation operator of (8), we obtain

$$\mathscr{L}[f(\varphi, \mathfrak{I})] = s^{\beta}\mathscr{L}[\Lambda(F(\varphi, \mathfrak{I}))] + s^{\beta}\mathscr{L}[\Xi(F(\varphi, \mathfrak{I}))] + s^{\beta}\mathscr{L}[u(\varphi, \mathfrak{I})], \quad (10)$$

Laplace transformation is applied to Caputo–Fabrizio (5) and Atangana–Baleanu (7) operators.

Step 3: on both sides, using the inverse Laplace transformation of equation (10), we obtain

$$F(\varphi, \mathfrak{I}) = H(\varphi, \mathfrak{I}) + \mathscr{L}^{-1}\left[s^{\beta}\mathscr{L}[\Lambda(F(\varphi, \mathfrak{I}))] + s^{\beta}\mathscr{L}[\Xi(F(\varphi, \mathfrak{I}))]\right]. \quad (11)$$

Step 4: applying the homotopy producer, the result of the above equations in a series form is defined by

$$F(\varphi, \mathfrak{I}, k) = \sum_{n=0}^{\infty} k^n F_n(\varphi, \mathfrak{I}), \qquad F(\varphi, \mathfrak{I}) = \lim_{k \longrightarrow 1} F(\varphi, \mathfrak{I}, k), \quad (12)$$

and the nonlinear terms can be expressed as

$$\Xi F(\varphi, \mathfrak{I}) = \sum_{n=1}^{\infty} k^n h_n(f(\varphi, \mathfrak{I})), \quad (13)$$

where $k \in (0, 1]$ is an embedding parameter and $h_n(F(x, \mathfrak{I}))$ are He's polynomials that can be provided by

$$h_n(F_0, \ldots, F_n) = \frac{1}{n!}\frac{\partial^n}{\partial k^k}\left[\Xi\left(\sum_{j=0}^{n} k^j F_j(\varphi, \mathfrak{I})\right)\right], \quad n \in \mathbb{N}. \quad (14)$$

Finally, the LHPTM is achieved by coupling the decomposition technique which is defined by

$$\sum_{j=0}^{\infty} k^n F_n(\varphi, \mathfrak{I}) = T(\varphi, \mathfrak{I}) + k\frac{1}{(m-1)!}\int_0^{\mathfrak{I}} (\mathfrak{I} - \tau)^{m-1} \cdot \left[u(\varphi, \mathfrak{I}) + \Lambda\left(\sum_{n=0}^{\infty} k^n F_n(\varphi, \mathfrak{I})\right) + \sum_{n=0}^{\infty} k^n h_n(F(\varphi, \mathfrak{I}))\right] d\tau, \quad (15)$$

where $T(\varphi, \mathfrak{I}) = H(\varphi, \mathfrak{I})$.

The terms, comparing with the same powers of k, produce results of many orders. The initial estimated of the approximation is $T(\varphi, \mathfrak{I})$, which is actually the Taylor series for the exact result of order β.

Using the aforementioned technique, we solved the fractional-order Whitham–Broer–Kaup equations in the Atangana–Baleanu and Caputo–Fabrizio senses using the LHPM.

4. Implementation of Caputo–Fabrizio Operator

Example 1. Let us consider the coupled system of fractional-order WBKEs in the CFC sense:

$$
\begin{aligned}
&{}^{CF}D_{\mathfrak{I}}^{\beta}\mu(\varphi,\mathfrak{I})+\mu(\varphi,\mathfrak{I})\frac{\partial\mu(\varphi,\mathfrak{I})}{\partial\varphi}+\frac{\partial\mu(\varphi,\mathfrak{I})}{\partial\varphi}+\frac{\partial\nu(\varphi,\mathfrak{I})}{\partial\varphi}=0,\\
&{}^{CF}D_{\mathfrak{I}}^{\beta}\nu(\varphi,\mathfrak{I})+\mu(\varphi,\mathfrak{I})\frac{\partial\nu(\varphi,\mathfrak{I})}{\partial\varphi}+\nu(\varphi,\mathfrak{I})\frac{\partial\mu(\varphi,\mathfrak{I})}{\partial\varphi}+3\frac{\partial^3\mu(\varphi,\mathfrak{I})}{\partial\varphi^3}-\frac{\partial^2\nu(\varphi,\mathfrak{I})}{\partial\varphi^2}=0,\quad 0<\beta\le 1,-1<\mathfrak{I}\le 1,-10\le\varphi\le 10,
\end{aligned}
\tag{16}
$$

under the initial conditions,

$$
\begin{aligned}
\mu(\varphi,0)&=\frac{1}{2}-8\tanh(-2\varphi),\\
\nu(\varphi,0)&=16-16\tanh^2(-2\varphi).
\end{aligned}
\tag{17}
$$

Using the Laplace transformation to equation (16), we obtain

$$
\begin{aligned}
\frac{s\mathscr{L}[\mu(\varphi,\mathfrak{I})](s)-\mu(\varphi,0)}{s+\beta(1-s)}&=-\mathscr{L}\left[\mu(\varphi,\mathfrak{I})\frac{\partial\mu(\varphi,\mathfrak{I})}{\partial\varphi}+\frac{\partial\mu(\varphi,\mathfrak{I})}{\partial\varphi}+\frac{\partial\nu(\varphi,\mathfrak{I})}{\partial\varphi}\right],\\
\frac{s\mathscr{L}[\nu(\varphi,\mathfrak{I})](s)-\nu(\varphi,0)}{s+\beta(1-s)}&=-\mathscr{L}\left[\mu(\varphi,\mathfrak{I})\frac{\partial\nu(\varphi,\mathfrak{I})}{\partial\varphi}+\nu(\varphi,\mathfrak{I})\frac{\partial\mu(\varphi,\mathfrak{I})}{\partial\varphi}+3\frac{\partial^3\mu(\varphi,\mathfrak{I})}{\partial\varphi^3}-\frac{\partial^2\nu(\varphi,\mathfrak{I})}{\partial\varphi^2}\right].
\end{aligned}
\tag{18}
$$

Simplify the above equation and use the initial conditions (17), and we obtain

$$
\begin{aligned}
\mathscr{L}[\mu(\varphi,\mathfrak{I})]&=\frac{\mu(\varphi,0)}{s}-\frac{s+\beta(1-s)}{s}\mathscr{L}\left[\mu(\varphi,\mathfrak{I})\frac{\partial\mu(\varphi,\mathfrak{I})}{\partial\varphi}+\frac{\partial\mu(\varphi,\mathfrak{I})}{\partial\varphi}+\frac{\partial\nu(\varphi,\mathfrak{I})}{\partial\varphi}\right],\\
\mathscr{L}[\nu(\varphi,\mathfrak{I})]&=\frac{\nu(\varphi,0)}{s}-\frac{s+\beta(1-s)}{s}\mathscr{L}\left[\mu(\varphi,\mathfrak{I})\frac{\partial\nu(\varphi,\mathfrak{I})}{\partial\varphi}+\nu(\varphi,\mathfrak{I})\frac{\partial\mu(\varphi,\mathfrak{I})}{\partial\varphi}+3\frac{\partial^3\mu(\varphi,\mathfrak{I})}{\partial\varphi^3}-\frac{\partial^2\nu(\varphi,\mathfrak{I})}{\partial\varphi^2}\right].
\end{aligned}
\tag{19}
$$

The inverse Laplace transformation is implemented to (19), and we obtain

$$
\begin{aligned}
\mu(\varphi,\mathfrak{I})&=\mu(\varphi,0)-\mathscr{L}^{-1}\left[\frac{s+\beta(1-s)}{s}\mathscr{L}\left\{\mu(\varphi,\mathfrak{I})\frac{\partial\mu(\varphi,\mathfrak{I})}{\partial\varphi}+\frac{\partial\mu(\varphi,\mathfrak{I})}{\partial\varphi}+\frac{\partial\nu(\varphi,\mathfrak{I})}{\partial\varphi}\right\}\right],\\
\nu(\varphi,\mathfrak{I})&=\nu(\varphi,0)-\mathscr{L}^{-1}\left[\frac{s+\beta(1-s)}{s}\mathscr{L}\left\{\mu(\varphi,\mathfrak{I})\frac{\partial\nu(\varphi,\mathfrak{I})}{\partial\varphi}+\nu(\varphi,\mathfrak{I})\frac{\partial\mu(\varphi,\mathfrak{I})}{\partial\varphi}+3\frac{\partial^3\mu(\varphi,\mathfrak{I})}{\partial\varphi^3}-\frac{\partial^2\nu(\varphi,\mathfrak{I})}{\partial\varphi^2}\right\}\right].
\end{aligned}
\tag{20}
$$

The LHPTM is used in (20), and we obtain

$$
\begin{aligned}
\sum_{n=0}^{\infty}\mu_n(\varphi,\mathfrak{I})&=\mu(\varphi,0)-p\mathscr{L}^{-1}\left[\frac{s+\beta(1-s)}{s}\mathscr{L}\left\{\sum_{n=0}^{\infty}p^nA_n+\frac{\partial}{\partial\varphi}\sum_{n=0}^{\infty}p^n\mu_n(\varphi,\mathfrak{I})+\frac{\partial}{\partial\varphi}\sum_{n=0}^{\infty}p^n\nu_n(\varphi,\mathfrak{I})\right\}\right],\\
\sum_{n=0}^{\infty}\nu_n(\varphi,\mathfrak{I})&=\nu(\varphi,0)-p\mathscr{L}^{-1}\left[\frac{s+\beta(1-s)}{s}\mathscr{L}\left\{\sum_{n=0}^{\infty}p^nB_n+\sum_{n=0}^{\infty}p^nC_n+3\frac{\partial^3}{\partial\varphi^3}\sum_{n=0}^{\infty}p^n\mu_n(\varphi,\mathfrak{I})-\frac{\partial^2}{\partial\varphi^2}\sum_{n=0}^{\infty}p^n\nu_n(\varphi,\mathfrak{I})\right\}\right].
\end{aligned}
\tag{21}
$$

The nonlinear can be found with the help of He's polynomial and can be defined as

$$\begin{aligned} A_0 &= \mu_0 \frac{\partial \mu_0}{\partial \varphi}, \\ A_1 &= \mu_0 \frac{\partial \mu_1}{\partial \varphi} + \mu_1 \frac{\partial \mu_0}{\partial \varphi}, \\ B_0 &= \mu_0 \frac{\partial \nu_0}{\partial \beta}, \\ B_1 &= \mu_0 \frac{\partial \nu_1}{\partial \beta} + \mu_1 \frac{\partial \nu_0}{\partial \beta}, \\ C_0 &= \nu_0 \frac{\partial \mu_0}{\partial \varphi}, \\ C_1 &= \nu_0 \frac{\partial \mu_1}{\partial \varphi} + \nu_1 \frac{\partial \mu_0}{\partial \varphi}. \end{aligned} \tag{22}$$

Comparing the coefficient of p, we have

$$\begin{aligned} p^0\colon \mu_0(\varphi, \mathfrak{I}) &= \mu(\varphi, 0) = \frac{1}{2} - 8\ \tanh(-2\varphi), \\ p^0\colon \nu_0(\varphi, \mathfrak{I}) &= \nu(\varphi, 0) = 16 - 16\tanh^2(-2\varphi), \\ p^1\colon \mu_1(\varphi, t) &= -\mathscr{L}^{-1}\left[\frac{s+\beta(1-s)}{s}\mathscr{L}\left\{A_0 + \frac{\partial}{\partial\varphi}\mu_0(\varphi, \mathfrak{I}) + \frac{\partial}{\partial\varphi}\nu_0(\varphi, \mathfrak{I})\right\}\right] = -8\ \sec h^2(-2\varphi)[\beta\mathfrak{I} + (1-\beta)], \\ p^1\colon \nu_1(\varphi, \mathfrak{I}) &= -p\mathscr{L}^{-1}\left[\frac{s+\beta(1-s)}{s}\mathscr{L}\left\{B_0 + C_0 + 3\frac{\partial^3}{\partial\varphi^3}\mu_0(\varphi, \mathfrak{I}) - \frac{\partial^2}{\partial\varphi^2}\nu_0(\varphi, \mathfrak{I})\right\}\right] \\ &= -32\ \sec h^2(-2\varphi)\tanh(-2\varphi)[\beta\mathfrak{I} + (1-\beta)], \\ p^2\colon \mu_2(\varphi, \mathfrak{I}) &= -\mathscr{L}^{-1}\left[\frac{s+\beta(1-s)}{s}\mathscr{L}\left\{A_1 + \frac{\partial}{\partial\varphi}\mu_1(\varphi, \mathfrak{I}) + \frac{\partial}{\partial\varphi}\nu_1(\varphi, \mathfrak{I})\right\}\right] \\ &= -16\ \sec h^2(-2\varphi)\Big(4\ \sec h^2(-2\varphi) - 8\ \tanh^2(-2\varphi) + 3\ \tanh(-2\varphi)\Big)\left[(1-\beta)^2 + 2\beta(1-\beta)\mathfrak{I} + \frac{\beta^2\mathfrak{I}^2}{2}\right], \\ p^2\colon \nu_2(\varphi, \mathfrak{I}) &= -p\mathscr{L}^{-1}\left[\frac{s+\beta(1-s)}{s}\mathscr{L}\left\{B_1 + C_1 + 3\frac{\partial^3}{\partial\varphi^3}\mu_1(\varphi, \mathfrak{I}) - \frac{\partial^2}{\partial\varphi^2}\nu_1(\varphi, \mathfrak{I})\right\}\right] \\ &= -32\ \sec h^2(-2\varphi)\Big\{40\ \sec h^2(-2\varphi)\tanh(-2\varphi) + 96\ \tanh(-2\varphi) - 2\ \tanh^2(-2\varphi) \\ &\quad -32\ \tanh^3(-2\varphi) - 25\ \sec h^2(-2\varphi)\Big\}\left[(1-\beta)^2 + 2\beta(1-\beta)\mathfrak{I} + \frac{\beta^2\mathfrak{I}^2}{2}\right], \\ &\ \vdots\ . \end{aligned} \tag{23}$$

We can calculate few terms of (16) which can be written as

$$\mu(\varphi,\mathfrak{I}) = \mu_0(\varphi,\mathfrak{I}) + \mu_1(\varphi,\mathfrak{I}) + \mu_2(\varphi,\mathfrak{I}) + \cdots,$$
$$\nu(\varphi,\mathfrak{I}) = \nu_0(\varphi,\mathfrak{I}) + \nu_1(\varphi,\mathfrak{I}) + \nu_2(\varphi,\mathfrak{I}) + \cdots,$$
$$\begin{aligned}\mu(\varphi,\mathfrak{I}) = {} & \frac{1}{2} - 8\tanh(-2\varphi) - 8\sec h^2(-2\varphi)[\beta\mathfrak{I} + (1-\beta)] - 16\sec h^2(-2\varphi) \\ & \times\left(4\sec h^2(-2\varphi) - 8\tanh^2(-2\varphi) + 3\tanh(-2\varphi)\right)\left[(1-\beta)^2 + 2\beta(1-\beta)\mathfrak{I} + \frac{\beta^2\mathfrak{I}^2}{2}\right] + \cdots,\end{aligned} \tag{24}$$
$$\begin{aligned}\nu(\varphi,\mathfrak{I}) = {} & 16 - 16\tanh^2(-2\varphi) - 8\sec h^2(-2\varphi)[\beta\mathfrak{I} + (1-\beta)] - 32\sec h^2(-2\varphi)\left\{40\sec h^2(-2\varphi)\tanh(-2\varphi)\right. \\ & \left. +96\tanh(-2\varphi) - 2\tanh^2(-2\varphi) - 32\tanh^3(-2\varphi) - 25\sec h^2(-2\varphi)\right\} \\ & \times\left[(1-\beta)^2 + 2\beta(1-\beta)\mathfrak{I} + \frac{\beta^2\mathfrak{I}^2}{2}\right] + \cdots.\end{aligned}$$

The exact solution of (16) is

$$\begin{aligned}\mu(\varphi,\mathfrak{I}) &= \frac{1}{2} - 8\tanh\left\{-2\left(\varphi - \frac{\mathfrak{I}}{2}\right)\right\}, \\ \nu(\varphi,\mathfrak{I}) &= 16 - 16\tanh^2\left\{-2\left(\varphi - \frac{\mathfrak{I}}{2}\right)\right\}.\end{aligned} \tag{25}$$

Figure 1 shows the actual and approximate solutions of $\mu(\varphi,\mathfrak{I})$ at $\beta = 1$, and Figure 2 shows the actual and approximate solutions of $\nu(\varphi,\mathfrak{I})$ at $\beta = 1$. Figures 3 and 4 show that the first graph has a different fractional order with respect to φ and the second graph has a different fractional order with respect to $\mathfrak{I}$ of Example 1. Tables 1 and 2 show the different fractional-order β of $\mu(\varphi,\mathfrak{I})$ and $\nu(\varphi,\mathfrak{I})$. Tables 3 and 4 show the comparisons with different methods.

Example 2. Let us consider the coupled system of fractional-order WBKEs in the CFC sense:

$$\begin{aligned}{}^{CF}D^{\beta}_{\mathfrak{I}}\mu(\varphi,\mathfrak{I}) + \mu(\varphi,\mathfrak{I})\frac{\partial\mu(\varphi,\mathfrak{I})}{\partial\varphi} + \frac{1}{2}\frac{\partial\mu(\varphi,\mathfrak{I})}{\partial\varphi} + \frac{\partial\nu(\varphi,\mathfrak{I})}{\partial\varphi} &= 0, \\ {}^{CF}D^{\beta}_{\mathfrak{I}}\nu(\varphi,\mathfrak{I}) + \mu(\varphi,\mathfrak{I})\frac{\partial\nu(\varphi,\mathfrak{I})}{\partial\varphi} + \nu(\varphi,\mathfrak{I})\frac{\partial\mu(\varphi,\mathfrak{I})}{\partial\varphi} - \frac{1}{2}\frac{\partial^2\nu(\varphi,\mathfrak{I})}{\partial\varphi^2} &= 0, \quad 0<\beta\le 1, 0<\mathfrak{I}\le 1, -100\le\varphi\le 100,\end{aligned} \tag{26}$$

under the initial conditions,

$$\begin{aligned}\mu(\varphi,0) &= \xi - \kappa\coth[\kappa(\varphi+\theta)], \\ \nu(\varphi,0) &= -\kappa^2\operatorname{cosech}^2[\kappa(\varphi+\theta)].\end{aligned} \tag{27}$$

Using the Laplace transformation to equation (26), we obtain

$$\begin{aligned}\frac{s\mathscr{L}[\mu(\varphi,\mathfrak{I})](s) - \mu(\varphi,0)}{s+\beta(1-s)} &= -\mathscr{L}\left[\mu(\varphi,\mathfrak{I})\frac{\partial\mu(\varphi,\mathfrak{I})}{\partial\varphi} + \frac{1}{2}\frac{\partial\mu(\varphi,\mathfrak{I})}{\partial\varphi} + \frac{\partial\nu(\varphi,\mathfrak{I})}{\partial\varphi}\right], \\ \frac{s\mathscr{L}[\nu(\varphi,\mathfrak{I})](s) - \nu(\varphi,0)}{s+\beta(1-s)} &= -\mathscr{L}\left[\mu(\varphi,\mathfrak{I})\frac{\partial\nu(\varphi,\mathfrak{I})}{\partial\varphi} + \nu(\varphi,\mathfrak{I})\frac{\partial\mu(\varphi,\mathfrak{I})}{\partial\varphi} - \frac{1}{2}\frac{\partial^2\nu(\varphi,\mathfrak{I})}{\partial\varphi^2}\right].\end{aligned} \tag{28}$$

Simplify the above equation and use the initial conditions (27), and we obtain

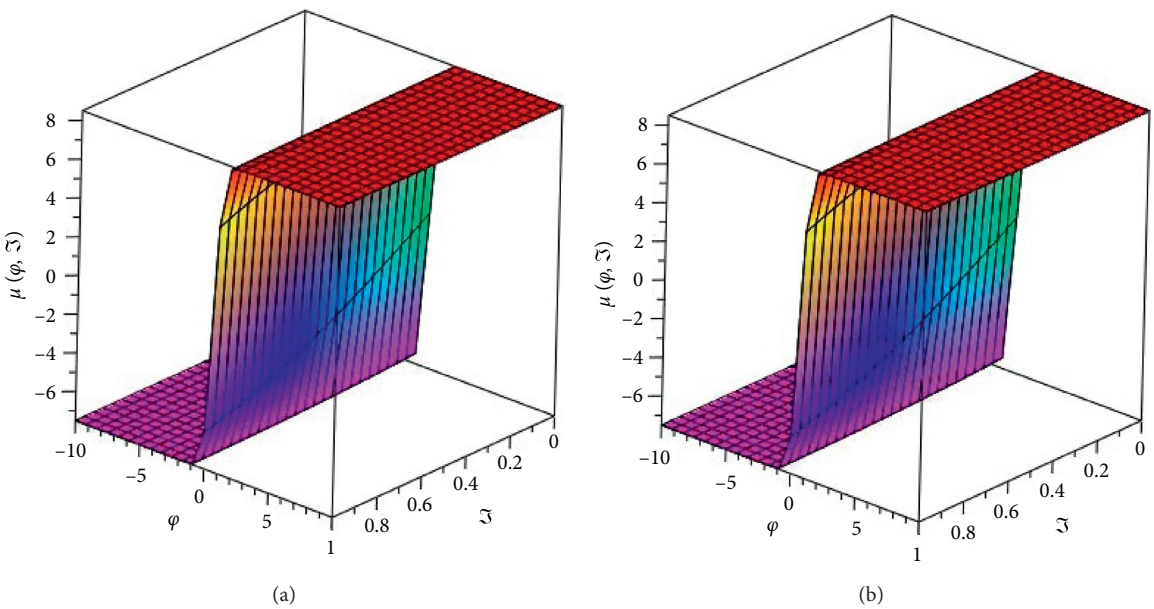

Figure 1: The exact and analytical solution with respect to the Caputo–Fabrizio operator of $\mu(\varphi, \mathfrak{I})$ at $\beta = 1$ of Example 1.

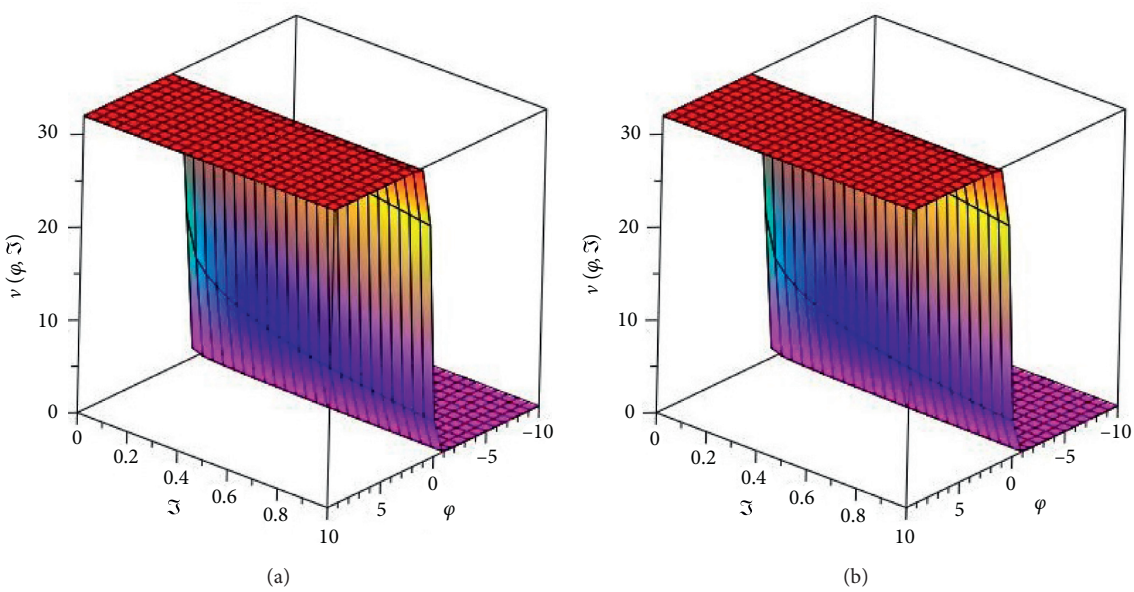

Figure 2: The exact and analytical solution with respect to the Caputo–Fabrizio operator of $\nu(\varphi, \mathfrak{I})$ at $\beta = 1$ of Example 1.

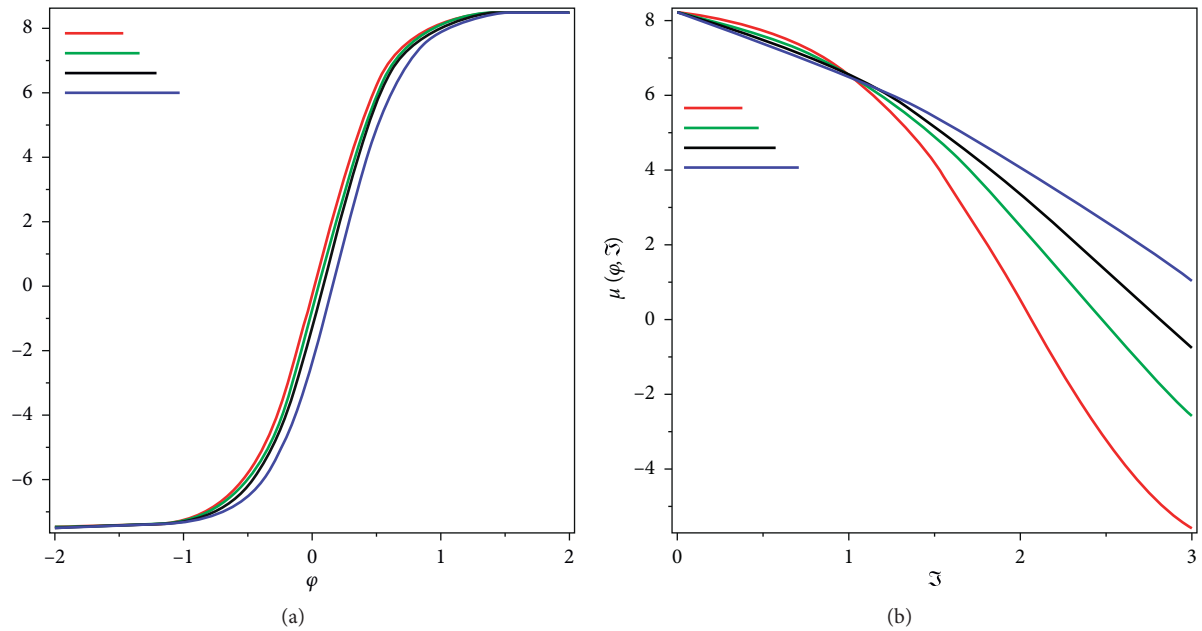

Figure 3: The different fractional-order solution with respect to the Caputo–Fabrizio operator of $\mu(\varphi, \mathfrak{I})$ at β of Example 1.

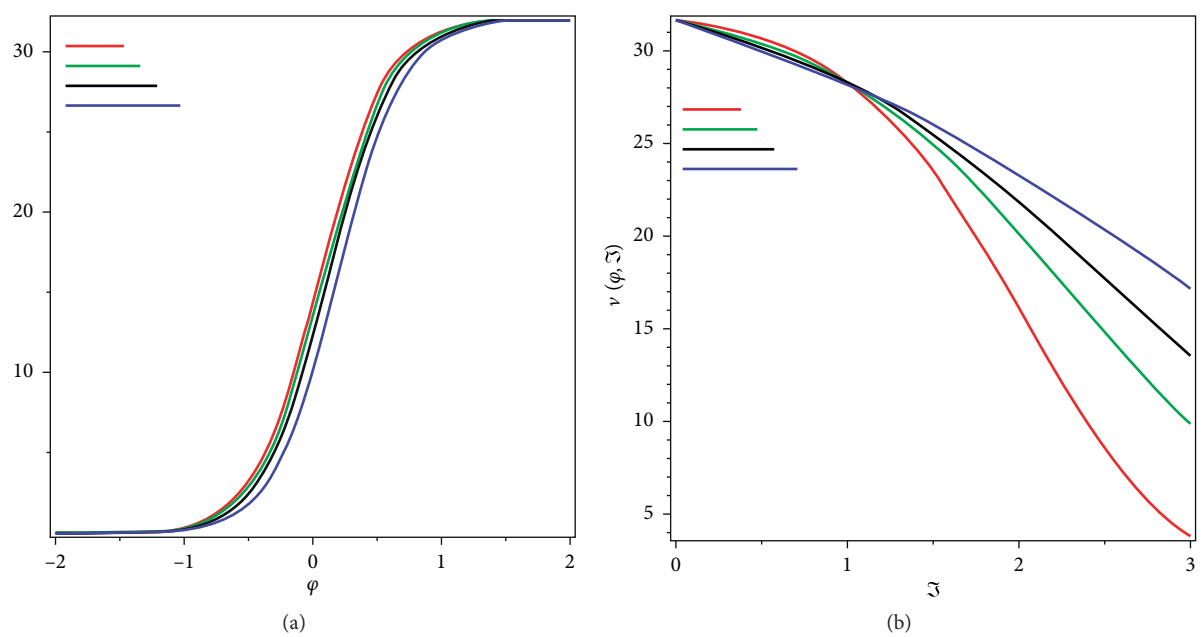

Figure 4: The different fractional-order solution with respect to the Caputo–Fabrizio operator of $\nu(\varphi, \mathfrak{I})$ at β of Example 1.

Table 1: HPTM for the approximate solution of Example 1.

$(\varphi, \mathfrak{I})$	$\mu(\varphi, \mathfrak{I})$ at $\beta = 0.5$	$\mu(\varphi, \mathfrak{I})$ at $\beta = 0.75$	$\mu(\varphi, \mathfrak{I})$ at $\beta = 1$	Exact solution
(0.1, 0.1)	−0.500817	−0.500795	−0.500782	−0.500782
(0.1, 0.3)	−0.500853	−0.500829	−0.50081	−0.50081
(0.1, 0.5)	−0.500878	−0.500857	−0.500837	−0.500837
(0.2, 0.1)	−0.49812	−0.498098	−0.498085	−0.498085
(0.2, 0.3)	−0.498154	−0.498131	−0.498112	−0.498112
(0.2, 0.5)	−0.498178	−0.498158	−0.498139	−0.498139
(0.3, 0.1)	−0.495491	−0.49547	−0.495458	−0.495458
(0.3, 0.3)	−0.495525	−0.495502	−0.495484	−0.495484
(0.3, 0.5)	−0.495548	−0.495529	−0.49551	−0.49551
(0.4, 0.1)	−0.49293	−0.492909	−0.492897	−0.492897
(0.4, 0.3)	−0.492963	−0.49294	−0.492922	−0.492922
(0.4, 0.5)	−0.492985	−0.492966	−0.492948	−0.492948
(0.5, 0.1)	−0.490433	−0.490413	−0.490401	−0.490401
(0.5, 0.3)	−0.490465	−0.490443	−0.490426	−0.490426
(0.5, 0.5)	−0.490487	−0.490469	−0.490451	−0.490451

Table 2: HPTM for the approximate solution of Example 1.

$(\varphi, \mathfrak{I})$	$\nu(\varphi, \mathfrak{I})$ at $\beta = 0.5$	$\nu(\varphi, \mathfrak{I})$ at $\beta = 0.75$	$\nu(\varphi, \mathfrak{I})$ at $\beta = 1$	Exact solution
(0.1, 0.1)	−0.0939215	−0.0939015	−0.09389	−0.09389
(0.1, 0.3)	−0.0939536	−0.0939319	−0.0939146	−0.0939146
(0.1, 0.5)	−0.0939757	−0.0939571	−0.0939391	−0.0939391
(0.2, 0.1)	−0.0915064	−0.091487	−0.0914759	−0.0914759
(0.2, 0.3)	−0.0915375	−0.0915165	−0.0914997	−0.0914997
(0.2, 0.5)	−0.0915589	−0.0915409	−0.0915235	−0.0915235
(0.3, 0.1)	−0.0891657	−0.0891469	−0.0891361	−0.0891361
(0.3, 0.3)	−0.0891958	−0.0891754	−0.0891592	−0.0891592
(0.3, 0.5)	−0.0892166	−0.0891992	−0.0891822	−0.0891822
(0.4, 0.1)	−0.0868965	−0.0868782	−0.0868678	−0.0868678
(0.4, 0.3)	−0.0869257	−0.0869059	−0.0868901	−0.08688901
(0.4, 0.5)	−0.0869458	−0.0869289	−0.0869125	−0.0869125
(0.5, 0.1)	−0.0846961	−0.0846784	−0.0846683	−0.0846683
(0.5, 0.3)	−0.0847244	−0.0847052	−0.0846899	−0.0846899
(0.5, 0.5)	−0.0847439	−0.0847275	−0.0847116	−0.0847116

$$\begin{aligned}
\mathscr{L}[\mu(\varphi, \mathfrak{I})] &= \frac{\mu(\varphi, 0)}{s} - \frac{s + \beta(1-s)}{s}\mathscr{L}\left[\mu(\varphi, \mathfrak{I})\frac{\partial \mu(\varphi, \mathfrak{I})}{\partial \varphi} + \frac{1}{2}\frac{\partial \mu(\varphi, \mathfrak{I})}{\partial \varphi} + \frac{\partial \nu(\varphi, \mathfrak{I})}{\partial \varphi}\right], \\
\mathscr{L}[\nu(\varphi, \mathfrak{I})] &= \frac{\nu(\varphi, 0)}{s} - \frac{s + \beta(1-s)}{s}\mathscr{L}\left[\mu(\varphi, \mathfrak{I})\frac{\partial \nu(\varphi, \mathfrak{I})}{\partial \varphi} + \nu(\varphi, \mathfrak{I})\frac{\partial \mu(\varphi, \mathfrak{I})}{\partial \varphi} - \frac{1}{2}\frac{\partial^2 \nu(\varphi, \mathfrak{I})}{\partial \varphi^2}\right].
\end{aligned} \tag{29}$$

The inverse Laplace transformation is implemented to (29), and we obtain

$$\begin{aligned}
\mu(\varphi, \mathfrak{I}) &= \mu(\varphi, 0) - \mathscr{L}^{-1}\left[\frac{s + \beta(1-s)}{s}\mathscr{L}\left\{\mu(\varphi, \mathfrak{I})\frac{\partial \mu(\varphi, \mathfrak{I})}{\partial \varphi} + \frac{1}{2}\frac{\partial \mu(\varphi, \mathfrak{I})}{\partial \varphi} + \frac{\partial \nu(\varphi, \mathfrak{I})}{\partial \varphi}\right\}\right], \\
\nu(\varphi, \mathfrak{I}) &= \nu(\varphi, 0) - \mathscr{L}^{-1}\left[\frac{s + \beta(1-s)}{s}\mathscr{L}\left\{\mu(\varphi, \mathfrak{I})\frac{\partial \nu(\varphi, \mathfrak{I})}{\partial \varphi} + \nu(\varphi, \mathfrak{I})\frac{\partial \mu(\varphi, \mathfrak{I})}{\partial \varphi} - \frac{1}{2}\frac{\partial^2 \nu(\varphi, \mathfrak{I})}{\partial \varphi^2}\right\}\right].
\end{aligned} \tag{30}$$

The LHPTM is used in (30), and we obtain

Table 3: HPTM for the approximate solution of Example 1.

$(\varphi, \mathfrak{I})$	Absolute error of ADM	Absolute error of VIM	Absolute error of OHAM	Absolute error HPTM
(0.1, 0.1)	1.04892×10^{-4}	1.23033×10^{-4}	1.07078×10^{-4}	1.67111×10^{-12}
(0.1, 0.3)	9.64474×10^{-5}	3.69597×10^{-4}	3.04565×10^{-4}	4.51196×10^{-11}
(0.1, 0.5)	8.88312×10^{-5}	6.16873×10^{-4}	4.81303×10^{-4}	2.08888×10^{-10}
(0.2, 0.1)	4.25408×10^{-4}	1.19869×10^{-4}	1.04388×10^{-4}	1.57879×10^{-12}
(0.2, 0.3)	3.91098×10^{-4}	3.60098×10^{-4}	2.97260×10^{-4}	4.26227×10^{-11}
(0.2, 0.5)	3.60161×10^{-4}	6.01006×10^{-4}	4.70138×10^{-4}	1.97328×10^{-10}
(0.3, 0.1)	9.71922×10^{-4}	1.16789×10^{-4}	1.01776×10^{-4}	1.49181×10^{-12}
(0.3, 0.3)	8.93309×10^{-4}	3.50866×10^{-4}	2.90150×10^{-4}	4.02799×10^{-11}
(0.3, 0.5)	8.22452×10^{-4}	5.85610×10^{-4}	4.59590×10^{-4}	1.86481×10^{-10}
(0.4, 0.1)	1.75596×10^{-3}	1.13829×10^{-4}	9.92418×10^{-5}	1.41043×10^{-12}
(0.4, 0.3)	1.61430×10^{-3}	3.41948×10^{-4}	2.83229×10^{-4}	3.80803×10^{-11}
(0.4, 0.5)	1.48578×10^{-3}	5.70710×10^{-4}	4.49118×10^{-4}	1.76298×10^{-10}
(0.5, 0.1)	2.79519×10^{-3}	1.10936×10^{-4}	9.67808×10^{-4}	1.33388×10^{-12}
(0.5, 0.3)	2.56714×10^{-3}	3.33274×10^{-4}	2.76492×10^{-4}	3.60145×10^{-11}
(0.5, 0.5)	2.36184×10^{-3}	5.56235×10^{-4}	4.38895×10^{-4}	1.66734×10^{-10}

Table 4: Comparison of different methods for the approximate solution of Example 1.

$(\varphi, \mathfrak{I})$	Absolute error of ADM	Absolute error of VIM	Absolute error of OHAM	Absolute error HPTM
(0.1, 0.1)	6.41419×10^{-3}	1.10430×10^{-4}	5.86860×10^{-5}	3.28081×10^{-12}
(0.1, 0.3)	5.99783×10^{-3}	3.31865×10^{-4}	3.04565×10^{-4}	8.85812×10^{-11}
(0.1, 0.5)	5.61507×10^{-3}	5.54071×10^{-4}	3.08812×10^{-4}	4.10099×10^{-10}
(0.2, 0.1)	1.33181×10^{-2}	1.07016×10^{-4}	5.56884×10^{-5}	3.07768×10^{-12}
(0.2, 0.3)	1.24441×10^{-2}	3.21601×10^{-4}	2.97260×10^{-4}	8.30963×10^{-11}
(0.2, 0.5)	1.16416×10^{-2}	5.36927×10^{-4}	2.92626×10^{-4}	3.84706×10^{-10}
(0.3, 0.1)	2.07641×10^{-2}	1.03737×10^{-4}	5.28609×10^{-5}	2.88849×10^{-12}
(0.3, 0.3)	1.93852×10^{-2}	3.11737×10^{-4}	2.90150×10^{-4}	7.79908×10^{-11}
(0.3, 0.5)	1.81209×10^{-2}	5.20447×10^{-4}	2.77382×10^{-4}	3.6107×10^{-10}
(0.4, 0.1)	2.88100×10^{-2}	1.00579×10^{-4}	5.01929×10^{-5}	2.71246×10^{-12}
(0.4, 0.3)	2.68724×10^{-2}	3.02245×10^{-4}	2.83229×10^{-4}	7.32356×10^{-11}
(0.4, 0.5)	2.50985×10^{-2}	5.04593×10^{-4}	2.63019×10^{-4}	3.39055×10^{-10}
(0.5, 0.1)	3.75193×10^{-2}	9.75385×10^{-5}	4.76741×10^{-5}	2.54828×10^{-12}
(0.5, 0.3)	3.49617×10^{-2}	2.93107×10^{-4}	2.76492×10^{-4}	6.88039×10^{-11}
(0.5, 0.5)	3.26239×10^{-2}	4.89335×10^{-4}	2.49480×10^{-4}	3.18537×10^{-10}

$$\begin{aligned}
\sum_{n=0}^{\infty} \mu_n(\varphi, \mathfrak{I}) &= \mu(\varphi, 0) - p\mathscr{L}^{-1}\left[\frac{s+\beta(1-s)}{s}\mathscr{L}\left\{\sum_{n=0}^{\infty} p^n A_n + \frac{1}{2}\frac{\partial}{\partial\varphi}\sum_{n=0}^{\infty} p^n \mu_n(\varphi, \mathfrak{I}) + \frac{\partial}{\partial\varphi}\sum_{n=0}^{\infty} p\nu_n(\varphi, \mathfrak{I})\right\}\right], \\
\sum_{n=0}^{\infty} \nu_n(\varphi, \mathfrak{I}) &= \nu(\varphi, 0) - p\mathscr{L}^{-1}\left[\frac{s+\beta(1-s)}{s}\mathscr{L}\left\{\sum_{n=0}^{\infty} p^n B_m + \sum_{n=0}^{\infty} p^n C_n - \frac{1}{2}\frac{\partial^2}{\partial\varphi^2}\sum_{n=0}^{\infty} p^n \nu_n(\varphi, \mathfrak{I})\right\}\right].
\end{aligned} \tag{31}$$

The nonlinear can be found with the help of He's polynomial and can be defined as

$$
\begin{aligned}
A_0 &= \mu_0 \frac{\partial \mu_0}{\partial \varphi}, \\
A_1 &= \mu_0 \frac{\partial \mu_1}{\partial \varphi} + \mu_1 \frac{\partial \mu_0}{\partial \varphi}, \\
B_0 &= \mu_0 \frac{\partial \nu_0}{\partial \beta}, \\
B_1 &= \mu_0 \frac{\partial \nu_1}{\partial \beta} + \mu_1 \frac{\partial \nu_0}{\partial \beta}, \\
C_0 &= \nu_0 \frac{\partial \mu_0}{\partial \varphi}, \\
C_1 &= \nu_0 \frac{\partial \mu_1}{\partial \varphi} + \nu_1 \frac{\partial \mu_0}{\partial \varphi}.
\end{aligned}
\tag{32}
$$

Comparing the coefficient of p, we have

$$
\begin{aligned}
p^0\colon\ \mu_0(\varphi, \mathfrak{I}) &= \mu(\varphi, 0) = \xi - \kappa \coth[\kappa(\varphi + \theta)], \\
p^0\colon\ \nu_0(\varphi, \mathfrak{I}) &= \nu(\varphi, 0) = -\kappa^2 \operatorname{cosech}^2[\kappa(\varphi + \theta)], \\
p^1\colon\ \mu_1(\varphi, \mathfrak{I}) &= -\mathscr{L}^{-1}\left[\frac{s + \beta(1-s)}{s} \mathscr{L}\left\{A_0 + \frac{1}{2}\frac{\partial}{\partial \varphi}\mu_0(\varphi, \mathfrak{I}) + \frac{\partial}{\partial \varphi}\nu_0(\varphi, \mathfrak{I})\right\}\right] \\
&= -\xi\kappa^2 \operatorname{cosech}^2[\kappa(\varphi + \theta)][\beta\mathfrak{I} + (1-\beta)], \\
p^1\colon\ \nu_1(\varphi, \mathfrak{I}) &= -p\mathscr{L}^{-1}\left[\frac{s + \beta(1-s)}{s} \mathscr{L}\left\{B_0 + C_0 - \frac{1}{2}\frac{\partial^2}{\partial \varphi^2}\nu_0(\varphi, \mathfrak{I})\right\}\right] \\
&= -\xi\kappa^2 \operatorname{cosech}^2[\kappa(\varphi + \theta)] \coth[\kappa(\varphi + \theta)][\beta\mathfrak{I} + (1-\beta)], \\
p^2\colon\ \mu_2(\varphi, \mathfrak{I}) &= -\mathscr{L}^{-1}\left[\frac{s + \beta(1-s)}{s} \mathscr{L}\left\{A_1 + \frac{1}{2}\frac{\partial}{\partial \varphi}\mu_1(\varphi, \mathfrak{I}) + \frac{\partial}{\partial \varphi}\nu_1(\varphi, \mathfrak{I})\right\}\right] \\
&= -\xi\kappa^4 \operatorname{cosech}^2[\kappa(\varphi + \theta)]\left(3\coth^2([\kappa(\varphi + \theta)] - 1)\right)\left[(1-\beta)^2 + 2\beta(1-\beta)\mathfrak{I} + \frac{\beta^2\mathfrak{I}^2}{2}\right] \\
&\quad + 2\xi^2\kappa^5 \operatorname{cosech}^2[\kappa(\varphi + \theta)]\left(3\beta\left(-2\beta + 1 + \beta^2\right)\mathfrak{I} + \frac{\beta^3\mathfrak{I}^3}{6} - \frac{3\beta^2(\beta-1)\mathfrak{I}^2}{2} + 3\beta^2 - 3\beta + 1 - \beta^3\right), \\
p^2\colon\ \nu_2(\varphi, \mathfrak{I}) &= -p\mathscr{L}^{-1}\left[\frac{s + \beta(1-s)}{s} \mathscr{L}\left\{B_1 + C_1 - \frac{1}{2}\frac{\partial^2}{\partial \varphi^2}\nu_1(\varphi, \mathfrak{I})\right\}\right] \\
&= 2\xi\kappa^5 \operatorname{cosech}^2[\kappa(\varphi + \theta)]\left\{\xi\kappa \operatorname{cosech}^2\left(3\coth^2([\kappa(\varphi + \theta)] - 1)\right) + 2\xi\kappa \operatorname{cosech}^2 \coth^2([\kappa(\varphi + \theta)])\right\} \\
&\quad \times\left(3\beta\left(-2\beta + 1 + \beta^2\right)\mathfrak{I} + \frac{\beta^3\mathfrak{I}^3}{6} - \frac{3\beta^2(\beta-1)\mathfrak{I}^2}{2} + 3\beta^2 - 3\beta + 1 - \beta^3\right) \\
&\quad - 2\xi\coth\left(3\operatorname{cosech}^2([\kappa(\varphi + \theta)] - 1)\right)\left[(1-\beta)^2 + 2\beta(1-\beta)\mathfrak{I} + \frac{\beta^2\mathfrak{I}^2}{2}\right], \\
&\quad \vdots
\end{aligned}
\tag{33}
$$

We can calculate few terms of (26) which can be written as

$$\begin{aligned}
\mu(\varphi,\mathfrak{I}) &= \mu_0(\varphi,\mathfrak{I}) + \mu_1(\varphi,\mathfrak{I}) + \mu_2(\varphi,\mathfrak{I}) + \cdots,\\
\nu(\varphi,\mathfrak{I}) &= \nu_0(\varphi,\mathfrak{I}) + \nu_1(\varphi,\mathfrak{I}) + \nu_2(\varphi,\mathfrak{I}) + \cdots,\\
\mu(\varphi,\mathfrak{I}) &= \xi - \kappa\coth[\kappa(\varphi+\theta)] - \xi\kappa^2\operatorname{cosech}^2[\kappa(\varphi+\theta)][\beta\mathfrak{I} + (1-\beta)]\\
&\quad - \xi\kappa^4\operatorname{cosech}^2[\kappa(\varphi+\theta)]\left(3\coth^2([\kappa(\varphi+\theta)]-1)\right)\left[(1-\beta)^2 + 2\beta(1-\beta)\mathfrak{I} + \frac{\beta^2\mathfrak{I}^2}{2}\right]\\
&\quad + 2\xi^2\kappa^5\operatorname{cosech}^2[\kappa(\varphi+\theta)]\left(3\beta\left(-2\beta+1+\beta^2\right)\mathfrak{I} + \frac{\beta^3\mathfrak{I}^3}{6} - \frac{3\beta^2(\beta-1)\mathfrak{I}^2}{2} + 3\beta^2 - 3\beta + 1 - \beta^3\right) + \cdots,
\end{aligned} \tag{34}$$

$$\begin{aligned}
\nu(\varphi,\mathfrak{I}) &= -\kappa^2\operatorname{cosech}^2[\kappa(\varphi+\theta)] - \xi\kappa^2\operatorname{cosech}^2[\kappa(\varphi+\theta)]\coth[\kappa(\varphi+\theta)][\beta\mathfrak{I} + (1-\beta)]\\
&\quad + 2\xi\kappa^5\cos ech^2[\kappa(\varphi+\theta)]\left[\left\{\xi\kappa\operatorname{cosech}^2\left(3\coth^2([\kappa(\varphi+\theta)]-1)\right) + 2\xi\kappa\operatorname{cosech}^2\coth^2([\kappa(\varphi+\theta)])\right\}\right.\\
&\quad \times\left(3\beta\left(-2\beta+1+\beta^2\right)\mathfrak{I} + \frac{\beta^3\mathfrak{I}^3}{6} - \frac{3\beta^2(\beta-1)\mathfrak{I}^2}{2} + 3\beta^2 - 3\beta + 1 - \beta^3\right)\\
&\quad \left. -2\xi\coth\left(3\operatorname{cosech}^2([\kappa(\varphi+\theta)]-1)\right)\left[(1-\beta)^2 + 2\beta(1-\beta)\mathfrak{I} + \frac{\beta^2\mathfrak{I}^2}{2}\right]\right] + \cdots.
\end{aligned}$$

The exact solution of (26) is

$$\begin{aligned}
\mu(\varphi,\mathfrak{I}) &= \xi - \kappa\coth[\kappa(\varphi+\theta-\xi\mathfrak{I})],\\
\nu(\varphi,\mathfrak{I}) &= -\kappa^2\operatorname{cosech}^2[\kappa(\varphi+\theta-\xi\mathfrak{I})].
\end{aligned} \tag{35}$$

5. Implementation of Atangana–Baleanu Operator

Example 3. Let us consider the coupled system of fractional-order WBKEs in the ABC sense:

$$\begin{aligned}
&{}^{AB}D_{\mathfrak{I}}^{\beta}\mu(\varphi,\mathfrak{I}) + \mu(\varphi,\mathfrak{I})\frac{\partial\mu(\varphi,\mathfrak{I})}{\partial\varphi} + \frac{\partial\mu(\varphi,\mathfrak{I})}{\partial\varphi} + \frac{\partial\nu(\varphi,\mathfrak{I})}{\partial\varphi} = 0,\\
&{}^{AB}D_{\mathfrak{I}}^{\beta}\nu(\varphi,\mathfrak{I}) + \mu(\varphi,\mathfrak{I})\frac{\partial\nu(\varphi,\mathfrak{I})}{\partial\varphi} + \nu(\varphi,\mathfrak{I})\frac{\partial\mu(\varphi,\mathfrak{I})}{\partial\varphi} + 3\frac{\partial^3\mu(\varphi,\mathfrak{I})}{\partial\varphi^3} - \frac{\partial^2\nu(\varphi,\mathfrak{I})}{\partial\varphi^2} = 0, \quad 0<\beta\le 1, -1<\mathfrak{I}\le 1, -10\le\varphi\le 10,
\end{aligned} \tag{36}$$

under the initial conditions,

$$\mu(\varphi,0)=\frac{1}{2}-8\tanh(-2\varphi),$$
$$\nu(\varphi,0)=16-16\tanh^2(-2\varphi). \tag{37}$$

Using the Laplace transformation to (36), we obtain

$$\frac{B(\beta)}{1-\beta}\frac{s\mathscr{L}[\mu(\varphi,\mathfrak{I})](s)-s^{\beta-1}\mu(\varphi,0)}{s+(\beta/(1-\beta))}=-\mathscr{L}\left[\mu(\varphi,\mathfrak{I})\frac{\partial\mu(\varphi,\mathfrak{I})}{\partial\varphi}+\frac{\partial\mu(\varphi,\mathfrak{I})}{\partial\varphi}+\frac{\partial\nu(\varphi,\mathfrak{I})}{\partial\varphi}\right],$$
$$\frac{B(\beta)}{1-\beta}\frac{s\mathscr{L}[\nu(\varphi,\mathfrak{I})](s)-s^{\beta-1}\nu(\varphi,0)}{s+(\beta/(1-\beta))}=-\mathscr{L}\left[\mu(\varphi,\mathfrak{I})\frac{\partial\nu(\varphi,\mathfrak{I})}{\partial\varphi}+\nu(\varphi,\mathfrak{I})\frac{\partial\mu(\varphi,\mathfrak{I})}{\partial\varphi}+3\frac{\partial^3\mu(\varphi,\mathfrak{I})}{\partial\varphi^3}-\frac{\partial^2\nu(\varphi,\mathfrak{I})}{\partial\varphi^2}\right]. \tag{38}$$

Simplify the above equation and use the initial conditions (37), and we obtain

$$\mathscr{L}[\mu(\varphi,\mathfrak{I})]=\frac{\mu(\varphi,0)}{s}-\frac{(1-\beta)s^{\beta}+\beta}{B(\beta)s^{\beta}}\mathscr{L}\left[\mu(\varphi,\mathfrak{I})\frac{\partial\mu(\varphi,\mathfrak{I})}{\partial\varphi}+\frac{\partial\mu(\varphi,\mathfrak{I})}{\partial\varphi}+\frac{\partial\nu(\varphi,\mathfrak{I})}{\partial\varphi}\right],$$
$$\mathscr{L}[\nu(\varphi,\mathfrak{I})]=\frac{\nu(\varphi,0)}{s}-\frac{(1-\beta)s^{\beta}+\beta}{B(\beta)s^{\beta}}\mathscr{L}\left[\mu(\varphi,\mathfrak{I})\frac{\partial\nu(\varphi,\mathfrak{I})}{\partial\varphi}+\nu(\varphi,\mathfrak{I})\frac{\partial\mu(\varphi,\mathfrak{I})}{\partial\varphi}+3\frac{\partial^3\mu(\varphi,\mathfrak{I})}{\partial\varphi^3}-\frac{\partial^2\nu(\varphi,\mathfrak{I})}{\partial\varphi^2}\right]. \tag{39}$$

The inverse Laplace transformation implement to (39), we obtain

$$\mu(\varphi,\mathfrak{I})=\mu(\varphi,0)-\mathscr{L}^{-1}\left[\frac{(1-\beta)s^{\beta}+\beta}{B(\beta)s^{\beta}}\mathscr{L}\left\{\mu(\varphi,\mathfrak{I})\frac{\partial\mu(\varphi,\mathfrak{I})}{\partial\varphi}+\frac{\partial\mu(\varphi,\mathfrak{I})}{\partial\varphi}+\frac{\partial\nu(\varphi,\mathfrak{I})}{\partial\varphi}\right\}\right],$$
$$\nu(\varphi,\mathfrak{I})=\nu(\varphi,0)-\mathscr{L}^{-1}\left[\frac{(1-\beta)s^{\beta}+\beta}{B(\beta)s^{\beta}}\mathscr{L}\left\{\mu(\varphi,\mathfrak{I})\frac{\partial\nu(\varphi,\mathfrak{I})}{\partial\varphi}+\nu(\varphi,\mathfrak{I})\frac{\partial\mu(\varphi,\mathfrak{I})}{\partial\varphi}+3\frac{\partial^3\mu(\varphi,\mathfrak{I})}{\partial\varphi^3}-\frac{\partial^2\nu(\varphi,\mathfrak{I})}{\partial\varphi^2}\right\}\right]. \tag{40}$$

The LHPTM is used in (40), and we obtain

$$\sum_{n=0}^{\infty}\mu_n(\varphi,\mathfrak{I})=\mu(\varphi,0)-p\mathscr{L}^{-1}\left[\frac{(1-\beta)s^{\beta}+\beta}{B(\beta)s^{\beta}}\mathscr{L}\left\{\sum_{n=0}^{\infty}p^nA_n+\frac{\partial}{\partial\varphi}\sum_{n=0}^{\infty}p^n\mu_n(\varphi,\mathfrak{I})+\frac{\partial}{\partial\varphi}\sum_{n=0}^{\infty}p^n\nu_n(\varphi,\mathfrak{I})\right\}\right],$$
$$\sum_{n=0}^{\infty}\nu_n(\varphi,\mathfrak{I})=\nu(\varphi,0)-p\mathscr{L}^{-1}\left[\frac{(1-\beta)s^{\beta}+\beta}{B(\beta)s^{\beta}}\mathscr{L}\left\{\sum_{n=0}^{\infty}p^nB_m+\sum_{n=0}^{\infty}p^nC_n+3\frac{\partial^3}{\partial\varphi^3}\sum_{n=0}^{\infty}p^n\mu_n(\varphi,\mathfrak{I})-\frac{\partial^2}{\partial\varphi^2}\sum_{n=0}^{\infty}p^n\nu_n(\varphi,\mathfrak{I})\right\}\right]. \tag{41}$$

The nonlinear can be found with the help of He's polynomial and can be defined as

Comparing the coefficient of p, we have

$$\begin{aligned}
A_0 &= \mu_0 \frac{\partial \mu_0}{\partial \varphi}, \\
A_1 &= \mu_0 \frac{\partial \mu_1}{\partial \varphi} + \mu_1 \frac{\partial \mu_0}{\partial \varphi}, \\
B_0 &= \mu_0 \frac{\partial \nu_0}{\partial \beta}, \\
B_1 &= \mu_0 \frac{\partial \nu_1}{\partial \beta} + \mu_1 \frac{\partial \nu_0}{\partial \beta}, \\
C_0 &= \nu_0 \frac{\partial \mu_0}{\partial \varphi}, \\
C_1 &= \nu_0 \frac{\partial \mu_1}{\partial \varphi} + \nu_1 \frac{\partial \mu_0}{\partial \varphi}.
\end{aligned} \tag{42}$$

$$\begin{aligned}
p^0\colon \mu_0(\varphi, \mathfrak{I}) &= \mu(\varphi, 0) = \frac{1}{2} - 8\ \tanh(-2\varphi), \\
p^0\colon \nu_0(\varphi, \mathfrak{I}) &= \nu(\varphi, 0) = 16 - 16\tanh^2(-2\varphi), \\
p^1\colon \mu_1(\varphi, \mathfrak{I}) &= -\mathscr{L}^{-1}\left[\frac{(1-\beta)s^\beta + \beta}{B(\beta)s^\beta}\mathscr{L}\left\{A_0 + \frac{\partial}{\partial \varphi}\mu_0(\varphi, \mathfrak{I}) + \frac{\partial}{\partial \varphi}\nu_0(\varphi, \mathfrak{I})\right\}\right] \\
&= -8\ \sec h^2(-2\varphi)\frac{1}{B(\beta)}\left[\frac{\beta \mathfrak{I}^\beta}{\Gamma(\beta+1)} + (1-\beta)\right], \\
p^1\colon \nu_1(\varphi, \mathfrak{I}) &= -p\mathscr{L}^{-1}\left[\frac{(1-\beta)s^\beta + \beta}{B(\beta)s^\beta}\mathscr{L}\left\{B_0 + C_0 + 3\frac{\partial^3}{\partial \varphi^3}\mu_0(\varphi, \mathfrak{I}) - \frac{\partial^2}{\partial \varphi^2}\nu_0(\varphi, \mathfrak{I})\right\}\right] \\
&= -32\ \sec h^2(-2\varphi)\tanh(-2\varphi)\frac{1}{B(\beta)}\left[\frac{\beta \mathfrak{I}^\beta}{\Gamma(\beta+1)} + (1-\beta)\right], \\
p^2\colon \mu_2(\varphi, \mathfrak{I}) &= -\mathscr{L}^{-1}\left[\frac{(1-\beta)s^\beta + \beta}{B(\beta)s^\beta}\mathscr{L}\left\{A_1 + \frac{\partial}{\partial \varphi}\mu_1(\varphi, \mathfrak{I}) + \frac{\partial}{\partial \varphi}\nu_1(\varphi, \mathfrak{I})\right\}\right] \\
&= -16\ \sec h^2(-2\varphi)\left(4\ \sec h^2(-2\varphi) - 8\ \tanh^2(-2\varphi) + 3\ \tanh(-2\varphi)\right) \\
&\quad \times \frac{1}{B^2(\beta)}\left[(1-\beta)^2 + \frac{2\beta(1-\beta)\mathfrak{I}^\beta}{\Gamma(\beta+1)} + \frac{\beta^2 \mathfrak{I}^{2\beta}}{\Gamma(2\beta+1)}\right], \\
p^2\colon \nu_2(\varphi, \mathfrak{I}) &= -p\mathscr{L}^{-1}\left[\frac{(1-\beta)s^\beta + \beta}{B(\beta)s^\beta}\mathscr{L}\left\{B_1 + C_1 + 3\frac{\partial^3}{\partial \varphi^3}\mu_1(\varphi, \mathfrak{I}) - \frac{\partial^2}{\partial \varphi^2}\nu_1(\varphi, \mathfrak{I})\right\}\right] \\
&= -32\ \sec h^2(-2\varphi)\left\{40\ \sec h^2(-2\varphi)\tanh(-2\varphi) + 96\ \tanh(-2\varphi) - 2\ \tanh^2(-2\varphi)\right. \\
&\quad \left. -32\ \tanh^3(-2\varphi) - 25\ \sec h^2(-2\varphi)\right\}\left[(1-\beta)^2 + \frac{2\beta(1-\beta)\mathfrak{I}^\beta}{\Gamma(\beta+1)} + \frac{\beta^2 \mathfrak{I}^{2\beta}}{\Gamma(2\beta+1)}\right], \\
&\ \vdots
\end{aligned} \tag{43}$$

We can calculate few terms of (36) which can be written as

$$\begin{aligned}
\mu(\varphi,\mathfrak{I}) &= \mu_0(\varphi,\mathfrak{I}) + \mu_1(\varphi,\mathfrak{I}) + \mu_2(\varphi,\mathfrak{I}) + \cdots,\\
\nu(\varphi,\mathfrak{I}) &= \nu_0(\varphi,\mathfrak{I}) + \nu_1(\varphi,\mathfrak{I}) + \nu_2(\varphi,\mathfrak{I}) + \cdots,\\
\mu(\varphi,\mathfrak{I}) &= \frac{1}{2} - 8\tanh(-2\varphi) - 8\sec h^2(-2\varphi)\left[\frac{\beta\mathfrak{I}^{\beta}}{\Gamma(\beta+1)} + (1-\beta)\right] - 16\sec h^2(-2\varphi)\\
&\quad \left(4\sec h^2(-2\varphi) - 8\tanh^2(-2\varphi) + 3\tanh(-2\varphi)\right)\frac{1}{B^2(\beta)}\left[(1-\beta)^2 + \frac{2\beta(1-\beta)\mathfrak{I}^{\beta}}{\Gamma(\beta+1)} + \frac{\beta^2\mathfrak{I}^{2\beta}}{\Gamma(2\beta+1)}\right] + \cdots,\\
\nu(\varphi,\mathfrak{I}) &= 16 - 16\tanh^2(-2\varphi) - 8\sec h^2(-2\varphi)\left[\frac{\beta\mathfrak{I}^{\beta}}{\Gamma(\beta+1)} + (1-\beta)\right] - 32\sec h^2(-2\varphi)\\
&\quad \times\left\{40\sec h^2(-2\varphi)\tanh(-2\varphi) + 96\tanh(-2\varphi) - 2\tanh^2(-2\varphi) - 32\tanh^3(-2\varphi) - 25\sec h^2(-2\varphi)\right\}\\
&\quad \times\left[(1-\beta)^2 + \frac{2\beta(1-\beta)\mathfrak{I}^{\beta}}{\Gamma(\beta+1)} + \frac{\beta^2\mathfrak{I}^{2\beta}}{\Gamma(2\beta+1)}\right] + \cdots.
\end{aligned} \tag{44}$$

The exact solution of (36) is

$$\begin{aligned}
\mu(\varphi,\mathfrak{I}) &= \frac{1}{2} - 8\tanh\left\{-2\left(\varphi - \frac{\mathfrak{I}}{2}\right)\right\},\\
\nu(\varphi,\mathfrak{I}) &= 16 - 16\tanh^2\left\{-2\left(\varphi - \frac{\mathfrak{I}}{2}\right)\right\}.
\end{aligned} \tag{45}$$

Figure 5 shows the actual and approximate solutions of $\mu(\varphi,\mathfrak{I})$ at $\beta = 1$, and Figure 6 shows the actual and approximate solutions of $\nu(\varphi,\mathfrak{I})$ at $\beta = 1$. Figures 7 and 8 show that the first graph has a different fractional order with respect to φ and the second graph has a different fractional order with respect to $\mathfrak{I}$ of Example 3.

Example 4. Let us consider the coupled system of fractional-order WBKEs in the ABC sense:

$$\begin{aligned}
&{}^{ABC}D_{\mathfrak{I}}^{\beta}\mu(\varphi,\mathfrak{I}) + \mu(\varphi,\mathfrak{I})\frac{\partial\mu(\varphi,\mathfrak{I})}{\partial\varphi} + \frac{1}{2}\frac{\partial\mu(\varphi,\mathfrak{I})}{\partial\varphi} + \frac{\partial\nu(\varphi,\mathfrak{I})}{\partial\varphi} = 0,\\
&{}^{ABC}D_{\mathfrak{I}}^{\beta}\nu(\varphi,\mathfrak{I}) + \mu(\varphi,\mathfrak{I})\frac{\partial\nu(\varphi,\mathfrak{I})}{\partial\varphi} + \nu(\varphi,\mathfrak{I})\frac{\partial\mu(\varphi,\mathfrak{I})}{\partial\varphi} - \frac{1}{2}\frac{\partial^2\nu(\varphi,\mathfrak{I})}{\partial\varphi^2} = 0, \quad 0<\beta\le 1, -1<\mathfrak{I}\le 1, -10\le\varphi\le 10,
\end{aligned} \tag{46}$$

under the initial conditions,

$$\begin{aligned}
\mu(\varphi,0) &= \xi - \kappa\coth[\kappa(\varphi+\theta)],\\
\nu(\varphi,0) &= -\kappa^2\operatorname{cosech}^2[\kappa(\varphi+\theta)].
\end{aligned} \tag{47}$$

Using the Laplace transformation to (46), we obtain

$$\begin{aligned}
\frac{B(\beta)}{1-\beta}\frac{s\mathscr{L}[\mu(\varphi,\mathfrak{I})](s) - s^{\beta-1}\mu(\varphi,0)}{s+(\beta/(1-\beta))} &= -\mathscr{L}\left[\mu(\varphi,\mathfrak{I})\frac{\partial\mu(\varphi,\mathfrak{I})}{\partial\varphi} + \frac{1}{2}\frac{\partial\mu(\varphi,\mathfrak{I})}{\partial\varphi} + \frac{\partial\nu(\varphi,\mathfrak{I})}{\partial\varphi}\right],\\
\frac{B(\beta)}{1-\beta}\frac{s\mathscr{L}[\nu(\varphi,\mathfrak{I})](s) - s^{\beta-1}\nu(\varphi,0)}{s+(\beta/(1-\beta))} &= -\mathscr{L}\left[\mu(\varphi,\mathfrak{I})\frac{\partial\nu(\varphi,\mathfrak{I})}{\partial\varphi} + \nu(\varphi,\mathfrak{I})\frac{\partial\mu(\varphi,\mathfrak{I})}{\partial\varphi} - \frac{1}{2}\frac{\partial^2\nu(\varphi,\mathfrak{I})}{\partial\varphi^2}\right].
\end{aligned} \tag{48}$$

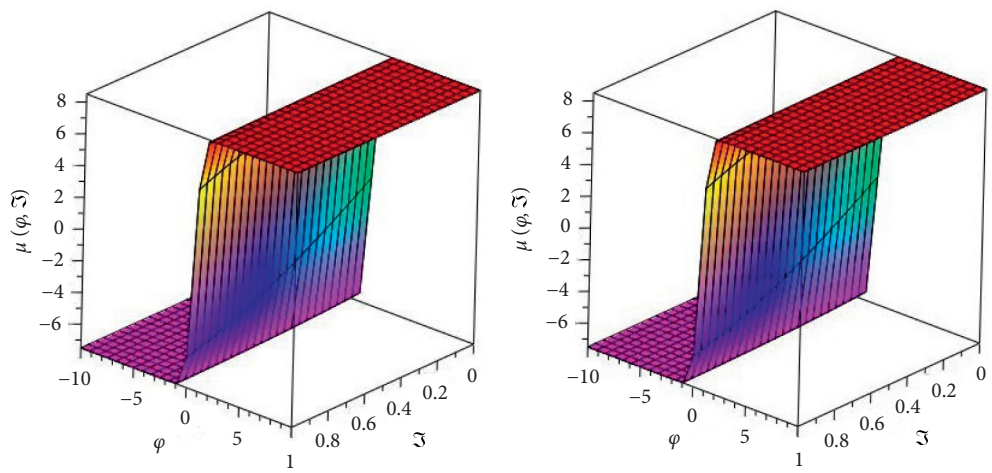

Figure 5: The exact and analytical solution with respect to the Atangana–Baleanu operator of $\mu(\varphi, \mathfrak{I})$ at $\beta = 1$ of Example 3.

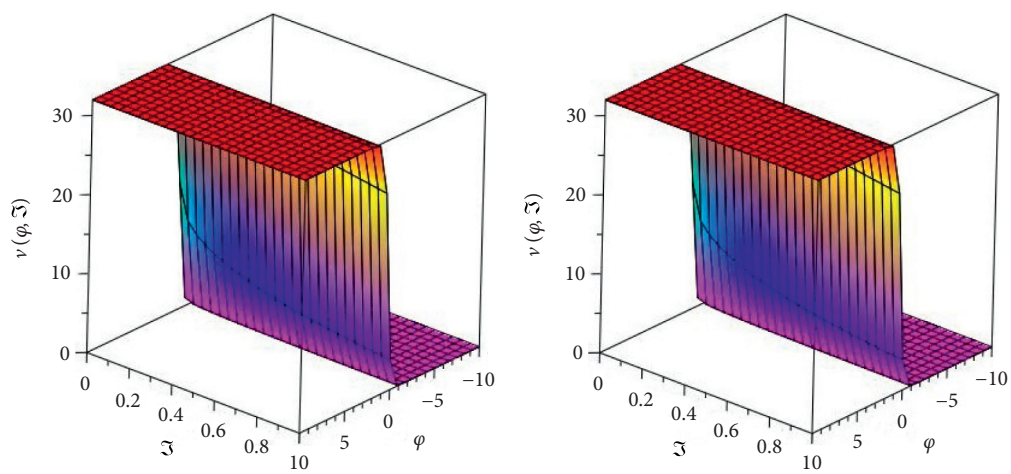

Figure 6: The exact and analytical solution with respect to the Atangana–Baleanu operator of $\nu(\varphi, \mathfrak{I})$ at $\beta = 1$ of Example 3.

Simplifying the above equation and using the initial conditions (47), we obtain

$$\begin{aligned}
\mathscr{L}[\mu(\varphi, \mathfrak{I})] &= \frac{\mu(\varphi, 0)}{s} - \frac{(1-\beta)s^{\beta} + \beta}{B(\beta)s^{\beta}} \mathscr{L}\left[\mu(\varphi, \mathfrak{I}) \frac{\partial \mu(\varphi, \mathfrak{I})}{\partial \varphi} + \frac{1}{2} \frac{\partial \mu(\varphi, \mathfrak{I})}{\partial \varphi} + \frac{\partial \nu(\varphi, \mathfrak{I})}{\partial \varphi}\right], \\
\mathscr{L}[\nu(\varphi, \mathfrak{I})] &= \frac{\nu(\varphi, 0)}{s} - \frac{(1-\beta)s^{\beta} + \beta}{B(\beta)s^{\beta}} \mathscr{L}\left[\mu(\varphi, \mathfrak{I}) \frac{\partial \nu(\varphi, \mathfrak{I})}{\partial \varphi} + \nu(\varphi, \mathfrak{I}) \frac{\partial \mu(\varphi, \mathfrak{I})}{\partial \varphi} - \frac{1}{2} \frac{\partial^2 \nu(\varphi, \mathfrak{I})}{\partial \varphi^2}\right].
\end{aligned} \tag{49}$$

The inverse Laplace transformation is implemented to (49), and we obtain

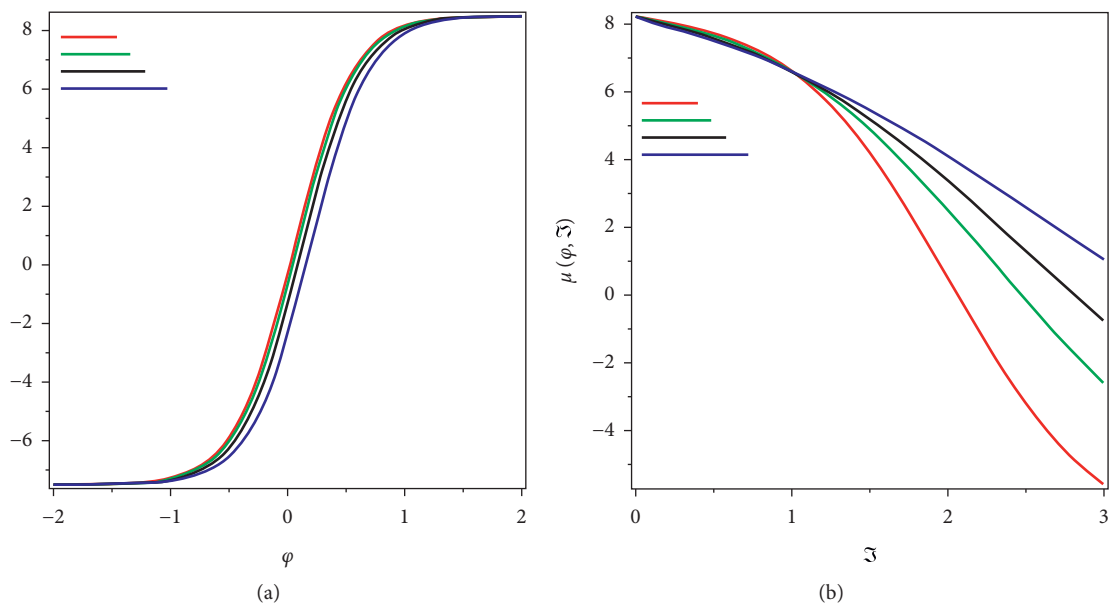

Figure 7: The different fractional-order solution with respect to the Atangana–Baleanu operator of $\mu(\varphi, \mathfrak{I})$ at β of Example 3.

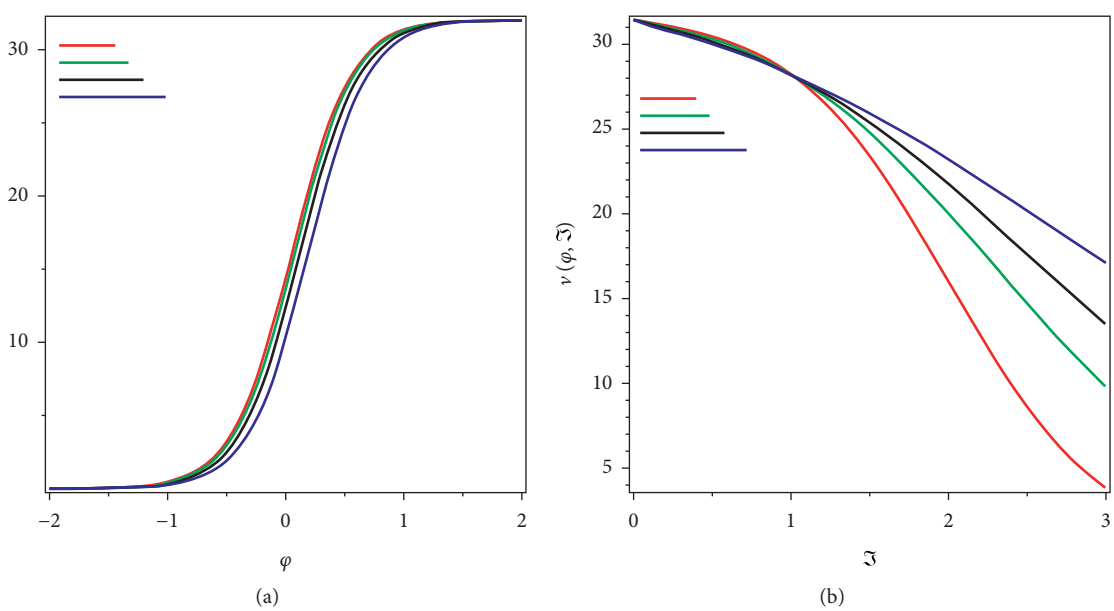

Figure 8: The different fractional-order solution with respect to the Atangana–Baleanu operator of $\nu(\varphi, \mathfrak{I})$ at β of Example 3.

$$\begin{aligned}
\mu(\varphi, \mathfrak{I}) &= \mu(\varphi, 0) - \mathscr{L}^{-1}\left[\frac{(1-\beta)s^{\beta}+\beta}{B(\beta)s^{\beta}}\mathscr{L}\left\{\mu(\varphi, \mathfrak{I})\frac{\partial\mu(\varphi, \mathfrak{I})}{\partial\varphi} + \frac{1}{2}\frac{\partial\mu(\varphi, \mathfrak{I})}{\partial\varphi} + \frac{\partial\nu(\varphi, \mathfrak{I})}{\partial\varphi}\right\}\right],\\
\nu(\varphi, \mathfrak{I}) &= \nu(\varphi, 0) - \mathscr{L}^{-1}\left[\frac{(1-\beta)s^{\beta}+\beta}{B(\beta)s^{\beta}}\mathscr{L}\left\{\mu(\varphi, \mathfrak{I})\frac{\partial\nu(\varphi, \mathfrak{I})}{\partial\varphi} + \nu(\varphi, \mathfrak{I})\frac{\partial\mu(\varphi, \mathfrak{I})}{\partial\varphi} - \frac{1}{2}\frac{\partial^2\nu(\varphi, \mathfrak{I})}{\partial\varphi^2}\right\}\right].
\end{aligned} \tag{50}$$

The LHPTM is used in (50), and we obtain

$$\sum_{n=0}^{\infty}\mu_n(\varphi,\mathfrak{I}) = \mu(\varphi,0) - p\mathscr{L}^{-1}\left[\frac{(1-\beta)s^{\beta}+\beta}{B(\beta)s^{\beta}}\mathscr{L}\left\{\sum_{n=0}^{\infty}p^nA_n + \frac{1}{2}\frac{\partial}{\partial\varphi}\sum_{n=0}^{\infty}p^n\mu_n(\varphi,\mathfrak{I}) + \frac{\partial}{\partial\varphi}\sum_{n=0}^{\infty}p^n\nu_n(\varphi,\mathfrak{I})\right\}\right],$$
$$\sum_{n=0}^{\infty}\nu_n(\varphi,\mathfrak{I}) = \nu(\varphi,0) - p\mathscr{L}^{-1}\left[\frac{(1-\beta)s^{\beta}+\beta}{B(\beta)s^{\beta}}\mathscr{L}\left\{\sum_{n=0}^{\infty}p^nB_n + \sum_{n=0}^{\infty}p^nC_n - \frac{1}{2}\frac{\partial^2}{\partial\varphi^2}\sum_{n=0}^{\infty}p^n\nu_n(\varphi,\mathfrak{I})\right\}\right]. \tag{51}$$

The nonlinear can be found with the help of He's polynomial and can be defined as

$$\begin{aligned}
A_0 &= \mu_0\frac{\partial\mu_0}{\partial\varphi},\\
A_1 &= \mu_0\frac{\partial\mu_1}{\partial\varphi} + \mu_1\frac{\partial\mu_0}{\partial\varphi},\\
B_0 &= \mu_0\frac{\partial\nu_0}{\partial\beta},\\
B_1 &= \mu_0\frac{\partial\nu_1}{\partial\beta} + \mu_1\frac{\partial\nu_0}{\partial\beta},\\
C_0 &= \nu_0\frac{\partial\mu_0}{\partial\varphi},\\
C_1 &= \nu_0\frac{\partial\mu_1}{\partial\varphi} + \nu_1\frac{\partial\mu_0}{\partial\varphi}.
\end{aligned} \tag{52}$$

Comparing the coefficient of p, we have

$$p^0\colon \mu_0(\varphi,\mathfrak{I}) = \mu(\varphi,0) = \xi - \kappa\coth[\kappa(\varphi+\theta)],$$

$$p^0\colon \nu_0(\varphi,\mathfrak{I}) = \nu(\varphi,0) = -\kappa^2\operatorname{cosech}^2[\kappa(\varphi+\theta)],$$

$$\begin{aligned}
p^1\colon \mu_1(\varphi,\mathfrak{I}) &= -\mathscr{L}^{-1}\left[\frac{(1-\beta)s^{\beta}+\beta}{B(\beta)s^{\beta}}\mathscr{L}\left\{A_0 + \frac{1}{2}\frac{\partial}{\partial\varphi}\mu_0(\varphi,\mathfrak{I}) + \frac{\partial}{\partial\varphi}\nu_0(\varphi,\mathfrak{I})\right\}\right]\\
&= -\xi\kappa^2\operatorname{cosech}^2[\kappa(\varphi+\theta)]\frac{1}{B(\beta)}\left[\frac{\beta\mathfrak{I}^{\beta}}{\Gamma(\beta+1)} + (1-\beta)\right],
\end{aligned}$$

$$\begin{aligned}
p^1\colon \nu_1(\varphi,\mathfrak{I}) &= -p\mathscr{L}^{-1}\left[\frac{(1-\beta)s^{\beta}+\beta}{B(\beta)s^{\beta}}\mathscr{L}\left\{B_0 + C_0 - \frac{1}{2}\frac{\partial^2}{\partial\varphi^2}\nu_0(\varphi,\mathfrak{I})\right\}\right]\\
&= -\xi\kappa^2\operatorname{cosech}^2[\kappa(\varphi+\theta)]\coth[\kappa(\varphi+\theta)]\frac{1}{B(\beta)}\left[\frac{\beta\mathfrak{I}^{\beta}}{\Gamma(\beta+1)} + (1-\beta)\right],
\end{aligned}$$

$$\begin{aligned}
p^2\colon \mu_2(\varphi,\mathfrak{I}) &= -\mathscr{L}^{-1}\left[\frac{(1-\beta)s^{\beta}+\beta}{B(\beta)s^{\beta}}\mathscr{L}\left\{A_1 + \frac{1}{2}\frac{\partial}{\partial\varphi}\mu_1(\varphi,\mathfrak{I}) + \frac{\partial}{\partial\varphi}\nu_1(\varphi,\mathfrak{I})\right\}\right]\\
&= -\xi\kappa^4\operatorname{cosech}^2[\kappa(\varphi+\theta)]\left(3\coth^2([\kappa(\varphi+\theta)]-1)\right)\frac{1}{B^2}\left[(1-\beta)^2 + \frac{2\beta(1-\beta)\mathfrak{I}^{\beta}}{\Gamma(\beta+1)} + \frac{\beta^2\mathfrak{I}^{2\beta}}{\Gamma(2\beta+1)}\right]\\
&\quad + 2\xi^2\kappa^5\operatorname{cosech}^2[\kappa(\varphi+\theta)]\frac{1}{B^3}\left[(1-\beta)^3 + \frac{3\beta(1-\beta)^2\mathfrak{I}^{\beta}}{\Gamma(2\beta+1)} + \frac{3\beta^2(1-\beta)\mathfrak{I}^{2\beta}}{\Gamma(2\beta+1)} + \frac{\beta^3\mathfrak{I}^{3\beta}}{\Gamma(3\beta+1)}\right],
\end{aligned}$$

$$
\begin{aligned}
p^2\colon \nu_2(\varphi,\mathfrak{I}) &= -p\mathscr{L}^{-1}\left[\frac{(1-\beta)s^{\beta}+\beta}{B(\beta)s^{\beta}}\mathscr{L}\left\{B_1+C_1-\frac{1}{2}\frac{\partial^2}{\partial\varphi^2}\nu_1(\varphi,\mathfrak{I}))\right\}\right]\\
&= 2\xi\kappa^5\operatorname{cosech}^2[\kappa(\varphi+\theta)]\left\{\xi\kappa\operatorname{cosech}^2\left(3\coth^2([\kappa(\varphi+\theta)]-1)\right)+2\xi\kappa\operatorname{cosech}^2\coth^2([\kappa(\varphi+\theta)])\right\}\\
&\quad\times\frac{1}{B^3}\left[(1-\beta)^3+\frac{3\beta(1-\beta)^2\mathfrak{I}^{\beta}}{\Gamma(2\beta+1)}+\frac{3\beta^2(1-\beta)\mathfrak{I}^{2\beta}}{\Gamma(2\beta+1)}+\frac{\beta^3\mathfrak{I}^{3\beta}}{\Gamma(3\beta+1)}\right]\\
&\quad-2\xi\coth\left(3\operatorname{cosech}^2([\kappa(\varphi+\theta)]-1)\right)\frac{1}{B^2}\left[(1-\beta)^2+\frac{2\beta(1-\beta)\mathfrak{I}^{\beta}}{\Gamma(\beta+1)}+\frac{\beta^2\mathfrak{I}^{2\beta}}{\Gamma(2\beta+1)}\right],\\
&\quad\vdots
\end{aligned}
\tag{53}
$$

We can calculate few terms of (46) which can be written as

$$
\begin{aligned}
\mu(\varphi,\mathfrak{I}) &= \mu_0(\varphi,\mathfrak{I})+\mu_1(\varphi,\mathfrak{I})+\mu_2(\varphi,\mathfrak{I})+\cdots,\\
\nu(\varphi,\mathfrak{I}) &= \nu_0(\varphi,\mathfrak{I})+\nu_1(\varphi,\mathfrak{I})+\nu_2(\varphi,\mathfrak{I})+\cdots,\\
\mu(\varphi,\mathfrak{I}) &= \xi-\kappa\coth[\kappa(\varphi+\theta)]-\xi\kappa^2\operatorname{cosech}^2[\kappa(\varphi+\theta)]\frac{1}{B(\beta)}\left[\frac{\beta\mathfrak{I}^{\beta}}{\Gamma(\beta+1)}+(1-\beta)\right]\\
&\quad-\xi\kappa^4\operatorname{cosech}^2[\kappa(\varphi+\theta)]\left(3\coth^2([\kappa(\varphi+\theta)]-1)\right)\frac{1}{B^2}\left[(1-\beta)^2+\frac{2\beta(1-\beta)\mathfrak{I}^{\beta}}{\Gamma(\beta+1)}+\frac{\beta^2\mathfrak{I}^{2\beta}}{\Gamma(2\beta+1)}\right]\\
&\quad+2\xi^2\kappa^5\operatorname{cosech}^2[\kappa(\varphi+\theta)]\frac{1}{B^3}\left[(1-\beta)^3+\frac{3\beta(1-\beta)^2\mathfrak{I}^{\beta}}{\Gamma(2\beta+1)}+\frac{3\beta^2(1-\beta)\mathfrak{I}^{2\beta}}{\Gamma(2\beta+1)}+\frac{\beta^3\mathfrak{I}^{3\beta}}{\Gamma(3\beta+1)}\right]+\cdots,\\
\nu(\varphi,\mathfrak{I}) &= -\kappa^2\operatorname{cosech}^2[\kappa(\varphi+\theta)]-\xi\kappa^2\operatorname{cosech}^2[\kappa(\varphi+\theta)]\coth[\kappa(\varphi+\theta)]\frac{1}{B(\beta)}\left[\frac{\beta\mathfrak{I}^{\beta}}{\Gamma(\beta+1)}+(1-\beta)\right]\\
&\quad+2\xi\kappa^5\operatorname{cosech}^2[\kappa(\varphi+\theta)]\left\{\xi\kappa\operatorname{cosech}^2\left(3\coth^2([\kappa(\varphi+\theta)]-1)\right)+2\xi\kappa\operatorname{cosech}^2\coth^2([\kappa(\varphi+\theta)])\right\}\\
&\quad\times\frac{1}{B^3}\left[(1-\beta)^3+\frac{3\beta(1-\beta)^2\mathfrak{I}^{\beta}}{\Gamma(2\beta+1)}+\frac{3\beta^2(1-\beta)\mathfrak{I}^{2\beta}}{\Gamma(2\beta+1)}+\frac{\beta^3\mathfrak{I}^{3\beta}}{\Gamma(3\beta+1)}\right]-2\xi\coth\left(3\operatorname{cosech}^2([\kappa(\varphi+\theta)]-1)\right)\\
&\quad\times\frac{1}{B^2}\left[(1-\beta)^2+\frac{2\beta(1-\beta)\mathfrak{I}^{\beta}}{\Gamma(\beta+1)}+\frac{\beta^2\mathfrak{I}^{2\beta}}{\Gamma(2\beta+1)}\right]+\cdots.
\end{aligned}
\tag{54}
$$

The exact solution of (46) is

$$
\begin{aligned}
\mu(\varphi,\mathfrak{I}) &= \xi-\kappa\coth[\kappa(\varphi+\theta-\xi\mathfrak{I})],\\
\nu(\varphi,\mathfrak{I}) &= -\kappa^2\operatorname{cosech}^2[\kappa(\varphi+\theta-\xi\mathfrak{I})].
\end{aligned}
\tag{55}
$$

6. Conclusions

In this paper, the LHPTM was considered to achieve an analytical result for the fractional-order Whitham–Broer–Kaup equations considering the Caputo–Fabrizio and Atangana–Baleanu operators. Analytical results were obtained for different fractional order β. Both suggested operators have shown to be critical mathematical tools for scientists working in numerous fields of applied sciences. The polynomial expansion well-thought-out in the LHPTM permits to achieve an infinite series result for the Whitham–Broer–Kaup equations. This technique established a general system to achieve fractional-order models' analytical results, and the results are obtained in the series form, which converges quickly; the LHPTM is used for investigating other nonlinear fractional systems of partial differential equations.

Abbrevation

HPTM: Homotopy perturbation transform method
lT: Laplace transform
FPDEs: Fractional partial differential equations
FC: Fractional calculus
WBKEs: Whitham–Broer–Kaup equations
ADM: Adomian decomposition method.

Data Availability

The numerical data used to support the findings of this study are included within the article.

Conflicts of Interest

The authors declare that there are no conflicts of interest regarding the publication of this article.

Acknowledgments

One of the co-authors (A. M. Zidan) extend his appreciation to the Deanship of Scientific Research at King Khalid University, Abha 61413, Saudi Arabia, for funding this work through research groups program, under Grant no. R.G.P-2/142/42. The authors are grateful to the Deanship of Scientific Research, King Saud University, for funding through Vice Deanship of Scientific Research Chairs..

References

[1] F. Xie, Z. Yan, and H. Zhang, "Explicit and exact traveling wave solutions of Whitham-Broer-Kaup shallow water equations," *Physics Letters A*, vol. 285, no. 1-2, pp. 76–80, 2001.

[2] M. I. Asjad, M. Aleem, A. Ahmadian, S. Salahshour, M. Ferrara, and M. Ferrara, "New trends of fractional modeling and heat and mass transfer investigation of (SWCNTs and MWCNTs)-CMC based nanofluids flow over inclined plate with generalized boundary conditions," *Chinese Journal of Physics*, vol. 66, pp. 497–516, 2020.

[3] A. A. Alderremy, K. M. Saad, S. Aly, D. Kumar, and J. Singh, "New models of fractional blood ethanol and two cell cubic autocatalator reaction equations," *Mathematical Methods in the Applied Sciences*, vol. 43, 2021.

[4] L. Wang and X. Chen, "Approximate analytical solutions of time fractional Whitham-Broer-Kaup equations by a residual power series method," *Entropy*, vol. 17, no. 9, pp. 6519–6533, 2015.

[5] M. Aleem, M. Imran Asjad, M. S. R. Chowdhury, and A. Hussanan, "Analysis of mathematical model of fractional viscous fluid through a vertical rectangular channel," *Chinese Journal of Physics*, vol. 61, pp. 336–350, 2019.

[6] K. M. Saad, M. Alqhtani, and M. Alqhtani, "Numerical simulation of the fractal-fractional reaction diffusion equations with general nonlinear," *AIMS Mathematics*, vol. 6, no. 4, pp. 3788–3804, 2021.

[7] S. M. El-Sayed and D. Kaya, "Exact and numerical traveling wave solutions of Whitham-Broer-Kaup equations," *Applied Mathematics and Computation*, vol. 167, no. 2, pp. 1339–1349, 2005.

[8] N. A. Shah, I. Khan, M. Aleem, and M. A. Imran, "Influence of magnetic field on double convection problem of fractional viscous fluid over an exponentially moving vertical plate: new trends of Caputo time-fractional derivative model," *Advances in Mechanical Engineering*, vol. 11, no. 7, 2019.

[9] K. M. Saad, M. Alqhtani, and J. F. Gómez-Aguilar, "Fractal-fractional study of the hepatitis C virus infection model," *Results in Physics*, vol. 19, Article ID 103555, 2020.

[10] J. Ahmad, M. Mushtaq, and N. Sajjad, "Exact solution of whitham-broer-kaup shallow water wave equations," *Journal of Science and Arts*, vol. 15, p. 1, 2015.

[11] M. Ahmad, M. A. Imran, M. Aleem, and I. Khan, "A comparative study and analysis of natural convection flow of MHD non-Newtonian fluid in the presence of heat source and first-order chemical reaction," *Journal of Thermal Analysis and Calorimetry*, vol. 137, no. 5, pp. 1783–1796, 2019.

[12] H. M. Srivastava and K. M. Saad, "A comparative study of the fractional-order clock chemical model," *Mathematics*, vol. 8, no. 9, p. 1436, 2020.

[13] B. A. Kupershmidt, "Mathematics of dispersive water waves," *Communications in Mathematical Physics*, vol. 99, no. 1, pp. 51–73, 1985.

[14] G. B. Whitham, "Variational methods and applications to water waves," *Proceedings of the Royal Society of London. Series A. Mathematical and Physical Sciences*, vol. 299, no. 1456, pp. 6–25, 1967.

[15] L. J. F. Broer, "Approximate equations for long water waves," *Applied Scientific Research*, vol. 31, no. 5, pp. 377–395, 1975.

[16] D. J. Kaup, "A higher-order water-wave equation and the method for solving it," *Progress of Theoretical Physics*, vol. 54, no. 2, pp. 396–408, 1975.

[17] D. D. Ganji, H. B. Rokni, M. G. Sfahani, and S. S. Ganji, "Approximate traveling wave solutions for coupled Whitham-Broer-Kaup shallow water," *Advances in Engineering Software*, vol. 41, no. 7-8, pp. 956–961, 2010.

[18] J. Biazar and H. Aminikhah, "Study of convergence of homotopy perturbation method for systems of partial differential equations," *Computers & Mathematics with Applications*, vol. 58, no. 11-12, pp. 2221–2230, 2009.

[19] A. Ali, K. Shah, and R. A. Khan, "Numerical treatment for traveling wave solutions of fractional Whitham-Broer-Kaup equations," *Alexandria Engineering Journal*, vol. 57, no. 3, pp. 1991–1998, 2018.

[20] S. T. Mohyud-Din and M. A. Noor, "Homotopy perturbation method for solving partial differential equations," *Zeitschrift Fur Naturforschung A*, vol. 64, no. 3-4, pp. 157–170, 2009.

[21] S. Saha Ray, "A novel method for travelling wave solutions of fractional Whitham-Broer-Kaup, fractional modified Boussinesq and fractional approximate long wave equations in shallow water," *Mathematical Methods in the Applied Sciences*, vol. 38, no. 7, pp. 1352–1368, 2015.

[22] S. T. Mohyud-Din, A. Yıldırım, G. Demirli, and G. Demirli, "Traveling wave solutions of Whitham-Broer-Kaup equations by homotopy perturbation method," *Journal of King Saud University-Science*, vol. 22, no. 3, pp. 173–176, 2010.

[23] A. Kadem and B. Dumitru, "On fractional coupled Whitham-Broer-Kaup equations," *Romanian Journal of Physics*, vol. 56, no. 5-6, pp. 629–635, 2011.

[24] H. R. Ghehsareh, M. Ahmad, and Z. Ali, "Lie symmetry analysis and conservation laws for time fractional coupled Whitham-Broer-Kaup equations," *UPB Scientific Bulletin, Series A: Applied Mathematics and Physics*, vol. 80, no. 3, pp. 153–168, 2018.

[25] Z. Zhang, X. Yong, and Y. Chen, "Symmetry analysis for Whitham-Broer-Kaup equations," *Journal of Nonlinear Mathematical Physics*, vol. 15, no. 4, pp. 383–397, 2008.
[26] Y. Wang, Y.-F. Zhang, Z.-J. Liu, and M. Iqbal, "A fractional Whitham-Broer-Kaup equation and its possible application to tsunami prevention," *Thermal Science*, vol. 21, no. 4, pp. 1847–1855, 2017.
[27] S. Arshed and M. Sadia, "G'/G-Expansion method: new traveling wave solutions for some nonlinear fractional partial differential equations," *Optical and Quantum Electronics*, vol. 50, no. 3, pp. 1–20, 2018.
[28] A. Rani, Q. M. Ul-Hassan, M. Ashraf, K. Ayub, and M. Y. Khan, "A novel technique for solving nonlinear WBK equations of fractionl-order," *Journal of Science and Arts*, vol. 18, no. 2, pp. 301–316, 2018.
[29] K. M. Owolabi and A. Atangana, "Analysis and application of new fractional Adams-Bashforth scheme with Caputo-Fabrizio derivative," *Chaos, Solitons & Fractals*, vol. 105, pp. 111–119, 2017.
[30] M. Naeem, A. M. Zidan, K. Nonlaopon, M. I. Syam, Z. Al-Zhour, and R. Shah, "A new analysis of fractional-order equal-width equations via novel techniques," *Symmetry*, vol. 13, no. 5, p. 886, 2021.
[31] M. Caputo and M. Fabrizio, "A new definition of fractional derivative without singular kernel," *Progress in Fractional Differentiation and Applications*, vol. 1, no. 2, pp. 1–13, 2015.
[32] R. K. Pandey and H. K. Mishra, "Homotopy analysis Sumudu transform method for time-fractional third order dispersive partial differential equation," *Advances in Computational Mathematics*, vol. 43, no. 2, pp. 365–383, 2017.
[33] J. Vahidi, "The combined Laplace-homotopy analysis method for partial differential equations," *Journal of Mathematics and Computer Science*, vol. 16, pp. 88–102, 2016.
[34] S. Choudhary and V. Daftardar-Gejji, "Invariant subspace method: a tool for solving fractional partial differential equations," *Fractional Calculus and Applied Analysis*, vol. 20, no. 2, pp. 477–493, 2017.
[35] N. A. Pirim and F. Ayaz, "A new technique for solving fractional order systems: Hermite collocation method," *Applied Mathematics*, vol. 7, no. 18, pp. 2307–2323, 2016.
[36] K. M. Saad, "Comparing the Caputo, Caputo-Fabrizio and Atangana-Baleanu derivative with fractional order: fractional cubic isothermal auto-catalytic chemical system," *The European Physical Journal Plus*, vol. 133, no. 3, pp. 1–12, 2018.
[37] M. Hamarsheh, A. I. Ismail, and Z. Odibat, "An analytic solution for fractional order Riccati equations by using optimal homotopy asymptotic method," *Applied Mathematical Sciences*, vol. 10, no. 23, pp. 1131–1150, 2016.
[38] S. Rathore, D. Kumar, J. Singh, and S. Gupta, "Homotopy analysis Sumudu transform method for nonlinear equations," *International Journal of Industrial Mathematics*, vol. 4, no. 4, pp. 301–314, 2012.
[39] A. Ghorbani, "Beyond Adomian polynomials: He polynomials," *Chaos, Solitons & Fractals*, vol. 39, no. 3, pp. 1486–1492, 2009.
[40] S. Abbasbandy and K. V. Elyas Shivanian, "A new approximate analytical technique for dual solutions of nonlinear differential equations arising in mixed convection heat transfer in a porous medium," *International Journal of Numerical Methods for Heat & Fluid Flow*, vol. 54, 2017.
[41] S.-J. Liao, "An approximate solution technique not depending on small parameters: a special example," *International Journal of Non-linear Mechanics*, vol. 30, no. 3, pp. 371–380, 1995.
[42] V. F. Morales-Delgado, J. F. Gómez-Aguilar, S. Kumar, and M. A. Taneco-Hernández, "Analytical solutions of the Keller-Segel chemotaxis model involving fractional operators without singular kernel," *The European Physical Journal Plus*, vol. 133, no. 5, p. 200, 2018.

Hindawi
Complexity
Volume 2021, Article ID 9998610, 11 pages
https://doi.org/10.1155/2021/9998610

Research Article

Numerical Simulation of Fractional Zakharov–Kuznetsov Equation for Description of Temporal Discontinuity Using Projected Differential Transform Method

Dianchen Lu,[1] **Muhammad Suleman**,[1,2] **Jamshaid Ul Rahman**,[1] **Samad Noeiaghdam**,[3,4] **and Ghulam Murtaza**[5]

[1]*Faculty of Science, Jiangsu University, 212013 Zhenjiang, China*
[2]*Department of Mathematics, COMSATS University, 44000 Islamabad, Pakistan*
[3]*Industrial Mathematics Laboratory, Baikal School of BRICS, Irkutsk National Research Technical University, 664074 Irkutsk, Russia*
[4]*Department of Applied Mathematics and Programming, South Ural State University, Lenin Prospect 76,454080, Chelyabinsk, Russia*
[5]*School of Science, Department of Mathematics, University of Management and Technology, 54000 Lahore, Pakistan*

Correspondence should be addressed to Dianchen Lu; dclu@ujs.edu.cn and Jamshaid Ul Rahman; jamshaidrahman@gmail.com

Received 4 March 2021; Accepted 21 June 2021; Published 5 July 2021

Academic Editor: Atila M. Bueno

The core aim of this study is to propose a novel computational procedure, namely, Elzaki transform iterative method to work out two-dimensional nonlinear time-fractional Zakharov–Kuznetsov equation numerically. We execute the suggested iterative procedure on two models and results are presented graphically in the form of surface plot and absolute error is compared with the VIM and HPM to show that the method is more powerful than VIM and HPM and deduce that the offered numerical pattern is more efficient in simulating linear and nonlinear fractional order models.

1. Introduction

Applications of fractional calculus are found in various fields such as social science, viscoelasticity, finance, electrochemistry, finance, mathematical physics, signal processing, and physics. In various prominent areas, numerous important models are being found using the fractional derivatives in control, signal theory, mechanics, chemical, acoustics, and fluid and in several other problems which arise in engineering and applied sciences. In real world, we cannot think that any model exits physically without fractional derivatives. There are numerous nonlinear models in this world, and particularly, we say it is not possible to find out the solution analytically of nonlinear fractional models. So, we solve the numerous nonlinear fractional models numerically and computationally. Derivatives and integral order fractional are of important aspects in fractional calculus. It has already been proved by many researchers that fractional order generalizations of integral order models portray the natural phenomenon in extremely proficient manner. The classical derivatives exhibit local nature whereas the Caputo fractional derivatives exhibit nonlocal nature. Such that, making use of the local derivative, we can examine the variation in neighborhood of a point, but applying Caputo fractional derivative, we can examine changes in the interval. Because of this differential characteristic of Caputo fractional derivative, it is appropriate to simulate more physical phenomenon such as vibration, ocean, dynamical system, climate, physics, atmospheric, earthquake, and polymers. Due to vast applications of fractional differential equations, many researchers, such as Senol et al. [1], Sahoo and Ray [2], Das and Saha [3], Porogo et al. [4], Kuo [5], HE [6–8], Liu et al. [9], Shang et al. [10], Wang and Liu [11], Wang et al. [12], Hu and He [13], Wu and Liang [14],

He [15–22], Liu et al. [23], Adamu and Ogenyi [24], El-Dib [25], Filobello-Nino et al. [26], Yildrim [27–29], He [30–34], Ahmad [35], Prakash and Kumar [36], Molliq et al. [37], Kumar et al. [38,39], Aruna and Ravi Kanth [40], Daftardar-Gejji et al. [41–44], Jafari et al. [45], Bhalekar and Daftardar-Gejji [46], Munro and Parkes [47], Sakharov and Kuznetsov [48], Kumar et al. [49, 50], Pandey and Mishra [51], Zhang et al. [52], Podlubny [53], Laskin [54], Sun et al. [55], Singh [56], Kumar et al. [57, 58], Yang et al. [59], Suleman et al. [60–64], and Ahmad et al. [65, 66], studied different types of differential equations to understand the physical phenomena. The key issues in physical sciences, such as mathematical physics, are modeled with the help of nonlinear partial differential equations. In the investigation of nonlinear physical phenomenon, fractional order plays a vital role in finding the solution for nonlinear evolution problems.

In this study, we introduced iterative Elzaki transform method to study the numerical solution of two-dimensional nonlinear Zakharov–Kuznetsov equations fractional in time. This iterative Elzaki transform method is a combination of Elzaki transform and projected differential transform method, which provides the solution in a convergent series form.

The Zakharov–Kuznetsov equation is a model describing the isotropic evolution of a nonlinear ion-acoustic wave; many phenomena reveal that the wave travels discontinuously in time, and some properties hidden in a nonlinear wave has to be observed in multiple time scales. For example, for a flow in a tube, the main flow property can be described by the laminar theory, but the vortex near the boundary has to be described in a more small time scale, and a fractional model is needed.

In the current study, nonlinear Zakharov–Kuznetsov equation fractional in time has been studied:

$$\frac{\partial^{\alpha}\varphi}{\partial t^{\alpha}} + a\frac{\partial \varphi^{p}}{\partial x} + b\frac{\partial^{3}\varphi^{q}}{\partial x^{3}} + c\frac{\partial^{3}\varphi^{r}}{\partial x\,\partial y^{2}} = 0, \tag{1}$$

where φ is a function of x and y, t and α are parameter characterizing fractional derivatives $0 < \alpha \le 1$, a, b, and c are real constants, and p, q, and r are natural numbers that deal with the behavior of ion-acoustic waves. These waves are barely nonlinear in plasma and consist of cold ions and hot isothermal electrons in the presence of a steady magnetic field. This type of nonlinear equation was in three dimensions and was obtained firstly during the studies of steady magnetized lossless plasma to illustrate weakly ion-acoustic waves. The vital inspiration to work on this idea is established, a computational procedure to investigate nonlinear fractional differential equations, which is reliable and efficient. Since, their application is being found in mathematical modeling of real-world problems.

In this study, we suggest the iterative Elzaki transform method to numerically solve the nonlinear Zakharov–Kuznetsov equation fractional in time. Before this, the Elzaki transform and projected differential transform method has been used by many researchers discretely due to their strong characteristics. We are well familiar that integral transform methods are very helpful in finding the solution of linear and nonlinear fractional, ordinary, and partial differential equations. Previously, lot of articles were found on applications of integral transforms such as Laplace, Fourier, Hankel, and Mellin, but hardly any articles were found on the power series of these integral transforms such as the Elzaki transform. Apparently, this transformation is used not extensively so far by many researchers. The Elzaki transform is very powerful tool to solve linear and nonlinear differential equation, but it has several remarkable advantages over the already used integral transforms. The most useful characteristics of the Elzaki transform is its unity feature, which reduces the computational time to compute nonlinear fractional problems arising in several branches of engineering and applied sciences. The development of the proposed method is based on combination of two strong methodologies and applicable to work with different types of fractional order linear and nonlinear ordinary and partial differential equation. We suggest the proposed method can minimize the work and computational time as compared to the already used methods, while the efficiency is maintained for the approximate results, decreasing the size amount in improvement of the implementation of proposed technique.

2. Basic Definitions of Fractional Calculus and Elzaki Transform

(1) On the domain of functions the Elzaki transform can be defined as

$$B = \left\{ g(k) | N.k_1.k_2 > 0. |g(k)| < Ne^{\left(|k|/k_j\right)}\ if\ k \in (-1)^j \times (0, \infty) \right\}. \tag{2}$$

Given formulae can be written in the form

$$E[g(k)] = \int_0^{\infty} g(uk)e^{-k}dk, \quad u \in (-k_1, k_2). \tag{3}$$

(2) The Elzaki transform is defined for the Caputo fractional derivative by the following formula:

$$E\left[D_x^{n\alpha}u(x,t)\right] = v^{-n\alpha}E[u(x,t)] - \sum_{k=0}^{m-1} v^{(-n\alpha+k)}u^{k}(0.t),$$
$$n-1 < n\alpha \le n. \tag{4}$$

(3) He's fractional derivative:

$$D_t^{\alpha} g(t) = D^{\alpha} \frac{d^n}{dt^n} (I^n g) = \frac{d^n}{dt^n} (I^{n-\alpha} g) = \frac{1}{\Gamma(n-\alpha)} \frac{d^n}{dt^n} \int_{t_0}^{t} (v-t)^{n-\alpha-1} [g_0(v) - g(v)] dv. \tag{5}$$

(4) Keeping the first term of $g_0(v)$, we give another application of He's fractional derivative in the form

$$D_t^{\alpha} g(t) = \frac{1}{\Gamma(n-\alpha)} \frac{d^n}{dt^n} \int_{t_0}^{t} (v-t)^{n-\alpha-1} [g(t_0) - g(v)] dv. \tag{6}$$

Note that g can be continuous but possibly not differentiable anywhere.

(5) Variational iteration method (VIM):

$$D_t^{\alpha} g(t) = \frac{1}{\Gamma(n-\alpha)} \frac{d^n}{dt^n} \int_{t_0}^{t} (v-t)^{n-\alpha-1} g(v) dv. \tag{7}$$

(6) Caputo fractional derivative can be defined in He's fractional derivative as

$$D_x^{\alpha} g(x) = \frac{1}{\Gamma(n-\alpha)} \int_{0}^{x} (x-t)^{n-\alpha-1} \frac{d^n g(t)}{dt^n} dt. \tag{8}$$

(7) Riemann Liouville derivative can be defined in He's fractional derivative as

$$D_x^{\alpha} g(x) = \frac{1}{\Gamma(n-\alpha)} \frac{d^n}{dx^n} \int_{0}^{x} (x-t)^{n-\alpha-1} g(t) dt. \tag{9}$$

(8) Local fractional derivative has attracted much attention due to its simple chain rule:

$$g^{(\alpha)}(x_0) = \frac{d^{\alpha} g(x)}{dx^{\alpha}}\Big|_{x=x_0} = \lim_{x \longrightarrow x_0} \frac{\Delta^{\alpha}(g(x) - g(x_0))}{(x - x_0)^{\alpha}}, \tag{10}$$

where

$$\Delta^{\alpha}(g(x) - g(x_0)) \cong \Gamma(1+\alpha) \Delta(g(x) - g(x_0)). \tag{11}$$

(9) Fractal derivative:

$$\frac{Du}{Dx^{\alpha}} = \lim_{\Delta x \longrightarrow L_0} \frac{(U(A) - U(B))}{k L_0^{\alpha}}. \tag{12}$$

(10) Alternatively,

$$\frac{Du}{Dx^{\alpha}} = \Gamma(1+\alpha) \lim_{\Delta x = x_A - x_B \longrightarrow L_0} \frac{(U(A) - U(B))}{(x_A - x_B)^{\alpha}}. \tag{13}$$

3. Description of Elzaki Transforms' Iterative Method

Consider the functional equation $u(z) = g(z) + Nu(z)$, where N is the nonlinear operator defined on Banach space A and g is any known function. The main objective is to acquire the solution in convergent series form. Assume $u(z) = \sum_{i=0}^{\alpha} u_i(z)$, whereas $Nu(z)$ nonlinear operator can be represented as

$$N[u(z)] = N\left[\sum_{i=0}^{\infty} u_i(z)\right] = N[u_0] + \sum_{i=1}^{\infty} \left[N\left(\sum_{j=0}^{i} u_j\right) - N\left(\sum_{j=0}^{i-1} u_j\right)\right]. \tag{14}$$

So, we obtain

$$u(z) = g(z) + N(u_0) + \sum_{i=1}^{\infty} \left[N\left(\sum_{j=0}^{i} u_j\right) - N\left(\sum_{j=0}^{i-1} u_j\right)\right]. \tag{15}$$

Comparing both sides, we have

$$\begin{aligned} u_0 &= g, \\ u_1 &= N(u_0), \\ u_{k+1} &= N(u_0 + u_1 +, \ldots, +u_k) - N(u_0 + u_1 +, \ldots, +u_{k-1}), \\ k &= 1.2 \ldots\ldots \end{aligned} \tag{16}$$

Now, consider

$$D_t^{\alpha} u(z,t) + Mu(z,t) = g(z,t), \tag{17}$$

with initial condition,

$$u(z,0) = h(z), \tag{18}$$

where nonlinear operator is denoted by M. Now, apply the Elzaki transform on either sides of equation (17), we obtain

$$E[D_t^{\alpha} u(z,t) + Mu(z,t)] = E[g(z,t)]. \tag{19}$$

Using the differential property of the Elzaki transform, we obtain

$$\overline{u} = u(z,0) + v^{\alpha}[E[g] - E[Mu]] = u(z,0) + v^{\alpha}E[g] - v^{\alpha}E[Mu] = G - v^{\alpha}E[Mu]. \tag{20}$$

Using the inverse Elzaki transform, we obtain

$$u = g(z,t) - E^{-1}[v^{\alpha}E[Mu]], \tag{21}$$

which is of the type as $u = g + Nu$, where $Nu = -E^{-1}[v^{\alpha}E[Mu]]$; then,

$$\begin{aligned} u_0 &= G, \\ u_1 &= -E^{-1}[v^{\alpha}E[Mu_0]], \\ u_{k+1} &= -E^{-1}\left[v^{\alpha}E\left\{M\sum_{j=0}^{i}u_j - M\sum_{j=0}^{i-1}u_j\right\}\right]. \end{aligned} \tag{22}$$

4. Error Analysis of Proposed Technique

In this section, the error analysis of proposed technique is presented.

Theorem 1. *If there exist a real number k, $0 < k < 1$, satisfying, $u_{i+1}(z,v) \le ku_i(z,v)$ for each values of i. Furthermore, if we use the truncated series $\sum_{i=0}^{l} u_i(z,v)$ to approximate solution of $u(z,t)$. We get the maximum truncated error:*

$$\left\| u(z,v) - \sum_{i=0}^{l} u_i(z,v) \right\| \le \frac{k^{l+1}}{(1-k)} \left\| u_0(z,v) \right\|. \tag{23}$$

Proof. We obtain

$$\begin{aligned} \left\| u(z,v) - \sum_{i=0}^{l} u_i(z,v) \right\| &= \left\| \sum_{i=l+1}^{\infty} u_i(z,v) \right\| \le \sum_{i=l+1}^{\infty} \left\| u_i(z,v) \right\| \le \sum_{i=l+1}^{\infty} k^i \left\| u_i(z,v) \right\| \\ &\le k^{l+1}\left[1 + (k)^1 + (k)^2 + \ldots\right] \left\| u_0(z,v) \right\| \le \frac{k^{l+1}}{(1-k)} \left\| u_0(z,v) \right\|, \end{aligned} \tag{24}$$

which completes the proof. □

5. Illustrative Examples

In this section, we execute the proposed iterative method on fractional Zakharov–Kuznetsov equation.

Example 1. Consider the nonlinear time-fractional Zakharov–Kuznetsov equation:

$$D_t^{\alpha} u + \left(u^2\right)_x + \frac{1}{8}\left(u^2\right)_{xxx} + \frac{1}{8}\left(u^2\right)_{xyy} = 0, \tag{25}$$

where $0 < \alpha < 1$ and given initial condition $u(x,y,0) = (1/3)\sigma(e^{(x+y)} - e^{-(x+y)})^2$, where σ is arbitrary constant.

Exact solution for $\alpha = 1$ is

$$u(x,y,0) = \frac{1}{3}\sigma\left(e^{(x+y-\sigma t)} - e^{-(x+y-\sigma t)}\right)^2. \tag{26}$$

Applying the Elzaki transform on both sides,

$$\overline{u} = \frac{1}{3}\sigma\left(e^{(x+y-\sigma t)} - e^{-(x+y-\sigma t)}\right)^2 + v^{\alpha}\left[E\left[-\left(u^2\right)_x - \frac{1}{8}\left(u^2\right)_{xxx} - \frac{1}{8}\left(u^2\right)_{xyy}\right]\right]. \tag{27}$$

Using inverse Elzaki transform, we obtain

$$
\begin{aligned}
u(x,y,t) &= \frac{1}{3}\sigma\left(e^{(x+y-\sigma t)} - e^{-(x+y-\sigma t)}\right)^2 + E^{-1}\left[v^{\alpha}E\left[-\left(u^2\right)_x - \frac{1}{8}\left(u^2\right)_{xxx} - \frac{1}{8}\left(u^2\right)_{xyy}\right]\right],\\
u_0(x,y,t) &= \frac{1}{3}\sigma\left(e^{(x+y-\sigma t)} - e^{-(x+y-\sigma t)}\right)^2,\\
u_1(x,y,t) &= -\frac{2}{3}\frac{\sigma^2 t^{\alpha}}{\Gamma(1+\alpha)}\left(e^{(x+y)} - e^{-(x+y)}\right)\left(e^{3(x+y)} - e^{-3(x+y)} + 3\left(e^{(x+y)} - e^{-(x+y)}\right)\right),\\
u_2(x,y,t) &= \frac{12800}{27}\frac{\Gamma(1+2\alpha)\sigma^4 t^{3\alpha}}{\Gamma(1+\alpha)^2\Gamma(1+3\alpha)}\left(e^{6(x+y)} - e^{-6(x+y)}\right) - \frac{2560}{81}\frac{\Gamma(1+2\alpha)\sigma^4 t^{3\alpha}}{\Gamma(1+\alpha)^2\Gamma(1+3\alpha)}\left(e^{2(x+y)} - e^{-2(x+y)}\right)\\
&\quad - \frac{5120}{81}\frac{\Gamma(1+2\alpha)\sigma^4 t^{3\alpha}}{\Gamma(1+\alpha)^2\Gamma(1+3\alpha)}\left(e^{4(x+y)} - e^{-4(x+y)}\right) - \frac{54400}{81}\frac{\Gamma(1+2\alpha)\sigma^4 t^{3\alpha}}{\Gamma(1+\alpha)^2\Gamma(1+3\alpha)}\left(e^{8(x+y)} - e^{-8(x+y)}\right)\\
&\quad + \frac{800}{9}\frac{\sigma^3 t^{2\alpha}}{\Gamma(1+2\alpha)}\left(e^{6(x+y)} - e^{-6(x+y)}\right) + \frac{416}{27}\frac{\sigma^3 t^{2\alpha}}{\Gamma(1+2\alpha)}\left(e^{2(x+y)} - e^{-2(x+y)}\right) - \frac{2240}{27}\frac{\sigma^3 t^{2\alpha}}{\Gamma(1+2\alpha)}\left(e^{4(x+y)} - e^{-4(x+y)}\right)\\
&\quad + \frac{16}{9}\frac{\sigma^2 t^{\alpha}}{\Gamma(1+\alpha)}\left(e^{2(x+y)} - e^{-2(x+y)}\right) - \frac{20}{9}\frac{\sigma^2 t^{\alpha}}{\Gamma(1+\alpha)}\left(e^{4(x+y)} - e^{-4(x+y)}\right)\\
&\quad + \frac{2}{3}\frac{\sigma^2 t^{\alpha}}{\Gamma(1+\alpha)}\left(e^{(x+y)} - e^{-(x+y)}\right)\left(e^{3(x+y)} - e^{-3(x+y)} + 3\left(e^{(x+y)} - e^{-(x+y)}\right)\right)\\
&\quad + \frac{14}{9}\frac{\sigma^2 t^{\alpha}}{\Gamma(1+\alpha)}\left(e^{3(x+y)} - e^{-3(x+y)} + 3\left(e^{(x+y)} - e^{-(x+y)}\right)\right).
\end{aligned}
\tag{28}
$$

Similarly, we can find the higher order terms of $u(x,y,t)$ using the proposed method. Finally, we get the approximate solution $u(x,y,t)$ denoted by equation (28) is $(x,y,0) = \sum_{i=0}^{\infty} u_i$.

For $\alpha = 1$, $t = 0.5$, and $\sigma = 0.001$, illustrate absolute error, numerical solution, and exact solution in Figures 1–3. On comparison, we found that numerical solution obtained by the Elzaki transform iterative method is identical to exact solution shown in Figures 1–3. We used third order approximation to estimate the efficiency, absolute error, and approximate solution obtained by the Elzaki transform iterative method. Comparison between approximate and exact solution to obtain absolute error for specific value of x and t with other techniques is presented in the tabular form (Table 1).

Example 2. Consider $(3,3,3)$ time-fractional Z-K equation:

$$D_t^{\alpha}u + \left(u^3\right)_x + 2\left(u^3\right)_{xxx} + 2\left(u^3\right)_{xyy} = 0, \quad 0 < \alpha < 1. \tag{29}$$

Initial condition:

$$u(x,y,0) = \frac{3}{4}\sigma\left(e^{(x+y/6)} - e^{-(x+y/6)}\right). \tag{30}$$

For $\alpha = 1$, the exact solution of equation (29) is

$$u(x,y,t) = \frac{3}{4}\sigma\left(e^{(x+y-\sigma t/6)} - e^{-(x+y-\sigma t/6)}\right). \tag{31}$$

Using the differential properties of Elzaki transformation on both sides of equation (29), we obtain

$$\overline{u} = \frac{3}{4}\sigma\left(e^{(x+y-\sigma t/6)} - e^{-(x+y-\sigma t/6)}\right) + v^{\alpha}E\left[-\left(u^3\right)_x - 2\left(u^3\right)_{xxx} - 2\left(u^3\right)_{xyy}\right]. \tag{32}$$

Applying the inverse Elzaki transform, we obtain

$$u(x,y,t) = \frac{3}{4}\sigma\left(e^{(x+y-\sigma t/6)} - e^{-(x+y-\sigma t/6)}\right) + E^{-1}\left[v^{\alpha}E\left[-\left(u^3\right)_x - 2\left(u^3\right)_{xxx} - 2\left(u^3\right)_{xyy}\right]\right]. \tag{33}$$

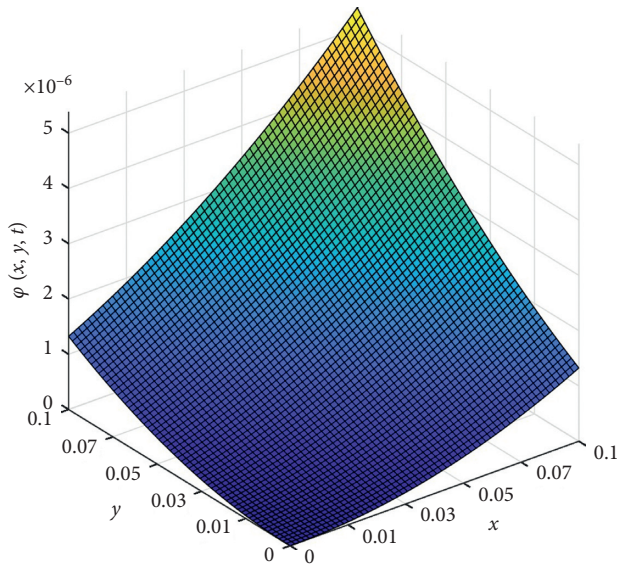

Figure 1: Represents exact solution of Example 1 at $\alpha = 1$.

Using the Elzaki iterative method, the successive terms are as follows:

$$
\begin{aligned}
u_0(x,y,t) &= \frac{3}{4}\sigma\left(e^{(x+y/6)} - e^{-(x+y/6)}\right),\\
u_1(x,y,t) &= -\frac{3\sigma^2 t^{\alpha}}{64\Gamma(1+\alpha)}\left(e^{(x+y/2)} - e^{-(x+y/2)} + 3\left(e^{(x+y/6)} - e^{-(x+y/6)}\right)\right),\\
u_2(x,y,t) &= \frac{23031\sigma^9 t^{4\alpha}\Gamma(1+3\alpha)}{65536\Gamma(1+\alpha)^3\Gamma(1+4\alpha)}\left(e^{(x+y/2)} - e^{-(x+y/2)}\right)\\
&\quad + \frac{295245\sigma^9 t^{4\alpha}\Gamma(1+3\alpha)}{262144\Gamma(1+\alpha)^3\Gamma(1+4\alpha)}\left(e^{(3x+3y/2)} - e^{-(3x+3y/2)}\right) - \frac{11475\sigma^9 t^{4\alpha}\Gamma(1+3\alpha)}{65536\Gamma(1+\alpha)^3\Gamma(1+4\alpha)}\left(e^{(5x+5y/6)} - e^{-(5x+5y/6)}\right)\\
&\quad - \frac{5325\sigma^9 t^{4\alpha}\Gamma(1+3\alpha)}{131072\Gamma(1+\alpha)^3\Gamma(1+4\alpha)}\left(e^{(x+y/6)} - e^{-(x+y/6)}\right) - \frac{246645\sigma^9 t^{4\alpha}\Gamma(1+3\alpha)}{262144\Gamma(1+\alpha)^3\Gamma(1+4\alpha)}\left(e^{(7x+7y/6)} - e^{-(7x+7y/6)}\right)\\
&\quad - \frac{2025\sigma^7 t^{3\alpha}\Gamma(1+2\alpha)}{16384\Gamma(1+\alpha)^2\Gamma(1+3\alpha)}\left(e^{(x+y/2)} - e^{-(x+y/2)}\right) - \frac{4155\sigma^7 t^{3\alpha}\Gamma(1+2\alpha)}{65536\Gamma(1+\alpha)^2\Gamma(1+3\alpha)}\left(e^{(x+y/6)} - e^{-(x+y/6)}\right)\\
&\quad + \frac{43605\sigma^7 t^{3\alpha}\Gamma(1+2\alpha)}{16384\Gamma(1+\alpha)^2\Gamma(1+3\alpha)}\left(e^{(5x+5y/6)} - e^{-(5x+5y/6)}\right) - \frac{49329\sigma^7 t^{3\alpha}\Gamma(1+2\alpha)}{16384\Gamma(1+\alpha)^2\Gamma(1+3\alpha)}\left(e^{(7x+7y/6)} - e^{-(7x+7y/6)}\right)\\
&\quad + \frac{105\sigma^5 t^{2\alpha}}{512\Gamma(1+2\alpha)}\left(e^{(x+y/6)} - e^{-(x+y/6)}\right) + \frac{2295\sigma^5 t^{2\alpha}}{1024\Gamma(1+2\alpha)}\left(e^{(5x+5y/6)} - e^{-(5x+5y/6)}\right)\\
&\quad - \frac{1863\sigma^5 t^{2\alpha}}{1024\Gamma(1+2\alpha)}\left(e^{(x+y/2)} - e^{-(x+y/2)}\right) + \frac{51\sigma^3 t^{\alpha}}{2048\Gamma(1+\alpha)}\left(e^{(x+y/2)} - e^{-(x+y/2)} + 3\left(e^{(x+y/6)} - e^{-(x+y/6)}\right)\right)\\
&\quad - \frac{27\sigma^3 t^{\alpha}}{64\Gamma(1+\alpha)}\left(e^{(x+y/2)} - e^{-(x+y/2)}\right) + \frac{15\sigma^3 t^{\alpha}}{64\Gamma(1+\alpha)}\left(e^{(x+y/6)} - e^{-(x+y/6)}\right)\\
&\quad + \frac{27\sigma^3 t^{\alpha}}{64\Gamma(1+\alpha)}\left(e^{(x+y/3)} - e^{-(x+y/3)} - 2\right)\left(e^{(x+y/6)} - e^{-(x+y/6)}\right).
\end{aligned}
\tag{34}
$$

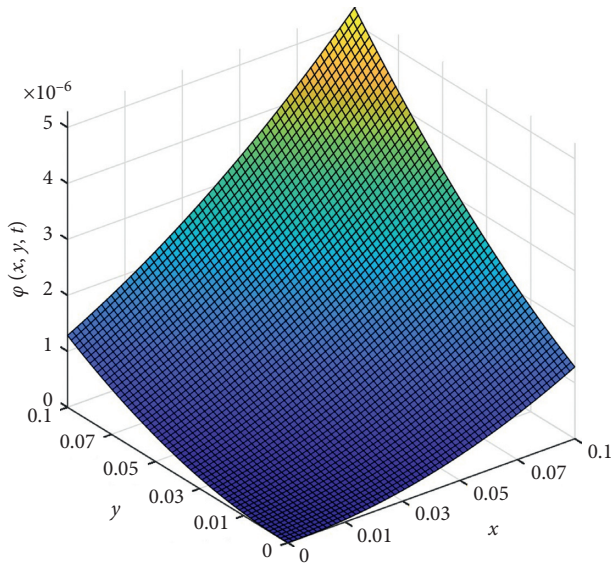

Figure 2: Represents numerical solution of Example 1 at $\alpha = 1$.

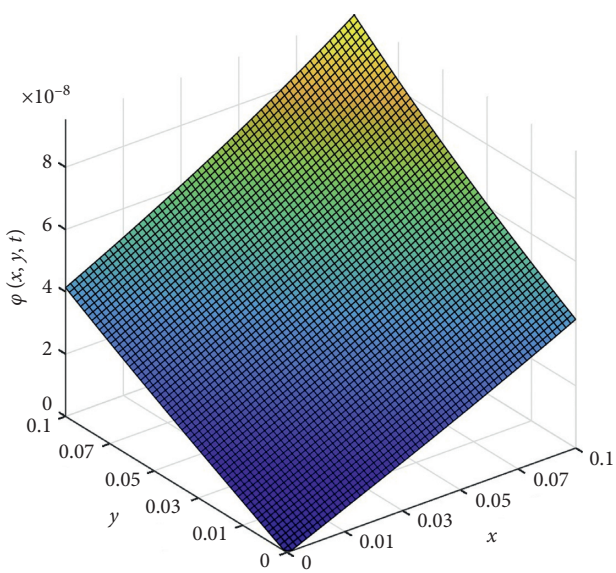

Figure 3: Represents absolute error of Example 1 at $\alpha = 1$.

Table 1: Comparison among different methods for absolute error when $\alpha = 1$ and $\sigma = 0.001$.

x	t	ETIM	VIM	HPTM	NISTM
0.0	0.0	2.00×10^{-8}	2.00×10^{-8}	2.00×10^{-8}	2.00×10^{-8}
	0.01	1.50×10^{-7}	3.99×10^{-6}	1.50×10^{-7}	1.40×10^{-7}
	0.03	3.06×10^{-7}	8.01×10^{-6}	3.06×10^{-7}	3.10×10^{-7}
	0.05	5.55×10^{-7}	1.59×10^{-5}	5.55×10^{-7}	5.55×10^{-7}
	0.07	7.66×10^{-7}	2.24×10^{-5}	7.80×10^{-7}	7.80×10^{-7}
	0.10	8.12×10^{-7}	2.01×10^{-5}	8.11×10^{-7}	8.12×10^{-7}
0.01	0.0	1.40×10^{-7}	3.95×10^{-6}	1.40×10^{-7}	1.40×10^{-7}
	0.01	3.25×10^{-7}	8.01×10^{-6}	3.01×10^{-7}	3.01×10^{-7}
	0.03	5.53×10^{-7}	9.19×10^{-6}	4.65×10^{-7}	4.65×10^{-7}
	0.05	7.32×10^{-7}	2.05×10^{-5}	6.35×10^{-7}	8.11×10^{-7}
	0.07	8.11×10^{-7}	2.11×10^{-5}	8.11×10^{-7}	8.11×10^{-7}
	0.10	9.98×10^{-7}	2.41×10^{-7}	9.99×10^{-7}	9.98×10^{-7}

Table 1: Continued.

x	t	ETIM	VIM	HPTM	NISTM
0.03	0.0	3.01×10^{-7}	7.90×10^{-7}	3.01×10^{-7}	3.01×10^{-7}
	0.01	4.75×10^{-7}	1.49×10^{-6}	4.66×10^{-7}	4.66×10^{-7}
	0.03	5.63×10^{-7}	1.89×10^{-6}	6.63×10^{-7}	6.63×10^{-7}
	0.05	8.91×10^{-7}	2.11×10^{-5}	8.11×10^{-7}	7.55×10^{-7}
	0.07	9.40×10^{-6}	2.23×10^{-5}	9.97×10^{-7}	8.11×10^{-6}
	0.10	1.2×10^{-6}	2.94×10^{-5}	2.41×10^{-6}	1.2×10^{-6}
0.05	0.0	4.66×10^{-7}	1.19×10^{-6}	4.66×10^{-7}	4.66×10^{-7}
	0.01	5.67×10^{-7}	1.34×10^{-6}	6.35×10^{-7}	6.35×10^{-7}
	0.03	7.22×10^{-7}	1.98×10^{-5}	8.12×10^{-7}	8.12×10^{-7}
	0.05	8.98×10^{-7}	2.00×10^{-5}	9.98×10^{-7}	9.98×10^{-7}
	0.07	1.01×10^{-7}	2.41×10^{-5}	1.20×10^{-7}	1.20×10^{-7}
	0.10	1.2×10^{-7}	3.27×10^{-5}	1.41×10^{-7}	1.41×10^{-7}
0.07	0.0	6.35×10^{-7}	1.55×10^{-6}	6.35×10^{-7}	6.35×10^{-7}
	0.01	1.38×10^{-7}	1.89×10^{-6}	7.12×10^{-7}	1.38×10^{-7}
	0.03	7.22×10^{-7}	2.11×10^{-6}	8.34×10^{-7}	7.22×10^{-7}
	0.05	8.98×10^{-7}	8.98×10^{-5}	9.98×10^{-7}	8.98×10^{-7}
	0.07	1.01×10^{-7}	3.52×10^{-5}	1.20×10^{-6}	1.01×10^{-7}
	0.10	1.2×10^{-7}	2.48×10^{-5}	1.56×10^{-6}	1.2×10^{-7}
0.10	0.0	8.12×10^{-7}	2.00×10^{-6}	8.12×10^{-7}	8.12×10^{-7}
	0.01	8.98×10^{-7}	2.21×10^{-6}	9.98×10^{-7}	8.98×10^{-7}
	0.03	7.22×10^{-6}	2.64×10^{-5}	522×10^{-6}	7.22×10^{-6}
	0.05	6.35×10^{-6}	3.27×10^{-5}	3.35×10^{-6}	6.35×10^{-6}
	0.07	4.66×10^{-6}	3.77×10^{-5}	2.66×10^{-6}	4.66×10^{-6}
	0.10	1.63×10^{-6}	4.11×10^{-6}	1.88×10^{-6}	1.63×10^{-6}

Similarly, we can find the higher order terms of $u(x, y, t)$ using the proposed method. Finally, we get the approximate solution $u(x, y, t)$ is given by $(x, y, 0) = \sum_{i=0}^{\infty} u_i$.

For $\alpha = 1$, $t = 0.5$, and $\sigma = 0.001$, illustrate absolute error, numerical solution, and exact solution in Figures 4–6. On comparison, we found that numerical solution obtained by the Elzaki transform iterative method is identical to the exact solution shown in Figures 4–6. We used third-order approximation to estimate the efficiency, absolute error, and approximate solution obtained by the Elzaki transform iterative method. Comparison between approximate and exact solution to obtain absolute error for different value of x and t with other methods is presented in Table 2.

6. Results and Discussion

On comparison of numerical and exact solution in Figures 1 and 2 at $\alpha = 1$, $t = 0.5$, and $\sigma = 0.001$ for nonlinear (2, 2, 2) Zakharov–Kuznetsov equation fractional in time and u strictly increases with the increase in x. Comparison shows exceptional concurrency between numerical and exact solutions. In Figure 3, we demonstrate if x increases at $y = 1$, $t = 1$, and $\sigma = 0.001$, respectively, and at $\alpha = 0.75$, 1. u strictly increases and $\alpha = 0.25$, 0.5. From Figure 4, it is now obvious that the solution depends on fractional derivative of time. In Figure 5, we evaluate exact and numerical solution for standard case of time-fractional Zakharov–Kuznetsov. When $\alpha = 1$, $t = 0.5$, $\sigma = 0.001$, then the nonlinear time (3, 3, 3) time-fractional Zakharov–Kuznetsov u increases strictly with the x increases. Figure 6 demonstrates α at $y = 1$, $t = 1$, and $\sigma = 0.001$, numerous values of fractional order, respectively. It is pragmatic from Figure 6

Table 2: Absolute error for Example 1 between two consecutive approximate terms at different values of α for unknown exact solution.

x	t	$\alpha = 0.5$ $\lvert\varphi_2 - \varphi_1\rvert$	$\alpha = 0.5$ $\lvert\varphi_3 - \varphi_2\rvert$	$\alpha = 0.75$ $\lvert\varphi_2 - \varphi_1\rvert$	$\alpha = 0.5$ $\lvert\varphi_3 - \varphi_2\rvert$
0.0	0.0	4.27×10^{-8}	6.57×10^{-11}	3.21×10^{-8}	2.97×10^{-11}
0.01	0.01	4.12×10^{-8}	8.98×10^{-11}	4.11×10^{-8}	3.98×10^{-11}
0.03	0.03	4.98×10^{-8}	7.22×10^{-10}	4.98×10^{-8}	6.88×10^{-10}
0.05	0.05	6.35×10^{-8}	1.35×10^{-9}	5.35×10^{-8}	1.65×10^{-9}
0.07	0.07	8.11×10^{-7}	4.66×10^{-9}	8.11×10^{-7}	3.33×10^{-9}
0.10	0.10	1.63×10^{-7}	7.63×10^{-9}	9.63×10^{-7}	5.98×10^{-9}

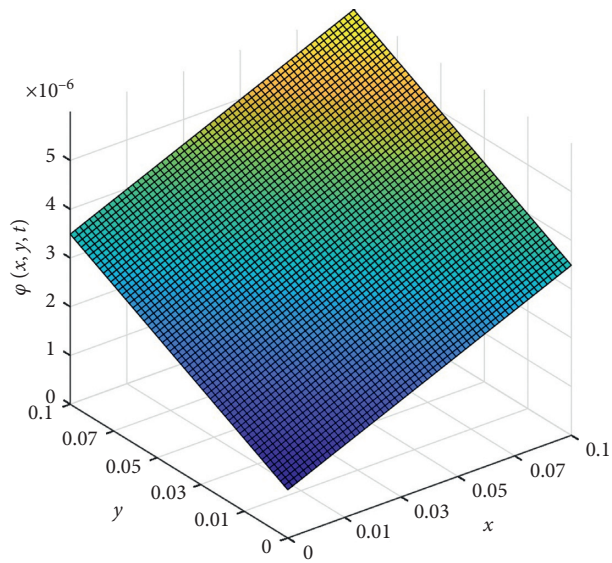

Figure 4: Represents exact solution of Example 2 at $\alpha = 1$.

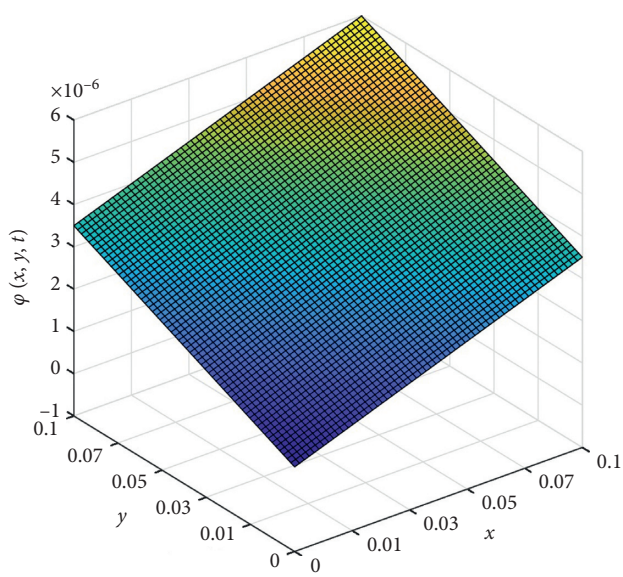

Figure 5: Represents numerical solution of Example 2 at $\alpha = 1$.

that u increases strictly with the increase in x. Table 2 demonstrates that the absolute error can be neglected between the consecutive iterations because it approaches 0, and Table 3 represents the absolute error for Example 1 between two consecutive approximate terms at different values of α for unknown exact solution.

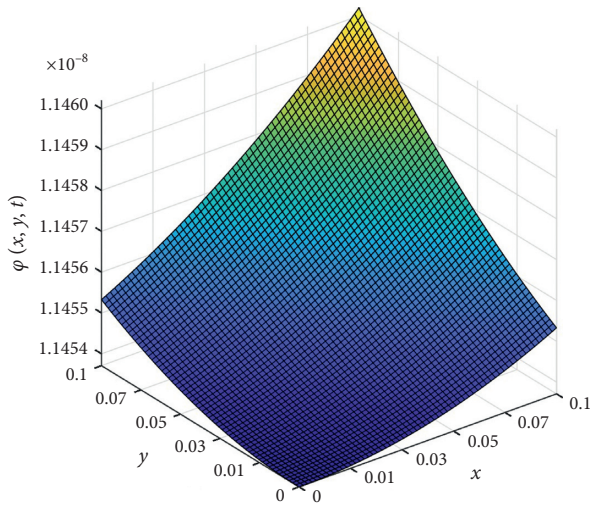

Figure 6: Represents absolute error of Example 2 at $\alpha = 1$.

Table 3: Absolute error for Example 1 between two consecutive approximate terms at different values of α for unknown exact solution.

x	t	$\alpha = 0.5$ $\lvert\varphi_2 - \varphi_1\rvert$	$\alpha = 0.5$ $\lvert\varphi_3 - \varphi_2\rvert$	$\alpha = 0.75$ $\lvert\varphi_2 - \varphi_1\rvert$	$\alpha = 0.5$ $\lvert\varphi_3 - \varphi_2\rvert$
0.0	0.0	1.98×10^{-10}	7.91×10^{-21}	1.91×10^{-10}	4.27×10^{-21}
0.01	0.01	1.98×10^{-10}	3.22×10^{-20}	1.91×10^{-10}	7.88×10^{-20}
0.03	0.03	1.99×10^{-10}	5.99×10^{-18}	1.92×10^{-10}	3.76×10^{-18}
0.05	0.05	1.99×10^{-10}	5.55×10^{-18}	1.92×10^{-10}	5.84×10^{-18}
0.07	0.07	2.00×10^{-10}	7.55×10^{-17}	1.93×10^{-10}	3.88×10^{-17}
0.10	0.10	2.00×10^{-10}	2.23×10^{-17}	1.93×10^{-10}	7.66×10^{-17}

Fractional order α number of iteration increases. This shows the application of proposed method for the fractional order.

7. Conclusion

In this study, we used ETNM to obtain the solution of nonlinear Zakharov–Kuznetsov equation fractional in time. We attain the solution in the convergent series form. The basic characterization of ETNM to find solution of nonlinear models is without using restrictive assumption, which is the improvement over other methods. Numerical comparison shows that this method is more powerful than VIM and HPM. These methods also work well for the unknown integer order. Consequently, we deduce that the presented numerical scheme is efficient and powerful in solving linear and nonlinear fractional order models.

Data Availability

The data used to support the findings of this study are included within the article.

Disclosure

The authors declare that this manuscript is original, has not been published before, and is not currently being considered for publication elsewhere.

Conflicts of Interest

The authors declare that they have no conflicts of interest.

Authors' Contributions

All authors contributed to this research. Material preparation, methodology, data collection, formal analysis, and software were performed by Muhammad Suleman, Jamshaid Ul Rahman, and Dianchen Lu. Initially, the manuscript was prepared by Muhammad Suleman and modified as per the suggestions by the other authors. Final version was reviewed and edited by Samad Noeiaghdam, Jamshaid Ul Rahman, and Ghulam Murtaza. All authors approved the final manuscript.

Acknowledgments

This work was supported by National Natural Science Foundation, China, and Faculty of Science, Jiangsu University, Zhenjiang, China.

References

[1] M. Senol, M. Alquran, and H. D. Kasmaei, "On the comparsion of perturbation-iteration algorithm and residual power series method to solve fractional Zakharov-Kuznetsov equation," *Results in Physics*, vol. 9, pp. 321–327, 2018.

[2] S. Sahoo and S. S. Ray, "Improved sub-equation method for (3+1) dimensional generalized fractional KdV-Zakharov-Kuznetsov equations," *Computers & Mathematics with Applications*, vol. 70, no. 2, pp. 158–166, 2015.

[3] A. Das and A. Saha, "Dynamical survey of the dual power Zakharov-Kuznetsov-Burgers equation with external periodic perturbation," *Computers & Mathematics with Applications*, vol. 76, no. 5, pp. 1174–1183, 2018.

[4] O. P. Porogo, B. Muatjeteja, and A. R. Adem, "Variational approach and exact solutions for a generalized coupled Zakharov-Kuznetsov system," *Computers & Mathematics with Applications*, vol. 73, no. 5, pp. 864–872, 2017.

[5] C. K. Kuo, "The new exact solitary and multi-soliton solutions for the (2+1) dimensional Zakhraov- Kuznetsov equation," *Computers & Mathematics with Applications*, vol. 75, no. 8, pp. 2851–2857, 2018.

[6] J.-H. He, "A tutorial review on fractal spacetime and fractional calculus," *International Journal of Theoretical Physics*, vol. 53, no. 11, pp. 3698–3718, 2014.

[7] J.-H. He, "Fractal calculus and its geometrical explanation," *Results in Physics*, vol. 10, no. S1, pp. 272–276, 2018.

[8] J.-H. He, "A new fractal derivation," *Thermal Science*, vol. 15, no. 1, pp. 145–147, 2011.

[9] H. Y. Liu, Z. M. Liu, and F. K. Ko, "A fractional model for heat transfer in Mongolian yurt," *Thermal Science*, vol. 21, no. 4, pp. 1861–1866, 2017.

[10] X. Shang, J. Wang, and X. Yang, "Fractal analysis for heat extraction in geothermal system," *Thermal Science*, vol. 21, no. 1, pp. 25–31, 2017.

[11] K. L. Wang and S. Y. Liu, "He's fractional derivative and its application for fractional Fornberg-Whitham equation," *Thermal Science*, vol. 21, no. 5, pp. 2049–2055, 2017.

[12] Y. Wang, Y. Zhang, and W. Rui, "Shallow water waves in porous medium for coast protection," *Thermal Science*, vol. 21, no. 1, pp. 145–151, 2017.

[13] Y. Hu and J.-H. He, "On fractal space-time and fractional calculus," *Thermal Science*, vol. 20, no. 3, pp. 773–777, 2016.

[14] X. E. Wu and Y. S. Liang, "Relationship between fractal dimensions and fractional calculus," *Nonlinear Science Letters A*, vol. 8, pp. 77–89, 2017.

[15] J. H. He, S. K. Elagan, and Z. B. Li, "Geometrical explanation of the fractional complex transform and derivative chain rule for fractional calculus," *Physics Letters A*, vol. 376, no. 4, pp. 257–259, 2012.

[16] J. H. He and Z. B. Li, "Converting fractional differential equations into partial differential equations," *Thermal Science*, vol. 16, no. 2, pp. 331–334, 2016.

[17] J.-H. He, "Homotopy perturbation technique," *Computer Methods in Applied Mechanics and Engineering*, vol. 178, no. 3-4, pp. 257–262, 1999.

[18] J.-H. He, "A coupling method of a homotopy technique and a perturbation technique for non-linear problems," *International Journal of Non-linear Mechanics*, vol. 35, no. 1, pp. 37–43, 2000.

[19] J.-H. He, "Some asymptotic methods for strongly nonlinear equations," *International Journal of Modern Physics B*, vol. 20, no. 10, pp. 1141–1199, 2006.

[20] J. H. He, "Homotopy perturbation method with an auxiliary term," *Abstract and Applied Analysis*, vol. 2012, Article ID 857612, 2012.

[21] J. H. He, "Homotopy perturbation method with two expanding parameters," *Indian Journal of Physics*, vol. 88, no. 2, pp. 193–196, 2014.

[22] Y. Wu and J.-H. He, "Homotopy perturbation method for nonlinear oscillators with coordinate-dependent mass," *Results in Physics*, vol. 10, pp. 270-271, 2018.

[23] Z.-J. Liu, M. Adamu, E. Suleiman, and J.-H. He, "Hybridization of homotopy perturbation method and Laplace transformation for the partial differential equations," *Thermal Science*, vol. 21, no. 4, pp. 1843–1846, 2017.

[24] M. Y. Adamu and P. Ogenyi, "Parameterized homotopy perturbation method," *Nonlinear Science Letters A*, vol. 8, no. 2, pp. 240–243, 2017.

[25] Y. O. El-Dib, "Multiple scales homotopy perturbation method for nonlinear oscillators," *Nonlinear Science Letters A*, vol. 8, pp. 352–364, 2017.

[26] U. Filobello-Nino, H. Vazquez-Leal, K. Boubaker et al., "Nonlinearities distribution homotopy perturbation method to find solution for Troesch's problem," *Nonlinear Science Letters A*, vol. 8, no. 3, pp. 279–291, 2018.

[27] A. Yildirim, "An algorithm for solving the fractional nonlinear Schrödinger equation by means of the homotopy perturbation method," *International Journal of Nonlinear Sciences and Numerical Simulation*, vol. 10, no. 4, pp. 445–450, 2009.

[28] A. Yildinm, "Analytical approach to Fokker-Planck equation with space- and time-fractional derivatives by means of the homotopy perturbation method," *Journal of King Saud University - Science*, vol. 22, no. 4, pp. 257–264, 2010.

[29] A. Yildirim and Y. Gulkanat, "Analytical approach to fractional Zakharov–Kuznetsov equations by He's homotopy perturbation method," *Communications in Theoretical Physics*, vol. 53, no. 6, pp. 1005–1010, 2010.

[30] J. H. He, "Variational iteration method- a kind of non-linear analytical technique: some examples," *International Journal of Non-Linear Mechanics*, vol. 34, no. 4, pp. 699–708, 1999.

[31] J. H. He, "Variational Iteration method- some recent results and new interpretations," *Journal of Computational and Applied Mathematics*, vol. 207, no. 1, pp. 3–17, 2007.

[32] J. H. He and X. H. Wu, "Variational iteration method: new development and applications," *Computers & Mathematics with Applications*, vol. 54, no. 7-8, pp. 881–894, 2007.

[33] J. He, "Variational iteration method for delay differential equations," *Communications in Nonlinear Science and Numerical Simulation*, vol. 2, no. 4, pp. 235-236, 1997.

[34] J. H. He, "An approximate solution technique depending on an artificial parameter: a special example," *Communications in Nonlinear Science and Numerical Simulation*, vol. 3, no. 2, pp. 92–97, 1998.

[35] H. Ahmad, "Auxiliary parameter in the variational iteration algorithm-II and its optimal determination," *Nonlinear Science Letters A*, vol. 9, no. 1, pp. 62–72, 2018.

[36] A. Prakash and M. Kumar, "He's variational iteration method for the solution of nonlinear Newell-Whitehead-Segel equation," *Journal of Applied Analysis & Computation*, vol. 6, no. 3, pp. 738–748, 2016.

[37] R. Y. Molliq, M. S. M. Noorani, I. Hashim, and R. R. Ahmad, "Approximate solutions of fractional Zakharov-Kuznetsov equations by VIM," *Journal of Computational and Applied Mathematics*, vol. 233, no. 2, pp. 103–108, 2009.

[38] S. Kumar, H. Kocak, and A. Yildirim, "A fractional model of gas dynamics equations and its analytical approximate solution using Laplace transform," *Zeitschrift für Naturforschung A*, vol. 67, no. 6-7, pp. 389–396, 2012.

[39] S. Kumar, A. Yildirim, Y. Khan, and L. Wei, "A fractional model of the diffusion equation and its analytical solution using Laplace transform," *Iranian Journal of Science and*

Technology, Transaction B: Engineering, vol. 19, no. 4, pp. 1117–1123, 2012.

[40] K. Aruna and A. S. V. Ravi Kanth, "Approximate solutions of nonlinear fractional Schrodinger equation via differential transform method and modified differential transform method," *National Academy Science Letters*, vol. 36, no. 2, pp. 201–221, 2013.

[41] V. Daftardar-Gejji and H. Jafari, "An iterative method for solving nonlinear functional equations," *Journal of Mathematical Analysis and Applications*, vol. 316, no. 2, pp. 753–763, 2006.

[42] V. Daftardar-Gejji and S. Bhalekar, "Solving fractional boundary value problems with Dirichlet boundary conditions using a new iterative method," *Computers & Mathematics with Applications*, vol. 59, no. 5, pp. 1801–1809, 2010.

[43] S. Bhalekar and V. Daftardar-Gejji, "New iterative method: application to partial differential equations," *Applied Mathematics and Computation*, vol. 203, no. 2, pp. 778–783, 2008.

[44] V. Daftardar-Gejji and S. Bhalekar, "Solving fractional diffusion-wave equations using the new iterative method," *Fractional Calculus and Applied Analysis*, vol. 11, no. 2, pp. 193–202, 2008.

[45] H. Jafari, S. Seifi, A. Alipoor, and M. Zabihi, "An iterative method for solving linear and nonlinear fractional diffusion-wave equation," *Journal of Nonlinear Fractional and Phenomenal Science in Engineering*, vol. 11, no. 2, 2007.

[46] S. Bhalekar and V. Daftardar-Gejji, "Solving evolution equations using a new iterative method," *Numerical Methods for Partial Differential Equations*, vol. 26, no. 4, pp. 906–916, 2010.

[47] S. Munro and E. J. Parkes, "Stability of solitary-wave solutions to a modified Zakharov–Kuznetsov equation," *Journal of Plasma Physics*, vol. 64, no. 4, pp. 411–426, 2000.

[48] V. E. Zakharov and E. A. Kuznetsov, "Three-dimensional solutions," *Soviet Physics Uspekhi*, vol. 39, pp. 285-286, 1974.

[49] D. Kumar, J. Singh, and S. Kumar, "Numerical computation of nonlinear fractional Zakharov-Kuznetsov equation arising in ion-acoustic waves," *Journal of the Egyptian Mathematical Society*, vol. 22, no. 3, pp. 373–378, 2014.

[50] D. Kumar, J. Singh, and D. Baleanu, "A hybrid computational approach for Klein-Gordon equations on Cantor sets," *Nonlinear Dynamics*, vol. 87, no. 1, pp. 511–517, 2016.

[51] R. K. Pandey and H. K. Mishra, "Numerical simulation for solution of space-time fractional telegraphs equations with local fractional derivatives via HAFSTM," *New Astronomy*, vol. 57, pp. 82–93, 2017.

[52] Y. Zhang, H. Sun, H. H. Stowell, M. Zayernouri, and S. E. Hansen, "A review of applications of fractional calculus in Earth system dynamics," *Chaos, Solitons & Fractals*, vol. 102, pp. 29–46, 2017.

[53] I. Podlubny, *Fractional Differential Equations*, Academic Press, New York, NY, USA, 1999.

[54] N. Laskin, "Time fractional quantum mechanics," *Chaos, Solitons & Fractals*, vol. 102, pp. 16–28, 2017.

[55] H. Sun, Z. Li, Y. Zhang, and W. Chen, "Fractional and fractal derivative models for transient anomalous diffusion: model comparison," *Chaos, Solitons & Fractals*, vol. 102, pp. 346–353, 2017.

[56] H. Singh, "Approximate solution of fractional vibration equation using Jacobi polynomials," *Applied Mathematics and Computation*, vol. 317, pp. 85–100, 2018.

[57] D. Kumar, J. Singh, and S. Kumar, "A fractional model of Navier-Stokes equation arising in unsteady flow of a viscous fluid," *Journal of the Association of Arab Universities for Basic and Applied Sciences*, vol. 17, no. 1, pp. 14–19, 2015.

[58] D. Kumar, J. Singh, and D. Baleanu, "Numerical computation of a fractional model of differential-difference equation," *Journal of Computational and Nonlinear Dynamics*, vol. 11, no. 6, 2016.

[59] S. Yang, H. Fu, and B. Yu, "Fractal analysis of flow resistance in tree like branching networks with roughened micro channels," *Fractals*, vol. 25, no. 1, Article ID 1750008, 2017.

[60] M. Suleman, D. Lu, J. He, U. Farooq, H. S. Ye, and J. Ul Rahman, "Numerical investigation of fractional HIV model using Elzaki projected differential transform method," *Fractals*, vol. 26, no. 5, Article ID 1850062, 2018.

[61] M. Suleman, D. Lu, J. He, U. Farooq, S. Noeiaghdam, and F. Ali Chandio, "Elzaki projected differential transform method for fractional order system of linear and nonlinear fractional partial differential equation," *Fractals*, vol. 26, no. 3, Article ID 1850041, 2018.

[62] J. Ul Rahman, M. Suleman, D. C. Lu, J.-H. He, and M. Ramzan, "He-Elzaki method for spatial diffusion of biological population," *Fractals*, vol. 27, no. 5, Article ID 1950069, 2019.

[63] D. Lu, M. Suleman, M. Ramzan, and J. Ul Rahman, "Numerical solutions of coupled nonlinear fractional KdV equations using He's fractional calculus," *International Journal of Modern Physics B*, vol. 35, no. 2, Article ID 2150023, 2020.

[64] J. Rahman, U. Khan, S. Ahmad et al., "Numerical simulation of Darcy-forchheimer 3D unsteady nanofluid flow comprising carbon nanotubes with cattaneo-christov heat flux and velocity and thermal slip conditions," *Processes*, vol. 7, no. 10, p. 687, 2019.

[65] M. Ahmad, M. A. Imran, M. Aleem, and I. Khan, "A comparative study and analysis of natural convection flow of MHD non-Newtonian fluid in the presence of heat source and first-order chemical reaction," *Journal of Thermal Analysis and Calorimetry*, vol. 137, no. 5, pp. 1783–1796, 2019.

[66] M. A. Imran, I. Khan, M. Ahmad, N. A. Shah, and M. Nazar, "Heat and mass transport of differential type fluid with non-integer order time-fractional Caputo derivatives," *Journal of Molecular Liquids*, vol. 229, pp. 67–75, 2017.

Hindawi
Complexity
Volume 2021, Article ID 3754922, 13 pages
https://doi.org/10.1155/2021/3754922

Research Article

Stagnation Point Flow of EMHD Micropolar Nanofluid with Mixed Convection and Slip Boundary

Shahzada Muhammad Atif,[1] Muhammad Abbas,[2] Umair Rashid,[3] and Homan Emadifar[4]

[1]*Department of Mathematics, Capital University of Science and Technology, Islamabad, Pakistan*
[2]*Department of Mathematics, University of Sargodha, Sargodha 40100, Pakistan*
[3]*CAS Key Laboratory of Mechanical Behavior and Design of Materials, Department of Modern Mechanics, University of Science and Technology of China, Hefei 230026, Anhui, China*
[4]*Department of Mathematics, Islamic Azad University, Hamedan Branch, Hamedan, Iran*

Correspondence should be addressed to Muhammad Abbas; muhammad.abbas@uos.edu.pk and Homan Emadifar; homan_emadi@yahoo.com

Received 10 April 2021; Revised 27 May 2021; Accepted 19 June 2021; Published 2 July 2021

Academic Editor: Muhammad Imran Asjad

The aim of this numerical research is to study the stagnation point flow of the electrical magnetohydrodynamic micropolar nanofluid with slip conditions past a stretching sheet. The phenomenon of linear thermal radiation, Ohmic and internal heating, has also been considered in the energy equation. The modelled PDEs are converted into ODEs via similarity transformation, and converted ODEs are tackled via the shooting technique. The features of assorted parameters on the axial and angular velocities and energy and concentration fields are sketched. The numerical values of the Sherwood and Nusselt numbers have been computed numerically and displayed in the form of tables. Our analysis shows that the heat transfer rate is decreased as the thermal slip parameter and the diffusion slip parameter are enhanced. The present study illustrates that the energy and concentration distribution are decreased with each of the mass free convection parameter, stagnation parameter, and thermal free convection parameter.

1. Introduction

The phenomenon of transfer of heat, which has significant application in many engineering and industry disciplines, is affected positively by the implementation of an appropriate magnetic field. The investigation of magnetohydrodynamic flow past a heated surface has gained significant attention due to its vast applications in engineering problems, i.e., magnetohydrodynamic power generators, petroleum industries, and crystal growth. Swedish scientist Alfven [1] was the first to introduce the magnetohydrodynamic fluid flow. He won the Nobel Prize in Physics for his work on MHD in 1970. He described the class of magnetohydrodynamic waves, which are now known as Alfven waves. Zheng et al. [2] reported the magnetohydrodynamic 2-D (dimensional) flow past a porous shrinking surface with slip conditions with conclusion that an acclivity in the shrinking parameter enhances the thermal boundary layer. By considering the slip effects in a porous medium, Ullah et al. [3] explored the magnetohydrodynamic (MHD) Casson fluid and noticed that boosting the unsteadiness parameter enhances the wall shear stress. Rahbari et al. [4] examined the magnetohydrodynamic Maxwell fluid flowing through parallel plates and determined that increase in the Deborah number increases the velocity. By investigating heat transfer in the magnetohydrodynamic flow past a radially shrinking/stretching sheet, Soid et al. [5] concluded that dual solutions exist only in case of suction and for small values of magnetic parameters. Decline in surface drag due to increment in the squeezed flow parameter in Carreau fluid with thermal radiation and magnetohydrodynamic effect past a sensor surface was reported by Atif et al. [6]. Transverse

magnetohydrodynamic effect on nonlinear stretching sheet was ascertained by Ramana et al. [7]. They used modified Fourier flux law and concluded that the relaxation and retardation time have opposite effects on the thermal profile. For further studies, see [8, 9].

Stagnation point flow is one of the fields in which scientists and engineers show keen interest. Some of the recent studies include the following: For MHD viscoelastic nanofluid, the dual solution of stagnation point past a porous stretching surface with radiation effect was reported by Juosh [10]. It was found that an acclivity in the Deborah number contributes to upsurge in the drag coefficient. Impact of MHD on stagnation point flow of a nanofluid with nonuniform thermal reservoir was analyzed by Rashid et al. [11]. Pal [12] put light on magnetohydrodynamic stagnation point flow with suction effect and reported that the Sherwood number was decreased as the Lewis number increased. Bioconvective stagnation point of Maxwell nanofluid flow past a convectively heated surface was reported by Abbasi et al. [13]. They observed that energy, concentration, and density profiles were higher for nonconvective surfaces than in convective heated surfaces. Lund et al. [14] performed the stability analysis and reported the dual solution of MHD stagnation point of Casson fluid. Their main observation was that the sign of the smallest eigenvalues shows that the first solution was stable. Effect of solar radiation on MHD stagnation point nanofluid flow was discussed by Ghasemia and Hatami [15] with a key finding that the energy profile is hiked as the Biot number is increased rapidly. The phenomena of thermal radiation have much significance in the transfer of heat and were discussed by many authors in the literature [16–19].

Micropolar fluids can be characterized as fluids which exhibit the micro-rotational effects and micro-rotational inertia. Analysis of the micropolar fluids has been an active field of interest for many researchers. This class of fluids possesses certain simplicity and elegance in their mathematical formulation which should appeal to mathematicians. The micropolar fluids can support couple stress and body couples only. Physically, they may represent adequately the fluids consisting of dipole elements. Certain anisotropic fluids e.g., liquid crystals which are made up of dumbbell molecules are of this type. In fact, animal blood happens to fall in this category. Other polymeric fluids and fluids containing minute amounts of additives may be represented by the mathematical model underlying micropolar fluids. Eringen [20, 21], through his pioneering work, invited the attention of the researchers' community in this interesting area of fluid dynamics. Sui et al. [22] investigated the nonlinear constitutive diffusion model in the micropolar fluid with the main finding that both the velocity and energy profiles are increased as the power exponent n is decreased from 1. Heat transfer of the free convective micropolar fluid with heat source past a shrinking sheet was noticed by Mishra et al. [23]. They observed that the fluid motion is declined as the heat generation coefficient is upsurged. Atif et al. [24] analyzed the bioconvective magnetohydrodynamic micropolar nanofluid with stratification and reported that the density distribution decreases as the density stratification and mixed number parameter are hiked. Micropolar nanofluid flow with nonlinear convection and multiple slip effects was examined by Zemedu and Ibrahim [25] with concluding remarks that boosting the solutal nonlinear convection parameter causes an increase in the velocity.

The heat transfer in base fluids like mineral oils, water, and ethylene glycol is not as much effective as in nanofluids [26–31]. Nanofluids have the ability to improve the heat transfer properties. Their ability to move through capillaries and microchannels without making any blockage in flow makes them unique. By considering the induced magnetic field, Atif et al. [32] investigated the magnetohydrodynamic micropolar Carreau nanofluid and found that the angular velocity is increased rapidly as the magnetic Prandtl number increases. Three-dimensional Eyring–Powell nanofluid with Arrhenius energy was reported by Taseer et al. [33]. Khan [34] reported that nanoparticle dispersion reduces the Nusselt number in a partially heated vertical annulus. For a solutal-dominated regime, both Nusselt and Sherwood numbers declined for micropolar nanofluid as reported by Manaa et al. [35].

In recent years, researchers have paid serious attention to electrical magnetohydrodynamics. Electrical magnetohydrodynamic stagnation point nanofluid with mixed convection and slip boundary over a stretching surface was scrutinized by Hsiao [36]. A major conclusion was that an acclivity in either the electrical or the magnetic parameter led to an upsurge in the temperature profile. Literature review indicates that the EMHD stagnation point micropolar nanofluid with mixed convection and slip boundary has not been investigated yet. In the present article, linear thermal radiation, Joule's heating, and heat source have also been incorporated in the energy equation. In this study, four aspects have been focused. First, the heat and mass transfer of micropolar nanofluid are addressed. Second, the impact of thermal radiation and electrical magnetohydrodynamics on different profiles is examined. Third, the stagnation point flow is analyzed. Fourth, the analysis of the mixed convection and slip boundary conditions is performed. The arising ordinary differential equations for the problem are tackled through the shooting method. The influence of all the prominent parameters is examined numerically and displayed graphically.

2. Mathematical Model

An incompressible, 2D, mixed convection micropolar nanofluid flow over a stretching sheet with slip effects has been analyzed. By using Ohm's law and Maxwell's equations, the continuity equation, linear and angular momentum, and fluid energy and concentration equations have been formulated. Joule's heating, thermal radiation, and heat source effects have also been considered in the energy equation. C, C_∞, T, and T_∞ denotes the surface concentration, ambient concentration surface temperature, and ambient temperature, respectively. The flow is assumed along the $x-$ axis which is considered to be in the upward direction, whereas the $y-$ axis is perpendicular to the sheet. A uniform magnetic field B_0 has been implemented towards

the y – axis as illustrated in Figure 1. It is also assumed that the magnetic Reynolds number is very small due to which induced magnetic number is ignored.

In the light of the above assumption, the governing equations of the modelled problem are as follows [36, 37]:

$$\frac{\partial u}{\partial x}+\frac{\partial v}{\partial y}=0, \tag{1}$$

$$\begin{aligned} u\frac{\partial u}{\partial x}+v\frac{\partial u}{\partial y}=U_\infty\frac{\partial U_\infty}{\partial x}+\left(\nu+\frac{k}{\rho}\right)\frac{\partial^2 u}{\partial y^2}+\frac{k}{\rho_f}\frac{\partial N}{\partial y}+\frac{1}{\rho}\sigma B_0^2(U-u)\\ +g_x\beta_t(T-T_\infty)+g_x\beta_c(C-C_\infty)+\frac{1}{\rho}\sigma E_0B_0, \end{aligned} \tag{2}$$

$$u\frac{\partial N}{\partial x}+v\frac{\partial N}{\partial y}=\frac{\gamma}{(\rho j)}\left(\frac{\partial^2 N}{\partial y^2}\right)-\frac{k}{(\rho j)}\left(2N+\frac{\partial u}{\partial y}\right), \tag{3}$$

$$\begin{aligned} u\frac{\partial T}{\partial x}+v\frac{\partial T}{\partial y}=\alpha\frac{\partial^2 T}{\partial y^2}-\frac{1}{(\rho C_p)}\frac{\partial q_r}{\partial y}+\frac{\sigma(uB_0-E_0)^2}{(\rho C_p)}+\tau\left[D_B\frac{\partial C}{\partial y}\frac{\partial T}{\partial y}+\frac{D_T}{T_\infty}\left(\frac{\partial T}{\partial y}\right)^2\right]\\ +\frac{Q_0}{(\rho C_p)}(T-T_\infty), \end{aligned} \tag{4}$$

$$u\frac{\partial C}{\partial x}+v\frac{\partial C}{\partial y}=D_B\frac{\partial^2 C}{\partial y^2}+\frac{D_T}{T_\infty}\frac{\partial^2 T}{\partial y^2}. \tag{5}$$

The related BCs are as follows:

$$\left.\begin{aligned} &\left.\begin{aligned} &u_w-cx=L\frac{\partial u}{\partial y},\\ &v=v_w=ax,\\ &N=0,\\ &T=T_w+k_1\frac{\partial T}{\partial y},\\ &C=C_w+k_2\frac{\partial C}{\partial y}, \end{aligned}\right\}\ \text{at } y=0,\\ &\left.\begin{aligned} &u\longrightarrow 0,\\ &N\longrightarrow 0,\\ &T\longrightarrow T_\infty,\\ &C\longrightarrow C_\infty, \end{aligned}\right\}\ \text{as } y\longrightarrow\infty. \end{aligned}\right\}. \tag{6}$$

In equation (3), the Rosseland radiative heat flux q_r is given by $q_r=-(4\sigma^*/3\kappa^*)(\partial T^4/\partial y)$. The spin gradient viscosity is given by $\gamma=(\mu+(k/2))j$, where $j=\nu/a$ and k represents the microinertia density and vortex viscosity, respectively. For nondimensionlization, the following transformation [36] has been considered:

$$\left.\begin{aligned} &\psi=x\sqrt{a\nu}\,f(\eta),\\ &N=ax\sqrt{\frac{a}{\nu}}\,g(\eta),\\ &\eta=y\sqrt{\frac{a}{\nu}},\\ &\theta(\eta)=\frac{T-T_\infty}{T_w-T_\infty},\\ &T=T_\infty+Ax\theta(\eta),\\ &\phi(\eta)=\frac{C-C_\infty}{C_w-C_\infty},\\ &C=C_\infty+Bx\phi(\eta). \end{aligned}\right\}. \tag{7}$$

Continuity equation (1) is satisfied automatically, and equations (2)–(5) yield the following:

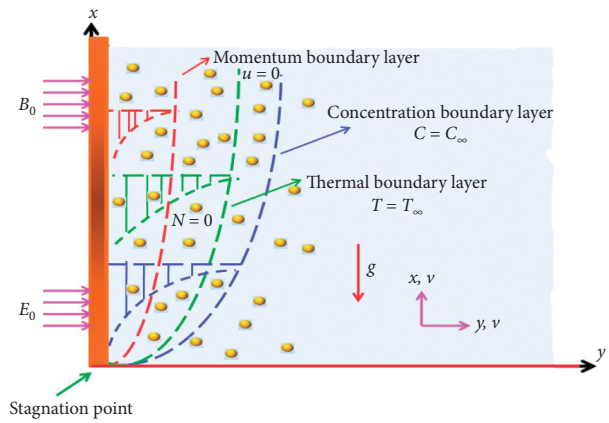

Figure 1: Flow configuration.

$$(1+K)f''' - f'^2 + ff'' + Kg' + S_0 - M(f' - 1 - E) + G_t\theta + G_c\phi = 0, \tag{8}$$

$$\left(1+\frac{K}{2}\right)g'' - gf' + fg' - K(2g + f'') = 0, \tag{9}$$

$$\left(1+\frac{4}{3}Rd\right)\theta'' + \Pr\left[f\theta' + \lambda\theta + Nb\theta'\phi' + Nt\theta'^2 + MEc\left(f'^2 + E^2 - 2Ef'\right)\right] = 0, \tag{10}$$

$$\phi'' + Scf\phi' + \frac{Nt}{Nb}\theta'' = 0. \tag{11}$$

The associated boundary conditions in the dimensionless form are as follows:

$$\left.\begin{aligned} f &= S, \\ f' &= 1 + \delta_1 f'', \\ g &= 0, \\ \theta &= 1 + \delta_2\theta', \\ \phi &= 1 + \delta_3\phi' \end{aligned}\right\} \text{at } \eta = 0, \qquad \left.\begin{aligned} f' &\longrightarrow 0, \\ g &\longrightarrow 0, \\ \theta &\longrightarrow 0, \\ \phi &\longrightarrow 0, \end{aligned}\right\} \text{as } \eta \longrightarrow \infty. \tag{12}$$

Here, $\Pr = \nu/\alpha$ denotes the Prandtl number, $S_0 = U_\infty^2(c + Lf''(0)\sqrt{a^3/\nu})^2/a^2u_w^2$ represents the stagnation parameter, $\mathrm{Ec} = a^2x^2/C_p(T_w - T_\infty)$ denotes the Eckert number, $\mathrm{Nb} = \tau D_B(C_w - C_\infty)/\nu$ denotes the Brownian motion parameter, $K = k/\mu$ represents the micropolar parameter, $G_t = g_x\beta_t(T_w - T_\infty)(c + Lf''(0)\sqrt{a^3/\nu})/a^2U_w$ represents the thermal free convection parameter, $M = \sigma B_0^2/a\rho$ represents the magnetic number, $E = E_0/B_0U$ represents the electric field parameter, $\mathrm{Nt} = \tau D_T(T_w - T_\infty)/\nu T_\infty$ denotes the thermophoresis parameter, $S = (c/a) + (L/a)f''(0)\sqrt{a^3/\nu}$ denotes the slip parameter, $\mathrm{Sc} = \nu/D_B$ denotes the Schmidt number, $G_c = g_x\beta_c(C_w - C_\infty)(c + Lf''(0)\sqrt{a^3/\nu})/a^2U_w$ denotes the mass free convection parameter, $\mathrm{Rd} = 4\sigma^*T_\infty^3/k\kappa^*$ denotes the thermal radiation parameter, $\lambda = Q_0/a(\rho C_p)$ denotes the heat generation coefficient, $\delta_1 = L\sqrt{a/\nu}$ represents the shear stress parameter, $\delta_2 = k_1\sqrt{a/\nu}$ represents the temperature slip parameter, and $\delta_3 = k_2\sqrt{a/\nu}$ represents the diffusion slip parameter, where k_1 and k_2 are the slip parameters associated with the reference temperature and concentration, respectively.

3. Quantities of Interest

The dimensionless Nusselt and dimensionless Sherwood numbers are the most concerning quantities in engineering and industries.

$$\mathrm{Nu} = \frac{xq_w}{k(T_w - T_\infty)}, \qquad \mathrm{Sh} = \frac{xj_w}{D_B(C_w - C_\infty)}. \tag{13}$$

In the nondimensional form, Nusselt and Sherwood numbers are given by

$$\mathrm{Nu}_x\mathrm{Re}_x^{-(1/2)} = -\left(1+\frac{4}{3}\mathrm{Rd}\right)\theta'(0), \qquad \mathrm{Sh}_x\mathrm{Re}_x^{-(1/2)} = -\phi'(0), \tag{14}$$

where $\mathrm{Re}_x = ax^2/\nu$.

4. Solution Methodology

The system of ODEs (8)–(11) along with BCs (12) is tackled numerically by the shooting technique. Now, we introduce $\varsigma_1 = f$, $\varsigma_2 = f'$, $\varsigma_3 = f''$, $\varsigma_4 = g$, $\varsigma_5 = g'$, $\varsigma_6 = \theta$, $\varsigma_7 = \theta'$, $\varsigma_8 = \phi$, and $\varsigma_9 = \phi'$ as follows:

$$\left.\begin{aligned}
\varsigma_1' &= \varsigma_2,\\
\varsigma_2' &= \varsigma_3,\\
\varsigma_3' &= \frac{1}{1+K}\left[\varsigma_2^2 - \varsigma_1\varsigma_3 - S_0 - K\varsigma_5 + M\left(\varsigma_2 - 1 - E\right) - G_t\varsigma_6 - G_c\varsigma_8\right],\\
\varsigma_4' &= \varsigma_5,\\
\varsigma_5' &= \frac{2}{2+K}\left[\varsigma_2\varsigma_4 - \varsigma_1\varsigma_5 + K\left(2\varsigma_4 + \varsigma_3\right)\right],\\
\varsigma_6' &= \varsigma_7,\\
\varsigma_7' &= -\frac{3\mathrm{Pr}}{3+4\mathrm{Rd}}\left[\varsigma_1\varsigma_7 + \lambda\varsigma_6 + MEc\left(\varsigma_2^2 + E^2 - 2E\varsigma_2\right) + \mathrm{Nb}\varsigma_7\varsigma_9 + \mathrm{Nt}\varsigma_7^2\right],\\
\varsigma_8' &= \varsigma_9,\\
\varsigma_9' &= -Sc\varsigma_1\varsigma_9 - \frac{\mathrm{Nt}}{\mathrm{Nb}}\varsigma_7'.
\end{aligned}\right\}. \tag{15}$$

The corresponding boundary conditions are

$$\left.\begin{aligned}
&\varsigma_1 = S,\\
&\varsigma_2 = 1 + \delta_1\varsigma_3,\\
&\varsigma_4 = 0, \qquad \text{at } \eta = 0,\\
&\varsigma_6 = 1 + \delta_2\varsigma_7,\\
&\varsigma_8 = 1 + \delta_3\varsigma_9\\
&\varsigma_2 \longrightarrow 0,\\
&\varsigma_4 \longrightarrow 0,\\
&\varsigma_6 \longrightarrow 0, \qquad \text{as } \eta \longrightarrow \infty.\\
&\varsigma_8 \longrightarrow 0
\end{aligned}\right\}. \tag{16}$$

4.1. Code Validation. For the verification of the correctness of the code, the results of the Nusselt and Sherwood numbers which were presented by Khan and Pop [38] and Hsiao [36] are successfully reproduced. Our simulations have a satisfactory agreement with the already published results of Khan and Pop [38] and Hsiao [36] in the literature which can be seen in Table 1.

5. Results and Discussion

Table 2 is displayed to view the effect of the sundry parameters on the dimensionless Nusselt number and Sherwood number. It is observed that a boost in each of the electric parameter E, slip parameter S, micropolar parameter K, thermal radiation parameter Rd, the stagnation parameter S_0, thermal free convection parameter G_t, diffusion slip parameter δ_3, and mass free convection parameter G_c, causes an increase in Nusselt number, whereas it decreases for a boost in each of the heat generation coefficient λ, shear stress parameter δ_1, magnetic parameter M, and the thermal slip parameter δ_2. The Sherwood number is hiked as each of the material parameter K, magnetic parameter M, thermal free convection parameter G_t, velocity slip parameter S, electric parameter E, b mass free convection parameter G_c, stagnation parameter S_0, and heat generation coefficient λ, and thermal radiation parameter Rd is boosted. However, it diminishes as the diffusion slip parameter δ_3, thermal slip parameter δ_2, and shear stress parameter δ_1 are increased.

Figures 2–14 are sketched to study the variations occurring due to dimensionless parameters in temperature distribution $\theta(\eta)$. For all graphs of the temperature dynamics, the values of $\mathrm{Rd} = 1$, $K = \mathrm{Ec} = \mathrm{Sc} = 0.2$, $\mathrm{Pr} = 10$, and $M = \lambda = \mathrm{Nt} = \mathrm{Nb} = S = E = S_0 = \delta_1 = \delta_2 = \delta_3 = G_t = G_c = 0.1$. Figure 2 is prepared to visualize the fluctuation in the temperature distribution $\theta(\eta)$ in response to the variation in the magnetic effect M. The temperature of the fluid is increased as M increases. This supports the general behaviour of the implementation of M. Resistance to the flow of the fluid is increased as M increases due to which $\theta(\eta)$ is enhanced. The temperature distribution $\theta(\eta)$ is diminished as the stagnation parameter S_0 is enhanced. This effect is evident from Figures 3 and 4 demonstrated to view the effect of Pr on temperature distribution $\theta(\eta)$. These graphs indicate that upsurge in the Prandtl number Pr causes depreciation in the thermal profile. There is decline in the thermal conductivity of the fluid due to which $\theta(\eta)$ is reduced. Fluctuation due to electrical parameter E in the temperature is divulged in Figure 5. An increment in E results in an enhancement in thermal profile. As the Lorentz force is associated with the magnetic and electric field, it

Table 1: Comparison of the presently computed values of $-\theta'(0)$ and $-\phi'(0)$.

		$-\theta'(0)$			$-\phi'(0)$		
Nt	Nb	[38]	[36]	Present	[38]	[36]	Present
0.1		0.9524	0.9524	0.952371	2.1294	2.1294	2.129356
0.2		0.6932	0.6932	0.693173	2.2740	2.2740	2.273956
0.3	0.1	0.5201	0.5201	0.520081	2.5286	2.5287	2.528542
0.4		0.4026	0.4026	0.402584	2.5752	2.5752	2.795041
0.5		0.3211	0.3211	0.321059	3.0351	3.0352	3.034979
0.1	0.2	0.5056	0.5056	0.505580	2.3819	2.3819	2.381840
	0.3	0.2522	0.2521	0.252156	2.4100	2.4100	2.409991
	0.4	0.1194	0.1194	0.119406	2.3997	2.3997	2.399625
	0.5	0.0543	0.0542	0.054254	2.3836	2.3836	2.383547

Table 2: Numerical values of $-\theta'(0)$ and $-\phi'(0)$ with Pr = 10 and Sc = 10.

K	M	S	E	Rd	λ	S_0	δ_1	δ_2	δ_3	G_t	G_c	$-\theta'(0)$	$-\phi'(0)$
0.2	0.1	0.1	0.1	1	0.1	0.1	0.1	0.1	0.1	0.1	0.1	2.208651	2.024640
0.5												2.232818	2.036448
												2.261914	2.050800
	0.5											2.184588	2.084730
	1											2.080667	2.150170
	2											1.739265	2.272888
		0.2										2.243757	2.041956
		0.3										2.275876	2.058062
		0.4										2.305543	2.073151
			0.2									2.218326	2.024963
			0.3									2.226200	2.025659
			0.4									2.232293	2.026724
				2								2.984161	2.071179
				3								3.592600	2.106463
				4								4.112293	2.133076
					0.2							1.942647	2.096437
					0.3							1.642765	2.176308
					0.4							1.297555	2.266894
1.0						0.2						2.642305	2.309297
						0.3						3.086188	2.579879
						0.4						3.535021	2.835314
							0.2					2.150432	1.993731
							0.3					2.101926	1.968131
							0.4					2.060676	1.946477
								0.2				2.040919	2.040302
								0.3				1.893540	2.054700
								0.4				1.763684	2.067856
									0.2			2.289550	1.628650
									0.3			2.345048	1.362008
									0.4			2.385455	1.170300
										1		2.274822	2.057306
										5		2.488543	2.166622
										10		2.670723	2.263403
											1	2.251821	2.045980
											5	2.405905	2.124113
											10	2.549245	2.199092

leads to an increment in the resistance causing the energy distribution to enhance. The influence of the thermal radiation parameter Rd on temperature distribution $\theta(\eta)$ is chalked out in Figure 6. These graphs reflect that an enhancement in Rd increases the energy profile. To visualize the behaviour of the thermophoresis parameter Nt on temperature, Figure 7 is sketched, which shows that there is an increment in $\theta(\eta)$ as Nt is hiked. Physically, in

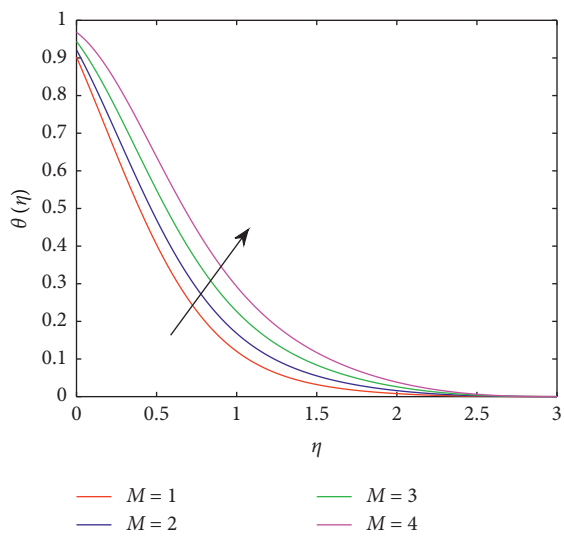

Figure 2: Variation due to M in $\theta(\eta)$.

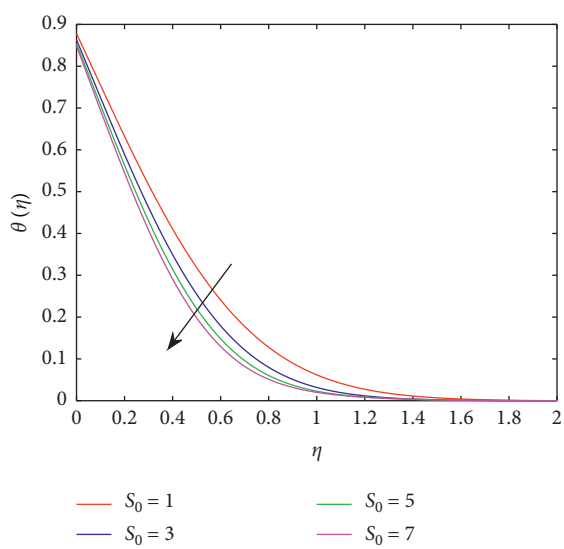

Figure 3: Variation due to S_0 in $\theta(\eta)$.

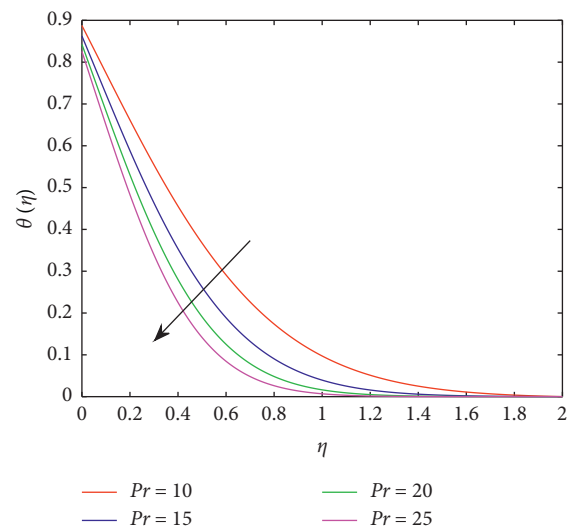

Figure 4: Variation due to Pr in $\theta(\eta)$.

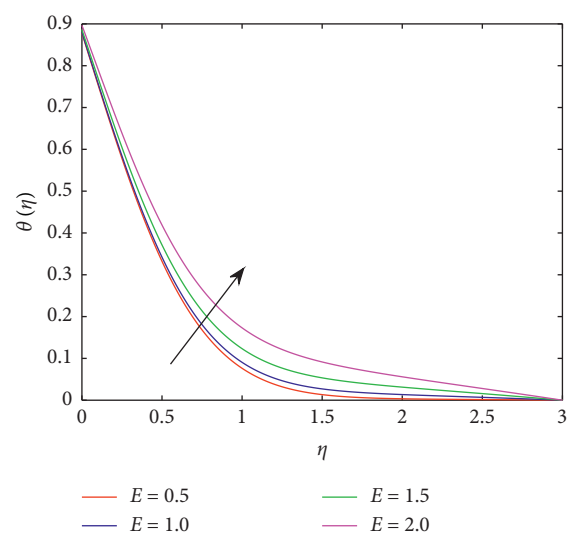

Figure 5: Variation due to E in $\theta(\eta)$.

thermophoresis, the particles apply force on the other particles due to which particles from the hotter region move towards the colder region. Larger values of Nt denotes more application of the force on the other particles and as a result, more fluid moves from the higher temperature region to the colder region. Figure 8 shows that $\theta(\eta)$ is increased as the Brownian motion parameter Nb increases. Physically, the Brownian motion heats up the fluid and also aggravates the particles away from the fluid regime and therefore a decrement is seen in concentration profile. Figure 9 is illustrated to view the effect of heat generation coefficient λ on $\theta(\eta)$, which shows that $\theta(\eta)$ is hiked for escalating values of λ. The viscous dissipation effect which is represented by the Eckert number Ec on energy field is analyzed in Figure 10. It is a number that represents the relation between the kinetic energy and the change in enthalpy. It is noticed that gradually boosting Ec leads to an increase in $\theta(\eta)$. Influence of the dimensionless slip parameter S on $\theta(\eta)$ is presented in Figure 11, and it shows that an upsurge in S encourages the energy distribution $\theta(\eta)$ to decline. The influence of the slip parameter δ_2 which is associated with temperature on the temperature field is chalked out in Figure 12. The energy profile is found to be increasing as slip parameter δ_2 goes up. The variation in the thermal profile due to the thermal free convection parameter G_t is shown in Figure 13. The energy distribution declined as the thermal free convection parameter G_t is hiked. Figure 14 depicts that the energy profile is decreases as G_c is boosted.

Figures 15–23 have been outlined to study the fluctuations in the concentration field $\phi(\eta)$ due to variation in the governing parameters. For all the graphical presentations of $\phi(\eta)$, we have considered $\mathrm{Pr} = 10, \mathrm{Nb} = 0.3, \mathrm{Ec} = Sc = K = 0.2$, and $M = \mathrm{Rd} = 1, \lambda = \mathrm{Nt} = S = E = S_0 = \delta_1 = \delta_2 = \delta_3 = G_t = G_c = 0.1$. Figure 15 is given to study the impact of

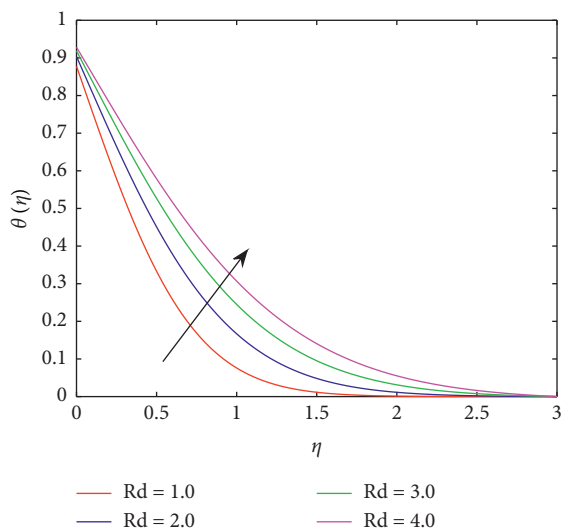

Figure 6: Variation due to Rd in $\theta(\eta)$.

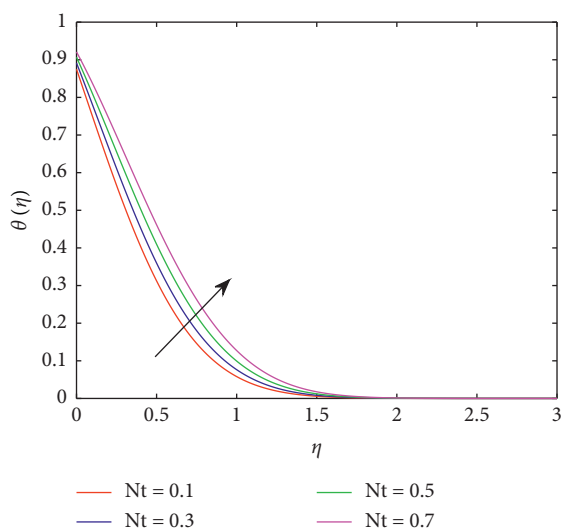

Figure 7: Variation due to Nt in $\theta(\eta)$.

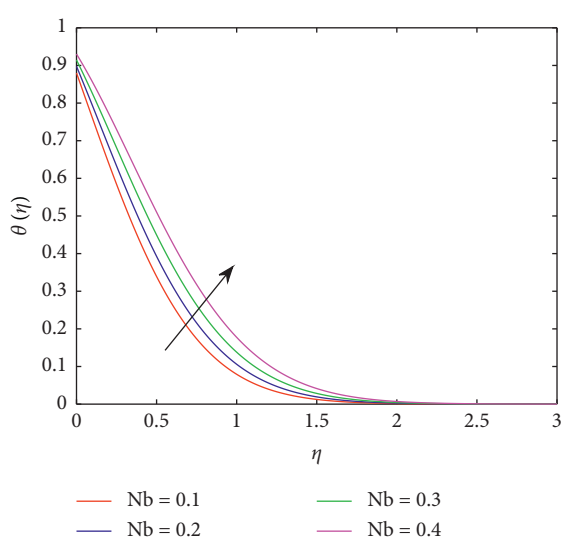

Figure 8: Variation due to Nb in $\theta(\eta)$.

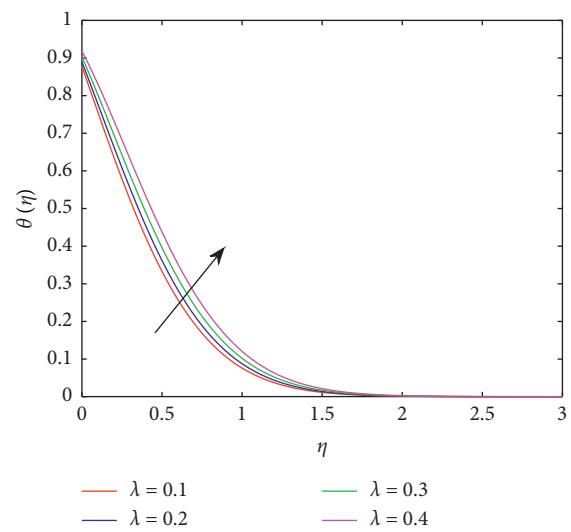

Figure 9: Variation due to λ in $\theta(\eta)$.

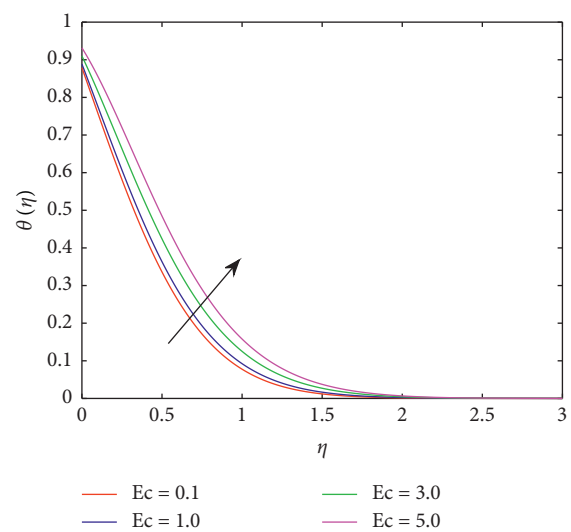

Figure 10: Variation due to Ec in $\theta(\eta)$.

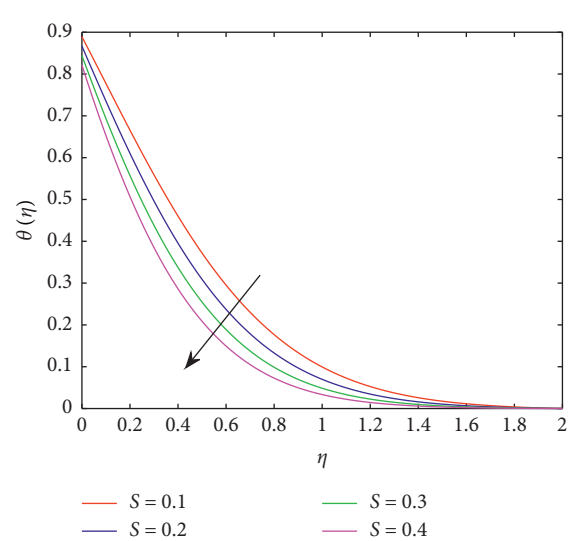

Figure 11: Variation due to S in $\theta(\eta)$.

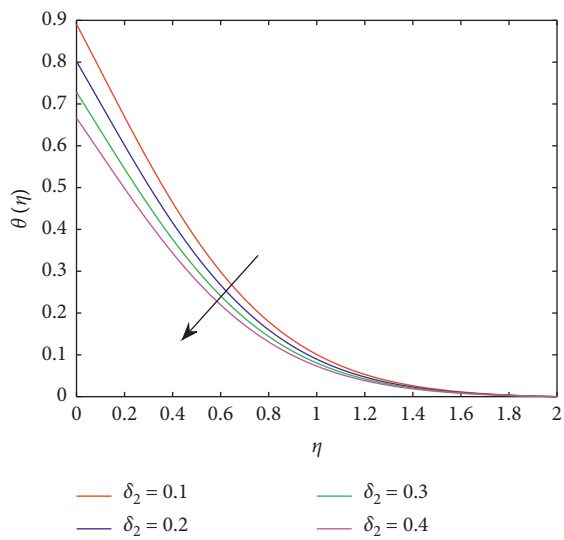

Figure 12: Variation due to δ_2 in $\theta(\eta)$.

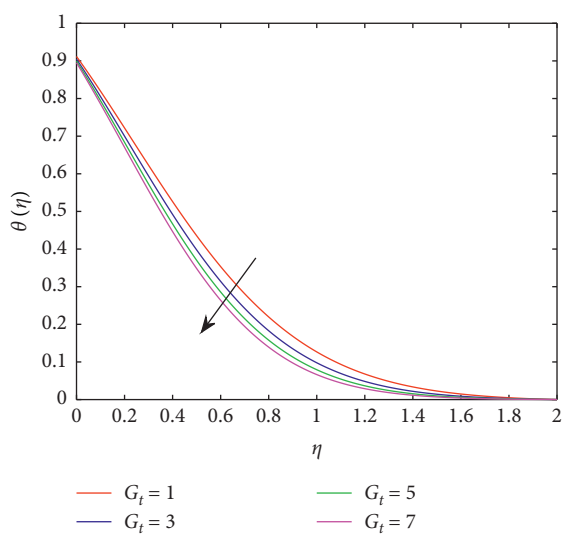

Figure 13: Variation due to G_t in $\theta(\eta)$.

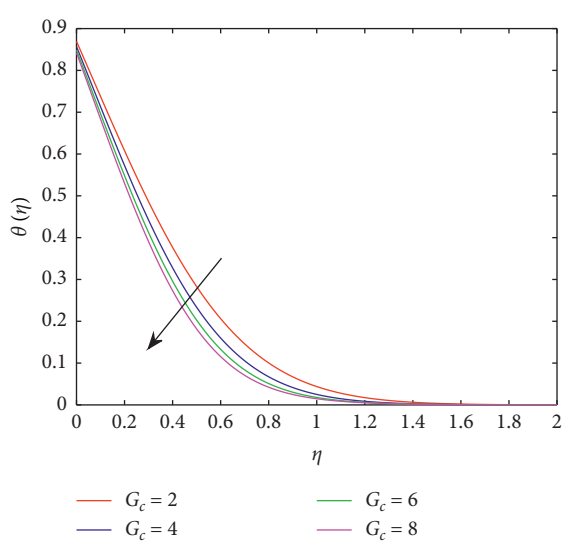

Figure 14: Variation due to G_c in $\theta(\eta)$.

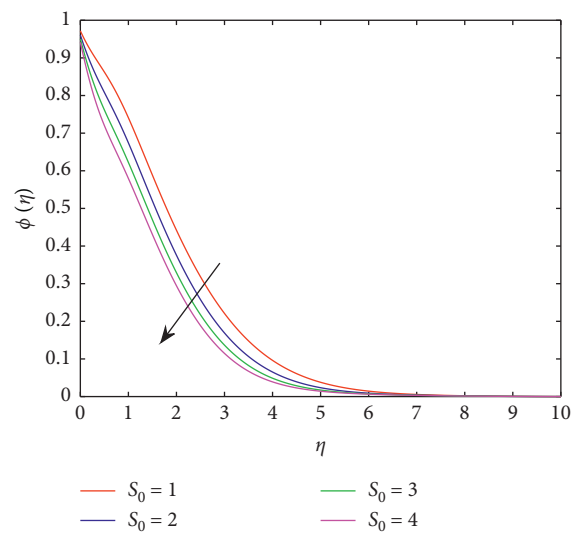

Figure 15: Variation due to S_0 in $\phi(\eta)$.

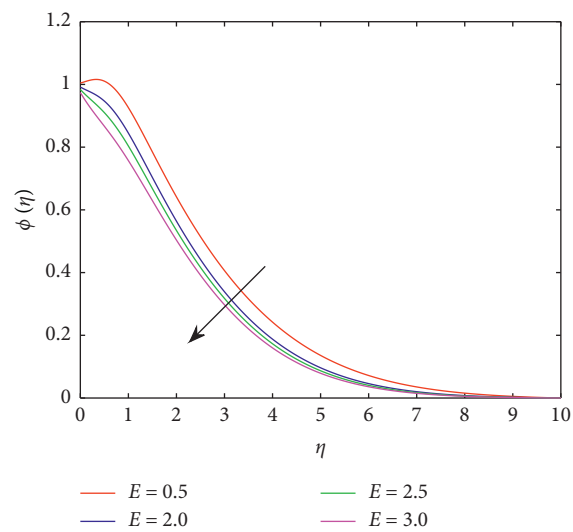

Figure 16: Variation due to E in $\phi(\eta)$.

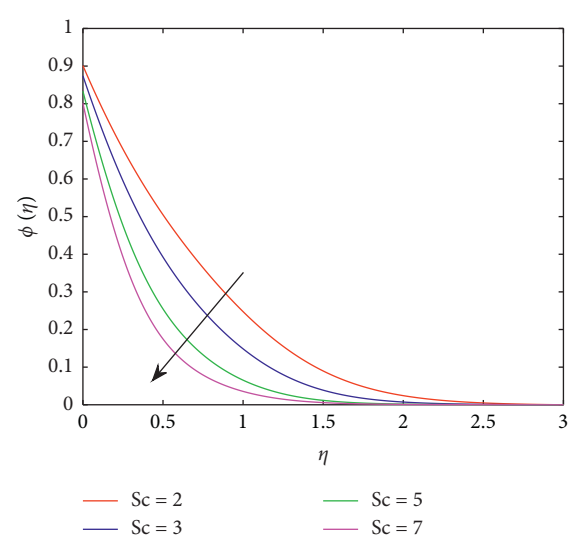

Figure 17: Variation due to Sc in $\phi(\eta)$.

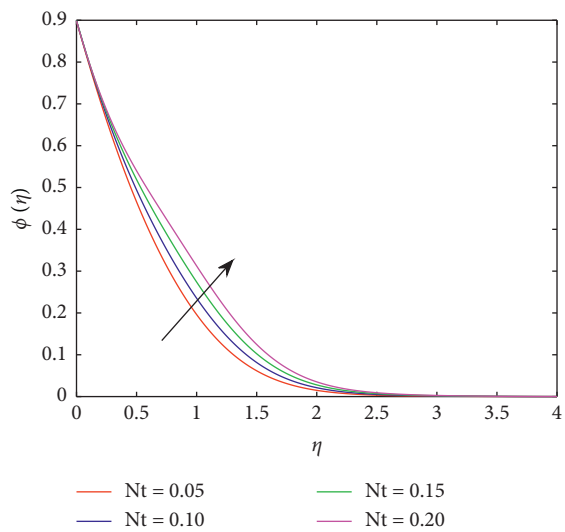

Figure 18: Variation due to Nt in $\phi(\eta)$.

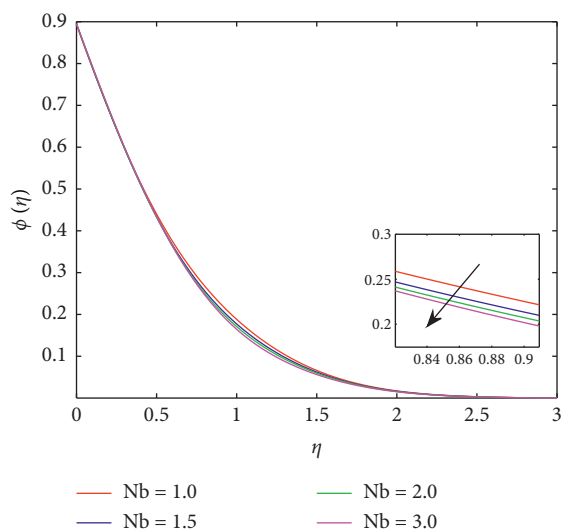

Figure 19: Variation due to Nb in $\phi(\eta)$.

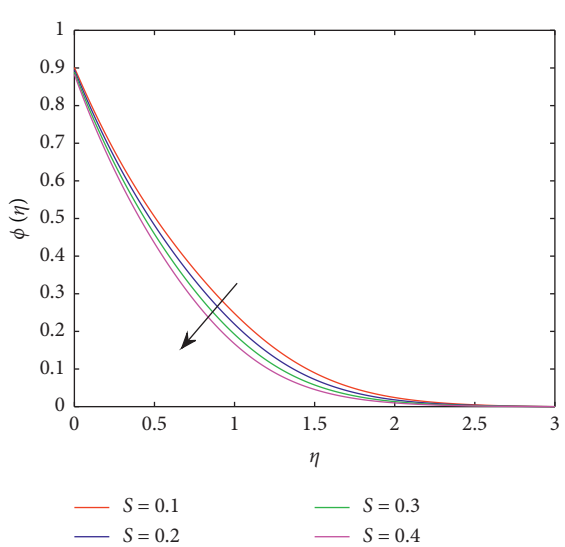

Figure 20: Variation due to S in $\phi(\eta)$.

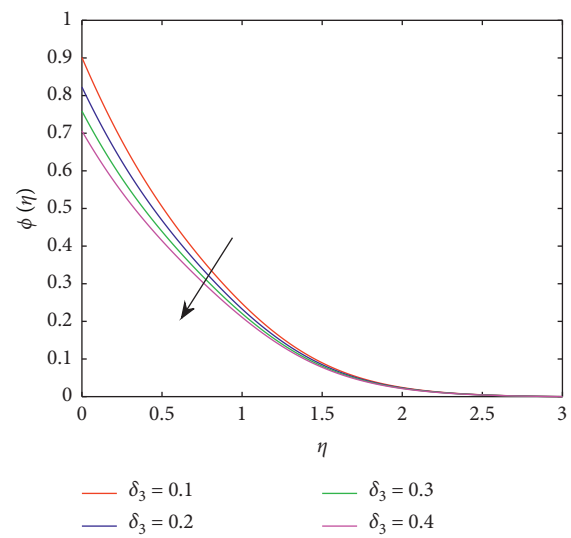

Figure 21: Variation due to δ_3 in $\phi(\eta)$.

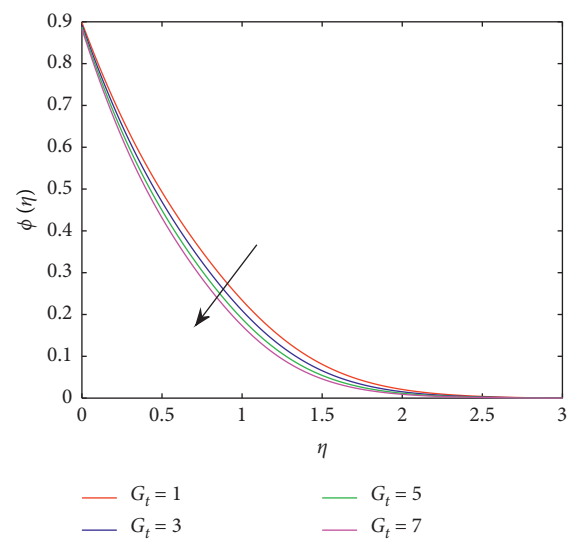

Figure 22: Variation due to G_t in $\phi(\eta)$.

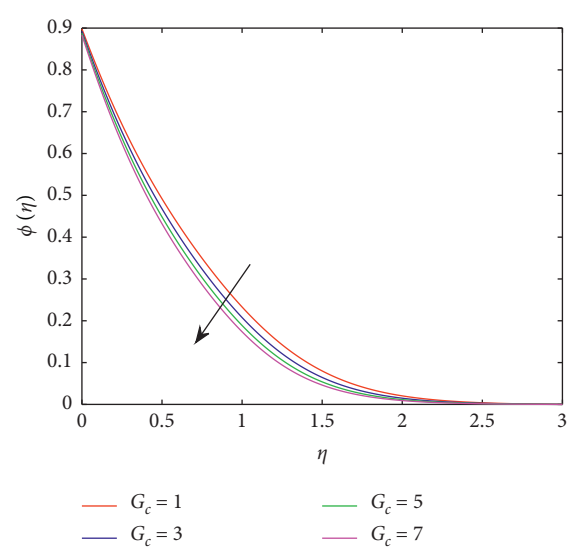

Figure 23: Variation due to G_c in $\phi(\eta)$.

stagnation parameter S_0 on $\phi(\eta)$. The concentration distribution $\phi(\eta)$ is diminished as the stagnation point parameter is enhanced. Figure 16 represents the graph of $\phi(\eta)$ for growing values of E. From these curves, it is clear that increasing electric parameter E diminishes $\phi(\eta)$. Figure 17 presents the role of Schmidt number Sc in the variation of $\phi(\eta)$. The concentration field $\phi(\eta)$ is diminished as Sc is rapidly increased. The effect of Nt on dimensionless concentration field $\phi(\eta)$ is reported in Figure 18. These graphs present that concentration field is enhanced as Nt is gradually increased. Figure 19 is presented to view the fluctuation in dimensionless $\phi(\eta)$ caused by the increase in Nb. An increase in dimensionless parameter Nb causes a reduction in $\phi(\eta)$. The impact of the variation of the dimensionless velocity slip parameter S on the dimensionless $\phi(\eta)$ is shown in Figure 20. These curves indicate that with an increment in the velocity slip parameter S, the dimensionless $\phi(\eta)$ declined. Figure 21 depicts the graphs of the concentration profile for various values of the dimensionless diffusion slip parameter δ_3. From these curves, it is noticed that an enhancement in the dimensionless diffusion slip parameter δ_3 causes a decrease in $\phi(\eta)$. The fluctuation in the dimensionless concentration distribution due to the thermal free convection parameter G_t is shown in Figure 22. The concentration field is reduced as thermal free convection parameter G_t is increased. Figure 23 depicts that $\phi(\eta)$ is decreased as the mass free convection parameter G_c is increased.

6. Concluding Remarks

In this study, two-dimensional free convection electrical magnetohydrodynamic micropolar nanofluid is analyzed. Some of the key observations are as follows:

(i) The energy field declined with an acclivity in the stagnation parameter S_0, slip parameter S, thermal free convection parameter G_t, and thermal slip parameter δ_2

(ii) The Nusselt number is escalated for the increasing values of slip parameter S, electric parameter E, stagnation parameter S_0, and thermal radiation parameter Rd

(iii) The concentration field is diminished with an increase in stagnation parameter S_0, electric parameter E, diffusion thermal slip parameter δ_3, and slip parameter S

(iv) The Sherwood number is increased as slip parameter S, electric parameter E, heat generation coefficient λ, stagnation parameter S_0, and mass free convection parameter G_c are increased

Nomenclature

B_0: Applied magnetic field
C: Fluid concentration inside the boundary layer
C_∞: Fluid concentration outside the boundary layer
C_f: Skin friction coefficient
C_p: Specific heat
C_w: Concentration at wall surface
D: Coefficient of mass diffusion
D_B: Brownian diffusion coefficient
D_T: Thermophoresis diffusion parameter
Ec: Eckert number
E: Electrical parameter
f: Reduced streamfunction
h_w: Local surface heat flux transfer coefficient
j: Microinertia density
j_w: Local mass flux
k_f: Thermal conductivity
K: Material parameter
M: Magnetic number
Nu_x: Nusselt number
Nt: Thermophoresis parameter
Nb: Brownian motion parameter
N: Angular velocity
Pr: Prandtl number
q_r: Radiative heat flux
G_t: Thermal free convection parameter
q_w: Heat transfer rate
Rd: Thermal radiation parameter
Re_x: Local Reynolds number
Sc: Schmidt number
T: Boundary layer temperature
T_w: Surface temperature
T_∞: Ambient temperature
t: Time
u: Velocity in x direction
u_w: Characteristics velocity
v: Velocity in y direction
v_w: Stretching rate
S_0: Stagnation parameter
S: Slip parameter
ν: Kinematic viscosity
ρ: Fluid density
μ: Dynamic viscosity
σ_m: Electric charge density
θ: Dimensionless temperature
ϕ: Dimensionless concentration
γ: Spin gradient viscosity
η: Dimensionless boundary layer thickness
δ_1: Dimensionless shear stress parameter
δ_2: Thermal slip parameter
δ_3: Diffusion mass slip parameter
$(\rho C_p)_p$: Heat capacity of the nanoparticles
$(\rho C_p)_f$: Heat capacity of the fluid
G_c: Mass free convection parameter.

Data Availability

The experimental data used to support the findings of this study are included within this paper.

Conflicts of Interest

The authors declare that they have no conflicts of interest regarding the study.

Authors' Contributions

All authors equally contributed to this work and read and approved the final manuscript.

Acknowledgments

The authors thank Dr. Muhammad Kashif Iqbal for his assistance in proofreading of the manuscript.

References

[1] H. Alfven, "Existence of electromagnetic-hydrodynamic waves," *Nature*, vol. 150, no. 3850, pp. 405-406, 1942.

[2] L. Zheng, J. Niu, X. Zhang, and Y. Gao, "MHD flow and heat transfer over a porous shrinking surface with velocity slip and temperature jump," *International Journal of Biomathematics*, vol. 56, no. 5-6, pp. 133–144, 2012.

[3] I. Ullah, K. Bhattacharyya, S. Shafie, and I. Khan, "Unsteady MHD mixed convection slip flow of Casson fluid over nonlinearly stretching sheet embedded in a porous medium with chemical reaction, thermal radiation, heat generation/absorption and convective boundary conditions," *PLoS One*, vol. 11, no. 10, Article ID e0165348, 2016.

[4] A. Rahbari, M. Abbasi, I. Rahimipetroudi, B. Sundén, D. Domiri Ganji, and M. Gholami, "Heat transfer and MHD flow of non-Newtonian Maxwell fluid through a parallel plate channel: analytical and numerical solution," *Mechanical Sciences*, vol. 9, no. 1, pp. 61–70, 2018.

[5] S. K. Soid, A. Ishak, and I. Pop, "MHD flow and heat transfer over a radially stretching/shrinking disk," *Chinese Journal of Physics*, vol. 56, no. 1, pp. 58–66, 2018.

[6] S. M. Atif, S. Hussain, and M. Sagheer, "Effect of thermal radiation and variable thermal conductivity on magnetohydrodynamics squeezed flow of Carreau fluid over a sensor surface," *Journal of Nanofluids*, vol. 8, no. 4, pp. 806–816, 2019.

[7] K. V. Ramana, K. Gangadhar, T. Kannan, and A. J. Chamkha, "Cattaneo–Christov heat flux theory on transverse MHD oldroyd-B liquid over nonlinear stretched flow," *Journal of Thermal Analysis and Calorimetry*, vol. 43, 2021.

[8] M. Bibi, A. Zeeshan, M. Y. Malik, and K. U. Rehman, "Numerical investigation of the unsteady solid-particle flow of a tangent hyperbolic fluid with variable thermal conductivity and convective boundary," *The European Physical Journal Plus*, vol. 134, pp. 156–164, 2019.

[9] S. Shah, S. M. Atif, and A. Kamran, "Radiation and slip effects on MHD Maxwell nanofluid flow over an inclined surface with chemical reaction," *Heat Transfer*, vol. 50, no. 4, pp. 4062–4085, 2021.

[10] R. Jusoh, R. Nazar, and I. Pop, "Dual solutions of magnetohydrodynamic stagnation point flow and heat transfer of viscoelastic nanofluid over a permeable stretching/shrinking sheet with thermal radiation," *Journal of Physics: Conference Series*, vol. 890, 2017.

[11] H. U. Rasheed, S. Islam, S. Noor et al., "Impact of magnetohydrodynamics on stagnation point slip flow due to nonlinearly propagating sheet with nonuniform thermal reservoir," *Mathematical Problems in Engineering*, vol. 2020, Article ID 1794213, 2020.

[12] D. Pal and G. Mandal, "Magnetohydrodynamic stagnation-point flow of Sisko nanofluid over a stretching sheet with suction," *Propulsion and Power Research*, vol. 9, no. 4, 2020.

[13] A. Abbasi, W. Farooq, and I. Riaz, "Stagnation point flow of Maxwell nanofluid containing gyrotactic micro-organism impinging obliquely on a convective surface," *Heat Transfer*, vol. 49, no. 5, pp. 2977–2999, 2020.

[14] L. A. Lund, Z. Omar, I. Khan, D. Baleanu, and K. S. Nisar, "Dual similarity solutions of MHD stagnation point flow of Casson fluid with effect of thermal radiation and viscous dissipation: stability analysis," *Scientific Reports*, vol. 10, 2020.

[15] S. E. Ghasemi and M. Hatami, "Solar radiation effects on MHD stagnation point flow and heat transfer of a nanofluid over a stretching sheet," *Case Studies in Thermal Engineering*, vol. 25, p. 100898, 2021.

[16] M. Irfan, W. A. Khan, M. Khan, and M. M. Gulzar, "Influence of arrhenius activation energy in chemically reactive radiative flow of 3D Carreau nanofluid with nonlinear mixed convection," *Journal of Physics and Chemistry of Solids*, vol. 125, pp. 141–152, 2019.

[17] S. M. Atif, S. Hussain, and M. Sagheer, "Effect of viscous dissipation and Joule heating on MHD radiative tangent hyperbolic nanofluid with convective and slip conditions," *Journal of the Brazilian Society of Mechanical Sciences and Engineering*, vol. 41, no. 4, pp. 189–206, 2019.

[18] S. M. Atif, S. Hussain, and M. Sagheer, "Heat and mass transfer analysis of time-dependent tangent hyperbolic nanofluid flow past a wedge," *Physics Letters A*, vol. 383, no. 11, pp. 1187–1198, 2019.

[19] M. Awais, K. U. Rehman, M. Y. Malik, A. Hussain, and T. Salahuddin, "A computational analysis subject to thermophysical aspects of Sisko fluid flow over a cylindrical surface," *The European Physical Journal Plus*, vol. 132, no. 9, pp. 392–407, 2017.

[20] A. Eringen, "Theory of micropolar fluids," *Indiana University Mathematics Journal*, vol. 16, no. 1, pp. 1–18, 1966.

[21] A. C. Eringen, "Theory of thermomicrofluids," *Journal of Mathematical Analysis and Applications*, vol. 38, no. 2, pp. 480–496, 1972.

[22] J. Sui, P. Zhao, Z. Cheng, L. Zheng, and X. Zhang, "A novel investigation of a micropolar fluid characterized by nonlinear constitutive diffusion model in boundary layer flow and heat transfer," *Physics of Fluids*, vol. 29, 2017.

[23] S. R. Mishra, I. Khan, Q. M. Al-Mdallal, and T. Asifa, "Free convective micropolar fluid flow and heat transfer over a shrinking sheet with heat source," *Case Studies in Thermal Engineering*, vol. 11, pp. 113–119, 2018.

[24] S. M. Atif, S. Hussain, and M. Sagheer, "Magnetohydrodynamic stratified bioconvective flow of micropolar nanofluid due to gyrotactic microorganisms," *AIP Advances*, vol. 9, no. 2, Article ID 025208, 2019.

[25] C. Zemedu and W. Ibrahim, "Nonlinear convection flow of micropolar nanofluid due to a rotating disk with multiple slip flow," *Mathematical Problems in Engineering*, vol. 2020, Article ID 4735650, 2020.

[26] S. U. S. Choi and J. A. Eastman, "Enhancing thermal conductivity of fluids with nanoparticles," *ASME Fluids Engineering*, vol. 231, pp. 99–105, 1995.

[27] S. O. Giwa, M. Sharifpur, and J. P. Meyer, "Experimental study of thermo-convection performance of hybrid nanofluids of Al_2O_3-MWCNT/water in a differentially heated square cavity," *International Journal of Heat and Mass Transfer*, vol. 148, 2020.

[28] W. A. Khan, F. Sultan, M. Ali, M. Shahzad, M. Khan, and M. Irfan, "Consequences of activation energy and binary chemical reaction for 3D flow of Cross-nanofluid with

radiative heat transfer," *Journal of the Brazilian Society of Mechanical Sciences and Engineering*, vol. 41, no. 4, 2019.

[29] M. R. Eid, K. Mahny, A. Dar, and T. Muhammad, "Numerical study for Carreau nanofluid flow over a convectively heated nonlinear stretching surface with chemically reactive species," *Physica A: Statistical Mechanics and its Applications*, vol. 540, 2020.

[30] S. M. Atif, A. Kamran, and S. Shah, "MHD micropolar nanofluid with non Fourier and non Fick's law," *International Communications in Heat and Mass Transfer*, vol. 122, Article ID 105114, 2021.

[31] U. Ali, M. Y. Malik, A. A. Alderremy, S. Aly, and K. U. Rehman, "A generalized findings on thermal radiation and heat generation/absorption in nanofluid flow regime," *Physica A: Statistical Mechanics and its Applications*, vol. 553, Article ID 124026, 2020.

[32] S. M. Atif, S. Hussain, and M. Sagheer, "Numerical study of MHD micropolar Carreau nanofluid in the presence of induced magnetic field," *AIP Advances*, vol. 8, 2018.

[33] T. Muhammad, H. Waqas, S. A. Khan, R. Ellahi, and S. M. Sait, "Significance of nonlinear thermal radiation in 3D Eyring–Powell nanofluid flow with Arrhenius activation energy," *Journal of Thermal Analysis and Calorimetry*, vol. 143, 2020.

[34] S. A. Khan and M. A. Siddiqui, "Numerical studies on heat and fluid flow of nanofluid in a partially heated vertical annulus," *Heat Transfer*, vol. 49, no. 3, pp. 1458–1490, 2020.

[35] N. Manaa, A. Abidi, A. C. Saleel, and M. N. Borjini, "Three-dimensional numerical analysis on performance enhancement of micropolar hybrid nanofluid in Comparison with simple nanofluid," *Heat Transfer Engineering*, pp. 1–21, 2020.

[36] K.-L. Hsiao, "Stagnation electrical MHD nanofluid mixed convection with slip boundary on a stretching sheet," *Applied Thermal Engineering*, vol. 98, pp. 850–861, 2016.

[37] M. Bilal, "Micropolar flow of EMHD nanofluid with nonlinear thermal radiation and slip effects," *Alexandria Engineering Journal*, vol. 59, no. 2, pp. 965–976, 2020.

[38] W. A. Khan and I. Pop, "Boundary-layer flow of a nanofluid past a stretching sheet," *International Journal of Heat and Mass Transfer*, vol. 53, no. 11-12, pp. 2477–2483, 2010.

Hindawi
Complexity
Volume 2021, Article ID 6052437, 11 pages
https://doi.org/10.1155/2021/6052437

Research Article

Generalization of Thermal and Mass Fluxes for the Flow of Differential Type Fluid with Caputo–Fabrizio Approach of Fractional Derivative

Asima Razzaque,[1] Anam Rani,[1] and Mudassar Nazar[2,3]

[1]*Department of Basic Science, Preparatory Year Deanship, King Faisal University Hofuf, Al Has, Hofuf, Saudia Arabia*
[2]*School of Mathematical Sciences, University of Science and Technology of China, Hefei, Anhui, China*
[3]*Centre for Advanced Studies in Pure and Applied Mathematics, Bahauddin Zakariya University, Multan, Pakistan*

Correspondence should be addressed to Mudassar Nazar; mudassar_666@yahoo.com

Received 14 May 2021; Accepted 21 June 2021; Published 30 June 2021

Academic Editor: Dumitru Vieru

In this research work, generalized thermal and mass transports for the unsteady flow model of an incompressible differential type fluid are considered. The Caputo–Fabrizio fractional derivative is used for the respective generalization of Fourier's and Fick's laws. A MHD fluid flow is considered near a flat vertical surface subject to unsteady mechanical, thermal, and mass conditions at boundary. The governing equations of flow model are solved by integral transform, and closed form results for generalized momentum, thermal, and concentration fields are obtained. Generalized thermal and mass fluxes at boundary are quantified in terms of Nusselt and Sherwood numbers, respectively, and presented in tabular form. The significance of the physical parameters over the momentum, thermal, and concentration profiles is characterized by sketching the graphs.

1. Introduction

Fractional calculus has been expanding rapidly in the present time for the sake of its applications in the modeling and physical explanation of natural phenomenon. The noninteger derivatives of fractional order have been applied successfully to the generalization of fundamental laws of nature specially in the transport phenomenon.

Several approaches [1–4] of fractional derivatives have been proposed and utilized for the different proposes by many theorists from different fields of sciences and technology [5]. Imran et al. [6] considered two different approaches of fractional differential operators for the flow of MHD Newtonian fluid under the arbitrary boundary conditions, namely, Atangana and Caputo–Fabrizio. Kumar et al. [7] explained the Cauchy reaction diffusion equations by fractional calculus. Qureshi et al. [8] applied the fractional derivative to model a blood flow and discussed the concentration level of ethanol in blood circulation system. Hristov [9] considered a steady-state heat conduction and obtained analytical solutions by applying the Caputo–Fabrizio approach of fractional derivative. Imran et al. [10, 11] considered the Caputo time fractional derivative to discuss the slippage flow over an exponentially accelerated plate and for the flow of differential fluid past stationary heated vertical plate. Ahmad et al. [12] compared two flow models, one with the power law kernel and the other with the nonsingular kernel. Khalid et al. [13] obtained the results for flow of micropolar fluid and applied the fractional derivative for heat and mass transport. Shukla et al. [14] presented a report regarding applications of fractional calculus. Kumar et al. [15] explored the results for free convectional motion with a uniform temperature through a porous media by utilizing the power, exponential, and Mittag–Leffler kernels of fractional operator. Singh et al. [16] constructed the dynamic fractional model to explain the smoking dynamics. Sun et al. [17] presented a collection of real world applications of fractional differential operators. Nazar et al. [18]

discussed the double convectional flow via two approaches of noninteger operators and compared the obtained results of thermal, mass, and momentum profiles. Gomez et al. [19] solved fractional diffusion-advection equation and obtained the analytical solution for supper diffusion. Tran et al. [20] discussed the stabilities of fractional differential equation. Recently, Tuan et al. [21] endorsed the fractional calculus to demonstrate the transition model of COVID-19. Hristov et al. [22] applied the mixed time-space derivative to obtain the result for transient flow of non-Newtonian fluid. Saqib et al. [23], Haq et al. [24], and Imran et al. [25] utilized the fractional differential operator with the nonsingular kernel to obtain the fractional result for the flow of Jeffery, and second grade fluids. Some more investigations regarding Caputo–Fabrizio fractional derivatives are found in [26–28].

Hristov et al. [29] suggested the generalized transient thermal transport with damping contribution, by considering the Caputo–Fabrizio idea of nonsingular kernel. Aleem et al. [30], Sheikh et al. [31] and Ahmad et al. [32] followed the track suggested in [29] and applied it to describe the generalized heat and mass transfer flow. In light of the above motivational investigations, we are interested in discussing the generalized thermal and mass transports with heat generation and chemical reaction for the flow of second grade fluid through a porous media, with the existence of a magnetic field.

2. Mathematical Formulation

Suppose that the second grade fluid is lying in the vicinity of a vertical plate with ambient temperature T_∞ and concentration level C_∞. The orientation of the plate in the coordinate system is placed with y-axis becoming normal to the plane of plate as shown in Figure 1. Initially, the physical system containing boundaries and fluid is in complete equilibrium. Suddenly, plate starts moving with velocity $U_0 f(t)$; at this moment, the temperature of plate and the concentration level near the plate rise or fall according to $T_\infty + (T_w - T_\infty)g(t)$ and $C_\infty + (T_w - C_\infty)h(t)$, respectively, where $f(\cdot)$, $g(\cdot)$, and $h(\cdot)$ are arbitrary functions and satisfy $f(0) = 0$, $g(0) = 0$, and $h(0) = 0$, respectively. The contribution of Lorentz force is also applied for the flow of fluid. Moreover, the induced magnetic field and heat dissipation are small and can be negligible. Subject to Boussinesq's approximation, the governing equations of respective flow take the following form [29, 30]:

$$\mu\left(1+\alpha_1\frac{\partial}{\partial t}\right)\frac{\partial^2 u(y,t)}{\partial y^2}-\rho\frac{\partial u(y,t)}{\partial t}-\sigma B_0^2 u(y,t)-\frac{\mu\phi}{K_1}u(y,t)=-\rho g\beta_C\left[C(y,t)-C_\infty\right]-\rho g\beta_T\left[T(y,t)-T_\infty\right], \tag{1}$$

$$\rho C_p\frac{\partial T(y,t)}{\partial t}-Q\left[T(y,t)-T_\infty\right]=k\frac{\partial^2 T(y,t)}{\partial y^2}, \tag{2}$$

$$\frac{\partial C(y,t)}{\partial t}-K_r\left[C(y,t)-C_\infty\right]=D\frac{\partial^2 C(y,t)}{\partial y^2}. \tag{3}$$

Initial and boundary conditions:

$$u=0, T=T_\infty, C=C_\infty, \quad \text{at } t=0, \text{ and, } y\in[0,\infty), \tag{4}$$

$$\begin{aligned} &u=U_0 f(t),\\ &T=T_\infty+(T_w-T_\infty)g(t),\\ &C=C_\infty+(T_w-C_\infty)h(t), \quad y=0, t>0, \end{aligned} \tag{5}$$

$$u\longrightarrow 0, T\longrightarrow T_\infty, C\longrightarrow C_\infty, \quad \text{as } y\longrightarrow\infty, t>0. \tag{6}$$

3. Generalized Model

The thermal balance with heat generation is expressed as follows:

$$\rho C_p\frac{\partial T(y,t)}{\partial t}=-\frac{\partial q}{\partial y}+Q\left[T(y,t)-T_\infty\right], \quad y,t>0, \tag{7}$$

and the generalized thermal flux with damping effect [29, 30] is

$$q(y,t)=-k_1\frac{\partial T(y,t)}{\partial y}-k_2{}^{CF}D_t^\alpha(1-\alpha)\frac{\partial T(y,t)}{\partial y}, \quad y,t>0, \tag{8}$$

where ${}^{CF}D_t^\alpha$ is the fractional differential operator suggested by Caputo–Fabrizio. The constant h_1 and h_2 are the effective heat conduction and elastic conduction parameters, respectively.

From equation (8), it is clear that, for $\alpha = 1$, the classical thermal flux is recovered. Similarly, the molecular balance with chemical reaction is expressed as

$$\frac{\partial C(y,t)}{\partial t}=-\frac{\partial J(y,t)}{\partial y}+K_r\left(C(y,t)-C_\infty\right), \quad y,t>0, \tag{9}$$

and the generalized Fick's Law with damping effect [29, 30] is

$$J(y,t)=-D_1\frac{\partial C(y,t)}{\partial y}-D_2{}^{CF}D_t^\alpha(1-\alpha)\frac{\partial C(y,t)}{\partial y}, \quad y,t>0, \tag{10}$$

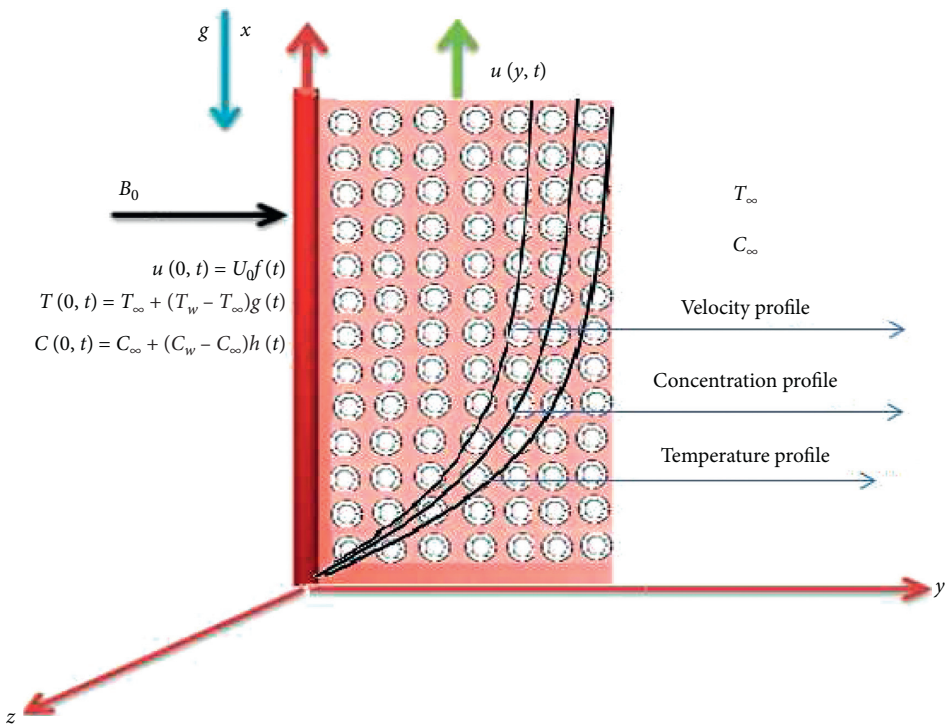

Figure 1: Flow geometry and coordinate system.

where D_1 and D_2 are the effective mass diffusion and the elastic diffusion, respectively.

Introduce the relations

$$\begin{aligned} v &= \frac{u}{U_0}, \\ \eta &= \frac{yU_0}{\nu}, \\ \tau &= \frac{tU_0^2}{\nu}, \\ \psi &= \frac{C - C_\infty}{C_w - C_\infty}, \\ \varphi &= \frac{T - T_\infty}{T_w - T_\infty}, \end{aligned} \tag{11}$$

in equations (1), (4)–(6), and (7)–(10), to get the shape free model.

The momentum balance takes the following form:

$$\left(1 + \alpha_2 \frac{\partial}{\partial \tau}\right) \frac{\partial^2 v(\eta, \tau)}{\partial \eta^2} - \frac{\partial v(\eta, \tau)}{\partial \tau} - Mv(\eta, \tau) - \frac{1}{K} v(\eta, \tau) = -Gr\varphi(\eta, \tau) - Gm\psi(\eta, \tau). \tag{12}$$

Dimensionless thermal balance is

$$\frac{\partial \varphi(\eta, \tau)}{\partial t} = \frac{1}{\mathrm{Pr}_1} \frac{\partial^2 \varphi(\eta, \tau)}{\partial \eta^2} + \frac{1}{\mathrm{Pr}_2} {}^{CF}D_t^{\alpha} (1 - \alpha) \frac{\partial^2 \varphi(\eta, \tau)}{\partial \eta^2} + Q_0 \varphi(\eta, \tau). \tag{13}$$

Dimensionless diffusion equation is

$$\frac{\partial \psi(\eta,\tau)}{\partial t} = \frac{1}{Sc_1}\frac{\partial^2 \psi(\eta,\tau)}{\partial \eta^2} + \frac{1}{Sc_2}{}^{CF}D_t^{\alpha}(1-\alpha)\frac{\partial^2 \psi(\eta,\tau)}{\partial \eta^2} + K_0\psi(\eta,\tau). \tag{14}$$

And the corresponding initial and boundary conditions are

$$\upsilon(\eta,0) = 0, \varphi(\eta,0) = 0, \psi(\eta,0) = 0, \quad \eta > 0, \tag{15}$$

$$\upsilon(0,\tau) = f(\tau), \varphi(0,\tau) = g(\tau), \psi(0,\tau) = h(\tau), \quad \tau > 0, \tag{16}$$

$$\upsilon(\eta,\tau) \longrightarrow 0, \varphi(\eta,\tau) \longrightarrow 0, \psi(\eta,\tau) \longrightarrow 0, \quad \text{as } \eta \longrightarrow 0, \tag{17}$$

where $\alpha_2 = (\alpha_1 U_0^2/\nu)$ is the dimensionless second grade parameter, $Gm = ((g\beta_C(C_w - C_\infty))/U_0^3)$ is the mass Grashof number, $Gr = ((g\beta_T(T_w - T_\infty))/U_0^3)$ is the thermal Grashof number, $M = (\nu\sigma/(\rho U_0^2))$ is the magnetic parameter, $(1/K) = (\nu^2\phi/(K_1 U_0^2))$ is the porosity parameter, $\mathrm{Pr}_1 = (\mu C_p/h_1)$ and $\mathrm{Pr}_2 = (\mu C_p/h_2)$ are Prandtl numbers, $Sc_1 = (\nu/D_1)$ and $Sc_2 = (\nu/D_2)$ are Schmidt numbers, $Q_0 = (Q\nu/(\rho C_p U_0^2))$ is the heat generation parameter, and $K_0 = (K_r\nu/U_0^2)$ is the chemical reaction parameter.

4. Solution of the Problem

The solution of generalized model is obtained by endorsing the Laplace transform.

4.1. Generalized Temperature Field. Endorsing the Laplace transform to equation (16), an ordinary differential equation is obtained as

$$q\overline{\varphi}(\eta,q) = \frac{1}{\mathrm{Pr}_1}\frac{\partial^2 \overline{\varphi}(\eta,s)}{\partial \eta^2} + \frac{1}{\mathrm{Pr}_2}(1-\alpha)\left[\frac{q}{q(1-\alpha)+\alpha}\right]\frac{\partial^2 \overline{\varphi}(\eta,q)}{\partial \eta^2} + Q_0\overline{\varphi}(\eta,q), \tag{18}$$

with the following transformed boundary conditions:

$$\overline{\varphi}(\eta,q) = G(q), \quad \text{and } \overline{\varphi}(\eta,q) \longrightarrow 0, \text{ as } \eta \longrightarrow \infty. \tag{19}$$

Equation (18) is solved with conditions (19), and its solution is expressed as

$$\overline{\varphi}(\eta,q) = G(q)\exp\left(-\eta\sqrt{\frac{(q-a_0)(q-Q_0)}{a_1(q+a_2)}}\right), \tag{20}$$

where $a_0 = (\alpha/(1-\alpha))$, $a_1 = ((\mathrm{Pr}_1 + \mathrm{Pr}_2)/\mathrm{Pr}_1\mathrm{Pr}_2)$, and $a_2 = (a_0\mathrm{Pr}_2/(\mathrm{Pr}_1 + \mathrm{Pr}_2))$.

Equation (20) is complicated, and it is not possible to invert the temperature field in t-domain by ordinary formula of Laplace inverse. Therefore, the inversion algorithms, namely, Stehfest and Tzou, are utilized to invert the transformed temperature profile, and the obtained results are presented in Figure 2(a) for $g(t) = 1$.

4.2. Generalized Concentration Field. Again endorsing the Laplace transform to equation (14), an ordinary differential equation is obtained as

$$q\overline{\psi}(\eta,q) = \frac{1}{\mathrm{Sc}_1}\frac{\partial^2 \overline{\psi}(\eta,s)}{\partial \eta^2} + \frac{1}{\mathrm{Sc}_2}(1-\alpha)\left[\frac{q}{q(1-\alpha)+\alpha}\right]\frac{\partial^2 \overline{\psi}(\eta,q)}{\partial \eta^2} + K_0\overline{\psi}(\eta,q), \tag{21}$$

$$\overline{\psi}(\eta,q) = H(q), \quad \text{and } \overline{\psi}(\eta,q) \longrightarrow 0, \text{ as } \eta \longrightarrow \infty. \tag{22}$$

Equation (21) is solved with conditions (22), and its solution is expressed as

$$\overline{\psi}(\eta,q) = H(q)\exp\left(-\eta\sqrt{\frac{(q-a_0)(q-K_0)}{b_1(q+b_2)}}\right), \tag{23}$$

where $b_1 = ((Sc_1 + Sc_2)/Sc_1 Sc_2)$ and $b_2 = (b_0 Sc_2/(Sc_1 + Sc_2))$.

Equation (23) is complicated, and it is not possible to invert the temperature field in t-domain by ordinary formula of Laplace inverse. Therefore, the inversion algorithms are

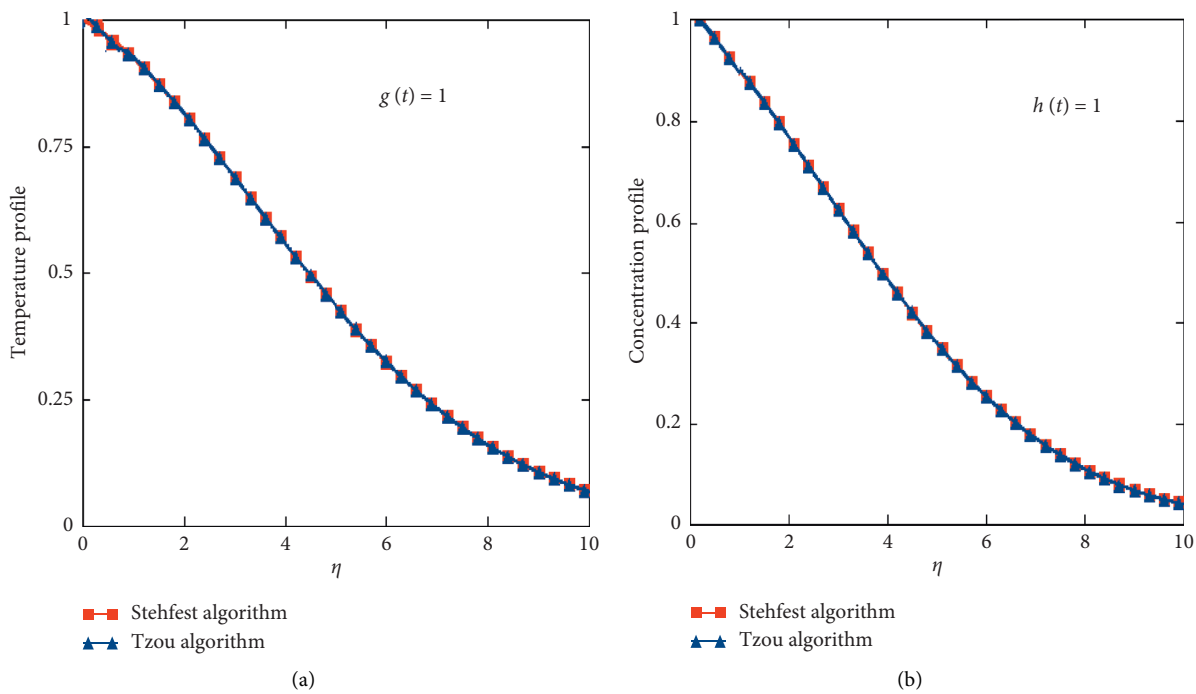

FIGURE 2: Profiles of inverted temperature and concentration with Stehfest's and Tzou's algorithms for (a) $g(t) = 1$ and (b) $h(t) = 1$.

utilized to obtain the temperature profile for $h(t) = 1$, and the obtained results are presented in Figure 2(b).

4.3. Velocity Field with Generalized Thermal and Mass Transport. Equation (13) is converted to an ordinary differential equation via Laplace transform as

$$(1+\alpha_2 q)\frac{\partial^2 \overline{v}(\eta,q)}{\partial \eta^2} - q\overline{v}(\eta,q) - M\overline{v}(\eta,q) - \frac{1}{K}\overline{v}(\eta,q) = -\mathrm{Gr}\overline{\varphi}(\eta,q) - \mathrm{Gm}\overline{\psi}(\eta,q), \tag{24}$$

with corresponding transformed boundary conditions

$$\overline{v}(0,q) = F(q), \quad \text{and } \overline{v}(\eta,q) \longrightarrow 0 \text{ as } \eta \longrightarrow \infty. \tag{25}$$

Equation (24), subject to condition (25), is solved for velocity field in q-domain as follows:

$$\begin{aligned}\overline{v}(\eta,q) = {} & F(q)\exp\left(-y\sqrt{\frac{q+M_0}{q+\alpha_3}}\right) \\ & + \frac{\mathrm{Gr}\alpha_3 G(q)\left[\exp\left(-y\sqrt{(q+M_0)/(q+\alpha_3)}\right) - \exp\left(-y\sqrt{((q+a_0)(q-Q_0))/a_1(q+a_2)}\right)\right]}{(q+\alpha_3)(q-a_0)(q-Q_0) - a_1(q+a_2)(q+M_0)} \\ & + \frac{\mathrm{Gm}\alpha_3 H(q)\left[\exp\left(-y\sqrt{(q+M_0)/(q+\alpha_3)}\right) - \exp\left(-y\sqrt{((q+b_0)(q-K_0))/b_1(q+b_2)}\right)\right]}{(q+\alpha_3)(q-b_0)(q-K_0) - b_1(q+b_2)(q+M_0)},\end{aligned} \tag{26}$$

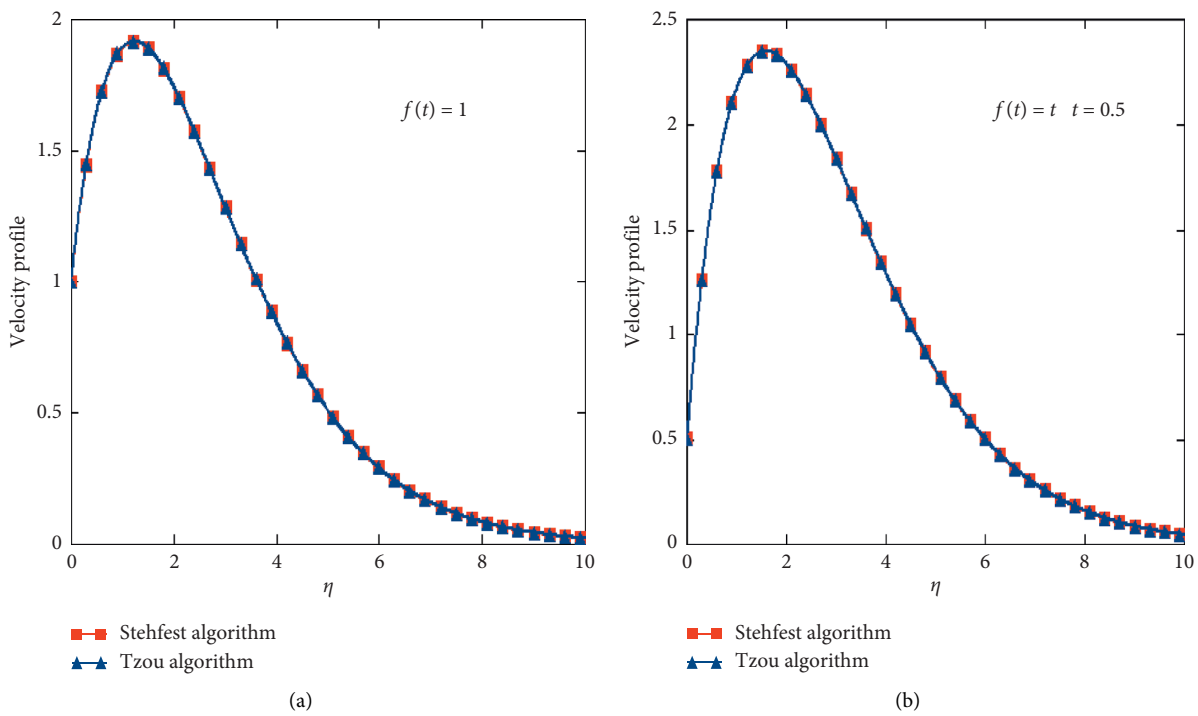

Figure 3: Profile of inverted velocity with Stehfest's and Tzou's algorithms for (a) $f(t) = 1$ and (b) $f(t) = t$.

where $\alpha_3 = (1/\alpha_2)$ and $M_0 = M + (1/K)$. Equation (26) is also complex, and it is inverted in t-domain with the help of inversion algorithms. The inverse Laplace of velocity for $f(t) = 1$, and $f(t) = t$ is demonstrated in Figures 3(a) and 3(b).

5. Results and Parametric Discussion

This article is designed for the analysis of generalized thermal and mass transport flow of differential type fluid under generalized boundary conditions. The effects of magnetic field, heat source, and chemical reaction are also considered for flow model. The respective governing equations of flow model are solved analytically via integral transform method, and closed form expressions for field variables are attained.

The effects of potent parameters are also discussed graphically by plotting some graphs of for variation of appeared parameters. Figures 4(a) and 4(b) are sketched to explain the effect of fractional parameter α and Pr over the temperature profile, and it is noted that the temperature of fluid is raised with the developing values of α. Also, it is detected that the temperature falls down with the increasing values of Pr, because the fluid is thick, and momentum diffusivity is dominant to the thermal diffusivity for the greater Pr; therefore, fluid velocity slows down for increasing Pr. Figure 4(c) is drawn for three specification of $g(t)$, and it is noted that temperature profiles satisfy the boundary conditions.

In Figure 5, the subjectivity of concentration is explained for variations of α, Sc, and three specification for the $g(t)$. The same behavior of concentration is seen for respective parameters as seen in temperature profiles.

Velocity profile is outlined in Figure 6(a) due variation of fractional parameters α. The figure pattern shows that the fluid gains more and more momentum as α tends to increase. The influence of Pr and Sc is signified in Figures 6(b) and 6(c). As Pr and Sc are quantified by the ratios of momentum diffusivity to thermal diffusivity and molecular diffusion coefficients, respectively, and for enhancing values of Pr and Sc referred to as the dominant momentum diffusivity, the fluid slows down for developing values of Pr and Sc.

Figure 7(a) is drawn to see the significance role of Gr for supporting the flow, and it is noted that the speed of fluid is elevated for developing values of Gr. As Gr is quantified by relative buoyancy force induced by the variations in temperature differences to the retarding force generates by the virtue of viscosity of the fluid, hence, for larger values of Gr, there is more convectional current, so fluid speeds up. The effects of thermal generation parameter Q_0, and chemical reaction parameters K_0 are discussed in Figures 7(b) and 7(c), and it is concluded that velocity profiles rise for enhancing values of Q_0 and K_0.

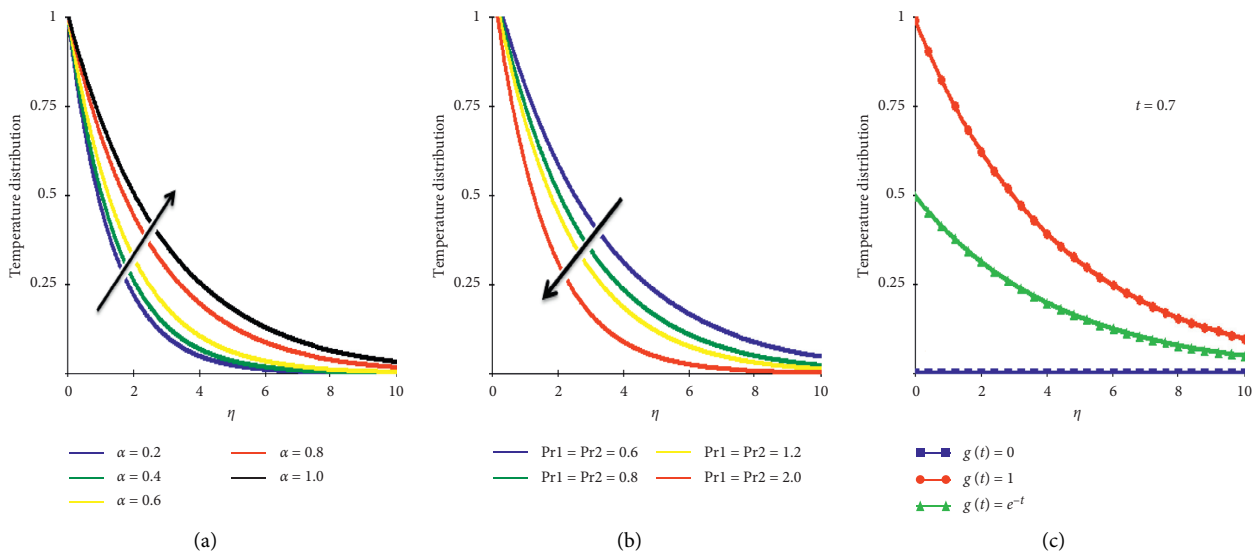

Figure 4: Sketch thermal profile for changing α, Pr, and $g(t)$.

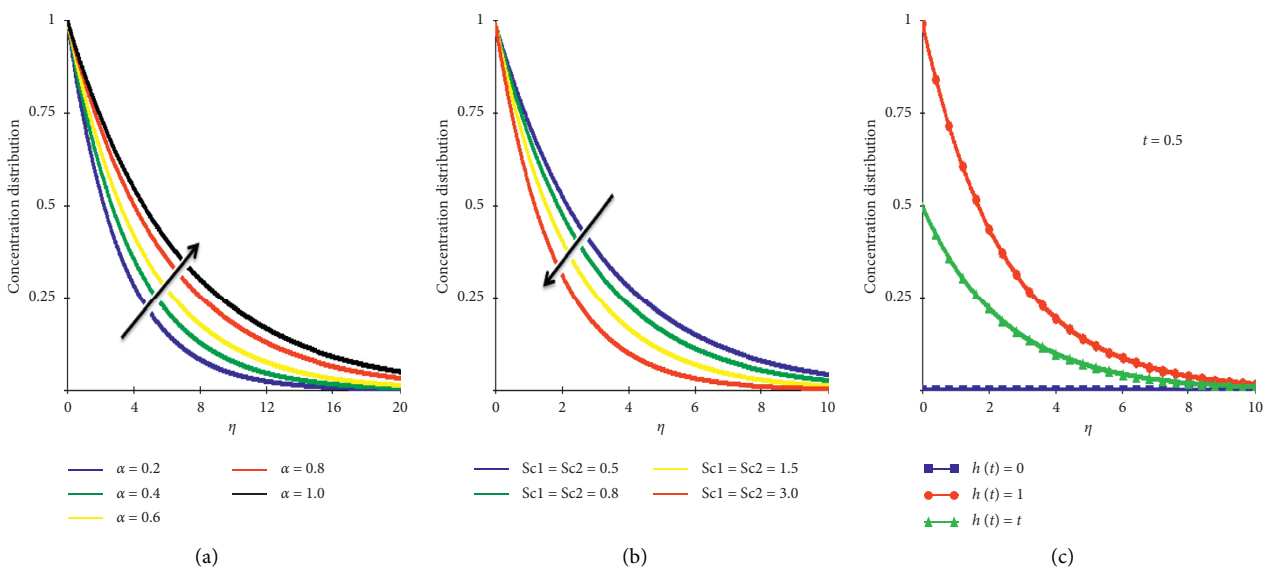

Figure 5: Sketch concentration profile for changing α, Sc, and $h(t)$.

The subjectivity of magnetic parameter M is highlighted in Figure 8(a) and from this figure, it is seen that profile lowers down for increasing values of M, because strong magnetic field creates more hindrance to the flow of fluid. Figure 8(b) shows the effect of K and it is seen that fluid speeds up with the increasing values of K. The increasing values of K refer to the decreasing effect of porosity, and hence, fluid velocity increases with the enhancing values of K. Figure 8(c) is plotted for three specifications of $f(t)$; from the profiles, it is clear that velocity profiles satisfy the boundary conditions for different $f(t)$. The present results for velocity and temperature are also compared with the existing results obtained by Sheh et al. [27] in Figures 9(a) and 9(b). The overlapping profiles confirm the validity of our results.

Further, heat and mass transfer at plate is discussed numerically in terms of Nusselt and Sherwood numbers, and results are presented in Tables 1 and 2. From these tables, it is clear that both Nusselt and Sherwood numbers are grown with elevating fractional parameter α for small time, while there is an opposite behavior for large time.

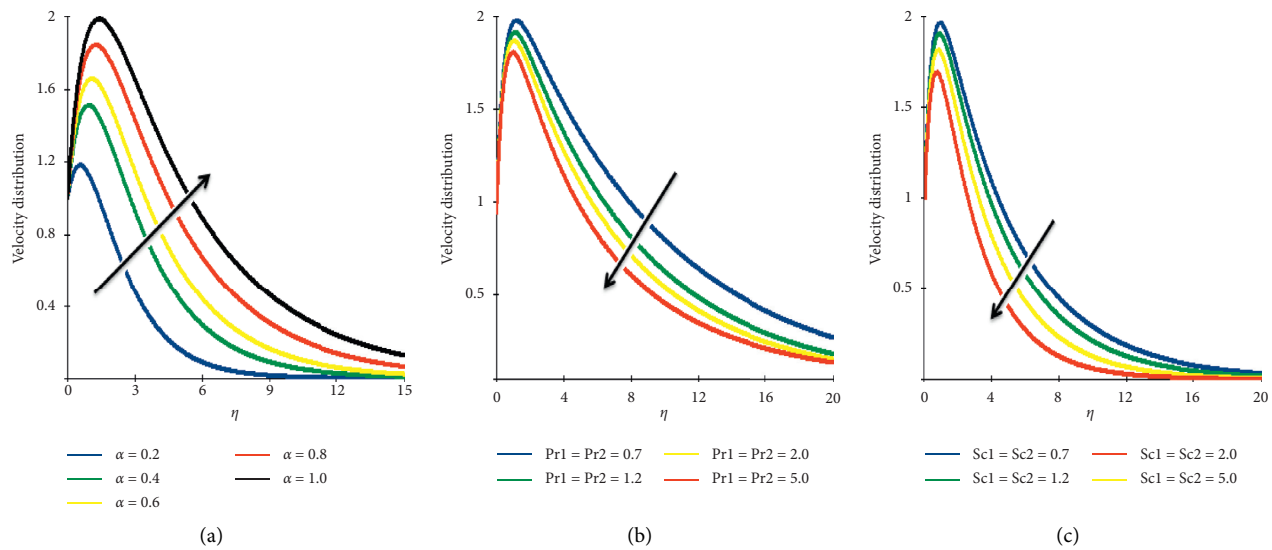

(a) (b) (c)

Figure 6: Sketch velocity profile for changing α, Pr, and Sc.

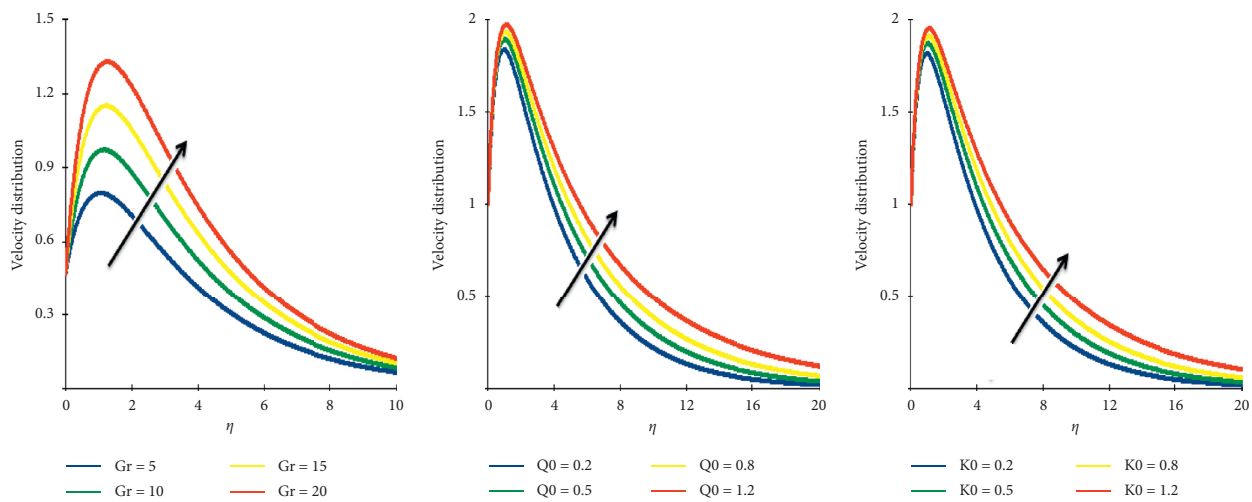

(a) (b) (c)

Figure 7: Sketch velocity profile for changing Gr, Q_0, and K_0.

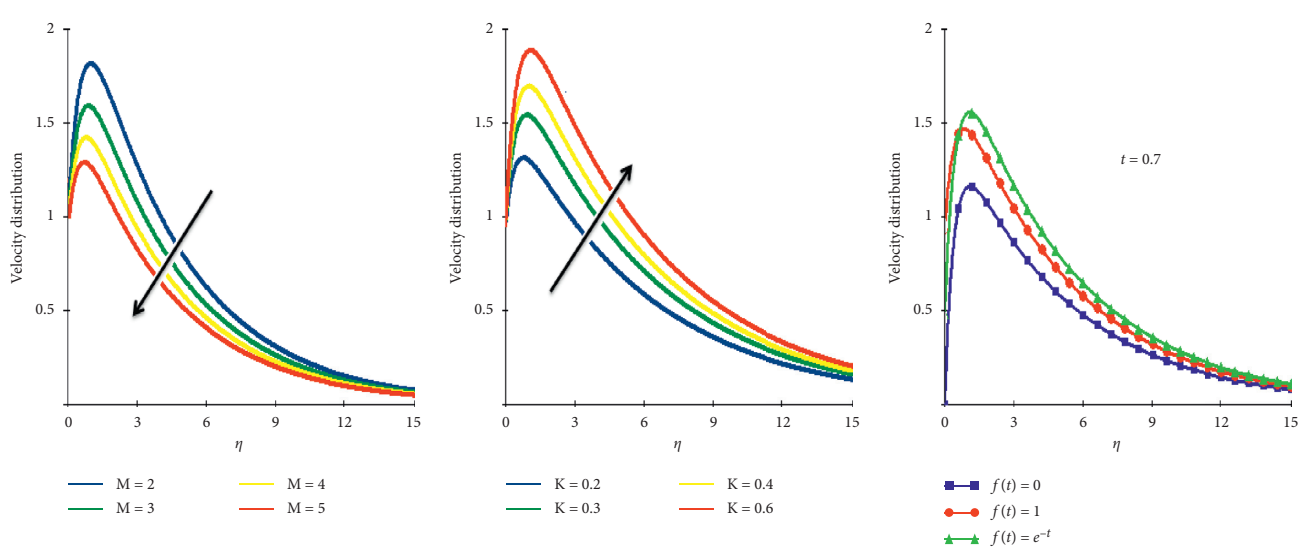

(a) (b) (c)

Figure 8: Sketch of velocity profile for changing values of M, K, and for $f(t)$.

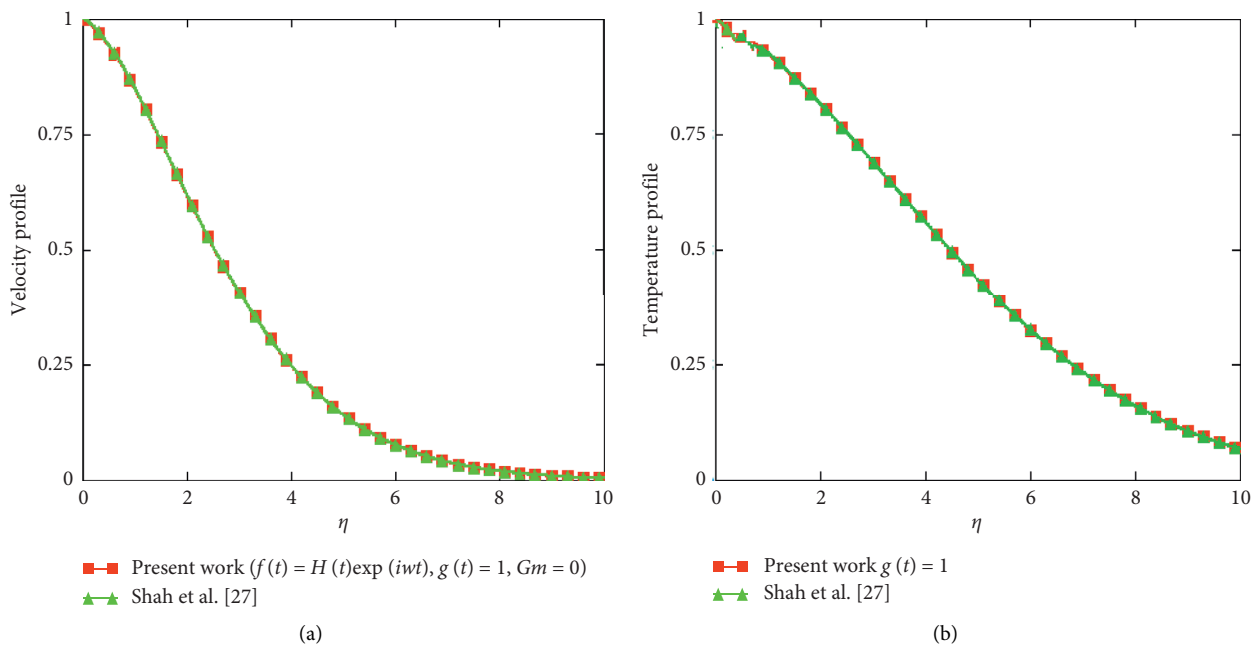

Figure 9: Sketch of velocity profile $[f(t) = H(t)\exp(iwt), g(t) = 1, Gm = 0]$ a comparison with Shah et al. [27].

Table 1: Subjectivity of Nusselt number due to α variation.

α	$\mathrm{Pr} = 2.0,\ t = 0.05$	$\mathrm{Pr} = 2.0,\ t = 0.5$	$\mathrm{Pr} = 2.0,\ t = 0.3$	$Q_0 = 0.3,\ t = 0.05$	$Q_0 = 0.3,\ t = 0.5$	$Q_0 = 0.3,\ t = 3$
0.1	1.28534684	1.63362404	1.58760351	1.366943741	0.367330281	0.10095136
0.2	2.01663381	1.76776695	1.08576315	1.895117488	0.458735913	0.10663781
0.3	2.93972368	1.91324675	0.83412160	2.748208635	0.543071730	0.09371372
0.4	4.47358865	2.34431009	0.48029944	3.249259012	0.680603872	0.08409179
0.5	5.49971941	2.70030862	0.27597129	3.593811291	0.898429253	0.07035624
0.6	6.28539361	3.23449479	0.10950250	3.849001709	1.022261776	0.04743416
0.7	6.92269321	3.67387267	0.07443112	4.046919659	1.143305599	0.03609199
0.8	7.45715981	4.05046294	0.04832345	4.205461089	1.246011475	0.10366066
0.9	7.91544825	4.38137291	0.03367067	4.335584398	1.335201230	0.11544229

Table 2: Subjectivity of Sherwood number due to α variation.

α	$\mathrm{Sc} = 1.5,\ t = 0.05$	$\mathrm{Sc} = 1.5,\ t = 0\ .5$	$\mathrm{Sc} = 1.5,\ t = 3$	$K_0 = 0.5,\ t = 0.05$	$K_0 = 0.5,\ t = 0.5$	$K_0 = 0.5,\ t = 3$
0.1	1.36694374	1.07412976	0.21908902	1.16694374	1.35433928	0.21095136
0.2	1.89511748	1.17645846	0.30983867	1.22263165	1.42893593	0.20663781
0.3	2.74820863	1.81147383	0.43817805	2.45807253	1.54357105	0.20371372
0.4	3.59381129	2.18028761	0.48989795	2.90622561	1.90603035	0.15091079
0.5	3.59381129	2.43499766	0.57965507	3.21440254	2.50425241	0.11935624
0.6	3.84900179	2.62480001	0.61967734	3.44265186	2.64561232	0.10743416
0.7	4.04691969	2.77288204	0.72663608	3.61967501	2.74330559	0.08609199
0.8	4.20546109	2.89214374	0.81975606	3.76147875	2.94601147	0.01366066
0.9	4.33558438	2.99049848	0.90332718	3.87786456	3.00220123	0.00544229

6. Conclusion

This investigation is designed to discuss the generalized thermal and mass transports and flow modeling for MHD second grade fluid subject to arbitrary conditions with the effect of heat generation and chemical reaction through a porous medium. The mathematical model is solved by integral transform method, and closed form relations for temperature, concentrations, and velocity fields are obtained. The effects of parameters for thermal and mass flow are discussed graphically. Also, thermal and mass

fluxes at boundary of flow domain are explained numerically for the due variation of α, and obtained results are given in the tabular form.

Some concluded bullets of this study are as follows:

(i) Temperature of the fluid is raised with incremental variation of α and Q_0, while it falls for the incremental variation of both Pr_1 and Pr_2

(ii) The thermal boundary conditions are also satisfied by temperature for different specifications of $g(t)$

(iii) The concentration level of the fluid is raised with incremental variation of α and K_0, whereas the level falls for the incremental variation of both Sc_1 and Sc_2

(iv) The concentration boundary conditions are also satisfied by the concentration for different specification of $h(t)$

(v) Velocity profile shows a growing trend for incremental increase in the values of α, Gr, Gm, Q_0, K_0, and K where as it retards for developing Pr_1 Pr_2, Sc_1, Sc_2, and M

(vi) The Nusselt number is boosted with the increasing values of α by taking large values of time, while it falls down with the increasing α for small time

(vii) The Sherwood number grows with the increasing values of α, for the large values of time, while it falls down with the increasing α for small time

Data Availability

All data are included within the article.

Conflicts of Interest

The authors declare that they have no conflicts of interest.

Acknowledgments

This project was sponsored by the Deanship of Scientific Research under Nasher Proposal No. 206207, King Faisal University.

References

[1] M. Caputo and M. Fabrizio, "A new definition of fractional derivative without singular kernel," *Progress in Fractional Differentiation and Applications*, vol. 1, no. 2, pp. 1–13, 2015.

[2] M. Caputo and M. Fabrizio, "Applications of new time and spatial fractional derivatives with exponential kernels," *Progress in Fractional Differentiation and Applications*, vol. 2, no. 1, pp. 1–11, 2016.

[3] D. Baleanu, A. Fernandez, and A. Akgül, "On a fractional operator combining proportional and classical differ-integrals," *Mathematics*, vol. 8, no. 3, pp. 360–372, 2020.

[4] C. Milici, G. Drgnescu, and J. T. Machado, *Introduction to Fractional Differential Equations*, Springer, Berlin Germany, VII edition, 2019.

[5] C. H. Yu, "Fractional derivatives of some fractional functions and their applications," *Asian Journal of Applied Science and Technology*, vol. 4, no. 1, pp. 147–158, 2020.

[6] M. A. Imran, M. Aleem, M. B. Riaz, R. Ali, and I. Khan, "A comprehensive report on convective flow of fractional (ABC) and (CF) MHD viscous fluid subject to generalized boundary conditions," *Chaos, Solitons & Fractals*, vol. 118, pp. 274–289, 2019.

[7] S. Kumar, A. Kumar, S. Abbas, M. A. Qurashi, and D. Baleanu, "A modified analytical approach with existence and uniqueness for fractional Cauchy reaction diffusion equations," *Advances in Difference Equations*, vol. 1, pp. 1–18, 2020.

[8] S. Qureshi, A. Yusuf, A. A. Shaikh, M. Inc, and D. Baleanu, "Fractional modeling of blood ethanol concentration system with real data application," *Chaos: An Interdisciplinary Journal of Nonlinear Science*, vol. 29, no. 1, Article ID 013143, 2019.

[9] J. Hristov, "Steady-state heat conduction in a medium with spatial non-singular fading memory: derivation of caputo-fabrizio space-fractional derivative from Canttaneo concept with Jeffrey's kernel and analytical solutions," *Thermal Science*, vol. 21, no. 2, pp. 827–839, 2017.

[10] M. A. Imran, S. Sarwar, and M. Nazar, "Influence of slip over an exponentially moving vertical plate with Caputo-time fractional derivative," *Journal of Thermal Analysis and Calorimetry*, 2020.

[11] M. A. Imran, I. Khan, M. Ahmad, N. A. Shah, and M. Nazar, "Heat and mass transport of differential type fluid with non-integer order time-fractional Caputo derivatives," *Journal of Molecular Liquids*, vol. 229, pp. 67–75, 2017.

[12] M. Ahmad, M. A. Imran, M. Aleem, and I. Khan, "A comparative study and analysis of natural convection flow of MHD non-Newtonian fluid in the presence of heat source and first-order chemical reaction," *Journal of Thermal Analysis and Calorimetry*, vol. 137, no. 5, pp. 1783–1796, 2019.

[13] A. Khalid, I. Khan, and S. Shafie, "Free convection flow of micropolar fluids over an oscillating vertical plate," *Malaysian Journal of Fundamental and Applied Sciences*, vol. 13, no. 4, pp. 654–658, 2017.

[14] R. K. Shukla and P. Sapra, "Fractional calculus and its applications for scientific professionals: a literature review," *International Journal of Modern Mathematical Sciences*, vol. 17, no. 2, pp. 111–137, 2019.

[15] D. Kumar, J. Singh, K. Tanwar, and D. Baleanu, "A new fractional exothermic reactions model having constant heat source in porous media with power, exponential and Mittag-Leffler laws," *International Journal of Heat and Mass Transfer*, vol. 138, pp. 1222–1227, 2019.

[16] J. Singh, D. Kumar, M. A. Qurashi, and D. Baleanu, "A new fractional model for giving up smoking dynamics," *Advances in Difference Equations*, vol. 88, pp. 1–16, 2017.

[17] H. Sun, Y. Zhang, D. Baleanu, W. Chen, and Y. Chen, "A new collection of real world applications of fractional calculus in science and engineering," *Communications in Nonlinear Science and Numerical Simulation*, vol. 64, pp. 213–231, 2018.

[18] M. Nazar, M. Ahmad, M. A. Imran, and N. A. Shah, "Double convection of heat and mass transfer flow of MHD generalized second grade fluid over an exponentially accelerated infinite vertical plate with heat absorption," *Journal of Mathematical Analysis*, vol. 8, pp. 1–10, 2017.

[19] F. Gómez, E. Escalante, C. Calderón, L. Morales, M. González, and R. Laguna, "Analytical solutions for the fractional diffusion-advection equation describing super-diffusion," *Open Physics*, vol. 14, no. 1, pp. 668–675, 2016.

[20] M. D. Tran, V. Ho, and H. N. Van, "On the stability of fractional differential equations involving generalized Caputo

fractional derivative," *Mathematical Problems in Engineering*, vol. 2020, pp. 1–14, 2020.

[21] N. H. Tuan, H. Mohammadi, and S. Rezapour, "A mathematical model for COVID-19 transmission by using the Caputo fractional derivative," *Chaos, Solitons & Fractals*, vol. 140, Article ID 110107, 2020.

[22] J. Hristov, "A transient flow of a non-Newtonian fluid modelled by a mixed time-space derivative: an improved integral-balance approach," *Nonlinear Systems and Complexity*, pp. 153–174, 2019.

[23] M. Saqib, F. Ali, I. Khan, N. A. Sheikh, S. A. A. Jan, and fnm Samiulhaq, "Exact solutions for free convection flow of generalized Jeffrey fluid: a Caputo-Fabrizio fractional model," *Alexandria Engineering Journal*, vol. 57, no. 3, pp. 1849–1858, 2018.

[24] S. Ul Haq, S. Jan, S. Ullah Jan, S. Inayat Ali Shah, I. Khan, and J. Singh, "Heat and mass transfer of fractional second grade fluid with slippage and ramped wall temperature using Caputo-Fabrizio fractional derivative approach," *AIMS Mathematics*, vol. 5, no. 4, pp. 3056–3088, 2020.

[25] M. A. Imran, N. A. Shah, M. Aleem, and I. Khan, "Heat transfer analysis of fractional second-grade fluid subject to Newtonian heating with Caputo and Caputo-Fabrizio fractional derivatives: a comparison," *The European Physical Journal Plus*, vol. 132, pp. 340–358, 2017.

[26] M. A. Khan, Z. Hammouch, and D. Baleanu, "Modeling the dynamics of hepatitis E via the Caputo-Fabrizio derivative," *Mathematical Modelling of Natural Phenomena*, vol. 14, no. 3, pp. 311–324, 2019.

[27] N. A. Shah and I. Khan, "Heat transfer analysis in a second grade fluid over and oscillating vertical plate using fractional Caputo-Fabrizio derivatives," *The European Physical Journal C*, vol. 76, no. 7, pp. 362–374, 2016.

[28] N. A. Sheikh, F. Ali, M. Saqib et al., "Comparison and analysis of the Atangana-Baleanu and Caputo-Fabrizio fractional derivatives for generalized Casson fluid model with heat generation and chemical reaction," *Results in Physics*, vol. 7, pp. 789–800, 2017.

[29] J. Hristov, "Transient heat diffusion with a non-singular fading memory from the Cattaneo constitutive equation with Jeffrey's kernel to the Caputo-Fabrizio time fractional derivative," *Thermal Sciences*, vol. 20, pp. 557–562, 2016.

[30] M. Aleem, M. Imran Asjad, M. S. R. Chowdhury, and A. Hussanan, "Analysis of mathematical model of fractional viscous fluid through a vertical rectangular channel," *Chinese Journal of Physics*, vol. 61, pp. 336–350, 2019.

[31] N. A. Sheikh, D. L. C. Ching, I. Khan, D. Kumar, and K. S. Nisar, "A new model of fractional Casson fluid based on generalized Fick's and Fourier's laws together with heat and mass transfer," *Alexandria Engineering Journal*, vol. 59, no. 5, pp. 2865–2876, 2020.

[32] M. Ahmad, M. A. Imran, and M. Nazar, "Mathematical modeling of $(CuAl_2O_3)$ water based Maxwell hybrid nanofluids with Caputo-Fabrizio fractional derivative," *Advances in Mechanical Engineering*, vol. 12, no. 9, pp. 1–11, 2020.

Hindawi
Complexity
Volume 2021, Article ID 9952562, 10 pages
https://doi.org/10.1155/2021/9952562

Research Article

Numerical Solution of the Multiterm Time-Fractional Model for Heat Conductivity by Local Meshless Technique

Bander N. Almutairi,[1] Ahmed E. Abouelregal,[2,3] Bandar Bin-Mohsin,[1] M. D. Alsulami,[4] and Phatiphat Thounthong[5]

[1]*Department of Mathematics, College of Science, King Saud University, Riyadh 11451, Saudi Arabia*
[2]*Department of Mathematics, College of Science and Arts, Jouf University, Al-Qurayyat, Saudi Arabia*
[3]*Department of Mathematics, Faculty of Science, Mansoura University, Mansoura 35516, Egypt*
[4]*University of Jeddah, College of Sciences and Arts at Alkamil, Department of Mathematics, Jeddah, Saudi Arabia*
[5]*Renewable Energy Research Centre, Department of Teacher Training in Electrical Engineering, Faculty of Technical Education, King Mongkut's University of Technology North Bangkok, 1518 Pracharat 1 Road, Bangsue, Bangkok 10800, Thailand*

Correspondence should be addressed to Ahmed E. Abouelregal; ahabogal@gmail.com

Received 24 March 2021; Revised 26 April 2021; Accepted 9 May 2021; Published 11 June 2021

Academic Editor: Nehad Ali Shah

Fractional partial differential equation models are frequently used to several physical phenomena. Despite the ability to express many complex phenomena in different disciplines, researchers have found that multiterm time-fractional PDEs improve the modeling accuracy for describing diffusion processes in contrast to the results of a single term. Nowadays, it attracts the attention of the active researchers. The aim of this work is concerned with the approximate numerical solutions of the three-term time-fractional Sobolev model equation using computationally attractive and reliable technique, known as a local meshless method. Because of the meshless character and the simple application in higher dimensions, there is a growing interest in meshless techniques. To assess the reliability and accuracy of the proposed method, three test problems and two types of irregular domains are taken into account.

1. Introduction

In recent years, fractional partial differential equations (FPDEs) have drawn the consideration of numerous researchers to their applications in various fields of science and technology. Partial derivatives provide a flexible model and an extraordinary tool for description of capturing the history of the variable and genetic characteristics of various dynamic systems. Extensive research has been carried out in the advancement of numerical and analytical solutions of linear and nonlinear FPDEs [1–6]. However, several researchers have not succeeded in deriving and modeling many complex phenomena utilizing linear or nonlinear PDEs with integer order [7]. Subsequently, the fractional is taken as account and is a good solution to this problem [8]. In the current work, three-term time-fractional Sobolev equation is considered which can be expressed as

$$\frac{\partial^{\beta_1}\mathscr{V}(y,z,t)}{\partial t^{\beta_1}}+\frac{\partial^{\beta_2}\mathscr{V}(y,z,t)}{\partial t^{\beta_2}}+\frac{\partial^{\beta_3}\mathscr{V}(y,z,t)}{\partial t^{\beta_3}}-\frac{\partial\nabla^2\mathscr{V}(y,z,t)}{\partial t}-\beta\nabla^2\mathscr{V}(y,z,t)+\gamma\nabla(\mathscr{V}(y,z,t)\nabla\mathscr{V}(\overline{z},t))$$
$$+\delta\mathscr{V}(y,z,t)=F(\overline{z},t),\quad (y,z)\in\Omega,\ 0<\beta_3\le\beta_2\le\beta_1\le 1,\ t>0. \tag{1}$$

With the conditions,

$$\begin{aligned}&\mathscr{V}(y,z,0)=\mathscr{V}_0(y,z),\\&\mathscr{V}(y,z,t)=g_1(y,z,t),\quad (y,z)\in\partial\Omega\ ,\end{aligned} \tag{2}$$

where ∇^2 is the Laplacian and ∇ denotes gradient operators, and β, γ, and δ the are known constants, whereas $(\partial^{\beta_1}/\partial t^{\beta_1})$, $(\partial^{\beta_2}/\partial t^{\beta_2})$, and $(\partial^{\beta_3}/\partial t^{\beta_3})$ represent the Caputo derivative operator of order $0<\beta_3\le\beta_2\le\beta_1\le 1$ for the function $\mathscr{V}(y,z,t)$.

In recent literature, various meshless methods have been utilized for the numerical solution of various PDE models almost in every discipline of science and engineering. In particular, the RBF-based meshless methods are the mainstream of these methods. The meshless nature is one of the main reasons behind the developing interest for such approaches. The meshless methods significantly reduce the complexity of dimensionality utilizing traditional methods such as the finite element and finite difference methods. Compared to mesh-based methods, these methods do not require mesh in the domain. The meshless methods have the ability to compute the solution in regular and irregular domain utilizing scattered or uniform nodes, which increases the priority and the advantages of meshless methods. As these facts show, these methods are really workable and useful numerical methods that can be applied to real-world challenging problems [9–17].

The RBF-based meshless methods have also some deficiencies like other numerical methods, in which the most important one is the dense ill-conditioned matrices and the selection of the optimal value of the shape parameter. To avoid these drawbacks, local meshless methods are the best alternatives, suggested by the researchers which are considered to be accurate and stable for the solution of diverse integer and fractional-order PDE models [18, 19]. The local meshless methods are less sensitive to the change in shape parameters than the global version, and it produces well-conditioned sparse matrices. Furthermore, local version of meshless methods is considered to be more effective and efficient than global ones. In recent years, the abilities of various sorts of local meshless methods in different applications have been explored [20–22].

In the current research, we have implemented the local meshless method to approximate the numerical solution of three-term time-fractional model equation (1). For this purpose, multiquadric (MQ) radial basis functions (RBFs) are used. Furthermore, two types of irregular domains are also taken in numerical examples.

2. Methodology of the Local Meshless Method

According to the local meshless method, to approximate the derivatives of $\mathscr{V}(\overline{\mathbf{z}},t)$ at the centers $\overline{\mathbf{z}}_h$ by the neighborhood of $\overline{\mathbf{z}}_h$, $\{\overline{\mathbf{z}}_{h1},\overline{\mathbf{z}}_{h2},\overline{\mathbf{z}}_{h3},\ldots,\overline{\mathbf{z}}_{hn_h}\}\subset\{\overline{\mathbf{z}}_1,\overline{\mathbf{z}}_2,\ldots,\overline{\mathbf{z}}_{N^n}\}$, $n_h\ll N^n$, where $h=1,2,\ldots,N^n$, we have used $\overline{\mathbf{z}}=y$ and $\overline{\mathbf{z}}=(y,z)$ for one-dimensional and two-dimensional cases, respectively.

Now, considering the following case for one-dimensional,

$$\mathscr{V}^{(m)}(y_h)\approx\sum_{k=1}^{n_h}\lambda_k^{(m)}\mathscr{V}(y_{hk}),\quad h=1,2,\ldots,N. \tag{3}$$

Substituting the multiquadric RBF $\psi(\|y-y_p\|)=\sqrt{1+(c\|y_{hk}-y_p\|)^2}$ in (3),

$$\psi^{(m)}\left(\left\|y_h-y_p\right\|\right)=\sum_{k=1}^{n_h}\lambda_{hk}^{(m)}\psi\left(\left\|y_{hk}-y_p\right\|\right),\quad p=h1,h2,\ldots,hn_h. \tag{4}$$

Equation (4) in matrix form is

$$\underbrace{\begin{bmatrix}\psi_{h1}^{(m)}(y_h)\\ \psi_{h2}^{(m)}(y_h)\\ \vdots\\ \psi_{hn_h}^{(m)}(y_h)\end{bmatrix}}_{\psi_{n_h}^{(m)}}=\underbrace{\begin{bmatrix}\psi_{h1}(y_{h1}) & \psi_{h2}(y_{h1}) & \cdots & \psi_{hn_h}(y_{h1})\\ \psi_{h1}(y_{h2}) & \psi_{h2}(y_{h2}) & \cdots & \psi_{hn_h}(y_{h2})\\ \vdots & \vdots & \ddots & \vdots\\ \psi_{h1}(yh_{n_h}) & \psi_{h2}(y_{hn_h}) & \cdots & \psi_{hn_h}(yh_{n_h})\end{bmatrix}}_{A_{n_h}}\underbrace{\begin{bmatrix}\lambda_{h1}^{(m)}\\ \lambda_{h2}^{(m)}\\ \vdots\\ \lambda_{hn_h}^{(m)}\end{bmatrix}}_{\lambda_{n_h}^{(m)}}, \tag{5}$$

where

$$\psi_p((y_k))=\psi\left(\left\|y_k-y_p\right\|\right),\quad p=h1,h2,\ldots,hn_h, \tag{6}$$

for each $k=i1,h2,\ldots,hn_h$. Equation (5) in simple form is

$$\boldsymbol{\psi}_{n_h}^{(m)}=\mathbf{A}_{n_h}\boldsymbol{\lambda}_{n_h}^{(m)}. \tag{7}$$

From (7), we obtain

$$\boldsymbol{\lambda}_{n_h}^{(m)} = \mathbf{A}_{n_h}^{-1}\boldsymbol{\psi}_{n_h}^{(m)}. \tag{8}$$

(3) and (8) implies

$$\mathscr{V}^{(m)}(y_h) = \left(\boldsymbol{\lambda}_{n_h}^{(m)}\right)^T \mathbf{V}_{n_h}, \tag{9}$$

where

$$\mathbf{V}_{n_h} = \left[\mathscr{V}(y_{h1}), \mathscr{V}(y_{h2}), \ldots, \mathscr{V}\left(y_{hn_h}\right)\right]^T. \tag{10}$$

The derivatives of $\mathscr{V}(y, z, t)$ w. r. t. y and z can be found as

$$\begin{aligned} \mathscr{V}_y^{(m)}(y_h, z_h) &\approx \sum_{k=1}^{n_h} \gamma_k^{(m)} \mathscr{V}(y_{hk}, z_{hk}), \quad h = 1, 2, \ldots, N^2, \\ \mathscr{V}_y^{(m)}(y_h, z_h) &\approx \sum_{k=1}^{n_h} \eta_k^{(m)} \mathscr{V}(y_{hk}, z_{hk}), \quad h = 1, 2, \ldots, N^2. \end{aligned} \tag{11}$$

For $\gamma_k^{(m)}$ and $\eta_k^{(m)}$ $(k = 1, 2, \ldots, n_h)$, we continue as

$$\begin{aligned} \boldsymbol{\gamma}_{n_h}^{(m)} &= \mathbf{A}_{n_h}^{-1}\boldsymbol{\Phi}_{n_h}^{(m)}, \\ \boldsymbol{\eta}_{n_h}^{(m)} &= \mathbf{A}_{n_h}^{-1}\boldsymbol{\Phi}_{n_h}^{(m)}. \end{aligned} \tag{12}$$

The time derivative $(\partial^{\beta_1}\mathscr{V}(\bar{\mathbf{z}}, t)/\partial t^{\beta_1})$ is discretized utilizing Caputo derivative [23], where $\beta_1 \in (0, 1)$ as

$$\frac{\partial^{\beta_1}\mathscr{V}(\bar{\mathbf{z}}, t)}{\partial t^{\beta_1}} = \begin{cases} \dfrac{1}{\Gamma(1-\beta_1)} \displaystyle\int_0^t \frac{\partial \mathscr{V}(\bar{\mathbf{z}}, \vartheta)}{\partial \vartheta}(t-\vartheta)^{-\beta_1} \mathrm{d}\vartheta, & 0 < \beta_1 < 1, \\ \dfrac{\partial \mathscr{V}(\bar{\mathbf{z}}, t)}{\partial t}, & \beta_1 = 1. \end{cases} \tag{13}$$

Let τ be the time step size, and for the interval $[0, t]$, consider $t_q = q\tau$, $q = 0, 1, 2, \ldots, Q$. We complete the time-fractional derivative term as

$$\begin{aligned} \frac{\partial^{\beta_1}\mathscr{V}\left(\bar{\mathbf{z}}, t_{q+1}\right)}{\partial t^{\beta_1}} &= \frac{1}{\Gamma(1-\beta_1)} \int_0^{t_{q+1}} \frac{\partial \mathscr{V}(\bar{\mathbf{z}}, \vartheta)}{\partial \vartheta}\left(t_{q+1} - \vartheta\right)^{-\beta_1} \mathrm{d}\vartheta, \\ &= \frac{1}{\Gamma(1-\beta_1)} \sum_{r=0}^{q} \int_{r\tau}^{(r+1)\tau} \frac{\partial \mathscr{V}(\bar{\mathbf{z}}, \vartheta)}{\partial \vartheta}(t_{r+1} - \vartheta)^{-\beta_1} \mathrm{d}\vartheta, \\ &\approx \frac{1}{\Gamma(1-\beta_1)} \sum_{r=0}^{q} \int_{r\tau}^{(r+1)\tau} \frac{\partial \mathscr{V}(\bar{\mathbf{z}}, \vartheta_r)}{\partial \vartheta}(t_{r+1} - \vartheta)^{-\beta_1} \mathrm{d}\vartheta. \end{aligned} \tag{14}$$

The term $(\partial \mathscr{V}(\bar{\mathbf{z}}, \vartheta_r)/\partial \vartheta)$ is approximated as follows:

$$\frac{\partial \mathscr{V}(\bar{\mathbf{z}}, \vartheta_r)}{\partial \vartheta} = \frac{\mathscr{V}(\bar{\mathbf{z}}, \vartheta_{r+1}) - \mathscr{V}(\bar{\mathbf{z}}, \vartheta_r)}{\vartheta} + \mathscr{O}(\tau). \tag{15}$$

Then,

$$\frac{\partial^{\beta_1}\mathscr{V}\left(\bar{\mathbf{z}},t_{q+1}\right)}{\partial t^{\beta_1}} \approx 1/\Gamma\left(1-\beta_1\right)\sum_{r=0}^{q}\mathscr{V}\left(\bar{\mathbf{z}},t_{r+1}\right)-\mathscr{V}\left(\bar{\mathbf{z}},t_r\right)/\tau\int_{r\tau}^{(r+1)\tau}\left(t_{r+1}-\vartheta\right)^{-\beta_1}\mathrm{d}\vartheta,$$

$$=\frac{1}{\Gamma\left(1-\beta_1\right)}\sum_{r=0}^{q}\frac{\mathscr{V}\left(\bar{\mathbf{z}},t_{q+1-r}\right)-\mathscr{V}\left(\bar{\mathbf{z}},t_{q-r}\right)}{\tau}\int_{r\tau}^{(r+1)\tau}\left(t_{r+1}-\vartheta\right)^{-\beta_1}\mathrm{d}\vartheta,$$

$$=\begin{cases}\dfrac{\tau^{-\beta_1}}{\Gamma\left(2-\beta_1\right)}\left(\mathscr{V}^{q+1}-\mathscr{V}^{q}\right)+\dfrac{\tau^{-\beta_1}}{\Gamma\left(2-\beta_1\right)}\displaystyle\sum_{r=1}^{q}\left(\mathscr{V}^{q+1-r}-\mathscr{V}^{q-r}\right)\left[(r+1)^{1-\beta_1}-r^{1-\beta_1}\right], & q\geq 1,\\[2ex] \dfrac{\tau^{-\beta_1}}{\Gamma\left(2-\beta_1\right)}\left(\mathscr{V}^{1}-\mathscr{V}^{0}\right), & q=0.\end{cases} \tag{16}$$

Letting $a_0=(\tau^{-\beta_1}/\Gamma(2-\beta_1))$ and $b_r=(r+1)^{1-\beta_1}-r^{1-\beta_1}$, $r=0,1,\ldots,q$, we have

$$\frac{\partial^{\beta_1}\mathscr{V}\left(\bar{\mathbf{z}},t_{q+1}\right)}{\partial t^{\beta_1}}\approx\begin{cases}a_0\left(\mathscr{V}^{q+1}-\mathscr{V}^{q}\right)+a_0\displaystyle\sum_{r=1}^{q}b_r\left(\mathscr{V}^{q+1-r}-\mathscr{V}^{q-r}\right), & q\geq 1,\\[2ex] a_0\left(\mathscr{V}^{1}-\mathscr{V}^{0}\right), & q=0.\end{cases} \tag{17}$$

The fractional derivative of order β_2 and β_3 can be found as above.

3. Numerical Experiments

This section examines the accuracy and applicability of the proposed method for the three-term time-fractional model (1). In the test problems, we have considered regular and irregular domains. This computation is considered to be regular and scattered nodes with regular and irregular domains. In this article, we have used the Crank–Nicholson scheme and multiquadric (MQ) RBF with shape parameter value $c=10$. Unless specifically stated, the spatial domain $[0,4]$ and time step size $\tau=0.002$ are used. Accuracy is measured as follows:

$$\begin{aligned}L_{\text{absolute}}&=|\widehat{\mathbb{V}}-\mathscr{V}|,\\ \text{Max}-\text{error}&=\max\left(L_{\text{absolute}}\right),\\ \text{RMS}&=\sqrt{\frac{\sum_{h=1}^{N^n}\left(\widehat{\mathbb{V}}_h-\mathscr{V}_h\right)^2}{N}},\end{aligned} \tag{18}$$

where $\widehat{\mathbb{V}}$ is the exact solution, and $\mathscr{V}$ is the approximate solution.

Problem 1. Consider the model equation:

$$\frac{\partial^{\beta_1}\mathscr{V}(y,z,t)}{\partial t^{\beta_1}}+\frac{\partial^{\beta_2}\mathscr{V}(y,z,t)}{\partial t^{\beta_2}}+\frac{\partial^{\beta_3}\mathscr{V}(y,z,t)}{\partial t^{\beta_3}}-\frac{\partial\nabla^2\mathscr{V}(y,z,t)}{\partial t}-\nabla^2\mathscr{V}(y,z,t)=F(y,z,t),$$
$$0<\beta_3\leq\beta_2\leq\beta_1\leq 1,$$
$$t>0. \tag{19}$$

Having the exact solution,

$$\mathscr{V}(y,z,t)=e^{-t}\sin(\pi y)\sin(\pi z),\quad (y,z)\in\Omega. \tag{20}$$

The proposed meshless method is implemented for generating the required numerical results for Problem 1, which are given in Table 1. Different values of a number of nodes N, fractional order $\beta_1=\beta_2=\beta_3$, and final time $t=1$ are used, whereas the error norms stand for max − error and RMS. These results revealed the fact that the recommended meshless method is capable of better results. Showing the accurate and efficient of the method, the results are compared with the exact solution for $\beta_1=\beta_2=\beta_3=0.1$, $\beta_1=\beta_2=\beta_3=0.3$, $\beta_1=\beta_2=\beta_3=0.5$, $t=1$, $t=2$, and for

Table 1: Problem 1, approximate results for $t = 1$.

	$\beta_1 = \beta_2 = \beta_3 = 0.2$		$\beta_1 = \beta_2 = \beta_3 = 0.5$		$\beta_1 = \beta_2 = \beta_3 = 0.8$	
N	Max − error	RMS	Max − error	RMS	Max − error	RMS
8^2	$8.5869e-08$	$3.9708e-08$	$3.8841e-07$	$1.2258e-07$	$4.9568e-06$	$1.7762e-06$
10^2	$8.2120e-08$	$3.9848e-08$	$4.8466e-07$	$1.4140e-07$	$5.8961e-06$	$1.9704e-06$
12^2	$8.8415e-08$	$3.9397e-08$	$5.2865e-07$	$1.6405e-07$	$6.1379e-06$	$2.1931e-06$

Table 2: Problem 1, approximate results using $N = 8^2$ and $\beta = \beta_1 = \beta_2 = \beta_3$.

	Max − error					
	$t = 1$			$t = 2$		
τ	$\beta = 0.1$	$\beta = 0.3$	$\beta = 0.5$	$\beta = 0.1$	$\beta = 0.3$	$\beta = 0.5$
0.2	$1.1044e-03$	$9.9648e-04$	$7.9676e-04$	$7.9063e-04$	$7.1256e-04$	$5.7016e-04$
0.02	$1.0790e-05$	$8.0577e-06$	$3.9095e-06$	$7.7071e-06$	$5.6947e-06$	$3.1952e-06$
0.002	$1.0500e-07$	$4.3655e-08$	$3.8841e-07$	$7.4936e-08$	$3.0435e-08$	$2.9006e-07$

various values of time step size τ. These results are computed using $N = 8^2$ and are given in Table 2. One can observe from this table that only in few iterations, the suggested meshless method produced better results, and as the number of time iteration increases, the accuracy increase and the error norm reached up to $\max - \text{error} \approx 10^{-10}$. As the condition number, stability, and accuracy of the RBF-based meshless methods heavily depend on the value of shape parameter c, a little change in shape parameter value causes instability and the results get diverge. But the suggested local meshless method is tested for Problem 1 in terms of condition number, stability, and accuracy as shown in Figure 1 for $N = 10^2$, $\beta_1 = \beta_2 = \beta_3 = 0.5$, and $t = 1$. This figure revealed that the suggested meshless method is stable, accurate, and given ideal low condition number ≈ 1 for a long range of c up to 2000. Figure 2 shows the absolute error using $\beta_1 = \beta_2 = \beta_3 = 0.1$ and $\beta_1 = \beta_2 = \beta_3 = 0.8$ for $N = 10^2$ and $t = 1$. Better accuracy of the recommended algorithm can be seen in this figure.

Problem 2. Consider the model equation:

$$\frac{\partial^{\beta_1}\mathscr{V}(y,z,t)}{\partial t^{\beta_1}} + \frac{\partial^{\beta_2}\mathscr{V}(y,z,t)}{\partial t^{\beta_2}} + \frac{\partial^{\beta_3}\mathscr{V}(y,z,t)}{\partial t^{\beta_3}} - \frac{\partial\nabla^2\mathscr{V}(y,z,t)}{\partial t} - \nabla^2\mathscr{V}(y,z,t) = F(y,z,t),$$
$$0 < \beta_3 \le \beta_2 \le \beta_1 \le 1, \tag{21}$$
$$t > 0.$$

Having the exact solution,

$$\mathscr{V}(y,z,t) = e^{y-z-t}\sin(\pi y)\sin(\pi z), \quad (y,z) \in \Omega. \tag{22}$$

In Table 3, we have implemented the suggested algorithm for generating the numerical results for Problem 2 for $N = 8^2$, $N = 10^2$, $N = 12^2$, $\beta_1 = \beta_2 = \beta_3 = 0.2$, $\beta_1 = \beta_2 = \beta_3 = 0.4$, $\beta_1 = \beta_2 = \beta_3 = 0.4$, and $t = 1$, $t = 2$. The results are assessed in term of max − error and RMS. Accurate results have been obtained in this problem as well. Showing the applicability and efficacy of the propose method, the results are compared with the exact solution for various values of $\beta_1 = \beta_2 = \beta_3\, t$ and τ using $N = 8^2$. These results are given in Table 4. One can observe from this table that only in few iterations, the suggested meshless method produced better results, and as the number of time iteration increases, the accuracy increase and the error norm reached up to $\text{RMS} \approx 10^{-9}$.

Just like the previous problem, the suggested method has been tested for Problem 2 in terms of condition number, stability, and accuracy as shown in Figure 3 for $N = 10^2$, $\beta = 0.5$, and $t = 1$. It can easily be seen from the figure that the suggest meshless method is stable, accurate, and given ideal low condition number ≈ 1 for a long range of c up to 2000, whereas in Figure 4, we have shown a comparison of exact and approximate solutions for various values of time t and brilliant match of both the solutions can be found in this figure.

One of the principle advantages of the meshless techniques over mesh-based techniques is the implementation in the irregular domain with ease. In this article, two types of challenging irregular domains are taken into account, which are displayed in Figure 5. In Table 5, we have shown the numerical results obtained by the suggested meshless method corresponding to the irregular domains for Problem 1 and Problem 2. We have considered the various value of β 's, and the results are shown in form of max − error and RMS. It is observed from the table that better accuracy has been achieved in both domains.

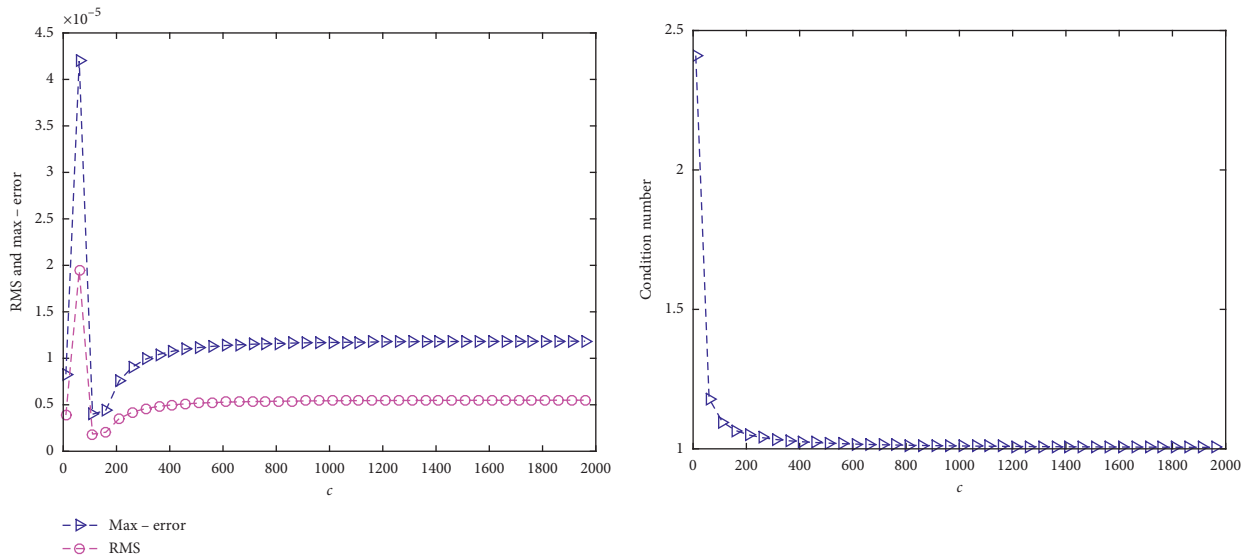

(a) (b)

Figure 1: Problem 1. (a) c and error norms, (b) c and condition number.

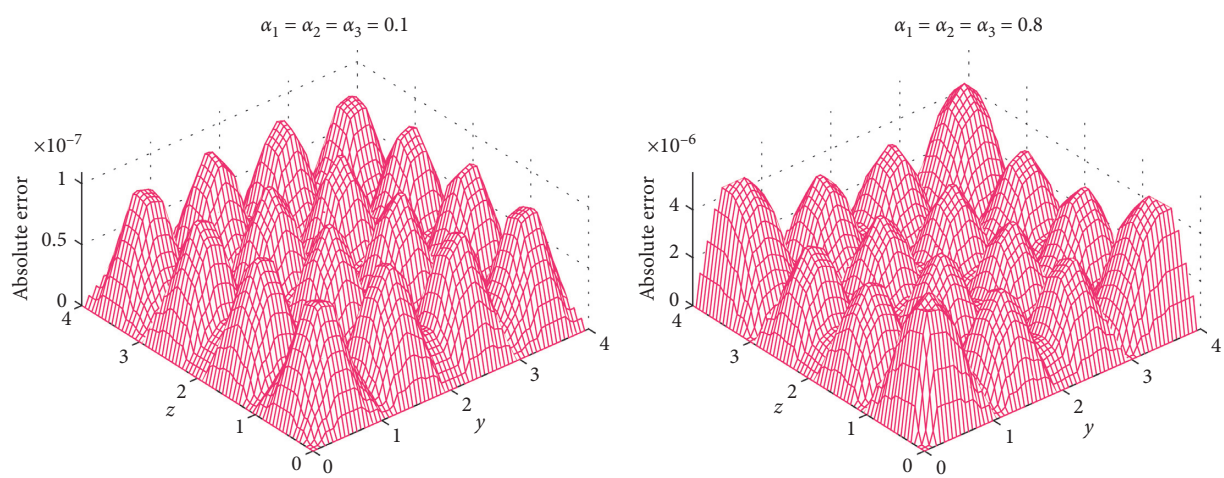

(a) (b)

Figure 2: Problem 1. Absolute error for $\beta = 0.1$ (a) and $\beta = 0.8$ (b), where $\beta = \beta_1 = \beta_2 = \beta_3$.

Table 3: Problem 2, approximate results for $t = 1$.

N	$\beta_1 = \beta_2 = \beta_3 = 0.2$		$\beta_1 = \beta_2 = \beta_3 = 0.4$		$\beta_1 = \beta_2 = \beta_3 = 0.6$	
	Max − error	RMS	Max − error	RMS	Max − error	RMS
8^2	$1.2325e-06$	$2.0404e-07$	$2.3271e-06$	$3.3074e-07$	$1.9346e-05$	$2.5361e-06$
10^2	$1.5895e-06$	$2.1784e-07$	$3.2329e-06$	$4.5136e-07$	$2.6251e-05$	$3.2570e-06$
12^2	$1.4030e-06$	$2.1123e-07$	$4.2754e-06$	$5.8259e-07$	$3.1278e-05$	$3.9590e-06$

Table 4: Problem 2, approximate results for $N = 8^2$.

τ	RMS					
	$t = 1$			$t = 2$		
	$\beta = 0.2$	$\beta = 0.4$	$\beta = 0.6$	$\beta = 0.2$	$\beta = 0.4$	$\beta = 0.6$
0.2	$2.6139e-03$	$2.2018e-03$	$1.5260e-03$	$1.8624e-03$	$1.5697e-03$	$1.0945e-03$
0.02	$2.3792e-05$	$1.2980e-05$	$4.3173e-05$	$1.6857e-05$	$9.2597e-06$	$3.3106e-05$
0.002	$2.0404e-07$	$3.3074e-07$	$2.5361e-06$	$1.4425e-07$	$2.4742e-07$	$1.9042e-06$
0.0002	$1.5812e-09$	$1.1891e-08$	$1.1014e-07$	$1.1152e-09$	$8.7439e-09$	$8.2401e-08$

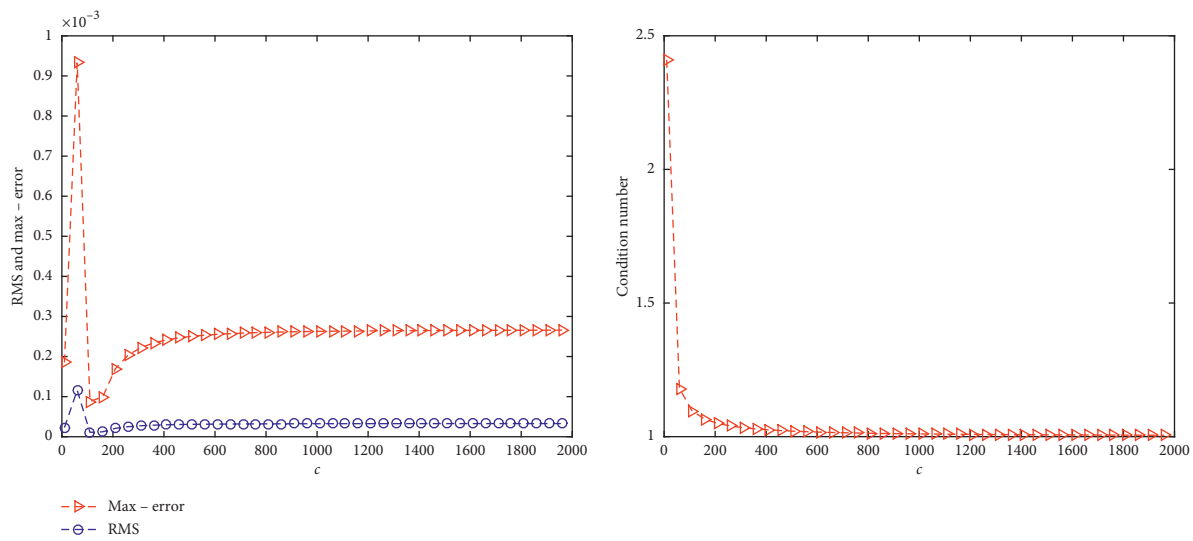

(a) (b)

Figure 3: Problem 2. (a) c and error norms. (b) c and condition number.

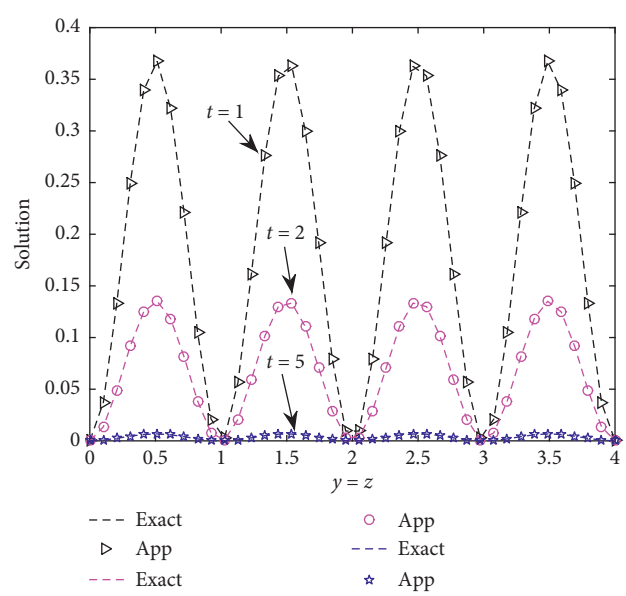

Figure 4: Problem 2, approximate and exact solution for indicated time.

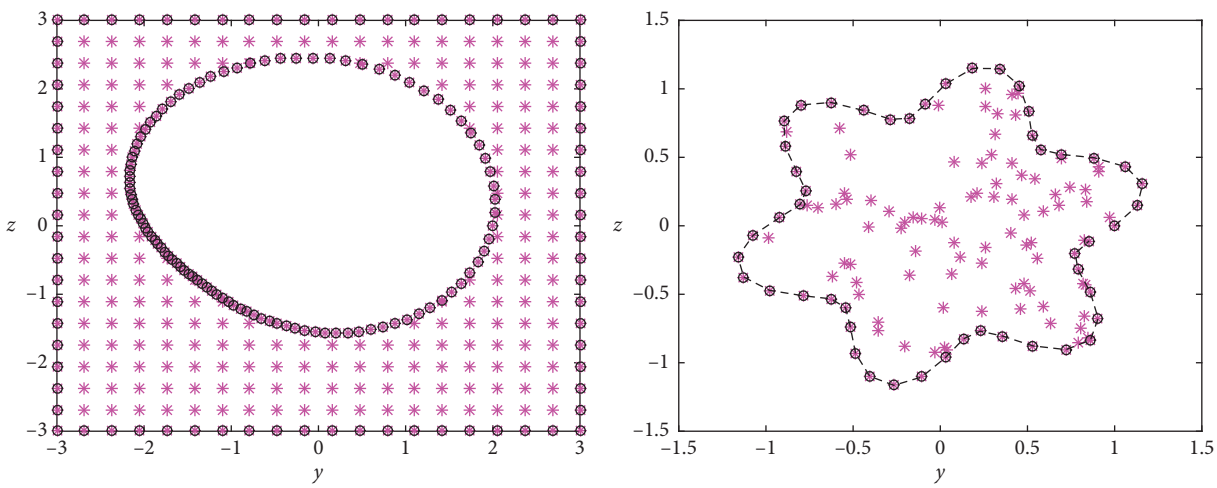

Figure 5: Computational domain 1 (a) and domain 2 (b).

Table 5: Approximate results corresponding to the irregular domains.

	Domain	$\beta = 0.2$		$\beta = 0.5$		$\beta = 0.8$	
		Max − error	RMS	Max − error	RMS	Max − error	RMS
Problem 1	Domain 1	$2.8188e-07$	$7.0294e-08$	$3.2180e-06$	$8.2127e-07$	$3.3601e-05$	$9.0154e-06$
	Domain 2	$1.9344e-06$	$3.4442e-07$	$2.0244e-05$	$3.8603e-06$	$1.1285e-04$	$2.6506e-05$
Problem 2	Domain 1	$9.0788e-06$	$1.1575e-06$	$9.5402e-05$	$1.0099e-05$	$1.0994e-03$	$1.1639e-04$
	Domain 2	$3.3707e-06$	$6.0517e-07$	$3.2748e-05$	$6.3853e-06$	$1.2824e-04$	$3.2931e-05$

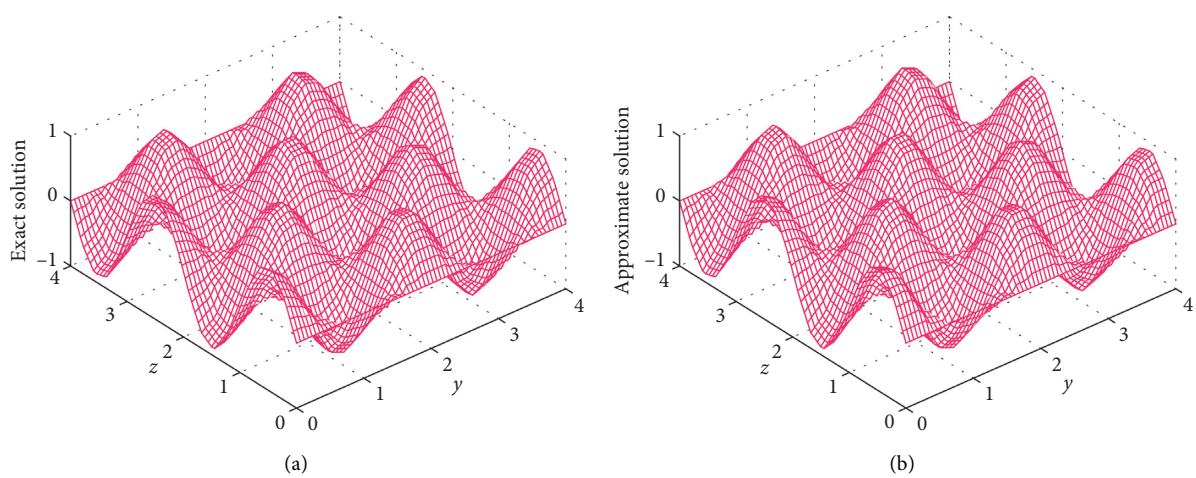

Figure 6: Problem 3. (a) Exact solution. (b) Numerical solution.

Problem 3. Consider the model equation:

$$\frac{\partial^{\beta_1}\mathscr{V}(y,z,t)}{\partial t^{\beta_1}}+\frac{\partial^{\beta_2}\mathscr{V}(y,z,t)}{\partial t^{\beta_2}}+\frac{\partial^{\beta_3}\mathscr{V}(y,z,t)}{\partial t^{\beta_3}}-\frac{\partial\nabla^2\mathscr{V}(y,z,t)}{\partial t}-\nabla^2\mathscr{V}(y,z,t)+\nabla(\mathscr{V}(y,z,t)\nabla\mathscr{V}(\bar{\mathbf{z}},t))$$
$$+\pi^2\mathscr{V}(y,z,t)=F(y,z,t),\quad (y,z)\in\Omega,\ 0<\beta_3\le\beta_2\le\beta_1\le 1,\ t>0. \tag{23}$$

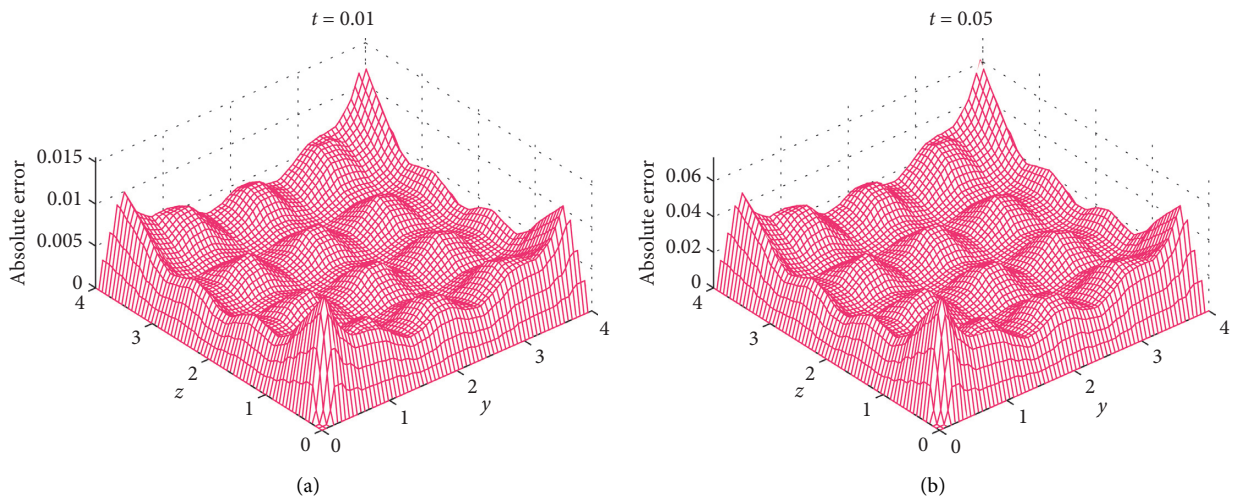

Figure 7: Problem 3, absolute error at (a) $t = 0.01$ and (b) $t = 0.05$.

Having the exact solution,

$$\mathscr{V}(y,z,t) = e^{t}\sin(\pi y)\sin(\pi z), \quad (y,z) \in \Omega. \tag{24}$$

In Figure 6, we have visualized the behavior of the exact and approximate solutions for the Problem 3 using $N = 20^2$, $\beta_1 = \beta_2 = \beta_3 = 0.5$, and $t = 0.1$, which show that the approximate solution is very compatible with the exact solution. In Figure 7, the absolute error is displayed for Problem 3.

4. Conclusion

In this study, our principle focused on the applicability and performance of the RBF-based local meshless method to approximate the numerical solution of three-term time-fractional Sobolev equations. The computed results show that the proposed technique can take care of these sorts of problems amazingly and accurately. The local procedure leads to a sparse system of linear equations, and the solution is approximated with good accuracy. Three test problems are taken into account to test the effectiveness and accuracy of the proposed meshless method utilizing rectangular and two irregular domains. The numerical results demonstrate the high accuracy and effectiveness of the method. Given the current research, the proposed technique is a surprisingly powerful and successful tool for solving numerical problems of multiterm time-fractional PDEs found in various fields of science and technology.

Data Availability

The data that support the findings of this study are openly available at https://hindawi.com/publish-research.

Conflicts of Interest

The authors declare that they have no conflicts of interest.

Acknowledgments

The authors extend their appreciation to the Deanship of Scientific Research of King Saud University for funding this work through research group no. RG-1441-327.

References

[1] I. Ahmad, H. Ahmad, P. Thounthong, Y.-M. Chu, and C. Cesarano, "Solution of multi-term time-fractional PDE models arising in mathematical biology and physics by local meshless method," *Symmetry*, vol. 12, no. 7, p. 1195, 2020.

[2] N. A. Shah, I. Dassios, and J. D. Chung, "Numerical investigation of time-fractional equivalent width equations that describe hydromagnetic waves," *Symmetry*, vol. 13, no. 3, p. 418, 2021.

[3] H. Ahmad, T. A. Khan, I. Ahmad, P. S. Stanimirović, and Y.-M. Chu, "A new analyzing technique for nonlinear time fractional Cauchy reaction-diffusion model equations," *Results in Physics*, vol. 19, Article ID 103462, 2020.

[4] M. Inc, M. N. Khan, I. Ahmad, S.-W. Yao, H. Ahmad, and P. Thounthong, "Analysing time-fractional exotic options via efficient local meshless method," *Results in Physics*, vol. 19, Article ID 103385, 2020.

[5] N. A. Shah and J. D. Chung, "The analytical solution of fractional-order whitham–broer–kaup equations by an elzaki decomposition method," *Numerical Methods for Partial Differential Equations*, 2021.

[6] I. Ahmad, M. N. Khan, M. Inc, H. Ahmad, and K. S. Nisar, "Numerical simulation of simulate an anomalous solute transport model via local meshless method," *Alexandria Engineering Journal*, vol. 59, no. 4, pp. 2827–2838, 2020.

[7] S. T. R. Rizvi, I. Afzal, and K. Ali, "Chirped optical solitons for Triki-Biswas equation," *Modern Physics Letters B*, vol. 33, no. 22, Article ID 1950264, 2019.

[8] R. Attia, D. Lu, and M. M. A. Khater, "Chaos and relativistic energy-momentum of the nonlinear time fractional duffing equation," *Mathematical and Computational Applications*, vol. 24, no. 1, p. 10, 2019.

[9] M. N. Khan, S. U. Islam, I. Hussain, I. Ahmad, and H. Ahmad, "A local meshless method for the numerical solution of space-

dependent inverse heat problems," *Mathematical Methods in the Applied Sciences*, vol. 44, 2020.

[10] M. Nawaz, I. Ahmad, and H. Ahmad, "A radial basis function collocation method for space-dependent inverse heat problems," *Journal of Applied and Computational Mechanics*, vol. 6, 2020.

[11] P. Thounthong, M. Khan, I. Hussain, I. Ahmad, and P. Kumam, "Symmetric radial basis function method for simulation of elliptic partial differential equations," *Mathematics*, vol. 6, no. 12, p. 327, 2018.

[12] N. A. Shah, I. Dassios, E. R. El-Zahar, J. D. Chung, and S. Taherifar, "The variational iteration transform method for solving the time-fractional fornberg-whitham equation and comparison with decomposition transform method," *Mathematics*, vol. 9, no. 2, p. 141, 2021.

[13] H. Ahmad, A. R. Seadawy, and T. A. Khan, "Study on numerical solution of dispersive water wave phenomena by using a reliable modification of variational iteration algorithm," *Mathematics and Computers in Simulation*, vol. 177, 2020.

[14] H. Ahmad, A. R. Seadawy, T. A. Khan, and P. Thounthong, "Analytic approximate solutions for some nonlinear parabolic dynamical wave equations," *Journal of Taibah University for Science*, vol. 14, no. 1, pp. 346–358, 2020.

[15] N. A. Shah, E. R. El-Zahar, M. D. Aljoufi, and J. D. Chung, "An efficient approach for solution of fractional-order helmholtz equations," *Advances in Difference Equations*, vol. 2021, no. 1, pp. 1–15, 2021.

[16] Y.-M. Chu, N. A. Shah, P. Agarwal, and J. D. Chung, "Analysis of fractional multi-dimensional Navier–Stokes equation," *Advances in Difference Equations*, vol. 2021, no. 1, pp. 1–18, 2021.

[17] H. Ahmad, T. A. Khan, P. S. Stanimirovic, and I. Ahmad, "Modified variational iteration technique for the numerical solution of fifth order KdV type equations," *Journal of Applied and Computational Mechanics*, vol. 6, 2020.

[18] I. Ahmad, M. Ahsan, I. Hussain, P. Kumam, and W. Kumam, "Numerical simulation of PDEs by local meshless differential quadrature collocation method," *Symmetry*, vol. 11, no. 3, p. 394, 2019.

[19] I. Ahmad, M. Ahsan, Z.-U. Din, A. Masood, and P. Kumam, "An efficient local formulation for time-dependent PDEs," *Mathematics*, vol. 7, no. 3, p. 216, 2019.

[20] I. Ahmad, S.-U. Islam, and A. Q. M. Khaliq, "Local RBF method for multi-dimensional partial differential equations," *Computers & Mathematics with Applications*, vol. 74, no. 2, pp. 292–324, 2017.

[21] C. Shu, *Differential Quadrature and its Application in Engineering*, Springer-Verlag, London, UK, 2000.

[22] I. Ahmad, H. Ahmad, A. E. Abouelregal, P. Thounthong, and M. Abdel-Aty, "Numerical study of integer-order hyperbolic telegraph model arising in physical and related sciences," *The European Physical Journal Plus*, vol. 135, no. 9, pp. 1–14, 2020.

[23] M. Caputo, "Linear models of dissipation whose Q is almost frequency independent--II," *Geophysical Journal International*, vol. 13, no. 5, pp. 529–539, 1967.

Hindawi
Complexity
Volume 2021, Article ID 5927070, 12 pages
https://doi.org/10.1155/2021/5927070

Research Article

Soret and Radiation Effects on Mixture of Ethylene Glycol-Water (50%-50%) Based Maxwell Nanofluid Flow in an Upright Channel

Kashif Sadiq,[1] Fahd Jarad,[2,3] Imran Siddique,[1] and Bagh Ali[4]

[1]*Department of Mathematics, University of Management and Technology, Lahore-54770, Pakistan*
[2]*Department of Mathematics, Cankaya University, Etimesgut, Ankara, Turkey*
[3]*Department of Medical Research, China Medical University Hospital, China Medical University, Taichung, Taiwan*
[4]*School of Mathematics and Statistics, Northwestern Polytechnical University, Xian 710129, China*

Correspondence should be addressed to Fahd Jarad; fahd@cankaya.edu.tr

Received 12 April 2021; Revised 4 May 2021; Accepted 18 May 2021; Published 27 May 2021

Academic Editor: Ali Akgül

In this article, ethylene glycol (EG) + waterbased Maxwell nanofluid with radiation and Soret effects within two parallel plates has been investigated. The problem is formulated in the form of partial differential equations. The dimensionless governing equations for concentration, energy, and momentum are generalized by the fractional molecular diffusion, thermal flux, and shear stress defined by the Caputo–Fabrizio time fractional derivatives. The solutions of the problems are obtained via Laplace inversion numerical algorithm, namely, Stehfest's. Nanoparticles of silver (Ag) are suspended in a mixture of EG + water to have a nanofluid. It is observed that the thermal conductivity of fluid is enhanced by increasing the values of time and volume fraction. The temperature and velocity of water-silver nanofluid are higher than those of ethylene glycol (EG) + water (H_2O)-silver (Ag) nanofluid. The results are discussed at 2% of volume fraction. The results justified the thermo-physical characteristics of base fluids and nanoparticles shown in the tables. The effects of major physical parameters are illustrated graphically and discussed in detail.

1. Introduction

Fluids like coolants (ethylene glycol and water), lubricants (oils), paraffin, biofluids, and polymer solutions are common conductive fluids. Nanofluids have better thermo-physical features such as viscosity, rate of heat transfer, thermal diffusion, and thermal conductivity compared with conventional fluids. Due to enhanced qualities, nanofluids have many applications in biomedical, engineering, and industries, for example, nanocryosurgery, magnetic drug, electronics cooling, vehicle cooling, smart fluids, industrial cooling, and heat transfer [1]. Heat exchangers, electric conductors, solar collectors, and piping are the most recent applications of heat transfer. These applications are used to reduce and enhance the heat of systems and depend on convection. Though, it is obvious that suitable fluids are essential for heat transfer.

Many researchers are investigating the Soret effect on natural convection mass and heat transport due to its applications in scientific systems and engineering. The gradients of temperature cause mass diffusion which is called the Soret effect. Isotopes separation, geosciences, hydrology, petrology, and chemical processing are applications of Soret effects [2–7]. RamReddy et al. [8] studied mass and heat transport in mixed convection nanofluid flow on a plate influenced by the Soret effect. Raju et al. [9] analyzed the nanofluid flow on a moving vertical plate influenced by magnetic field, thermal radiation, and Soret effect.

Ganesh et al. [10] investigated the flow of ethylene glycol ($C_2H_6O_2$) + water (H_2O) (50 : 50) comprising the nanoparticles of boehmite alumina with Sakiadis and Blasius slip. Arani et al. [11] applied the simple algorithm to analyze the flow of a mixture of $C_2H_6O_2$–H_2O (50 : 50) and different shapes of nanoparticles of boehmite alumina in a channel. They found that the nanoparticles of spherical shape affect the thermal conductivity significantly. Monfared et al. [12] studied the effects of shapes of nanoparticles of boehmite alumina on entropy generation and thermal conductivity on

the flow of a nanofluid in a heat exchanger double pipe. They concluded that the entropy generation has a maximum frictional rate for the nanoparticles of platelet shape. Nisar et al. [13] numerically investigated EG-water (50 : 50) based mixed convection hybrid nanofluid flow within two disks with thermal radiation.

In diverse problems of physical sciences and engineering integer, order or classical derivative cannot represent the complex dynamics conditions entirely. In these cases, the fractional-order derivatives are more suitable approaches, in viscous flows, biology, biomedical sciences, signal and image handling, chemical reaction, treatment, and cancer diagnosis. Fractional-order derivatives can demonstrate the memory results of flow and describe the traditional properties. It is significant to discuss that fractional derivatives have numerous applications in the field of modern technology and science which consists of viscoelasticity, relaxation process, diffusion, and electrochemistry [14]. Markis et al. [15] investigated the fractional model of Maxwell's fluid flow. They concluded that by changing the value of the fractional parameter, the results can be adjusted close to the experimental results. Zafer and Fetecau [16] used Caputo–Fabrizio fractional derivative to examine the Newtonian fluid flow on a vertical plate. Siddique and Bukhari [17] analyzed the effect of generalized fractional Fourier's and Fick's laws on convective flows of non-Newtonian fluid subject to Newtonian heating. Alkahtani and Atangana [18] applied diverse fractional methods to study heat transfer and memory effect. They developed new numerical techniques for the solution of fractional equations. Siddique et al. [19] studied the heat transfer analysis in convective flows of fractional second grade fluids with Caputo–Fabrizio and Atangana–Baleanu derivative subject to Newtonion heating. Abro et al. [20] calculated exact analytical results for Oldroyd-B fluid flow in a pipe. Siddique et al. [21] studied the unsteady flow of Walter's-B fluid subject to a consistent inclined magnetic field at an angle of inclination over the boundary of transverse xy-plane with fractional thermal transport. In this paper, they found the semianalytical solutions of the dimensionless temperature and velocity fields by using the Laplace inversion numerical algorithms such as Stehfest's and Tzou's. Vieru et al. [22] investigated the exact results of the flow of viscous fluid for the fractional model on a vertical plate with Newtonian heating and mass diffusion.

Motivated by the above study, focus of this work is to examine the flow of mass and heat in an unsteady Maxwell nanofluid flow inside two vertical parallel plates with combined effect of Soret and thermal radiation. The numerical inverse Laplace transform is used to compute the solutions of equations. The graphical illustration of the significant constraints on concentration, heat, and flow profiles is presented and discussed in detail. The fractional model of nanofluid is developed to generalize the standard constitutive equations by using equation of shear stress, Fourier's law, and molecular diffusion. It is obvious that most investigations considered water as base fluid. The inspiration of this examination is consequently to study the heat presentation of nanofluid using EG-water (50 : 50) as base fluid and nanoparticles of Ag. EG is a natural fluid of low instability and viscosity, which is totally mixable with water; hence, it very well may be utilized as a base fluid all alone or blended in with water to frame EG-water base fluid. The impacts of Soret effect on the concentration of fluid are additionally explored. The graphical description of the relevant parameters on the flow of fluid, mass, and heat exchange attributes is shown and completely examined.

2. Mathematical Model

An incompressible, unsteady, viscous 2D flow of Maxwell nanofluid within two infinite parallel plates having distance d between them in the presence of Soret and thermal radiation effects is considered. The nanofluid is prepared by adding nanoparticles of silver into the mixture of EG-water (50 : 50) at a fixed volume fraction ϕ. The Maxwell nanofluid is viewed as optically thick. Thus, the Rosseland estimations can be used for radiation impacts.

X-axis is taken along the plates and y-axis is taken normal to the plates as demonstrated in Figure 1. At first, both nanofluid and plates are in equilibrium at fixed temperature T_0 and concentration C_0.The right plate slides at $\tilde{t} \geq 0$ in the plane along x-axis with the velocity U_0. Simultaneously, concentration and temperature levels rise to C_1 and T_1. The radiative heat flux q_r is outlined in the temperature equation.

Thermo-physical features of EG-H_2O, H_2O, and silver are given in Table 1, which are assumed to be constant. It is also considered that the fluid and nanoparticles are in thermal stability, and slippage among them is neglected. The viscous diffusion in the heat equation is ignored because of its little size in natural convection flows in spite of the fact that it can lessen the heat presentation of nanofluids which changes with the rate of flow. Then again, the dissipating of nanoparticles in a fluid is joined by a development of the viscosity which diminishes its flow. Subsequently, the scattering of nanoparticles in a base fluid cannot be subjective. It must be investigated or even improved.

Since the boundaries of channel are infinitely long in the x- and z-axis, we can expect that all actual parameters describing heat transfer and the flow of fluid are elements of $\tilde{t}$ and $\tilde{y}$ only.

The equation of continuity is uniformly justified for the velocity field $\mathbf{v} = (\tilde{u}(\tilde{y}, \tilde{t}), 0, 0)$, and the typical Boussinesq's approximation is utilized. The expressions of the unsteady flow when pressure gradient is neglected are as follows [23]:

The linear momentum equation is as follows:

$$\rho_{nf} \frac{\partial \tilde{u}}{\partial \tilde{t}} = \frac{\partial \tilde{\tau}}{\partial \tilde{y}} + g(\rho\beta_T)_{nf}\left[\tilde{T} - T_0\right] + g(\rho\beta_C)_{nf}\left[\tilde{C} - C_0\right]. \tag{1}$$

The shear stress is as follows:

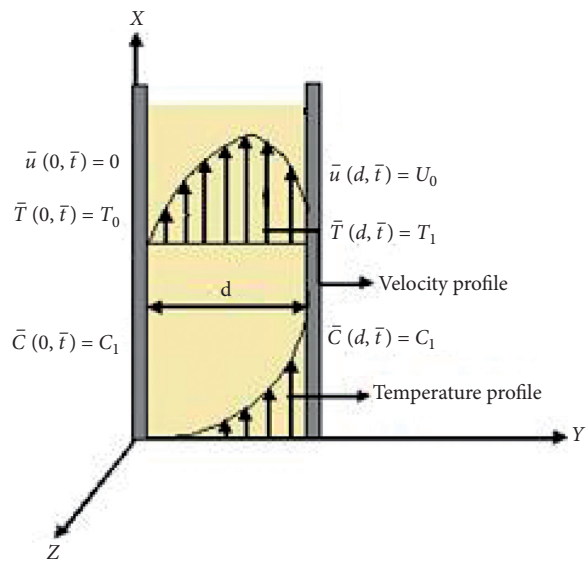

Figure 1: Flow geometry.

Table 1: Thermo-physical features of nanoparticles and EG [13].

Material	EG-H_2O (50 : 50)	H_2O	Silver (Ag)
ρ	1056	997.1	10500
c_p	3288	4179	235
k	0.425	0.613	429
$\beta \times 10^{-5}$	0.00341	21	1.89
Pr	29.86	6.2	—

$$\left(1 + \tilde{\lambda}\frac{\partial}{\partial \tilde{t}}\right)\tilde{\tau} = \mu_{nf}\frac{\partial \tilde{u}}{\partial \tilde{y}}. \tag{2}$$

The energy equation is as follows:

$$\left(\rho c_p\right)_{nf}\frac{\partial \tilde{T}}{\partial \tilde{t}} = -\frac{\partial \tilde{q}}{\partial \tilde{y}} - \frac{\partial q_r}{\partial \tilde{y}}. \tag{3}$$

The thermal flux is as follows:

$$\tilde{q} = -k_{nf}\frac{\partial \tilde{T}}{\partial \tilde{y}}. \tag{4}$$

The diffusion equation is as follows:

$$\frac{\partial \tilde{C}}{\partial \tilde{t}} = -\frac{\partial \tilde{j}}{\partial \tilde{y}} + \frac{D_{nf}k_T}{T_m}\frac{\partial^2 T}{\partial y^2}. \tag{5}$$

The molecular diffusion is as follows:

$$\tilde{j} = -D_{nf}\frac{\partial \tilde{C}}{\partial \tilde{y}}, \tag{6}$$

with corresponding conditions such as

$$\begin{aligned} &\tilde{u}(0,\tilde{t}) = 0,\\ &\tilde{u}(y,0) = 0,\\ &\tilde{u}(d,\tilde{t}) = U_0, \end{aligned} \tag{7}$$

$$\begin{aligned} &\tilde{T}(0,\tilde{t}) = T_0,\\ &\tilde{T}(y,0) = T_0,\\ &\tilde{T}(d,\tilde{t}) = T_1, \end{aligned} \tag{8}$$

$$\begin{aligned} &\tilde{C}(y,0) = C_0,\\ &\tilde{C}(0,\tilde{t}) = C_0,\\ &\tilde{C}(d,\tilde{t}) = C_1. \end{aligned} \tag{9}$$

The thermal-physical properties of nanofluid are defined by [24]

$$\begin{aligned}
\frac{\mu_{nf}}{\mu_f} &= \frac{1}{(1-\phi)^{2.5}},\\
\frac{\rho_{nf}}{\rho_f} &= (1-\phi)+\phi\frac{\rho_s}{\rho_f},\\
\frac{(\rho c_p)_{nf}}{(\rho c_p)_f} &= (1-\phi)+\phi\frac{(\rho c_p)_s}{(\rho c_p)_f},\\
\frac{D_{nf}}{D_f} &= \frac{1}{(1-\phi)},\\
\frac{(\rho\beta_T)_{nf}}{(\rho\beta_T)_f} &= (1-\phi)+\phi\frac{(\rho\beta_T)_s}{(\rho\beta_T)_f},\\
\frac{(\rho\beta_C)_{nf}}{(\rho\beta_C)_f} &= (1-\phi)+\phi\frac{(\rho\beta_C)_s}{(\rho\beta_C)_f},\\
\frac{k_{nf}}{k_f} &= \left[\frac{k_s+2k_f-2\phi(k_f-k_s)}{k_s+2k_f+\phi(k_f-k_s)}\right].
\end{aligned} \tag{10}$$

Introducing the dimensionless parameters, variables, and functions,

$$\begin{aligned}
u &= \frac{u}{U_0},\\
t &= \frac{\nu_f\tilde{t}}{d^2},\\
y &= \frac{y}{d},\\
\theta &= \frac{T-T_0}{T_1-T_0},\\
C &= \frac{C-C_0}{C_1-C_0},\\
\lambda &= \frac{\lambda\nu_f}{d^2},\\
q &= \frac{q}{q_0},\\
q_0 &= \frac{k_{nf}(T_1-T_0)}{d},\\
\tau &= \frac{\tilde{\tau}}{\tau_0},\\
\tau_0 &= \mu_{nf}\frac{U_0}{d},\\
j &= \frac{y}{j_0},\\
j_0 &= \frac{D_{nf}(C_1-C_0)}{d},\\
a_1 &= \frac{\mu_{nf}}{\rho_{nf}\nu_f},\\
a_2 &= Gr\frac{(\beta_T)_{nf}}{(\beta_T)_f},\\
a_3 &= Gm\frac{(\beta_C)_{nf}}{(\beta_C)_f},\\
a_4 &= \frac{1}{\Pr}\frac{k_{nf}(\rho c_p)_f}{k_f(\rho c_p)_{nf}},\\
a_5 &= \frac{Nr}{\Pr}\frac{(\rho c_p)_f}{(\rho c_p)_{nf}},\\
a_6 &= \frac{1}{Sc}\frac{D_{nf}}{D_f},\\
a_7 &= Sr\frac{D_{nf}}{D_f},\\
Gr &= \frac{g(\beta_T)_f(T_1-T_0)d^2}{U_0\nu_f},\\
Sc &= \frac{\nu_f}{D_f},\\
Sr &= \frac{D_f k_T(T_1-T_0)}{T_m(C_1-C_0)\nu_f},\\
Gm &= \frac{g(\beta_C)_f(C_2-C_1)d^2}{U_0\nu_f},\\
Nr &= \frac{16\sigma' T_1^3}{3k' k_f},\\
\Pr &= \frac{(\rho c_p)_f\nu_f}{k_f},
\end{aligned} \tag{11}$$

where U_0, τ_0, q_0, and j_0 are characteristic scales.

By switching equation (11) into equations (1)–(9), we get

$$\frac{\partial u}{\partial t} = a_1\frac{\partial\tau}{\partial y} + a_2\theta + a_3 C, \tag{12}$$

$$\left(1+\lambda\frac{\partial}{\partial t}\right)\tau = \frac{\partial u}{\partial y}, \tag{13}$$

$$\frac{\partial\theta}{\partial t} = -a_4\frac{\partial q}{\partial y} + a_5\frac{\partial^2\theta}{\partial y^2}, \tag{14}$$

$$q(y,t) = -\frac{\partial\theta}{\partial y}, \tag{15}$$

$$\frac{\partial C(y,t)}{\partial t} = -a_6\frac{\partial j(y,t)}{\partial y} + a_7\frac{\partial^2\theta}{\partial y^2}, \tag{16}$$

$$j(y,t) = -\frac{\partial C(y,t)}{\partial y}, \tag{17}$$

with corresponding conditions such as

$$\begin{aligned} u(y,0) &= 0, \\ u(0,t) &= 0, \\ u(1,t) &= 1, \end{aligned} \tag{18}$$

$$\begin{aligned} \theta(y,0) &= 0, \\ \theta(0,t) &= 0, \\ \theta(1,t) &= 1, \end{aligned} \tag{19}$$

$$\begin{aligned} C(y,0) &= 0, \\ C(0,t) &= 0, \\ C(1,t) &= 1. \end{aligned} \tag{20}$$

To discuss the time fractional derivative models, the researchers consider the developed generalization of the standard constitutive equations (13), (15), and (17) by using the equation of shear stress as follows:

$$\left(1+\lambda\frac{\partial}{\partial t}\right)\tau(y,t) = -{}^{CF}D_t^{\alpha}\frac{\partial u(y,t)}{\partial y}, \quad 0 \le \alpha < 1. \tag{21}$$

Fourier's law is as follows:

$$q(y,t) = -{}^{CF}D_t^{\beta}\frac{\partial \theta(y,t)}{\partial y}, \quad 0 \le \beta < 1, \tag{22}$$

and Fick's law is as follows:

$$j(y,t) = -{}^{CF}D_t^{\gamma}\frac{\partial C(y,t)}{\partial y}, \quad 0 \le \gamma < 1. \tag{23}$$

In the above equations, ${}^{CF}D_t^{\zeta}(\cdot)$ represents the Caputo–Fabrizio time fractional derivative described by [25]

$${}^{CF}D_t^{\xi}\Psi(\eta,t) = \frac{1}{1-\xi}\int_0^t \exp\left(\frac{-\xi(t-\Omega)}{1-\xi}\right)\frac{\partial \Psi(\eta,\Omega)}{\partial \Omega}\mathrm{d}\Omega, \quad 0 \le \xi < 1. \tag{24}$$

The Laplace transform of equation (24) is as follows:

$$L\left\{{}^{CF}D_t^{\xi}\Psi(\eta,t)\right\} = \frac{sL\{\Psi(\eta,t)\} - \Psi(\eta,0)}{(1-\xi)s+\xi}. \tag{25}$$

Remark. If $\Psi(\eta,0) = 0$ and $\xi \longrightarrow 0$, equation (25) becomes $L\left\{{}^{CF}D_t^{\xi}\Psi(\eta,t)\right\} = L\{\Psi(\eta,t)\}$. Then, generalized shear stress, thermal flux, and molecular diffusion equations (21)–(23) reduce to the classical equations (13), (15), and (17).

Eliminating $\tau$from (12) and (21), we get

$$\left(1+\lambda\frac{\partial}{\partial t}\right)\frac{\partial u}{\partial t} = a_1{}^{CF}D_t^{\alpha}\frac{\partial^2 u}{\partial y^2} + a_2\left(1+\lambda\frac{\partial}{\partial t}\right)\theta + a_3\left(1+\lambda\frac{\partial}{\partial t}\right)C. \tag{26}$$

Eliminating $q$from (14) and (22), we get

$$\frac{\partial \theta}{\partial t} = a_4{}^{CF}D_t^{\beta}\frac{\partial^2 \theta}{\partial y^2} + a_5\frac{\partial^2 \theta}{\partial y^2}. \tag{27}$$

Now, eliminating j from (16) and (23), we have

$$\frac{\partial C}{\partial t} = a_6{}^{CF}D_t^{\gamma}\frac{\partial^2 C}{\partial y^2} + a_7\frac{\partial^2 \theta}{\partial y^2}. \tag{28}$$

3. Solution of the Problems

Applying the Laplace transform to equations (26)–(28) and using conditions (18)–(20), we obtain the following results:

$$\begin{aligned} \overline{u}(y,s) = {} & \frac{\sinh[y\sqrt{w(s)}]}{s\sinh[\sqrt{w(s)}]} + \frac{s+e_1}{e_0 s[p(s)-w(s)]}\left[\frac{a_3 p(s)(s+d_1)}{s[d_0 p(s)-s-d_1]} - a_2(1+\lambda s)\right]\left[\frac{\sinh[y\sqrt{p(s)}]}{s\sinh[\sqrt{p(s)}]} - \frac{\sinh[y\sqrt{w(s)}]}{s\sinh[\sqrt{w(s)}]}\right] \\ & + \frac{a_3 d_0(s+e_1)}{e_0 s[s+d_1-d_0 w(s)]}\left[1+\frac{a_7 p(s)(s+d_1)}{s[d_0 p(s)-s-d_1]}\right]\left[\frac{\sinh[y\sqrt{w(s)}]}{s\sinh[\sqrt{w(s)}]} - \frac{\sinh\left[y\sqrt{((s+d_1)/d_0)}\right]}{s\sinh\left[\sqrt{((s+d_1)/d_0)}\right]}\right], \end{aligned} \tag{29}$$

$$\overline{\theta}(y,s) = \frac{\sinh[y\sqrt{p(s)}]}{s\sinh[\sqrt{p(s)}]}, \tag{30}$$

$$\overline{C}(y,s) = \frac{\sinh\left[y\sqrt{((s+d_1)/d_0)}\right]}{s\sinh\left[\sqrt{((s+d_1)/d_0)}\right]} + \frac{a_7 p(s)(s+d_1)}{s[d_0 p(s)-s-d_1]}\left[\frac{\sinh\left[y\sqrt{((s+d_1)/d_0)}\right]}{s\sinh\left[\sqrt{((s+d_1)/d_0)}\right]} - \frac{\sinh[y\sqrt{p(s)}]}{s\sinh[\sqrt{p(s)}]}\right], \tag{31}$$

where

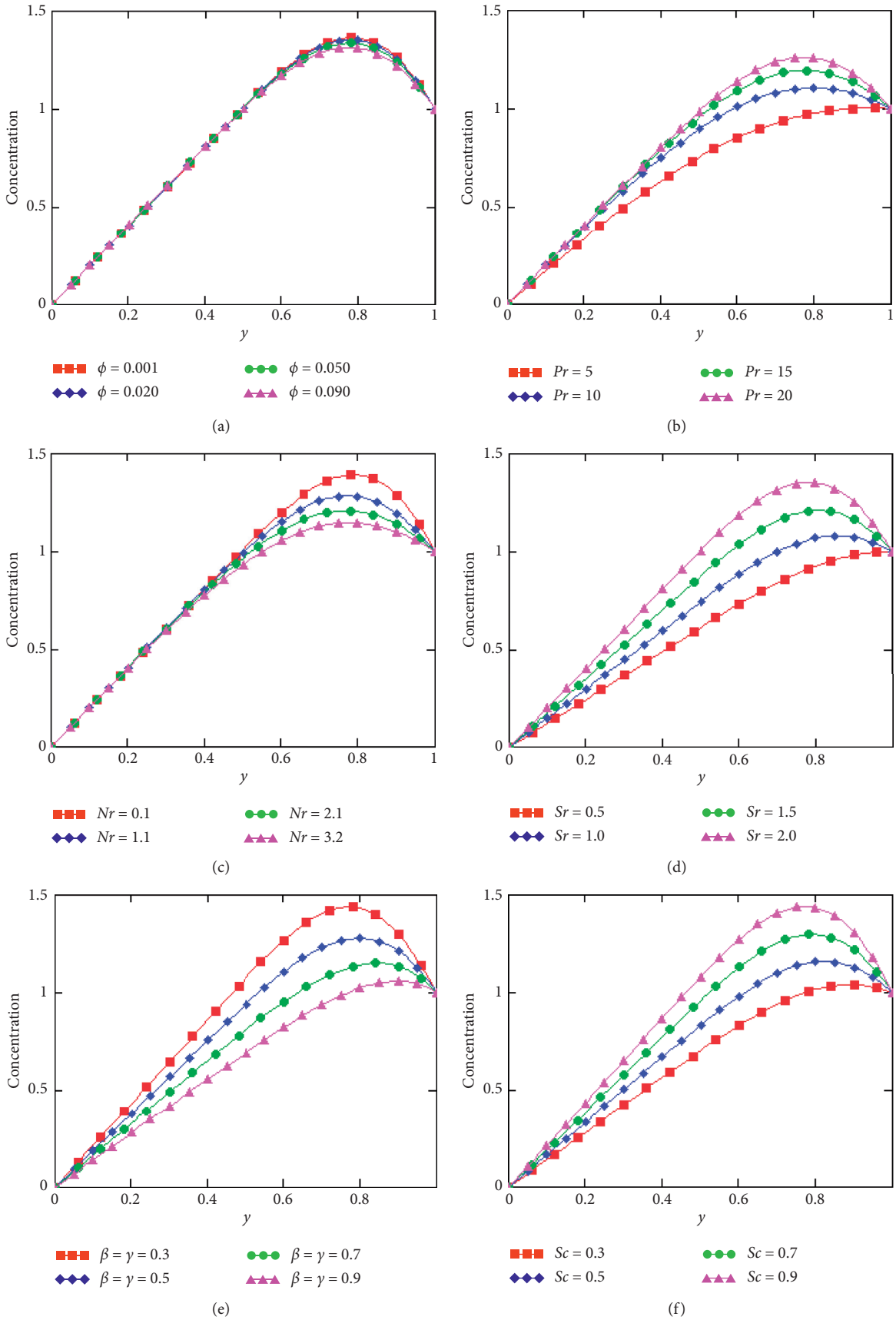

Figure 2: Continued.

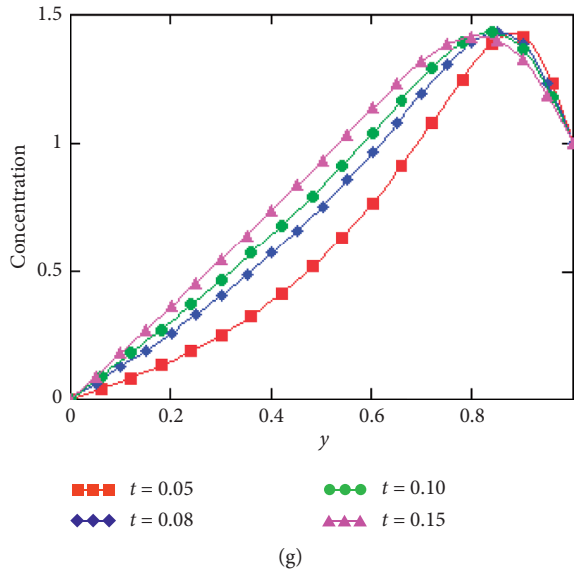

Figure 2: Variation of concentration.

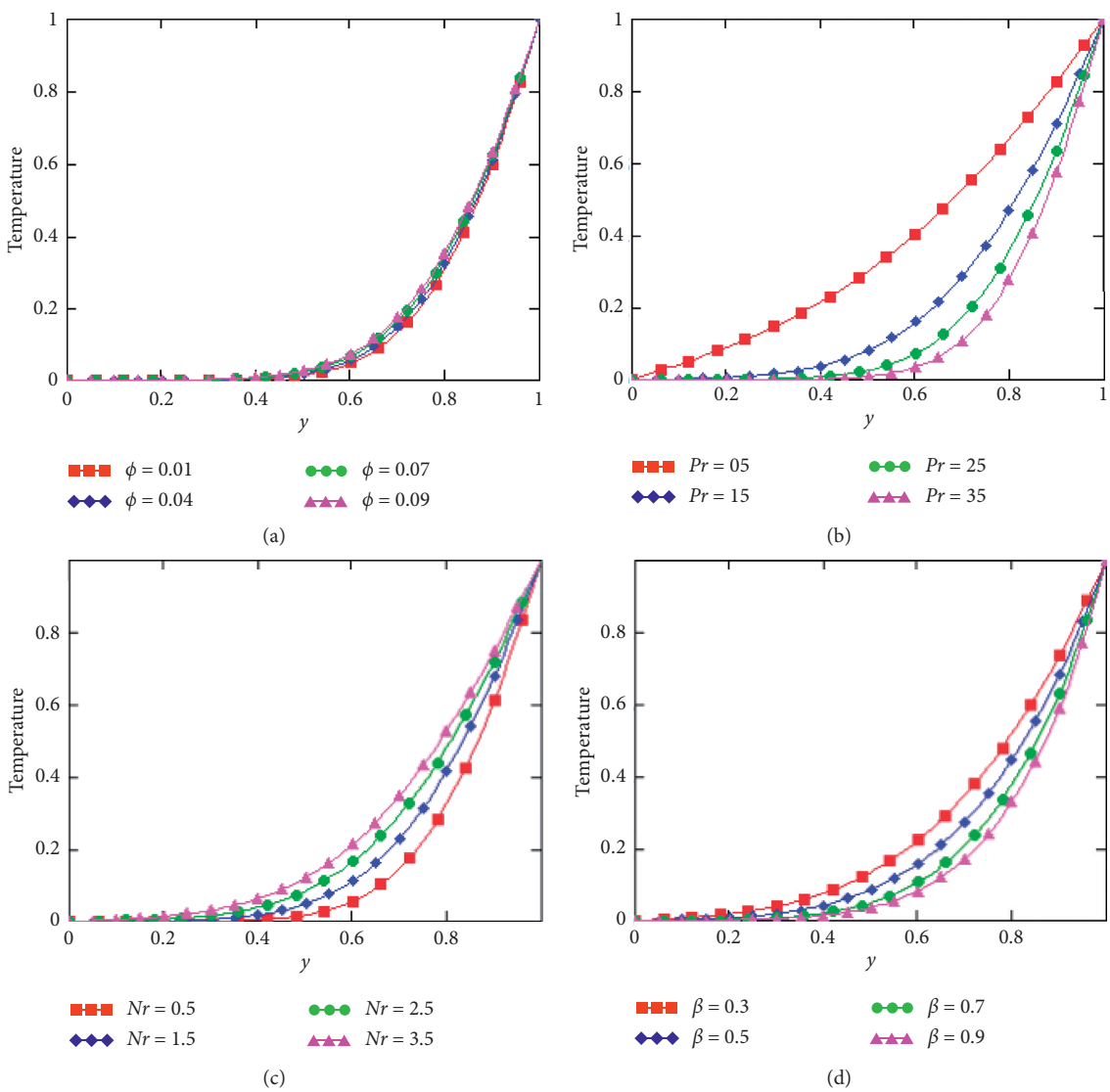

Figure 3: Continued.

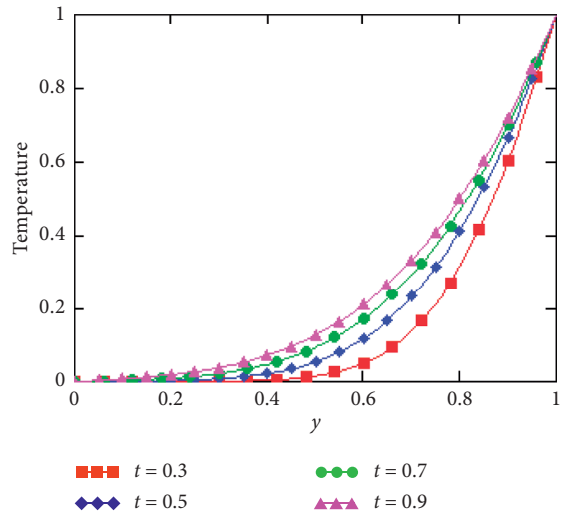

(e)

Figure 3: Variation of temperature.

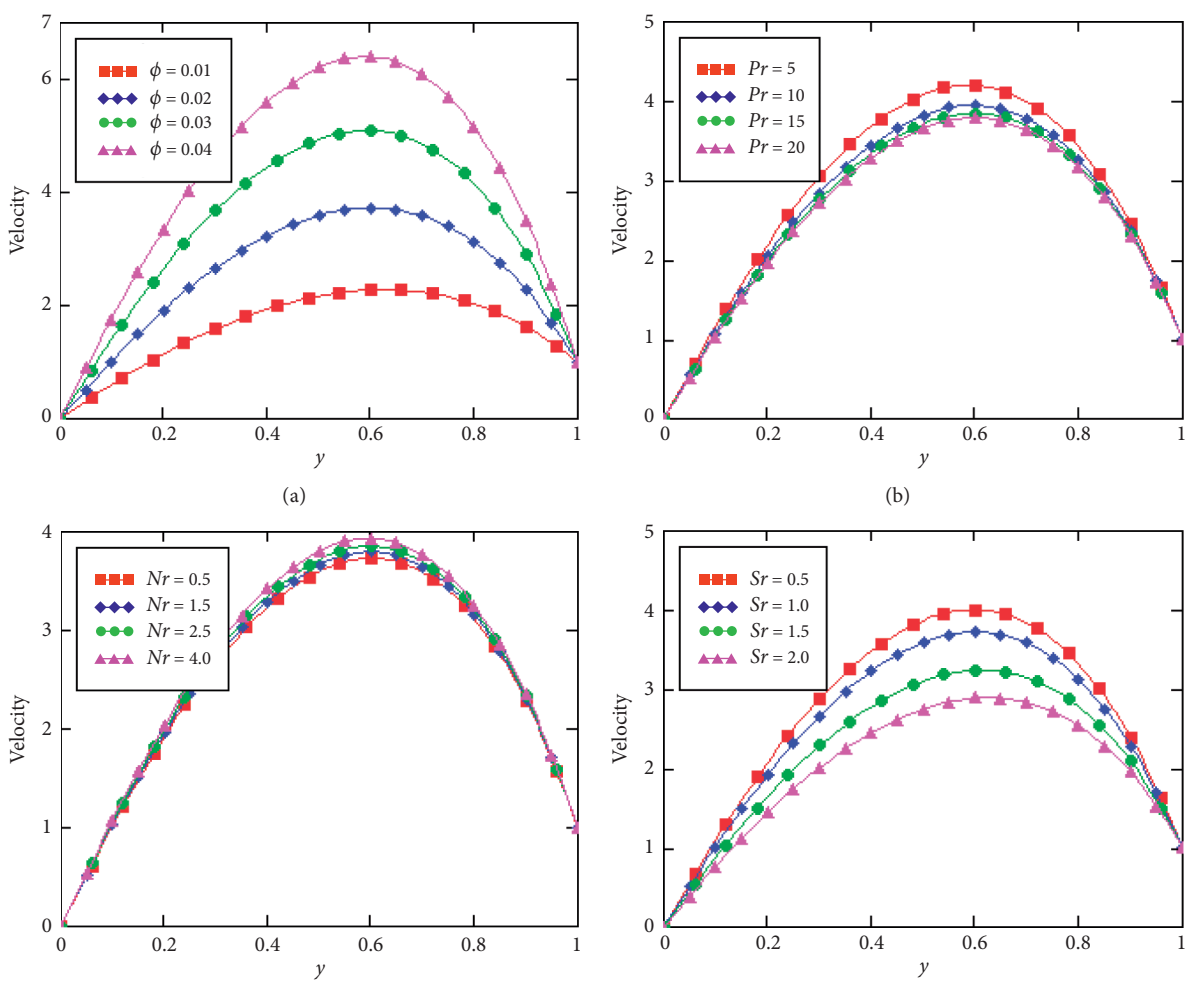

Figure 4: Continued.

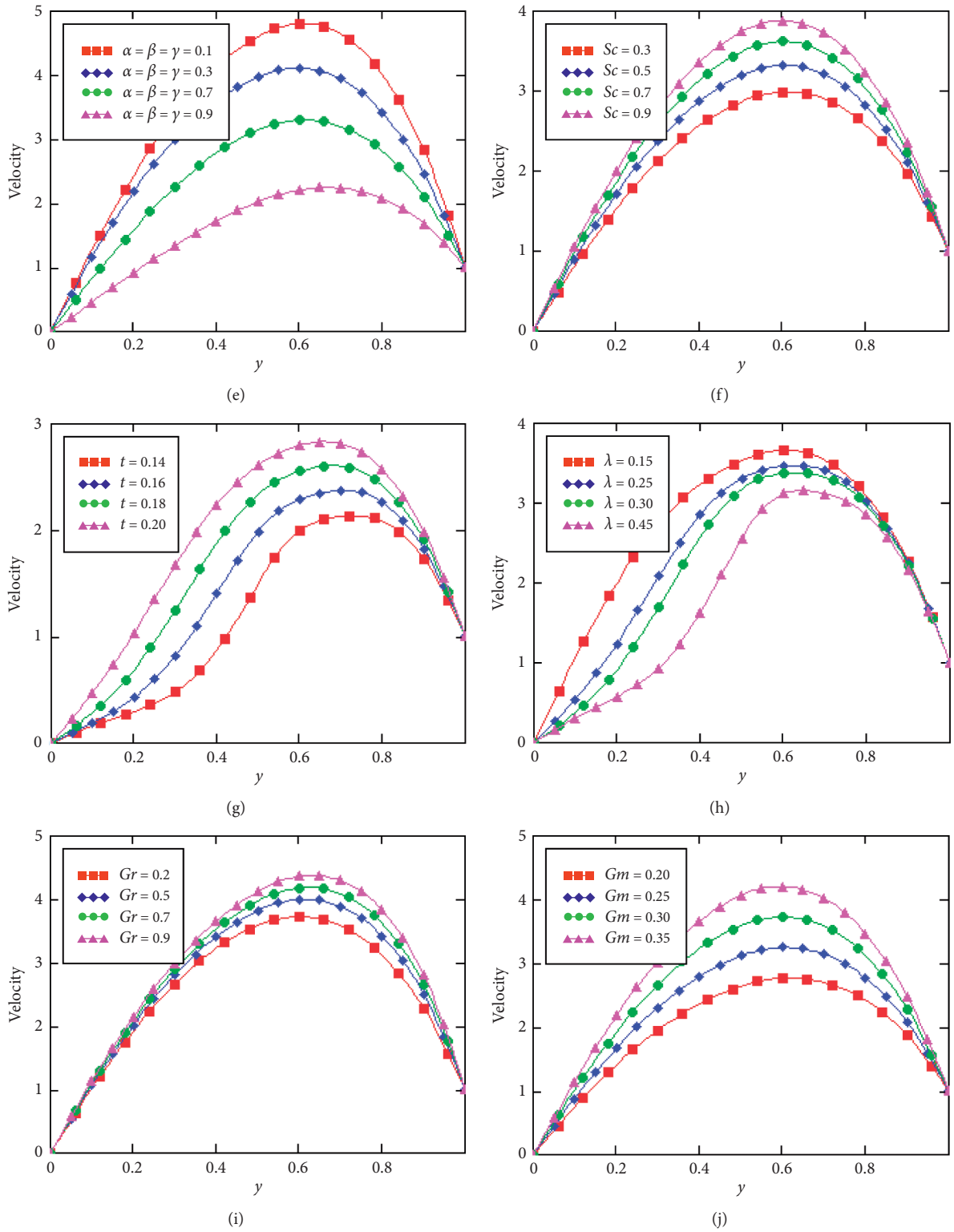

Figure 4: Variation of velocity.

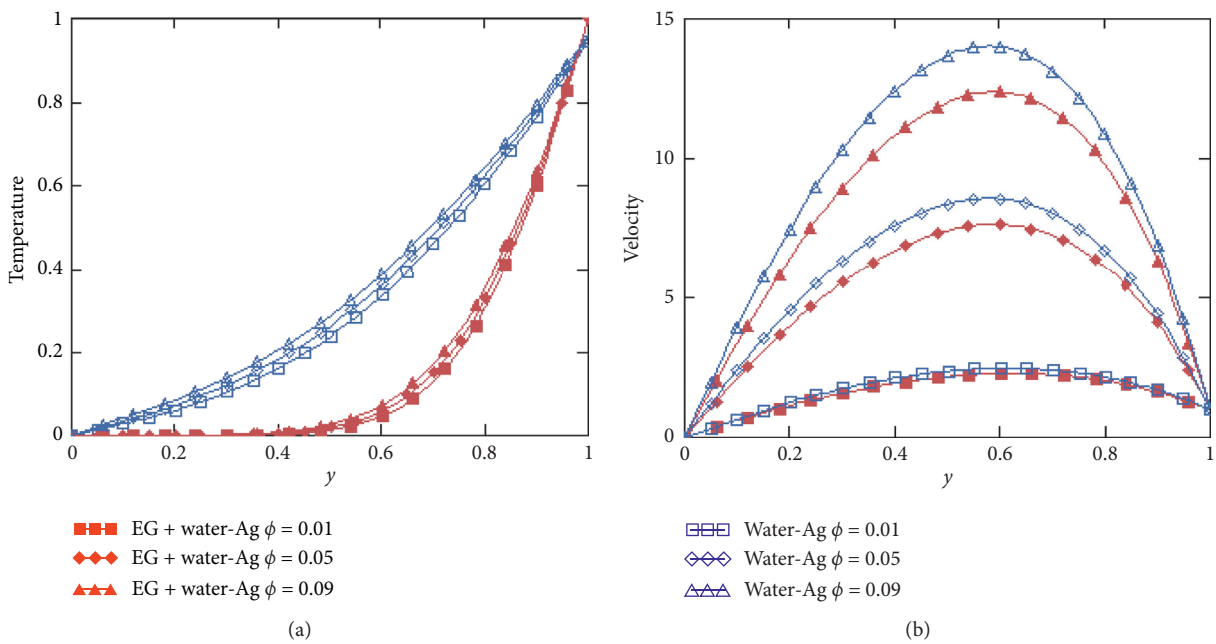

Figure 5: Variation of temperature (a) and velocity (b) of nanofluids.

$$
\begin{aligned}
b_0 &= \frac{a_4}{1-\beta},\\
b_1 &= \frac{\beta}{1-\beta},\\
p(s) &= \frac{s(s+b_1)}{(b_0+a_5)s+a_5 b_1},\\
e_0 &= \frac{a_1}{1-\alpha},\\
e_1 &= \frac{\alpha}{1-\alpha},\\
w(s) &= \frac{(s+e_1)(1+\lambda s)}{e_0},\\
d_0 &= \frac{a_6}{1-\gamma},\\
d_1 &= \frac{\gamma}{1-\gamma}.
\end{aligned}
\tag{32}
$$

To obtain the inverse of equations (29)–(31) numerically, Stehfest's algorithm [26] is used.

$$
u(y,t) \approx \frac{\ln(2)}{t}\sum_{j=1}^{2p} \mathrm{d}_j \overline{u}\left(y, j\frac{\ln(2)}{t}\right), \tag{33}
$$

where

$$
d_j = (-1)^{j+p}\sum_{i=[(j+1)/2]}^{\min(j,p)} \frac{i^p(2i)!}{(p-i)!i!(i-1)!(j-1)!(2i-j)!}, \tag{34}
$$

where p is a positive integer.

4. Graphical Results and Discussion

In this section, the graphical analysis of temperature, concentration, and velocity profiles for fractional and flow parameter is carried out in detail. The fractional fluid model is solved by means of the Laplace transform method. Semianalytical results for concentration, temperature, and velocity fields are computed by applying the Laplace inversion numerical algorithm, namely, Stehfest's.

The results obtained shows the influences of the nondimensional governing parameters, namely, Maxwell fluid parameter (λ), nanoparticles volume parameters (ϕ), mass and thermal Grashof numbers (Gm and Gr), Soret effect (Sr), radiation parameter (Nr), Prandtl number (Pr), Schmidt number (Sc), and fractional parameters (α, β, γ) on the flow, temperature, and concentration profiles and are discussed and presented graphically in Figures 2–4. For numerical results, we used $Sc = 0.78$, $\lambda = 0.1$, $\phi = 0.02$, $\alpha = \beta = \gamma = 0.4$, $Sr = 2$, $Pr = 29.86$, $Gr = 0.2$, $Nr = 0.4$, $Gm = 0.3$, and $t = 0.3$. These values are kept common in entire study except the varied values in respective figures. Thermophysical properties of base fluids ($EG + H_2O$) and nanoparticle Ag are given in Table 1.

Figures 2(a), 3(a), and 4(a) depict the effect of volume fraction of nanoparticle ϕ on concentration, temperature, and velocity profiles for ($EG + H_2O$)–Ag nanofluid. It is observed from figures that increase in volume fraction of nanoparticle decreases the concentration profile while increasing the velocity and temperature profiles of the flow. Generally increase in volume fraction of nanoparticles improves the thermal conductivity which makes the fluid hot. These improve the thermal boundary layer thickness along with velocity boundary layers.

Figures 2(b), 3(b), and 4(c) represent the effect of Prandtl number Pr on concentration, temperature, and velocity profiles. It is clear from figures that a raise in the value of Pr enhances the concentration profile and reduces the temperature and velocity profiles. As expected, it is due to the fact that increase in the values of Pr reduces the thermal conductivity making fluid more thick and reducing thickness of thermal boundary layer. Figures 2(c), 3(c), and 4(c) illustrate the effect of radiation parameter Nr on concentration, velocity, temperature, and velocity profiles. We observed from figures that increase in Nr decreases the concentration profile while increasing the velocity and temperature profiles of the flow. Clearly, with the increase in the values of Nr, the amount of heat transfers to the fluid increases which increases the temperature of the fluid and in turn enhances the flow of fractional nanofluid. Figures 2(d) and 4(d) depict the effect of Soret Sr on concentration and velocity profiles. It can be seen from figures that increase in Sr decreases the concentration profile while increasing the velocity profiles of the flow.

Figures 2(e), 3(d), and 4(e) symbolize the effect of fractional parameters α, β, and γ on concentration, temperature, and velocity profiles. It is obvious from figures that raise in the values of α reduces the concentration, temperature, and velocity profiles. Figures 2(f) and 4(f) represent the effect of Schmidt number Sc on concentration and velocity profiles. It is evident from figures that a raise in the value of Sc enhances the concentration and velocity profiles. Figures 2(g), 3(e), and 4(g) represent the effect of time t on concentration, temperature, and velocity profiles. From these figures, it is observed that concentration, temperature, and velocity increases for increasing values of t.

Figure 4(h) signifies the effect of Maxwell fluid parameter λ on velocity profile. This figure shows that the velocity is a decreasing function λ.

Figures 5(a) and 5(b) show a comparison of two different nanofluids when nanoparticles of Ag were added to the two kings of base fluids EG + H_2O and H_2O. It is interesting to mention that the enhancement in temperature and velocity profiles of H_2O–Ag nanofluid is more than that of EG + H_2O–Ag nanofluid.

5. Conclusions

In this study, we analyzed the influence of thermal radiation and Soret parameters of an unsteady Maxwell fractional nanofluid flow in a vertical channel by considering EG + water (50 : 50)-Ag and water-Ag nanofluids. The fractionalized governing equations modeled with Caputo–Fabrizio time fractional derivative are solved via the Laplace transform method. Numerical inversion Laplace transforms technique, namely, Stehfest's is used in MATHCADE software to find the inverse Laplace transform for concentration, temperature, and velocity graphically. Some important outcomes of this study are as follows:

(1) The EG + water based Maxwell nanofluid has lesser heat transfer rate than water-based nanofluid

(2) The heat transfer rate enhances with the higher concentration of nanoparticles

(3) The velocity reduces for higher values of Maxwell fluid parameterλ

(4) Temperature and velocity of the fluid can be controlled by using volume fraction and also by using mixture of conventional fluids as base fluid

(5) Greater values of volume fraction ϕ demonstrated considerable effect on mass, energy, and momentum profiles

(6) The influence of Gr and Gm stabilizes the growth of momentum boundary layer

(7) The existence of Sr and substantial species increases the concentration

(8) The suspension of nanoparticles in EG + water provides a potential in increasing the heat transport performance

Nomenclature

$\tilde{u}$: Velocity (m/s)
$\tilde{C}$: Concentration (kg/m^3)
$\tilde{T}$: Temperature (K)
g: Gravitational acceleration (m/s^2)
k: Thermal conductivity (W/m K)
D: Mass diffusivity (m^2/s)
c_p: Specific heat (J/kg K)
Gr: Thermal Grashof number
Nr: Thermal radiation
Gm: Mass Grashof number
Sc: Schmidt number
Sr: Soret effect
Pr: Prandtl number.

Greek Symbols

$\tilde{\lambda}$: Maxwell fluid parameter
λ: Dimensionless parameter
μ: Dynamic viscosity (kg/m s)
σ: Electric conductivity (S/m)
ρ: Density (kg/m^3)
ν: Kinematic viscosity (m^2/s)
$k\prime$: Absorption coefficient
k_T: Thermal diffusion
$\sigma\prime$: Stefan Boltzmann constant
T_m: Mean temperature
β_T: Thermal expansion coefficient (K^{-1})
θ: Dimensionless temperature
β_C: Mass volumetric coefficient (K^{-1})
ϕ: Volume fraction.

Subscript

nf: Nanofluid
f: Fluid.

Data Availability

The data used to support the findings of this study are available from the corresponding author upon request.

Conflicts of Interest

The authors declare that there are no conflicts of interest regarding the publication of this paper.

References

[1] W. N. Mutuku and O. D. Makinde, "On hydromagnetic boundary layer flow of nanofluids over a permeable moving surface with Newtonian heating," *Latin American Applied Research*, vol. 44, no. 1, pp. 57–62, 2014.

[2] A. J. Omowaye, A. I. Fagbade, and A. O. Ajayi, "Dufour and Soret effects on steady MHD convective flow of a fluid in a porous medium with temperature dependent viscosity: homotopy analysis approach," *Journal of the Nigerian Mathematical Society*, vol. 34, no. 3, pp. 343–360, 2015.

[3] S. S. K. Raju, M. Narahari, and P. Rajashekhar, "Soret and chemical reaction effects on unsteady two-dimensional natural convection along a vertical plate," *AIP Conference Proceedings*, vol. 1621, p. 154, 2014.

[4] G. V. R. Reddy, "Soret and Dufour Effects on MHD free convective flow past a vertical porous plate in the presence of heat generation," *International Journal of Applied Mechanics and Engineering*, vol. 21, no. 3, pp. 649–665, 2016.

[5] D. R. Srinivas, G. S. Sreedhar, and K. Govardhan, "Effect of viscous dissipation, Soret and Dufour effect on free convection heat and mass transfer from vertical surface in a porous medium," *Procedia Materials Science*, vol. 10, pp. 563–571, 2015.

[6] S. Tippa, M. Narahari, and P. Rajashekhar, "Dufour effect on unsteady natural convection flow past an infinite vertical plate with constant heat and mass fluxes," *AIP Conference Proceedings*, vol. 1621, p. 470, 2014.

[7] I. J. Uwanta and H. Usman, "On the influence of Soret and Dufour effects on MHD free convective heat and mass transfer flow over a vertical channel with constant suction and viscous dissipation," *International Scholarly Research Notices*, vol. 2014, Article ID 639159, 11 pages, 2014.

[8] C. RamReddy, P. V. S. N. Murthy, A. J. Chamkha, and A. M. Rashad, "Soret effect on mixed convection flow in a nanofluid under convective boundary condition," *International Journal of Heat and Mass Transfer*, vol. 64, pp. 384–392, 2013.

[9] C. S. K. Raju, M. J. Babu, N. Sandeep, V. Sugunamma, and J. V. R. Reddy, "Radiation and Soret effects of MHD nanofluid flow over a moving vertical moving plate in porous medium," *Chemical and Process Engineering Research*, vol. 30, pp. 9–23, 2015.

[10] N. V. Ganesh, Q. M. Al-Mdallal, K. Reena, and S. Aman, "Blasius and Sakiadis slip flow of H2O-C2H6O2 (50:50) based nanoliquid with different geometry of boehmite alumina nanoparticles," *Case Studies in Thermal Engineering*, vol. 16, Article ID 100546, 2019.

[11] A. A. A. Arani, S. Sadripour, and S. Kermani, "Nanoparticle shape effects on thermal-hydraulic performance of boehmite alumina nanofluids in a sinusoidal-wavy mini-channel with phase shift and variable wavelength," *International Journal of Mechanical Sciences*, vol. 128-129, pp. 550–563, 2017.

[12] M. Monfared, A. Shahsavar, and M. R. Bahrebar, "Second law analysis of turbulent convection flow of boehmite alumina nanofluid inside a double-pipe heat exchanger considering various shapes for nanoparticle," *Journal of Thermal Analysis and Calorimetry*, vol. 135, no. 2, pp. 1521–1532, 2019.

[13] K. S. Nisar, U. Khan, A. Zaib, I. Khan, and D. Baleanu, "Numerical simulation of mixed convection squeezing flow of a hybrid nanofluid containing magnetized ferroparticles in (50%:50%) of ethylene glycol–water mixture base fluids between two disks with the presence of a non-linear thermal radiation heat flux," *Frontiers Chemistry*, vol. 8, p. 792, 2020.

[14] M. Saqib, I. Khan, and S. Shafie, "Application of Atangana-Baleanu fractional derivative to MHD channel flow of CMC-based-CNT's nanofluid through a porous medium," *Chaos, Solitons & Fractals*, vol. 116, pp. 79–85, 2018.

[15] N. Makris, G. F. Dargush, and M. C. Constantinou, "Dynamic analysis of generalized viscoelastic fluids," *Journal of Engineering Mechanics*, vol. 119, no. 8, pp. 1663–1679, 1993.

[16] A. A. Zafar and C. Fetecau, "Flow over an infinite plate of a viscous fluid with non-integer order derivative without singular kernel," *Alexandria Engineering Journal*, vol. 55, no. 3, pp. 2789–2796, 2016.

[17] I. Siddique and S. M. Bukhari, "Analysis of the effect of generalized fractional Fourier's and Fick's laws on convective flows of non-Newtonian fluid subject to Newtonian heating," *The European Physical Journal Plus*, vol. 135, no. 1, pp. 1–21, 2020.

[18] B. S. T. Alkahtani and A. Atangana, "Modeling the potential energy field caused by mass density distribution with eton approach," *Open Physics*, vol. 14, no. 1, pp. 106–113, 2016.

[19] I. Siddique, I. Tlili, S. M. Bukhari, and Y. Mahsud, "Heat transfer analysis in convective flows of fractional second grade fluids with Caputo–Fabrizio and Atangana–Baleanu derivative subject to Newtonion heating," *Mechanics of Time-dependent Materials*, pp. 1–21, 2020.

[20] K. A. Abro, I. Khan, and J. F. Gómez-Aguilar, "A mathematical analysis of a circular pipe in rate type fluid via Hankel transform," *The European Physical Journal Plus*, vol. 133, no. 10, p. 397, 2018.

[21] I. Siddique, N. A. Shah, and K. A. Abro, "Thermography of ferromagnetic Walter's-B fluid through varying thermal stratification," *South African Journal of Chemical Engineering*, vol. 36, pp. 118–126, 2021.

[22] D. Vieru, C. Fetecau, and C. Fetecau, "Time-fractional free convection flow near a vertical plate with Newtonian heating and mass diffusion," *Thermal Science*, vol. 19, no. 1, pp. 85–98, 2015.

[23] M. Ahmad, M. A. Imran, and M. Nazar, "Mathematical modeling of (Cu-Al2O3) water based Maxwell hybrid nanofluids with Caputo-Fabrizio fractional derivative," *Advances in Mechanical Engineering*, vol. 12, no. 9, pp. 1–11, 2020.

[24] S. Kakac and A. Pramuanjaroenkij, "Review of convective heat transfer enhancement with nanofluids," *International Journal of Heat Mass Transfer*, vol. 52, no. 13-14, pp. 3187–3196, 2009.

[25] M. Caputo and M. Fabrizio, "A new definition of fractional derivative without singular kernel," *Progress in Fractional Differentiation and Applications*, vol. 1, no. 2, pp. 73–85, 2015.

[26] H. Stehfest, "Algorithm 368: numerical inversion of Laplace transforms [D5]," *Communications of the ACM*, vol. 13, no. 1, pp. 47–49, 1970.

Hindawi
Complexity
Volume 2021, Article ID 9951162, 9 pages
https://doi.org/10.1155/2021/9951162

Research Article

Impact of Nanofluid Flow over an Elongated Moving Surface with a Uniform Hydromagnetic Field and Nonlinear Heat Reservoir

Haroon U. R. Rasheed,[1] Saeed Islam,[1] Zeeshan Khan,[2] Sayer O. Alharbi,[3] Hammad Alotaibi,[4] and Ilyas Khan[3]

[1]*Department of Mathematics, Abdul Wali Khan University Mardan, Mardan 23200, Khyber Pakhtunkhwa, Pakistan*
[2]*Sarhad University of Science and Information Technology, Peshawar 25000, Khyber Pakhtunkhwa, Pakistan*
[3]*Department of Mathematics, College of Science Al-Zulfi, Majmaah University, Al-Majmaah 11952, Saudi Arabia*
[4]*Department of Mathematics, College of Science, Taif University, P.O. Box 11099, Taif 21944, Saudi Arabia*

Correspondence should be addressed to Ilyas Khan; ilyaskhan@tdtu.edu.vn

Received 6 March 2021; Revised 9 April 2021; Accepted 29 April 2021; Published 24 May 2021

Academic Editor: Ali Akgül

The increasing global demand for energy necessitates devoted attention to the formulation and exploration of mechanisms of thermal heat exchangers to explore and save heat energy. Thus, innovative thermal transport fluids require to boost thermal conductivity and heat flow features to upsurge convection heat rate, and nanofluids have been effectively employed as standard heat transfer fluids. With such intention, herein, we formulated and developed the constitutive flow laws by utilizing the Rossland diffusion approximation and Stephen's law along with the MHD effect. The mathematical formulation is based on boundary layer theory pioneered by Prandtl. Governing nonlinear partial differential flow equations are changed to ODEs via the implementation of the similarity variables. A well-known computational algorithm BVPh2 has been utilized for the solution of the nonlinear system of ODEs. The consequence of innumerable physical parameters on flow field, thermal distribution, and solutal field, such as magnetic field, Lewis number, velocity parameter, Prandtl number, drag force, Nusselt number, and Sherwood number, is plotted via graphs. Finally, numerical consequences are compared with the homotopic solution as a limiting case, and an exceptional agreement is found.

1. Introduction

In the recent development, nanofluid has gained considerable attention from researchers, engineers, scientists, and mathematicians due to its significant implementations in diverse fields of sciences. These applications cover the following areas: chemical engineering, space science, nuclear science, solar energy collection, and several other areas. The nanofluid applications can also be employed in other real-world problems which include engine oils, heat exchangers, and thermal conductivity [1]. The word nanofluid is considered to incorporate small nanoparticles whose dimension is up to 1–100 nm in the base liquid; biofluid, lubricants, oil, and ethylene are the common examples of nanofluids [2]. Eastman et al. [3] studied to develop the thermal behavior of nanofluids by incorporating various nanosized material particles to base fluids. Chamkha et al. [4] examined radiation effects on mixed convection in view of the vertical cone embedded in the porous medium with the nanoliquid. The influence of hydromagnetic free convective and heat transfer was analyzed by Sheikholeslami et al. [5]. The consequences of MHD flow and viscous dissipation on the momentum boundary layer of the nanoliquid were evaluated by Abbas and Sayed [6]. The hydromagnetic flow of nanofluids over a revolving disk was reported by Mahanthesh et al. [7]. Later on, various potential investigations have been carried out by many researchers and engineers into the development and implications of these fluids [8–11]. Heat transfer rheology in convective flow nanofluids with thermal conductivity and electrical behavior received exceptional importance for their

fruitful applications in life sciences and engineering development. Such applications include solar energy, nuclear reactor, and cooling and heating mechanisms. Using Buongiorno's model, Shehzad et al. [12] examined the effect of convective heat flow of the nanoliquid. Shen et al. [13] investigated the heat flow of a nanoliquid by a stretching surface with thermal radiation effect and velocity slip. Jahan et al. [14] evaluated the numerical solution to understand heat transfer aspects in nanomaterials over a convectively permeable stretching surface with radiation effect. Hamad and Pop [15] described thermal radiation effects on unsteady nanoliquid over an oscillatory moving plate with the heat reservoir. Sheikholeslami and Ganji [16] conducted a numerical consequence to analyze the three-dimensional nanoliquid with thermal radiation effects in a revolving system. Hussain et al. [17] illustrated analytical results by employing Laplace transform to explore unsteady hydromagnetic flow over a rotating system subject to chemical reaction and Hall current. Several mathematicians and investigators reported the thermal conductivity and electrical conductivity nature of nanofluids under different conditions with various geometry convective heat transfer effects in [18–23]. Mahanthesh et al. [24] evaluated the impact of suspended nanoparticles on the convective flow of nanomaterial in view of the vertical surface with radiation effects. Kumar et al. [25] conducted a numerical study by employing the RK-4 method to analyze radiative Jeffrey nanofluid flow with convective boundary conditions. Raza et al. [26] numerically studied the influence of viscous dissipation and magnetic field of molybdenum disulfide nanoliquid with the shape effect. Al-Odat et al. [27] addressed the interaction of magnetic effects and boundary layer flow of the fluid by an exponentially stretchable sheet. Chamkha and Aly [28] presented the numerical solution to magnetohydrodynamic free convection flow of a nanoliquid by a vertical plane in view of the porous medium and radiation effects. Aliakbar et al. [29] studied the analytical solution to hydromagnetic flow of upper convective Maxwell fluid past a stretchable extended surface. Khan et al. [30] evaluated the numerical solution by utilizing the explicit finite difference method (FDM) with stability analysis to unsteady nanofluid flow by a stretching surface. Ibrahim and Shankar [31] employed the shooting technique to inspect magnetohydrodynamic boundary layer flow of nanomaterial over the stretching sheet with the slip condition. Sparrow and Cess [32], Ozisik [33], Siegel and Howell [34], Howell [35], Takhar et al. [36], and Hossain and Takhar [37] all contributed well to radiative heat transfer analysis.

2. Basic Flow Equations

Here, we considered steady magnetohydrodynamic boundary layer nanofluid flow with a uniform velocity U moving towards an infinite plate. The velocity of the infinite plate is defined by the relation $U_w = \lambda U$; here, λ denotes the velocity parameter. The nanofluid flow is confined at $0 \leq y$. The coordinate system is chosen in the form such that the $y-$ axis is normal to the direction of flow, and the magnetic interaction is employed normal to the plate. Let T_w be the fluid temperature and C_w be the concentration at the wall, and free-stream numbers are T_∞ and C_∞. The proposed model is described by the following set of differential equations. The flow map and coordinates axes are presented in Figure 1.

$$\frac{\partial u}{\partial x} + \frac{\partial v}{\partial y} = 0, \tag{1}$$

$$u\frac{\partial u}{\partial x} + v\frac{\partial u}{\partial y} = \nu\frac{\partial^2 v}{\partial y^2} - u\frac{\sigma B_0^2}{\rho_f}, \tag{2}$$

$$u\frac{\partial T}{\partial x} + v\frac{\partial T}{\partial y} = \alpha\frac{\partial^2 T}{\partial y^2} - \frac{\alpha}{k}\frac{\partial q_r}{\partial y} + \tau\left(D_B\frac{\partial C}{\partial y}\frac{\partial T}{\partial y} + \frac{D_T}{T_\infty}\left(\frac{\partial T}{\partial y}\right)^2\right), \tag{3}$$

$$u\frac{\partial u}{\partial x} + v\frac{\partial u}{\partial y} = D_B\left(\frac{\partial^2 C}{\partial y^2}\right) + \frac{D_T}{T_\infty}\left(\frac{\partial^2 T}{\partial y^2}\right). \tag{4}$$

Here, (u, v) are the velocity components in coordinates axes, ν is the kinematic viscosity, k is the thermal conductivity parameter, q_r denotes the heat flux, D_B represents Brownian diffusion coefficient, D_T represents the thermophoresis diffusion coefficient, B_0 denotes the field strength, σ is the electrical conductivity parameter, τ represents the ratio of the nanoparticle heat capacity to the base fluid heat capacity, τ_w is the shear stress, $\alpha = k/(\rho c)_f$ represents thermal diffusivity, λ is the velocity parameter, $\lambda > 0$ corresponds to the downstream motion of the plate from the origin, and $\lambda < 0$ corresponds to the upstream motion.

The appropriate extreme values are

$$\begin{aligned} &y = 0\colon\ v = 0, u = \lambda U, T = T_w, C = C_w, \\ &y \longrightarrow \infty\colon\ U_w \longrightarrow U, T \longrightarrow T_\infty, C \longrightarrow C_\infty. \end{aligned} \tag{5}$$

Utilizing the Rosseland diffusion approximation [35], thermal flux is defined as

$$q_r = \frac{-4\sigma^*}{3K_s}\frac{\partial T^4}{\partial y}, \tag{6}$$

where σ^* is the Stefan–Boltzman constant and K_S is the Rosseland mean absorption coefficient. The difference in the nanofluid temperature within the fluid is sufficiently small such that T^4 can be written as a linear function of temperature:

$$T^4 \cong 4TT_\infty^3 - 3T_\infty^4. \tag{7}$$

Substituting (6) and (7) in (3), we attained

$$\frac{\partial q_r}{\partial y} = \frac{-16\sigma^* T_\infty^3}{3K_s}\frac{\partial^2 T}{\partial y^2}. \tag{8}$$

Introduce the similarity transformations:

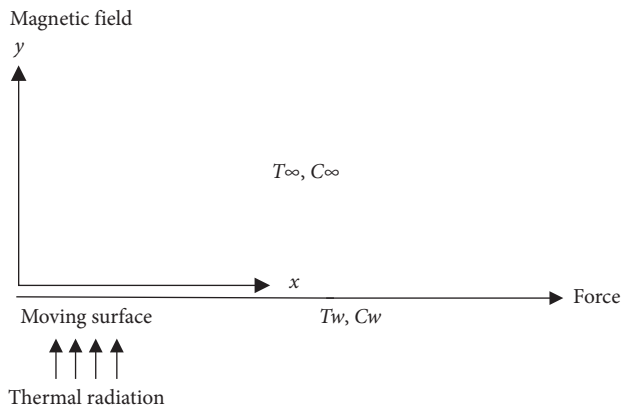

Figure 1: The flow map diagram.

$$\psi = (2Uvx)^{(1/2)} f(\eta),$$
$$\theta(\eta) = \frac{T - T_\infty}{T_w - T_\infty},$$
$$\varphi(\eta) = \frac{C - C_\infty}{C_w - C_\infty}, \tag{9}$$
$$\eta = (U/2vx)^{(1/2)}.$$

The stream function ψ may be expressed as

$$u = \frac{\partial \psi}{\partial y},$$
$$v = -\frac{\partial \psi}{\partial x}. \tag{10}$$

Equation (1) is justified automatically, while equations (2)–(5) have the forms

$$f'''(\eta) + f(\eta) f''(\eta) - (\mathrm{Ha}) f'(\eta) = 0, \tag{11}$$

$$\frac{1}{\mathrm{pr}}(3 + 4R)\theta''(\eta) + f(\eta)\theta'(\eta) + \mathrm{Nb}\varphi'(\eta)\theta'(\eta) + \mathrm{Nt}\left(\theta'(\eta)\right)^2 = 0, \tag{12}$$

$$\varphi''(\eta) + (\mathrm{Le}) f(\eta)\varphi'(\eta) + \left(\frac{\mathrm{Nt}}{\mathrm{Nb}}\right)\theta''(\eta) = 0, \tag{13}$$

$$\begin{aligned} f(0) &= 0, \\ f'(0) &= \lambda, \\ \theta(0) &= 1, \\ \varphi(0) &= 1, \\ f'(\infty) &\longrightarrow 1, \\ \theta(\infty) &\longrightarrow 0, \\ \varphi(\infty) &\longrightarrow 0. \end{aligned} \tag{14}$$

The governing variables appearing in (11)–(13) are defined as follows.

$R = (4\alpha\delta T_\infty^3/kk)$, $\mathrm{Pr} = (\nu/\alpha)$, $\mathrm{Le} = (\nu/D_B)$, $\mathrm{Ha} = (2xB_0^2/U\rho_f)$, $\mathrm{Nb} = (((\rho c)_p D_B(\varphi_w - \varphi_\infty))/\nu(\rho c)_f)$, $\mathrm{Nt} = (((\rho c)_p D_B(T_w - T_\infty))/\nu(\rho c)_f T_\infty)$, $C_f = (\tau_w/\rho u^2)$, $\mathrm{Nu}_x = (q_w/(T_w - T_\infty)k)$, and $\mathrm{Sh}_x = (xq_m/D_B(C_w - C_\infty)k)$ label the radiation constraint, Prandtl number, Lewis number, Hartmann number, Brownian parameter, thermophoretic force, drag force, and Nusselt and Sherwood numbers.

The local Reynolds number is given by the equation $\mathrm{Re}_x = Ux/\nu$.

Using similarity variables in C_f, Nu_x, and Sh_x, we get the dimensionless form as

$$\begin{aligned} (2\mathrm{Re})^{0.5} C_f &= f''(0), \\ \left(\frac{\mathrm{Re}_x}{2}\right)^{-1} 2\mathrm{Nu}_x &= -\theta'(0), \\ \left(\frac{\mathrm{Re}_x}{2}\right)^{-1} 2\mathrm{Nu}_x &= -\varphi'(0). \end{aligned} \tag{15}$$

3. Numerical Solution and Convergence Analysis

The nonlinear flow expressions (ODEs) in (11)–(13) subject to boundary conditions in (14) are first transformed into 1st-order ODEs and then tackled numerically by employing a built-in computational algorithm BVPh2 in Mathematica software. The routine flow numerical code is demonstrated in Figure 2. Step size $\Delta\eta = 0.001$, and relative tolerance error 10^{-6} is set; in addition, the choice of $\eta_\infty = 7$ confirms that all numerical approximations approach correctly to asymptotic values.

Let us introduce the transformation variables as $f(\eta) = w_1, f'(\eta) = w_2, f''(\eta) = w_3, \theta(\eta) = w_4, \theta'(\eta) = w_5$, $\phi(\eta) = w_6$, and $\phi'(\eta) = w_7$; hence, the following system of 1st-order seven differential equations are generated:

$$\begin{aligned} w_1' &= w_2, \\ w_2' &= w_3, \\ w_3' + w_1 w_3 - (\mathrm{Ha}) w_2 &= 0, \\ w_4' &= w_5, \\ \frac{1}{\mathrm{pr}}(3 + 4R) w_5' + w_1 w_5 + (\mathrm{Nb}) w_5 w_7 + \mathrm{Nt}\left(w_5\right)^2 &= 0, \\ w_6' &= w_7, \\ w_7' + (\mathrm{Le}) w_1 w_7 + \left(\frac{\mathrm{Nt}}{\mathrm{Nb}}\right) w_5 &= 0. \end{aligned} \tag{16}$$

The transfer conditions are

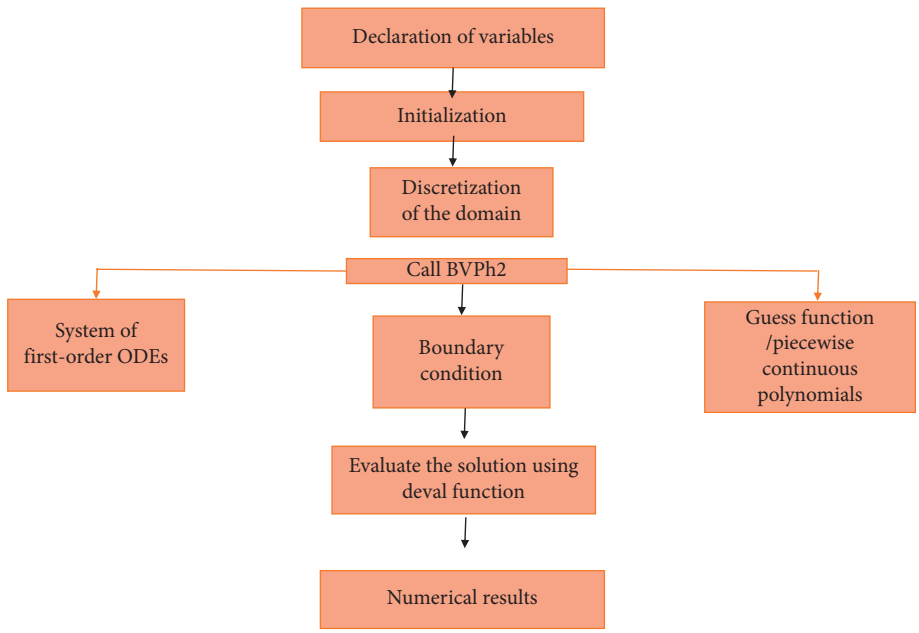

Figure 2: BVPh2 routine algorithm in Mathematica software.

$$\begin{aligned} w_1(0) &= 0, \\ w_2(0) &= \lambda, \\ w_4(0) &= 1, \\ w_6(0) &= 1, \\ w_2(\infty) &= 1, \\ x_4(\infty) &= 0, \\ x_6(\infty) &= 0. \end{aligned} \tag{17}$$

For authentication purpose, the computational results are further tested by the use of an analytical scheme (HAM), and a reasonable agreement has been obtained in two solutions. The attributes of two solutions via graphs are shown in Figures 3–5, and the tabularized data for velocity and thermal and solutal fields are presented in Tables 1–3. Finally, the residual error analysis has been evaluated and shown in Figure 6. A decrease in error is perceived for higher-order deformations.

4. Discussion

The current computational results accomplished by a numerical algorithm BVP2 unveil the influence of pertinent governing constraints on velocity, thermal field, and concentration profile. The impact of various emerging parameters in flow equations (11)–(13) is plotted through Figures 7–19. The numerical values of these flow factors are regarded as $\mathrm{Ha} = 0.5, \lambda = 0.3, \mathrm{Nt} = 0.5, \mathrm{Nb} = 0.5$, $\mathrm{Le} = 1.0$, $\mathrm{Pr} = 2.0$, and $R = 0.4$.

Figure 7 describes the Hartmann number Ha effect on the nanofluid velocity profile $f'(\eta)$. As anticipated, $f'(\eta)$ dwindles when subject to upsurge in Ha. In reality, this figure revealed that augmentation in Ha boosts Lorentz force. In consequence, velocity $f'(\eta)$ diminishes. The

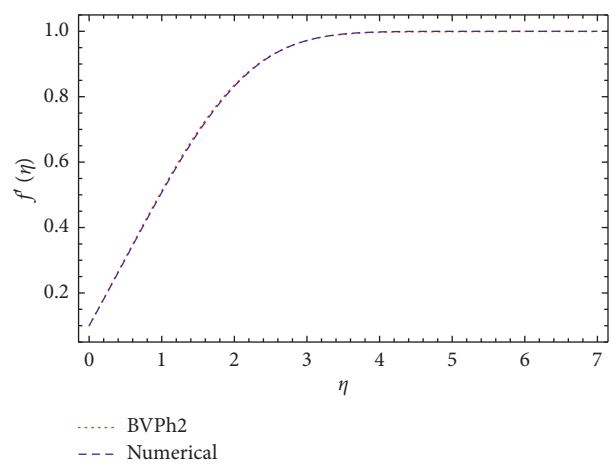

Figure 3: Graphical comparison for two solutions in case of the velocity profile.

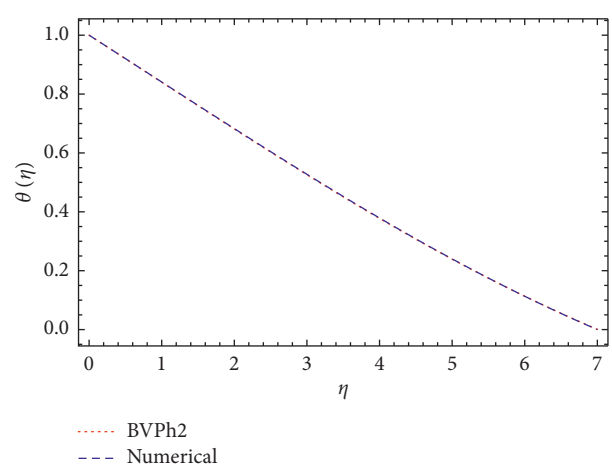

Figure 4: Graphical comparison for two solutions in case of the temperature profile.

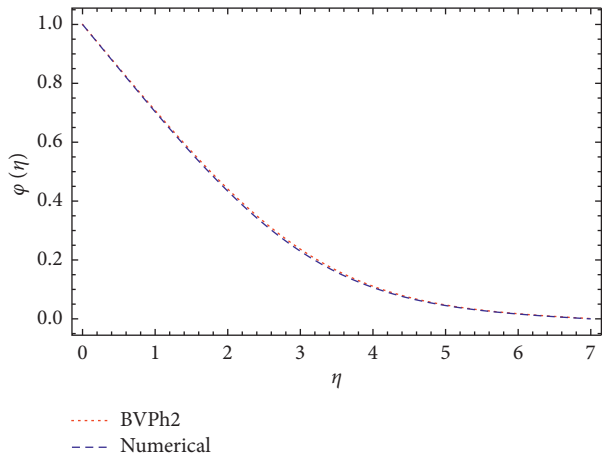

Figure 5: Graphical comparison for two solutions in case of the concentration profile.

Table 1: Numerical solution via the analytical solution for the velocity $f'(\eta)$ profile.

η	Numerical solution	HAM solution	Absolute error
0.0	0.000000	1.260600×10^{-11}	1.260600×10^{-11}
1.0	0.304039	0.306972	0.002933
2.0	0.987469	0.995322	0.007853
3.0	1.904260	1.913580	0.009316
4.0	2.893680	2.902320	0.008634
5.0	3.893100	3.900560	0.007458
6.0	4.893080	4.899550	0.006471
7.0	5.893080	5.898930	0.005845

Table 2: Numerical solution via the analytical solution for the temperature $\theta(\eta)$ profile.

η	Numerical solution	HAM solution	Absolute error
0.0	1.000000	1.000000	7.586150×10^{-13}
1.0	0.840974	0.840241	0.000733
2.0	0.682654	0.681360	0.001294
3.0	0.527582	0.526044	0.001539
4.0	0.379004	0.377623	0.001381
5.0	0.240021	0.239184	0.000837
6.0	0.113119	0.113103	0.000016
7.0	7.995770×10^{-10}	0.000912	0.000912

Table 3: Numerical solution via the analytical solution for the nanoparticle concentration $\varphi(\eta)$ profile.

η	Numerical solution	HAM solution	Absolute error
0.0	1.000000	1.000000	2.065240×10^{-12}
1.0	0.703260	0.707816	0.004557
2.0	0.433740	0.441075	0.007335
3.0	0.229562	0.236590	0.007028
4.0	0.106379	0.110674	0.004295
5.0	0.045187	0.047072	0.001885
6.0	0.016303	0.017325	.001021
7.0	$-2.066080'' \times 10^{-8}$	0.000912	0.000912

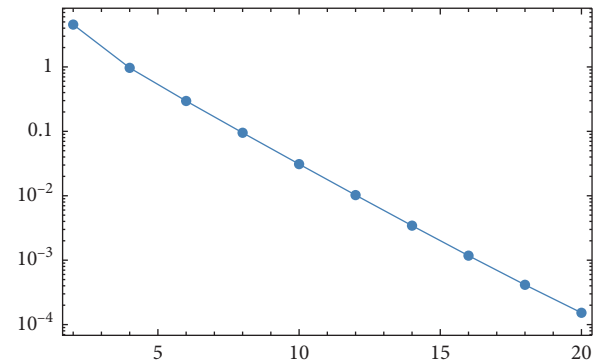

Figure 6: Total residual error via the order of approximation.

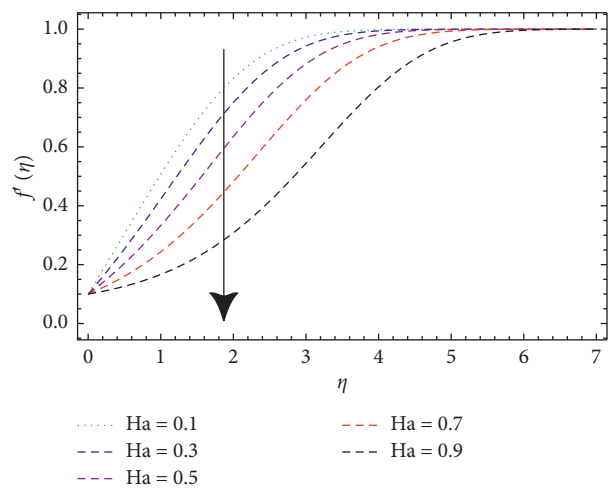

Figure 7: Influence of the velocity $f'(\eta)$ profile via Ha.

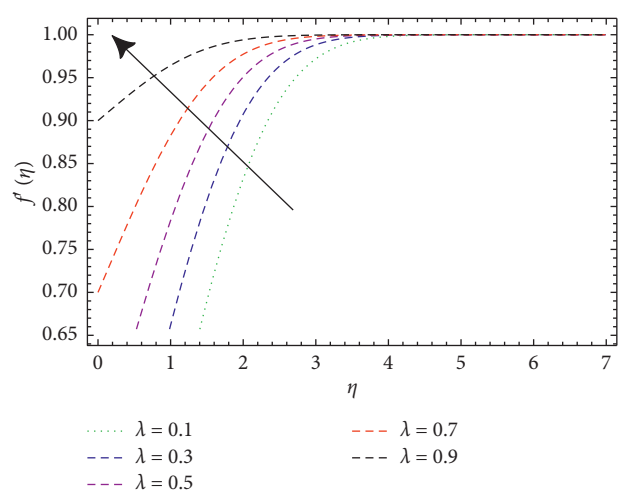

Figure 8: Influence of the velocity $f'(\eta)$ profile via λ.

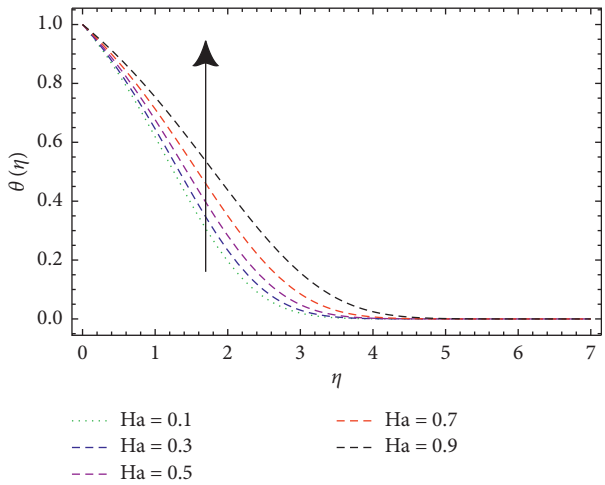

Figure 9: Influence of the temperature $\theta(\eta)$ profile via Ha.

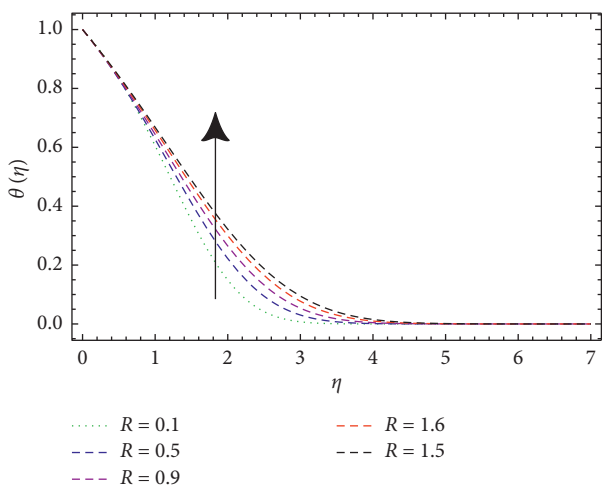

Figure 10: Influence of the temperature $\theta(\eta)$ profile via R.

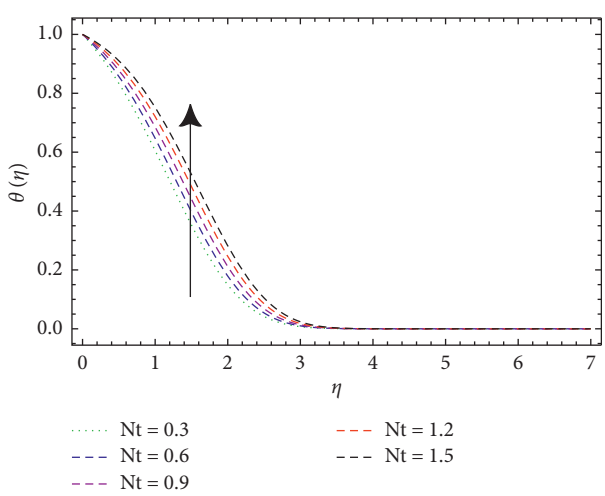

Figure 11: Influence of the temperature $\theta(\eta)$ profile via Nt.

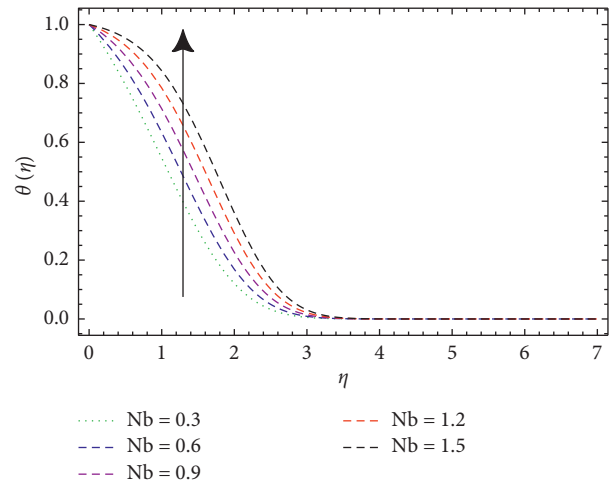

Figure 12: Influence of the $\theta(\eta)$ profile via Nb.

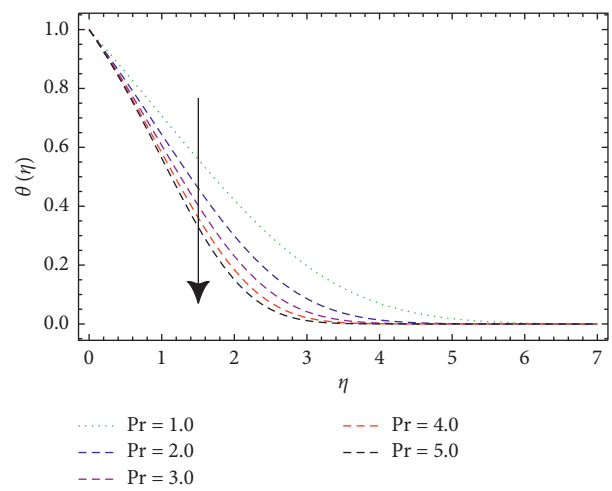

Figure 13: Influence of the $\theta(\eta)$ profile via Pr.

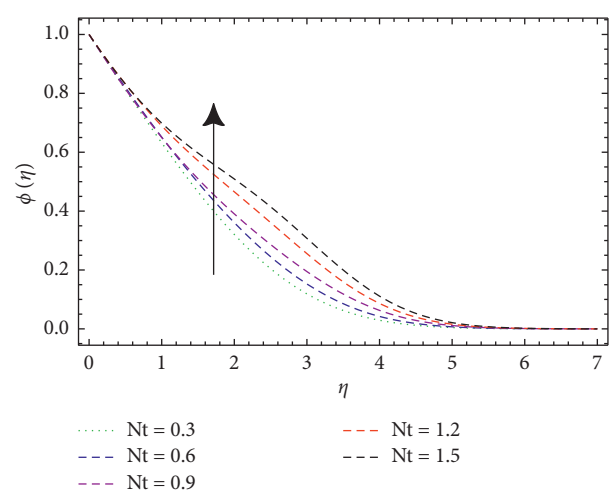

Figure 14: Influence of the temperature $\phi(\eta)$ profile via Nt.

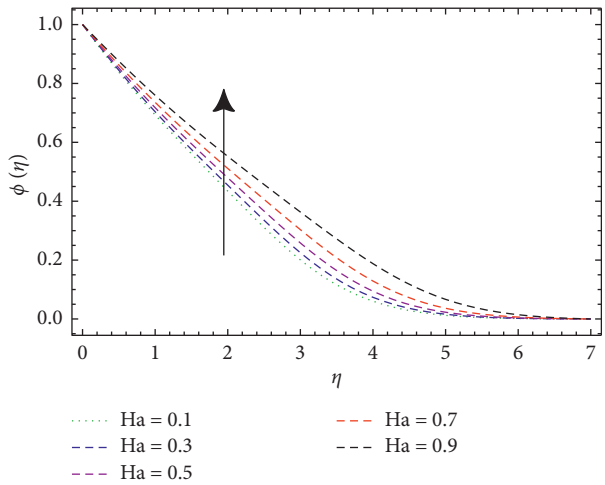

Figure 15: Influence of the $\phi(\eta)$ profile via Ha.

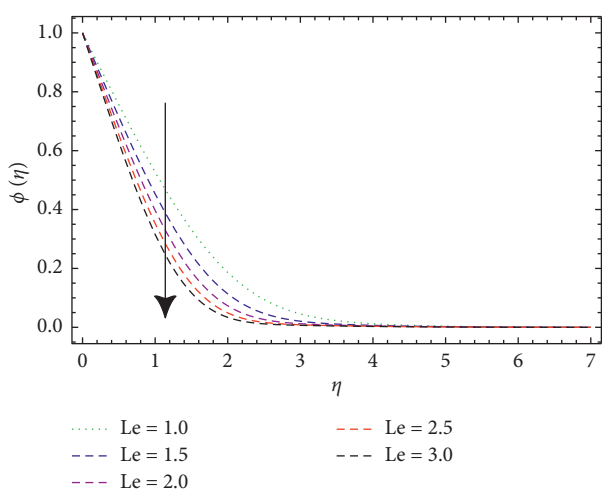

Figure 16: Influence of the $\phi(\eta)$ profile via Le.

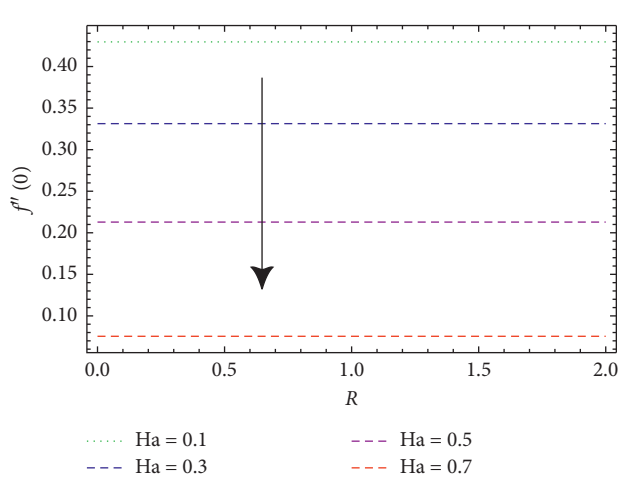

Figure 17: Skin friction/drag force via R for different values of Ha.

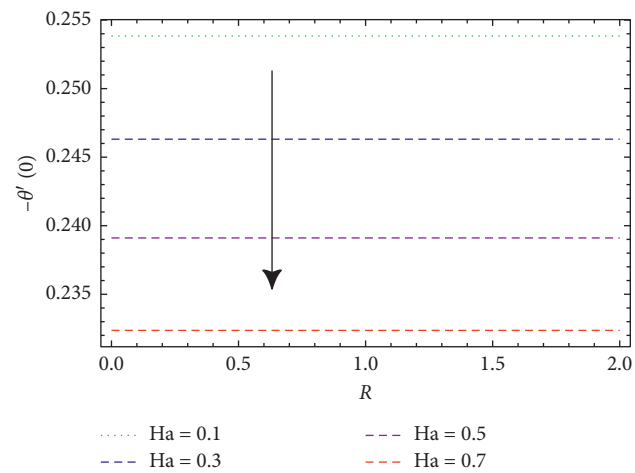

Figure 18: Nusselt number via R for different values of Ha.

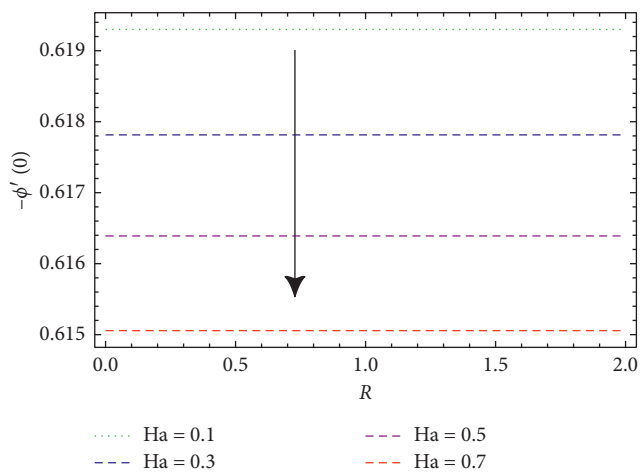

Figure 19: Sherwood number via R for changed values of Ha.

contribution of velocity parameter λ on nanofluid velocity profile $f'(\eta)$ is evaluated through Figure 8. As perceived, in this figure, fluid velocity enhances when λ upsurges. Hence, $f'(\eta)$ upsurges. The attributes of thermal field $\theta(\eta)$ curves for Ha magnetic field are disclosed in Figure 9. One can perceive that $\theta(\eta)$ is a growing function of Ha. In reality, the heat transfer rate of nanofluid particles boosts up through larger Ha. Consequently, $\theta(\eta)$ escalates. Such a scenario is perceived because higher Ha implies larger Lorentz force provides more resistance which makes increases the fluid flow. In consequence, $\theta(\eta)$ augments. Figure 10 explains variations in thermal field $\theta(\eta)$ subjected to radiation parameter R. This figure unveils $\theta(\eta)$ enhancement for higher values of (R). In fact, working nanofluid acquires extra heat subject to the radiation factor. In consequence, $\theta(\eta)$ upsurges. ;Figure 11 reveals variations in $\theta(\eta)$ subject to thermophoresis parameter Nt. Here, thermal field increases with increasing Nt. Physically, the thermophoretic force rises as Nt parameter is escalated. Such force is responsible to move small size particles by hotter towards colder region. Consequently, $\theta(\eta)$ escalates. Figure 12 explains the Brownian motion parameter Nb effect on $\theta(\eta)$. As

anticipated, thermal field $\theta(\eta)$ enhances through larger Nb parameter. In nanofluids, Brownian motion ascends due to small-size nanoparticles, and at this point, nanoparticle motion rate and its effect against the fluid have a vital vibrant role regarding heat transport. In consequence, upsurges in Nb produce active nanoparticle motion within the base fluid. The result of disordered nanoparticle motion develops kinetic energy of the nanoparticles, and eventually, thermal behavior $\theta(\eta)$ of the fluid augments. The contribution of Prandtl number Pr on $\theta(\eta)$ is evaluated through Figure 13. Here, thermal field diminishes against larger Prandtl number estimations. Attributes of Nt on solutal field $\varphi(\eta)$ are interpreted in Figure 14. We perceived an increase in $\varphi(\eta)$ subjected to higher thermophoresis parameter estimations. In reality, an upsurge in thermophoresis force is viewed through greater Nt parameter which is responsible for moving the fluid particles from higher temperature to lower temperature. In consequence, $\varphi(\eta)$ profile boosts. Solutal field $\varphi(\eta)$ curves for Hartmann number Ha are unveiled in Figure 15. Clearly, the solutal field is the augmenting function of the Hartmann number. Mass transfer augments when Ha is enhanced. Accordingly, $\varphi(\eta)$ increases. The attributes of Lewis number parameter Le on solutal field $\varphi(\eta)$ are interpreted in Figure 16. Clearly, $\varphi(\eta)$ diminishes when Le is increased. Physically, Lewis number Le signifies the influence of thermal diffusion on mass diffusion in the boundary layer region. Such a scenario is noticed because higher Le implies lessening in the solutal field and boundary layer.

Effects of pertinent variables against physical quantities $(f''(0), -\theta'(0), \text{and} -\varphi'(0))$ are described in Figures 17–19. These figures highlight decay in $f''(0)$, $-\theta'(0)$, and $-\varphi'(0)$ for larger R and Ha estimations.

5. Closing Remarks

The aim of this research is to analyze two-dimensional incompressible viscoelastic magnetonanofluid flow with the Buongiorno model. This investigation further includes results of heat generation/absorption with convective conditions. Current investigation enables us to explain the following key outcomes:

(i) Velocity field $f'(\eta)$ lessens when subject to increment in the Hartmann number Ha, and thermal field $\theta(\eta)$ develops with magnetic strength

(ii) Velocity profile augmented with larger velocity parameter λ

(iii) Thermal field $\theta(\eta)$ upsurges when radiation parameter R and Hartmann number Ha are improved

(iv) A similar feature is viewed qualitatively for higher thermophoretic parameter Nt and Brownian motion variable Nb

(v) Solutal field $\varphi(\eta)$ boosts through larger Hartmann number Ha, and $\varphi(\eta)$ field dwindles while Lewis number Le augments

(vi) Larger values of radiation parameter R and Hartmann number Ha diminish $f''(0)$ skin friction (drag force), Nusselt number $-\theta'(0)$, and Sherwood number $-\varphi'(0)$

Data Availability

The data used to support the findings of this study are included within the article.

Conflicts of Interest

The authors declare that they have no conflicts of interest.

Acknowledgments

The authors extend their appreciation to the Deanship of Scientific Research at Majmaah University for funding this work under the project number (RGP-2019-6).

References

[1] T. Hayat, R. Sajjad, A. Alsaedi, T. Muhammad, and R. Ellahi, "On squeezed flow of couple stress nanofluid between two parallel plates," *Results in Physics*, vol. 7, pp. 553–561, 2017.

[2] S. U. S. Choi and J. A. Eastman, "Enhancing thermal conductivity of fluids with nanoparticles," in *Proceedings of the ASME International Mechanical Engineering Congress and Exposition*, pp. 99–105, San Francisco, CA, USA, January 1995.

[3] J. A. Eastman, S. U. S. Choi, S. Li, W. Yu, and L. J. Thompson, "Anomalously increased effective thermal conductivities of ethylene glycol-based nanofluids containing copper nanoparticles," *Applied Physics Letters*, vol. 78, pp. 718–720, 2001.

[4] A. J. Chamkha, S. Abbasbandy, A. M. Rashad, and K. Vajravelu, "Radiation effects on mixed convection about a cone embedded in a porous medium filled with a nanofluid," *Meccanica*, vol. 48, pp. 275–285, 2013.

[5] M. Sheikholeslami, M. M. Rashidi, T. Hayat, and D. D. Ganji, "Free convection of magnetic nanofluid considering MFD viscosity effect," *Journal of Molecular Liquids*, vol. 218, pp. 393–399, 2016.

[6] W. Abbas and E. A. Sayed, "Hall current and joule heating effects on free convection flow of a nanofluid over a vertical cone in presence of thermal radiation," *Thermal Science*, vol. 21, pp. 2603–2614, 2017.

[7] B. Mahanthesh, B. Gireesha, I. Animasaun, T. Muhammad, and N. Shashikumar, "MHD flow of SWCNT and MWCNT nanoliquids past a rotating stretchable disk with thermal and exponential space dependent heat source," *Physica Scripta*, vol. 94, Article ID 085214, 2019.

[8] I. L. Animasaun, O. K. Koriko, K. S. Adegbie et al., "Comparative analysis between 36 nm and 47 nm alumina-water nanofluid flows in the presence of Hall effect," *Journal of Thermal Analysis and Calorimetry*, vol. 135, pp. 873–886, 2019.

[9] I. Ullah, S. Shafie, I. Khan, and K. L. Hsiao, "Brownian diffusion and thermophoresis mechanisms in Casson fluid over a moving wedge," *Results in Physics*, vol. 9, pp. 183–194, 2018.

[10] P. B. S. Kumar, B. J. Gireesha, R. S. R. Gorla, and B. Mahanthesh, "Magnetohydrodynamic flow of Williamson nanofluid due to an exponentially stretching surface in the

presence of thermal radiation and chemical reaction," *Journal of Nanofluids*, vol. 6, pp. 264–272, 2017.

[11] X. Zhou, Y. Jiang, X. Li et al., "Numerical investigation of heat transfer enhancement and entropy generation of natural convection in a cavity containing nano liquid-metal fluid," *International Communications in Heat and Mass Transfer*, vol. 106, pp. 46–54, 2019.

[12] N. Shehzad, A. Zeeshan, R. Ellahi, and K. Vafai, "Convective heat transfer of nanofluid in a wavy channel: Buongiorno's mathematical model," *Journal of Molecular Liquids*, vol. 222, pp. 446–455, 2016.

[13] B. Shen, L. Zheng, C. Zhang, and X. Zhang, "Bioconvection heat transfer of a nanofluid over a stretching sheet with velocity slip and temperature jump," *Thermal Science*, vol. 21, pp. 2347–2356, 2017.

[14] S. Jahan, H. Sakidin, R. Nazar, and I. Pop, "Analysis of heat transfer in nanofluid past a convectively heated permeable stretching/shrinking sheet with regression and stability analyses," *Results in Physics*, vol. 10, pp. 395–405, 2018.

[15] M. A. A. Hamad and I. Pop, "Unsteady MHD free convection flow past a vertical permeable flat plate in a rotating frame of reference with constant heat source in a nanofluid," *Heat and Mass Transfer*, vol. 47, pp. 1517–1524, 2011.

[16] M. Sheikholeslami and D. D. Ganji, "Three-dimensional heat and mass transfer in a rotating system using nanofluid," *Powder Technology*, vol. 253, pp. 789–796, 2014.

[17] S. M. Hussain, J. Jain, G. S. Seth, and M. M. Rashidi, "Free convective heat transfer with Hall effects, heat absorption and chemical reaction over an accelerated moving plate in a rotating system," *Journal of Magnetism and Magnetic Materials*, vol. 422, pp. 112–123, 2017.

[18] X. Zhou, Y. Jiang, Y. Hou, and M. Du, "Thermocapillary convection instability in annular two-layer system under various gravity levels," *Microgravity Science and Technology*, vol. 31, pp. 641–648, 2019.

[19] Y. Jiang and X. Zhou, "Heat transfer and entropy generation analysis of nanofluids thermocapillary convection around a bubble in a cavity," *International Communications in Heat and Mass Transfer*, vol. 105, pp. 37–45, 2019.

[20] Y. Jiang, X. Zhou, and Y. Wang, "Effects of nanoparticle shapes on heat and mass transfer of nanofluid thermocapillary convection around a gas bubble," *Microgravity Science and Technology*, vol. 32, pp. 1–11, 2019.

[21] Y. Jiang, X. Zhou, and Y. Wang, "Comprehensive heat transfer performance analysis of nanofluid mixed forced and thermocapillary convection around a gas bubble in mini-channel," *International Communications in Heat and Mass Transfer*, vol. 110, Article ID 104386, 2020.

[22] B. Mahanthesh, B. J. Gireesha, R. S. R. Gorla, F. M. Abbasi, and
S. A. Shehzad, "Numerical solutions for magnetohydrodynamic flow of nanofluid over a bidirectional non-linear stretching surface with prescribed surface heat flux boundary," *Journal of Magnetism and Magnetic Materials*, vol. 417, pp. 189–196, 2016.

[23] N. Bhaskar Reddy, T. Poornima, and P. Sreenivasulu, "Influence of variable thermal conductivity on MHD boundary layer slip flow of ethylene-glycol based cu nanofluids over a stretching sheet with convective boundary condition," *International Journal of Engineering Mathematics*, vol. 2014, Article ID 905158, 10 pages, 2014.

[24] B. Mahanthesh, J. Gireesha, and I. L. Animasaun, "Exploration of non-linear thermal radiation and suspended nanoparticles effects on mixed convection boundary layer flow of nano-liquids on a melting vertical surface," *Journal of Nanofluids*, vol. 7, pp. 833–843, 2018.

[25] P. S. Kumar, B. Mahanthesh, B. Gireesha, and S. Shehzad, "Quadratic convective flow of radiated nano-Jeffrey liquid subject to multiple convective conditions and Cattaneo Christov double diffusion," *Applied Mathematics and Mechanics*, vol. 39, pp. 1311–1326, 2018.

[26] J. Raza, F. Mebarek-Oudina, and A. Chamkha, "Magnetohydrodynamic flow of molybdenum disulfide nanofluid in a channel with shape effects," *Multidiscipline Modeling in Materials and Structures*, vol. 15, pp. 737–757, 2019.

[27] M. Q. Al-Odat, R. A. Damesh, and T. A. Al-Azab, "Thermal boundary layer on an exponentially stretching continuous surface in the presence of magnetic field effect," *International Journal of Applied Mechanics and Engineering*, vol. 11, pp. 289–299, 2006.

[28] A. J. Chamkha and A. M. Aly, "MHD free convection flow of a nanofluid past a vertical plate in the presence of heat generation or absorption effects," *Chemical Engineering Communications*, vol. 198, pp. 425–441, 2011.

[29] V. Aliakbar, A. Alizadeh-Pahlavan, and K. Sadeghy, "The influence of thermal radiation on MHD flow of Maxwellian fluids above stretching sheets," *Communications in Nonlinear Science and Numerical Simulation*, vol. 14, no. 3, pp. 779–794, 2009.

[30] M. S. Khan, M. M. Alam, and M. Ferdows, "Effects of magnetic field on radiative flow of a nanofluid past a stretching sheet," *Procedia Engineering*, vol. 56, pp. 316–322, 2013.

[31] W. Ibrahim and B. Shankar, "MHD boundary layer flow and heat transfer of a nanofluid past a permeable stretching sheet with velocity, thermal and solutal slip boundary conditions," *Computers & Fluids*, vol. 75, pp. 1–10, 2013.

[32] M. E. Sparrow and D. R. Cess, *Radiation Heat Transfer*, Brooks/Cole, Belmont, CA, USA, 1970.

[33] N. M. Ozisik, *Radiative Transfer and Interaction with Conduction and Convection*, John Wiley & Sons, New York, NY, USA, 1973.

[34] R. Siegel and J. R. Howell, *Thermal Radiation Heat Transfer*, Hemisphere, New York, NY, USA, 2nd edition, 1992.

[35] J. Howell, "Radiative transfer in porous media," in *Handbook of Porous Media*, K. Vafai, Ed., CRC Press, New York, NY, USA, 2000.

[36] H. S. Takhar, R. S. R. Gorla, and V. M. Soundalgekar, "Radiation effects on MHD free convection flow of a gas past a semi-infinite vertical plate," *International Journal of Numerical Methods For Heat And Fluid Flow*, vol. 6, pp. 77–83, 1996.

[37] M. A. Hossain and H. S. Takhar, "Radiation effect on mixed convection along a vertical plate with uniform surface temperature," *Heat and Mass Transfer*, vol. 31, pp. 243–248, 1996.